UNIVERSITY OF LIVERPOOL

Investigating the interplay between the Parkinson's Disease proteins VPS35 and LRRK2 in an isogenic cell model system

Katy Rebecca McCarron

Thesis submitted in accordance with the requirements of

University of Liverpool for the Degree of Doctor in Philosophy

July 2023

Investigating the interplay between the Parkinson's Disease proteins VPS35 and LRRK2 in an isogenic cell model system

Katy Rebecca McCarron

Abstract

In familial Parkinson's Disease (PD), which makes up 10-15% of all PD cases, causative mutations in seventeen genes have been discovered. Study of these genes has revealed two common themes: dysfunction in endolysosomal trafficking and mitochondrial function. The emergence of these two overarching processes suggests that these genes may constitute common pathways underpinning pathology.

A [D620N] mutation within vacuolar protein sorting 35 (VPS35), a component of the endosomal sorting complex retromer, causes autosomal dominant PD and is reported to induce endolysosomal trafficking defects, mitochondrial dysfunction, and hyperactivation of the PD-related kinase leucine-rich repeat kinase 2 (LRRK2). A subset of Rab GTPases has been identified as substrates for LRRK2 and PD-linked variants of VPS35 and LRRK2 enhance the phosphorylation of these substrate Rabs. Several functions for LRRK2 have been proposed, including in regulating trafficking, ciliogenesis, and the response to endolysosomal damage.

The mechanism by which VPS35 enhances LRRK2 kinase activity, and its functional significance, is not yet clear. This project aimed to gain a deeper understanding of this relationship.

I have generated isogenic hTERT-RPE1 cell lines expressing either wild-type or [D260N] mutant VPS35 in an inducible fashion.

Using this model, I have found the effect of the [D620N] mutation is subtle at steady state, with only two changes observed: decreased WASH complex association and increased LRRK2-dependent Rab phosphorylation.

Despite a decreased physical interaction with the WASH complex, the localisation of WASH complex components to the endosome is unchanged. Furthermore, no perturbations in endosomal trafficking could be observed. Similarly, expression of the [D620N] mutation did not lead to an aberrant mitochondrial phenotype. Mitochondrial morphology and basal mitochondrial membrane potential were equivalent to wild type VPS35-expressing cells. Moreover, VPS35[D620N] did not impair the initiation of depolarisation-induced mitophagy.

I have shown that at steady state, expression of VPS35[D620N] causes an increase in the membrane-bound total and phosphorylated pool of Rab12. This appears to 'prime' LRRK2 to respond to endolysosomal damage, resulting in amplified phosphorylation of Rab10 and Rab12. This sensitisation does not affect lysosomal repair or the secretion of lysosomal contents outside of the cell which have previously been shown to be LRRK2 dependent mechanisms. Expression of VPS35 [D620N] leads to a failure in the clearance of LC3-positive damaged lysosomes, suggesting that recovery from damage is impaired. Furthermore, I have identified that VPS35 is required for full activation of LRRK2 triggered by treatment with endolysosomal damaging agents nigericin, LLOMe and chloroquine.

These findings provide further insight into the relationship between LRRK2 and VPS35 and suggest that lysosomal dysfunction plays a key role in PD pathogenesis. Moreover, it hints at promise that patients with VPS35 [D620N] will benefit from therapeutics that inhibit LRRK2.

Table of contents

List of figures

List of tables

Abbreviations

ALG2	Apoptosis-Linked Gene 2
ALIX	Apoptosis-Linked Gene-2 Interacting Protein X
ALR	Autophagic Lysosome Reformation
ALS	Amyotrophic Lateral Sclerosis
ANK	Ankyrin
ANOVA	Analysis Of Variance
AO	Antimycin A and oligomycin A
ARM	Armadillo
Arp2/3	Actin-Related Protein 2/3
ATG	Autophagy-Related
ATP13A2	ATPase Cation Transporting 13A2
BAR	Bin/Amphiphysin/RVS
BECN1	Beclin 1
BNIP3	BCL2-interaction protein 3
BNIP3L	BNIP3-like, NIX
BSA	Bovine Serum Albumin
CASM	Conjugation of ATG8s to Single Membranes
CatD	Cathepsin D
CCCP	Carbonyl Cyanide 3-Chlorophenylhydrazone
CCDC	Coiled-Coil Domain Containing
CHMP	Charged Multivesicular Body Protein
CIMPR	Cation-Independent Mannose 6-Phosphate Receptor
CLEAR	Coordinated Lysosomal Expression and Regulation
CMA	Chaperone-Mediated Autophagy
CMV	Cytomegalovirus
COMMD	Copper Metabolism Gene MURR1 Domain
COR	C-terminal of Roc
CSC	Cargo-Selective Complex
CTCF	Corrected Total Cell Fluorescence
DAPI	4’,6’diamidino-2-phenylindole
DENND	DENN Domain-Containing
DMEM	Dulbecco’s Modified Eagle’s Medium
DMSO	Dimethyl Sulfoxide
DNA	Deoxyribonucleic Acid
DNAJC	DnaJ Heat Shock Protein Family (Hsp40) Member
Dox	Doxycycline
DRP1	Dynamin-Related Protein 1
DTT	Dithiothreitol
DUB	Deubiquitylases
EDTA	Ethylenediaminetetraacetic
EEA1	Early Endosome Antigen 1

EGFR	Epidermal Growth Factor Receptor
ELDR	Endo-Lysosomal Damage Response
ER	Endoplasmic Reticulum
ERC	Endosomal Recycling Compartment
ESCPE	Endosomal SNX-BAR Sorting Complex for Promoting Exit
ESCRT	Endosomal complexes required for transport
EtOH	Ethanol
Exp	Exposure
F-actin	Filamentous Actin
FACS	Fluorescence-Activated Cell Sorting
FBOX	F-box only with Uncharacterized Domains
FBS	Foetal Bovine Serum
FIP200	Focal Adhesion Kinase Family Interacting Protein of 200 kDa
FIS1	Mitochondrial Fission 1 Protein
FLCN	Folliculin
FNIP	Folliculin Interacting Protein
FRT	Flp Recombination Target
FYVE	Fab 1, YOTB, Vac1, EEA1
GABARAP	GABA Receptor-Associated Protein
GABARAPL	GABARAP-like
Gal	Galectin
GAP	GTPase Activating Protein
GARP	Golgi-Associated Retrograde Protein
GCase	β-Glucocerebrosidase
GDF	GDI Displacement Factor
GDI	GDP Dissociation Inhibitor
GEF	Guanine Nucleotide Exchange Factor
GLUE	GRAM-Like Ubiquitin Binding in EAP45
HOPS	Homotypic Fusion and Protein Sorting
HRS	Hepatocyte Growth Factor-Regulated Tyrosine Kinase Substrate
Hsc70	Heat Shock Cognate 70 kDa Protein
HSP60	Heat Shock Protein 60
ILV	Intraluminal Vesicles
iPSC	Induced Pluripotent Stem Cell
IPTG	Isopropyl ß-D-1-Thiogalactopyranoside
JIP	c-JNK-Interacting Protein
LAMP	Lysosomal-Associated Membrane Protein
LC3	Microtubule-Associated Protein Light Chain 3
LIR	LC3 Interacting Region
LLOMe	L-Leucyl-L-Leucine Methyl Ester
LRR	Leucine-Rich Repeat
LRRK2	Leucine-Rich Repeat Kinase 2
M6P	Mannose 6-Phosphate

M6PR	Mannose 6-Phosphate Receptor
MDV	Mitochondrial Derived Vesicle
MEF	Mouse Embryonic Fibroblast
MFF	Mitochondrial Fission Factor
MFN	Mitofusin
MiT/TFE	microphthalmia/transcription factor E
MID	Mitochondrial Dynamics Protein
MiNA	Mitochondrial Network Analysis
Miro1	GTPase Mitochondrial Rho GTPase 1
MMP	Mitochondrial Membrane Potential
mTOR	Mammalian Target of Rapamycin
mTORC1	Mammalian Target of Rapamycin Complex 1
MUL1	Mitochondrial E3 Ubiquitin Protein Ligase 1
MVB12	Multivesicular Body Sorting Factor 12
NDP52	Nuclear dot protein 52 kDa
NRBF2	Nuclear Receptor-Binding Factor 2
OPA1	Optic atrophy 1
OPTN	Optineurin
p150	Protein of 150 kDa
PAGE	Polyacrylamide Gel Electrophoresis
PARL	Presenilins-Associated Rhomboid-Like Protein
PBS	Phosphate-Buffered Saline
PCR	Polymerase Chain Reaction
PD	Parkinson's Disease
PDZ	Post Synaptic Density 95-Discs Large-Zonula Occulens-1
PE	Phosphatidylethanolamine
PFA	Paraformaldehyde
PH	Pleckstrin Homology
PI	Phosphoinositide
PI	Phosphatidylinositol
PI3K	Phosphatidylinositol 3-Kinase
PI4K2A	Phosphatidylinositol 4-Kinase Type 2 Alpha
PIKFYVE	1-Phosphatidylinositol 3-Phosphate 5-Kinase
PINK1	PTEN Induced Putative Kinase 1
PITT	Phosphoinositide-Initiated Membrane Tethering and Lipid Transport
PNS	Post Nuclear Supernatant
PP2A	Protein Phosphatase 2A
PPM1H	Protein Phosphatase Mg2+/Mn2+ Dependent 1H
PROPPIN	β-Propellers that Bind Phosphoinositides
PS	Phosphatidylserine
PtdIns	Phosphatidylinositol
PX	Phox Homology
R7BD	Rab7a Binding Domain

Rab	Rab GTPase
RE	Restriction Endonuclease
REP	Rab Escort Protein
RILP	Rab-Interacting Lysosomal Protein
RILPL	Rab Interacting Lysosomal Protein Like
RIPA	Radioimmunoprecipitation Assay
RME-8	Receptor Mediated Endocytosis-8
Roc	Ras of Complex
ROS	Reactive Oxygen Species
RPE	Retinal Pigment Epithelium
RPM	Revolutions per Minute
RTK	Receptor Tyrosine Kinase
SD	Standard Deviation
SDS	Sodium Dodecyl Sulphate
SE	Sorting Endosome
siRNA	Small Interfering RNA
SNARE	N-Ethylmaleimide-Sensitive Factor Attachment Protein Receptor
SNX	Sorting Nexin
SOC	Super Optimal Broth with Catabolite Repression
sorLA	Sortilin-Related Receptor
STAM	Signal Transducing Adaptor Molecule
STAMBP	STAM-Binding Protein
SV40	Simian Virus 40
SYNJ1	Synaptojanin1
TAE	Tris-Acetate-EDTA
TBC1D	Tre-2, BUB2p, Cdc16p-1-Domain
TBS	Tris-Buffered Saline
TBS-T	Tris-Buffered Saline with 0.1% Tween
TCA	Trichloroacetic Acid
TEN	Tubular Endosomal Network
TetR	Tet Repressor
TGN	*trans*-Golgi Network
TGN46	*trans*-Golgi Network Glycoprotein 46
TIMM44	Translocase of Inner Mitochondrial Membrane 44
TMEM230	Transmembrane Protein 230
TMRE	Tetramethylrhodamine, Ethyl Ester, Perchlorate
TMRM	Tetramethylrhodamine, Methyl Ester, Perchlorate
TOM	Trans-Outer Mitochondrial Membrane
TPS	Total Protein Stain
TRIM	Tripartite Motif Containing
TSG101	Tumour Susceptibility Gene 101 Protein
Ub	Ubiquitin
ULK	Unc-51-Like Kinase

UPS	Ubiquitin-Proteasome System
USP	Ubiquitin-Specific Protease 8
UPS	Ubiquitin-Proteasome System
UV	Ultraviolet
v-ATPase	Vacuolar Adenosine Triphosphatase
VDAC	Voltage-Dependent Anion Channels
VPS	Vacuolar Protein Sorting
VPS35L	VPS35-Like
WASH	Wiskott-Aldrich Syndrome Protein and Scar Homologue
WIPI	WD Repeat Interacting with Phosphoinositides
WT	Wild Type
x *g*	Relative centrifugal force

Acknowledgements

Although it has not been without its challenges, I have thoroughly enjoyed the last few years in Liverpool completing my PhD. I could not have done it without the support of so many people around me.

Firstly, I would like to thank my PhD supervisors Sylvie Urbé and Michael Clague, I am extremely grateful for the time, support, and guidance they have given me over the past three years. I would also like to thank the MRC DiMeN DTP for funding my project and giving me the opportunity to do a PhD.

I've been extremely lucky to be a part of such a supportive lab who are willing to share their time and expertise, and so owe my thanks to the members of MSCU, past and present: Ailbhe Brazel, Andreas Kallinos, Anne Clancy, Emma Rusilowicz-Jones, Erithelgi Bertsoulaki, Francesca Frigenti, Francesca Querques, Francesco Barone, Georgia Guilbert, Hannah Elcocks, Hannah Glover, Ioanna Georgiou, Jane Jardine, Joana Gomes Neto, Liam Pollock, Lois Rooney, Pei Yee Tey, Svetlana Telnova, Victoria Ciampani. I would like to give special thanks to Hannah Elcocks for training me when I first started, all her help on the LRRK2-VPS35 project and listening to me moan. Thanks to Anne Clancy for her all her help and her endless patience answering all my silly questions. I'm also grateful for the fun times outside of the lab that have made my time here so enjoyable; from socially distanced beers on the balcony to pub trips and games of pool when the world finally reopened.

I would also like to thank my secondary supervisor Heather Mortiboys for hosting me at SiTraN and all her support while I was there. It was an incredible experience and would also like to thank all her lab for making me feel so welcome but special thanks goes to Alicja and Toby for giving up so much of their time to help me.

I must also thank all those outside of the lab who have supported me. Thank you to my housemates and climbing partners Helen and Georgia for making my time in Liverpool even more enjoyable and providing an escape from time in the lab. Thank you to all my wonderful friends who are always there when I need them. Finally, I am incredibly lucky to have such a loving and supporting family back home, without whom I would not be the person I am today. I would like to especially thank my mum, for always being there for me, for nursing me back to health after surgery, for listening to me when times in the lab were tough, for her sage advice (even if I didn't always want to hear it) and for always believing in me. Thank you.

1 Introduction

1.1 The Endosomal Network

The endosomal network consists of a set of dynamic membranous compartments which act in concert to transport integral membrane proteins around the cell. Endocytosed cargoes from the plasma membrane are delivered to the early endosome where they are sorted for either degradation or recycling (**Figure 1.1**). The different membrane compartments can be distinguished according to their size and morphology, luminal pH, phosphoinositide composition and Rab GTPase localisation (Huotari and Helenius, 2011).

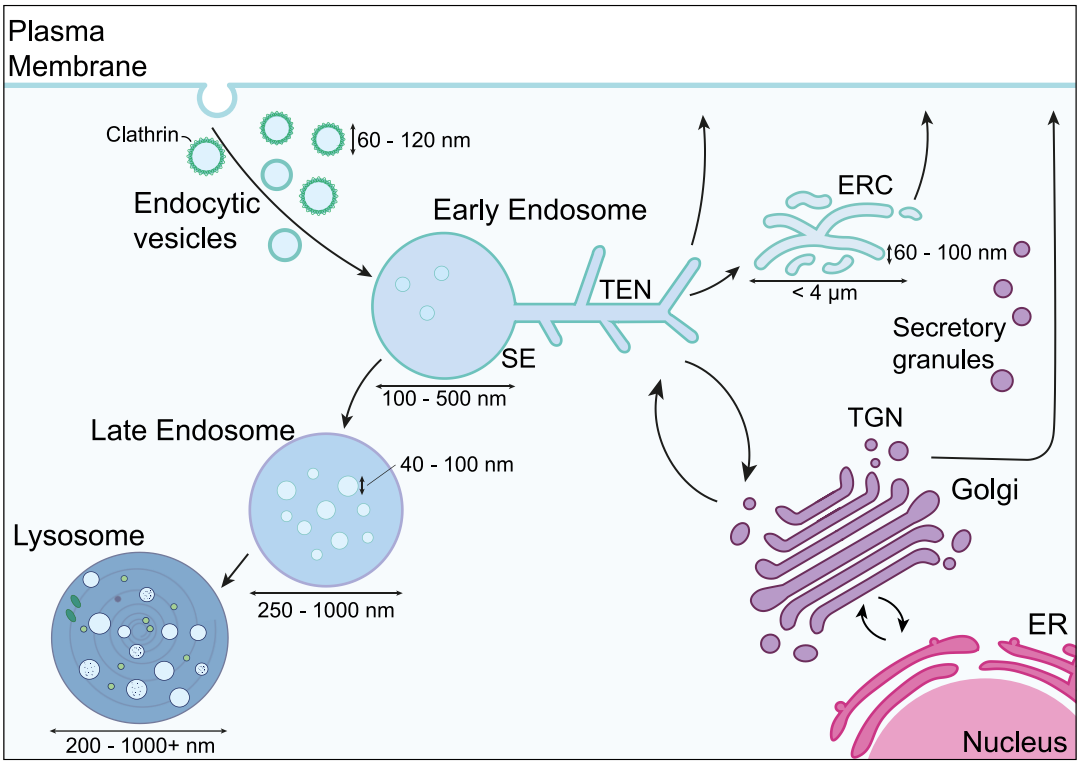

Figure 1.1 Endosomal trafficking pathways

Proteins from the cell membrane are endocytosed within vesicles, which fuse with the sorting endosome (SE). From here, protein cargo may be delivered to the lysosomes via late endosomes for degradation or recycled to the Golgi or plasma membrane. Cargo recycling from the SE back to the plasma membrane may take several routes: directly via the 'fast recycling' pathway, or indirectly or indirectly via the endocytic recycling compartment (ERC) by 'slow recycling'.

TEN, tubular endosomal network; TGN, *trans*-Golgi network

1.1.1 The endocytic pathway

Transmembrane proteins and their bound ligands are internalised at the plasma membrane via endocytosis, which involves membrane invagination, coat assembly, budding, and the generation of small vesicles 60-120 nm in diameter (Klumperman

and Raposo, 2014). Endocytosis may be clathrin-mediated, which is the major route, or clathrin-independent (Kaksonen and Roux, 2018; Mayor et al., 2014). Endocytic cargoes are involved in a variety of physiological functions, including nutrient uptake, neurotransmission, cell signalling and cell adhesion, but have one initial destination – the early endosome (Kaksonen and Roux, 2018).

The early endosome forms the nexus of trafficking pathways within the cell and comprises a network of different endosomal structures. Typically, the early endosome is made up of a central vacuole 100-500 nm in diameter with multiple tubular extensions (Klumperman and Raposo, 2014). The central vacuole is the site at which endocytic vesicles fuse with early endosome and cargo is sorted for degradation or recycling, and so is commonly referred to as the 'sorting endosome' (SE). Alternatively, nascent or recycled proteins may arrive at the early endosome from the Golgi apparatus via anterograde trafficking pathways. The tubules extending from the SE form the 'tubular endosomal network' (TEN), which is the site at which protein sorting complexes associate with the early endosome for cargo recycling. Early endosomal tubules that are not attached to the SE may also be present, forming what is known as the 'endosomal recycling compartment' (ERC) or recycling endosome. The pH within the early endosome is 5.6-6.0, whereas the ERC has a mildly higher pH of 6.4-6.5 (Maxfield, 2014).

Once cargoes arrive at the early endosome, they are sorted for either recycling or degradation. Proteins destined for degradation will be set on a path towards the lysosome via late endosomes. If a protein is recycled, it may take several routes. Firstly, it may be delivered straight back to the plasma membrane from the TEN, a process termed 'rapid recycling'. Cargo may also be transported to the ERC before returning to the plasma membrane via the 'slow recycling' pathway. Examples of cargoes recycled to the plasma membrane are cell adhesion receptors, nutrient transporters and mitogenic signalling receptors (Burd and Cullen, 2014). Alternatively, cargo may be transported to the *trans*-Golgi network (TGN) via retrograde trafficking, where cargo can be packaged into secretory vesicles and targeted towards its destination in the same manner as newly synthesised proteins.

Protein cargoes that are targeted for degradation are internalised into intraluminal vesicles (ILVs), 40-100 nm in diameter, within the SE central vacuole (Klumperman and Raposo, 2014; Stoorvogel et al., 1991). Endosomes continuously fuse with each other, growing in size, and continue to generate ILVs (Gautreau et al., 2014). This increase in size and number of ILVs signifies the transition into late endosomes, which

are larger (250 – 1000 nm in diameter), contain more than eight ILVs and have a pH of 5.0-6.0 (Gautreau et al., 2014; Klumperman and Raposo, 2014; Maxfield, 2014). Late endosomes can also be distinguished by a change in their membrane composition and protein population (Gautreau et al., 2014).

In the final step of the degradative endolysosomal pathway, late endosomes fuse with lysosomes to deliver their contents, forming a hybrid endolysosome compartment (Luzio et al., 2014). Of all components of the endolysosomal system, lysosomes are the most heterogenous, varying greatly in size from 200 nm to over 1 μm (Klumperman and Raposo, 2014). Small, dense core storage lysosomes are inactive and have a neutral pH but become highly acidic (pH 5.0) and active following fusion with late endosomes (Bright et al., 2016; Maxfield, 2014).

1.1.2 The lysosome

Lysosomes were first discovered by Christian de Duve in 1955 (Appelmans and De Duve, 1955). Once considered merely the end-point in degradation, lysosomes are now understood to play a more complex role in the cell, with involvement in nutrient sensing and signalling, cell adhesion, tumour metastasis and antigen presentation (Luzio et al., 2014; Pu et al., 2016).

There are over 100 lysosomal transmembrane proteins, the most abundant being LAMP1 (lysosomal-associated membrane protein 1) and LAMP2 (lysosomal-associated membrane protein 2) which make up around half of the lysosomal transmembrane protein population (Luzio et al., 2014). The highly glycosylated luminal tails of LAMPs function to protect the lysosomal membrane from degradation by the hydrolases that they confine (Pu et al., 2016).

Lysosomes contain over 50 soluble acid hydrolases (phosphatases, nucleases, glycosidases, proteases, peptidases, sulphatases and lipases) which participate in the degradation of macromolecules (Luzio et al., 2014). Following their synthesis, acid hydrolases are post-translationally modified to incorporate mannose 6-phosphate (M6P) residues (Kornfeld et al., 1999; Rohrer and Kornfeld, 2001). This facilitates their recognition by M6P receptors (M6PR), which mediate their transport from the Golgi apparatus to the lumen of early endosomes (Saftig and Klumperman, 2009). Two M6P receptors exist in mammalian cells, a 46kDa cation-dependent M6PR (CDMPR), which primarily exists as a dimer, and a 300 kDa cation-independent M6PR (CIMPR). Both receptors function in the delivery of hydrolases to lysosomes, but CIMPR has an additional role at the plasma membrane in the endocytosis of lysosomal hydrolases and other ligands, such as retinoic acid (Braulke and Bonifacino, 2009). Due to the

lower pH of the late endosome, here the hydrolase-M6PR complexes dissociate and the M6PRs are recycled back to the *trans*-Golgi network (TGN) for further rounds of hydrolase delivery (Hirst et al., 1998; Olson et al., 2008). As endosomes mature, become more acidic and fuse with lysosomes, the hydrolases become active and degrade their substrate macromolecules to allow recycling of the break-down products (e.g. amino acids, fatty acids) (Huotari and Helenius, 2011).

The activity of these hydrolases is dependent on the maintenance of two properties within the lysosomal lumen: a high Cl^- concentration and a low pH (Feng et al., 2023). The lysosomal Cl^-/H^+ exchanger CLC-7 maintains intralysosomal Cl^- concentration and an acidic environment is achieved through the action of the vacuolar ATPase (v-ATPase) proton pump (Ohkuma et al., 1982; Wu et al., 2023; Zhang et al., 2023).

The v-ATPase comprises two main subcomplexes, a V_0 mechanical domain and a V_1 catalytic domain, which function together as a molecular rotor that propels H^+ across the lysosomal membrane. The V_0 mechanical domain sits within the lysosomal membrane and comprises five subunits which form a pore through which H^+ transits into lysosomes (Freeman et al., 2023). Comprised of eight subunits, the V_1 domain assembles on the cytosolic face of the V_0 domain and forms the rotor portion of the v-ATPase. Hydrolysis of ATP at the catalytic site on V_1 drives the rotor ring to turn unidirectionally, thus propelling the H^+ through the V_0 pore (Freeman et al., 2023).

Assembly and disassembly of the v-ATPase allows further regulation of lysosomal pH. For instance, amino acid starvation, lysosomal damage and pathogen infection all drive the engagement of V_0 and V_1 (Hooper et al., 2022; Stransky and Forgac, 2015). The activity of the v-ATPase is also regulated by the Rab7a (hereafter Rab7) effector Rab-interacting lysosomal protein (RILP), which controls v-ATPase stability and localisation (De Luca et al., 2014). Interactions between the v-ATPase and PI(4)P and $PI(3,5)P_2$ are proposed to regulate V_0-V_1 assembly and H^+ pumping force (Freeman et al., 2023). By promoting the activation of Rag GTPases, the v-ATPase also plays an important role in the TFEB-dependent upregulation of lysosomal and autophagy genes in response to amino acid starvation or lysosomal stress (Zoncu et al., 2011).

1.1.3 Maintaining membrane identity

The membrane-bound compartments within cells carry out distinct specialised functions. The phosphoinositide (PI) family of lipids and the Rab GTPase proteins (hereafter referred to as Rabs) are key players in regulating these compartments as they both recruit and activate the protein machineries which carry out these

specialised processes. Therefore, phosphoinositide and Rab composition are key definers of membrane, or organelle, identity.

1.1.3.1 Phosphoinositides

Phosphoinositides are phospholipids that localise to the cytosolic face of phospholipid bilayers and function in signalling cascades and the recruitment of effector proteins. The chemical structures of phosphoinositide family phospholipids consist of a *myo*-inositol head group with an acyl chain. All derive from phosphatidylinositol (PtdIns), which is synthesised in the ER and delivered to organelles through the endosomal network, biosynthetic pathway, or via membrane contact sites (Posor et al., 2022). The hydroxy groups at positions 3, 4 and 5 of the inositol ring can be phosphorylated in different combinations to yield PI(3)P, PI(4)P, PI(5)P, PI(3,4)P_2, PI(3,5)P_2, PI(4,5)P_2 and PI(3,4,5)P_3.

The different PIs can be rapidly generated via the action of spatially and temporally restricted kinases and phosphatases. This control of phosphatase and kinase localisation facilitates the enrichment of specific phosphoinositides at distinct membrane compartments to maintain membrane identity (**Figure 1.2**). The plasma membrane is predominantly composed of PI(4,5)P_2, however PI(4)P, PI(3,4)P_2 and PI(3,4,5)P_3 may also be present. The primary PI constituent of early endosomes is PI(3)P, generated directly from PtdIns by the action of the kinase vacuolar protein sorting 34 (VPS34) (Gillooly et al., 2000; Posor et al., 2022; Schu et al., 1993). On late endosomes, a portion of PI(3)P is converted to PI(3,5)P_2 by 1-Phosphatidylinositol 3-Phosphate 5-Kinase (PIKfyve) (McEwen et al., 1999; Sbrissa et al., 1999; Shisheva et al., 2001). Lysosomes contain a much more heterogenous mix of PIs than other compartments, and can comprise PI(3)P, PI(4)P, PI(3,4)P_2, PI(3,5)P_2 and PI(4,5)P_2 (Posor et al., 2022).

Rab5 recruits VPS34 to the early endosome to mediate the generation of PI(3)P (Christoforidis et al., 1999). Evolutionary conserved domains have been identified that facilitate PI(3)P binding, including PH (Pleckstrin Homology), PX (Phox Homology), FYVE (Fab 1, YOTB, Vac1, EEA1) and PROPPIN (β-propellers that bind phosphoinositides) (Lystad and Simonsen, 2016). Many proteins which reside and function at the early endosome are recruited by PI(3)P via such domains; including early endosome antigen 1 (EEA1), hepatocyte growth factor-regulated tyrosine kinase substrate (HRS) and VPS36 (Lawe et al., 2000; Mills et al., 1998; Slagsvold et al., 2005; Urbé et al., 2000). Therefore, the proper functioning of the early endosome is critically dependent on PI(3)P.

PIKfyve is recruited by PI(3)P to early endosomes via its FYVE domain, where it converts PI(3)P into PI(3,5)P_2 (Cabezas et al., 2006; Dove et al., 2002; Sbrissa et al., 1999). This is a key step in endosome maturation as PI(3,5)P_2 is required for retriever-dependent recycling pathways (discussed in **Section 1.2.2.3**) and influences lysosomal ion homeostasis by controlling the ion channels CLC-7, TPC1, TRPML1 and, possibly, the v-ATPase (Giridharan et al., 2022; Leray et al., 2022; Rivero-Ríos and Weisman, 2022).

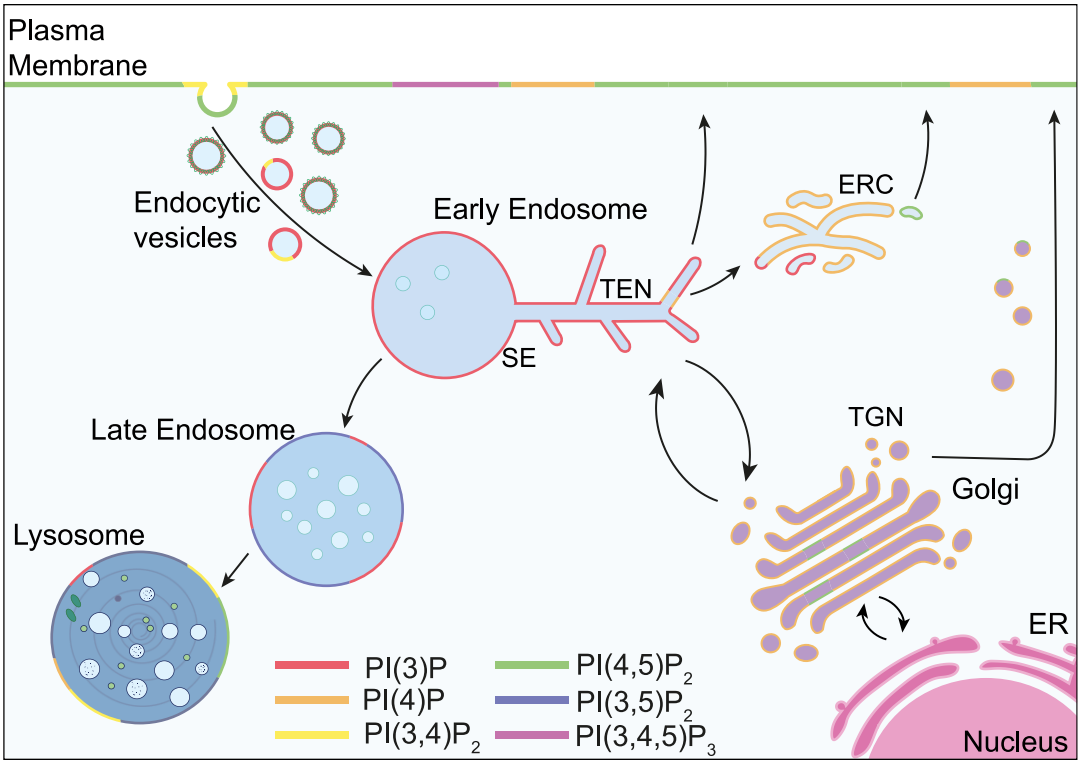

Figure 1.2 Subcellular localisation of phosphoinositides in the endolysosomal network
The identity of subcellular compartments within the endolysosomal system is governed by the enrichment of different phosphoinositide (PI) species. The different PI species present at membranes are indicated by the colours shown. Phosphatidylinositol (PtdIns) and PI(5)P localisation are not shown. Figure adapted from (Posor et al., 2022).

1.1.3.2 Rab GTPases

Another determinant of membrane identity is a family of over 60 small Rab GTPases named Rabs (Zahraoui et al., 1989). Marino Zerial and his colleagues first discovered that different Rab proteins localise to different membrane compartments (Chavrier et al., 1990). Some Rabs are present at several domains, whilst others localise exclusively to one compartment. Rab5 is present at the plasma membrane, early endosomes, phagosomes and caveosomes, whereas Rab11 is only present at recycling endosomes (Stenmark, 2009; Ullrich et al., 1996). Some compartments may contain multiple Rabs, such as the early endosome and recycling compartment,

where distinct Rabs govern the trafficking pathways of different integral membrane proteins (Wandinger-Ness and Zerial, 2014). Therefore, the enrichment of specific Rabs at membranes provides a marker for these distinct compartments (**Figure 1.3**).

In addition, Rabs also control the identity of these membranes and facilitate different functions within each compartment. Rab5 provides one of the best examples of defining membrane identity within the endolysosomal system. Rab5 is involved in clathrin-dependent endocytosis and the fusion of these vesicles with the early endosome (Gorvel et al., 1991). At the early endosome, Rab5 recruits VPS34 to the endosomal membrane surface, which initiates PI(3)P synthesis (Christoforidis et al., 1999). Many proteins bind to PI(3)P in the endosomal membrane, including the retromer-associated sorting nexins and members of the ESCRT machinery. Through this recruitment process, Rab5 controls both the composition of the membrane and the proteins which are associated with it. The tethering factor EEA1 is another Rab5 effector, and is one of the most commonly used early endosomal markers (Christoforidis et al., 1999; Mu et al., 1995; Simonsen et al., 1998). EEA1 also binds to PI(3)P, illustrating the coincidence detection mechanism that exists at membranes whereby Rabs and PI species act together to control effector localisation and therefore, membrane identity (Carlton and Cullen, 2005). Given its many functions at the early endosome, it is perhaps unsurprising that loss of Rab5 leads to impaired recycling and abnormal morphology (Bucci et al., 1992).

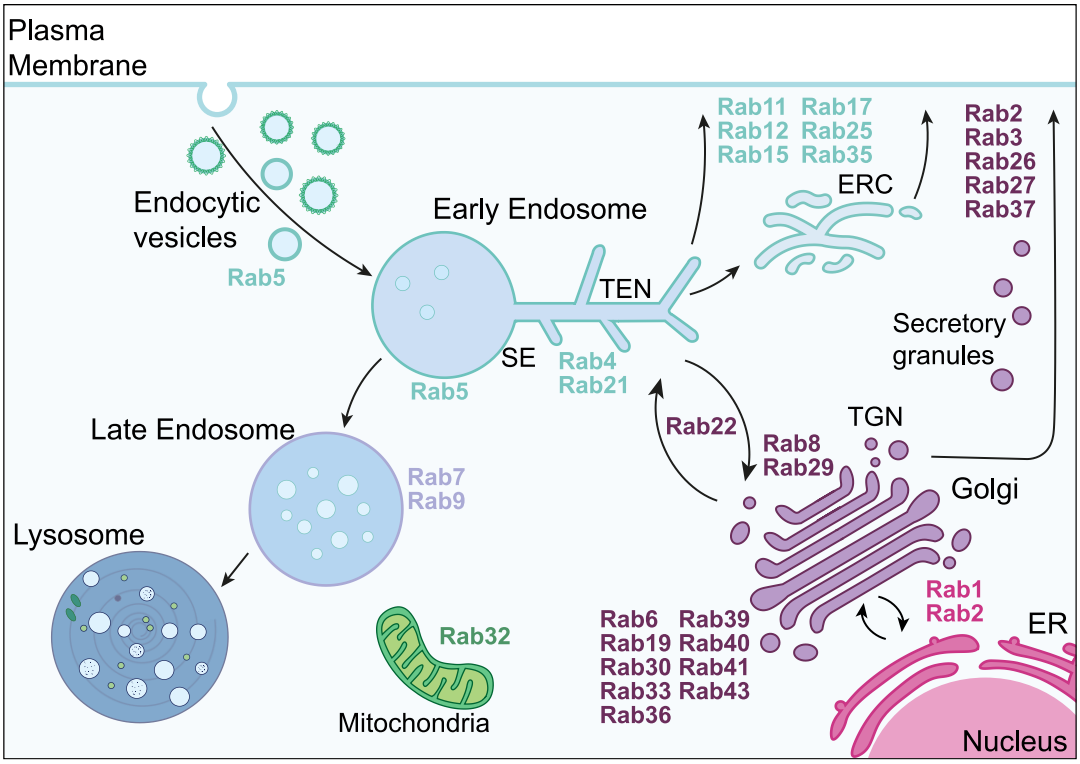

Figure 1.3 Localisation of Rabs in the endolysosomal network

The identity of subcellular compartments within the endolysosomal system is governed by the enrichment of different Rabs. Figure adapted from (Zhen and Stenmark, 2015).

1.2 Co-ordinating membrane traffic

One of the key roles of the endolysosomal network is the transportation of cargoes between membrane-bound compartments, known as membrane traffic. Several complex processes are involved in the transport of cargoes within membrane-bound vesicles from one compartment to another. Firstly, vesicle formation requires sequential events promoting membrane curvature, vesicle coating and release from the membrane by scission. Sorting of cargoes is key to ensure correct and efficient trafficking, often determining its fate. Finally, recognition and fusion of the vesicle with the target membrane is necessary to retrieve the incoming cargo. All these events are tightly controlled by proteins and protein complexes.

1.2.1 Rab GTPases – 'master' regulators membrane trafficking

Rabs are considered to be master regulators of membrane traffic because they act as molecular switches to control several membrane trafficking events; including vesicle sorting, motility, tethering and fusion (Stenmark, 2009). The conversion of Rabs between their GTP- and GDP-bound states not only controls their activity but also their membrane association. The activity cycle of Rabs is mediated by two classes of proteins, guanine nucleotide exchange factors (GEFs) and GTPase activating proteins (GAPs) (**Figure 1.4**).

After synthesis, Rabs are post-translationally modified by prenylation (Itzen and Goody, 2011). The irreversible addition of geranylgeranyl groups to one or two adjacent C-terminal cysteines in the hypervariable region allows Rabs to associate with lipid membranes (Edler and Stein, 2019; Itzen and Goody, 2011). At steady state, generally around half of a Rab species population is localised to membranes and half remains in the cytosol, although this differs between Rabs (Pfeffer, 2017).

In the cytosol, Rabs exist in their inactive GDP-bound state and are sequestered through high affinity association with GDP dissociation inhibitors (GDIs), which have a strong preference for Rabs in their GDP-bound state (Araki et al., 1990; Shapiro and Pfeffer, 1995; Wu et al., 2010). Two GDIs have been identified in humans and one in yeast and are capable of binding to all Rab GTPases (Pfeffer, 2017). Crystal structures of yeast GDI-Rab complexes show three interactions sites: a GDI-Rab binding platform, a GDI C-terminus coordinating region, and a prenyl-lipid binding pocket which accommodates the geranylgeranyl chains of the Rab (Ignatev et al., 2008; Pylypenko et al., 2006). The first association made is between the Rab binding

platform and the switch I region of the Rab, which recognises Rabs in their GDP-bound form and prevent release of GDP, stabilising Rabs in their inactive conformation. The insertion of the geranylgeranylated residues of Rabs into the binding pocket of GDI prevents Rab association with membranes (Edler and Stein, 2019). The formation of the Rab-GDI complex stabilises Rabs in their inactive state in the cytosol (Araki et al., 1990; Dirac-Svejstrup et al., 1994; Matsui et al., 1990; Sasaki et al., 1990). GDIs are also thought to act as chaperones for Rabs, directing them to and from membranes (Soldati et al., 1994, 1993; Ullrich et al., 1994, 1993). Rab escort proteins (REPs) have high structural similarity to GDIs and play a similar role in the delivery of Rabs to membranes, but only with newly synthesised Rabs (Alexandrov et al., 1994; Stenmark, 2009).

GDI displacement factor (GDF) catalyses the dissociation of Rab-GDI complexes, allowing Rab activation and membrane association (Sivars et al., 2003). So far only one GDF has been identified (Pfeffer, 2017; Sivars et al., 2003). GEFs act to accelerate the rate of GDP release from Rabs, which occurs spontaneously at an extremely slow rate (Itzen and Goody, 2011). The binding of GEFs to Rabs induces a conformational change that opens the nucleotide binding site, weakening Rab-GDP interactions to facilitate GDP release (Itzen and Goody, 2011). This allows for replacement with GTP, thus converting the Rab into its active GTP-bound state. It has been shown that the hypervariable domain of Rabs acts as a recognition site for GEFs to confer substrate specificity (Thomas et al., 2019). Loss of GEFs has also been shown to cause loss of Rab localisation, suggesting they also play a role in the targeting of Rabs to the membrane (Cabrera and Ungermann, 2013; Gerondopoulos et al., 2012; Thomas and Fromme, 2016). Furthermore, artificial manipulation of GEF localisation causes relocalisation of Rabs (Blümer et al., 2013; Gerondopoulos et al., 2012). In the active, membrane-bound form, Rabs recruit multiple effectors to carry out membrane trafficking functions. This includes GEFs for other Rab proteins, forming a cascade of Rab activation at a membrane compartment (Pfeffer, 2017).

The intrinsic GTPase activity of Rabs is low and so GAPs acts to catalyse this process, hydrolysing GTP and inactivating the Rab protein, which allows tight control of trafficking events (Itzen and Goody, 2011; Pfeffer, 2017). The GDP-bound inactive Rab is then extracted from the membrane by GDI, completing the Rab activity cycle.

One of the best characterised Rab cascades is the ‘Rab5-Rab7’ switch, a critical process in the maturation of early endosomes to late endosomes (Rink et al., 2005). Rab5 recruits the Rab7 GEF Mon1-Ccz1 (which also binds to PI(3)P in the endosomal

membrane), activating Rab7 and displacing the Rab5 GEF rabex-5, leading to Rab5 inactivation (Poteryaev et al., 2010). GTP-Rab7 is then able recruit numerous effectors, including RILP and retromer (discussed in **Section 1.2.2.2**) (Cantalupo et al., 2001; Jordens et al., 2001; Rojas et al., 2008; Seaman et al., 2009).

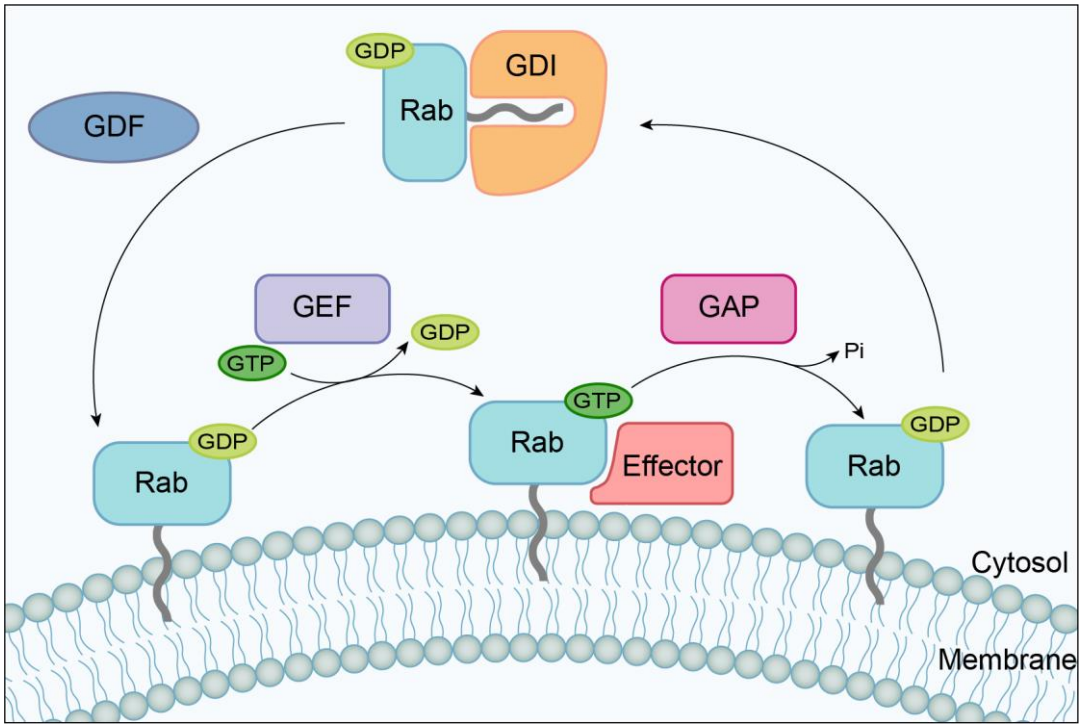

Figure 1.4 Rab-GTPase activity cycle

Rabs are sequestered in the cytosol in their inactive GDP-bound state via interaction with a GDP dissociation inhibitor (GDI). Rabs are released from this Rab-GDI complex through the action of GDI dissociation factor (GDF). Dissociation from GDI reveals the Rab geranylgeranylated carboxy terminal which is then capable of associating with membranes. A guanine exchange factor (GEF) catalyses the exchange of GDP for GTP, activating the Rab as it can bind to multiple effector proteins in the GTP-bound form. The active Rab is inactivated through GTP hydrolysis, catalysed by a GTPase-activating protein (GAP). Thus, the Rab is once again in an inactive conformation which can be recognised by GDI.

1.2.2 Endosomal sorting

The transport of protein cargo from the early endosome to other cellular compartments is integral for homeostasis (McNally and Cullen, 2018). It allows tight regulation of membrane composition and an adaptive response to be mounted to conditions such as starvation (Cullen and Steinberg, 2018; Curnock et al., 2019; McNally and Cullen, 2018). At the endosomal membrane, cargoes are enriched at discrete subdomains according to their fate, either degradation or recycling.

This sorting process is orchestrated by several protein complexes (Cullen and Steinberg, 2018). The ESCRT machinery is involved in the sorting of cargo for degradation. The ESCRT complexes act sequentially to recognise and sort ubiquitylated cargo into ILVs within the endosome, which are then degraded upon fusion of the late endosome with the lysosome (Cullen and Steinberg, 2018; McNally and Cullen, 2018). To save cargo from a degradative fate, cargo must be actively retrieved. This is coordinated by multiple protein complex machineries; retromer, ESCPE-1, the CCC-retriever commander complex, and the WASH complex (Naslavsky and Caplan, 2018).

1.2.2.1 ESCRT-dependent cargo degradation

The endosomal complexes required for transport (ESCRT) machinery orchestrate the internalisation of ubiquitylated cargo at the endosome into ILVs, which are ultimately degraded by the lysosome. Five protein complexes (ESCRT-0, -I, -II, -III and Vps4) and a host of accessory proteins make up the ESCRT machinery and act in concert to generate degradative subdomains on the endosomal membrane surface, enrich these with ubiquitylated cargo, promote membrane deformation, and finally, cause vesicle scission (**Figure 1.5**) (Williams and Urbé, 2007).

Components of the ESCRT machinery were first discovered by Scott Emr in a yeast screen for genes which caused defects in the sorting of proteins to the vacuole, hence their naming prefix *vacuolar protein sorting* (Vps) (Raymond et al., 1992). The ESCRT proteins have been designated as belonging to the Class E Vps mutants which show a distinct phenotype of accumulation of protein cargo within enlarged endosomes (Raymond et al., 1992).

The ESCRT-0 complex, a heterodimer consisting of HRS and signal transducing adaptor molecule (STAM), initiates the process of ILV formation. The ESCRT-0 complex is recruited to early endosomes via the FYVE zinc finger domain of HRS (Urbé et al., 2000). At the endosome, it binds to multiple ubiquitylated cargoes via ubiquitin binding domains present on HRS and STAM (Frankel and Audhya, 2018; Raiborg et al., 2001). In addition, HRS recruits clathrin, which assembles into lattice structures that corral cargo within discrete patches on the endosomal membrane to create a distinct degradative subdomain (Norris and Grant, 2020; Sachse et al., 2002). To continue the process of ESCRT-mediated sorting, ESCRT-0 recruits the protein complex ESCRT-I (Frankel and Audhya, 2018).

ESCRT-I is a heterotetrameric complex comprised of VPS37, tumour susceptibility gene 101 protein (TSG101), VPS28 and multivesicular body sorting factor 12

(MVB12; also referred to as ubiquitin associated protein 1, UBAP1). ESCRT-I is recruited to the endosomal membrane via the interactions of TSG101 with HRS and ubiquitylated cargo (Frankel and Audhya, 2018).

ESCRT-II is a heterotetrameric complex, consisting of VPS36, SNF8 (VPS22) and two VPS25 subunits. ESCRT-II is recruited to the endosome via an interaction between VPS28 of ESCRT-I and the GRAM-like ubiquitin binding in EAP45 (GLUE) domain of VPS36 (Cullen and Steinberg, 2018). The GLUE domain of VPS36 is also capable of binding ubiquitin on modified cargoes and PI(3)P in the endosomal membrane (Schmidt and Teis, 2012). Together, ESCRT-0, ESCRT-I and ESCRT-II make up the 'early' ESCRT machinery and are believed to mainly function in sorting of ubiquitylated cargo into concentrated zones (Schmidt and Teis, 2012).

Unlike the early ESCRT machinery, ESCRT-III is not a stable complex, and only transient associations form between its four core subunits, charged multivesicular body protein 6 (CHMP6; VPS20), CHMP4 (SNF7), CHMP3 (VPS24) and CHMP2 (VPS2). CHMP6 catalyses the formation of long filaments of CHMP4 which form a spiral around the degradative subdomain, with ubiquitylated cargo at the centre (**Figure 1.5**) (McCullough et al., 2015; Norris and Grant, 2020; Schmidt and Teis, 2012). The spiral structure generates tension for membrane curvature, promoting the inward budding of the membrane to eventually form an ILV (Cullen and Steinberg, 2018). To prevent further oligomerisation, CHMP3 caps the end of the filament, which then recruits CHMP2, and subsequently VPS4 (Schmidt and Teis, 2012). The CHMP4 oligomers may provide a diffusion barrier for cargo to contain it within the subdomain after deubiquitylation (Norris and Grant, 2020). The VPS4 complex is a Type I AAA-ATPase which acts with ESCRT-III in membrane deformation and vesicle neck constriction and also mediates ESCRT complex disassembly (Adell et al., 2014; Babst et al., 2002a, 2002b, 1998, 1997).

The deubiquitylating enzymes (DUBs) STAM-binding protein (STAMBP, also known as AMSH) or USP8 (ubiquitin-specific protease 8; ubiquitin carboxyl-terminal hydrolase 8, also known as UBPY) associate with CHMP2 and CHMP3 of the ESCRT-III complex and remove ubiquitin moieties from cargo before they are incapsulated into ILVs (Clague and Urbé, 2006). Including facilitating the recycling of ubiquitin, these DUBs may have additional functions in ESCRT-mediated degradation as AMSH and USP8 have been shown to exert opposite effects on the rate of EGFR degradation, and USP8 has been shown to stabilise the ESCRT-0 complex (Clague and Urbé, 2006; Row et al., 2007).

In addition to the role of the ESCRT complex in internalisation of integral membrane proteins at the endosome, ESCRT complexes also function in other processes which require membrane sealing. These include cytokinesis, lysosome repair and nuclear envelope repair (Zhen et al., 2021). The ESCRT-associated protein apoptosis-linked gene-2 interacting protein X (ALIX) is also capable of bridging the interaction between ESCRT-I and ESCRT-III complexes and is understood to play an important role in these other ESCRT machinery functions, despite being dispensable for cargo degradation (Bissig and Gruenberg, 2014; Skowyra et al., 2018).

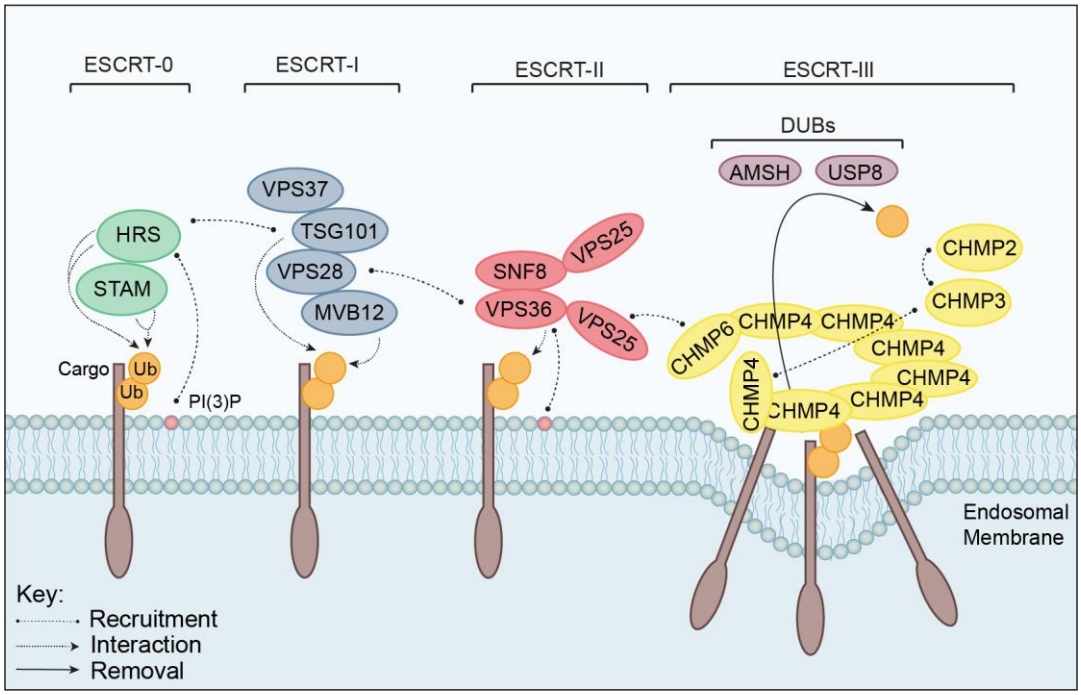

Figure 1.5 ESCRT-mediated internalisation of ubiquitylated cargo

The ESCRT-0 complex associates to the cytosolic face of the endosomal membrane via binding to PI(3)P. To initiate cargo sorting, the ESCRT-0 components HRS and STAM bind ubiquitylated cargo via four ubiquitin binding domains. ESCRT-0 recruits the ESCRT-I complex via an interaction between HRS and TSG101 to continue the process of cargo sorting. The ESCRT-I components TSG101 and MVB12 bind ubiquitin conjugated to the cargo. ESCRT-II is recruited to the endosomal membrane by ESCRT-I. The VPS36 subunit of ESCRT-II simultaneously binds to PI(3)P in the endosomal membrane and one ubiquitin moiety. The ESCRT-III complex is recruited by ESCRT-II via an interaction between CHMP6 and VPS25. CHMP6 catalyses the formation of spiral filaments of CHMP4 oligomers around cargo within the degradative subdomain. This prevents diffusion of cargo and provides tensile force to promote inward budding of the membrane and ILV formation. The DUBs AMSH and USP8 remove ubiquitin moieties from cargo before they are internalised into ILVs.

AMSH, STAM-binding protein; CHMP, charged multivesicular body protein; DUB, deubiquitylases; ESCRT, endosomal sorting complexes required for transport; HRS, hepatocyte growth factor-regulated tyrosine kinase substrate; ILV, intra-luminal vesicle; MVB12, multivesicular body sorting factor 12; PI(3)P, phosphatidylinositol 3-phosphate; STAM, signal transducing adaptor molecule;

TSG101, tumour susceptibility gene 101; Ub, ubiquitin; USP8, ubiquitin specific protease 8; VPS, vacuolar protein sorting.

1.2.2.2 Retromer

Retromer is an ancient, highly conserved protein complex that is a major conductor of endosomal sorting (Burd and Cullen, 2014). First discovered in the budding yeast *Saccharomyces cerevisiae*, retromer was shown to be a heteropentameric complex comprised of two sub-complexes, a Vps5 and Vps17 Sorting Nexin family (SNX)-Bin/Amphiphysin/RVS (BAR) dimer, and a Vps26, Vps29 and Vps35 trimer known as the cargo-selective complex (CSC) (Seaman et al., 1998). In this study, the retromer complex was shown to be involved in the recycling of carboxypeptidase receptor Vps10 from the endosome to the TGN (Seaman et al., 1998).

The CSC is conserved across eukaryotes, with mammalian retromer also containing VPS26, VPS29 and VPS35 (Koumandou et al., 2011). In humans, three orthologs of Vps26p exist, VPS26A, VPS26B, VPS26C (also known as DSCR3) (Koumandou et al., 2011). Proteomic analysis has revealed that VPS26A and VPS26B have largely redundant functions, however the importance of the two isoforms may lie in their differential expression within the body (McNally et al., 2017; Simoes et al., 2021). VPS26B is enriched within the *trans*-entorhinal cortex within the brain, a region particularly susceptible to Alzheimer's disease pathology (Simoes et al., 2021). VPS26C is a subunit of the retriever complex (discussed in **Section 1.2.2.3** below) which diverged early in the evolutionary origins of VPS26, suggesting that retriever is a similarly ancient sorting complex (Gallon et al., 2014; McNally et al., 2017).

In contrast, the SNX proteins have shown greater divergence. The yeast SNX dimer proteins each have multiple mammalian orthologs, SNX1 and SNX2 are orthologs of Vps5, and SNX5, SNX6 and SNX32 are orthologs of Vps17 (Koumandou et al., 2011). In higher eukaryotes, the core retromer trimer (VPS35, VPS26, VPS29) and SNX-BAR dimer (SNX1/SNX2 and SNX5/SNX6/SNX32) act as independent complexes capable of recycling of different cargo (Kvainickas et al., 2017; Simonetti et al., 2017). In mammalian systems, the VPS heterotrimer is referred to as 'retromer' and the SNX-BAR dimer is known as the Endosomal SNX-BAR Sorting Complex for Promoting Exit-1 (ESCPE-1).

Retromer does not contain membrane binding domains, and therefore relies on interactions with sorting nexins and Rab7 for recruitment to the endosome (Lucas et al., 2016; Rojas et al., 2008; Seaman et al., 2009). The SNX proteins bind at the VPS26:VPS35 interface of retromer and Rab7 binds to VPS35 (Jia et al., 2016; Lucas

et al., 2016). Resolution of the crystal structure of retromer by cryo-electron microscopy has revealed that it is capable of assembling into higher-order structures around endosomal tubules (Kovtun et al., 2018; Leneva et al., 2021). In this arrangement, two retromer complexes form an arch-shaped dimer where the VPS26 subunits sit closest to the endosomal membrane, the VPS35 subunits form the main body of the arch with the two opposing C-termini interacting with each other at the apex, and the VPS29 subunits sitting at the top of the arch (**Figure 1.6**).

Retromer is involved in the trafficking of cargo from the endosome to multiple destinations, including the plasma membrane, TGN and to lysosome-related organelles (McNally and Cullen, 2018). Over 100 plasma membrane proteins have been shown to be recycled via retromer-dependent mechanisms, including metal ion transporters, nutrient sensing, signalling receptors (Steinberg et al., 2013). In addition to mediating endosomal association of retromer, SNX3 and SNX27 act to confer selectivity and directionality in cargo retrieval through differential recognition of conserved short peptide motifs within the cytoplasmic domains of integral membrane proteins (**Figure 1.6**). The retromer-SNX3 complex recognises the sequence Øx[L/M/V], where Ø is a bulky aromatic residue, and directs cargo to the *trans*-Golgi network. Cargo containing this sequence include Wntless, the divalent cation transporter DMT1-II and possibly the cation-independent mannose-6-phosphate receptor (discussed further in **Section 1.2.2.3**) (Cui et al., 2018; Harterink et al., 2011; Lucas et al., 2016; Zhang et al., 2011). The SNX27-retromer complex facilitates recycling of cargo to the plasma membrane, including GLUT1, β_2-adrenoceptor and the copper transporter ATP7A (Lauffer et al., 2010; Steinberg et al., 2013). SNX27 contains a post synaptic density 95-discs large-zonula occulens-1 (PDZ) domain which recognises a type-I PDZ binding motif near the C-termini of these cargo (Lauffer et al., 2010; Steinberg et al., 2013; Temkin et al., 2011).

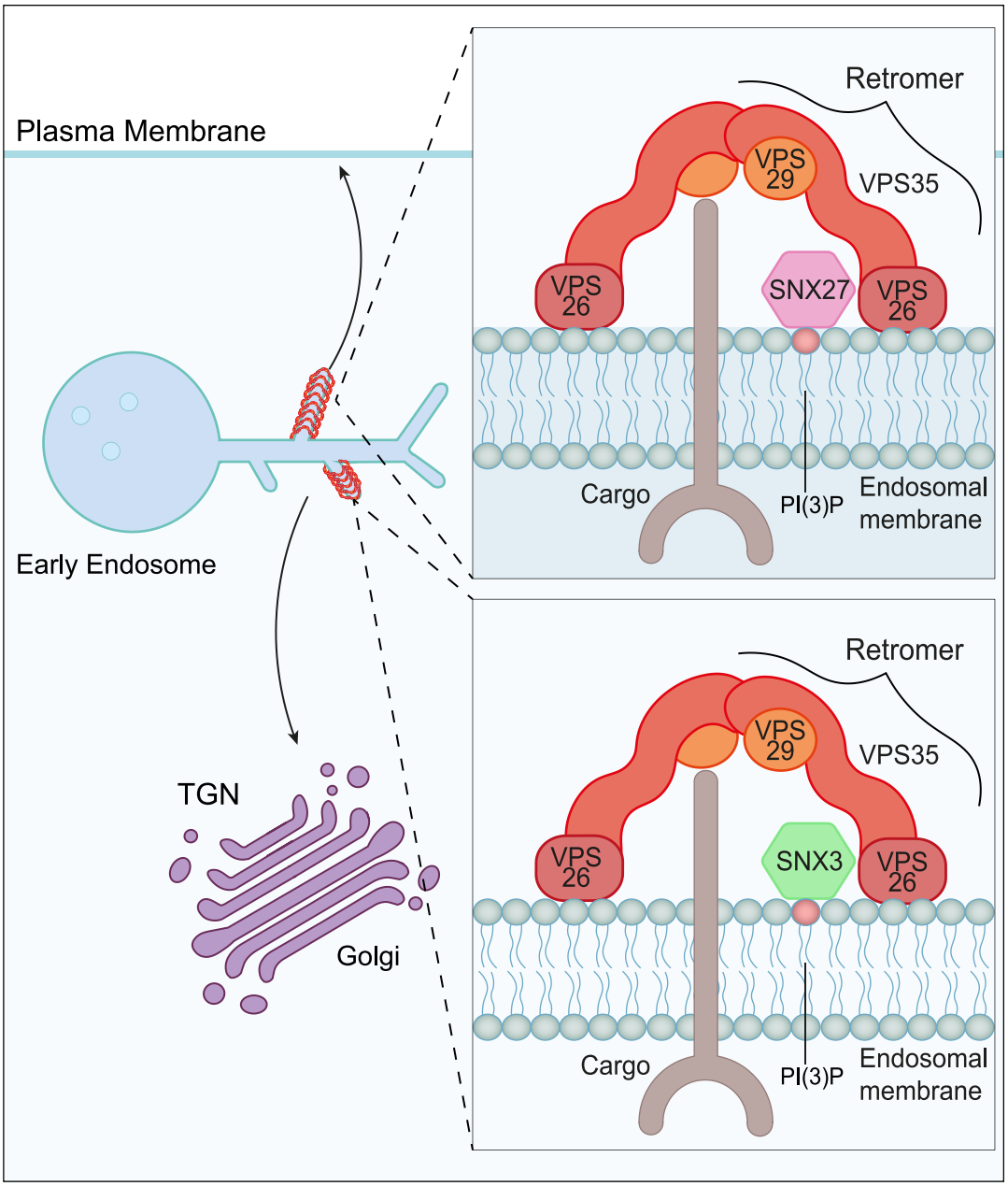

Figure 1.6 Retromer complex function

The VPS35-VPS29-VPS26 trimer comprises retromer, an endosomal cargo sorting complex which recycles cargo to the plasma membrane and the *trans*-Golgi network (TGN). Retromer assembles into a coat around endosomal tubules by forming repeated homodimeric 'arches'. Membrane association of retromer is mediated by a sorting nexin (SNX) protein which associates with the membrane via PI(3)P. The identity of the SNX protein determines the sorting destination. SNX3-retromer delivers cargo to the TGN and SNX27-retromer directs cargo to the plasma membrane.

In addition to its role in cargo recognition and sorting, retromer also associates with a host of accessory proteins which control endosome morphology and identity. The retromer complex promotes the recruitment of the Wiskott-Aldrich syndrome protein and scar homologue (WASH) complex to endosomes, an ancient complex composed

of five proteins: FAM21 A/B/C (WASHC2A/B/C), CCDC53 (WASHC3), SWIP (strumpellin and WASH interacting protein; WASHC4) and strumpellin (WASHC5). This is facilitated by an interaction between VPS35 and the C-terminal tail of FAM21 (Harbour et al., 2012). The WASH complex acts as a nucleation promoting factor for Actin-related protein 2/3 (Arp2/3) complex which promotes the formation of branched actin networks at the base of endosomal tubules. These filamentous actin polymers are thought to act as a scaffold to stabilise tubules and recruit further complexes involved in sorting (McNally and Cullen, 2018).

A recently proposed role for retromer in maintaining membrane identity has been put forward based on the interactions of the VPS29 subunit with Tre-2, BUB2p, Cdc16p-1-Domain family member 5 (TBC1D5) and VPS9-ankyrin repeat protein (VARP) (Jimenez-Orgaz et al., 2018). Recruitment of retromer to the endosomal membrane is dependent on Rab7, which in turn recruits the Rab7 GAP TBC1D5 (Seaman et al., 2009). TBC1D5 then catalyses Rab7-GTP hydrolysis, inactivating Rab7 and promoting its removal from the endosomal membrane. Therefore, retromer plays an integral role in the activity cycling of Rab7 at endosomes. Loss of the retromer-TBC1D5 interaction leads to accumulation of hyperactivated Rab7 at enlarged large endosomes (Daly et al., 2023; Jimenez-Orgaz et al., 2018). As Rab7 has myriad functions in the endosome maturation process, the removal of Rab7 from endosomal membranes by retromer-TBC1D5 acts as a brake to prevent progression to a late endosome/lysosomal identity (Daly et al., 2023; Jimenez-Orgaz et al., 2018).

VARP has multiple reported functions in endosomal trafficking, acting as a GEF for Rab21, an effector for Rab32 and Rab38, which are important in trafficking of cargo to the lysosome-related organelle melanosomes (Fukuda, 2016). In the context of maintaining identity, VARP binds to and inactivates the R-N-ethylmaleimide-sensitive factor attachment protein receptor (R-SNARE) VAMP7 which, when active, is important for fusion between late endosomes and lysosomes (Schäfer et al., 2012).

1.2.2.3 Retromer-independent recycling

Although retromer appears to be the major mediator of endosomal cargo recycling, and is certainly the most extensively studied, many cargoes have been identified that are trafficked via retromer-independent mechanisms (McNally et al., 2017; Steinberg et al., 2012).

The ESCPE-1 complex consists of heterodimer of SNX1/SNX2 and SNX5/SNX6/SNX32 which function as a coat for endosomal tubulation and a sorting complex for cargo recycling (Kvainickas et al., 2017; Lopez-Robles et al., 2023;

Simonetti et al., 2019, 2017). SNX1/2 mediates membrane association to PI(3)P or other phosphoinositides, whereas SNX5/6 binds to the cytoplasmic domain of cargo (Lopez-Robles et al., 2023). The PX domains of SNX5 and SNX6 associate with a cytoplasmic sorting motif, ΦxΩxΦ(x)nΦ, within transmembrane proteins to capture cargo for retrieval (Simonetti et al., 2019, 2017). This includes the cation-independent mannose-6-phosphate receptor (CIMPR), a cargo that has been classically thought to be trafficked via retromer (Simonetti et al., 2017). Independently, a study published by the Steinberg lab showed that knockout of SNX5/6 or SNX1/2, but not VPS35, caused a redistribution of CIMPR to peripheral endosomes in HeLa cells (Kvainickas et al., 2017). Following this, the authors called for a re-evaluation of whether CIMPR was truly a retromer cargo. A follow-up study utilised a 'knock-sideways' approach which acutely inactivates a protein by trapping it on an unrelated organelle, to show that inactivation of ESCPE-1, but not retromer, led to defects in CIMPR localisation (Evans et al., 2020). The authors also observed in H4 neuroglioma cells that knockout of retromer led to increased expression of CIMPR and its ligand cathepsin D, despite not altering its localisation to the TGN. They postulated that the changes in CIMPR localisation following perturbation of the retromer complex that have been observed by previous studies are not due to a direct relationship between retromer and CIMPR, but rather are due to longer term compensatory mechanism following disturbed lysosomal homeostasis (Evans et al., 2020).

A large, multi-multiprotein 'Commander' complex has been discovered to participate in endosomal recycling (McNally et al., 2017). This 16-subunit complex comprises three main regions: a trimeric sorting complex named retriever, a copper metabolism gene MURR1 domain (COMMD) ring and a scaffold consisting of coiled-coil domain containing 93 (CCDC93) and coiled-coil domain containing 22 (CCDC22). In addition, the commander complex also contains an accessory protein, DENN domain containing 10 (DENND10).

Retriever is a highly conserved heterotrimeric complex composed of VPS35-like (VPS35L, also referred to as C16orf62), VPS29 and VPS26C. Retriever associates with sorting nexin SNX17 and regulates the trafficking of more than 100 plasma membrane proteins, including integrins, nutrient transporters and signalling receptors (McNally et al., 2017; Steinberg et al., 2012). The retriever-SNX17 interaction is thought to be via the VPS26C subunit, like the interaction between VPS26A/B of retromer and sorting nexins SNX3 and SNX27 (McNally, 2017). Retriever and SNX17 co-localise with retromer on the same endosomal subdomains, distinct from ESCRT degradative domains (McNally, 2017).

Retriever and retromer both share a VPS29 subunit and adopt a similar conformation, but retriever is more twisted and compacted (Boesch et al., 2023; Healy et al., 2023; Laulumaa et al., 2023). Furthermore, VPS35L contains a largely unstructured N-terminal region that is not present on VPS35. The tail region spans the length of the retriever complex and interacts with VPS29 and the C-terminal region of VPS35L. Importantly, it functions to occlude the binding site on VPS29 which interacts with VARP and TBC1D5 when assembled in the retromer complex, providing a distinction between retromer and retriever function in recruitment of accessory factors (Healy et al., 2023).

Together CCDC22, CCDC93 and the COMMD ring comprise the CCC complex. CCDC22 and CCDC93 form a heterodimer which acts as a scaffold for assembly of the commander complex by interacting with VPS35L, several subunits of the COMMD ring and with DENND10 (Boesch et al., 2023; Healy et al., 2023; Laulumaa et al., 2023). The COMMD ring comprises one of each of the ten different COMMD proteins (Healy et al., 2023). The importance of the proper assembly of the commander complex is evidenced by the fact that mutation or loss of one subunit causes a decrease in the expression of other complex members and leads to Ritscher-Schinzel syndrome (Fedoseienko et al., 2018; Kato et al., 2020; Otsuji et al., 2023).

The 16th subunit is an accessory protein, DENND10, which is part of a family of Rab GEFs. However, its significance within the commander complex is unknown as, unlike other commander subunits, DENND10 is not required for complex stability or cargo recycling (Singla et al., 2019). In the commander complex structure, the Rab-interacting DENND domain is occluded and so would prevent its GEF activity (Boesch et al., 2023; Healy et al., 2023; Laulumaa et al., 2023). Further work will be required to understand the importance and role of DENND10 within the commander complex at the endosome.

1.2.2.4 Maintaining endosomal subdomains

On the endosomal membrane, discrete domains exist to segregate cargo degradation and cargo recycling activities. The degradative subdomain is clathrin-coated and is the site where the ESCRT machinery functions to internalise ubiquitylated cargo into ILVs for degradation by the lysosome. At the recycling subdomain, a host of protein complexes involved in sorting exist – commander, ESCPE-1 and retromer – along with the accessory protein complex, WASH. Several proteins have been implicated in the maintenance of these domains, including the WASH complex, filamentous actin (F-actin), receptor mediated endocytosis-8 (RME-8) and clathrin (**Figure 1.7**).

The WASH complex interacts with multiple endosomal proteins, including VPS35, SNX27, the CCC complex, RME-8 and HRS (Freeman et al., 2014; Harbour et al., 2012; Lee et al., 2016; MacDonald et al., 2018; McNally et al., 2017; Phillips-Krawczak et al., 2015). Several modes of endosomal WASH recruitment have been identified, including via a direct interaction between SWIP of the WASH complex and phosphoinositides in the endosomal membrane, and indirectly via retromer and HRS (Dostál et al., 2023; Harbour et al., 2012; MacDonald et al., 2018). WASH then acts to activate Arp2/3, which polymerises actin at the endosomes (Derivery et al., 2009). These F-actin networks are proposed to promote and stabilise tubule formation, spatially restrict cargo within the recycling subdomain and facilitate cargo transport via an interaction with the microtubule motor protein complex dynein/dynactin (Derivery et al., 2009; Puthenveedu et al., 2010; Simonetti and Cullen, 2019). Actin itself also acts as a sorting mechanism for recycling by directly binding to cargo that is sorted into endosomal tubules for recycling (MacDonald et al., 2020, 2018; Puthenveedu et al., 2010). Depolymerisation of actin leads to the convergence of discrete WASH domains on early endosomes, suggesting that F-actin promotes the segregation of different recycling domains within an endosome (Derivery et al., 2012). It has also been suggested that the CCC complex controls levels of PI(3)P on the endosomal membrane to negatively regulate WASH recruitment (Singla et al., 2019). The multiple interactions between WASH and components of the sorting and degradation machinery support a model in which WASH plays a key role in overseeing the maintenance, proper functioning, and architecture of the endosomal subdomains.

RME-8, also known as DnaJ Heat Shock Protein Family (Hsp40) Member C13 (DNAJC13), is localised to early endosomal membranes where it binds to PI(3)P (Xhabija et al., 2011; Xhabija and Vacratsis, 2015). Through its interaction with SNX1 and FAM21, RME-8 has been proposed to play a key role in the segregation of the degradative and recycling endosomal subdomains (McNally and Cullen, 2018; Popoff et al., 2009). Loss of RME-8 or SNX1 results in the mixing of these domains and disrupts retrograde trafficking (Norris et al., 2017; Popoff et al., 2009). Depletion of RME-8 also leads to excessive endosome tubulation, which is thought to occur via the loss of interaction between RME-8 and FAM21 (Freeman et al., 2014; Popoff et al., 2009). It is possible that RME-8 functions to spatially and temporally control the formation of endosomal recycling tubules containing its effector SNX1 by restricting the polymerisation of actin by WASH (Freeman et al., 2014; Norris et al., 2017). RME-8 recruits and activates the ATPase Hsc70 (Heat shock cognate 70 kDa protein) which disassembles clathrin coats (Chang et al., 2004; Norris et al., 2017; Popoff et

al., 2009). Therefore, RME-8 functions as a negative regulator of clathrin lattice formation at the degradative subdomain. However, depletion of clathrin also leads to the dysregulation of subdomain segregation (Norris et al., 2017). Clathrin is also recruited by HRS to maintain the degradative subdomain (Saftig and Klumperman, 2009). These findings highlight that RME-8 and clathrin are important players in the maintenance of endosomal subdomain architecture.

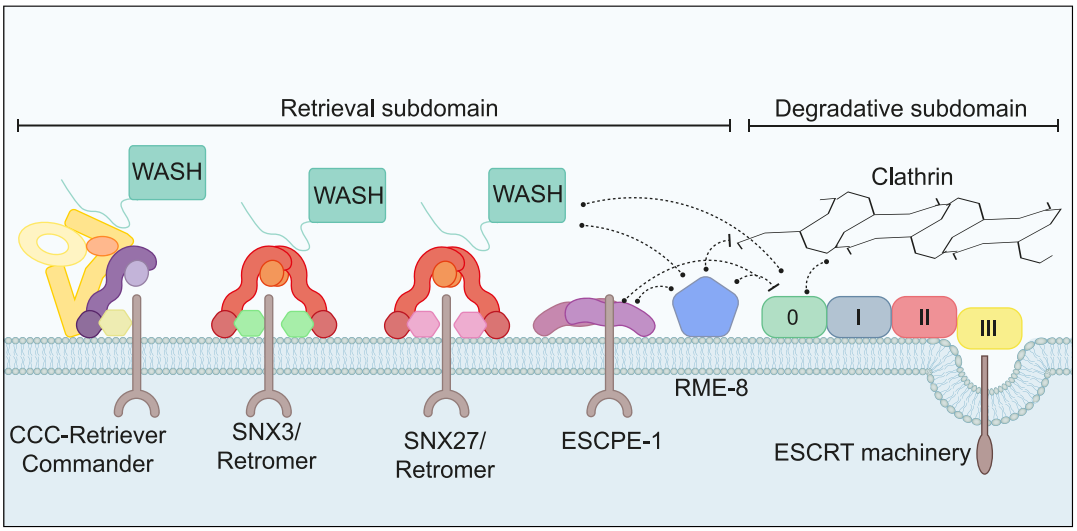

Figure 1.7 The sorting endosome

The sorting endosome is segregated into subdomains which function in cargo retrieval and cargo degradation. Degradation of ubiquitylated cargo is mediated by the ESCRT machinery. Recycling of cargo is orchestrated by the action of several multiprotein complexes: retromer, ESCPE-1 and commander. The maintenance of discrete recycling and degradative subdomains is facilitated by the action of the WASH complex, RME-8, HRS and clathrin.

1.3 Cellular quality control

To maintain homeostasis, cells have evolved two major quality control systems: the ubiquitin-proteasome system (UPS) and autophagy. Action of these pathways allows the cell to respond to a changing environment, fine-tune cellular processes and prevent the build-up of damaging material. These two processes are interconnected and largely rely on the same small molecule, ubiquitin (Clague and Urbé, 2010).

1.3.1 Ubiquitin

Ubiquitin is a small, 76-amino acid protein that is post-translationally added to protein substrates. It acts as a signalling molecule to control a myriad of cellular processes, including protein degradation, cell division and intracellular trafficking (Damgaard, 2021). The attachment of a ubiquitin moiety onto a substrate is catalysed by a set of sequential enzymatic reactions (Heride et al., 2014). The initial step involves transfer

of ubiquitin onto an E1 activating enzyme, which is driven by ATP. Ubiquitin is then transferred onto an E2 conjugating enzyme. The final step of the cascade involves the transfer of ubiquitin onto a lysine residue in the substrate which is mediated by an E3 ligase (Heride et al., 2014).

Ubiquitin itself contains several lysine (K) residues (K6, K11, K27, K29, K33, K48, K63), facilitating the formation of different types of ubiquitin chains. In addition, polyubiquitin may also be assembled by ubiquitylation at the N-terminal methionine (Met1) of successive ubiquitin moieties (Swatek and Komander, 2016). These polyubiquitin chains can consist of a single type of lysine site linkage or mixed chains, which can be linear or branched. This diversity in polyubiquitin chains is termed the 'ubiquitin code' and has been shown to confer a layer of specificity with respect to the downstream cellular signal. For instance, the most common chain type is K48-linked, which targets proteins for degradation by the proteasome. Whereas, K63-linked chains act as a signal for autophagy, intracellular trafficking and non-degradative processes such as NF-kB (nuclear factor kappa-light-chain-enhancer of activated B cells) signalling (Akutsu et al., 2016; Clague et al., 2015; Damgaard, 2021).

Opposing the E1-E2-E3 cascade, deubiquitylases (DUBs) function in the removal of ubiquitin from substrates. Over 99 DUBs exist, many of which exhibit chain type-selectivity (Clague et al., 2019). Removal of ubiquitin by DUBs provides two main functions, controlling ubiquitin-mediated signalling and degradation and replenishing a cytosolic pool of free ubiquitin for future conjugation reactions.

1.3.2 Ubiquitin proteasome system

The proteasome is a multi-protein complex composed of a 20S core particle and one or two 19S regulatory particles which function in substrate protein degradation and recognition, respectively (Collins and Goldberg, 2017). As discussed, the addition of polyubiquitin chains onto substrates serves as the main signal for targeting for proteasomal degradation (Finley, 2009). Degradation by the UPS functions to degrade misfolded proteins and control the levels of certain proteins within the cell. Therefore, the UPS is a major determinant of protein half-life, with some proteins having half-lives of minutes and others over 100 hours (Pohl and Dikic, 2019; Rusilowicz-Jones et al., 2022). Degradation via the UPS is limited by substrate size and so an alternative mechanism is required for degradation of larger substrates, such as protein aggregates, pathogens and organelles (Pohl and Dikic, 2019). Herein lies the role of autophagy.

1.3.3 Autophagy

Autophagy describes the process by which cytoplasmic material (e.g. proteins, pathogens or organelles) is degraded via the lysosome to maintain homeostasis (Galluzzi et al., 2017). Three types of autophagy have been described, microautophagy, chaperone mediated autophagy and macroautophagy (Galluzzi et al., 2017).

Microautophagy is the process by which the lysosome engulfs cytoplasmic content directly via membrane invagination (Galluzzi et al., 2017). Like in the endocytic degradative pathway, microautophagy requires the ESCRT machinery for inward budding of the lysosomal membrane (Galluzzi et al., 2017). Degradation of cytoplasmic proteins via microautophagy may occur in bulk or selectively following substrate recognition by HSC70 (Galluzzi et al., 2017).

Chaperone-mediated autophagy (CMA) involves the delivery of cytosolic proteins directly into the lysosome via the action of a HSC70-LAMP2A complex. The cytosolic chaperone protein HSC70 recognises a KFERQ motif on cytosolic proteins and, together with several other cochaperones, unfolds the CMA substrate and directs it to the cytosolic region of LAMP2A on the lysosomal membrane (Yim and Mizushima, 2020). Association between HSC70, the CMA substrate and LAMP2A triggers the formation of a multimeric LAMP2A complex which forms a pore through which the CMA substrate is translocated into the lysosomal lumen where it is degraded by lysosomal proteases (Yim and Mizushima, 2020).

Macroautophagy is the best characterised form of autophagy and involves the engulfment of cytoplasmic material by a double-membraned vesicle, termed an autophagosome, which fuses with the lysosome to degrade its contents (Yang and Klionsky, 2010). This can be either non-selective, where cytoplasmic content is degraded at random in response to nutrient starvation, or selective, where specific cargo is targeted for degradation (Vargas et al., 2023). Selective autophagy, hereafter named autophagy, mediates the removal of specific nutrients, proteins, pathogens and organelles, with each pathway named according to their target: glycophagy (glycogen), ferritinophagy (ferritin), aggrephagy (RNA or protein aggregates), xenophagy (intracellular pathogens), lipophagy (lipid droplets), mitophagy (mitochondria), pexophagy (peroxisomes), lysophagy (lysosomes), ribophagy (ribosomes), ER-phagy (endoplasmic reticulum), Golgiphagy (Golgi) (Nthiga et al., 2021; Vargas et al., 2023).

Autophagy is orchestrated by the AuTophaGy-related (ATG) proteins, which are evolutionarily conserved from yeast to mammals (Nakatogawa, 2020; Tsukada and Ohsumi, 1993). The 20 core ATG proteins can be sub-classified into six functional groups which, in mammals, comprise the ULK kinase complex, ATG9A-containing vesicles, the autophagy specific class III PI3K complex I, the ATG2-WD repeat protein interacting with phosphoinositides (WIPI) complex, the ATG16L1 complex, and the Atg8-protein lipidation system (**Table 1.1**). These proteins co-ordinate autophagosome biogenesis, which can be divided into five main steps: initiation, nucleation, expansion, closure, and maturation.

Table 1.1 Mammalian ATG proteins that form the core autophagy machinery
(Nakatogawa, 2020; Van Vliet et al., 2022)
ATG, autophagy- related; BECN1, beclin 1; ER, endoplasmic reticulum; FIP200, focal adhesion kinase family interacting protein of 200 kDa; GABARAP, GABA receptor-associated protein; GABARAPL, GABARAP-like; LC3, microtubule-associated protein light chain 3; NRBF2, nuclear receptor-binding factor 2; p150, protein of 150 kDa; PE, phosphatidylethanolamine; PI3K, phosphatidylinositol 3-kinase; PI(3)P, phosphatidylinositol 3-phosphate; Ub, ubiquitin; ULK, unc-51-like kinase; WIPI, WD repeat interacting with phosphoinositides.

Protein		Function
ULK complex		**Initiation of autophagy, recruitment of downstream autophagy machinery**
	ULK1/2	Ser/Thr kinase
	FIP200	Scaffolding protein
	ATG13	Complex formation
	ATG101	Complex stabilisation
ATG9A-containing vesicles		**Generation and expansion of phagophore**
	ATG9A	Vesicle targeting, lipid scramblase
PI3K complex I		**Generation of PI(3)P on the phagophore**
	VPS34	Class III PI 3-kinase
	BECN1	Complex stabilisation
	ATG14L	Complex targeting
	p150	Ser/Thr kinase
	NRBF2	Complex stabilisation
ATG2-WIPI complex		**Phagophore expansion**
	ATG2A/B	ER-phagophore tethering, lipid transfer
	WIPI1/2/3/4	PI(3)P effector, ATG16L1 complex recruitment, ATG2 recruitment
ATG16L1 complex		**Orchestrating ATG8-family lipidation**
	ATG5	Conjugates ATG12
	ATG7	E1 for ATG12 and ATG8-family proteins

	ATG10	E2 for ATG12
	ATG12	Ub-like protein
	ATG16L1	Complex targeting
ATG8-family lipidation system		**Cargo recognition, phagophore expansion**
	LC3A/B/C, GABARAP, GABARAPL1/2	Ub-like molecule conjugated to PE on phagophore
	ATG4A/B/C/D	C-terminal processing of ATG8-family proteins, ATG8-family delipidation
	ATG7	E1 for ATG8-family proteins
	ATG3	E2 for ATG8-family proteins

1.3.3.1 Autophagosome biogenesis

At the site of autophagosome biogenesis, an autophagosome precursor membrane develops, which grows and bends until it completely englobes the autophagy substrates, forming a mature autophagosome. The autophagosome then fuses with late endosomes or lysosomes to mediate the degradation of its contents (**Figure 1.8**).

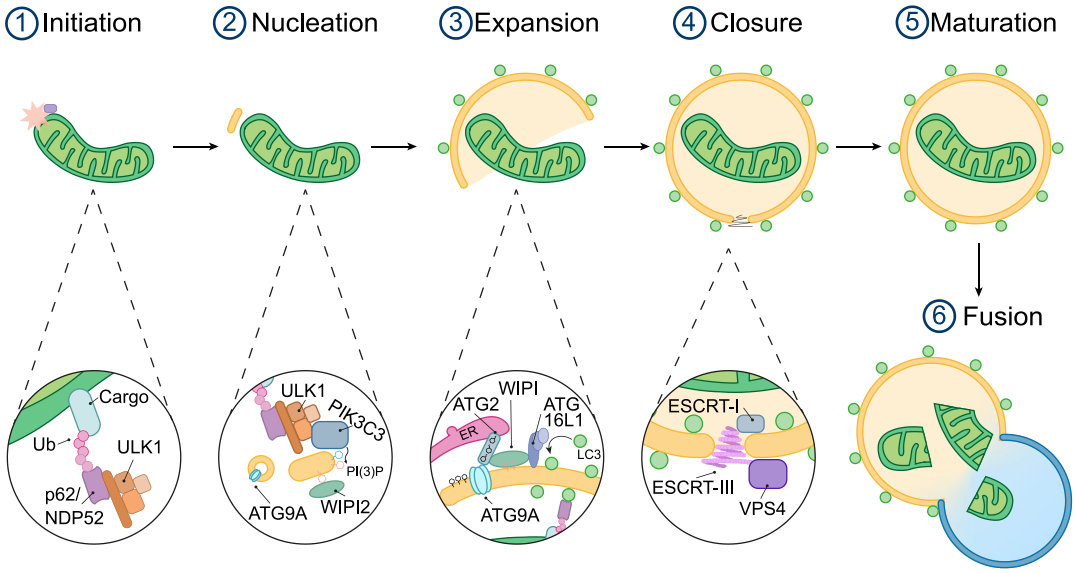

Figure 1.8 Stages of selective autophagy

Autophagy receptors (e.g. p62, NDP52) bind to ubiquitylated substrate cargo and FIP200 of the ULK1 complex. Autophagosome biogenesis commences as the ULK1 complex recruits the PI3K complex. The PI3K subunit VPS34 generates PI(3)P on the phagophore. ATG9A vesicles localise to the site of autophagosome biogenesis and are thought to provide the initial progenitor membrane. PI(3)P recruits the WIPI family of proteins to the phagophore which, in turn, recruit ATG2 and the ATG16L1 complex. The phagophore expands by receiving lipids from the ER via the ATG2-ATG9A lipid transporter complex. During expansion, the ATG16L1 complex mediates the conjugation of LC3 to the phagophore. Closure of the phagophore is orchestrated by the ESCRT machinery, forming a mature autophagosome. In the final stage of autophagy, the autophagosome fuses with a lysosome to allow degradation of the autophagic substrates.

In general, during selective autophagy, the accumulation of ubiquitin chains on cargo provides a signal for the initiation of autophagy. This recruits selective autophagy receptors such as nuclear dot protein 52 kDa (NDP52), optineurin (OPTN) and p62 (also known as sequestosome 1, SQSTM1). The selective autophagy receptors contain a ubiquitin-binding domain and a microtubule-associated protein light chain 3 (LC3)-interacting region (LIR) domain (Vargas et al., 2023). An exception is the case of the selective autophagy receptors BCL2-interaction protein 3 (BNIP3) and BNIP3-like (BNIP3L, also known as NIX) which lack a ubiquitin binding domain and instead insert directly into membrane of mitochondria and peroxisomes (Barone et al., 2023; Hanna et al., 2012; Novak et al., 2010; Wilhelm et al., 2022). The selective autophagy receptors also recruit the ULK complex via an interaction with FIP200 (Nakatogawa, 2020; Turco et al., 2020). The close assembly of multiple ULK complexes promotes their auto-activation and the recruitment and activation of downstream ATG machinery (Turco et al., 2020).

Recruitment of the PI3K complex promotes autophagosome biogenesis. The VPS34 subunit of the PI3K complex phosphorylates PtdIns to PI(3)P on the phagophore. In selective autophagy, it is believed that the phagophore forms *de novo* (Melia et al., 2020). The generation of a pool of PI(3)P facilitates the recruitment of the PI(3)P effector proteins WIPI1-4 (Bakula et al., 2017; Polson et al., 2010). Interaction of WIPI2b with ATG16L1 facilitates the recruitment of the ATG16L1 complex to the site of autophagosome biogenesis, whereas WIPI4 forms a complex with the lipid transfer protein ATG2A (Bakula et al., 2017; Dooley et al., 2014). In selective autophagy, the ULK1 complex and selective autophagy receptors also function as a scaffold for the recruitment of WIPIs, the ATG16L1 complex and the PI3K complex (Mercer et al., 2018).

ATG9A-containing vesicles originating from the *trans*-Golgi network localise to the site of autophagosome formation, however their exact role is not fully understood. It is debated whether they act as an initial seed for phagophore formation, serve as a membrane source for phagophore expansion, or whether they simply deliver components necessary for the progression of autophagy (Melia et al., 2020; Sawa-Makarska et al., 2020). A complex between ATG2A and ATG9A has recently been shown to function in the expansion of the phagophore (Van Vliet et al., 2022). ATG2A acts as a lipid shunt from donor membranes to the phagophore which then reach the lipid scramblase ATG9A on the phagophore that incorporates the incoming lipids into the membrane, allowing growth of the phagophore.

A critical step in phagophore expansion is the recruitment of LC3, which relies on a ubiquitin-like conjugation system. LC3 (and its other family members, GABARAP and GABARAPL1/2) exist in the cytosol in an unlipidated pro-form which is cleaved by the cysteine protease ATG4 to form LC3-I. Upon initiation of autophagy, the E1-like protein ATG7, E2-like protein ATG3 and E3-like protein ATG16L1 act to conjugate LC3 to the lipid phosphatidylethanolamine (PE) in the phagophore membrane (Nakatogawa, 2020). This lipidated form of LC3 (LC3-II) is thought to promote further expansion of the phagophore by recruiting additional ATG machinery, including ULK1 (Nakatogawa, 2020). In selective autophagy, the selective autophagy receptors bind to LC3, forming a bridge between the substrate and the autophagosome.

Eventually, the phagophore almost completely encloses the autophagic substrates, with only a small pore remaining. The closure of this pore is mediated by the ESCRT machinery (Nakatogawa, 2020).

Fully-formed autophagosomes then fuse with late endosomes or lysosomes to form amphisomes or autolysosomes, respectively (Galluzzi et al., 2017). This fusion is facilitated by much the same process as endosome-lysosome fusion. The autophagosome and lysosome are brought into close apposition by a tethering complex and the two membranes fuse through the action of a SNARE complex. Tethering of autophagosomes and lysosomes is facilitated by the concerted action of the HOPS complex, PLEKHM1 and EPG5 (Yim and Mizushima, 2020). Both PLEKHM1 and EPG5 tether the autophagosome to the endolysosome via an interaction with GTP-bound Rab7 (Yim and Mizushima, 2020). Therefore, activation and localisation of Rab7 to endolysosomes is key for autophagy progression. Following the coalescence of the autophagosome and the lysosome, autophagy substrates are degraded by the action of lysosome luminal hydrolases and proteases (Galluzzi et al., 2017).

An additional important step in autophagy is autophagic lysosome reformation (ALR) which functions to replenish the pool of functional lysosomes. This involves the formation of tubules emanating from the autolysosome, which then sever from the main vacuolar body and form proto-lysosomes, which ultimately become new lysosomes (Yim and Mizushima, 2020).

1.3.3.2 Non-canonical autophagy

An alternative pathway for degradation is ‘non-canonical’ autophagy, which has the unique feature that ATG8 family members are conjugated directly onto the single membrane of the target endolysosome or lysosome-related organelle. As such, non-

canonical autophagy is termed CASM (Conjugation of ATG8s to Single Membranes). Initiation and progression of CASM is independent of much of the initial autophagy machinery, including the ULK kinase complex, PI3K complex I and the ATG2-WIPI complex. However, they share the later proteins required for Atg8-family lipidation, the ATG16L1 complex and the ATG8 conjugation machinery (Durgan and Florey, 2022).

Several pathways have been shown to activate CASM, including LC3-associated phagocytosis and entosis, where cells are engulfed and degraded by a neighbouring cell. CASM can also be activated pharmacologically using drugs that disrupt the lysosomal pH and ion concentration, including ionophores, TRPML1 agonists and the lysosome-rupturing agent L-leucyl L-leucyl methyl ester (LLOMe) (Durgan and Florey, 2022). These stimuli are thought to converge on a unifying mechanism whereby they induce pH or ionic imbalances within endolysosomes, which drives engagement of V_0 and V_1 subunits of the v-ATPase (Durgan and Florey, 2022). The assembled v-ATPase then recruits ATG16L1 to the lysosomal membrane (Fletcher et al., 2018). Like in canonical autophagy, ATG16L1 targets LC3 to the site of autophagy. However, a unique feature of CASM is that LC3 is conjugated not only to phosphatidylethanolamine (PE), but also phosphatidylserine (PS) (Durgan et al., 2021). The LC3 on the endolysosomal vesicle promotes fusion with functional lysosomes to enable their degradation (Martinez et al., 2015)

1.4 Multi-layered organelle quality control

Quality control within cells is critical for homeostasis and cell survival, and can be achieved at a molecular, organellar and cellular level. The action of the ubiquitin-proteasome and autophagic systems play a key role in achieving this, discussed above (**Section 1.3**). Given the importance of being able to respond to a changing environment or potential harm, it is perhaps unsurprising that quality control is multi-faceted. This allows different degrees and types of damage to be responded to appropriately. It also provides a fail-safe mechanism if one pathway goes wrong or is overcome. Multiple, hierarchical mechanisms exist at both the mitochondria and lysosome to maintain homeostasis and respond to damage, providing a multi-layered system of organelle quality control.

1.4.1 Maintaining lysosomal homeostasis

In addition to being the terminal compartment for the endocytic and autophagic pathways, lysosomes play a critical role in nutrient sensing, cholesterol homeostasis

and immunity (Papadopoulos et al., 2020; Yang and Tan, 2023). As such, lysosomes are highly dynamic and undergo continual remodelling of their size, distribution, and composition to adjust to the changing needs of the cell. Given their importance to cellular homeostasis, damage to lysosomes can have catastrophic consequences, including cell death (Boya and Kroemer, 2008). To prevent this, multiple mechanisms exist to repair and remove dysfunctional lysosomes and replace the lysosomal pool (**Figure 1.9**).

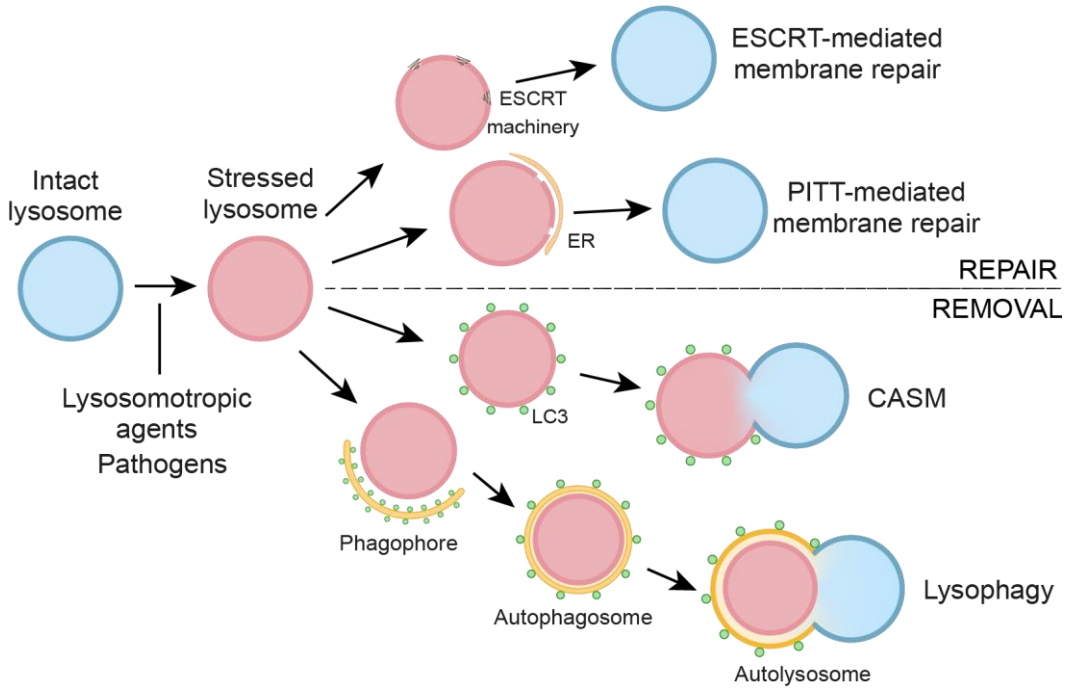

Figure 1.9 Multi-layered lysosomal quality control

When lysosomes become damaged the leakage of lysosomal hydrolases into the cytosol can have catastrophic consequences. If the damage is limited, lysosomes may be repaired. Repair of the lysosomal membrane can occur via membrane closure by the ESCRT machinery or via the phosphoinositide-initiated membrane tethering and lipid transport (PITT) pathway which delivers additional lipids and cholesterol to the lysosome from the endoplasmic reticulum (ER). If the damage is extensive, the lysosomes must be removed. The autophagic clearance of damaged lysosomes may be executed by the canonical autophagy machinery (lysophagy). Alternatively, LC3 may be conjugated directly onto the lysosomal membrane to activate clearance by CASM.

1.4.1.1 Lysosome biogenesis and distribution

Lysosomes are highly dynamic organelles which respond to the changing needs of the cell. The number of lysosomes and their positioning within the cell are altered in response to an assortment of different stimuli, including changes in pH or nutrient availability and lysosomal damage (Willett et al., 2017; Zoncu and Perera, 2022).

Lysosomes are trafficked throughout the cell along microtubules and, in general, form two populations – a highly mobile, peripheral population and largely static pool located perinuclearly at the microtubule organising centre (Zoncu and Perera, 2022). In nutrient-replete conditions and when the extracellular pH is acidic, lysosomes are peripherally distributed (Cabukusta and Neefjes, 2018; Rozhin et al., 1994). Upon nutrient starvation and lysosomal damage, lysosomes cluster in the perinuclear area, which is thought be critical for autophagosome-lysosome fusion (Cabukusta and Neefjes, 2018; Kluss et al., 2022; Korolchuk et al., 2011; Willett et al., 2017). Several different protein complexes have been discovered that link lysosomes to the motor proteins dynein/dynactin and kinesin to mediate their anterograde and retrograde transport, respectively. For anterograde transport to the perinuclear area, these complexes include Rab7:RILP, TRPML1:ALG2 and TMEM55B:JIP4. Retrograde transport of lysosomes to the periphery is mediated by Arl8 and its effector SKIP, and Rab7 and FYCO1 (Cabukusta and Neefjes, 2018). Recent evidence also suggests that the Rab8A/Rab10/Rab12 effector RILPL1 can function in anterograde lysosome transport, possibly in a complex with TMEM55B (Ito et al., 2023; Pal et al., 2023).

Lysosome biogenesis is controlled at the transcriptional level by the microphthalmia/transcription factor E (MiT/TFE) family of transcription factors, which in humans comprise MiTF, TFE3, TFEB and TFEC (Zoncu and Perera, 2022). The constitutive inactivation of MiT/TFE factors is mediated by mammalian target of rapamycin complex 1 (mTORC1). In turn, the activity of mTORC1 is controlled by a multi-subunit complex at the lysosome, consisting of v-ATPase, a dimer of Rag GTPases (RagA/B and RagC/D), the RagA/B GEF Ragulator, the RagA/B GAP GATOR1, the RagC/D GEF folliculin (FLCN)/ folliculin interacting protein (FNIP) complex, and Rheb GTPase (Yang and Wang, 2021). In nutrient-replete conditions, TFEB is phosphorylated in an mTORC1-dependent manner which promotes its association with 14-3-3 chaperone proteins, retaining it in the cytosol (Martina et al., 2012). In response to nutrient starvation, mTORC1 dissociates from the Rags at the lysosome and is inactivated. mTORC1 is therefore unable to phosphorylate MiT/TFE factors, leading to their nuclear translocation. MiT/TFE factors can also be dephosphorylated and activated by calcineurin and protein phosphatase 2A (PP2A) in response to calcium efflux (Yang and Tan, 2023). All MiT/TFE family members bind to CLEAR (Coordinated Lysosomal Expression and Regulation) sites in DNA, which are present in multiple lysosomal genes and genes involved in autophagy, exocytosis and endocytosis to promote their transcription and facilitate lysosome biogenesis

(Palmieri et al., 2011; Sardiello et al., 2009; Settembre et al., 2011; Settembre and Ballabio, 2014).

1.4.1.2 Lysosome repair

A number of different agents can cause a disruption to lysosome membrane integrity, including lysosomotropic dipeptide drugs, silica, changes in lysosome cholesterol composition and amyloid-β aggregates (Vargas et al., 2023). Disruption of the lysosomal membrane risks the leakage of hydrolytic enzymes into the cytosol, which can damage other organelles and cause cell death (Boya and Kroemer, 2008; Bussi et al., 2022). Two pathways have been identified that act to repair these breaks: the ESCRT pathway and the PITT pathway.

Treatment with silica crystals, pathogens and the lysosomotropic agent LLOMe trigger the recruitment of ESCRT machinery components to the sites of lysosomal membrane damage (López-Jiménez et al., 2018; Radulovic et al., 2018; Skowyra et al., 2018). Lysosomal membrane permeabilization leads to calcium ion efflux, which causes the recruitment of the calcium binding protein apoptosis-linked gene 2 (ALG2) to the lysosomal membrane which, in turn, recruits the ESCRT-I component TSG101 and the accessory protein ALIX (Shukla et al., 2022; Skowyra et al., 2018). Recruitment of either of these ESCRT machinery components facilitates the assembly of the ESCRT-III machinery and VPS4 at the sites of damage, which function to seal and repair the membrane hole (Radulovic et al., 2018; Shukla et al., 2022; Skowyra et al., 2018). The ESCRT machinery can also be recruited by galectin-3 (Gal3), a protein which binds to exposed carbohydrates in the lysosomal lumen following lysosome membrane damage (discussed in further detail in **Section 1.4.1.3**) (Jia et al., 2020). Gal3-dependent ESCRT recruitment is proposed to act in a secondary slower phase of ESCRT-mediated membrane repair following the acute, Ca^{2+}-dependent phase (Jia et al., 2020). It has also been shown that leucine-rich repeat kinase 2 (LRRK2) and Rab8a are required for the recruitment of ESCRT-III components to sites of lysosomal damage, however how LRRK2 and Rab8a regulate ESCRT-mediated membrane repair is not yet understood (Herbst et al., 2020).

In the absence of ESCRT machinery components, damaged lysosomes still undergo membrane repair, suggesting that alternative repair mechanisms must exist (Radulovic et al., 2018; Skowyra et al., 2018). Indeed, a second membrane repair pathway involving cholesterol and phosphatidylserine (PS) transfer from the endoplasmic reticulum (ER) has recently been discovered by two independent groups (Radulovic et al., 2022; Tan and Finkel, 2022). This pathway is termed the

phosphoinositide-initiated membrane tethering and lipid transport (PITT) pathway. One group used a lipidomic approach to identify that lysosomes became enriched for PS and cholesterol following treatment with LLOMe (Radulovic et al., 2022). Coming from a different angle, the other group used unbiased proteomics to identify that treatment with LLOMe lead to an increase in phosphatidylinositol 4-Kinase Type 2 Alpha (PI4K2A) and the PI(4)P effectors ORP9 and 11 (Tan and Finkel, 2022). Following these findings, both groups discovered a mechanism by which LLOMe treatment activates PI42KA to phosphorylate PI, generating PI(4)P on the lysosomal membrane. This recruits the PI(4)P effectors ORP9, ORP10, ORP11, ORPL1 and OSBP, which interact with VAPA/B on the endoplasmic reticulum to form ER-lysosome contact sites. These membrane tethering complexes mediate the transfer of PI(4)P from the lysosome to the ER, and PS and cholesterol from the ER to the lysosome. Accumulation of PS on the lysosome recruits and activates ATG2 which transfers lipids from the ER to the lysosome to generate new lysosomal membrane (Tan and Finkel, 2022). It is not completely understood how cholesterol mediates membrane repair, however it has been suggested that it may be due to cholesterol's ability to increase membrane stability and rigidity (Tan and Finkel, 2022).

1.4.1.3 Lysosome turnover

Lysosomal membrane proteins can be degraded by being internalised into the lysosome in a manner akin to the ubiquitin- and ESCRT-dependent endocytic degradative pathway (Zhang et al., 2021). This mechanism allows the lysosome membrane proteome to be remodelled according to the changing needs of the cell. The ESCRT-mediated membrane repair pathway (**Section 1.4.1.2**) is also proposed to remove damaged parts of the lysosomal membrane and the resident proteins via internalisation into intra-luminal vesicles (Zoncu and Perera, 2022).

In response to glucose starvation or osmotic stress, lysosomes can internalise specific lysosomal membrane proteins via microautophagy to regulate lysosome size and protein composition (Lee et al., 2020). This process is dependent on LC3 conjugation to the lysosome but does not require the canonical autophagy machinery (Lee et al., 2020). How LC3 triggers the internalisation of these vesicles is not understood.

If the damage to the lysosomes is too extensive and therefore irreparable, lysosomes can be selectively removed by autophagy, so-called lysophagy. This can occur through both canonical and non-canonical mechanisms. Osmotic imbalance, pore-forming toxins, LLOMe and TRPML1 activation can all activate non-canonical

autophagy mechanisms at the lysosome (Cross et al., 2023; Durgan and Florey, 2022). These different stimuli cause ionic or pH imbalances within the lysosomal lumen which trigger the assembly of v-ATPase complexes on the lysosomal membrane. The increased V_0-V_1 assembly of the v-ATPase pump can attempt to correct the pH imbalance but, more critically, recruits ATG16L1, driving lipidation of LC3 on the lysosomal membrane (Durgan and Florey, 2022; Hooper et al., 2022). The LC3-decorated then fuses with lysosomes to degrade its content.

Multiple different mechanisms mediating canonical autophagy have been identified but share two common features – they are initiated by galectin binding and are ubiquitin-dependent. Permeabilisation of the lysosomal membrane exposes the glycosylated luminal tails of lysosomal transmembrane proteins which triggers the recruitment of a subset of galectins (Gal), a family of carbohydrate-binding lectin proteins (Aits et al., 2015). The galectins recruited to the lysosome following permeabilization are galectin-1, galectin-3, galectin-8 and galectin-9 (Aits et al., 2015). The binding of different galectins appears to confer diversity in the response to lysosomal damage, with Gal3 functioning in lysosomal repair and lysophagy, and Gal8 functioning in lysophagy and lysosome biogenesis (Jia et al., 2020, 2018; Thurston et al., 2012).

Gal8 has been shown to interact directly with the selective autophagy receptor NDP52 to promote autophagosome formation (Thurston et al., 2012). Gal3 recruits the ULK1 machinery and interacts with the E3 ligases Tripartite Motif Containing 16 (TRIM16) and F-box only with uncharacterized domains 27 (FBXO27), which ubiquitylate the luminal tails of lysosomal proteins such as LAMP1, LAMP2 and TMEM192 (Chauhan et al., 2016; Yoshida et al., 2017). The ubiquitin chains recruit multiple autophagy receptors to drive lysophagy, including p62, OPTN, NDP52 and TAX1BP1 (Bussi et al., 2018; Eapen et al., 2021; Koerver et al., 2019; Yoshida et al., 2017). The formation of both K63-linked and K48-linked ubiquitin chains have been observed at sites of lysosomal damage and both are critical for lysophagy to proceed, with K63-linked chains appearing during an acute phase and K48-linked forming over a longer time frame (Koerver et al., 2019; Papadopoulos et al., 2017). The E2 enzyme UBE2QL1 orchestrates the formation of both types of ubiquitin chain, but appears to exert a preference for K48 chain formation (Koerver et al., 2019). It has been proposed that K48 chains are important in the removal of lysosomal proteins that may hinder efficient lysophagy (Papadopoulos et al., 2018). Substrates with K48-linked ubiquitin chains are removed by the endo-lysosomal damage response (ELDR) complex, consisting of the AAA-ATPase p97, UBXD1, PLAA and the DUB YOD1 (Papadopoulos et al.,

2018). One such ELDR complex substrate is calponin-2, which is recruited in the acute phase of lysosomal damage and acts to stabilise actin filaments to promote phagophore formation, but must be removed for lysophagy to be accomplished (Kravić et al., 2022)

1.4.1.4 Lysosome regeneration

For the clearance of damaged lysosomes and cell survival, a pool of functional lysosomes must exist. The replenishment of the functional lysosomal pool is primarily mediated by the TFEB-dependent transcription of lysosomal genes. Following disruption of the lysosomal membrane, Gal8 and Gal9 are recruited to the lysosome and converge on a pathway which leads to activation of TFEB (Aits et al., 2015; Jia et al., 2018). Gal8 interacts with the lysosomal Rag-Ragulator complex and suppresses mTOR activity, leading to TFEB activation. Whereas, Gal9 activates AMPK, which inhibits mTOR and, in turn, activates TFEB (Jia et al., 2018).

Lysosome membrane damage or osmotic stress can also lead to calcium-dependent activation of TFEB. Permeabilisation of the lysosomal membrane can lead to loss of calcium from breaks in the lysosome membrane (Skowyra et al., 2018). Alternatively, LC3 conjugated onto the lysosomal membrane has been reported to bind to and activate TRPML1, leading to calcium efflux (Lee et al., 2020). In the cytosol, calcium activates calcineurin, which dephosphorylates TFEB, promoting its translocation to the nucleus (Medina et al., 2015; Nakamura et al., 2020). Furthermore, activation of the TRPML1 channel and CASM have been shown to recruit GABARAP which recruits the FLCN/FNIP complex (Goodwin et al., 2021). This sequesters FLCN/FLIP away from the Rag-Ragulator complex, preventing mTOR activation, which leads to activation of TFEB. It has been proposed that other mechanisms must also exist to trigger FLCN/FLIP sequestration-dependent TFEB activation because the ionophore monensin also causes recruitment of FLCN/FLIP to the lysosome and activation of TFEB, but in a manner independent of TRPML1 and GABARAP (Goodwin et al., 2021).

An additional TFEB-independent mechanism for regeneration of lysosomes has recently been discovered (Bhattacharya et al., 2023). The authors report that in the initial phase of lysosome damage, the Rab7 GAP TBC1D15 is recruited to the lysosome via an interaction with ATG8-family proteins. TBC1D15 then recruits the dynamin-2, clathrin and kinesin-5B to promote the formation of tubules from damaged lysosomes, which then bud off and form proto-lysosomes. This process is akin to the ALR process in autophagy. This provides a biphasic nature to lysosome recovery,

where new lysosomes are initially generated via tubulation and then in a later phase, TFEB-dependent lysosomal biogenesis takes place (Bhattacharya et al., 2023).

1.4.2 Maintaining mitochondrial homeostasis

Given the critical role of the mitochondria within the cell, it is important to ensure their proper functioning. The maintenance of mitochondrial homeostasis is achieved through continual fission and fusion of mitochondrial networks, so-called mitochondrial dynamics. In addition to mitochondrial dynamics, several processes exist to exact quality control: the action of mitochondrial proteases, ubiquitin-mediated proteasomal degradation, mitochondrial derived vesicle (MDV) formation, and mitophagy (**Figure 1.10**). These processes are understood to be largely hierarchical, with the process employed largely depending on the degree and nature of the damage (Sugiura et al., 2014).

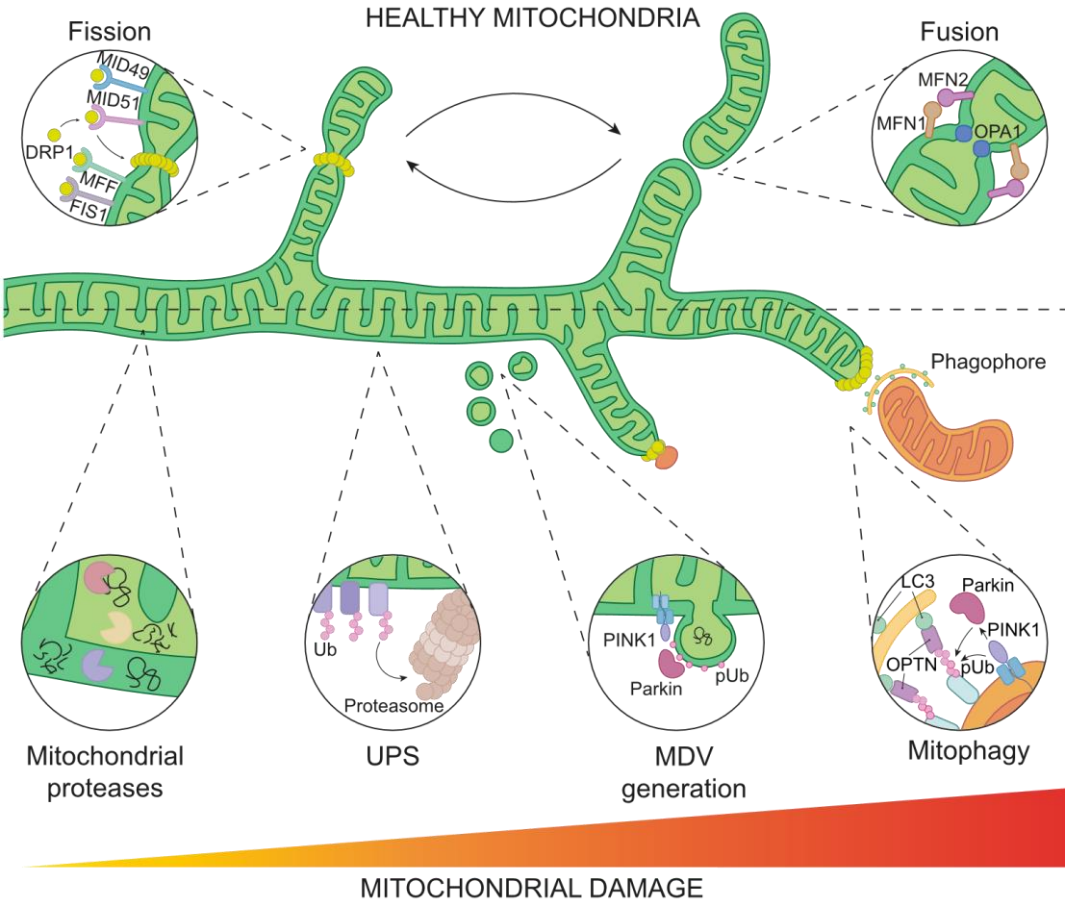

Figure 1.10 Multi-layered mitochondrial quality control

Mitochondrial homeostasis is maintained through a variety of pathways. Mitochondria constantly undergo fusion and fission to respond to metabolic stress, generate new mitochondria and respond to ATP levels. A hierarchical set of pathways exist to maintain mitochondrial quality control. Inner mitochondrial membrane and matrix resident proteases degrade damaged or misfolded proteins. Damaged outer mitochondrial membrane proteins can be targeted for proteasomal degradation by

ubiquitylation. Greater oxidative damage leads to the PINK1/Parkin-dependent generation of mitochondrial-derived vesicles which are trafficked to the lysosome for degradation. More extensive damage leads to mitophagy as a final line of defence. The fission machinery separates the damaged part of the mitochondria from the network. PINK1 is stabilised on damaged mitochondria where it phosphorylates ubiquitin on outer mitochondrial membrane proteins and activates Parkin. The generation of phospho-ubiquitin and ubiquitin chains recruits selective autophagy receptors such as optineurin, which bind LC3 and trigger the autophagic degradation of the mitochondria.
FIS1, mitochondrial fission 1 protein; LC3, microtubule-associated protein 1A/1B-light chain 3; MDV, mitochondrial derived vesicle; MFF, mitochondrial fission factor; MFN1, mitofusin 1; MFN2, mitofusin 2; MID49, mitochondrial dynamics protein of 49 kDa; MID51, mitochondrial dynamics protein of 51 kDa; OPA1, optic atrophy type 1; OPTN, optineurin; PINK1, PTEN induced putative kinase 1; pUb, phospho-ubiquitin; Ub, ubiquitin; UPS, ubiquitin-proteasome system.

1.4.2.1 Mitochondrial dynamics

Mitochondrial fusion is particularly important for the generation of new mitochondria and increasing ATP production under conditions of stress and is orchestrated by Optic Atrophy 1 (OPA1) and the GTPases mitofusin 1 (MFN1) and mitofusin 2 (MFN2) (Farmer et al., 2018). Mitochondrial fission is an important step during cell division and during the removal of mitochondria by mitophagy (Farmer et al., 2018). Fission is carried out by the formation of circular oligomers of dynamin-related protein 1 (DRP1) around mitochondria, which is recruited via the mitochondrial DRP1 receptors mitochondrial fission 1 protein (FIS1), mitochondrial fission factor (MFF) and mitochondrial dynamics protein of 49 and 51 kDa (MID49/MID51) (Farmer et al., 2018).

1.4.2.2 Molecular quality control

To maintain the mitochondrial proteome and remove damaged or incorrectly folded proteins, mitochondrial proteases residing within the mitochondria matrix and intramembrane space act to degrade protein substrates. This process is not well understood and the signals for degradation are not known (Szczepanowska and Trifunovic, 2022).

Mislocalised or damaged proteins on the outer mitochondrial membrane are ubiquitylated by E3 ligases, targeting them for degradation by the UPS. Proteins within the mitochondria can be retrotranslocated to the cytosol via the trans-outer mitochondrial membrane (TOM) complex, making them accessible for ubiquitylation and subsequent proteasomal degradation (Ravanelli et al., 2020).

1.4.2.3 Mitochondrial-derived vesicles

The next layer of quality control at the mitochondria involves the packaging of mitochondrial DNA, proteins and lipids into vesicles, so-called mitochondrial-derived vesicles (MDVs), which are transported to the lysosome for degradation (König et al., 2021; Soubannier et al., 2012a).

Generation of MDVs occur at steady state and is upregulated in response to oxidative stress to remove damaged material (Cadete et al., 2016; Soubannier et al., 2012b). MDVs are also involved in the trafficking of proteins to peroxisomes for homeostasis and biogenesis (Neuspiel et al., 2008; Sugiura et al., 2017). The composition, constituents and mechanism of generation of MDVs alters according the stressor and the target destination (König et al., 2021; McLelland et al., 2014; Soubannier et al., 2012b). MDVs can contain just the outer mitochondrial membrane or include the inner mitochondrial membrane and matrix (Sugiura et al., 2014). TOM complexes, voltage-dependent anion channels (VDAC) and the matrix protein PDH are example cargoes of lysosome-targeted MDVs (König et al., 2021; Soubannier et al., 2012a). Whereas, MDVs destined for the peroxisome are enriched with the mitochondrial outer membrane protein MUL1 (Mitochondrial E3 ubiquitin protein ligase 1) (Neuspiel et al., 2008). Mitochondria MDVs may also contain mitochondrial DNA nucleoids for degradation which, when released from the mitochondria, active the cGAS-STING innate immune response pathway (Zecchini et al., 2023).

The steady-state generation of MDVs involves the generation of tubules which emanate from mitochondria and undergo DRP1-dependent scission to form vesicles which are transported to the lysosome along microtubules (König et al., 2021). In response to stress, PINK1 and Parkin drive the generation of MDVs towards the lysosome, a process which precedes mitophagy (**Section 1.4.2.4 below**) (McLelland et al., 2014). This process requires Rab9, the SNARE syntaxin17, and vesicle scission occurs independently of DRP1 (Matheoud et al., 2016; McLelland et al., 2016, 2014). Retromer has also been implicated in the MDV trafficking pathway. Retromer is required for MDV trafficking to peroxisomes and mutations in retromer have been shown to increase turnover of DRP1 via MDVs destined for the lysosome (Braschi et al., 2010; Wang et al., 2016).

1.4.2.4 Mitophagy

When the damage to mitochondria is widespread, or the preceding quality control mechanisms have failed, entire dysfunctional mitochondria are selectively removed by mitophagy. Multiple different mitophagy pathways have been identified, which can

occur basally, or in response to varying stimuli. Iron depletion and hypoxia drive the transcription of BNIP3 and NIX, which localise to the mitochondrial membrane and bind to LC3 (Ganley and Simonsen, 2022; Li et al., 2021). Mitochondrial depolarisation can trigger mitophagy via multiple pathways, which can be Parkin-dependent or independent (Ganley and Simonsen, 2022). The most intensively studied of these is the PINK1/Parkin mitophagy pathway.

Basally, PTEN induced putative kinase 1 (PINK1) is continually imported into the mitochondria via the TOM complex, where it is cleaved by the inner mitochondrial membrane protease presenilins-associated rhomboid-like protein (PARL), released into the cytosol, and then degraded via the UPS (Greene et al., 2012; Jin et al., 2010; Narendra et al., 2010; Yamano and Youle, 2013). Upon mitochondrial depolarisation, PINK1 import fails, leading to the accumulation of full-length PINK1 on the mitochondrial membrane where it phosphorylates the serine 65 (Ser65) residue of ubiquitin moieties conjugated to outer mitochondrial membrane proteins (Kane et al., 2014; Kazlauskaite et al., 2015; Koyano et al., 2014). Phospho-ubiquitin recruits the E3 ligase Parkin to the mitochondria, which is then phosphorylated by PINK1 to become fully active (Pollock et al., 2021). The accumulation of ubiquitin and phospho-ubiquitin chains on the mitochondria recruits specific autophagy receptors, such as OPTN, p62 and NDP52, initiating mitophagy (Lazarou et al., 2015).

1.5 Parkinson's Disease

In 1817, James Parkinson published 'An Essay on the Shaking Palsy' on six subjects suffering from an as yet unclassified neurological condition that caused progressively worsening motor ability (Parkinson, 2002). Parkinson meticulously described the symptoms of each case, which included a resting tremor, stooped posture, and a shortened and shuffling gait, alongside non-motor symptoms including sleep disturbance, constipation, dysphagia. In acknowledgement of this seminal work, Jean-Martin Charcot, considered the father of neurology, suggested this condition be named 'Parkinson's Disease' (Obeso et al., 2017).

Parkinson's disease (PD) is estimated to affect 1% of the population over 60 years of age, making it the second most common neurodegenerative disorder (Reeve et al., 2014). Although primarily a movement disorder, PD is characterised by both motor and non-motor symptoms. The motor symptoms include the four cardinal features of PD: resting tremor, rigidity, bradykinesia, and postural instability. PD is progressive, and symptoms worsen through the course of the disease.

1.5.1 Cellular pathology

The cellular hallmarks of PD are the selective loss of dopaminergic neurons in the substantia nigra *pars compacta* (SNpc) and the presence of intra-neuronal and intra-axonal inclusions containing α-synuclein (Lewy bodies and Lewy neurites) (Antony et al., 2013; Spillantini et al., 1997). The substantia nigra lies within the midbrain and is an area rich in the pigment neuromelanin, which gives the region its characteristic dark appearance (**Figure 1.11**). A loss of pigmentation in the substantia nigra is a key feature in the brains of PD patients. The SNpc sub-region is a component of the basal ganglia, which functions in motor control. In PD, atrophy of dopaminergic neurons within the SNpc causes disruption to the neurocircuitry of the basal ganglia, leading to loss of motor co-ordination, giving rise to the key motor symptoms of the disorder (Bove and Travagli, 2019).

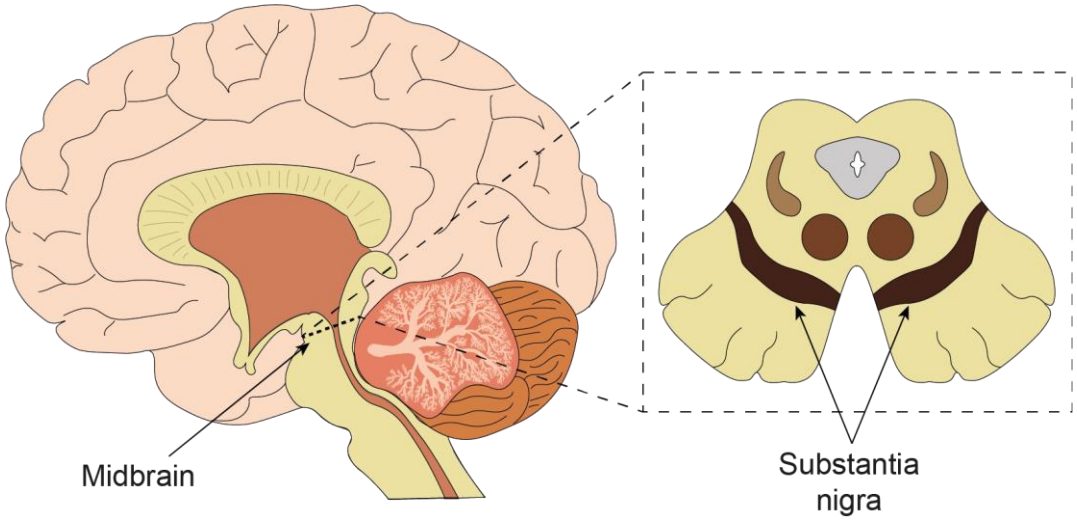

Figure 1.11 The substantia nigra
The substantia nigra is located within the midbrain and is a component of the basal ganglia. It has a characteristic dark appearance due to the abundance of the pigment neuromelanin. In Parkinson's disease, dopaminergic neurons within the substantia nigra degenerate, and this pigmentation is lost.

1.5.2 Aetiology and the genetic basis of Parkinson's Disease

The aetiology of Parkinson's disease is not well understood. Environmental exposure, genetic predisposition and epigenetics all appear to play a part in development of PD (van Heesbeen and Smidt, 2019). Study of environmental toxicants, such as paraquat and rotenone, and PD-linked genes has implicated several processes in PD pathology; mitochondrial function, endolysosomal trafficking, autophagy, protein degradation and oxidative stress (Ebanks et al., 2020).

In approximately 10% of cases, PD is inherited in a Mendelian fashion, with a single gene mutation leading to the development of PD (Karimi-Moghadam et al., 2018). A number of causal genes have been identified, and through genome-wide association studies several other gene loci have been linked to increased susceptibility (Ebanks et al., 2020; Karimi-Moghadam et al., 2018). These genes can be broadly categorised based on the cellular process they are involved in, and predominately function in endolysosomal trafficking, protein degradation or mitochondrial quality control (**Table 1.2**).

Table 1.2 PD-associated genes and loci

AD, autosomal dominant; AR, autosomal recessive; RF; risk factor.

(Deng et al., 2018; Dolgacheva et al., 2019; Ebanks et al., 2020; Karimi-Moghadam et al., 2018; Klein and Westenberger, 2012; Lesage et al., 2016; Rahman and Morrison, 2019)

PARK loci	Gene	Inheritance	Onset	Physiological function
PARK 1/4	SNCA	AD	Early/ Late	Endolysosomal trafficking/ Protein aggregation/ Autophagy
PARK 2	PRKN	AR	Early	Mitochondrial function and quality control
PARK 5	UCHL1	AD	Late	Ubiquitin-proteasome system
PARK 6	PINK1	AR	Late	Mitochondrial function and quality control
PARK 7	DJ-1	AR	Early	Stress response/ Mitochondrial function and quality control
PARK 8	LRRK2	AD	Late	Endolysosomal trafficking/ Mitochondrial function and quality control
PARK 9	ATP13A2	AD	Early	Endolysosomal trafficking/ Mitochondrial function and quality control
PARK 11	GIGYF2	AD	Late	Insulin signalling
PARK 13	Omi/ HTRA2	AD	Late	Mitochondrial function and quality control / Apoptosis
PARK 14	PLA2G6	AR	Early	Mitochondrial function and quality control / Iron homeostasis
PARK 15	FBXO7	AR	Early	Mitochondrial function and quality control / Ubiquitin-proteasome system
PARK 16	Rab29	RF	Late	Endolysosomal trafficking
PARK 17	VPS35	AD	Late	Endolysosomal trafficking/ Protein aggregation/ Mitochondrial function and quality control / Autophagy
PARK 18	EIF4G1	AD	Late	Protein synthesis
PARK 19	DNAJC6	AR	Early	Endolysosomal trafficking
PARK 20	SYNJ1	AR	Early	Endolysosomal trafficking/ Autophagy
PARK 21	DNAJC13	AD	Early	Endolysosomal trafficking
PARK 21	TMEM230	AD	Late	Endolysosomal trafficking

PARK 22	CHCHD2	AD	Late	Mitochondrial function and quality control
PARK 23	VPS13C	AR	Early	Endolysosomal trafficking/ Mitochondrial function and quality control
-	GBA	AD / RF	-	Lysosomal function/ Protein aggregation
-	Rab39b	RF	-	Synaptic vesicle trafficking
-	DNAJC26	RF	-	Endolysosomal trafficking/ Cellular adhesion
-	SYT11	RF	-	Autophagy / vesicle fusion

1.5.3 Accumulation of protein aggregates

Accumulation of protein aggregates is a hallmark of many neurodegenerative diseases, including Alzheimer's disease, Huntington's disease, Parkinson's disease and amyotrophic lateral sclerosis/motor neuron disease.

The offending protein in PD is α-synuclein (Spillantini et al., 1997). Encoded by the *SNCA* gene, α-synuclein is a small 14.4 kDa (140 amino acids) protein expressed predominantly in the brain (Burré et al., 2018). Highly enriched at the presynaptic terminal, α-synuclein is understood to facilitate vesicle fusion with membranes by promoting SNARE complex assembly via binding to synaptobrevin-2 (Burré et al., 2018; Lin et al., 2019). Monomeric α-synuclein is soluble and not inherently toxic. However, when it forms organised β-sheet structures and fibrils it becomes insoluble, toxic and resistant to degradation (de Oliveira and Silva, 2019; Zhang et al., 2018). These fibrils are also capable of converting native proteins into amyloidogenic forms, thus seeding a 'prion-like' spread of aggregated protein accumulation (Volpicelli-Daley et al., 2011).

An autosomal dominant form of PD can be caused by gene duplication, triplication, or single nucleotide mutation of *SNCA*, the most common being the A53T mutation (Burré et al., 2018; Polymeropoulos et al., 1997). Mutated forms of α-synuclein are more prone to oligomerisation and aggregation and have been shown to cause wide-scale disruption within the cell, impairing mitochondrial function, ER-to-Golgi trafficking, protein degradation and synaptic transmission (Burré et al., 2018; Lin et al., 2019).

1.5.4 Defects in mitochondrial function

Parkinson's disease pathology has been inextricably linked with mitochondrial dysfunction, with evidence coming from idiopathic patient samples, familial forms of the disease and the effects of environmental toxicants (Antony et al., 2013). The

pesticides rotenone and paraquat inhibit complex I of the mitochondrial respiratory chain and have been reported to a cause Parkinson-like syndrome (Wen et al., 2020). Furthermore, in the brains of sporadic patients, the activity of complex I is severely reduced (Bindoff et al., 1989; Schapira et al., 1990). Finally, several genes associated with familial forms of PD are linked with mitochondrial function and homeostasis, including PINK1, PRKN, DJ-1, FBXO7, CHCHD2 and VPS13C (Blauwendraat et al., 2020; Funayama et al., 2015).

PRKN encodes the E3 ligase Parkin which, along with PINK1 kinase, functions in the selective removal of damaged mitochondria by mitophagy (Matsuda et al., 2010; Narendra et al., 2008, 2010). Mutations in PRKN and PINK1 are considered to be loss of function and lead to rare, early-onset, autosomal recessive forms of PD (Blauwendraat et al., 2020). Furthermore, Parkin has been shown ubiquitylate VPS35, which is suggested to regulate retromer function rather than targeting it for proteasomal degradation (Martinez et al., 2017; Williams et al., 2018). VPS35 overexpression ameliorates some parkin-mutant phenotypes in *Drosophila*, including climbing defects and paraquat sensitivity, further supporting a functional interaction between these two proteins (Malik et al., 2015). FBXO7 is a component of an E3 ligase complex which localises to mitochondria and may regulate PINK1/Parkin mitophagy in some cell types (Delgado-Camprubi et al., 2017; Kraus et al., 2023).

Nineteen different mutations in DJ-1 have been linked to autosomal recessive PD (Dolgacheva et al., 2019). Although, it is currently unclear just how DJ-1 mutations cause PD pathogenesis, it is likely related to oxidative stress. Several functions for DJ-1 as a sensor of oxidative stress have been proposed, including limiting the effects of reactive oxygen species (ROS) by upregulating transcription of anti-oxidant genes and acting directly as a ROS scavenger (Lind-Holm Mogensen et al., 2023). A pool of DJ-1 localises to mitochondria and has been suggested to regulate mitochondrial redox responses, dynamics and mitophagy (Di Nottia et al., 2017; Hao et al., 2010; Wang et al., 2012a; Zhang et al., 2005).

VPS13C is a member of the VPS13 family of proteins which facilitate bulk lipid transport between membrane compartments (Kumar et al., 2018; Li et al., 2020). Mutations in VPS13C are thought to result in a loss of function (Lesage et al., 2016). Silencing of VPS13C has been shown to cause mitochondrial fragmentation, reduce mitochondrial function, and promote Parkin-dependent mitophagy (Lesage et al., 2016). These findings implicate VPS13C in mitochondrial dysfunction in relation to PD. However, more recent evidence has demonstrated localisation of VPS13C to ER-

endolysosome contact sites, suggesting it could also play a role in the endolysosomal system (Kumar et al., 2018).

CHCHD2 is a poorly characterised protein which localises to mitochondria and is thought to regulate mitochondrial respiration and morphology (Huang et al., 2018). Under hypoxic conditions and oxidative stress, CHCHD2 is no longer imported into the mitochondria and instead localises to the nucleus, where it acts as a transcription factor to upregulate cytochrome c oxidase levels (Kee et al., 2021). Mitochondrial depolarisation, on the other hand, leads to the stabilisation of CHCHD2 at mitochondria (Huang et al., 2018). PD-causing mutations in CHCHD2 are reported to cause a reduction in CHCHD2 levels, a decrease in mitochondrial complex I and IV activity, and increased ROS levels (Lee et al., 2018).

1.5.5 Defects in the endolysosomal network

Many of the familial and risk factor Parkinson's genes encode proteins which function at different points in the endolysosomal network, highlighting its centrality to PD pathogenesis. Two closely related proteins involved in endocytosis are mutated in familial PD, auxilin and synaptojanin1 (SYNJ1). SYNJ1 is a phosphoinositide phosphatase responsible for the dephosphorylation of $PI(4,5)P_2$ on clathrin-coated endocytic vesicles, a key step in coat disassembly (Cremona et al., 1999; McPherson et al., 1996). Dephosphorylation of $PI(4,5)P_2$ facilitates co-recruitment of auxilin and HSC70 to the vesicular membrane which breaks clathrin-clathrin interactions to promote their shedding (Kaksonen and Roux, 2018).

Loss of SYNJ1 in mammalian cell lines has been shown to result in enlargement of early endosomes, aberrant lysosome morphology and impaired transferrin receptor recycling, suggesting that SYNJ1 may play a more global role in membrane traffic, rather than just at synaptic terminals (Fasano et al., 2018). When the PD-linked [R258Q] mutation is knocked-in to *Drosophila* SYNJ1, PI(3)P and $PI(3,5)P_2$ accumulate at autophagosome membranes, suggesting a possible disruption to autophagy (Vanhauwaert et al., 2017). In an auxilin [R927G] mutant knockin mouse model, clinical PD symptoms were phenocopied, including bradykinesia and gait disturbance (Roosen et al., 2019). At a molecular level, the study showed [R927G] auxilin had impaired interaction with clathrin. Interestingly, LRRK2 phosphorylates auxilin within its clathrin-binding domain at Ser267 (Nguyen and Krainc, 2018). Using LRRK2 mutant patient-derived dopaminergic neurons, they showed that LRRK2 phosphorylation of auxilin interferes with clathrin binding, leading to widescale disruption of the endocytic system; impaired synaptic endocytosis, accumulation of

oxidised dopamine, decreased glucocerebrosidase activity, and accumulation of increased α-synuclein. These phenotypes could be partially rescued by overexpression of wild type auxilin (Nguyen and Krainc, 2018).

Located on the PARK21 locus, *DNAJC13* encodes RME-8 which, as discussed in **Section 1.2.2.4**, functions in endosomal trafficking and maintaining endosomal subdomain identity (McNally and Cullen, 2018; Popoff et al., 2009). Mutations in RME-8 have been linked to rare cases of familial Parkinson's Disease. This has been disputed and there is an argument that it is in fact transmembrane protein 230 (TMEM230) on the PARK21 locus that is mutated in PD (Deng et al., 2018). TMEM230 has been shown to localise to synaptic vesicles, the early endosome and recycling endosome, suggesting a role in vesicular trafficking (Deng et al., 2016). The proposed PD-linked [N855S] mutation in RME-8 has been shown to cause defects in endosomal trafficking, impairing transport of EGFR and transferrin receptor from early endosomes (Vilariño-Güell et al., 2014; Yoshida et al., 2018). The [N855S] mutation does not disrupt binding to SNX1 or retromer-WASH complexes, but promotes SNX1 tubule formation, similar to that seen with depletion, suggestive of a dominant-negative gain-of-function (Follett et al., 2019). Mutation of RME-8 has also been shown to cause disruption of autophagy due to mislocalisation of ATG9A (Besemer et al., 2020). Interestingly, this effect on ATG9A distribution phenocopies the effect of the PD-linked VPS35[D620N] mutation on ATG9A trafficking (Zavodszky et al., 2014).

Another early endosomal protein, VPS35, encoded by *PARK17*, is mutated in PD (Vilariño-Güell et al., 2011; Zimprich et al., 2011). Furthermore, the retromer components VPS35 and VPS26 are reduced in the brains of Alzheimer's patients, further linking retromer dysfunction to neurodegenerative disease (Small et al., 2005). The pathogenic effects of the PD-linked mutation in VPS35 are not fully understood, and many potential mechanisms have been suggested. These are discussed in detail in **Section 1.5.6**.

ATP13A2, located within the PARK9 locus, encodes the lysosomal transporter ATPase cation transporting 13A2 (ATP13A2) (Ramirez et al., 2006). Mutations in ATP13A2 have been linked to an autosomal recessive, early-onset form of parkinsonism known as Kufor-Rakeb syndrome (Park et al., 2015; Ramirez et al., 2006). ATP13A2 has been implicated in many cellular processes, including bivalent cation homeostasis, lysosomal function, proteostasis, lipid digestion and mitochondrial bioenergetics (Bento et al., 2016; Dehay et al., 2012; Demirsoy et al., 2017; Marcos et al., 2019; Tan et al., 2011; Tsunemi and Krainc, 2014; Usenovic et

al., 2012). Mutation or depletion of ATP13A2 has been shown by multiple studies to disrupt lysosomal function, affecting lysosomal pH, size and hydrolase activity (Dehay et al., 2012; Tsunemi and Krainc, 2014; Usenovic et al., 2012). It has been suggested that this effect is mediated by zinc, as loss of ATP13A2 prevents sequestration of Zn^{2+} in lysosomes (Tsunemi and Krainc, 2014). In line with lysosomal dysfunction, loss or mutation of ATP13A2 cause defects in autophagosome clearance (Bento et al., 2016; Gusdon et al., 2012; Ramonet et al., 2012; Usenovic et al., 2012). Increased levels of ATP13A2 have been recorded in sporadic and LRRK2 [G2019S] PD patients, supporting a role for ATP13A2 in PD pathogenesis (Henry et al., 2015; Ramirez et al., 2006; Ramonet et al., 2012). Given that ATP13A2 mutations lead to a loss of function, but levels of ATP13A2 are increased in PD patients, it may be that ATP13A2 has a protective role.

GBA1 encodes β-glucocerebrosidase (GCase), a lysosomal membrane-bound protein involved in the hydrolysis of glucose moieties from glycolipids. Mutations in *GBA1* cause the lysosomal storage disorder Gaucher Disease and are associated with increased susceptibility to early-onset PD (Aharon-Peretz et al., 2004; Berge-Seidl et al., 2017; Blauwendraat et al., 2018; Clark et al., 2007; Do et al., 2019; Lwin et al., 2004; Nalls et al., 2014; Neumann et al., 2009; Pankratz et al., 2012; Sidransky et al., 2009). GCase deficiency has been reported in brain samples from both sporadic and GBA1 mutation PD, particularly within the substantia nigra (Gegg et al., 2012; Murphy et al., 2014). Induced pluripotent stem cell (iPSC)-derived neurons from patients with GBA mutations showed increased levels of α-synuclein, ER stress, mitochondrial dysfunction, autophagy defects and dysregulated calcium levels, suggesting that these effects are relevant to disease pathology (Fernandes et al., 2016; Schöndorf et al., 2014).

LRRK2, also known as dardarin (derived from the Basque word for tremor) is encoded by the *PARK8* locus and is the most commonly mutated gene in familial PD, making up approximately 5% cases. Mutations in the *PARK8* locus were identified as a common cause of late-onset autosomal dominant inherited PD (Funayama et al., 2002). Later, two groups identified mutations in a novel protein, LRRK2, to be responsible for PARK8 PD (Paisán-Ruíz et al., 2004; Zimprich et al., 2004). Within cells, LRRK2 is present throughout the cytosol but also localises to membrane-bound vesicles and organelles (Berwick et al., 2019; Nichols et al., 2010). The function of LRRK2 and the effect of PD-linked mutations are described in detail in **Section 1.5.7**.

1.5.6 VPS35

VPS35 forms part of the endosomal sorting complex retromer, which functions to recycle protein cargo from the endosome to the *trans*-Golgi network and plasma. The role of retromer within the endolysosomal system is discussed in detail in **Section 1.2.2.2**.

1.5.6.1 VPS35 and Parkinson's disease

Two independent studies first linked the [D620N] mutation in VPS35 to a rare form of late-onset autosomal dominant PD (Vilariño-Güell et al., 2011; Zimprich et al., 2011). Although many polymorphisms in VPS35 have since been identified, [D620N] is the only mutation that has been confirmed as pathogenic (Rahman and Morrison, 2019). Levels of VPS35 have been shown to be reduced in the substantia nigra of PD patients, further implicating VPS35 in the pathology of PD (MacLeod et al., 2013).

1.5.6.2 VPS35 and endolysosomal dysfunction

The [D620N] mutation has been shown to reduce the affinity of VPS35 with FAM21 of WASH complex, leading to defects in endosomal trafficking (McGough et al., 2014; Zavodszky et al., 2014). However, the precise effects of the [D620N] mutation on cargo recycling are disputed. Several independent groups have reported that the [D620N] mutation causes defective recycling of CIMPR to the TGN (Follett et al., 2014; MacLeod et al., 2013; McGough et al., 2014), however others have found this pathway to be functional (Tsika et al., 2014; Zavodszky et al., 2014). Similarly, trafficking of GLUT1 to the plasma membrane has been reported to be impaired in one study (Zavodszky et al., 2014) and unchanged in another (McGough et al., 2014), despite taking similar methodological approaches in the same cell line. A study in which VPS35[D620N] was overexpressed in primary cortical neurons found that the mutation did not disrupt the trafficking of the lysosomal hydrolase receptors sortilin and sortilin-related receptor (sorLA) (Tsika et al., 2014).

Defects in retromer function have also been associated with lysosomal dysfunction. Loss of retromer causes impaired delivery of hydrolases to the lysosome, thereby reducing its degradative capacity (Arighi et al., 2004; Cui et al., 2018). Deletion of retromer has also been reported to cause enlargement of the lysosomal compartment and hyperaccumulation of Rab7 on the lysosomal membrane (Cui et al., 2018; Daly et al., 2023; Jimenez-Orgaz et al., 2018). Finally, PD patient-derived fibroblasts harbouring the VPS35[D620N] have been shown to have reduced LAMP1 and LAMP2 expression, smaller lysosomes and impaired degradative capacity (Hanss et al., 2021).

The observation that deletion of retromer enhances autophagy suggests that VPS35 may play a suppressive role in this process (Cui et al., 2018; Kvainickas et al., 2017). Loss of retromer has also been shown to upregulate autophagy by impairing mTORC1 translocation to the lysosome, enhancing TFEB signalling and CLEAR gene transcription (Kvainickas et al., 2019). The [D620N] mutation in VPS35 has been shown to impair autophagy (Tang et al., 2015b; Zavodszky et al., 2014). HeLa cells stably expressing VPS35[D620N] have been shown to display impaired autophagy due to disrupted trafficking of ATG9A (Zavodszky et al., 2014). Furthermore, a study has shown that SNpc dopaminergic neurons from VPS35[D620N] knockin mice displayed accelerated degradation of LAMP2A, a critical receptor in chaperone-mediated autophagy (Tang et al., 2015a). As α-synuclein is degraded by this process, it is suggested that this may account for the accumulation of α-synuclein seen in VPS35[D620N] transgenic mice (Tang et al., 2015a), although not all studies have found α-synuclein accumulation in VPS35[D620N] mouse models (Chen et al., 2019).

1.5.6.3 VPS35 and mitochondrial homeostasis

Perturbation of VPS35 has been linked with decreased mitochondrial function. Loss of VPS35 has been shown to cause reduced mitochondrial membrane potential, increased generation of ROS and reduced respiration (Tang et al., 2015b). However, overexpression of wild type VPS35 also causes these same phenotypes (Wang et al., 2016). This could suggest that when VPS35 is overexpressed it may act in a dominant negative fashion, which has implications for the interpretation of studies that look at the effect of the [D620N] mutation with high exogenous overexpression. Several studies have reported that the [D620N] mutation causes a decrease in respiration, mitochondrial membrane potential, increased ROS, and reduced ATP levels (Hanss et al., 2021; Ma et al., 2021; Niu et al., 2021; Wang et al., 2017, 2016). Some of these studies used overexpression systems, however, others used heterozygous knockin models and PD patient-derived cells, giving weight to the view that this is a physiologically relevant effect.

Several studies have implicated VPS35 in mitochondrial dynamics. Depletion of VPS35 has reported to cause mitochondrial fragmentation, which can be rescued by the reintroduction of wild type, but not [D620N] mutant, VPS35 in murine dopaminergic neurons (Tang et al., 2015b). However, another study found that knockdown of VPS35 in human neuroblastoma M17 cells caused mitochondria to become more elongated (Wang et al., 2016). Overexpression of either wild type or [D620N] mutant VPS35 has been reported to cause mitochondrial fragmentation, suggesting that at high levels of overexpression VPS35 may have a dominant

negative effect (Wang et al., 2017, 2016). Cells from the SNpc of homozygous [D620N] knockin mice have been shown to display more fragmentated mitochondria (Tang et al., 2015b). This finding has been supported by subsequent studies using heterozygous [D620N] knockin SH-SY5Y cells, PD patient-derived fibroblasts and PD-derived induced dopaminergic neurons which have found increased mitochondrial fragmentation (Hanss et al., 2021; Ma et al., 2021; Niu et al., 2021; Wang et al., 2017, 2016). This suggests that control of mitochondrial dynamics may be relevant to PD pathogenicity (Hanss et al., 2021; Wang et al., 2016).

The VPS35 [D620N] mutation has been shown to increase ubiquitin-mediated proteasomal degradation of the fusion protein MFN2 by impairing the removal of the E3 ligase MUL1 via MDVs (Tang et al., 2015b). Increased ubiquitylation of MFN2 by MUL1 promotes its degradation, leading to fewer fusion events. This tips the balance of mitochondrial dynamics towards fission, resulting in mitochondrial fragmentation. VPS35 has also been implicated in mitochondrial fission by mediating the transport of inactive DRP1 oligomers to the lysosome via MDVs (Wang et al., 2016). This interaction is increased by the [D620N] mutation, enhancing its turnover, thus allowing for more active DRP1 on the mitochondrial surface, promoting fission and fragmentation (Wang et al., 2016).

Two studies have linked the [D620N] mutation to dysfunctional mitophagy, but found different parts of the mitophagy process to be impaired (Hanss et al., 2021; Ma et al., 2021). In a heterozygous [D620N] knockin SH-SY5Y cell model, CCCP treatment failed to induce mitochondrial PINK1 stabilisation and Parkin recruitment, leading to fewer mitolysosomes being formed (Ma et al., 2021). Thus, initiation of mitophagy was impaired. The authors found that this was because VPS35[D620N] expression led to a reduction in basal mitochondrial membrane potential which rendered mitochondria less sensitive to mitochondrial depolarisation by CCCP. Conversely, a study using induced dopaminergic neurons derived from a PD patient harbouring the VPS35[D620N] mutation found that the number of mitolysosomes in response to CCCP treatment was elevated compared to control cells (Hanss et al., 2021). They noted that the patient-derived induced neurons expressing VPS35[D620N] had smaller lysosomes, reduced LAMP1 and LAMP2 levels, and impaired autophagic flux. Therefore, the clearance of dysfunctional mitochondria engulfed by autophagosomes was impaired.

1.5.7 LRRK2

LRRK2 is a large (2527 amino acid) multi-domain protein with two catalytic domains and four protein-protein interaction domains (**Figure 1.12**). The Ras of complex (Roc) GTP-binding domain and the accompanying C-terminal of Roc (COR) domain form the Roco catalytic domain which exhibits GTPase activity (Taylor and Alessi, 2020). The second catalytic domain of LRRK2 is a serine/threonine kinase that phosphorylates substrates, such as a subset of Rab GTPases, and autophosphorylates the S1292 residue within LRRK2 (Sheng et al., 2012; Steger et al., 2017, 2016). The Armadillo (ARM), ankyrin (ANK), leucine-rich repeat (LRR) and WD40 domains are believed to facilitate interactions with other proteins, possibly in a scaffolding role (Berwick, 2019). One such interaction is with the cytosolic chaperone 14-3-3, which binds following the phosphorylation of LRRK2 at the S935 residue (Dzamko et al., 2010; Nichols et al., 2010). Interaction with 14-3-3 is believed to prevent the self-association of LRRK2 into dimers, thus controlling its activity and localisation (Mamais et al., 2014; Nichols et al., 2010).

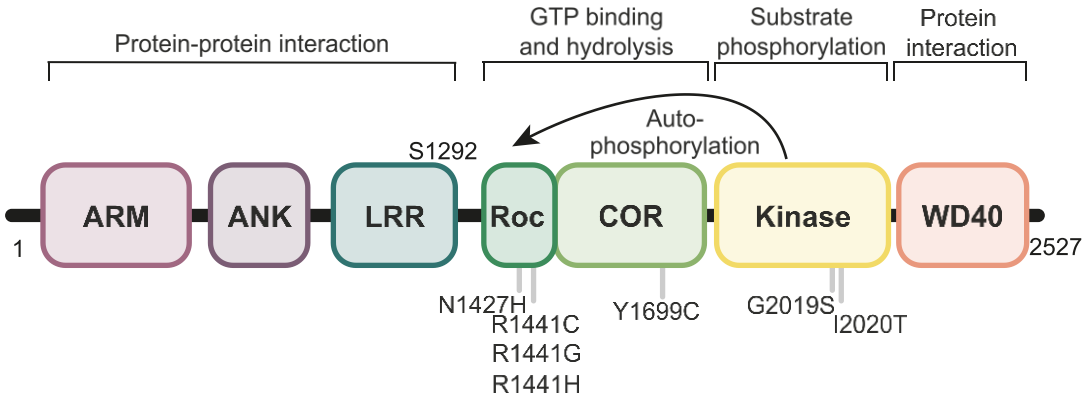

Figure 1.12 LRRK2 structure

Structure of LRRK2 domains, their proposed function and the location of pathogenic mutations associated with PD.

ANK, Ankyrin; ARM, Armadillo; COR, carboxy-terminal of Roc; LRR, Leucine-rich repeat; PD, Parkinson's disease; Roc, Ras of complex.

LRRK2 is widely distributed in human tissues, but with high expression in the immune cells, lung, kidney and intestine (Taylor and Alessi, 2020). Interestingly, only LRRK2, and not its homolog LRRK1, is present in the striatum, the main site of pathology in PD (Westerlund et al., 2008). The function of LRRK2 is not well understood and has been implicated in mitochondrial homeostasis, membrane trafficking, autophagy, neurite growth, ciliogenesis, centrosome positioning and immune signalling (Berwick et al., 2019; Wallings and Tansey, 2019). The major substrate of LRRK2 is a subset

of Rab GTPases: Rab3A/B/C/D, Rab8A/B, Rab10, Rab12, Rab35, Rab43 and possibly Rab29 (Steger et al., 2017, 2016). The localisation and known functions of LRRK2 substrate Rabs, and the location of the LRRK2 phosphosite in their *Homo sapien* forms are outlined in **Table 1.3**.

Table 1.3 LRRK2 substrate Rabs

(Eguchi et al., 2018; Goud et al., 2018; Ito et al., 2023; Jeong et al., 2018; Klinkert and Echard, 2016; Li and Marlin, 2015; Purlyte et al., 2018; Steger et al., 2017, 2016; Wauters et al., 2019; Yamano et al., 2018; Zhen and Stenmark, 2015)

Rab protein	LRRK2 phosphosite	Localisation	Function
Rab1A	T75	ER	ER-Golgi transport
Rab1B	T75		
Rab3A	T86	Secretory vesicles	Vesicle exocytosis
Rab3B	T86		
Rab3C	T94		
Rab3D	T86		
Rab5A	S84	Early endosomes, autophagosomes	Endosome fusion and motility, endocytic trafficking, mitophagy, autophagosome formation
Rab5B	S84		
Rab5C	S85		
Rab8A	T72	Secretory vesicles, *trans*-Golgi network, lysosomes, primary cilia	Cilia biogenesis, lysosome repair
Rab8B	T72		
Rab10	T73	Lysosomes, mitochondria, GLUT4 vesicles	Mitophagy, GLUT4 trafficking,
Rab12	S106	Recycling endosomes, lysosome	Retrograde transport, lysosome positioning
Rab29	T71, S72	*trans*-Golgi network	LRRK2 activation
Rab35	T72	Recycling endosomes	Endocytic trafficking, cell migration, neurite outgrowth
Rab43	T82	Golgi	Golgi-endosome transport, ER-Golgi transport, trafficking through Golgi

1.5.7.1 Mechanism of LRRK2 activation and function

In addition to Rabs being LRRK2 substrates, they also mediate the membrane recruitment and activation of LRRK2 (**Figure 1.13**). Three Rab-binding sites have

been identified on LRRK2, with each performing a different role to cumulatively regulate LRRK2 activity.

'Site 1' within the ARM domain of LRRK2 is capable of binding to Rab29, Rab8A and Rab10. Interaction at this site recruits LRRK2 to the membrane and promotes activation of LRRK2 autophosphorylation and substrate Rab phosphorylation (Vides et al., 2022). Overexpression of Rab29 drives localisation of LRRK2 to the Golgi, however the significance of this at endogenous levels is not known (Purlyte et al., 2018). Rab29 belongs to a sub-family of closely-related Rabs consisting of Rab29, Rab32 and Rab38, all of which are reported to interact with LRRK2 (McGrath et al., 2021; Waschbüsch et al., 2014). Overexpression of Rab32 has been shown to promote localisation of LRRK2 to late endosomes and a recent pre-print has shown that endogenous Rab38 promotes membrane recruitment in melanocytes (Unapanta et al., 2022; Waschbüsch et al., 2014). Rab32 has been shown to interact with LRRK2 at its ARM domain (McGrath et al., 2021), therefore it seems likely that all these Rabs bind to LRRK2 'Site 1' and promote membrane recruitment. LRRK2 Rab-binding 'Site 2' lies within the N-terminal region of LRRK2 and binds with high affinity to phosphorylated Rab8A and Rab10 (Vides et al., 2022). This is thought to facilitate a feed-forward mechanism to maintain LRRK2 membrane localisation to drive further Rab phosphorylation. Finally, a third Rab-binding site, 'Site 3', has recently been discovered which binds Rab12 (Dhekne et al., 2023). This interaction is thought to promote the configuration of LRRK2 into a conformation with maximal kinase activity. The existence of a fourth Rab-binding site which would act to correctly position LRRK2 towards its substrate Rabs has been proposed (Dhekne et al., 2023).

LRRK2 phosphorylates its substrate Rabs at a conserved threonine/serine site within their switch II motif (Steger et al., 2016). The phosphorylation of Rabs by LRRK2 can prevent their extraction from membranes by interfering with their interaction with GDI and may also decrease interaction with their GAPs (Eguchi et al., 2018; Liu et al., 2018; Steger et al., 2016) (**Figure 1.13**). Furthermore, a group of effectors have been identified that preferentially bind to phosphorylated Rabs: RILPL1, RILPL2, JIP3 and JIP4 (Steger et al., 2017; Waschbüsch et al., 2020). As such, phosphorylation of Rabs by LRRK2 can alter their normal functioning.

RILPL1 has been shown to interact with phosphorylated Rab8A and Rab10, RILPL2 with Rab8A, Rab10 and Rab12, JIP3 with Rab10, and JIP4 with Rab10 (Ito et al., 2023; Steger et al., 2016; Waschbüsch et al., 2020). Rab interacting lysosomal protein like 1 (RILP1) and Rab interacting lysosomal protein like 2 (RILP2) have been shown

to regulate cilia formation (Schaub and Stearns, 2013). LRRK2 activation impedes ciliogenesis through RILPL1 and RILPL2 (Dhekne et al., 2018; Lara Ordónez et al., 2019). Activation of LRRK2 has also been shown to promote recruitment of RILPL1 to lysosomes to promote their retrograde transport (Ito et al., 2023). JIP3 and JIP4 belong to the c-Jun NH_2-terminal kinase (JNK)-interacting protein (JIP) family of scaffolding proteins that possess an RH1 domain which facilitates interaction with cytoskeletal motor proteins. Both JIP3 and JIP4 have been implicated in lysosome motility (Rafiq et al., 2022; Willett et al., 2017). Activation of LRRK2 promotes recruitment of JIP4 and RILPL1 to lysosomes, regulating their positioning and lysosomal tubulation (Bonet-Ponce et al., 2020; Ito et al., 2023; Kluss et al., 2022). The effect of LRRK2 activation on JIP3 function is not known.

The Golgi-localised phosphatase protein phosphatase Mg^{2+}/Mn^{2+} dependent 1H (PPM1H) has been shown to dephosphorylate LRRK2-dependent phosphorylation of Rab8A and Rab10 (Berndsen et al., 2019) (**Figure 1.13**). However, PPM1H does not affect the phosphorylation status of other LRRK2 substrates, such as Rab12, therefore, other phosphatases that counter the kinase action of LRRK2 must exist (Berndsen et al., 2019).

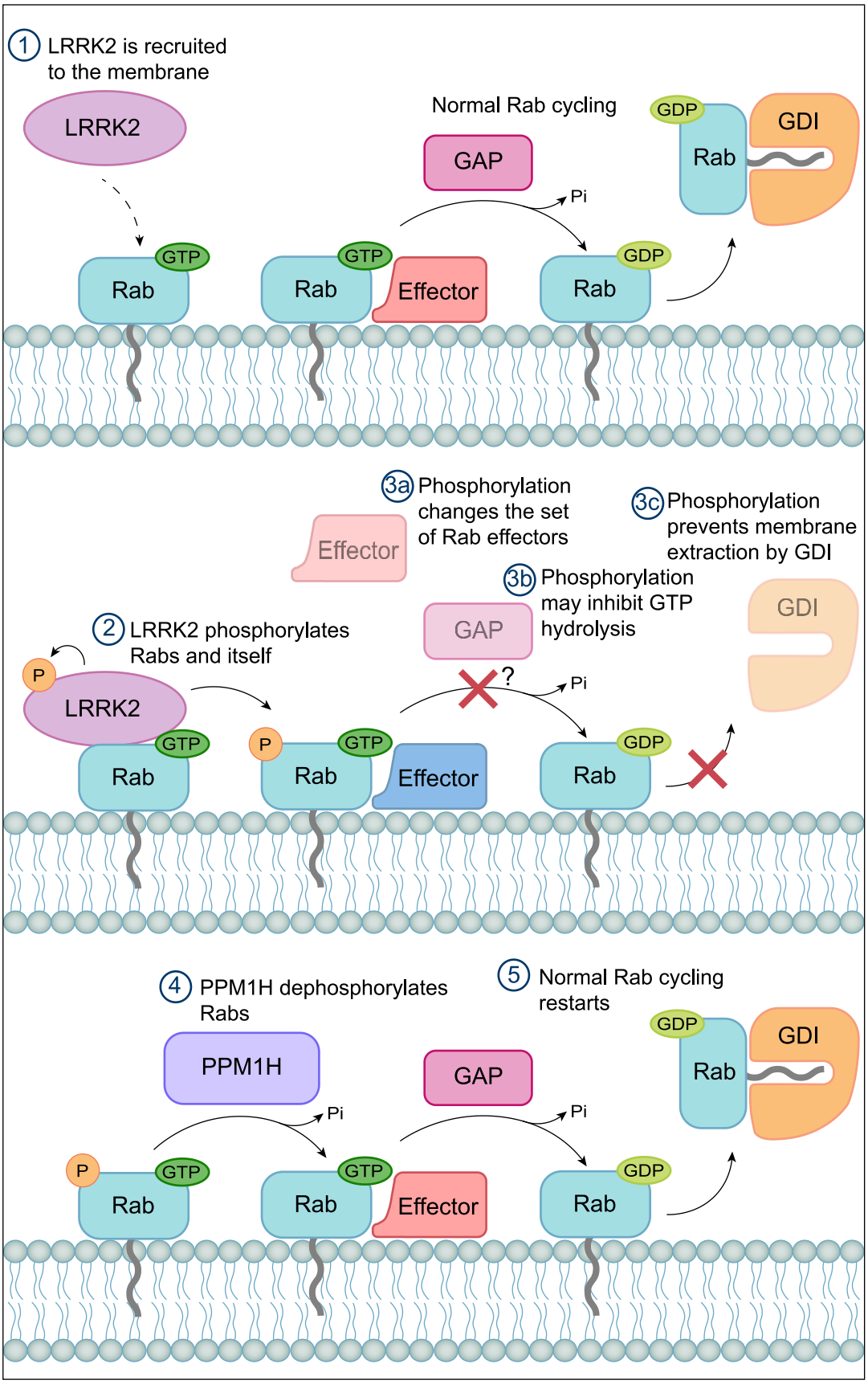

Figure 1.13 Overview of phosphorylation of Rabs by LRRK2

LRRK2 is recruited and activated at membranes via GTP-bound Rabs. LRRK2 then phosphorylates itself at S1292 and substrate Rabs at a conserved serine/threonine residue within the Switch II motif.

Rab phosphorylation leads to dissociation from their usual effectors and promotes binding to a new set of phospho-dependent effectors. Phosphorylation of Rabs also prevent their membrane extraction by GDIs, trapping them at membranes. It may also interfere with GTP hydrolysis by the Rab GAP proteins. Dephosphorylation at the serine/threonine residue of certain LRRK2 substrate Rabs is mediated by the phosphatase PPM1H.

1.5.7.2 LRRK2 and Parkinson's disease

Six pathogenic gain-of-function mutations in LRRK2 are associated with PD and are all located within the catalytic regions: [R1441C/G/H,] [Y1699C], [G2019S] and [I2020T] (**Figure 1.12**). As well as being linked to familial PD, LRRK2 has also been identified as a risk factor for susceptibility to PD through genome-wide association studies (Chang et al., 2017; International Parkinson Disease Genomics Consortium et al., 2011). The mutations [R1441C/G/H] and [Y1699C] lie within the Roco GTPase domain and are reported to decrease GTPase activity (Daniëls et al., 2011; Lewis et al., 2007). Lying within the kinase domain of LRRK2, the mutations [G2019S] and [I2020T] increase LRRK2 kinase activity (Gloeckner et al., 2006; West et al., 2005). Despite the [R1441C/G/H] and [Y1699C] mutations not being located in the kinase domain, they also increase Rab phosphorylation, suggesting the kinase activity of LRRK2 and its ability to phosphorylate Rabs plays a critical role in its pathogenicity (Liu et al., 2018; Steger et al., 2016). Furthermore, phosphoRabs have the potential to be used as biomarkers for LRRK2 activity in clinical trials as they can be detected in human peripheral mononuclear blood cells (Thirstrup et al., 2017). Binding of 14-3-3 is also disrupted by PD-linked mutations, causing increased activity of LRRK2 (Li et al., 2011; Muda et al., 2014; Nichols et al., 2010).

1.5.7.3 LRRK2 and the endolysosomal system

LRRK2 has been implicated in several processes in the endolysosomal network, including synaptic vesicle recycling, retrograde trafficking, autophagy and the response to endolysosomal stress (Taylor and Alessi, 2020). Loss of Rab29 and overexpression of LRRK2[G2019S] have been shown to impair CIMPR retrograde trafficking, which can be rescued by overexpression of VPS35 (MacLeod et al., 2013). Another study found pathogenic LRRK2 led to impaired recycling of transferrin (Mamais et al., 2021). Furthermore, LRRK2 has been shown to interact with the Golgi-localised tethering complex Golgi-associated retrograde protein (GARP), further supporting a role for LRRK2 in regulating trafficking (Beilina et al., 2020). Expression of pathogenic LRRK2 has been shown to cause a delay in the Rab5-Rab7 endocytic switch, decreased Rab7 activity and a delay in receptor-mediated degradation

(Gómez-Suaga et al., 2014). The authors suggest that the impairment in endosome maturation and trafficking is due to LRRK2 regulating Rab7. However, later work has shown that LRRK2 phosphorylates Rab5, so it is conceivable that these effects are due to the inability of phosphorylated Rab5 to recruit the Rab7 GEF Mon1-Ccz1 (Steger et al., 2017). In support of their hypothesis, Gómez-Suaga and colleagues cite a study which shows that the pathogenic mutations in the *Drosophila* LRRK2 homologue *LRRK* promote Rab7-dependent lysosome clustering (Dodson et al., 2012; Gómez-Suaga et al., 2014). However, unlike humans which possess *LRRK1* and *LRRK2* genes, *Drosophila* possess only one orthologue, *LRRK* (Seegobin et al., 2020). It is therefore possible that the effect on Rab7-dependent lysosome positioning is linked to an equivalent function of human LRRK1, which is known to phosphorylate Rab7 (Malik et al., 2021).

LRRK2 and VPS35 have been reported to act together in synaptic vesicle recycling in *Drosophila* but, again, interpretation of this result has the caveat that there is only one LRRK ortholog in flies (Inoshita et al., 2017). Overexpression of VPS35 in flies expressing human pathogenic LRRK2 has been shown to lessen locomotor deficits and dopaminergic neurodegeneration, respectively, suggesting a common pathway between these proteins exists (Linhart et al., 2014). In support of LRRK2 as part of network of interacting PD genes, LRRK2 has also been shown to interact with Parkin and the PD risk factor genes GAK and Rab29 (Beilina et al., 2014; Ng et al., 2009).

Expression of pathogenic LRRK2 variants has been reported to cause multiple lysosomal phenotypes, including swelling, perinuclear clustering, impaired acidification, and reduced degradative capacity (Henry et al., 2015; Ho et al., 2019; Hockey et al., 2015; Ito et al., 2023; MacLeod et al., 2013; Schapansky et al., 2018; Ysselstein et al., 2019). Expression of [G2019S] or [R1441C] LRRK2 leads to trapping of Rab8a at lysosomes (Mamais et al., 2021). Furthermore, it has been shown that LRRK2 negatively regulates lysosomal GCase activity in a Rab10-dependent manner, which is exacerbated by PD-linked LRRK2 mutations and could be relieved by LRRK2 kinase inhibition (Ysselstein et al., 2019). In addition to supporting a role for LRRK2 at the lysosome, this provides another link between two PD-associated genes. LRRK2 has also been reported to interact with the v-ATPase V_0 subunit a1, which is abolished by the [R1141C] mutation, causing an increase in lysosomal pH and decreased autolysosome fusion (Wallings et al., 2019). A recent pre-print has found that LRRK2 negatively regulates lysosomal degradative capacity at a transcriptional level through inhibition of MiT/TFE transcription factors, consequently suppressing lysosomal biogenesis (Yadavalli and Ferguson, 2023).

Several studies support a role for LRRK2 in the response to endolysosomal stress. LRRK2 is recruited to endolysosomal structures in response to damage and the lysosome-related organelle phagophores in response to infection (Bonet-Ponce et al., 2020; Eguchi et al., 2018; Herbst et al., 2020; Kuwahara et al., 2020). Recruitment of LRRK2 subsequently leads to increased phosphorylation at these membrane compartments. Several roles for LRRK2 in the response to endolysosomal stress have been proposed. These include the regulation of lysosomal size and contents in response to lysosome overload by promoting lysosomal exocytosis (Eguchi et al., 2018), regulating ESCRT-mediated repair of damaged endomembranes (Herbst et al., 2020), and the removal of damaged lysosomal content to functional lysosomes via lysosomal tubulation (Bonet-Ponce et al., 2020).

1.5.7.4 LRRK2 and mitochondrial homeostasis

There is a growing body of evidence to support a role for LRRK2 at the mitochondria. Mutations in LRRK2 have been widely reported to impair mitochondrial function, with cells displaying reduced mitochondrial membrane potential, increased ROS, and reduced respiration and, subsequently, reduced ATP levels (Hsieh et al., 2016; Mortiboys et al., 2010; Niu et al., 2012; Toyofuku et al., 2020; Wang et al., 2012b; Wauters et al., 2019). Multiple independent studies have reported a direct interaction between LRRK2 and the fission protein DRP1 (Niu et al., 2012; Perez Carrion et al., 2018; Stafa et al., 2014; Wang et al., 2012b). LRRK2 has been shown to promote the recruitment of DRP1 to mitochondria leading to increased fission, which is enhanced by pathogenic LRRK2 mutation (Niu et al., 2012; Wang et al., 2012b). However, another study reported that LRRK2 impairs the interaction of DRP1 with its receptor MID51 under depolarising conditions (Bonello et al., 2019). LRRK2 has also been reported to interact with the DRP1 receptor FIS1 (Niu et al., 2012) and the fusion proteins MFN1, MFN2 and OPA1 (Stafa et al., 2014). Together, these results suggest a role for LRRK2 in regulating mitochondrial dynamics. In different studies, the [G2019S] has been reported to cause elongated mitochondrial networks (Mortiboys et al., 2010), network fragmentation (Niu et al., 2012; Wang et al., 2012b) and no change to mitochondrial morphology (Hsieh et al., 2016; Singh et al., 2021). Clearly, more work is needed to understand the role LRRK2 plays in mitochondrial fission and fusion, and whether this is situation- or cell-type specific. Furthermore, loss of LRRK2 or expression of the [G2019S] mutation has shown to impair ER-mitochondrial contacts, suggesting a role for LRRK2 in the regulation of these contact sites (Toyofuku et al., 2020).

LRRK2 has been shown to suppress basal, PINK1-independent mitophagy in a kinase dependent manner (Singh et al., 2021; Tasegian et al., 2021). Consequently, the hyperactivating LRRK2[G2019S] mutation results in impaired mitophagy. LRRK2 has also been implicated in depolarisation-induced mitophagy (Bonello et al., 2019; Hsieh et al., 2016; Wauters et al., 2019). However, there is disagreement in the literature as to whether LRRK2 is acting upstream, downstream, or in a pathway parallel to Parkin. Bonello and colleagues reported that LRRK2 impairs the initiation of mitophagy by interfering with the interactions between DRP1 and MID51, DRP1 and Parkin, and Parkin and TOM40 (Bonello et al., 2019). On the other hand, Wauters and colleagues propose that LRRK2 interferes with mitophagy at a point downstream of Parkin. Fibroblasts from PD patients harbouring LRRK2 [G2019S] or [R1441C] fail to accumulate Rab10 at mitochondria in response to depolarisation, therefore it is no longer present to recruit the autophagy receptor optineurin (Wauters et al., 2019). The authors propose that this is because phosphorylated Rab10 is trapped at another membrane compartment (Wauters et al., 2019). Finally, Hsieh and colleagues showed that LRRK2 acts in a pathway parallel to PINK1 and Parkin to facilitate the clearance of damaged mitochondria. They show that LRRK2 interacts with the mitochondrial GTPase Mitochondrial Rho GTPase 1 (Miro1) which functions in the tethering of mitochondria to microtubules. In response to depolarisation, Miro1 is degraded to stop movement of damaged mitochondria and promote their clearance by mitophagy. The LRRK2 [G2019S] mutation was shown to stabilise Miro1 at mitochondria, delaying mitophagy (Hsieh et al., 2016).

1.5.8 An interconnected PD network

Whilst examining the functions of the gene products mutated in Parkinson's Disease highlights the importance of endolysosomal trafficking and mitochondrial dysfunction in pathogenesis, looking at these two processes separately may be a reductive view.

Several genes have been found to have both mitochondrial and endolysosomal trafficking roles, suggesting crosstalk between these two processes. Although ATP13A2 is located at the lysosome, knockdown disrupts mitochondrial networks, leads to increased ROS production, and accumulation of mitochondrial mass (Gusdon et al., 2012; Ramonet et al., 2012). VPS13C has been implicated in both endolysosomal-ER and mitochondrial-ER contact sites (Leonzino et al., 2021). Although the major role for Parkin appears to be in mediating mitophagy, it has also been implicated in endosomal sorting through the ubiquitylation of Rab7 (Song et al., 2016). As discussed previously (see **Sections 1.5.6.2**, **1.5.6.3**, **1.5.7.3** and **1.5.7.4**),

pathogenic mutations in VPS35 and LRRK2 have been extensively linked to dysfunctions in mitochondrial homeostasis (**Figure 1.14**) and in the endolysosomal system (**Figure 1.15**).

Moreover, many of these PD genes interact functionally with each other, suggesting that common pathways may exist that underpin disease pathology. The best characterised example of this is the PINK1/Parkin-dependent mitophagy pathway. However, the finding that the [D620N] mutation in VPS35 hyperactivates LRRK2 suggests that these proteins may also form a common axis to cause neurodegeneration (Mir et al., 2018).

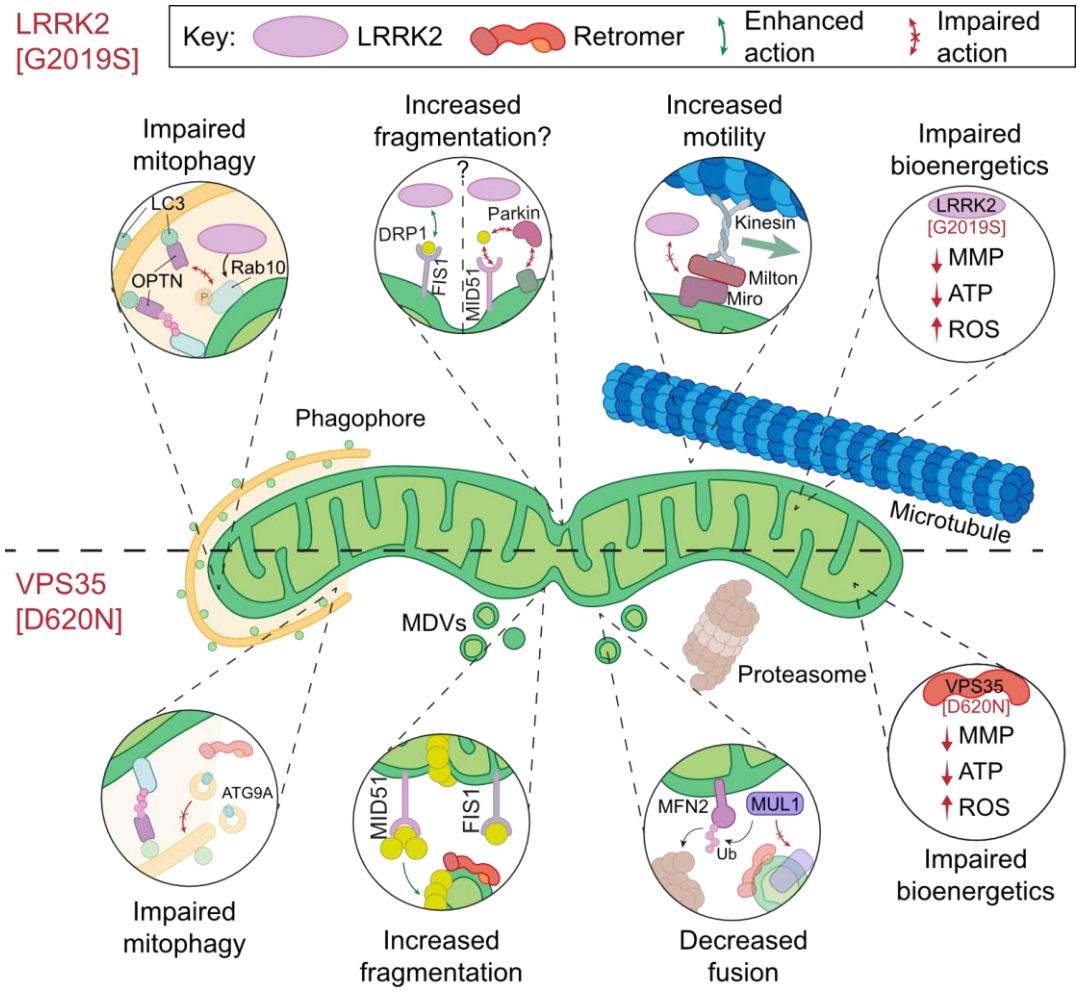

Figure 1.14 PD mutations in LRRK2 and VPS35 cause mitochondrial defects

The LRRK2[G2019S] has been reported to impair mitophagy due to reduced Rab10-dependent optineurin recruitment to mitochondria, stabilisation of Miro1, which prevents mitochondrial arrest prior to mitophagy initiation, and decreased recruitment of Parkin. The effect on LRRK2[G2019S] on mitochondrial morphology is disputed. The mutation been reported to enhance and impair DRP1 recruitment and cause mitochondrial elongation and fragmentation. The VPS35[D620N] mutation has been reported to impair mitophagy by preventing the delivery of ATG9A vesicles to the growing phagophore. The mutation has been shown to cause increased mitochondrial fusion by enhancing

the removal of inactive DRP1 oligomers via MDVs. VPS35[D620N] has also been reported to cause decreased fusion due to reduced removal of the E3 ligase MUL1 via MDVs, leading to enhanced proteasomal degradation of the fusion protein MFN2. Both VPS35[D620N] and LRRK2[G2019S] impair mitochondrial bioenergetics.

ATG, autophagy-related; DRP1, dynamin-related protein 1; FIS1, mitochondrial fission protein 1; LC3, microtubule-associated protein 1A/1B-light chain 3; MID51, mitochondrial dynamics protein of 51 kDa; MMP, mitochondrial membrane potential; OPTN, optineurin; ROS, reactive oxygen species; Ub, ubiquitin.

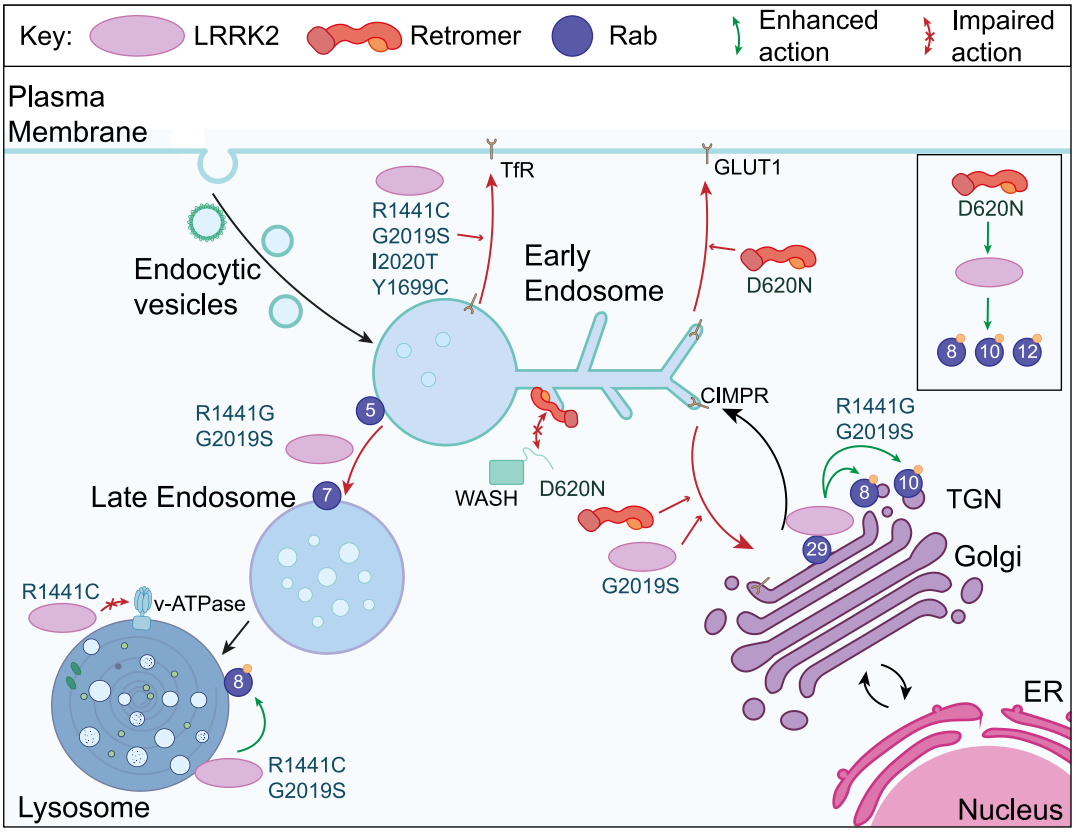

Figure 1.15 PD mutations in LRRK2 and VPS35 cause defects in the endolysosomal system

Pathogenic mutations in LRRK2 and VPS35 cause disruption in endocytic trafficking and cargo recycling. The VPS5[D620N] mutation impairs the interaction of retromer with the WASH complex. Pathogenic LRRK2 mutations cause increased phosphorylation of Rabs at membrane compartments. LRRK2 [R1441C] displays decreased interaction with v-ATPase, raising lysosomal pH and impairing autophagy. Mutations in LRRK2 cause lysosomal enlargement.

1.6 Aims

Recent work has shown the Parkinson's Disease proteins VPS35 and LRRK2 act in a common axis, whereby the [D620N] mutation in VPS35 causes hyperphosphorylation of LRRK2 substrate Rabs. However, how these two proteins interact and the functional consequences of [D620N]-mediated hyperactivation of LRRK2 are not understood.

In this thesis, I set out to further explore the relationship between LRRK2 and VPS35. **Chapter 3**, describes the generation and characterisation of a set of tools to facilitate the study of pathogenic VPS35 and LRRK2. This includes the generation of an isogenic pair of cell lines expressing either wild type or [D620N] mutant VPS35. I then use these tools to investigate the consequences of the VPS35[D620N] mutation on endosomal trafficking (**Chapter 4**) and mitochondrial dynamics and mitophagy (**Chapter 5**), with the aim to investigate whether there is any involvement of LRRK2. Finally, **Chapter 6** reports efforts to investigate whether VPS35 affects LRRK2's role in the response to endolysosomal damage.

2 Materials and Methods

2.1 Molecular Biology

2.1.1 Materials and Reagents

The reagents and materials used in molecular biology experiments are outlined in Table 2.1. If not otherwise stated, chemicals were purchased from Merck/Sigma-Aldrich. All primers were purchased from Eurofins Scientific.

Table 2.1 Molecular biology reagents and materials

REAGENT	SOURCE	CAT. NO.
Bacterial Cells		
Subcloning Efficiency™ DH5α Competent cells	ThermoFisher Scientific (Invitrogen)	#18265017
BL21 Competent *E. coli*	New England BioLabs	#C2530H
Media		
SOC (Super Optimal Broth with Catabolite Repression) Medium	ThermoFisher Scientific (Invitrogen)	#15544034
Gel electrophoresis reagents		
Tris-acetate-EDTA (TAE) buffer, 50x	National Diagnostics	#EC-872
Ultrapure™ Agarose powder	ThermoFisher Scientific (Invitrogen)	#16500500
SYBR™ Safe DNA gel stain	ThermoFisher Scientific (Invitrogen)	#S33102
1 kb DNA ladder	New England Biolabs	#N3232
100 bp DNA ladder	New England Biolabs	#N3231
Gel Loading Dye, Purple (6x), no SDS	New England Biolabs	#B7025S
Kits		
MinElute Gel Extraction Kit	Qiagen	#28604
QIAprep Spin MiniPrep Kit	Qiagen	#27106
HiSpeed Plasmid Maxi Kit	Qiagen	#12663
QIAquick PCR Purification Kit	Qiagen	#28104
PCR reagents		
PfuUltra II Fusion HotStart DNA Polymerase (and associated buffer)	Agilent	#600670
PCR nucleotide mix, 25mM	Promega	#U1431
Nuclease free water	Merck (Sigma-Aldrich)	#W4502
Restriction digest and ligation reagents		
Restriction Endonuclease Enzymes	New England Biolabs	Various
CutSmart Buffer	New England Biolabs	-
T4 DNA Ligase	New England Biolabs	#M0202
T4 DNA Ligase Reaction Buffer	New England Biolabs	-
Protein Purification Reagents		
Bacterial protease inhibitors	Merck (Sigma-Aldrich)	#P8465
Deoxyribonuclease I from bovine pancreas (DNase)	Merck (Sigma-Aldrich)	#DN25

GSTrap™ HP columns	Cytiva (GE)	#17528101
Isopropyl ß-D-1-thiogalactopyranoside (IPTG)	Merck (Sigma-Aldrich)	#I6758
Lysozyme	Merck (SAFC)	#1052810001
NuPAGE™ 4 to 12%, Bis-Tris, 1.0mm, Mini Protein Gel, 10-well	ThermoFisher Scientific (Invitrogen)	#NP0321BOX
NuPAGE™ MES SDS Running Buffer (20x)	ThermoFisher Scientific (Invitrogen)	#NP000202
PD10 Desalting columns	Merck (Cytiva)	#GE17-0851-01
Reduced L-glutathione	Merck (Sigma-Aldrich)	#G4251
SimplyBlue™ SafeStain	ThermoFisher Scientific (Invitrogen)	#LC6060
XCell *SureLock*™ Mini-Cell Electrophoresis System	ThermoFisher Scientific (Invitrogen)	#EI001

Plasmids used in this project are listed in **Table 2.2**.

Table 2.2 Table of plasmids

Plasmid name	Obtained from	Cat. No
pcDNA5-FRT/TO HA-VPS35 WT	MRC PPU	#DU26467
pcDNA5-FRT/TO HA-VPS35 [D620N]	MRC PPU	#DU26878
pcDNA5-FRT/TO NeoR	Generated in-house	
pEGFP-C1-Rab7	Gift from Harald Stenmark	
pEGFP-C1-Rab7-DN [T22N]	Gift from Tobias Zech	
pGEX-4T-3-mR7BD	Addgene	#79149
pGEX-6P-1	Merck (Cytiva)	#GE28-9546-48

2.1.2 Polymerase Chain Reaction (PCR)

DNA amplification by PCR was performed using PfuUltra II Fusion HS DNA Polymerase. The primer sequences used are shown in **Table 2.3**.The PCR reaction was set up according to **Table 2.4** and run according to the thermal cycler programme shown in **Table 2.5**.

Table 2.3 List of PCR primers used

Capital letters in the primer sequence represent the recognition sites for KpnI (forward, F) and NotI (reverse, R) restriction enzymes.

Target	Primer No.	5'-3'	
HA-VPS35 WT	2545	F	gacGGTACCgccaccatgtacccatacg
	2546	R	atgaaggtctcatcctttaaGCGGCCgctt

Table 2.4 PCR Reaction Mix for DNA amplification

Reagent	Volume required (µl)
Sterile water	x
10x Pfu-buffer	5
dNTPs (25mM)	1
Forward Primer	1.25
Reverse Primer	1.25
Template (50 ng)	y
PfuUltra HF DNA Polymerase	1
Total volume	50

Table 2.5 Thermocycler programme

Segment	Step	No. cycles	Temp. (°C)	Duration
1	Initial denaturation	1	95	2 min
2	Denaturation	30	95	30 sec
	Annealing		T_m - 5	30 sec
	Extension		68	1 min/kb
3	Final Extension	1	68	30 min

2.1.3 Restriction enzyme digestion

Restriction digests were set up according to **Table 2.6**. For each digest reaction, 1 µg of DNA was used. Reaction mixtures were incubated at 37 °C for 90 minutes (min).

Table 2.6 Restriction Digest Reaction Mix

RE, restriction endonuclease.

Reagent	Volume required (µl)			
	Uncut	Single Digest	Single Digest	Double Digest
Sterile water	x	x	x	x
CutSmart Buffer	4	4	4	4
DNA (1 µg)	y	y	y	y
RE enzyme 1	0	1	0	1
RE enzyme 2	0	0	1	1
Total volume	40	40	40	40

2.1.4 Ligation

T4 DNA ligation was performed to ligate insert DNA into a vector using an insert to vector molar ratio determined based on the size of each fragment. The reaction was set up as shown in **Table 2.7** and incubated in a thermocycler at 16 °C for 18 hours (h) then kept at 4 °C until use.

Table 2.7 Ligation Reaction Mix

Reagent	Volume required (µl)
Sterile water	x
10x T4 DNA Ligase Buffer	2
Vector (5 kb – 50 ng)	y
Insert (2.5 kb – 150 ng)	z
T4 DNA Ligase	1
Total volume	20

2.1.5 Agarose gel electrophoresis and gel extraction

Agarose gels were prepared by dissolving electrophoresis grade agarose powder in TAE buffer (40 mM Tris-acetate, 1 mM Na_2-EDTA) by heating in a microwave for approximately 4 minutes. After leaving to cool slightly, SYBR Safe stain was added at 1:10,000 dilution to allow visualisation of DNA by ultraviolet (UV) light. The gel was then poured into a cassette and left to set at room temperature. Before loading, 6x DNA loading dye was added to DNA samples. Gels were run in TAE buffer at 136 V for 45 minutes. DNA bands were visualised using a UV light. When necessary, DNA was extracted from gels using a QIAquick Gel Extraction kit.

2.1.6 Bacterial transformation

Transformation of bacteria was carried out using either BL21, DH5α *Escherichia coli* or TOP10 cells. Per transformation, a 50 µl aliquot of competent bacteria was thawed on ice before adding 5 µl of ligated DNA (from 20 µl total ligation reaction) or 100 ng of DNA. The bacterial suspension was incubated on ice for 20 minutes before undergoing heat-shock for 60 seconds (secs) in a water bath set to 42 °C, and then placed on ice for 2 minutes. 350 µl of SOC media was added to the bacteria, which were then incubated at 37 °C for 1 hour with shaking (250 revolutions per minute, rpm). Bacteria were then inoculated onto LB agar plates with the appropriate antibiotic selection marker (100 mg/ml ampicillin, 10 mg/ml kanamycin) and incubated overnight at 37 °C. For ligations, 200 µl of bacterial suspension was plated. For transformation with plasmid DNA, 50 µl of bacterial suspension was plated.

Individual bacterial colonies were picked from the plates, and each used to inoculate 5 ml of LB broth containing the appropriate selection antibiotic. Cultures were incubated overnight at 37 °C with shaking (250 rpm). DNA was purified from the bacterial cultures using a Qiagen MiniPrep Kit according to manufacturer instructions. Purified DNA samples were test-digested and, if positive, sent for sequencing at the DNA Sequencing Service (University of Dundee, UK). Sequence-verified plasmids

were transformed into bacteria as above, and an individual colony was used to inoculate 150 ml LB broth under antibiotic selection which was incubated overnight at 37 °C with shaking (250 rpm). Purified plasmid DNA was extracted using Qiagen MiniPrep Kit according to manufacturer instructions and a glycerol stock was prepared, as detailed in **Section 2.1.7**.

2.1.7 Glycerol stock

Five millilitres of overnight bacterial culture in LB broth and appropriate antibiotic was centrifuged at 4,000 rpm to pellet the bacteria. The pellet was then resuspended in 40% glycerol and LB broth and stored at -80 °C.

2.1.8 Strategy for cloning HA-VPS35 plasmids

The pcDNA5D-FRT/TO-HA-VPS35 WT and [D620N] plasmids contained a hygromycin resistance gene which made them incompatible for use as a selection marker for the FlpIn system in RPE1 cells as RPE1 cells already harbour hygromycin B resistance (Bodnar et al., 1998). It was therefore necessary to clone the HA-VPS35 inserts into the vector pcDNA5-FRT/TO-NeoR which instead contains a neomycin resistance (NeoR) cassette. A schematic of this process is illustrated in **Figure 2.1**.

PCR was used to amplify HA-VPS35 and to insert a KpnI restriction site at the 5' end and include a NotI site at the 3' end, forming KpnI-HA-VPS35-NotI. The PCR product was run on a 1% agarose gel by electrophoresis and a band at the expected molecular mass was extracted using a MinElute Gel Extraction Kit. This product was then restriction digested using KpnI and NotI restriction endonuclease enzymes and the digested product subjected to purification using a PCR purification kit. The pcDNA5-FRT/TO NeoR destination vector was also digested with KpnI and NotI and the two digestion products were ligated together using T4 DNA ligase. The ligation mixture was transformed into bacteria and DNA was extracted from cultures grown from the resulting colonies to be sequence verified. This strategy was successful for cloning pcDNA5 FRT/TO NeoR HA-VPS35 WT but failed for HA-VPS35 [D620N].

Efforts to make pcDNA5 FRT/TO NeoR VPS35 [D620N] by inserting PCR-amplified VPS35 D620N into pcDNA5 FRT/TO NeoR were unsuccessful, so the end-product was assembled via subcloning the gene of interest from pcDNA5 FRT/TO VPS35 [D620N] into pcDNA5-FRT/TO-NeoR HA-VPS35 WT, and in the process removing HA-VPS35 WT. This work was carried out in collaboration with Hannah Elcocks.

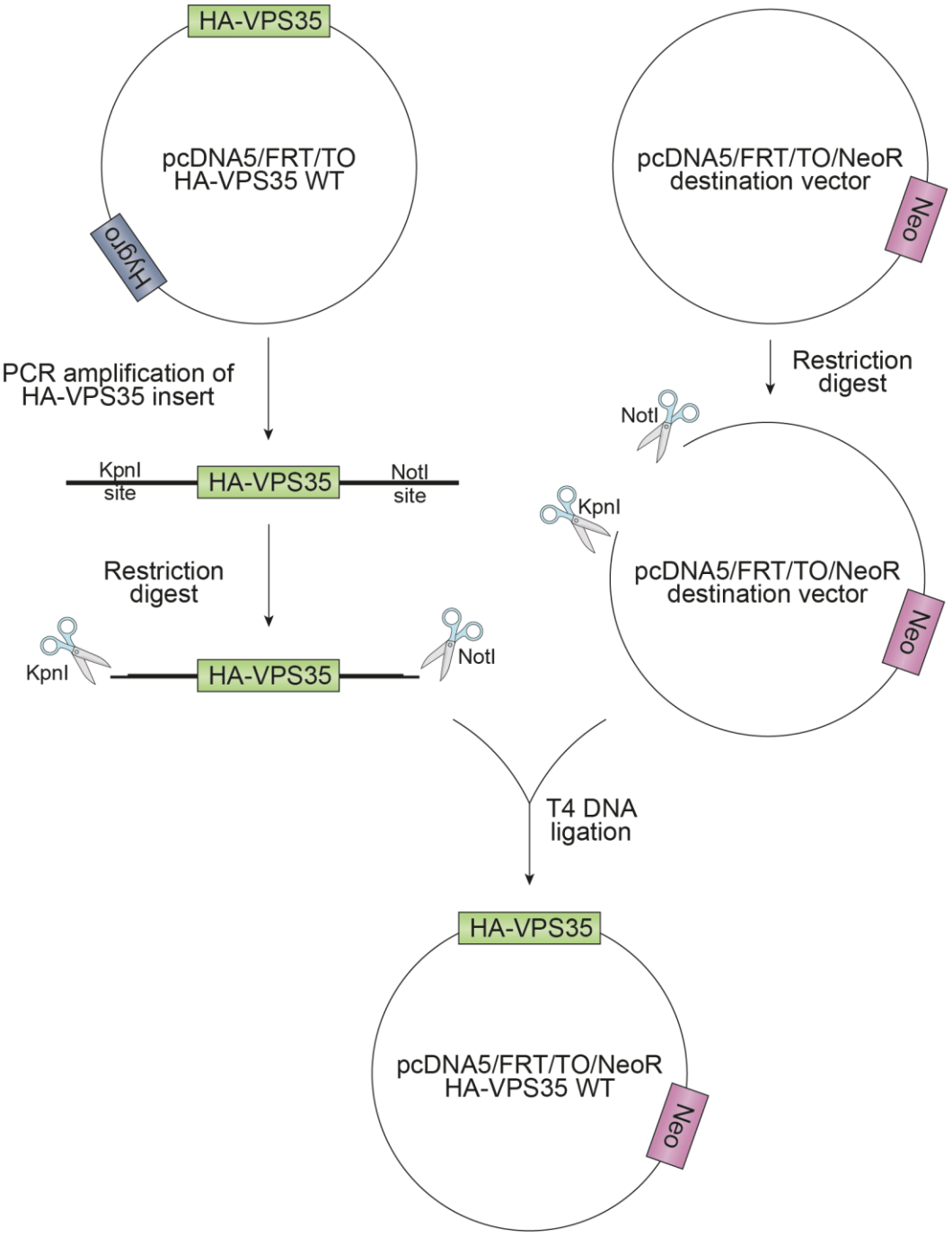

Figure 2.1 Cloning process for the creation of pcDNA5/FRT/TO/NeoR HA-VPS35 WT plasmid
HA-VPS35 cDNA was amplified from pcDNA5/FRT/TO/HA-VPS35 WT by PCR using primers designed to create KpnI and preserve NotI restriction sites. The PCR product and pcDNA5/FRT/TO/NeoR destination vector were subjected to restriction digest and the relevant products ligated together to create pcDNA5/FRT/TO/NeoR HA-VPS35 WT.

2.1.9 Production of GST-RILP

2.1.9.1 Protein production

To produce GST-RILP for use in the active Rab7 binding assay, GST-mouse Rab7 binding domain of RILP (GST-RILP) was subcloned out of pGEX-4T-3-mR7BD and into the pGEX-6P-1 backbone. Double digests of both constructs were run on a 1% agarose gel and the drop-out insert band and digested pGEX-6P-1 vector were extracted and ligated to form pGEX-6P-1-RILP using T4 DNA ligation (**Section 2.1.4**).

For protein production, pGEX-6P-1-RILP was transformed into BL21 bacteria as in **Section 2.1.6**. Colonies were grown on LB Agar plates under ampicillin and picked to inoculate a 10ml LB broth, which was incubated for 16 hours at 37 ºC with shaking (250 rpm). The following day, the starter culture was inoculated into 2 litres of LB broth with ampicillin and grown to an OD_{600} of 0.6-0.8. Protein production was then induced with 0.5 mM IPTG for 20 hours at 20 ºC, with shaking (250 rpm). Pre-induction and post-induction samples were collected to test induction efficiency (see **Section 2.1.9.2**). Bacteria were pelleted in a Jouan centrifuge at 4500 rpm for 15 minutes at 4 ºC. The pellets were washed in ice-cold PBS and pelleted as previously described. Bacterial pellets were flash frozen with liquid nitrogen and stored at -80 ºC until lysis. Lysis was performed using ice-cold PBS supplemented with lysozyme (0.5 mg/ml), DNase (10 µg/ml) and bacterial protease inhibitors (1:500) on ice for 30 minutes. The lysates were then sonicated using a probe set to high for 10 rounds of 20 seconds on ice. Lysates were then clarified in an ultracentrifuge at 100,000 x *g* for 25 minutes at 4 ºC. The supernatant was then filtered with a 0.2 µm filter before being loaded onto an ÄKTA pure protein purification system (Cytiva).

2.1.9.2 Assessing GST-RILP induction

Samples from the bacterial culture before and after induction with IPTG were pelleted and resuspended in hot lysis buffer (2 % SDS, 1 mM EDTA, 50 mM NaF) and incubated at 110 °C for 10 minutes, vortexing at 2-minute intervals. Sample buffer (10x) was added to samples before boiling at 95 °C for 5 minutes. Samples were spun at maximum speed on a tabletop centrifuge to pellet debris and 10 µl of each sample was resolved by sodium dodecyl sulphate polyacrylamide gel electrophoresis (SDS-PAGE) (described in **Section 2.3.8**). Proteins were visualised by incubating with SimplyBlue SafeStain for one hour, followed by a one-hour and an overnight wash in distilled water.

2.1.9.3 Purification of GST-RILP

Lysates were loaded onto a 1 ml GSTrap Column on an ÄKTA pure protein purification system (Cytiva). The column was washed with three column volumes of PBS and bound protein was eluted with 50mM Tris-HCl and 10 mM reduced glutathione. Fractions were collected in 500 µl volumes and the UV trace was used to determine which should contain GST-RILP protein. Samples from each fraction were resolved by SDS-PAGE and visualised using SimplyBlue SafeStain to assess their purity. Relevant fractions were pooled for buffer exchange using PD10 desalting columns. As per the manufacturer's instructions, the PD10 columns were equilibrated with GST storage buffer (50 mM Tris pH 7.4, 150 mM NaCl, 5 mM MgCl2, 1 mM dithiothreitol (DTT), 10% glycerol) and then the sample was applied to the columns three times, thus removing reduced glutathione and exchanging GST-RILP protein into GST storage buffer. The collected samples were pooled, and the concentration of the purified protein was calculated using a Pierce 660 nm assay (**Section 2.3.3)**. Single-use aliquots of the purified protein were flash frozen in liquid nitrogen and stored at -80 ºC until they were to be used in the assay. This work was carried out in collaboration with Hannah Elcocks.

2.2 Cell Biology

2.2.1 Materials and Reagents

The reagents and materials used in cell biology experiments are outlined in **Table 2.8**. If not otherwise stated, chemicals were purchased from Merck/Sigma-Aldrich. All siRNA oligonucleotides were purchased from Horizon Discovery (UK).

Table 2.8 Cell biology reagents and materials

REAGENT	SOURCE	CAT. NO.
Cell lines		
HEK293 Flp-In™ T-REx™	Invitrogen (UK)	R78007
hTERT RPE1 FRT/TR	Dr Jonathon Pines (ICR, London)	-
hTERT RPE1 FlpIn mitokeima	Generated by Dr Elena Marcassa and Dr Hannah Elcocks (MCSU, Liverpool) from hTERT RPE1 FRT/TR from Dr Jonathon Pines (ICR, London)	-
Cell culture media and supplements		
Dulbecco's Modified Eagle's Medium (DMEM), low glucose, GlutaMAX™ Supplement, pyruvate, Gibco™	ThermoFisher Scientific	#21885025

DMEM/F-12, GlutaMAX™ Supplement, Gibco™	ThermoFisher Scientific	#31331093
Opti-MEM™ Reduced Serum Medium, GlutaMAX™ Supplement, Gibco™	ThermoFisher Scientific	#51985034
Fetal Bovine Serum (FBS), qualified, Brazil, Gibco™	ThermoFisher Scientific	#10270106
MEM Non-Essential Amino Acids Solution (100x), Gibco™	ThermoFisher Scientific	#11140035
Trypsin-EDTA (0.5%), no phenol red (10x), Gibco™	ThermoFisher Scientific	#15400054
Transfection Reagents		
GeneJuice® Transfection Reagent	Merck Millipore	#70967
Lipofectamine™ RNAiMAX	Invitrogen	#13778075
Selection antibiotics		
Blasticidin S	ThermoFisher Scientific (Invitrogen)	#R21001
G418	Merck (Sigma-Aldrich)	#4727878001
Zeocin	ThermoFisher Scientific (Invitrogen)	#R25005
Induction antibiotics		
Doxycycline hyclate	Merck (Sigma-Aldrich)	#D9891
Treatment compounds		
Antimycin A	Merck (Sigma-Aldrich)	#A8674
Apilimod dimesylate	Tocris Bioscience	#7283
Carbonyl cyanide 3-chlorophenylhydrazone (CCCP)	Merck (Sigma-Aldrich)	#C2759
Chloroquine diphosphate salt	Merck (Sigma-Aldrich)	#C6628
Concanamycin A	Merck (Sigma-Aldrich)	#C9705
Epoxomicin	Merck (Sigma-Aldrich, Calbiochem)	#324800
L-Leucyl-L-Leucine methyl ester (LLOMe) hydrochloride	Cambridge Bioscience (Cayman Chemicals)	#CAY16008
MLi-2	Tocris (Abingdon, UK)	#5756
MLN-4924 (Pevonedistat)	Chemgood	#C-1231
Nigericin sodium salt	Merck (Sigma-Aldrich)	#N7143
Oligomycin A	Merck (Sigma-Aldrich)	#75351

Viral vectors used in this project are listed in **Table 2.9**.

Table 2.9 Table of lentiviruses

Viral vector	Obtained from	Cat. No
LV-CMV-eGFP-LRRK2 wild-type	KU Leuven	PD-12-197.2
LV-CMV-eGFP-LRRK2 G2019S	KU Leuven	PD-12-289
LV-CMV-eGFP-LRRK2 G2019S/D1994A	KU Leuven	PD-12-279

2.2.2 Cell Culture

RPE1 FlpIn Parental (hTERT RPE1 FRT/TR) and hTERT RPE1 FlpIn mitokeima cells were maintained in Dulbecco's Modified Eagle's Medium: Nutrient Mixture F-12 (DMEM/F-12) + GlutaMAX™. Parental HEK293 FlpIn (HEK293 Flp-In™ T-REx™) cells were maintained in Dulbecco's Modified Eagle's Medium (DMEM). Media were supplemented with 10 % heat-inactivated foetal bovine serum (FBS) and 1 % MEM non-essential amino acids (NEAA). All RPE1 FlpIn HA-VPS35 cell lines were maintained in the presence of 400 µg/ml G418 and 5 µg/ml blasticidin to retain expression of the constructs. All cells were maintained at 37 °C in a humidified 5% CO_2 atmosphere and split 1:5 – 1:10 when sub-confluent, as appropriate, to be passaged again after 2-3 days.

2.2.3 The *lac*Zeo Flp-In T-REx System

Developed by ThermoFisher Scientific, the *lac*Zeo Flp-In™ T-REx™ system (hereafter referred to as the FlpIn system) is used to generate stable cell lines carrying a gene of interest, the expression of which is under the control of a tetracycline repressor. The FlpIn system takes advantage of a site-specific DNA recombinase derived from *S. cerevisiae* to integrate the gene of interest into a host cell line.

The benefits of the FlpIn system are its efficiency, ease, and multi-use once a FlpIn Parental cell line has been generated. The gene of interest is only integrated into the host genome once, at a specific site, allowing for limited disruption of existing genes. As expression can be controlled by tetracycline-class antibiotics, it allows expression of the gene of interest to be titrated and facilitates study of genes where constitutive expression would lead to toxicity.

FlpIn Parental cells are generated by the integration of two plasmids, pcDNA6/TR and pFRT/*lac*Zeo, into the selected host cell line (**Figure 2.2**). The pcDNA6/TR plasmid encodes a Tet repressor (*Tet*R) gene and a gene conferring blasticidin resistance. Both genes are constitutively expressed under the control of a human cytomegalovirus (CMV) promoter and simian virus 40 (SV40) early promoter, respectively. The pFRT/*lac*Zeo plasmid encodes a Flp recombination target site (FRT) and a lacZ-Zeocin fusion gene. The FRT region is the site of binding of the enzyme Flp recombinase which orchestrates DNA recombination.

Following transfection, cells are maintained under blasticidin and zeocin selection to ensure that all cells have stable integration of the two plasmids. It is also important when selecting a FlpIn Parental cell clone that there is only a single insertion of the

FRT site and that there is high TetR expression to allow strong control of expression of the gene of interest.

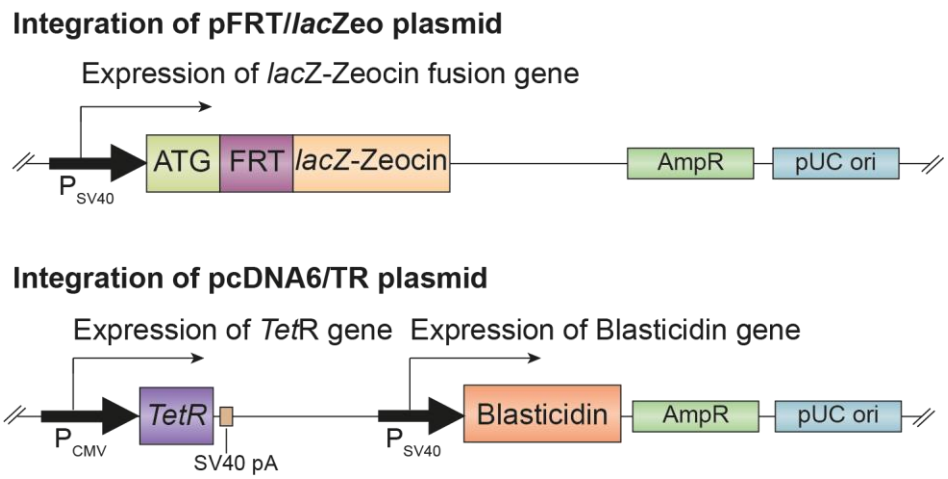

Figure 2.2 FRT/*lac*Zeo and TR genes are stably and randomly integrated into the genome of the host cell line

The RPE1 *lac*Zeo Flp-In T-REx Parental cell line is generated by transfection with pFRT/*lac*Zeo and pcDNA6/TR plasmids. Adapted from Flp-In™ T-REx™ Core Kit manual (Invitrogen).

AmpR, ampicillin resistance; FRT, Flp Recombinase Target; P_{CMV}, cytomegalovirus promoter; P_{SV40}, simian virus 40 early promoter; pUC ori, origin of replication; SV40 pA, SV40 polyadenylation signal; TetR, tetracycline repressor.

Introduction of the gene of interest into the FlpIn Parental cells requires co-transfection of the pCDNA5/FRT/TO expression vector with pOG44, which encodes a Flp recombinase. The pCDNA5/FRT/TO expression vector contains the gene of interest under the control of a tetracycline-inducible promotor (TO), an FRT site, and an antibiotic resistance gene lacking its ATG initiator codon. The pOG44 vector encodes a Flp recombinase which mediates DNA recombination at FRT sites.

The Flp recombinase mediates homologous recombination between the FRT site in genome, originating from the pFRT/lacZeo plasmid, and the FRT site in the pCDNA5/FRT/TO expression vector (**Figure 2.3**). Integration of the pCDNA5/FRT/TO/NeoR expression vector within the FRT site in the genome disrupts the lacZ-Zeocin gene, leading to loss of zeocin resistance and β-galactosidase activity. The ATG initiator codon for lacZeo is then in frame for neomycin resistance. Random integration would not confer neomycin resistance, allowing selection of clones only where the gene of interest has been inserted within the FRT site.

Expression of the gene of interest is under the control of a tetracycline-regulated, hybrid human cytomegalovirus promoter (CMV/2x$TetO_2$) (**Figure 2.4**). Homodimers of Tet repressor protein, encoded by the *TetR* gene originating from the pcDNA6/TR

plasmid, bind with high affinity to the two Tet operator regions ($TetO_2$) in the pcDNA5/FRT/TO/NeoR sequence. As a result, transcription is repressed. Upon addition of tetracycline-class antibiotics, such as tetracycline or doxycycline, the antibiotic binds to TetR, causing its dissociation from the Tet operator. Transcription is thus derepressed, permitting expression of the gene of interest.

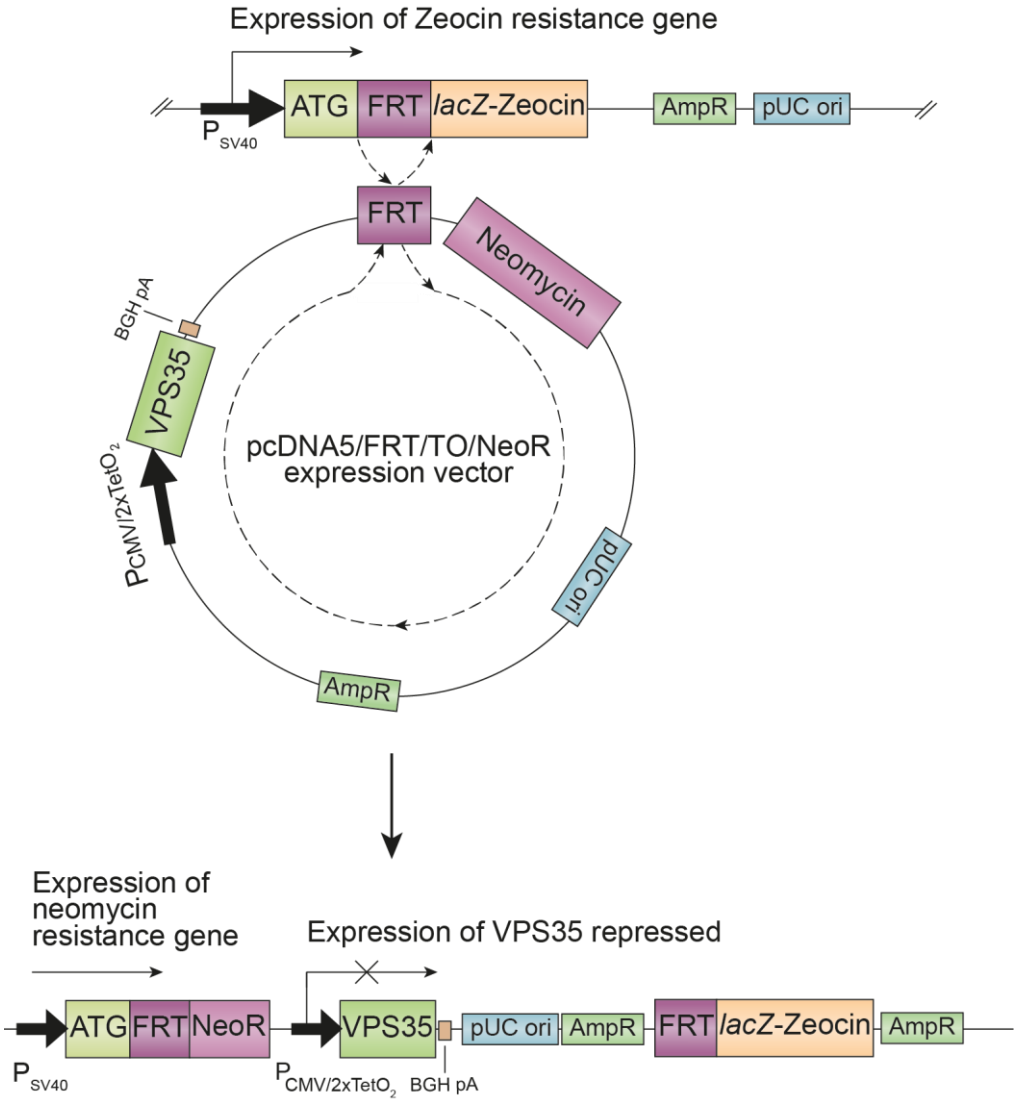

Figure 2.3 Integration of gene of interest into host cell line genome by Flp-mediated DNA recombination

Co-transfection of a pcDNA5/FRT/TO/NeoR expression vector and pOG44 encoding a Flp recombinase into a Flp-In T-REx parental cell line leads to the integration of the gene of interest (VPS35) into the host genome. Adapted from Flp-In™ T-REx™ Core Kit manual (Invitrogen).

AmpR, ampicillin resistance; BGH pA, Bovine Growth Hormone polyadenylation signa; FRT, Flp Recombinase Target; NeoR, neomycin resistance gene; P_{CMV}, cytomegalovirus promoter; P_{SV40}, simian virus 40 early promoter; pUC ori, origin of replication; SV40 pA, SV40 polyadenylation signal; $P_{CMV/TetO_2}$, hybrid cytomegalovirus/ 2x tetracycline operator promoter; TetR, tetracycline repressor; VPS35, vacuolar protein sorting 35.

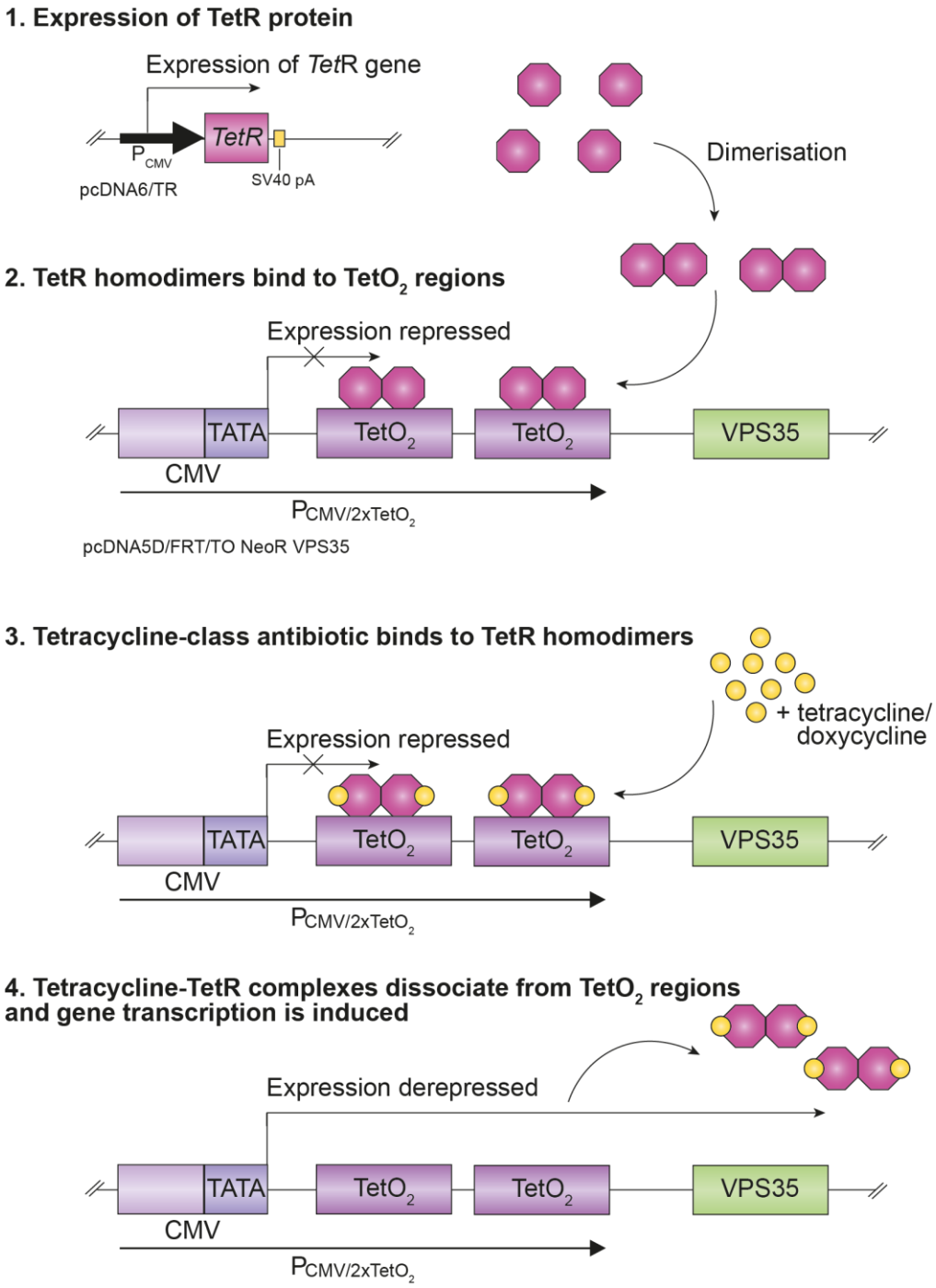

Figure 2.4 Tetracycline-inducible expression of gene of interest

The *Tet*R gene, originating from pcDNA5D/TR plasmid, is constitutively expressed in the host cell line, resulting in the production of TetR protein. Homodimers of TetR bind with high affinity to $TetO_2$ regions, repressing transcription of genes under the control of a CMV/2x$TetO_2$ promoter. Upon addition of tetracycline-class antibiotics such as tetracycline or doxycycline, they bind to TetR causing a conformational change that leads to dissociation from $TetO_2$, derepressing gene transcription. Adapted from Flp-In™ T-REx™ Core Kit manual (Invitrogen).

CMV, cytomegalovirus; P_{CMV}, cytomegalovirus promoter; $P_{CMV/TetO_2}$, hybrid cytomegalovirus/ 2x tetracycline operator promoter; SV40 pA, simian virus 40 polyadenylation signal; $TetO_2$, Tetracycline operator 2; TetR, tetracycline repressor; VPS35, vacuolar protein sorting 35.

2.2.4 Generation of VPS35 FlpIn Cell Lines

For one week prior to transfection, RPE1 FlpIn parental cells were maintained in 10% FBS DMEM/F-12 media containing 10 µg/ml blasticidin and 100 µg/ml zeocin. Using GeneJuice DNA transfection (see **Section 2.2.7**), 200,000 RPE1 FlpIn parental cells were co-transfected with a 10:1 ratio of pOG44-Flp plasmid (900 ng) and pCDNA5 FRT/TO NeoR harbouring either an HA-VPS35 WT or [D620N] mutant insert (100 ng). A control transfection was also performed using a GFP plasmid to assess transfection efficiency, which was approximately 30 % after 24 hours.

Twenty-four hours post-transfection, cells were split 1:4 from a 6-well plate to a 10cm dish and incubated with selection media (10% FBS DMEM/F-12, 1% NEAA, 400 µg/ml G418, 10 µg/ml blasticidin) to yield single colonies expressing both plasmids. Single cell-derived colonies were then left to grow, and once visible were picked and transferred into 24-well plates. Clonal cultures were expanded once confluent into gradually larger culture vessels.

For screening of HA-VPS35 induction, clones were seeded onto 6-well plates and treated with doxycycline (1 µg/ml) for 24 hours. Cells were then lysed and assessed by western blotting for HA and VPS35 (see **Section 2.3.8**).

2.2.5 Isolating monoclonal populations by single-cell dilution

Single cell dilution was performed on RPE1 FlpIn VPS35 WT C4 and [D620N] M9 cell lines to isolate a pure population.

Cell lines were trypsinised and resuspended in DMEM/F12 media containing 400 µg/ml G418 and 10 µg/ml blasticidin. From the homogenised solution, a dilute cell solution of 5 cells/mL was prepared. Cells were seeded into two 96 well plates at 100 µL cell solution per well. This achieves an average density of 0.5 cells/well to increase the likelihood that several wells will receive a single cell and decrease the chance of wells receiving more than one cell. The plates were then left undisturbed for 10 days, at which point they were checked to see if there were observable colonies. Once colonies had grown, they were trypsinised and moved to successively larger culture vessels and then screened.

2.2.6 Generation of VPS35 FlpIn Cell Lines stably expressing eGFP-LRRK2

RPE1 FlpIn VPS35 WT 3B4 and [D620N] 1F3 clones obtained by single-cell dilution (**Section 2.2.5**) were transduced with wildtype, hyperactive [G2019S], or kinase dead [G2019S/D1994A] eGFP-LRRK2 lentivirus at a multiplicity of infection of 0.8 in full media containing polybrene. After 48 hours, media were exchanged. Lentiviral transduction was carried out by Hannah Elcocks. To isolate transduced cells, GFP-positive cells were sorted using fluorescence-activated cell sorting (FACS). In brief, cells were trypsinised, washed in PBS and then resuspended in FACS buffer (PBS + 1% FBS) before being sorted by flow cytometry, using a polybrene only control to set the gate. FACS was carried out by Dr Ailbhe Brazel. Positive cells were expanded and screened by live cell imaging and western blotting for eGFP-LRRK2 expression. To obtain cell lines with homogenous eGFP-LRRK2 expression, the pooled cells were single cell diluted using the methods described in **Section 2.2.5**.

2.2.7 DNA Transfection

Cells were seeded into 6-well plates 24 hours prior to transfection. For transient DNA transfections, 6 µl GeneJuice was added to 250 µl Opti-MEM media per well, gently mixed, then incubated for 5 minutes at room temperature. Plasmid DNA was then added to the mixture, mixed gently, then incubated for 15 minutes at room temperature. The transfection mix was added dropwise to cells in 1750 µl fresh full media. After 24 hours, cells were harvested.

2.2.8 siRNA Transfection

RPE1 FlpIn cells were seeded 24 hours prior to transfection. Cells incubated in serum-free DMEM/F12 media were transfected with 40 nM siRNA in Opti-MEM media using Lipofectamine RNAiMAX in Opti-MEM at a 1:1 ratio. Serum-free DMEM/F12 media were exchanged for full DMEM/F12 media after 6 hours. In general, knockdowns were left for 72 hours and then cells were fixed or lysed. For double hit knockdowns, at 72 hours post-transfection cells were transfected again with 40 nM siRNA using the same method and left for 96 hours. To prevent cells becoming over-confluent in double hit knockdowns, cells were split 24 hours after each transfection. For GST-RILP assays, transfected cells were expanded from a 6 cm dish to a 15 cm dish 24 hours after siRNA transfection. siRNA oligonucleotides used in this project are listed in **Table 2.10**.

Table 2.10 Sequences of ON-TARGETplus siRNA oligonucleotides used for transfection
All siRNAs were purchased from Horizon Discovery (UK) and targeted against the human gene.

Reagent	Catalogue No.	Target sequence
LRRK2 (SMARTpool)	L-006323-00	GAAAUUAUCAUCCGACUAU
		GGAGGGAUCUUCUUUAAUU
		UUACCGAGAUGCCGUAUUA
		CAAGUUAUUUCAAGGCAAA
Rab10 (SMARTpool)	L-010823-00	GCAAGGGAGCAUGGUAUUA
		CACGUUAGCUGAAGAUAUC
		GAUGAUGCCUUCAAAUACUA
		GAAUAGACUUCAAGAUCAA
Rab29 (SMARTpool)	L-010556-00	GAGAACGGUUUCACAGGUU
		CAGGACAGCUUCAGCAAAC
		GGACCAGAUUGACCGGUUC
		GCUAGUAGUGUUUGGCUUA
TBC1D5 (SMARTpool)	L-020775-01	AGAUAAAGAACUUCGAUCA
		GAAUUAAGAGCAUGGUAUA
		CCGAAUCACAAUUUAGAAU
		AUCCAAGACCAGUGACUUA
VPS26A (SMARTpool)	L-013195-00	SEQUENCES NOT PROVIDED
VPS29 (SMARTpool)	L-009764-01	AUGUGAAAGUAGAACGAAU
		CAAGUGAAACUACGGAUAU
		UGAGAGGAGACUUCGAUGA
		AUAUUAAAGUGGACGAGAU
VPS35 (D5)	J-010894-05	GAACAUAUUGCUACCAGUA
VPS35 (D6)	J-010894-06	GAAAGAGCAUGAGUUGUUA
VPS35 (D7)	J-010894-07	GUUGUAAACUGUAGGGAUG
VPS35 (D8)	J-010894-08	GAACAAAUUUGGUGCGCCU
VPS35 (SMARTpool)	L-010894-00	GAACAUAUUGCUACCAGUA
		GAAAGAGCAUGAGUUGUUA
		GUUGUAAACUGUAGGGAUG
		GAACAAAUUUGGUGCGCCU
Non-targeting Control (Control #1)	D-001810-01	TGGTTTACATGTCGACTAA

2.2.9 Drug Treatments

Antimycin A, apilimod, CCCP, epoxomicin, LLOMe, MLi-2, MLN4924 and oligomycin A were solubilised in DMSO. Chloroquine was solubilised in filtered sterile water. Nigericin was solubilised in 100 % ethanol. Drug treatments were performed in full media and added to cells at 0.1 % of the total volume of media. Control cells were treated with vehicle at 0.1 % of the total volume of media for the longest incubation time point in a particular experiment.

2.3 Protein Biochemistry

2.3.1 Materials and Reagents

The reagents and materials used in biochemistry experiments are outlined in **Table 2.11**. If not otherwise stated, chemicals were purchased from Merck/Sigma-Aldrich.

Table 2.11 Protein biochemistry reagents and materials

REAGENT	SOURCE	CAT. NO.
Inhibitors		
Protease Inhibitor Cocktail	Merck (Sigma-Aldrich)	#P8340
cOmplete™, Mini, EDTA-free Protease Inhibitor Cocktail	Merck (Sigma-Aldrich)	#1183617001
PhosSTOP™	Merck (Roche)	#4906837001
Immunoprecipitation Reagents		
Pierce™ Anti-HA Magnetic Beads	ThermoFisher Scientific	#88836
Glutathione Sepharose 4B	Merck (GE/Cytiva)	#GE17-056-01
MagnaRack™ Magnetic Separation Rack	ThermoFisher Scientific (Invitrogen)	#CS15000
Subcellular fractionation Reagents		
Trypan Blue Stain (0.4%)	ThermoFisher Scientific (Invitrogen)	#T10282
Commercial protein assays		
Pierce™ 660nm Protein Assay Kit	ThermoFisher Scientific	#22662
Pierce™ BCA Protein Assay Reagent A	ThermoFisher Scientific	#23223
Pierce™ BCA Protein Assay Reagent B	ThermoFisher Scientific	#23224
IgG from bovine serum, lyophilised powder	Merck (Sigma-Aldrich)	#I5506
IgG from bovine serum, buffered aqueous solution	Merck (Sigma-Aldrich)	#I9640
Precast gels and molecular weight markers		
NuPAGE™ 4 to 12%, Bis-Tris, 1.0mm, Mini Protein Gel, 10-well	ThermoFisher Scientific (Invitrogen)	#NP0321BOX
NuPAGE™ 4 to 12%, Bis-Tris, 1.5mm, Mini Protein Gel, 10-well	ThermoFisher Scientific (Invitrogen)	#NP0335BOX
NuPAGE™ 4 to 12%, Bis-Tris, 1.0mm, Mini Protein Gel, 15-well	ThermoFisher Scientific (Invitrogen)	#NP0336BOX
NuPAGE™ 4 to 12%, Bis-Tris, 1.0mm, Midi Protein Gel, 20-well	ThermoFisher Scientific (Invitrogen)	#WG1402BOX
Unstained Protein Standard, Broad Range (10-200 kDa)	New England BioLabs	#P7717
Amersham™ ECL™ Rainbow™ Marker – Full range	Merck (Cytiva)	#RPN800E
2-Mercaptoethanol	Merck (Sigma-Aldrich)	#M6250
Running buffers		

NuPAGE™ MOPS SDS Running Buffer (20x)	ThermoFisher Scientific (Invitrogen)	#NP000102
NuPAGE™ MES SDS Running Buffer (20x)	ThermoFisher Scientific (Invitrogen)	#NP000202
Equipment		
XCell *SureLock*™ Mini-Cell Electrophoresis System	ThermoFisher Scientific (Invitrogen)	#EI001
XCell *SureLock*™ Midi-Cell Electrophoresis System	ThermoFisher Scientific (Invitrogen)	#WR0100
Genie Blotter with platinised titanium anode, 15 x 17 cm	IDEA Scientific company	#4017
Western Blot Products		
Amersham™ Protran® Western blotting membranes, nitrocellulose, pore size 0.2 µm	Merck (Cytiva)	#GE10600001
Amersham™ Protran® Western blotting membranes, nitrocellulose, pore size 0.45 µm	Merck (Cytiva)	#GE10600002
Ponceau S solution	Merck (Sigma-Aldrich)	#P7170
Revert™ 700 Total Protein Stain	LI-COR	#926-11021
Marvel Original Dried Skimmed Milk Powder	Premier Brands (UK)	-
Bovine Serum Albumin (BSA)	First Link (UK)	#40-00410

2.3.2 Cell Lysis

For routine western blotting, a monolayer of adherent cells were washed twice with ice-cold PBS then lysed in radioimmunoprecipitation assay (RIPA) buffer (150 mM NaCl, 1% sodium deoxycholate, 10 mM Tris-HCl, pH 7.5, 0.1% SDS, 1% Triton X-100) or NP40 cell lysis buffer (100 mM NaCl, 25 mM Tris-HCl pH 7.5, 50 mM NaF, 0.5% NP40) supplemented with mammalian protease inhibitor cocktail (1:250) for 15 minutes on ice, with rocking. If phosphorylation was to be investigated, a phosSTOP phosphatase inhibitor tablet was also added to the lysis buffer (1 tablet per 10 ml). Lysates were cleared by centrifugation at 21,000 x *g* for 30 minutes, and the supernatant collected.

For the GST-RILP active Rab7 pulldown assay (see **Section 2.3.4 below**), which required greater amounts of protein, cells were scraped in ice-cold PBS using a rubber scraper, then spun down at 1000 x *g* for 2 minutes at 4 °C. The cell pellet was then resuspended in high magnesium 'Rab7 lysis buffer' (20 mM Tris HCl, pH 7.8, 50 mM NaCl, 0.5% Triton X-100, 1 mM $MgCl_2$) supplemented with Roche protease inhibitor without EDTA. Lysates were clarified by centrifugation for 30 minutes at 21,000 x *g* at 4 °C and the supernatant collected.

2.3.3 Protein Assay

To determine the protein concentration of cell lysates, two colorimetric assays were used. In most cases a BCA assay was performed, with bovine IgG used to establish a standard curve. **Table 2.12** shows the set-up for a typical BCA assay, which was incubated at 37 °C for 30 minutes before being read at OD_{562} using a BioRad plate reader.

Table 2.12 BCA Protein Assay
Typical BCA protein assay. * BCA Working Reagent made by mixing 50 parts BCA Reagent A with 1 part BCA Reagent B.

	Standard Curve (x2)						**Sample (x3)**
Water (µl)	10	8	6	4	2	0	10
IgG (µl)	0	2	4	6	8	10	0
Lysis Buffer (µl)	3	3	3	3	3	3	-
Cell Lysate (µl)	-						3
BCA Working Reagent* (µl)	200						

For some experiments, protein concentration was ascertained using a Pierce 660nm Protein assay kit. Duplicates of the provided pre-diluted albumin standards were used to create a standard curve. After adding Pierce 660nm Protein Reagent, samples were incubated for 5 minutes at room temperature before being read at OD_{660} on a BioRad plate reader.

After determining protein concentrations, samples were diluted in lysis buffer and 5x sample buffer (312.5mM Tris-HCl, pH6.8, 15% w/v SDS, 50% w/v glycerol, 16% w/w 2-Mercaptoethanol, 0.05% w/v Bromophenol Blue) to standardise concentrations, then boiled for 5 minutes at 95 °C.

2.3.4 GST-RILP active Rab7 pulldown assay

Glutathione sepharose beads (20 µl per condition) were washed three times with PBS. To the washed beads, 5 or 10 µg GST-RILP fusion protein was added, and the mixture was rotated on a wheel overnight at 4 °C.

The next day, the beads were washed in ‘Rab7 lysis buffer’. Cells were harvested with ‘Rab7 lysis buffer’ (see **Section 2.3.2**) and protein concentration was determined (see **Section 2.3.3**). A 10 µg ‘Input’ sample was taken for each condition, equalised to the same protein concentration, diluted in 5x sample buffer, and boiled at 95 °C for 5 minutes. The GST-RILP coupled beads were washed three times with ‘Rab7 lysis buffer’ and incubated with cell lysates according to the maximum amount of protein

available in all cell lysate samples (i.e. µg protein in the least concentrated sample). The sample and bead mixtures were then incubated for 2 hours at 4 °C on a spinning wheel. After incubation, beads were washed twice in 'Rab7 wash buffer' (20 mM Tris HCl, pH 7.8, 50 mM NaCl, 3 mM $MgCl_2$), followed by a final wash in 10 mM Tris-HCl (pH 7.5). After the final spin, the supernatant was removed, and bound Rab7 was eluted from immobilised GST-RILP using 2.5x sample buffer. Samples were boiled at 95 °C for 5 minutes and then resolved by gel electrophoresis (see **Section 2.3.8**).

2.3.5 Immunoprecipitation

For immunoprecipitation experiments, cells were lysed in NP40 lysis buffer supplemented with MPIs and HA-precipitated using anti-HA magnetic beads. Approximately 10% of lysate was retained as an input sample and prepared as usual for western blotting (**Section 2.3.8**). For each condition, 25 µl of magnetic anti-HA bead slurry was washed three times with TBS / 0.05% Tween-20 (TBS-T) using a magnetic stand. Cell lysates were then added to the pre-washed beads and incubated on a wheel for 90 minutes at 4 ºC. After incubation, samples were washed twice in NP40 buffer and once in 10 mM Tris-HCl (pH 7.5). To elute proteins, 40 µL of 1x sample buffer was added to each tube and mixed gently before being heated at 95 ºC for 10 minutes. Samples were vortexed for 5-10 seconds and the beads magnetically separated from the final sample. Samples were then subjected to the standard immunoblotting protocol, with the entire sample being loaded onto the gel (**Section 2.3.8**).

2.3.6 Cathepsin D secretion assay

For assessment of basal secretion, cells were washed three times in warmed PBS and media were exchanged for serum-free Opti-MEM (1 ml per well of a 6-well plate) and incubated for 16 hours. For endolysosomal stress experiments, cells were washed three times in warmed PBS and media were exchanged for serum-free Opti-MEM media containing treatments (1 ml per well of a 6-well plate) and incubated for 3 hours. Conditioned media were collected, and the adherent cells were washed twice with ice-cold PBS and lysed in NP40 buffer (**see Section 2.3.2**). Media were spun at 3,000 x *g* for 10 minutes at 4 °C to pellet dead cells and cell debris, then 900 µl was transferred to a new tube. Haemoglobin/PBS was then added (100 µL) to aid protein precipitation and visualisation of the pellet. Sodium deoxycholate was added to the media at final concentration of 0.02%, which was then vortexed and incubated on ice for 30 minutes. Trichloroacetic acid (TCA) (100% w/v) was added to a final concentration of 10% w/v, mixed, then incubated on ice for one hour. Media samples

were then centrifuged at 21 000 x *g* for 30 minutes at 4 °C to pellet the protein precipitates. The supernatant was removed, and the resulting pellet was washed twice in ice-cold acetone. After the final acetone wash, pellets were left at room temperature for 10 minutes to allow any remaining acetone to evaporate. The pellet was then resuspended in 1x SDS sample buffer. If the sample buffer turned yellow, unbuffered Tris (1M) was added in 1 µl increments until it turned blue. Samples were then boiled at 95 °C for 5 minutes and subjected to the standard immunoblotting protocol, with the entire media samples being loaded onto the gel (**Section 2.3.8**).

2.3.7 Subcellular fractionation

All elements of the subcellular fractionation procedure were performed using ice-cold reagents and equipment that was pre-cooled and maintained at 4 °C. Two 15 cm dishes per condition were washed twice with ice-cold PBS and then each scraped in 5 ml PBS using a rubber scraper. Cell suspensions from the duplicate dishes were combined and centrifuged for 2 minutes at 1000 x *g*. The resulting cell pellets were washed in 5 ml HIM buffer and centrifuged for 5 minutes at 1000 x *g*. The cells were resuspended in 1 ml HIM buffer supplemented with MPIs and mechanically homogenised by shearing through a 23 gauge needle between three and six times. Efficient homogenisation was confirmed using Trypan Blue staining. Cell homogenates were centrifuged at 600 x *g* for 10 minutes to pellet nuclei and obtain a post nuclear supernatant (PNS). A 100 µl sample of PNS was retained and the remaining sample was further separated by ultracentrifugation at 100,000 x *g* for 30 minutes to obtain cytosol supernatant and membrane pellet fractions. The membrane pellet was resuspended in 200 µl HIM buffer. The protein concentration of the samples was determined by BCA assay (see **Section 2.3.3**) and samples within each fraction were adjusted to the same final concentration. Equivalent amounts of PNS, membrane and cytosol fractions were analysed by western blotting (**Section 2.3.8**).

2.3.8 SDS-PAGE and Western Blotting

Equal amounts of protein from each sample were loaded onto 4-12 % Bis-Tris precast NuPAGE gels. A pre-stained rainbow molecular weight marker and an unstained broad range marker were run alongside samples as standards. Gels were resolved at 100 V for 20 minutes then at 150 V for 70 minutes. In general, MOPS buffer was used. When resolving mainly low molecular weight proteins MES buffer was used.

Resolved gels were then transferred onto nitrocellulose membrane in transfer buffer (25 mM Tris, 192 mM Glycine, 20 % v/v methanol). When looking at low molecular weight proteins, 0.2 µm nitrocellulose was used. Otherwise, 0.45 µm nitrocellulose

membrane was used as standard. Transfers were performed at ~1 A / 25 V for 2 hours on ice or 1 hour at room temperature. Ponceau S stain was used to check transfer efficiency and loading consistency. An image of the Ponceau-stained blot was taken using a light box. Where appropriate, membranes were cut horizontally, using the molecular weight markers for reference, to maximise the number of proteins that could be probed for per blot. Ponceau was then washed off the blot with TBS-T (0.1 % w/v Tween-20) for 5 minutes.

Membranes were blocked for one hour in 5 % Marvel skimmed milk powder / TBS-T. Primary antibodies were incubated with the membranes according to the conditions shown in **Table 2.13** in 5% Marvel/TBS-T for most antibodies, apart from phospho-Rab10 and phospho-Rab12 antibodies which were incubated in 5% BSA/TBS-T. Membranes were washed 3 times for 5 minutes each in TBS-T before incubation with the appropriate secondary antibody (see **Table 2.14**) for 45-60 minutes at room temperature. Membranes were visualised using a LI-COR Odyssey Imaging System. Quantification was performed using LI-COR Odyssey Image Studio. Line traces were generated using Fiji software.

Table 2.13 Primary antibodies used in Western Blotting

M - mouse; Rb – rabbit; Sh – sheep; G – goat; O/N – overnight; RT - room temperature.

Protein	Species	Source	Catalogue no.	Dilution	Incubation conditions
Actin	M	Proteintech	66009-1-IG	1:10000	O/N, 4 ºC or 20 min, RT
Actin	Rb	Proteintech	20536-1-AP	1:2000	1 h, RT
ALIX	M	Santa Cruz	sc-53540	1:1000	O/N, 4 ºC
Cathepsin D	Rb	Calbiochem	219361	1:2000	O/N, 4 ºC or 1 h, RT
CIMPR	Rb	Gift from Paul Luzio		1:1000	O/N, 4 ºC
Cullin 2	Rb	Bethyl	A302-476A	1:2000	O/N, 4 ºC
FIS1	Rb	Proteintech	10956-1-AP	1:1000	O/N, 4 ºC
HA	M	Covance	MMS-101P	1:1000	O/N, 4 ºC or 1 h, RT
HRS	M	Axxora	ALX-804-382-C050	1:3000	O/N, 4 ºC
HSP60	G	Santa Cruz	sc-1052	1:1000	O/N, 4 ºC
JIP4	Rb	Cell Signalling Technology	5519 (D72F4)	1:1000	O/N, 4 ºC
LC3	M	Nanotools	5F10	1:200	1 h, RT
LRRK2	M	NeuroMab	N241A/34	1:50	O/N, 4 ºC
MFN2	M	Abcam	Ab56889	1:1000	O/N, 4 ºC
MUL1	Rb	Invitrogen	PA5-29550	1:1000	O/N, 4 ºC
OPA1	Rb	Abcam	ab42364	1:1000	O/N, 4 ºC

p62/SQSTM1 – Lck ligand	M	BD Biosciences	610833	1:1000	O/N, 4 ºC
PINK1	Rb	Cell Signalling	6946	1:1000	O/N, 4 ºC
Rab10	Rb	CST	8127 (D36C4)	1:1000	O/N, 4 ºC
Rab10 pT73	Rb	Abcam	ab230261	1 µg/ml	O/N, 4 ºC or 1 h, RT
Rab12	Sh	MRC PPU	SA227	1 µg/ml	O/N, 4 ºC
Rab12 pS106	Rb	Abcam	ab256487	1:1000	O/N, 4 ºC or 1 h, RT
Rab29	Sh	MRC PPU	DU50291	1:400	O/N, 4 ºC
Rab7	Rb	Abcam	ab137039	1:1000	O/N, 4 ºC
Sortilin	Rb	Abcam	ab16640	1:1000	O/N, 4 ºC
TBC1D5	M	Santa Cruz	sc-376296	1:1000	O/N, 4 ºC
TOM20	Rb	Proteintech	11802-1-AP	1:1000	O/N, 4 ºC
TOM40	Rb	Novus Biotechne	NBP2-38289	1:1000	O/N, 4 ºC
Ubiquitin pS65	Rb	Millipore	05-1308	1:1000	O/N, 4 ºC
Ubiquitin pS65	Rb	Cell Signalling	62802	1:1000	O/N, 4 ºC
VDAC1	M	Abcam	ab14734	1:1000	O/N, 4 ºC
VPS26A	Rb	Abcam	ab23892	1:1000	O/N, 4 ºC
VPS29	Rb	Abcam	ab98929	1:500	O/N, 4 ºC
VPS35	G	Abcam	ab10099	1:1000	O/N, 4 ºC
WASHC1	Rb	Sigma Aldrich	HPA002689	1:2000	O/N, 4 ºC

Table 2.14 Secondary antibodies used in Western Blotting

Secondary Antibody	Source	Catalogue no.	Dilution
Donkey anti-mouse IRDye 800CW	LI-COR	#926-32212	1:10,000
Donkey anti-mouse IRDye 680CW	LI-COR	#926-32222	1:10,000
Donkey anti-rabbit IRDye 800CW	LI-COR	#926-32213	1:10,000
Donkey anti-rabbit IRDye 680CW	LI-COR	#926-32223	1:10,000
Donkey anti-goat IRDye 800CW	LI-COR	#925-32214	1:10,000
Donkey anti-sheep IRDye 680CW	LI-COR	#926-32224	1:10,000

2.4 Microscopy

2.4.1 Materials and reagents

The reagents and materials used in imaging experiments are outlined in **Table 2.11**. If not otherwise stated, chemicals were purchased from Merck/Sigma-Aldrich.

Table 2.15 Protein biochemistry reagents and materials

REAGENT	SOURCE	CAT. NO.
Fixed-cell reagents		
Pierce™ 16% Formaldehyde (w/v), Methanol-free ampoules	ThermoFisher Scientific	#28908
Bovine Serum Albumin (BSA)	First Link (UK)	#40-00410
Goat Serum Donor Herd	Merck (Sigma-Aldrich)	#G6767

DAPI (4',6'diamidino-2-phenylindole)	ThermoFisher Scientific (Invitrogen)	#D1306
MOWIOL® 4-88 Reagent	Merck (Millipore)	#475904-M
Live-cell Imaging Reagents		
µ-Slide 8 Well Chamber Slide	ibidi	#80821
µ-Dish 35 mm, high	ibidi	#81156
DMEM/F12, no phenol red	Fisher Scientific (Gibco)	#21041025
Hoechst 33342	ThermoFisher Scientific (Invitrogen)	#62249
LysoTracker™ Red DND-99	ThermoFisher Scientific (Invitrogen)	#L7528
MitoTracker™ Green FM	ThermoFisher Scientific (Invitrogen)	# M7514
Tetramethylrhodamine, Ethyl Ester, Perchlorate (TMRE)	ThermoFisher Scientific (Invitrogen) Gift from Shankar Varadarajan	#T669

2.4.2 Immunofluorescence

When using paraformaldehyde (PFA) fixation, all steps were performed at room temperature using room temperature reagents. Cells adhered to coverslips were washed twice with PBS before being incubated with 4% PFA/PBS for 15 minutes. The PFA was then quenched using 50 mM ammonium chloride (NH_4Cl) for 10 minutes. After washing twice again with PBS, cell membranes were permeabilised by incubation with 0.2% Triton X-100 for 4 minutes. In some instances, methanol fixation and permeabilisation was employed. Cells were washed with room temperature PBS followed by incubation with ice-cold methanol for 5 minutes at -20 °C. In general, methanol fixation was used when TGN46 and LC3 primary antibodies were used.

Following either method of fixation, cells were blocked for 30 minutes in either 10 % goat serum /PBS or 3 % BSA/PBS. In general, BSA was used when LAMP antibodies were used or when one of the primary antibodies was raised in goat. After blocking, cells were incubated with primary antibodies for 1 hour (**Table 2.16**). Cells were then washed twice in PBS before incubating with secondary antibody in the same incubation buffer used for the primary antibodies for 30 minutes (

Table 2.17). After two washes in PBS, coverslips were dipped in PBS, then in Millipore H_2O and then mounted onto glass slides with Mowiol containing DAPI (1:5000). Coverslips were left to dry overnight in a dark room before being stored at 4 °C.

Table 2.16 Primary antibodies used for immunofluorescence staining

M - mouse; Rb – rabbit; Sh – sheep; G – goat

Target	Species	Source	Cat. No.	Dilution
ALIX	M	Santa Cruz	Sc-53540	1:500
CD63	M	DSHB	H5C6	1:500
CHMP2B	Rb	Abcam	ab157208	1:500
CIMPR	Rb	Gift Paul Luzio		1:500
EEA1	M	BD	610456	1:500
FAM21C	Rb	Merck	ABT79	1:1000
HA	G	Novus Biotechne	NB600-362	1:400
HA	M	Covance	MMS-101P	1:500
HA	Rat	Roche	11867423001	1:500
HRS	M	Axxora	ALX-804-382-C050	1:500
HSP60	G	Santa Cruz	sc01952	1:500
LAMP1	M	DSHB	H4A3	1:200
LAMP1	Rb	Cell Signalling Technology	9091 (D2D11)	1:200
LAMP2	M	DSHB	H4B4	1:500
LC3	M	Nanotools	5F10	1:200
p230	M	Biorad	611281	1:500
Rab7	Rb	Abcam	ab137029	1:500
Sortilin	Rb	Abcam	ab16640	1:1000
TGN46	Sh	Biorad	AHP500	1:500
TIMM44	Rb	Sigma	HPA043052	1:500
TOM20	M	BD Transduction	612278	1:500
TOM20	Rb	Sigma	HPA01152	1:100
VPS26A	Rb	Abcam	ab23892	1:800
VPS35	G	Abcam	ab10099	1:150
WASHC1	Rb	Sigma Aldrich	HPA002689	1:100

Table 2.17 Secondary antibodies used for immunofluorescence staining

Secondary Antibody	Source (Catalogue no.)	Dilution
Donkey anti-mouse AlexaFluor-488	Invitrogen (A21202)	1:500
Donkey anti-rabbit AlexaFluor-488	Invitrogen (A21206)	1:500
Donkey anti-sheep AlexaFluor-488	Invitrogen (A11015)	1:500
Donkey anti-mouse AlexaFluor-594	Invitrogen (A21203)	1:500
Donkey anti-rabbit AlexaFluor-594	Invitrogen (A21207)	1:500
Donkey anti-rat AlexaFluor-594	Invitrogen (A21209)	1:500
Donkey anti-sheep AlexaFluor-594	Invitrogen (A11018)	1:500
Donkey anti-mouse AlexaFluor-647	Invitrogen (A32787)	1:500
Donkey anti-rabbit AlexaFluor-647	Invitrogen (A32795)	1:500
Donkey anti-goat AlexaFluor-647	Invitrogen (A21447)	1:500
Goat anti-rat AlexaFluor-488	Invitrogen (A11006)	1:500
Goat anti-rat AlexaFluor-594	Invitrogen (A11007)	1:500
Goat anti-rat AlexaFluor-647	Invitrogen (A48265)	1:500

2.4.3 Live cell staining

For Mitotracker and Lysotracker assays, cells were seeded into 35 mm glass bottomed ibidi dishes. Cells were stained with 50 nM Mitotracker Green for 30 minutes, after which the media were exchanged, and cells were stained with 500 nM

Lysotracker Red DND-99 for 5 minutes. Cells were washed twice with PBS and incubated with DMEM/F12 without Phenol Red for 15 minutes before live cell imaging.

For assessment of mitochondrial membrane potential, cells were seeded into 35 mm glass bottomed ibidi dishes. Cells were stained with 50 nM TMRE and 0.5 µg/ml Hoechst 33342 for 30 minutes before being washed in PBS and the media exchanged for fresh DMEM/F12. Dishes were left to equilibrate for at least 20 minutes prior to imaging.

2.4.4 Image acquisition

Brightfield and fluorescence images for fixed samples were taking using a Nikon Ti-Eclipse brightfield microscope equipped with a CFI Plan Fluor DLL 10x air objective, a CFI Plan Apo 40x air objective or a CFI Plan Apochromat VC 63x oil objective lens. Confocal images were acquired on a Zeiss LSM800 or LSM900 confocal microscope with Airyscan using an APO 63x 1.4 NA oil objective or 40x LD C-Apochromat water objective.

For live cell confocal microscopy, cells were placed in a humidified chamber with 5% CO_2 at 37 °C. Confocal images were acquired with a 3i Marianas spinning disk confocal microscope (3i, Intelligent Imaging Innovations, Germany), using either a 40x 1.3 NA oil or a Plan-Apo 63x/1.4 NA oil objective lens or a Zeiss LSM900 confocal microscope with Airyscan with an 40x LD C-Apochromat water objective. For lysokeima assays, cells were seeded into ibidi 8-well chamber slides. Prior to imaging, media were exchanged for DMEM/F12 without phenol red. Lysokeima and mitokeima imaging was performed on a 3i Marianas spinning disk confocal microscope (photometrics Evolve EMCCD camera, acquisition software Slide Book 3i v3.0) Images were acquired sequentially (445 nm excitation, 617/73 nm emission; 561 nm excitation, 617/73 nm emission).

2.4.5 Image processing

Images were processed using Fiji, OMERO.web version 5.5 and Adobe Photoshop (2023). Figures were assembled using Abode Illustrator (2023).

2.4.6 Image analysis

2.4.6.1 Corrected total cell fluorescence

The fluorescence intensity within individual cells was determined by calculating the Corrected Total Cell Fluorescence (CTCF) using Fiji. The outline of individual cells was manually traced using the Freehand Selection Tool and the area, integrated

density and mean grey value measured. Two to three areas of background were also selected and their mean grey values were used to calculate the average background fluorescence. The CTCF was calculated using the following equation:

CTCF = Cell Integrated density – (area of selected cell x mean background fluorescence)

2.4.6.2 Particle analysis

The ‘Analyze Particle’ command on Fiji was used to quantify and measure objects within images. First, cell outlines were manually traced using the Freehand Selection Tool. Images were processed using a ‘Median’ or ‘Gaussian Blur’ filter to remove noise. The images were then segmented using either a manual or automatic threshold as appropriate for the particular experiment. If necessary, ‘Fill Holes’ and ‘Watershed’ functions were used to fill in hollow objects or separate overlapping objects, respectively. The ‘Analyse Particles’ command was then performed on the binary image using the ‘Summarize’ function to count the number of objects within each cell, their average size, total area, and the proportion of the cell occupied by the objects.

For measurement of the intensity of the particles, image segmentation was performed on a duplicate image and the ‘Analyse Particles’ command was set to redirect measurements so they were taken from the unsegmented image.

2.4.6.3 Organelle distribution analysis

The distribution of lysosomes and endosomes was analysed using a method adapted from (Starling et al., 2016). Cell outlines were manually traced using the Freehand selection tool. The cell area shape was scaled in 10% decrements to create concentric regions of interest around the centre of the cell. For each region, the integrated density was calculated and plotted as a function of the integrated density of the whole cell to generate the cumulative integrated signal intensity. Data points were then plotted to generate a positioning curve to inform on the distribution of organelles (**Figure 2.5**). A leftward shift of the curve indicates indicates clustering towards the cell center, whereas a rightward shift of the curve indicates a more peripheral distribution.

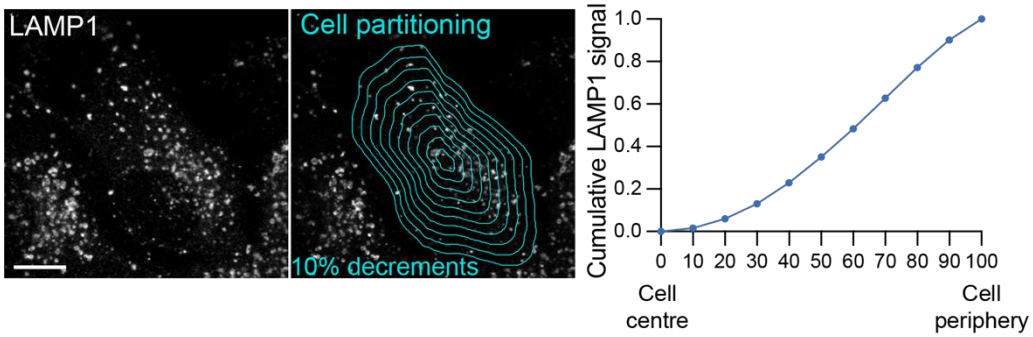

Figure 2.5 Example of organelle distribution analysis

Example of organelle distribution analysis workflow. RPE1 FlpIn VPS35 WT 3B4 cells stained for LAMP1 (right). Individual cells are outlined manually using the Freehand Selection Tool. The whole cell region of interest is used to generate concentric regions at 10% size decrements (middle). The integrated density of LAMP1 signal is measured for each region and calculated as a function of the integrated density for the whole cell area to generate the cumulative LAMP1 signal intensity. Mean values for each decile are calculated from the cells analysed and plotted to generate a positioning curve (left). Scale bar 10 µm.

2.4.6.4 Co-localisation analysis

The co-localisation of two proteins of interest was calculated using the Coloc 2 plugin in Fiji. The outlines of individual cells were manually traced using the Freehand Selection Tool and Coloc 2 co-localisation analysis was performed to calculate the Pearson's correlation coefficient.

2.4.6.5 Mitochondrial network analysis

The MiNA (Mitochondrial Network Analysis) plugin was used to characterise the morphology of the mitochondrial network using the mitochondrial marker TOM20 (Valente et al., 2017). Briefly, the Freehand Selection Tool was used to manually trace individual cell outlines. If necessary, images were pre-processed using an 'Unsharp Mask' and a 'Median' filter to reduce noise. Within the MiNA plugin, a binary mask of the mitochondrial network is generated and used to calculate the area of the cell occupied by the mitochondrial network, the so-called 'mitochondrial footprint' (**Figure 2.6**). The binary mask is then skeletonised and used to compute several parameters about the mitochondrial network morphology, including the mean number of branches per cell (number of mitochondrial branches stemming from a junction node) and the mean branch length.

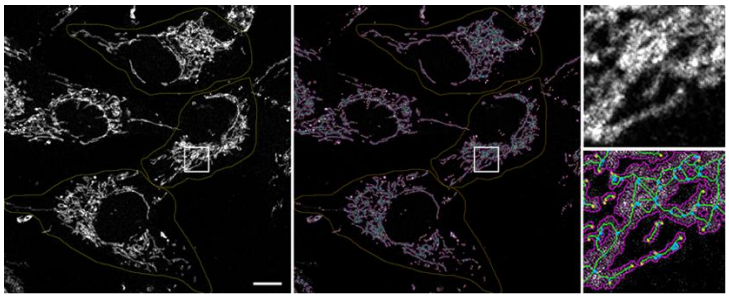

Figure 2.6 Example of MiNA plugin analysis

Exemplar image of implementation of MiNA Fiji plugin on RPE1 FlpIn VPS35 WT 3B4 cells stained for TOM20. Individual cells are outlined manually using the Freehand Selection Tool. From the original image (left), the MiNA plugin creates a binary mask of the mitochondrial network which is used calculate the area of the cell occupied by mitochondria (purple outline). The binary mask is skeletonised to compute information on the network morphology. Blue dots represent network junction nodes. Yellow dots represent network endpoints. Green lines indicate mitochondrial network branches. Scale bar 10 μm.

2.4.6.6 Mitophagy quantification

Mitophagy was quantified using the 'mito-QC Counter' plugin in Fiji, described in (Montava-Garriga et al., 2020). Briefly, outlines of cells were manually traced using the Freehand Selection Tool and added as overlays onto the image which was then saved as a separate image file. This was repeated for all images. Optimal settings for the radius for smoothing images, the ratio threshold (tolerance) and red channel threshold standard deviation above the mean were determined using a test set of images from each condition. The mitolysosomes identified by the counter were compared to manual counting and visual inspection of the original images. The following parameters were used: radius for smoothing images = 1, ratio threshold = 0.6, and red channel threshold = mean + 1 SD. Next, the mito-QC counter plugin was run in batch mode on all images to calculate the number of mitolysosomes per cell and the mean mitolysosome area (μm^2) per cell.

2.5 Statistical Methods

Graphs were prepared and statistical analyses were performed using GraphPad Prism 10. *n* represents the number of independent experimental repeats. Graphs indicate mean and standard deviation (when $n \geq 3$) or range (when $n = 2$). For experiments with at least three independent repeats, statistical significance was determined. In experiments with two conditions, unpaired or paired t-tests were used. In experiments with more than two conditions, statistical significance was determined using an ordinary one-way analysis of variance (ANOVA) with either Tukey's or Šídák's multiple comparisons tests, as indicated in the corresponding figure legends. P-values are represented as *P < 0.05, **P < 0.01, ***P < 0.001 and ****P < 0.0001.

3 Assembling the tools to explore the VPS35-LRRK2 connection

3.1 Introduction

When analysing the functions of the *PARK* gene products, two overarching biological processes stand out; endolysosomal trafficking and mitochondrial function. Given the emergence of these common themes, it suggests dysfunction in these processes is integral to disease pathology. This begs the question as to whether a subset of these *PARK* genes are causing dysfunction in common pathways, as has been shown in the case of cancer, where multiple genes in the Receptor Tyrosine Kinase (RTK)/ Ras GTPase/ MAP kinase pathway are found to be mutated (Sanchez-Vega et al., 2018). This notion was confirmed by the discovery that the PD genes PINK1 and Parkin act in concert to mediate the removal of damaged mitochondria by mitophagy (Clark et al., 2006; Narendra et al., 2008; Park et al., 2006).

Likewise, Parkinson's mutations in both VPS35 and LRRK2 have been shown to cause similar cellular phenotypes, including disrupted endocytic trafficking, defects in autophagy and mitochondrial dysfunction (Erb and Moore, 2020; Singh et al., 2019; Williams et al., 2017). Trafficking defects caused by mutant LRRK2 can be rescued by overexpression of wild type VPS35, suggesting a common axis involving these proteins (MacLeod et al., 2013). Furthermore, defects in dopamine transporter trafficking and striatal dopamine transmission observed in VPS35[D620N] knockin mice can be ameliorated by LRRK2 kinase inhibition, suggesting that VPS35 may lie upstream in this pathway (Bu et al., 2023). The [D620N] mutation in VPS35 has been shown to cause hyperphosphorylation of a number of Rab proteins through the action of LRRK2, (Mir et al., 2018). This finding has since been reproduced by independent groups, however, how VPS35 causes hyperactivation of LRRK2 function is not yet understood (Bu et al., 2023; Kadgien et al., 2021). Evidence for a direct interaction between LRRK2 and VPS35 is lacking. Two studies have shown that endogenous LRRK2 and VPS35 can be co-immunoprecipitated from mouse brain lysates (Kadgien et al., 2021; MacLeod et al., 2013), and when over-expressed in SH-SY5Y cells (MacLeod et al., 2013), however Inoshita and colleagues reported a failure to detect an interaction (data not shown in paper, methodology unclear) (Inoshita et al., 2017).

The small GTPase Rab7 plays a fundamental role in the endolysosomal system, controlling trafficking, endosome maturation and lysosome function, positioning and biogenesis (Guerra and Bucci, 2016). VPS35 has been shown to play an integral role

in the cycling of Rab7 from active to inactive and membrane bound to cytosolic states, where deletion of VPS35 causes accumulation of active Rab7 at lysosomes (Jimenez-Orgaz et al., 2018). PD-linked mutations in LRRK2 have been reported to decrease Rab7 activity (Gómez-Suaga et al., 2014). Given that VPS35 and LRRK2 have been shown to be functionally linked and that both affect Rab7 activity, it is possible that Rab7 dysfunction plays a part in this VPS35-LRRK2 axis.

The following chapter outlines the generation and characterisation of tools that I made to further explore the link between VPS35 and LRRK2, which includes:

- Assessing the suitability of RPE1 cells as a model to study VPS35 and LRRK2
- Creating isogenic cell lines expressing wild type and [D620N] VPS35 in RPE1 cells using the Flp-In™ T-Rex™ system
- Generating RPE1 FlpIn HA-VPS35 cells stably overexpressing LRRK2 through lentiviral transduction
- Establishing the GST-RILP assay in the lab as a method to measure active Rab7

The generation of cell lines and development of the GST-RILP assay described in this chapter was carried out in collaboration with Hannah Elcocks.

3.2 RPE1 cells as a system for looking at VPS35 and LRRK2

3.2.1 RPE1 cells express endogenous VPS35 and LRRK2

To choose a cell line to use in this project, the endogenous levels of LRRK2, VPS35, Rab7 and Rab29 were assessed by western blotting across a panel of cell lines from several origins; pigmented (MNT1, 501mel) and non-pigmented (WM266.4, A375P) melanoma, neuroblastoma (SH-SY5Y, SKNBE2), retinal pigment epithelium (RPE1) and osteosarcoma (U2OS) (**Figure 3.1**).

The expression of VPS35 was similar between cell lines, but the highest levels were seen in MNT1 cells (**Figure 3.1B**). In contrast, the levels of Rab7 varied greatly between different cell lines. The highest levels of Rab7 were observed in melanoma cells, particularly the pigmented lines 501mel and MNT1. Of the non-melanoma cell lines, RPE1, SKNBE2 and SH-SY5Y cells all had similar Rab7 expression (**Figure 3.1C**). The expression of Rab29 was also higher in melanoma cell lines compared to those from other origins but did not follow the same pattern as Rab7 and was not higher in the pigmented melanoma lines (**Figure 3.1E**).

LRRK2 expression differed greatly between the cell lines tested, ranging from highest expression in the non-pigmented melanoma WM266.4 cells, to almost undetectable in pigmented melanoma line 501mel and the two neuroblastoma cell lines SH-SY5Y and SKNBE2 (**Figure 3.1D**). This is in accordance with data from the Cancer Cell Line Encyclopaedia (CCLE) which shows that across a database of cancer cell lines, LRRK2 mRNA abundance was high in melanoma and cancers of the bone (Ewing's sarcoma and Giant cell tumour), and low in neuroblastoma (Barretina et al., 2012). In the U2OS sample, two bands were visible for LRRK2 at ~200 kDa and 150 kDa. This has been reported before in neutrophils and has been attributed to a proteolysed form of LRRK2 (Mir et al., 2018).

As RPE1 cells expressed endogenous VPS35 and LRRK2 and we had RPE1 cells stably expressing the Flp-In™ T-Rex™ system available in the laboratory, I decided to use this line for my project. This cell line also has the advantage of being 'near-diploid' compared to the aberrant karyotypes seen in immortalised cancer cell lines.

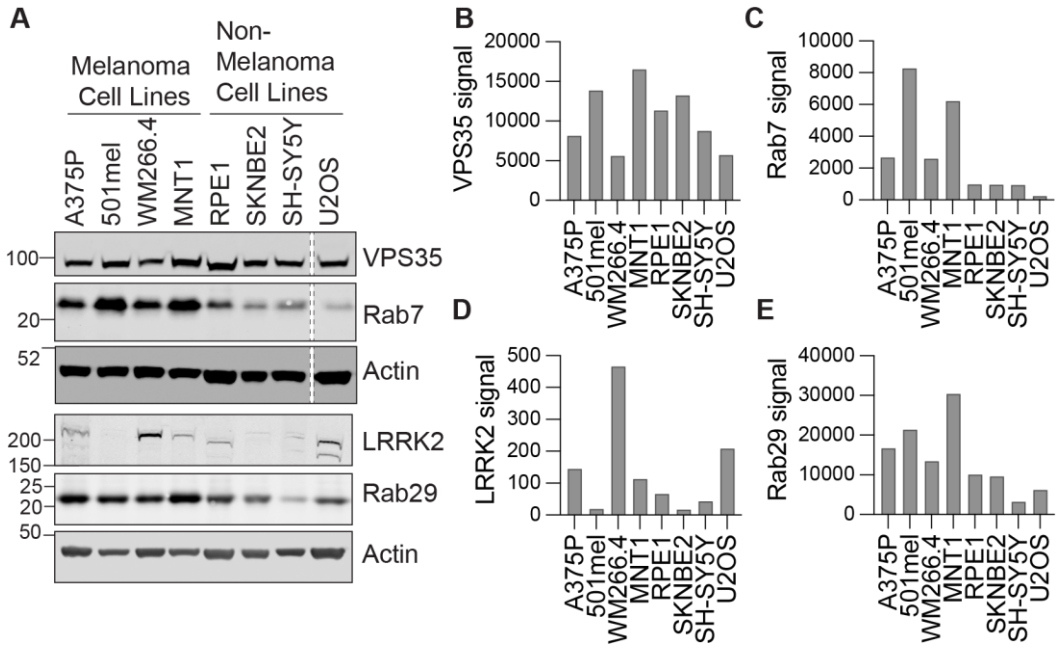

Figure 3.1 VPS35 and LRRK2 expression in a panel of cell lines

A A375P, WM266.4, 501mel, MNT1, RPE1, SKNBE2, SH-SY5Y and U2OS cell lysates were analysed by immunoblotting for expression of VPS35, Rab7, LRRK2 and Rab29. Dashed line indicates a lane that has been removed. **B-E** Quantification of western blots shown in A. Values normalised to actin. Data from a single experiment, *n* = 1.

3.2.2 Optimisation of retromer knockdown

To allow the study of retromer function in RPE1 cells, I first confirmed the efficiency of depleting cells of retromer sub-units using siRNA-mediated gene silencing.

Previous lab members had employed a double-hit protocol to knockdown the retromer complex in other cell lines where 72 hours after cells were first transfected with siRNA, they are transfected again and left for another 72-81 hours before lysis, totalling either 144 or 165 hours. The rationale behind the extended, double-hit knockdown protocol was based on the fact that the half-life of VPS35 is reportedly 138 hours (Schwanhäusser et al., 2011). I compared the efficiency of retromer knockdown using the single- and double-hit protocols in RPE1 cells (**Figure 3.2**). Using immunoblotting to look at the levels of retromer subunits after knockdown of VPS35 or VPS29, I found that 72 hour knockdown was sufficient to cause substantial depletion of the targeted protein and little to no further loss was evident at the 144-hour time-point (**Figure 3.2A**).

Depletion of VPS35 caused a concomitant reduction of VPS26A and VPS29. Similarly, VPS35 and VPS26 were depleted following knockdown of VPS29. This co-regulatory effect on other retromer components was also apparent by immunofluorescence microscopy. After depletion of VPS35, qualitatively there was an overall decrease in the VPS26A fluorescent signal, and the pool localised to EEA1-positive endosomes was lost (**Figure 3.2B**).

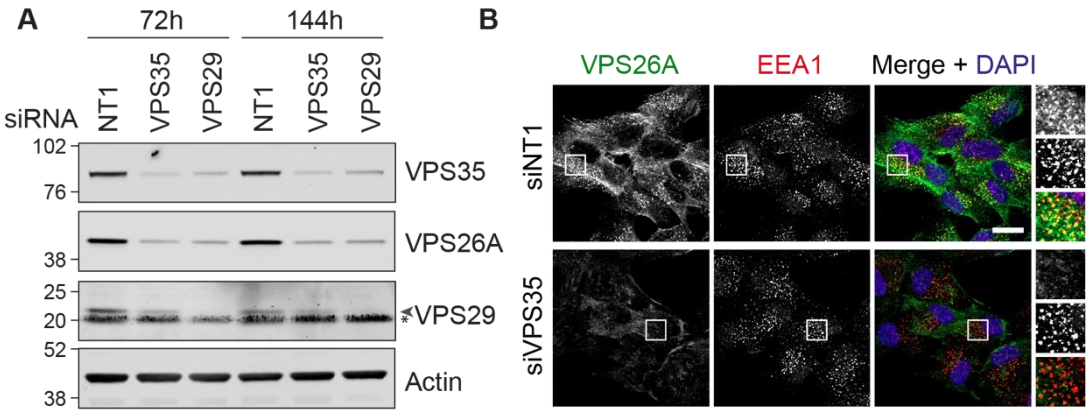

Figure 3.2 VPS35 knockdown destabilises retromer

A RPE1 FlpIn Parental cells were subjected to siRNA knockdown for 72 or 144 hours with control (non-targeting #1; NT1) or a pool of VPS29 or VPS35 targeting oligonucleotides before being lysed in RIPA buffer and analysed by immunoblotting. Arrowhead indicates specific band, asterisk indicates non-specific band. Data from a single experiment, *n* = 1. **B** RPE1 FlpIn Parental cells were subjected to siRNA knockdown for 72 hours with NT1 or VPS35 targeting oligonucleotides before being fixed and stained with the indicated antibodies and DAPI (DNA). z-stack images (5 slices, 0.2 µm step) were acquired on a Zeiss LSM900 confocal microscope using a 63x objective. Scale bar 20 µm. Data from a single experiment, *n* = 1.

3.2.3 Measuring endogenous LRRK2 activity in RPE1 cells

After confirming that LRRK2 was expressed endogenously in RPE1 cells, I set out to assess whether it is possible to measure basal LRRK2 activity. Following the discovery that LRRK2 phosphorylates a subset of Rab proteins, specific antibodies against Rab10 and Rab12 phosphorylated at the conserved serine/threonine residue have been developed which allow LRRK2 activity to be measured indirectly by western blotting (Lis et al., 2018; Mir et al., 2018). To test whether the basal pT73-Rab10 signal is specific in RPE1 cells, and as such could be used as a read-out of LRRK2, I took two approaches - manipulating Rab10 levels by siRNA knockdown and inhibiting LRRK2 with the specific inhibitor MLi-2.

Knockdown of Rab10 by siRNA reduced total Rab10 levels by 83%, whereas the reduction of pT73-Rab10 signal was only reduced by 39% (**Figure 3.3A and B**). As it is estimated that only around 1-3% of Rabs are phosphorylated at basal levels (Berndsen et al., 2019; Ito et al., 2016; Karayel et al., 2020), the incomplete disappearance of the pT73-Rab10 signal may signify that not all of the signal is specific, or that there is sufficient Rab10 remaining after the knockdown to maintain the phosphorylated pool.

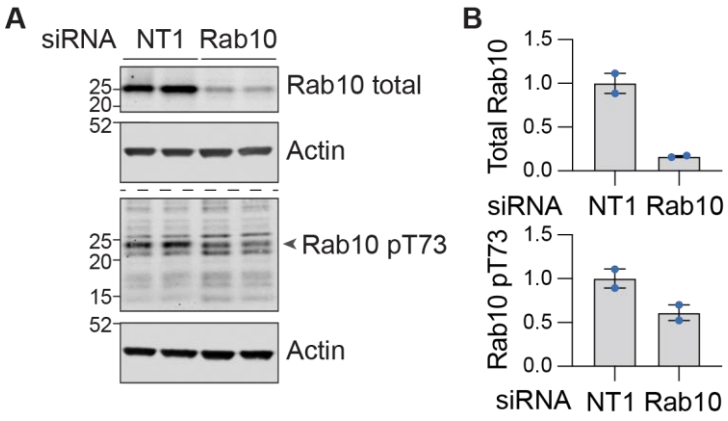

Figure 3.3 Rab10 is phosphorylated at steady state in RPE1 cells

A RPE1 FlpIn Parental cells were subjected to siRNA knockdown for 72 hours with control (non-targeting #1; NT1) or a pool of Rab10 targeting oligonucleotides before being lysed in RIPA buffer and analysed by immunoblotting. Grey arrowhead indicates band corresponding to phosphorylated Rab10. **B** Quantification of total and phosphorylated Rab10 expression normalised to NT1 control. Data from a single experiment with duplicate samples, *n* = 1. Bars represent mean ± range.

After identifying that a population of Rab10 was phosphorylated under baseline conditions in RPE1 cells, I assessed whether this could be modulated by altering LRRK2 activity pharmacologically. Several potent and specific inhibitors against LRRK2 have been developed, one of which has recently entered Phase III clinical

trials (BIIB122/DNL151) (Biogen, 2023). Two types of LRRK2 kinase inhibitor have been developed, Type I, which bind to the kinase domain in its closed active conformation and compete with ATP binding, and Type II, which lock the kinase domain in an open and inactive conformation (Azeggagh and Berwick, 2022). Both Type I (e.g. GSK3357679A, LRRK2-IN-1, MLi-2) and Type II (e.g. ponatinib, rebastinib, GZD-824) inhibit Rab10 and Rab12 phosphorylation, however only Type I inhibitors reduce phosphorylation of LRRK2 at S935 (Tasegian et al., 2021). Another difference between the two types of LRRK2 inhibitors is that Type II inhibitors show a greater potency towards wild type LRRK2 compared to the [G2019S] variant (Liu et al., 2013; Tasegian et al., 2021).

I monitored Rab10 phosphorylation by western blotting after a one-hour treatment of MLi-2 at a range of concentrations (**Figure 3.4**). At concentrations above 5 nM, MLi-2 treatment significantly decreased Rab10-T73 phosphorylation. Above 50 nM MLi-2, there was no further decrease in Rab10 phosphorylation, remaining at approximately 50-60% of the level in the vehicle control. This is akin to what I observed with Rab10 knockdown, suggesting this may represent the dynamic range of the effect of LRRK2 on Rab10 phosphorylation that can be measured in RPE1 cells. It has also been suggested that residual signal of Rab10 phosphorylation after LRRK2 inhibition may represent the action of another as yet unknown kinase (Karayel et al., 2020). I chose 100 nM as the optimal concentration to use for further experiments as Rab10 phosphorylation does not seem to further decrease at concentrations above this, and the use of high concentrations may increase the likelihood of off-target effects.

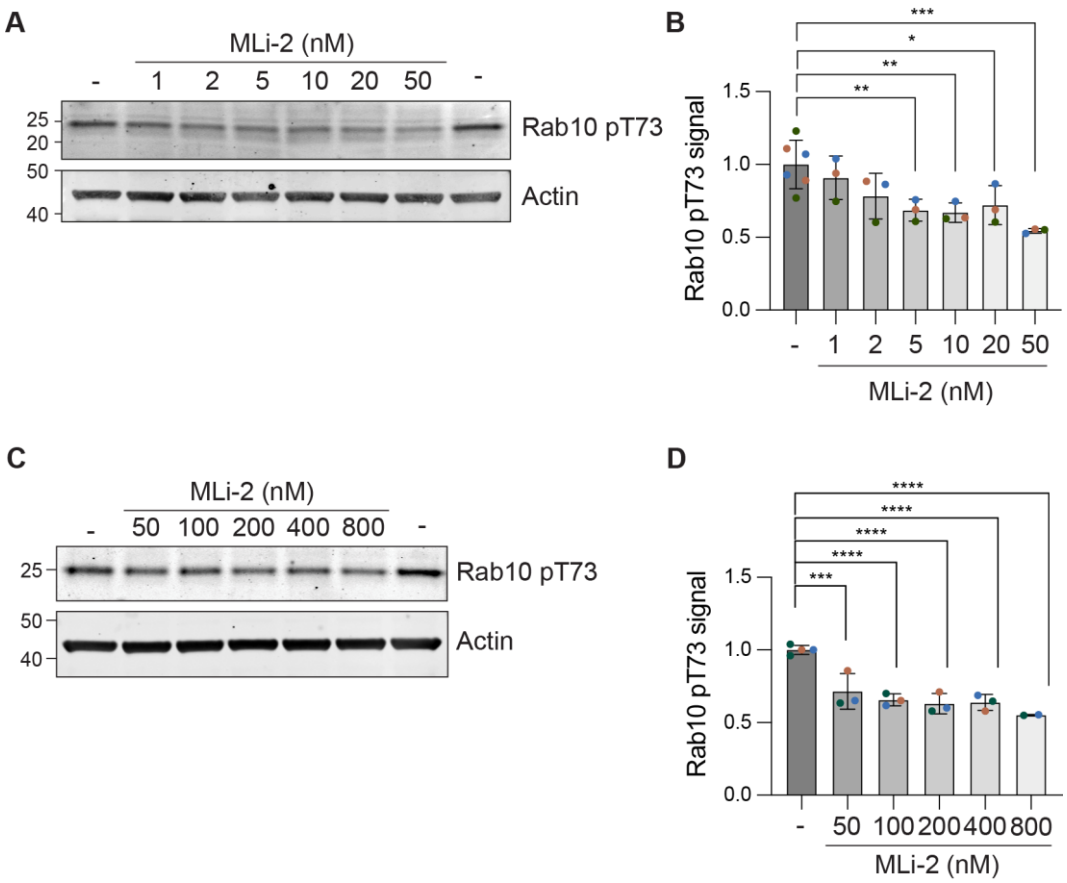

Figure 3.4 Inhibition of LRRK2 reduces Rab10 phosphorylation in RPE1 cells

A and **C** RPE1 FlpIn parental cells were treated with MLi-2 at the concentrations indicated or vehicle (DMSO) for 1 hour before being lysed in RIPA buffer and analysed by western blotting. A representative western blot is shown. **B** and **D** Quantification of Rab10 pT73 expression normalised to DMSO. *n* = 3. Each independent experiment is colour-coded. Bars represent mean ± SD. One-way ANOVA with Dunnett's multiple comparisons test performed on values normalised to mean of signal within a replicate. * P < 0.05, ** P < 0.01, *** P < 0.001, **** P < 0.0001.

3.3 Generating isogenic RPE1 FlpIn HA-VPS35 cells

To enable the study of the PD-linked pathogenic VPS35[D620N] mutation, I generated isogenic cell lines stably expressing either wild type or [D620N] mutant VPS35. To do this, I made use of the Flp-In™ T-Rex™ system (see **Section 2.2.3**) to integrate HA-tagged VPS35 into RPE1 cells, a method which had been used in the lab previously for other genes of interest. The small nature of the HA tag (9 amino acids) means that it is less likely to interfere with the protein distribution and function than larger tags such as GFP (238 amino acids). The advantage of the FlpIn system compared to random integration is that it results in integration of only a single copy of the gene of interest at a specific site in the same locus, meaning all cells should express similar levels of the protein, both within the wild type and mutant VPS35-expressing cell populations and between the cell line pair. Integration at the same

locus means that there will be less variation in gene expression caused by cis-acting elements such as promoters and enhancers. The expression of HA-tagged VPS35 in this system is also inducible with doxycycline, allowing for titration of exogenous VPS35 expression to a 1:1 ratio with endogenous VPS35. This recapitulates the scenario in the autosomal dominant PD patient, who have one wild type and one mutated allele of VPS35.

3.3.1 Screening of RPE1 FlpIn VPS35 cell lines

RPE1 FlpIn parental cells were co-transfected with pcDNA5D/FRT/TO NeoR VPS35 (WT/[D620N]) plasmid and pOG44 Flp recombinase plasmids in a 6-well plate, and after two days, ¼ of the cells were transferred into a 10cm dish and grown under selection with G418 and blasticidin. After approximately 2 weeks, single colonies were picked and subsequently expanded.

The cells were then screened for HA-VPS35 expression. Cells were treated with 1 µg/ml doxycycline (dox) for 24 hours before lysis and analysed by western blotting for endogenous and exogenous VPS35 expression (**Figure 3.5**). All colonies had integrated the HA-VPS35 plasmid and showed similar expression to each other. Clone M7 expressed HA-VPS35 both with and without doxycycline induction, suggesting that this colony may have lost expression of the Tet repressor. It is also possible that the sample was accidentally treated with doxycycline. A faint HA band was also visible in the other cell lines in the absence of doxycycline, which could be due to leakiness of the plasmid or small amounts of tetracycline in the FBS in the growth medium. However, the level of expression was very low compared to the doxycycline treated conditions and not apparent when probing for VPS35.

From the multiple cell lines, I selected ‘C4’ wild type and ‘M9’ mutant clones to take forward for further investigation, based on the near-endogenous level of HA-VPS35 expression which approximates the 1:1 ratio between exogenous and endogenous VPS35.

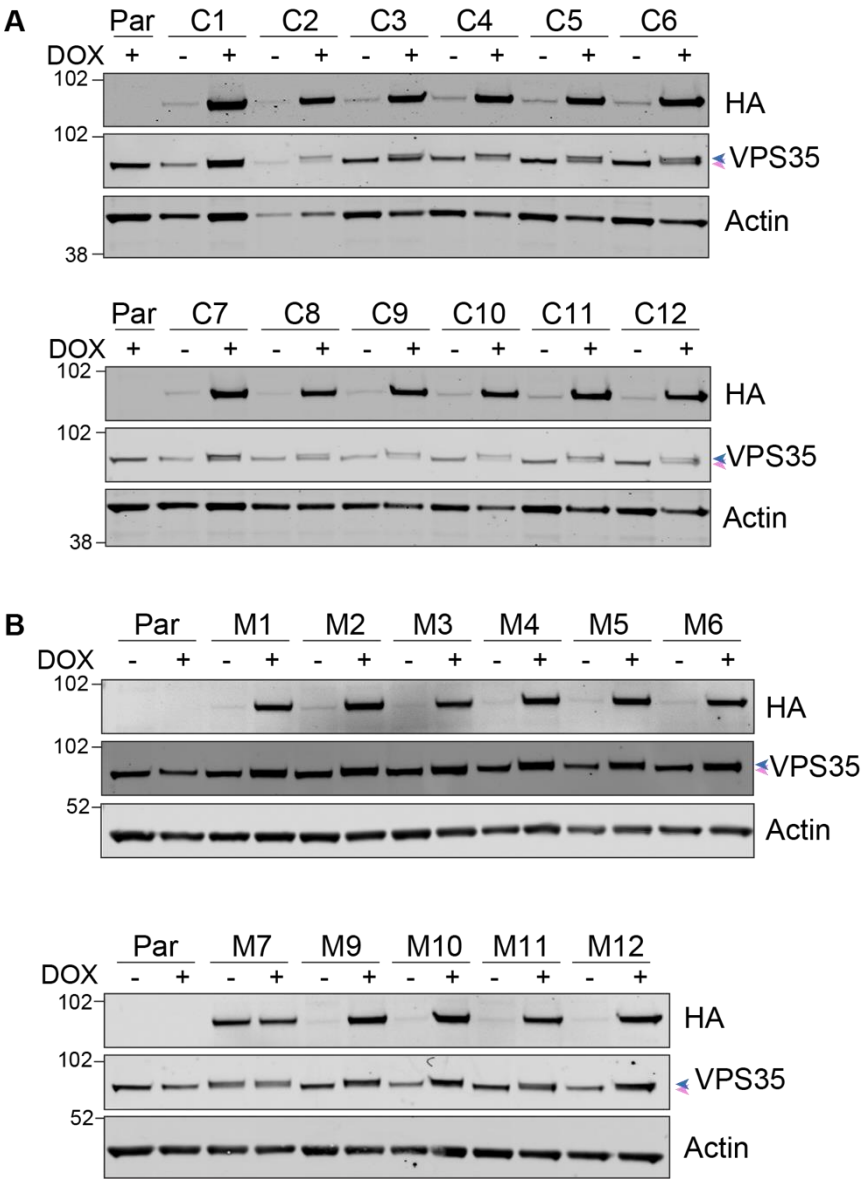

Figure 3.5 Screening RPE1 FlpIn VPS35 cell lines for doxycycline-inducible VPS35 expression
Control RPE1 FlpIn parental cells (Par) and colonies picked from RPE1 FlpIn cells transfected with **A** wild type (C) or **B** [D620N] (M) pCDNA5-FRT/TO-NeoR-HA-VPS35 constructs were screened for HA-VPS35 expression after induction of expression with 1 µg/ml doxycycline (dox) for 24 hours. Cells were then lysed in RIPA buffer and analysed by western blotting. Pink arrowhead indicates endogenous VPS35, blue arrowhead indicates HA-VPS35. Data from a single experiment, *n* = 1.

3.3.2 Optimisation of induction of HA-VPS35 expression

Next, I performed a time-course to determine the optimum length of induction with doxycycline and tested this at two different concentrations, 0.1 µg/ml and 1 µg/ml (**Figure 3.6**). Both WT and [D620N] cell lines expressed similar levels of HA-VPS35, as is expected with the FlpIn system. A higher concentration of doxycycline did not result in higher levels of expression so I decided that 0.1 µg/ml would be used going forward. As increasing concentrations of doxycycline have been shown to be cytotoxic

and concentrations as low as 1 µg/ml have been found to alter metabolism in human cell lines, this lower concentration should also minimise these deleterious side effects (Ahler et al., 2013; Xie et al., 2008). Using 0.1 µg/ml doxycycline for induction, I then performed a time-course experiment with more time points ranging from one to 24 hours. Expression of HA-VPS35 was apparent after 4 hours and became more pronounced at the longer time points, plateauing after 20 hours (**Figure 3.7**). In these experiments the expression of HA-tagged VPS35 only increased by 50%, unlike that seen in **Figure 3.5**. The same batch of doxycycline was used for all experiments, so we wondered whether some cells had lost expression of the transgene and decided to look at the cells by immunofluorescence microscopy and stain for HA.

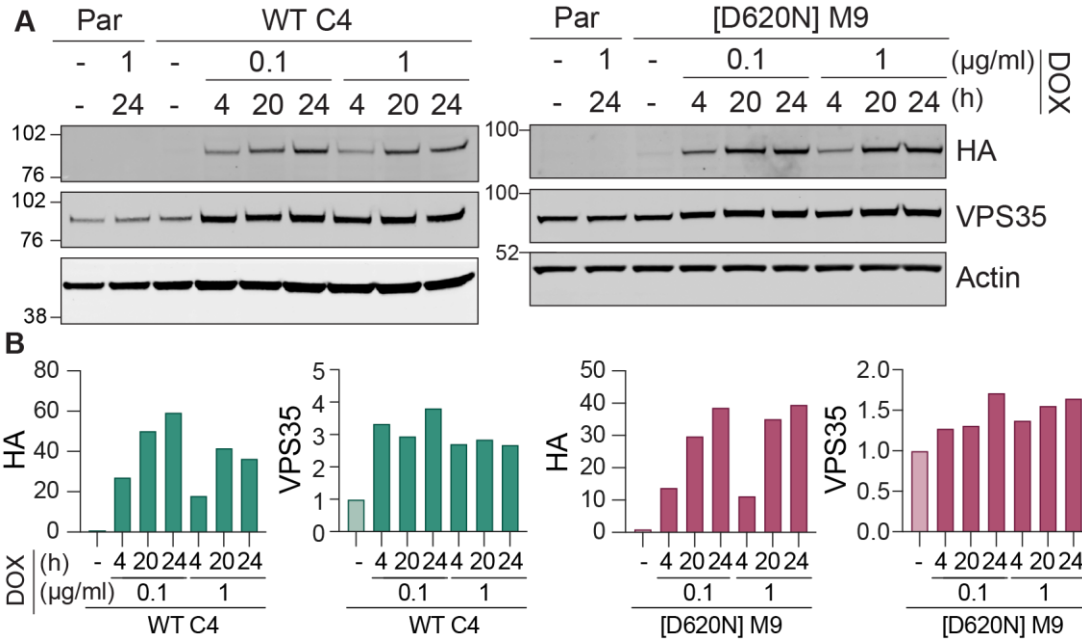

Figure 3.6 Optimisation of dox-induced HA-VPS35 expression in RPE1 FlpIn VPS35 cell lines
A RPE1 FlpIn Parental (Par) and FlpIn VPS35 WT C4 and [D620N] M9 cells were treated with either 0.1 or 1 µg/ml doxycycline for 4, 20 and 24 hours. Cells were then lysed in RIPA buffer and analysed by western blotting. **B** Quantification of results shown in A. Signal intensity values were normalised to actin then to uninduced condition for each cell line. Data from a single experiment, *n* = 1.

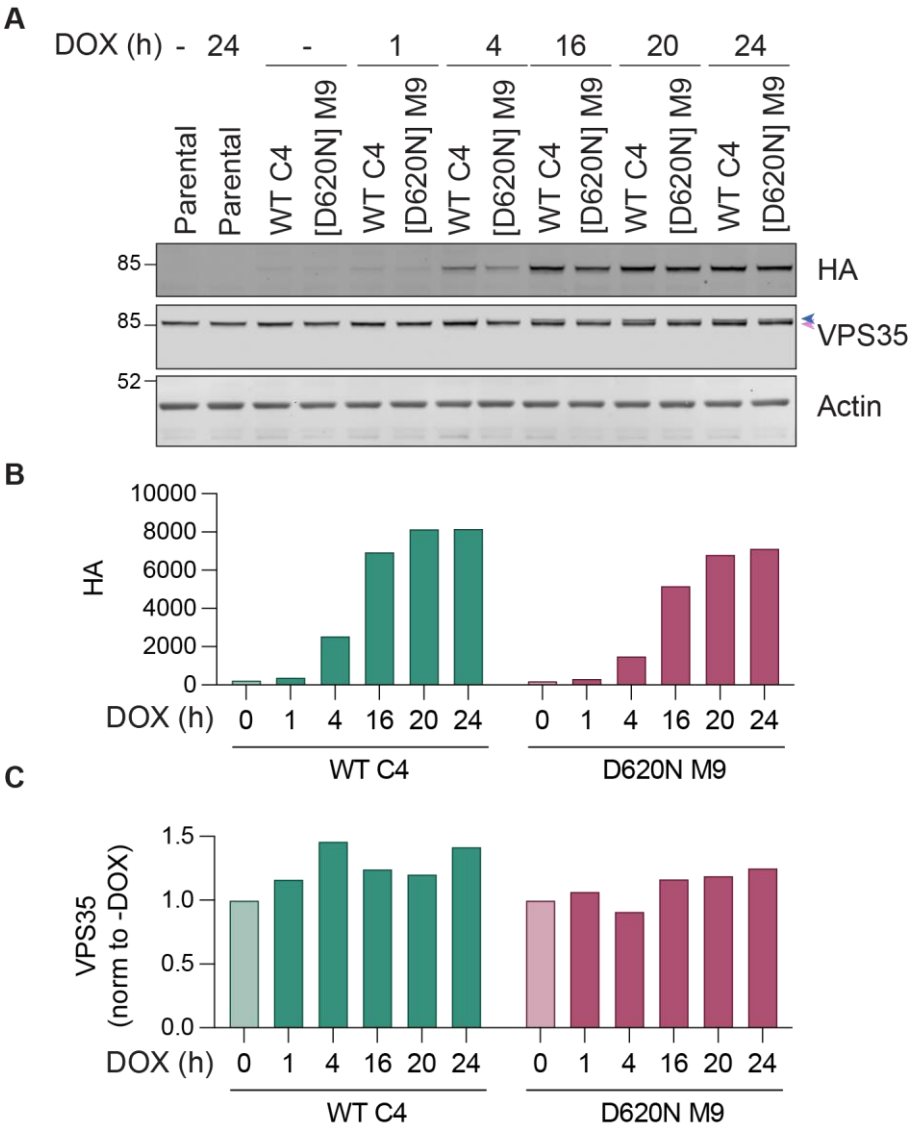

Figure 3.7 Extended doxycycline induction time course in RPE1 FlpIn VPS35 cell lines
A RPE1 FlpIn Parental (Par) and FlpIn VPS35 WT C4 and [D620N] M9 cells were treated with 0.1 µg/ml doxycycline for the indicated time points. Cells were then lysed in RIPA buffer and analysed by western blotting. Pink arrowhead indicates endogenous VPS35, blue arrowhead indicates HA-VPS35 **B** Quantification of results shown in A. **C** Quantification of results shown in A. Values normalised to -dox condition for each cell line. Data from a single experiment, *n* = 1.

3.3.3 Initial RPE1 FlpIn HA-VPS35 cell line characterisation by IF

To assess expression of HA-VPS35 by immunofluorescence, cells were induced with doxycycline for 24 hours, fixed, then stained for HA and the early endosomal marker EEA1 (**Figure 3.8A**). This revealed that not all the cells were expressing the construct. 58% of C4 were positive for HA expression and 44% for M9 (**Figure 3.8B**). The same was also seen with other clones (**Figure 3.8B**). Going forward, these cells were only used for IF experiments where I was able to compare HA-VPS35 positive and

negative cells side-by-side. To obtain a homogenously expressing, monoclonal population, WT C4 and [D620N] M9 cell lines were single cell diluted.

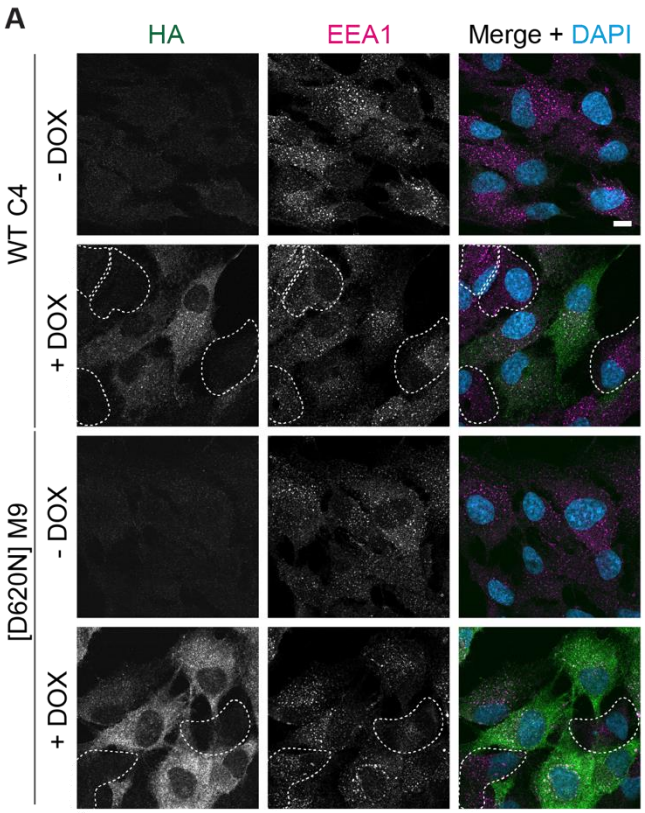

B

Cell Line	HA positive (*n*)
WT C4	58 % (*62*)
WT C5	41 % (*58*)
[D620N] M9	44 % (*70*)
[D620N] M10	45 % (*81*)

Figure 3.8 Heterogenous expression of HA-VPS35 in RPE1 FlpIn TRex cells
A RPE1 FlpIn VPS35 WT C4 and [D620N] M9 cells were treated with 0.1 µg/ml doxycycline for 24 hours, fixed and stained with the indicated antibodies and DAPI (DNA). Single slice images were acquired on a Zeiss LSM800 confocal microscope using a 63x objective. Scale bar 10 µm. Dashed outlines highlight HA-negative cells. **B** Quantification of HA-positive cells in selected RPE1 FlpIn HA-VPS35 cell lines. *n* = number of cells quantified. Data from a single experiment, *n* = 1.

3.3.4 Single cell dilution of RPE1 FlpIn VPS35 cell lines

Several clones expressing either WT and [D620N] HA-VPS35 were obtained by limited dilution and screened by both western blotting and immunofluorescence to assess their relative HA-VPS35 expression and their purity, respectively. All clones expressed HA-VPS35 after doxycycline induction (**Figure 3.9**) and appeared to be homogenous (**Figure 3.10**). The fold overexpression of VPS35 was similar between the mutant clones tested and more variable in the wild type clones (**Figure 3.9B**). The lines ‘WT 3B4’ and ‘[D620N] 1F3’ were selected for used for future work. The 2-fold increase in VPS35 expression seen upon induction with doxycycline in these lines was verified across four biological replicates (**Figure 3.11A and B**). This corresponds to a 1:1 ratio of WT:WT or WT:[D620N] VPS35. Just as for the original WT C4 and

[D620N] M9 clones, HA-VPS35 correctly localised to EEA1-positive endosomes (**Figure 3.11C**). The new '3B4' and '1F3' lines were amplified and aliquots were stored in liquid nitrogen. Unfortunately, I have observed that after thawing vials of these cells, not all the cells are HA-positive. When kept in selection, a 90% HA-VPS35 positive population can be achieved, however this also begins to decrease over time. To control for this, cells were regularly checked for HA expression.

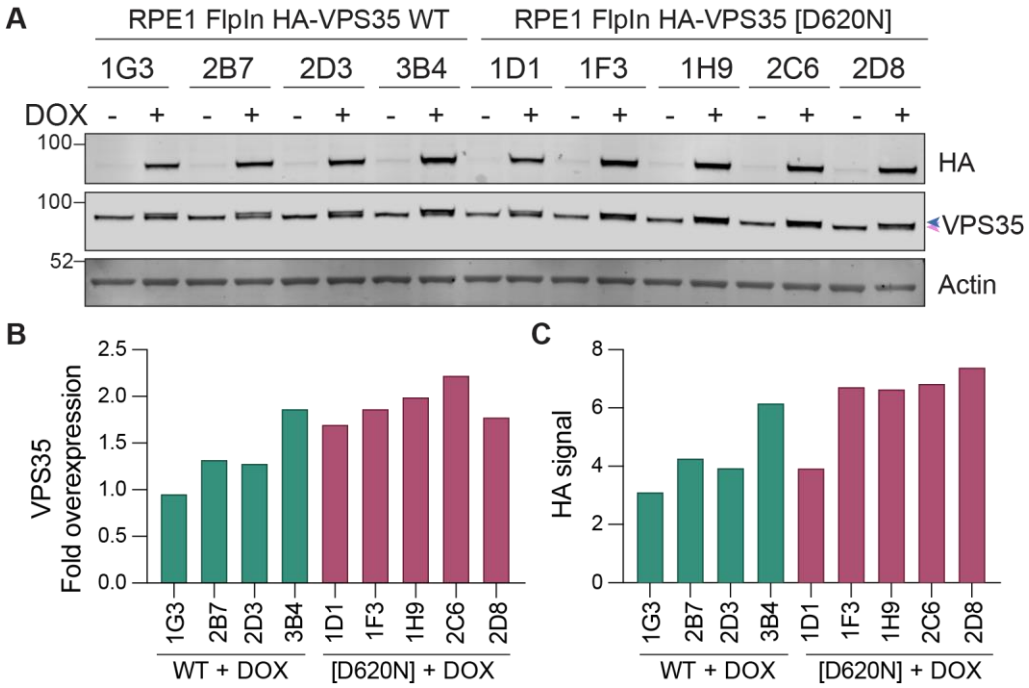

Figure 3.9 Screening of RPE1 FlpIn VPS35 single cell clones by western blotting

A RPE1 FlpIn VPS35 WT and [D620N] cell lines obtained by limited dilution were treated with 0.1 µg/ml doxycycline for 24 hours and screened for HA-VPS35 expression. Cells were lysed in RIPA buffer and analysed by western blotting. Pink arrowhead indicates endogenous VPS35, blue arrowhead indicates HA-VPS35 **B** Quantification of VPS35 expression in A, normalised to actin then to - Dox for each cell line. **C** Quantification of HA expression of + Dox samples in A, normalised to actin. Data from a single experiment, *n* = 1.

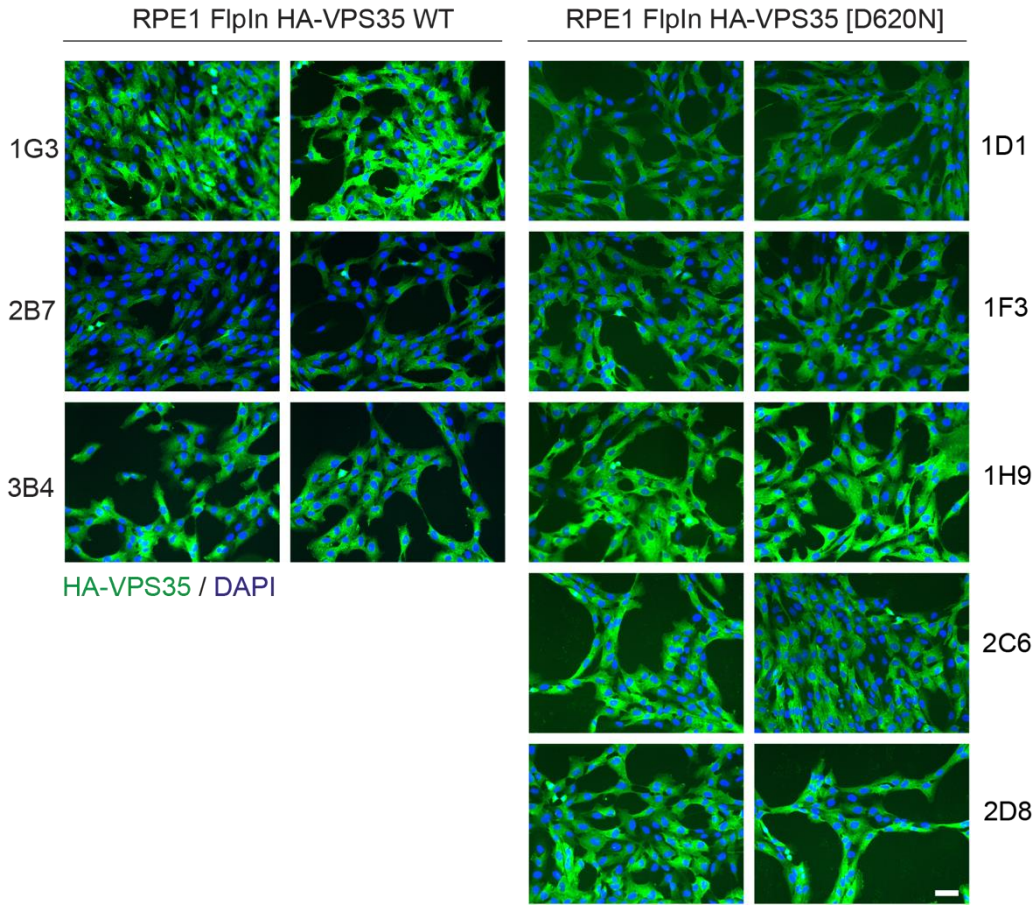

Figure 3.10 Screening of RPE1 FlpIn VPS35 single cell clones by immunofluorescence
RPE1 FlpIn VPS35 WT and [D620N] cell lines obtained by limited dilution were treated with 0.1 µg/ml doxycycline for 24 hours and screened for HA-VPS35 expression. Cells were fixed and stained with an antibody against HA and DAPI (DNA). Single slice images were acquired on a Nikon Ti-Eclipse widefield microscope using a 20x objective. Scale bar 50 µm. Data from a single experiment, *n* = 1.

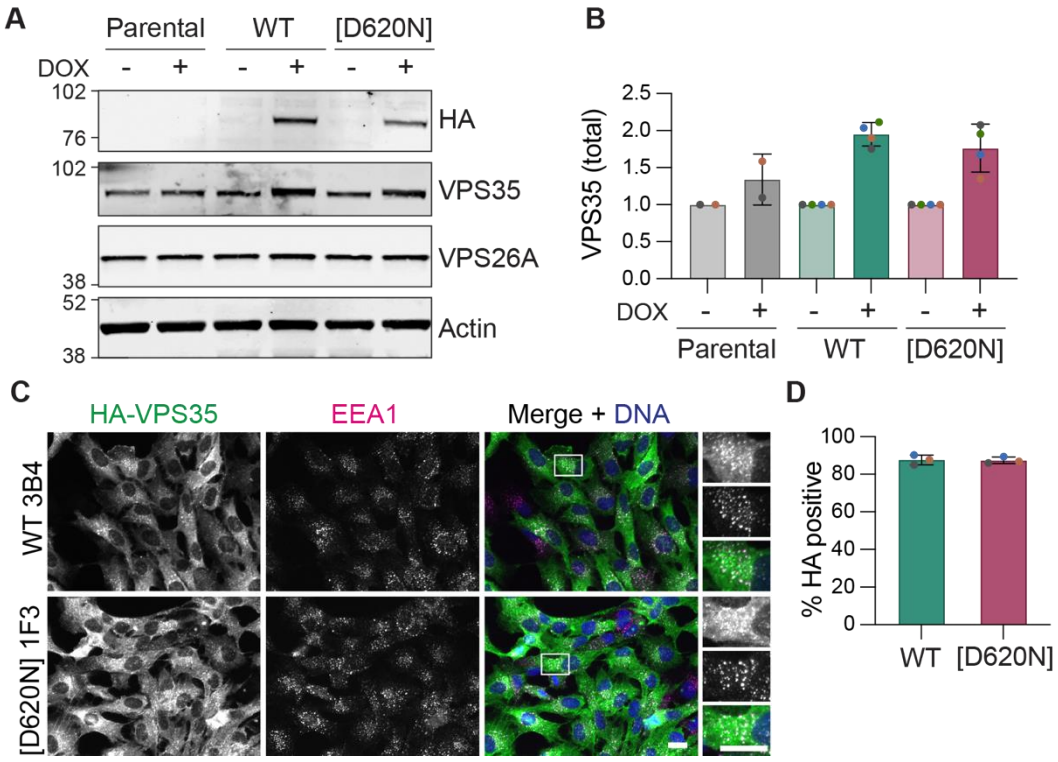

Figure 3.11 Selected RPE1 FlpIn VPS35 single cell clones

A RPE1 FlpIn VPS35 WT 3B4 and [D620N] 1F3 cells were treated with 0.1 µg/ml doxycycline for 24 hours and screened for HA-VPS35 expression. Cells were lysed in RIPA buffer and analysed by western blotting. **B** Quantification of total VPS35 expression normalised over actin then to '- dox' for each cell line. *n* = 2-4. Each independent experiment is colour-coded. Bars represent mean ± SD. **C** RPE1 FlpIn VPS35 WT 3B4 and [D620N] 1F3 cells were treated with 0.1 µg/ml doxycycline for 24 hours, fixed and stained with the indicated antibodies and DAPI (DNA). Single slice images were acquired on a Nikon Ti-Eclipse widefield microscope using a 40x objective. Scale bar 20 µm. **D** Quantification of percentage of cell population expressing HA-VPS35, as assessed by microscopy. *n* = 3, >135 cells counted per condition per experiment. Each independent experiment is colour-coded. Bars represent mean ± SD.

3.3.5 Initial characterisation of HA-VPS35 "single clone" lines

To assess the stability of HA-VPS35 wild type and mutant constructs, I induced expression with doxycycline for 24 hours and then withdrew the doxycycline by replacing the culture media with fresh media without doxycycline. I then lysed cells after increasing lengths of time following doxycycline withdrawal and analysed the levels of HA-VPS35 (**Figure 3.12A**). This revealed that the HA-VPS35 is very stable, with levels remaining steady even after 48 hours of doxycycline withdrawal (**Figure 3.12C**). This was the case for both wild type and mutant VPS35 suggesting that, at least over this time frame, the [D620N] mutation does not affect VPS35 stability. Interestingly, in the WT 3B4 cell line the endogenous band for VPS35 appeared to decrease after prolonged wash-out, resulting in a decrease in total VPS35 signal,

suggesting an autoregulatory effect in which overexpression of VPS35 leads to downregulation of endogenous VPS35 levels (**Figure 3.12B and D**). This effect was absent in the VPS35[D620N] mutant-expressing cell line. Expression of the HA-VPS35 also caused a small increase in VPS26 levels in both WT 3B4 and [D620N] 1F3 cell lines (**Figure 3.12E**).

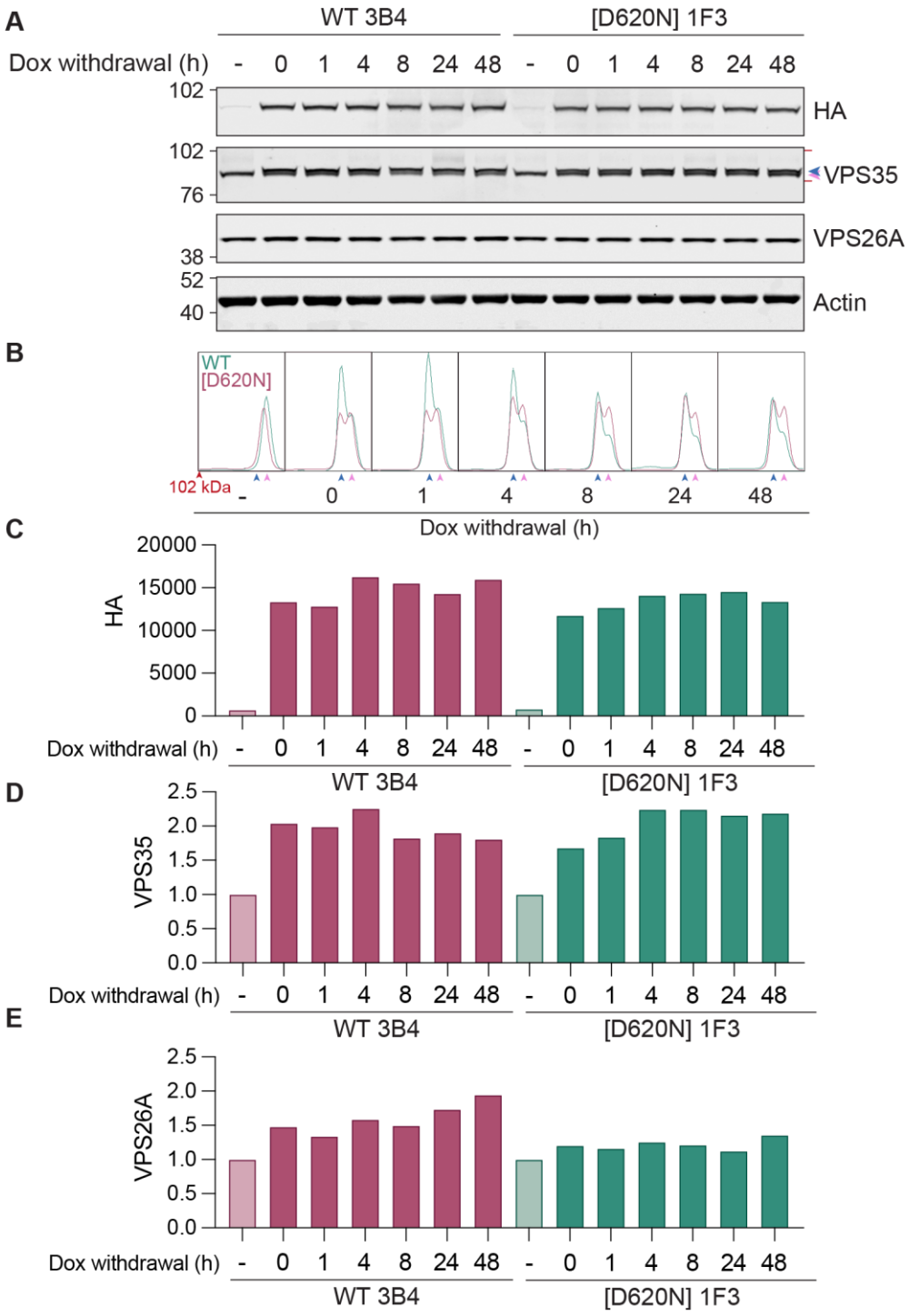

Figure 3.12 The [D620N] mutation does not affect stability of VPS35

A RPE1 FlpIn VPS35 WT 3B4 and [D620N] 1F3 cells were treated with 0.1 µg/ml doxycycline for 24 hours and then media were exchanged for fresh media without doxycycline. The cells were incubated for the times indicated before being lysed in RIPA buffer and analysed by western blotting. Pink arrowhead indicates endogenous VPS35, blue arrowhead indicates HA-VPS35. **B** Line graph of VPS35 signal measured between red lines indicated in A. **C** Quantification of HA-VPS35 expression normalised to actin. **D** Quantification of VPS35 expression in A normalised to actin then to uninduced control for each cell line. **D** Quantification of VPS26A expression normalised actin then to uninduced control for each cell line. Data from a single experiment, $n = 1$.

To look at the distribution of wild type and [D620N] HA-VPS35, I employed subcellular fractionation by differential centrifugation to isolate total membranes from the cytosol from a post-nuclear supernatant (**Figure 3.13A**). In uninduced cells, approximately 50-60% of VPS35 resided at membranes. This ratio was slightly decreased upon expression of HA-VPS35, 37% and 38% for WT and [D620N] VPS35, respectively (**Figure 3.13B**). Similarly, the percentage of HA present in the membrane fraction was 33% for WT VPS35 and 38% for [D620N] VPS35 (**Figure 3.13B**). This suggests that the [D620N] mutation does not affect the ability of retromer to be recruited to membranes. The decrease in distribution after induction may reflect a point at which no further VPS35 can be recruited to membranes due to lack of available binding sites. The resolution of endogenous and exogenous VPS35 bands is insufficient to quantify these separately, but by eye it appears that the 1:1 stoichiometry of exogenous to endogenous is retained at membranes in both cell lines.

Supporting this mixed distribution of retromer, HA-VPS35 localisation was part cytosolic and part punctate by confocal microscopy (**Figure 3.13C and D**). The RPE1 parental cells that were plated as a negative control on the same coverslips with the HA-VPS35 expressing cell lines show that both these HA staining patterns are specific. Co-staining with the early endosome marker EEA1 and the retromer component VPS26A shows that HA-VPS35 co-localises with VPS26A at a distinct EEA1-negative subdomain within early endosomes (**Figure 3.13E**). This suggests that the exogenous VPS35 is successfully incorporated into retromer complexes and recruited to the recycling subdomains of early endosomes. Additionally, expression of wild type and [D620N] HA-VPS35 did not perturb early endosome morphology as their appearance was indistinguishable from those in the neighbouring RPE1 parental cells (**Figure 3.13C**).

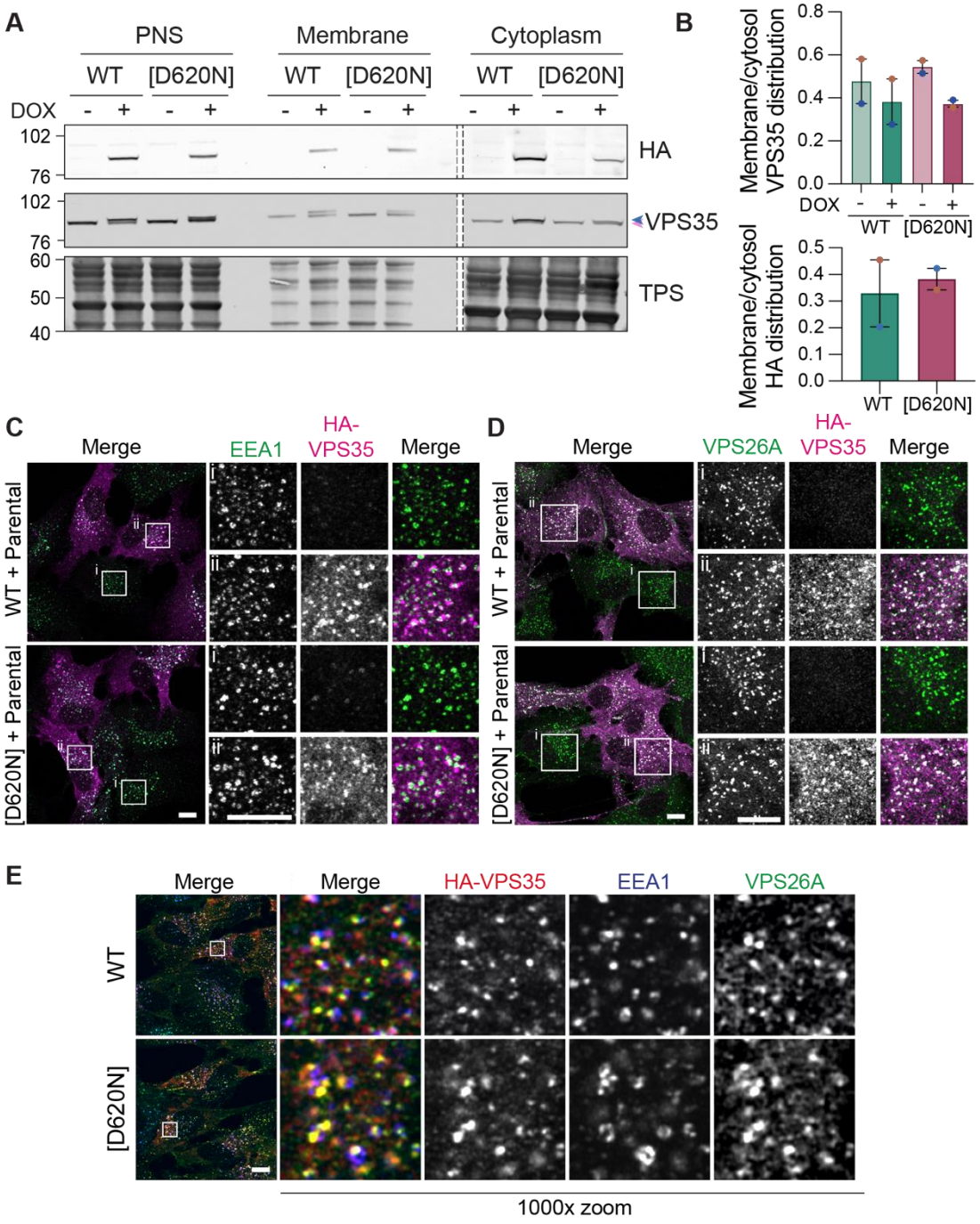

Figure 3.13 HA-VPS35 distribution in RPE1 FlpIn VPS35 isogenic cell lines

A RPE1 FlpIn VPS35 WT 3B4 and [D620N] 1F3 cells were treated with 0.1 µg/ml doxycycline for 24 hours before being homogenised in HIM buffer + MPIs. Post nuclear supernatants (PNS) were isolated by centrifugation at 600 x *g* for 10 minutes. Membrane and cytosolic fractions were separated by centrifugation at 100,000 x *g* for 30 minutes. Equal proportions of fractions corresponding to 30 µl PNS were loaded onto SDS-PAGE gels and analysed by immunoblotting. A representative western blot is shown. Dashed line represents where a lane has been cropped out. Pink arrowhead indicates endogenous VPS35, blue arrowhead indicates HA-VPS35. **B** Quantification of A. Bars represent mean ± range. *n* = 2. Each independent experiment is colour-coded. **C** and **D** RPE1 FlpIn VPS35 WT 3B4 and [D620N] 1F3 cells were treated with 0.1 µg/ml doxycycline and after 72 hours fixed and stained for the indicated antibodies. z-stack images (3 slices, 0.31 µm step) were acquired on a Zeiss LSM800 confocal

microscope using a 63x objective. Scale bar 10 µm. Data from a single experiment, *n* = 1. **E** RPE1 FlpIn VPS35 WT 3B4 and [D620N] 1F3 cells were treated with 0.1 µg/ml doxycycline for 24 hours, fixed and stained for the indicated antibodies. Single slice images were acquired on a Zeiss LSM800 confocal microscope in Airyscan mode using a 63x objective. Scale bar 10 µm. Data from a single experiment, *n* = 1.

3.3.6 RPE1 FlpIn VPS35 [D620N] cells display elevated Rab phosphorylation

To evaluate the suitability of the RPE1 FlpIn VPS35 model for studying the relationship between VPS35 and LRRK2, I set out to assess the finding by Mir and colleagues that the [D620N] mutation in VPS35 leads to enhancement of LRRK2 activation (Mir et al., 2018). To do this I induced wild type and [D620N] HA-VPS35 expression with doxycycline for 24 hours before lysing the cells and analysing phosphoRab levels by immunoblotting (**Figure 3.14**). In RPE1 FlpIn VPS35 WT 3B4 cells, expression of wild type VPS35 had no effect on the levels of pT73-Rab10 or pS106-Rab12. On the other hand, expression of [D620N] VPS35 in RPE1 FlpIn VPS35 [D620N] 1F3 cells lead to an 1.55-fold increase in Rab12 phosphorylation and a 1.4-fold increase in Rab10 phosphorylation when normalised to WT 3B4 uninduced samples (**Figure 3.14B**). Expression of total Rab10 and Rab12 was unaffected by expression of wild type or mutant VPS35, indicating this is a phosphorylation-specific effect. Furthermore, addition of MLi-2 one hour prior to lysis reduced this to below untreated uninduced levels, confirming that this effect is dependent on LRRK2. This result confirms that the [D620N] mutation causes hyperphosphorylation of Rab proteins via the action of LRRK2.

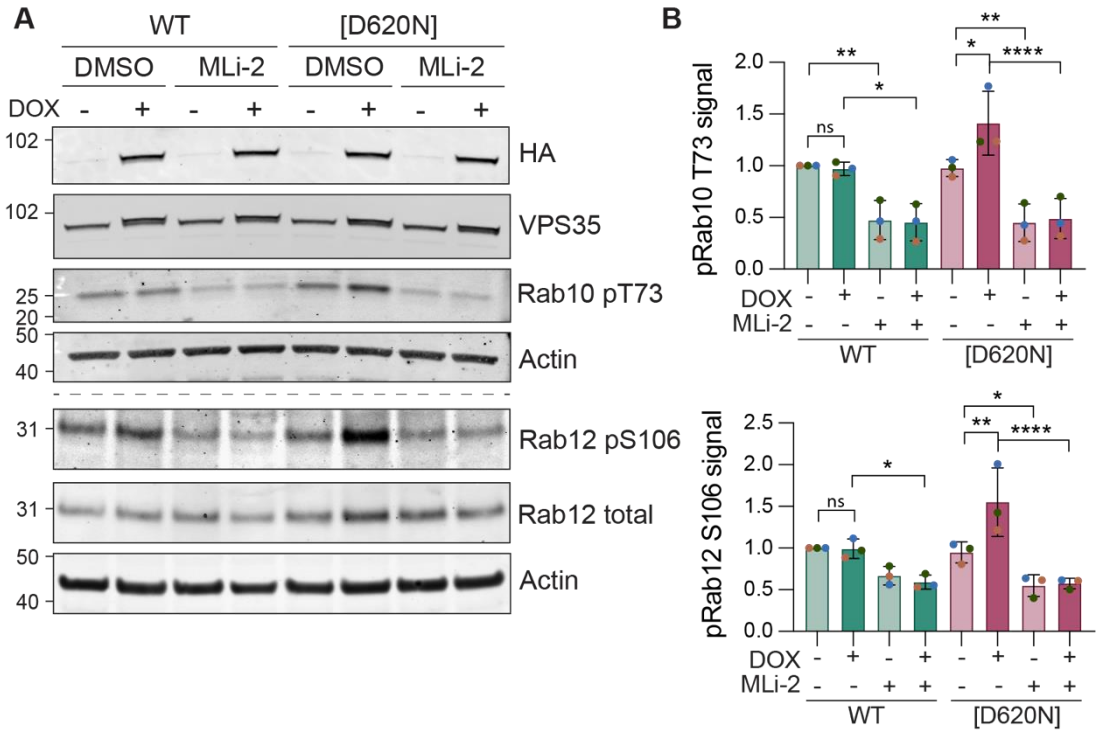

Figure 3.14 HA-VPS35 [D620N] enhances basal LRRK2-dependent Rab phosphorylation

A RPE1 FlpIn VPS35 WT 3B4 and [D620N] 1F3 cells were treated with 0.1 µg/ml doxycycline for 24 hours and treated with 100 nM MLi-2 or vehicle (DMSO) for one hour prior to lysis. Samples were analysed by immunoblotting. A representative western blot is shown. **B** Quantification of A. Values were normalised to 'WT – DOX' for each experiment. *n* = 3 independent experiments. Each independent experiment is colour-coded. Bars represent mean ± SD. One-way ANOVA with Tukey's multiple comparisons test performed on values normalised to sum of the signal within a replicate. * $P < 0.05$, ** $P < 0.01$, **** $P < 0.0001$.

3.4 Creation of RPE1 FlpIn HA-VPS35 lines expressing eGFP-LRRK2

To generate cell lines overexpressing LRRK2, RPE1 FlpIn HA-VPS35 WT (3B4) and [D620N] (1F3) were transduced with either wild type, hyperactive [G2019S] or kinase dead [G2019S/D1994A], N-terminally eGFP-tagged LRRK2 with lentiviruses. This was performed by a colleague, Hannah Elcocks. A multiplicity of infection of 0.8 was used to increase the likelihood of only one viral integration per cell. Cells were then sorted using FACS by another colleague, Dr Ailbhe Brazel, to isolate the transduced eGFP-positive populations. The eGFP-positive pools for each cell line were expanded and assessed for eGFP-LRRK2 expression. Expression levels were variable across the cell populations and thus monoclonal populations were obtained by limited dilution. Monoclonal populations were screened for eGFP signal by live-cell imaging and those with low-to-medium levels of expression were selected for further screening

by western blotting and immunofluorescence (**Figure 3.15**). This confirmed that the cell lines showed comparable LRRK2 expression to one another. Using Rab10 phosphorylation as a read-out for kinase activity, I confirmed that the constructs were behaving as expected, with the hyperactivating [G2019S] mutation (clones G3 and DG1) increasing Rab10 phosphorylation compared to WT (clones W1, DW2 and DW3), and the kinase-dead [D1994A] (clones D3 and DD1) decreasing it. The clone RPE1 FlpIn HA-VPS35 WT eGFP-LRRK2 [G2019S] G1 had undetectable levels of LRRK2 by immunoblotting yet gave an eGFP signal when analysed by microscopy. It is possible that in this clone the construct harbours a random mutation in its sequence leading to the generation of an early stop codon or a frameshift such that it expresses a truncated eGFP-tagged product. This could be assessed by western blotting by probing the entire membrane for LRRK2 and GFP to look for lower molecular weight species. In RPE1 VPS35 WT eGFP-LRRK WT W1, induction of HA-VPS35 expression led to a small increase in Rab10 phosphorylation, which was not present in the equivalent VPS35 [D620N] cell line. This result is only preliminary and would need to be repeated to be ensure that this is a true result. It is possible that by introducing such a high level of LRRK2 we oversaturate the system by which VPS35 [D620N] hyperactivates LRRK2 and so a differential cannot be seen.

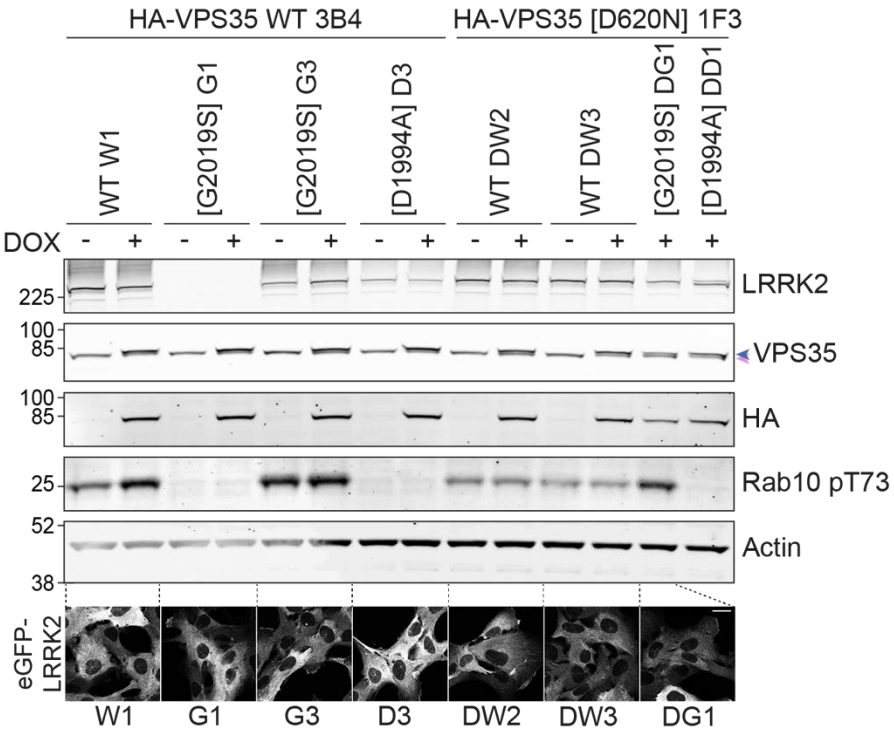

Figure 3.15 Screening RPE1 FlpIn HA-VPS35 + eGFP-LRRK2 single cell clones

A RPE1 FlpIn VPS35 WT 3B4 and [D620N] 1F3 eGFP-LRRK2 lentiviral cell lines were treated with 0.1 µg/ml doxycycline for 24 hours and screened for LRRK2 expression and Rab10 phosphorylation. Cells

were lysed in RIPA buffer and analysed by western blotting. Pink arrowhead indicates endogenous VPS35, blue arrowhead indicates HA-VPS35. Data from a single experiment, *n* = 1. **B** RPE1 FlpIn VPS35 WT 3B4 and [D620N] 1F3 GFP-LRRK2 lentiviral cell lines were treated with 0.1 µg/ml doxycycline for 24 hours and fixed. Single slice images were acquired on a Zeiss LSM800 confocal microscope using a 63x objective. Scale bar 20 µm. Data from a single experiment, *n* = 1.

3.5 Establishing GST-RILP active Rab7 binding assay

To measure levels of Rab7 activity, we set up the 'active Rab7 binding assay' in the lab, which has been characterised and used by several independent groups (Gómez-Suaga et al., 2014; Jimenez-Orgaz et al., 2018; Sun et al., 2009). The assay uses a GST fusion protein containing the Rab7a binding domain (R7BD) of RILP, which is exclusively able to bind active GTP-bound Rab7 (Sun et al., 2009). This fusion protein can then be immobilised on glutathione coupled sepharose beads to isolate active Rab7 from whole cell lysates. The production of GST-RILP fusion protein and the validation of the assay described in this section and methods **Section 2.1.9** was carried out in collaboration with Hannah Elcocks.

3.5.1 Production of GST-RILP fusion protein

When testing the induction of GST-RILP protein expression from BL21 bacteria transformed with pGEX-4T3-mR7BD, we noted that there was almost the same amount of free GST expressed as GST-RILP, suggesting a significant amount of spontaneous cleavage of the fusion protein at the thrombin site between the GST and the Rab7 binding domain of RILP (**Figure 3.16A**). In an effort to reduce this cleavage, we subcloned the mR7BD fragment into the vector pGEX-6P-1 that instead has a PreScission™ protease cleavage site. This enzyme recognition site is longer and more stable than the thrombin cleavage site in pGEX-4T3. This successfully yielded a higher proportion of uncleaved GST-RILP compared to the pGEX-4T3 vector after induction with IPTG (**Figure 3.16B**).

GST-RILP fusion protein was purified using a GSTrap™ column on an ÄKTA purification system. Bound proteins were eluted with reduced glutathione and the UV trace was used to determine the fractions containing the bulk of the eluted protein (**Figure 3.17A**). Fractions A2 to A11 were analysed by SDS-PAGE to confirm these contained eluted protein and to determine purity (**Figure 3.17B**). Fractions A3 to A9 contained most of the GST-RILP so were pooled and run through PD10 desalting columns to remove the glutathione. A proportion of the eluted protein was GST tag alone, which was expected from the induction gels. The concentration of the

preparation was determined, and aliquots were frozen to then be added to beads the day before an experiment.

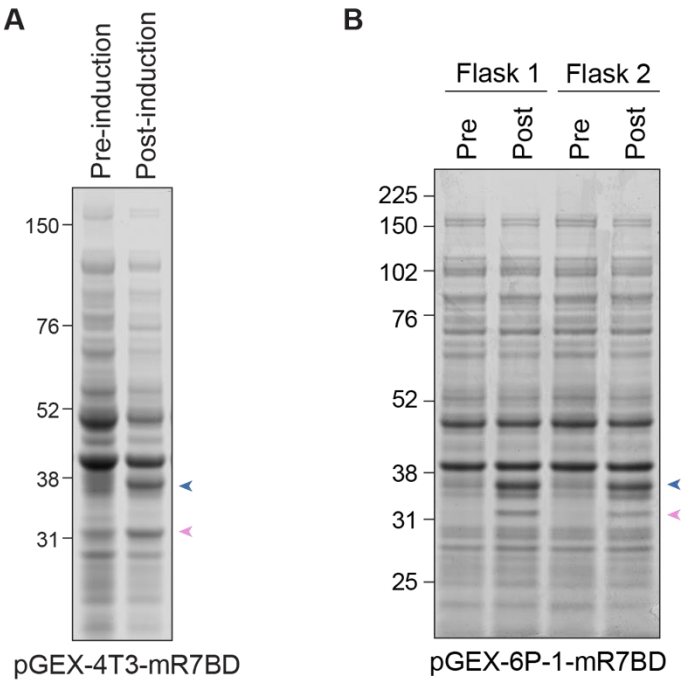

Figure 3.16 Induction of recombinant GST-RILP fusion protein expression in BL21 bacteria
BL21 bacteria were transformed with either pGEX-4T3-mR7BD (**A**) or pGEX-6P1-mR7BD (**B**) and grown on agar plates under ampicillin selection. Individual colonies were picked to inoculate a starter culture which was then diluted into 1 litre maxi cultures. Cultures were grown to an OD_{600} of 0.6 then induced with 0.25 mM IPTG and shaken for 20 hours at 20 °C. Pre- and post-induction samples were analysed by SDS-PAGE. Total protein was visualised with SimplyBlue Stain. Blue arrowhead indicates GST-RILP, pink arrowhead indicates GST alone.

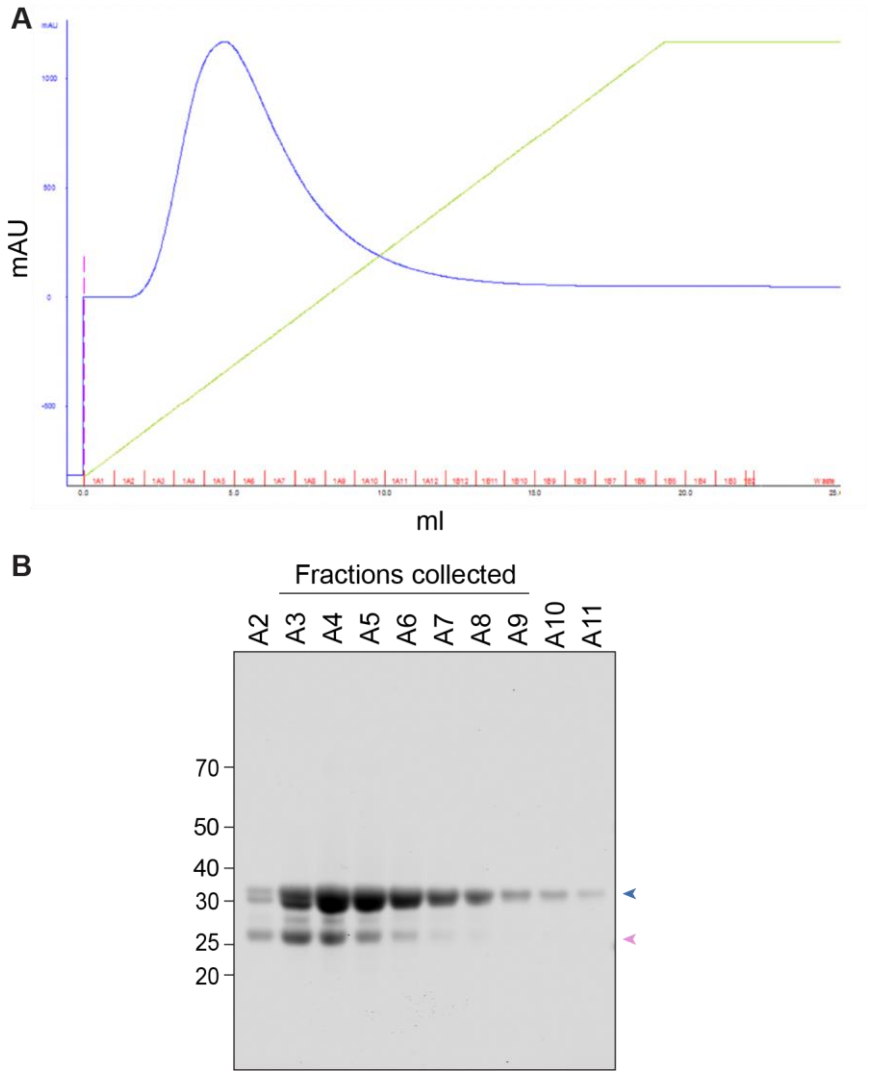

Figure 3.17 Purification of GST-RILP fusion protein

GST-tagged protein was purified from bacterial lysates transformed with pGEX-6P1-mR7BD using a GSTrap column on an ÄKTA Protein Purification System. Bound proteins were eluted with 10 mM reduced glutathione. **A** The UV trace was used to determine which fractions contained GST-tagged protein. **B** Fractions were visualised by SDS-PAGE to ascertain purity of GST-RILP protein prep. Blue arrowhead indicates GST-RILP, pink arrowhead indicates GST alone.

3.5.2 Validation of active Rab7 binding assay

To validate the active Rab7 binding assay using the GST-RILP fusion protein we had produced, I carried out a test experiment in HEK293 FlpIn parental cells which are commonly used in the lab for pulldown experiments as they yield high protein amounts after lysis relative to other cell lines. HEK293 FlpIn parental cells were transfected with GFP-tagged wild type or dominant negative mutant Rab7[T22N] for 24 hours, lysed and then the GST-RILP assay was carried out on the resulting cell lysates (**Figure 3.18A**).

A strong band at the expected molecular weight of GFP-Rab7 (50-60kDa) and fainter band corresponding to endogenous Rab7 (23kDa) was visible in the pulldowns, indicating that the assay is capable of isolating and detecting overexpressed and endogenous Rab7. The amount of dominant negative [T22N] GFP-Rab7 pulled down is reduced compared to wild type, even though the inputs show similar amounts of overexpressed protein, demonstrating that the assay is sensitive to changes in Rab7 activity.

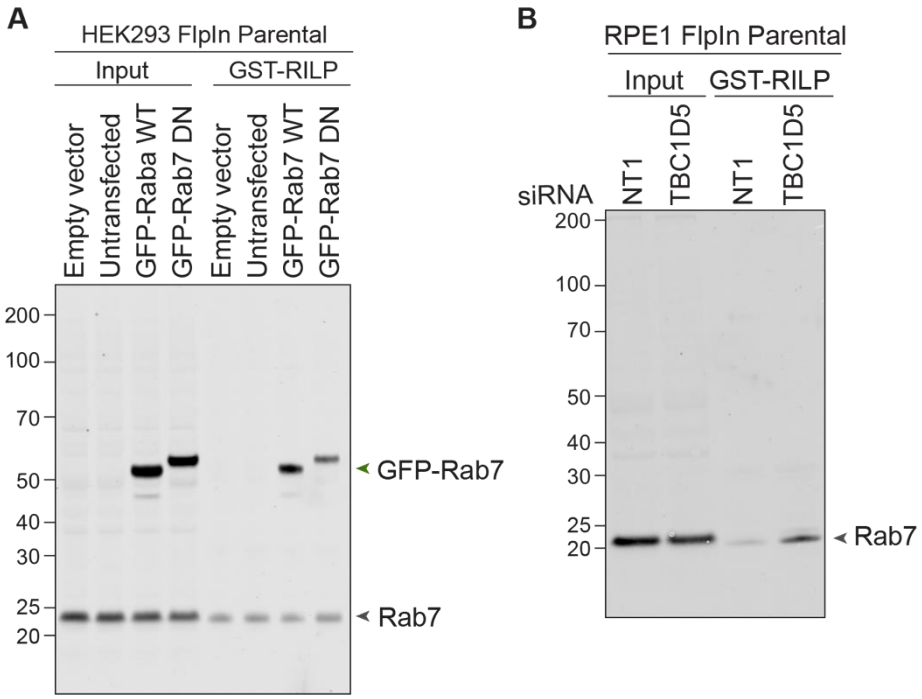

Figure 3.18 Validation of active Rab7 binding assay

A HEK293 FlpIn Parental cells were transfected with pEGFP empty vector or pEGFP-Rab7 (WT, wild type; DN, dominant negative [T22N]) for 24 hours. Lysates were incubated with immobilised GST-RILP for 2 hours and the resulting eluates were analysed by immunoblotting for active (GST-RILP-bound) Rab7. Green arrowhead indicates GFP-tagged Rab7. Grey arrowhead indicates endogenous Rab7. Data from a single experiment, *n* = 1. **B** RPE1 FlpIn Parental cells were subjected to siRNA knockdown for 72 hours with control (non-targeting #1; NT1) or TBC1D5 (pooled) targeting oligonucleotides before being lysed and incubated with immobilised GST-RILP for 2 hours. Eluted GST-RILP-bound Rab7 was analysed by immunoblotting. Grey arrowhead indicates endogenous Rab7. Data from a single experiment, *n* = 1.

I next tested the GST-RILP assay in RPE1 cells, as this would be the cell line I would use for future experiments. TBC1D5 is one of several Rab7 GAPs that are responsible for the conversion of the GTP bound to Rab7 to GDP. Knockdown of the Rab7 GAP TBC1D5 led to an increase in the levels of active Rab7, indicating an increase in GTP bound Rab7. This result further validates that the active Rab7 binding assay can detect changes to Rab7-GTP levels. It was necessary to load substantially more

protein onto the beads to obtain a good endogenous Rab7 signal when using RPE1 cells compared to HEK293 cells (800µg vs 300µg), which may mean that there is a smaller pool of Rab7 that is active at baseline conditions in this cell line.

3.5.3 Optimisation of active Rab7 binding assay

Given the low level of endogenous active Rab7 signal observed in the RILP pulldown from RPE1 lysates, I carried out further optimisation of the assay to try to enhance this signal. I compared the lysis buffer used in my validation experiments and by Jimenez-Orgaz and colleagues to a higher stringency buffer containing more sodium chloride that was used in a manuscript from Gómez-Suaga and colleagues to see if this decreased background binding and increased Rab7 signal (**Figure 3.19**) (Gómez-Suaga et al., 2014; Jimenez-Orgaz et al., 2018). There was a marginal decrease in background binding with the high stringency buffer as assessed by total protein staining, however the total active Rab7 signal was also reduced. I also tested the effect of increasing the amount of GST-RILP immobilised to the sepharose beads from 5 µg to between 10 and 20 µg. There was an increase in Rab7 signal with 10 µg of GST-RILP but this was not enhanced further when using greater amounts of GST-RILP. From these results I chose to continue to use the low stringency buffer but increased the amount of GST-RILP added to 10 µg for future experiments to achieve a stronger active Rab7 signal.

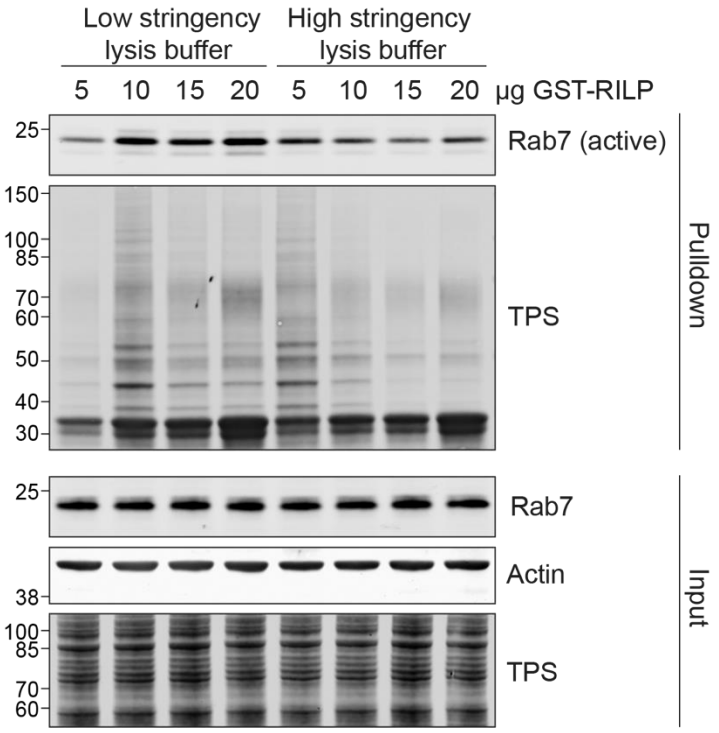

Figure 3.19 Optimisation of active Rab7 binding assay

RPE1 FlpIn Parental cells were lysed in low stringency (20mM Tris-HCl pH 7.8, 50 mM NaCl, 0.5 % Triton X-100, 1 mM $MgCl_2$) or high stringency (20 mM HEPES pH 7.4, 100 mM NaCl, 1 % Triton X-100, 5 mM $MgCl_2$) buffer and incubated with different amounts of GST-RILP fusion protein immobilised to Glutathione Sepharose beads. Bound proteins were eluted in sample buffer and analysed by immunoblotting. TPS, total protein stain. Data from a single experiment, $n = 1$.

3.6 Discussion

In this chapter I have outlined the steps I took to establish a set of tools to enable me to study the relationship between VPS35 and LRRK2.

3.6.1 RPE1 cells as a model system for studying VPS35 and LRRK2

I first screened a panel of cell lines for expression of VPS35, LRRK2, Rab29 and Rab7. While VPS35 was ubiquitously expressed in all cell lines, the levels of the other proteins were more variable. Rab7 expression was much higher in melanoma cell lines compared to non-melanoma cells. Up-regulation of Rab7 levels has been shown to be critical in driving initial melanoma progression, which is then reduced in a 'phenotypic switch' when melanomas gain invasive potential (Alonso-Curbelo et al., 2014). The authors of this manuscript also showed an enrichment of lysosomal genes in melanoma cell lines compared to other cancer cell types, including colon, leukaemia and renal, but did not investigate whether any of the other lysosomal genes also respond in the same manner as Rab7 to the phenotypic switch. This may explain why we also saw higher levels of Rab29 in the melanoma lines, as Rab GTPases are critical regulators of vesicular trafficking events in the endolysosomal system. Although Rab29 is not traditionally considered a lysosomal Rab, Eguchi *et al.* (2018) have shown that lysosomal stress can trigger its recruitment to lysosomal membranes, suggesting it may have some function at this organelle.

In the cell lines that I tested, levels of LRRK2 varied greatly. LRRK2 was expressed highest in WM266.4 and A375P cells, which a previous PhD student in the lab, Hannah Elcocks, has found is inversely proportional to their pigmentation and invasion potential. This suggests LRRK2 may be another marker for melanoma phenotypic switching and invasiveness, but in a manner opposite to Rab7, with LRRK2 being up-regulated in later stages of melanoma progression. I chose RPE1 cells as the model cell line for my project as I felt they had the best balance of expression of all these proteins, while also being diploid and good for imaging experiments.

LRRK2 contains several serines which have been shown to be differentially phosphorylated in the presence of familial PD mutations and have been used previously as read-outs for kinase activity. These include the autophosphorylation site S1292 and a cluster of serines between the ANK and LRR domain (S910/935/955/973) (Marchand et al., 2020; Sheng et al., 2012). LRRK2 inhibition causes dephosphorylation at S935, but only with Type I inhibitors and not Type II. Using commercially available antibodies against pS1292-LRRK2 and pS935-LRRK2, I was unable to detect any signal in RPE1 cells with endogenous levels of LRRK2. Therefore, to measure LRRK2 activity I measured LRRK2 substrate Rab phosphorylation using the phosphosite specific antibodies against pT73-Rab10 and pS106-Rab12 as a proxy readout of LRRK2. By immunoblotting for pT73-Rab10, I confirmed that endogenous LRRK2 is active basally in RPE1 cells, albeit at quite low levels. The small dynamic range between basal Rab10 phosphorylation and the residual LRRK2 independent signal measured in the presence of LRRK2 inhibitors may present difficulties when trying to assess a reduction in phosphorylation in future experiments. However, there should be no problem assessing hyperactivation, which is the most important aspect for my project, as we can see a very strong signal when exogenous wild type and [G2019S] variant eGFP-LRRK2 are introduced. This suggests the limiting factor for Rab10 phosphorylation in these cells is the activity and expression of LRRK2 rather than levels of total Rab10 or PPM1H, the LRRK2 phosphosite-specific phosphatase of Rab10 (Berndsen et al., 2019).

Another commonly used antibody to detect LRRK2 activity is one raised against pT72-Rab8A. However, this antibody is not specific and cross-reacts with phosphorylated Rab3A, Rab10, Rab35 and Rab43. Despite this, it still holds value in its use as a ‘pan-phospho-Rab’ antibody.

3.6.2 Generation of RPE1 cell lines expressing exogenous VPS35 and LRRK2

Using the Flp-In™ TRex™ system I have generated an isogenic pair of cell lines which express wild type or [D620N] mutant HA-VPS35. After performing immunofluorescence staining on the cell lines, we found that not all the cells expressed HA-VPS35. I hypothesised that this was because the colonies that were picked after transfection were not pure and contained untransfected cells. To obtain pure clones, the cell lines were single cell diluted and screened by immunofluorescence for HA staining. I have since found that expression is lost in 40-60% of the cells immediately after rethawing. This suggests that the reason that not

all cells express HA-VPS35 is that there has been loss or repression of the cassette. The Invitrogen protocol for generating Flp-In cell lines reports that down-regulation of the CMV promoter and loss of gene expression is observed in 3T3 and BHK cells (Invitrogen, 2012), and so this may also be the case for the RPE1 FlpIn cells. In some, but not all, cases, maintaining the cells under antibiotic selection increased the percentage of HA positive cells to up to 90%, which are then more suitable for use in biochemical experiments to allow us to better see any differences caused by the mutation.

It is likely that this is also the reason that the original 'mixed' clones were impure - I did not have the opportunity to screen them by immunofluorescence before freezing them down due to the covid lockdown. Ultimately, this means that care needs to be taken with these cell lines to ensure that a suitable proportion of the cells are expressing HA-VPS35 and at similar levels between the WT and [D620N] pair to reveal any subtle differences caused by the mutation in biochemical experiments. This is achieved by regular screening by immunofluorescence. For fixed immunofluorescence microscopy experiments, both the original mixed cells and 'pure' clones can be used at any percentage of positive cells provided that the cells are co-stained with HA to identify expressing cells.

I also generated clones of the WT and [D620N] VPS35 FlpIn cells expressing lentivirus transfected eGFP-LRRK2 at equivalent levels. Overexpression of LRRK2 could help overcome the low basal Rab phosphorylation observed in the RPE1 cells due to low endogenous LRRK2 expression. These cell lines will facilitate the study of wild type, hyperactive and kinase-dead LRRK2 in RPE1 cells, and in combination with the VPS35[D620N] mutant. However, it is possible that the large increase in Rab phosphorylation due to overexpression of LRRK2 may have such a strong effect that it masks any effect of [D620N]VPS35 which we have aimed to only express at near-endogenous levels in this model. It has been suggested that the placement of larger tags such as eGFP on the N-terminus of LRRK2 may disrupt membrane localisation (Vides et al., 2022). In our cell lines, the majority of eGFP-LRRK2 is cytosolic, with only the occasional punctate structure. This is in line with previous reports that have found LRRK2 to be 90% cytosolic at steady state (Berger et al., 2010; Purlyte et al., 2018). Many over-expression studies also show LRRK2 to have a cytoplasmic localisation but have also shown its presence at punctate structures, including endosomes and lysosomes, and at mitochondria (Biskup et al., 2006; Eguchi et al., 2018; Henry et al., 2015; Purlyte et al., 2018). Compounds which cause endolysosomal stress, such as chloroquine and LLOMe, have been shown to trigger

the recruitment of LRRK2 to lysosomal membranes (Eguchi et al., 2018; Herbst et al., 2020). Treatment with one of these agents could be used to check whether eGFP-tagged LRRK2 is able to be properly recruited to membranes in our cell lines. Alternatively, this could be tested by overexpressing Rab29, which drives LRRK2 recruitment at the Golgi (Purlyte et al., 2018).

3.6.3 Characterisation of RPE1 FlpIn VPS35 cell lines

Through cellular fractionation and immunofluorescence microscopy I have shown that [D620N] mutant VPS35 is able to properly localise to membranes and that its distribution and localisation to EEA1 positive early endosomes is unchanged, consistent with previous studies (Follett et al., 2014; McGough et al., 2014; Tsika et al., 2014).

Expression levels of retromer components are highly co-regulated. Depletion of either VPS35 or VPS29 by siRNA transfection also depleted cells of the other retromer subunits, indicating that loss of one retromer subunit causes destabilisation of the trimeric complex and its degradation. This has been observed previously in multiple studies (Fuse et al., 2015; Jimenez-Orgaz et al., 2018; Simonetti et al., 2017). By assessing HA-VPS35 levels in the RPE1 FlpIn VPS35 cells after withdrawal of doxycycline, I found that HA-VPS35 is very stable and persists at a similar level even 48 hours after withdrawal, and that this is not affected by the [D620N] mutation. This is consistent with previous studies looking at stability and assembly of the retromer core (McGough et al., 2014; Tsika et al., 2014; Zavodszky et al., 2014). According to the Invitrogen handbook for generating Flp-In T-REx cell lines, doxycycline has a half-life of 48 hours (Invitrogen, 2012). Therefore, combined with washing and exchange of media, it is unlikely that a significant amount of HA-VPS35 is still being transcribed. Upon induction of HA-VPS35 expression we also observe a small increase in VPS26, supporting the notion that the levels of retromer core components are highly dependent on each other.

Interestingly, after eight hours of doxycycline withdrawal there appeared to be a reduction in endogenous VPS35 in the WT 3B4 cells. VPS35 has recently been shown to undergo autoregulation in primary neuron cultures, whereby introduction of high titres of exogenous VPS35 causes a decrease in endogenous VPS35 to maintain total VPS35 levels (Qureshi et al., 2022). The authors attributed this to the instability of VPS35 when not part of the retromer complex (Fuse et al., 2015; Jimenez-Orgaz et al., 2018; Qureshi et al., 2022; Simonetti et al., 2017). That we do not see this auto-regulatory effect in the [D620N] cell may be due to the slightly lower levels of

exogenous expression so there is less competition for incorporation into retromer subunits. By fractionation we can see similar levels of wild type and [D620N] HA-VPS35 present in the membrane fraction, but more in the PNS and cytoplasmic fraction in the wild type cells which may have a stronger autoregulatory effect on endogenous VPS35 levels. However, further study would be needed to confirm that this difference in impact on endogenous VPS35 levels is due to differential expression levels and not due to the [D620N] mutation.

I confirmed the validity of the RPE1 FlpIn VPS35 system as a model for investigating the relationship between endogenous LRRK2 and VPS35 by showing that expression of VPS35[D620N] leads to an increase in Rab phosphorylation. The enhanced Rab phosphorylation was sensitive to LRRK2 inhibition, confirming that this effect is via a VPS35-LRRK2-Rab axis. The increase in Rab phosphorylation seen in the RPE1 cells is modest compared to what has previously been reported (Mir et al., 2018). For instance, Rab10 phosphorylation was elevated 4-5-fold in heterozygous knockin VPS35[D620N] mouse embryonic fibroblasts (MEFs) (Mir et al., 2018). This difference may reflect the relatively low expression and activity of LRRK2 in RPE1 cells.

3.6.4 RILP assay

Loss of VPS35 has been shown to increase Rab7 activity through subsequent loss of TBC1D5 control over Rab7, however it is not known what effect the [D620N] mutation has on levels of active Rab7 (Jimenez-Orgaz et al., 2018). Despite Rab7 not being a direct substrate for LRRK2, PD-causing mutations in LRRK2 have been shown to decrease Rab7-GTP levels (Gómez-Suaga et al., 2014). As perturbation of VPS35 levels and LRRK2 activity both affect levels of active Rab7, it is possible they act in a shared pathway to affect this change. As Rab7 is known to be a key player in the functioning of the endolysosomal system, this could be of relevance to the numerous trafficking and autophagy defects that have been reported in models of Parkinson's disease, including those with VPS35 and LRRK2 mutations.

To explore the effect of the [D620N] mutation on levels of active Rab7, we have established the GST-RILP active Rab7 binding assay in the lab. In this chapter, I have described the production of GST-RILP fusion protein to be used to isolate GTP-bound Rab7 from cell lysates, optimisation of the assay and its validation using TBC1D5 knockdown and expression of Rab7 wild type and dominant negative constructs.

Together, the tools I have generated in this chapter provide a platform for investigating the effects of the VPS35[D620N] mutation, with a focus on the relationship between VPS35, LRRK2 and Rab7.

4 VPS35, LRRK2 and endosomal trafficking

4.1 Introduction

Dysfunction in the endolysosomal system has been implicated in several neurodegenerative diseases, highlighting the importance of its normal function in the central nervous system. Retromer itself has been linked to the pathology of several neurodegenerative diseases, including Alzheimer's disease, Parkinson's Disease and Amyotrophic Lateral Sclerosis (ALS) (Williams et al., 2022). Perhaps the most compelling link between retromer dysfunction and neurodegeneration is that the missense mutation Asp620Asn, [D620N], in VPS35 causes autosomal dominant familial Parkinson's disease.

In 2014, two independent groups showed that the [D620N] mutation impaired the interaction of VPS35 with the tail of FAM21 of the WASH complex (McGough et al., 2014; Zavodszky et al., 2014). The functional consequences of this decreased association with the WASH complex remain unclear, both with regards to the effect on the WASH complex and on the trafficking function of retromer. Zavodszky and colleagues reported that the [D620N] mutation decreased WASH complex localisation to the endosome (Zavodszky et al., 2014), whereas McGough and colleagues found this to be unchanged (McGough et al., 2014).

These two studies also investigated the effect of the mutation on cargo recycling but again came to different conclusions, despite using similar approaches and operating in overlapping cell lines. Zavodszky and colleagues reported that stable expression of VPS35[D620N] in HeLa cells depleted of endogenous VPS35 led to defects in GLUT1, but not CIMPR, sorting, suggesting a defect in retrograde transport to the plasma membrane (Zavodszky et al., 2014). Conversely, the parallel study by McGough and colleagues found that expression of VPS35[D620N] was able to rescue GLUT1 mis-sorting following depletion of VPS35 in HeLa cells (McGough et al., 2014). The authors also showed that expression of VPS35[D620N] failed to rescue CIMPR trafficking defects in RPE1 cells depleted of VPS35. Furthermore, they observed CIMPR distribution was altered in VPS35[D620N] patient fibroblasts compared to a healthy control (McGough et al., 2014). From these results, the authors surmised that the [D620N] mutation causes a defect in trafficking to the *trans*-Golgi network. Studies using transient overexpression of VPS35[D620N] in other immortalised mammalian cell lines have also seen a defect in CIMPR trafficking (Follett et al., 2014; MacLeod et al., 2013), whereas in rat primary cortical neurons overexpressing VPS35[D620N]

and patient-derived fibroblasts sorting of CIMPR was found to be unaffected (Tsika et al., 2014). The latter study also showed sortilin and sorLA trafficking were unaffected by the [D620N] mutation when overexpressed in primary cortical neurons (Tsika et al., 2014).

It is worth noting that recent evidence has called into question the role of retromer in CIMPR trafficking, leading to the suggestion that CIMPR may be recycled via a different sorting complex, ESCPE-1 (Evans et al., 2020; Kvainickas et al., 2017). ESCPE-1 comprises the SNX-BAR dimer, SNX1/2 and SNX5/6, which acts together with the core retromer trimer of VPS35-VPS29-VPS26 in yeast but can function independently in mammals (Kvainickas et al., 2017; Seaman et al., 1998; Simonetti et al., 2017). This complicates the task of identifying the effect of the [D620N] mutation in my chosen system when the role of retromer in the trafficking of one of its once widely accepted cargoes is debated.

A recently proposed additional role for retromer is acting as a checkpoint protein in endosome maturation through its control of Rab7 activity and localisation (Daly et al., 2023). By recruiting the Rab7 GAP TBC1D5, retromer limits the amount of active Rab7 present at endosomes. Without retromer, active Rab7 accumulates on late endosomes/lysosomal structures (Daly et al., 2023; Jimenez-Orgaz et al., 2018). This is proposed to cause disruption to endosome maturation by promoting the rate of endolysosome fusion, whilst also causing a failure in lysosome reformation from the hybrid endolysosome organelles. This concept extends the role of retromer from sorting cargo at the endosome to being a master regulator of endosome-lysosome homeostasis. The effect of the VPS35[D620N] mutant on Rab7 has not yet been investigated.

In summary, despite the intensive study of the effect of the VPS35[D620N] mutation on trafficking, a clear consensus is lacking. Different conclusions have been made as to whether retrograde trafficking is affected in the direction of the *trans*-Golgi network, or the plasma membrane, in both, or in neither (**Table 4.1**). I hypothesised that the conflicting results may arise from the different experimental models used in the studies, such as re-expression of wild type or [D620N] mutant VPS35 in a knockout background, stably expressing VPS35 cell lines with knockdown of endogenous VPS35, transient overexpression and patient-derived fibroblasts. It would thus be beneficial to systematically test the different endosomal phenotypes that have been previously reported in different cell models in the literature using the RPE1 FlpIn

VPS35 cell system I have described in **Chapter 3**, wherein wildtype and [D620N] mutant VPS35 are expressed at a 1:1 ratio with endogenous VPS35.

Table 4.1 Summary of the effects of depletion and [D620N] mutation of VPS35 on the endosomal network

PM, plasma membrane; TGN, *trans*-Golgi network.

Phenotype	Retromer loss/inactivation		VPS35 [D620N]	
	Effect	Reference	Effect	Reference
CIMPR trafficking to the TGN	Impaired	(Arighi et al., 2004; Hao et al., 2013; MacDonald et al., 2018; MacLeod et al., 2013; McGough et al., 2014; Seaman, 2004)	Impaired	(Follett et al., 2014; MacLeod et al., 2013; McGough et al., 2014)
	Unchanged	(Evans et al., 2020; Kvainickas et al., 2017)	Unchanged	(Tsika et al., 2014; Zavodszky et al., 2014)
GLUT1 trafficking to the PM	Impaired	(McGough et al., 2014; Piotrowski et al., 2013; Steinberg et al., 2013)	Impaired	(Zavodszky et al., 2014)
			Unchanged	(McGough et al., 2014)
Sortilin trafficking	Impaired	(Canuel et al., 2008)	Unchanged	(Tsika et al., 2014)
SorLA trafficking	Impaired	(Fjorback et al., 2012)	Unchanged	(Tsika et al., 2014)
Rab7 activity	Increased	(Jimenez-Orgaz et al., 2018)	Not tested	
Rab7 localisation	Accumulation on lysosomes	(Daly et al., 2023; Jimenez-Orgaz et al., 2018)	Not tested	

In this chapter, I describe the work I performed to investigate the effect of the [D620N] mutation in VPS35 on some of these endosomal phenotypes in RPE1 cells and how this contrasts with the effect of VPS35 depletion. The phenotypes studied include:

- The interaction of the WASH complex with retromer
- Endosomal localisation of the WASH complex
- Trafficking of the lysosomal hydrolase receptors CIMPR and sortilin

- Localisation and activity of Rab7

Parkinson's disease-causing mutations in LRRK2 have been linked to delayed EGFR receptor trafficking, CIMPR mis-sorting and decreased Rab7 activity, suggesting that LRRK2 plays a role within the endosomal network (Gómez-Suaga et al., 2014; MacLeod et al., 2013). Overexpression of wild type VPS35 is capable of rescuing the CIMPR trafficking defects, suggesting the existence of a VPS35-LRRK2 axis in endosomal trafficking (MacLeod et al., 2013). In this chapter, I also set out to investigate whether any endosomal defects caused by the VPS35[D620N] mutation could be rescued by LRRK2 inhibition.

4.2 VPS35 and the WASH complex

4.2.1 VPS35[D620N] impairs WASH association but not its localisation

To assess whether the [D620N] mutation causes a decrease in WASH complex association, I performed immunoprecipitation experiments using anti-HA magnetic beads to pull down HA-VPS35 and look at the binding of interactors by western blotting (**Figure 4.1A**). Addition of doxycycline caused a strong increase in HA signal in the pulldown blot showing HA-VPS35 was successfully isolated by the anti-HA magnetic beads. The small amount of signal present in the negative control condition performed in the absence of doxycycline is likely due to some leakiness of the construct as a faint HA bind is visible in the uninduced (- DOX) conditions in the whole cell lysates. The binding of VPS26 to wild type and [D620N] mutant VPS35 was similar, suggesting that this interaction is minimally affected by the [D620N] mutation (**Figure 4.1B**). On the other hand, binding of WASHC1, a sub-unit of the WASH complex, was clearly reduced by 60% for the [D620N] mutant (**Figure 4.1C**). This confirms that WASH complex association with VPS35 is impaired by the [D620N] mutation in my cell system.

Next, I used immunofluorescence microscopy to see if the distribution of the WASH complex was affected by its reduced association with retromer. I seeded RPE1 FlpIn HA-VPS35 wild type or [D620N] cells mixed at a 2:1 ratio with RPE1 FlpIn parental cells into 6-well plates and induced HA-VPS35 expression with 0.1 µg/ml doxycycline. After 24 hours, I replated the cell mixtures onto coverslips and grew them in the absence of doxycycline for 48 hours before fixing and staining them for HA and the WASH complex subunits WASHC1 and FAM21. This experimental set-up allowed me

to compare WASH complex localisation in wild-type and [D620N] VPS35-expressing cells directly to parental cells that do not express the constructs on the same coverslips.

Staining for FAM21 revealed a punctate distribution with some cytosolic staining. These punctate structures co-localised with HA-VPS35 in the wild type and [D620N] expressing cells (**Figure 4.1D**). Quantification of the number of FAM21C puncta showed a small increase in VPS35-expressing cells compared to controls, however this was a minor effect when considering the spread of the data (**Figure 4.1E**). This increase may reflect that there is more VPS35 at the endosomes in these cells to recruit the WASH complex. The number nor the size of FAM21C puncta were changed comparing wild type and [D620N] cells. As expected, WASHC1 showed the same punctate distribution as FAM21C (**Figure 4.1F**). The number and size of WASHC1 puncta appeared to increase in the presence of the [D620N] mutation compared to wild-type, however this difference was not apparent when compared to parental cells on the same coverslip (**Figure 4.1G**). This suggests the increase in size and number of WASHC1 puncta may reflect some difference between the samples (coverslips), such as differing confluency or quality of antibody staining, rather than a biological difference between cells expressing wild type and mutant VPS35.

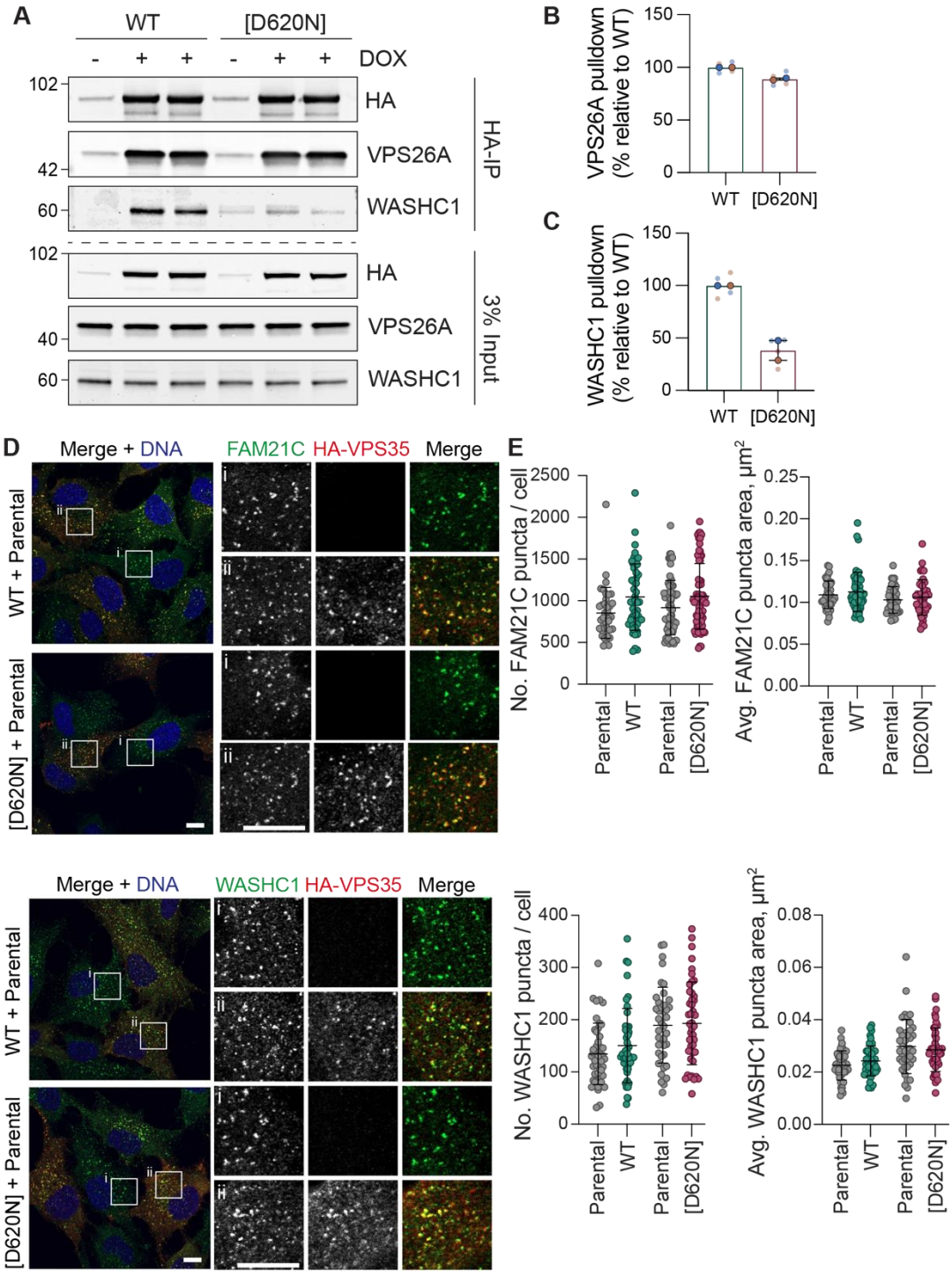

Figure 4.1 The [D620N] mutation impairs the interaction of WASH complex with retromer but not its endosomal association

A RPE1 FlpIn VPS35 WT 3B4 and [D620N] 1F3 cells were treated with 0.1 µg/ml doxycycline for 24 hours. Cells were lysed in NP40 buffer and subjected to immunoprecipitation (IP) using anti-HA magnetic beads. A representative western blot is shown. **B** Quantification of VPS26 binding in the HA-IP relative to the mean of WT + DOX condition per experiment. *n* = 2 independent experiments with duplicate samples. Each independent experiment is colour-coded. Transparent circles with no outline represent values for each sample in an experiment, opaque circles with black outlines correspond to mean values for each experiment. Bars represent mean ± range. **C** Quantification of

WASHC1 binding in the HA-IP relative to mean of WT + DOX condition per experiment. *n* = 2 independent experiments with duplicate samples. Each independent experiment is colour-coded. Transparent circles with no outline represent values for each sample in an experiment, opaque circles with black outlines correspond to mean values for each experiment. Bars represent mean ± range. **D** RPE1 FlpIn VPS35 WT 3B4 and [D620N] 1F3 cells were treated with 0.1 µg/ml doxycycline to induce HA-VPS35 expression. After 24 hours cells were mixed with RPE1 FlpIn Parental cells (green only in the merge) and replated onto coverslips. Cells were fixed 48 hours after replating and stained for the indicated antibodies. z-stack images (3 slices, 0.31 µm step) were acquired on a Zeiss LSM800 confocal microscope using a 63x objective. Scale bar 10 µm. **E** Quantification of the number and size of FAM21 particles, >38 cells counted per condition. Bars represent mean ± SD. Data from a single experiment. **F** RPE1 FlpIn VPS35 WT 3B4 and [D620N] 1F3 cells were treated with 0.1 µg/ml doxycycline to induce HA-VPS35 expression. After 24 hours cells were mixed with RPE1 FlpIn Parental cells (green only in the merge) and replated onto coverslips. Cells were fixed 48 hours after replating and stained for the indicated antibodies. z-stack images (3 slices, 0.31 µm step) were acquired on a Zeiss LSM800 confocal microscope using a 63x objective. Scale bar 10 µm. **G** Quantification of WASHC1 particles, >38 cells counted per condition. Bars represent mean ± SD. Data from a single experiment.

Actin polymerisation at endosomes mediated by the WASH complex is proposed to maintain and segregate distinct degradative and recycling endosomal subdomains (Simonetti and Cullen, 2019). I sought to investigate whether the [D620N] mutation in VPS35 perturbed the ability of WASH to regulate endosomal subdomain organisation. To do so, I stained RPE1 FlpIn HA-VPS35 wild type and [D620N] cells with antibodies against HRS, FAM21 and HA after 72 hours of induction with doxycycline (**Figure 4.2**). To enable the distinction between the different endosomal subdomains, cells were imaged using a Zeiss LSM900 microscope with Airyscan 2 which allows for confocal super-resolution. Using this method, HRS and FAM21 punctate structures appeared in close apposition to each other but showed little co-incidence, whereas there was significant overlap between HA-VPS35 and FAM21 puncta. This demonstrates the ability to differentiate between the HRS-positive degradative and VPS35 and FAM21 positive recycling subdomains. Expression of HA-VPS35 [D620N] caused no apparent change in the overlap between HRS and FAM21. This suggests that the [D620N] mutation does not affect the maintenance of discrete subdomains at the endosome.

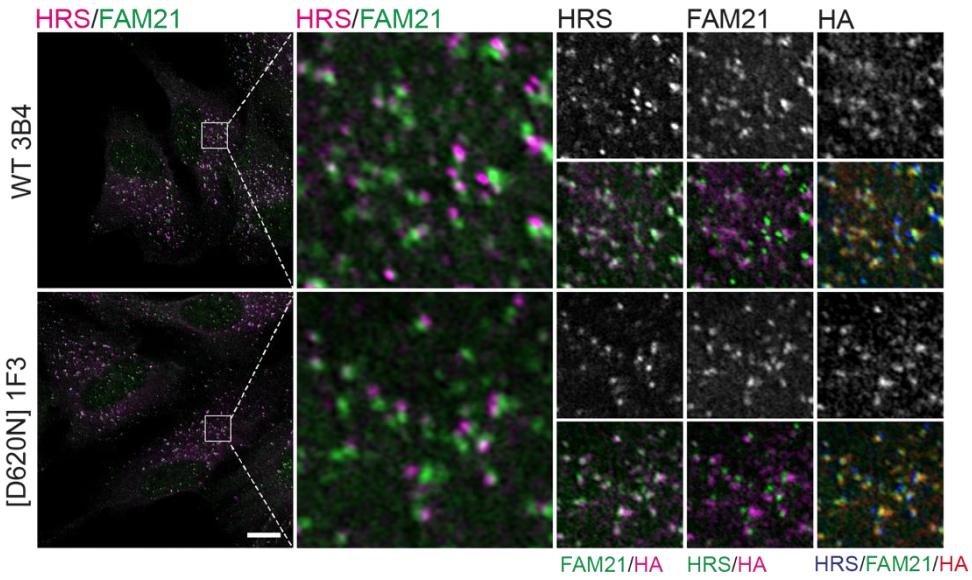

Figure 4.2 The [D620N] mutation does not disrupt the segregation of recycling and degradative endosomal subdomains

RPE1 FlpIn VPS35 WT 3B4 and [D620N] 1F3 cells were treated with 0.1 µg/ml doxycycline and after 72 hours fixed and stained with the indicated antibodies. Images were acquired on a Zeiss LSM900 confocal microscope in Airyscan 2 mode using a 63x objective. Scale bar 10 µm. Data from a single experiment, *n* = 1.

4.2.2 Depletion of VPS35 causes loss of endosomal WASH

The lack of effect of the [D620N] mutation on the localisation of the WASH complex to endosomes lies in stark contrast with the effect of depletion of VPS35 in RPE1 Parental cells. Knockdown of VPS35 for 72 hours caused a marked decrease in the number of FAM21C and WASHC1 puncta at EEA1-positive early endosomes when assessed qualitatively (**Figure 4.3**). A small portion of WASH complex remained at endosomes following depletion of retromer, indicating the existence of a retromer-independent mechanism of WASH complex recruitment. It has been shown that HRS is also required for WASH complex association, and so this may be one mechanism for recruiting the residual WASH complex seen at endosomes in VPS35-depleted RPE1 cells (MacDonald et al., 2018). A recent study has also identified a retromer-independent mechanism for WASH complex endosome association whereby the SWIP sub-unit binds phosphoinositide species within the endosomal membrane, primarily PI(3,5)P_2 (Dostál et al., 2023).

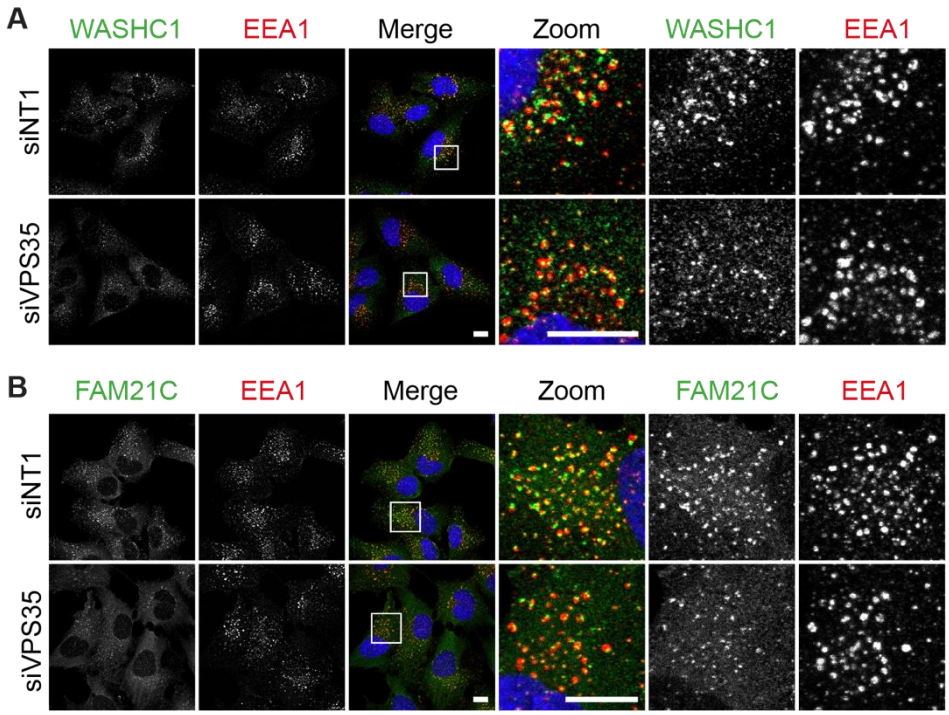

Figure 4.3 WASH complex association to the endosome is dependent on VPS35
RPE1 FlpIn Parental cells were subjected to siRNA knockdown for 72 hours with control (non-targeting #1; NT1) or VPS35 (pooled) targeting oligonucleotides before being fixed and stained for EEA1, DAPI (DNA) and either WASHC1 (**A**) or FAM21C (**B**). z-stack images (3 slices, 0.2µm step) were acquired on a Zeiss LSM900 confocal microscope using a 63x objective. Max projection shown. Scale bar 10 µm. Representative images shown from one of two independent experiments, *n* = 2.

4.3 VPS35 and cargo recycling

4.3.1 VPS35[D620N] and CIMPR trafficking

The trafficking of the cation-independent mannose-6-phosphate receptor (CIMPR) has been shown to be perturbed by the VPS35[D620N] mutation in some studies (Cui et al., 2021; Follett et al., 2014; MacLeod et al., 2013; McGough et al., 2014), but not others (Tsika et al., 2014; Zavodszky et al., 2014). I sought to investigate whether the [D620N] mutation affected CIMPR trafficking in the RPE FlpIn isogenic cell model system. **Figure 4.4A** shows the distribution of CIMPR by immunofluorescence microscopy in cells induced for HA-VPS35 expression for 72 hours. In uninduced control WT 3B4 and [D620N] 1F3 cells, CIMPR staining showed a strong co-localisation with the *trans*-Golgi marker *trans*-Golgi Network Glycoprotein 46 (TGN46). Expression of wild type or mutant VPS35 did not alter this distribution when assessed qualitatively. I have also looked at the localisation of CIMPR after a shorter, 24-hour induction and likewise did not find any disruption to its localisation.

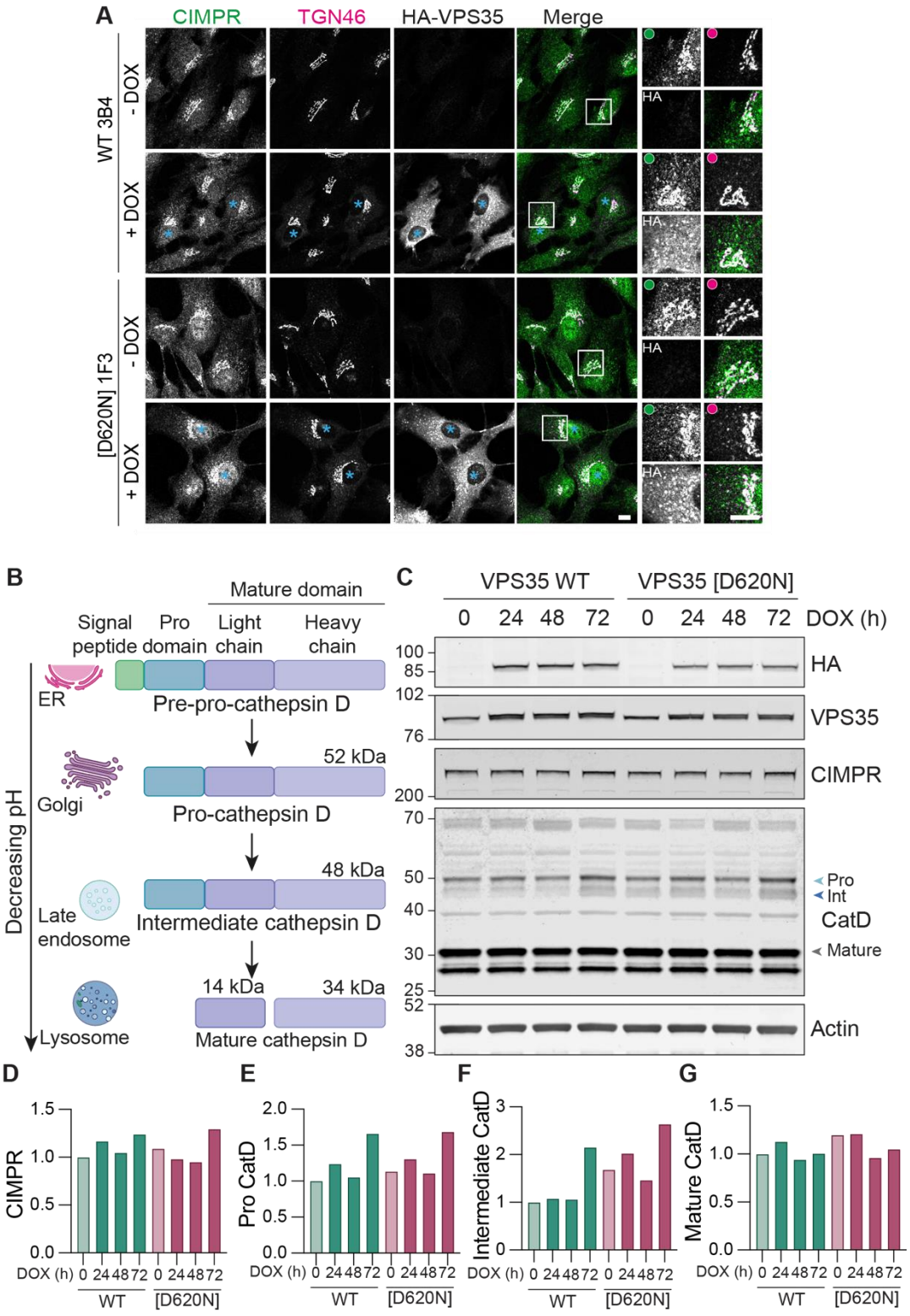

Figure 4.4 VPS35[D620N] does not affect steady-state CIMPR distribution

A RPE1 FlpIn VPS35 WT 3B4 and [D620N] 1F3 cells were treated with 0.1 µg/ml doxycycline and after 72 hours fixed and stained with the indicated antibodies. Images were acquired on a Zeiss LSM800 confocal microscope using a 63x objective. Scale bar 10 µm. Images are representative of two experiments, *n* = 2. Blue asterisks indicate cells expressing HA-VPS35. **B** Schematic of Cathepsin D (CatD) processing. **C** RPE1 FlpIn VPS35 WT 3B4 and [D620N] 1F3 cells were treated with 0.1

µg/ml doxycycline then lysed at the indicated time points and analysed by immunoblotting. **D** Quantification of C**.** Signals were quantified and normalised to actin signal and WT 0h Dox condition. Graphs represent CIMPR (D), pro CatD (E), intermediate CatD (F) and mature CatD (G). Data from a single experiment, *n* = 1.

In addition, I looked at the total levels of CIMPR and cathepsin D by western blotting. Cathepsin D is a lysosomal protease which CIMPR is responsible for delivering to the endolysosomal system from the *trans*-Golgi network (Pohlmann et al., 1995; Press et al., 1998). Pre-pro-cathepsin D is synthesised in the ER and transits to the Golgi where the signal peptide is removed to generate inactive 52 kDa precursor pro-cathepsin D. This precursor form is then trafficked to early and late endosomes by CIMPR, where it loses the N-terminal pro-peptide residues to become an enzymatically active intermediate 48 kDa form (Saftig and Klumperman, 2009; Szulc-Dąbrowska et al., 2020). Intermediate cathepsin D then undergoes autocatalysis in the low pH environment of the lysosome to form the active, mature double-chain form of cathepsin D (**Figure 4.4B**) (Szulc-Dąbrowska et al., 2020).

I compared the levels of CIMPR and the proportion of the different cathepsin D forms upon expression of HA-VPS35 wild type or [D620N] mutant for 24 to 72 hours (**Figure 4.4C**). I speculated that 24 hours may not be long enough to see impaired trafficking of *de novo* synthesised cathepsin D and so also included a longer induction time. I observed no marked difference in CIMPR levels upon expression of wild-type or [D620N] VPS35 expression (**Figure 4.4D**). Immunoblotting for cathepsin D revealed several bands, corresponding to the pro, intermediate and mature forms. Basally, the majority of cathepsin D exists in the mature form in RPE1 cells. Expression of wild-type VPS35 did not alter the levels of any form of cathepsin D at 24- and 48-hours post-induction (**Figure 4.4E-G**). After 72 hours of induction there was increased pro- and intermediate cathepsin D in both wild-type and [D620N] VPS35 conditions. Expression of intermediate cathepsin D was at least 1.5-fold higher at all time-points in VPS35 [D620N] 1F3 cells compared to VPS35 WT 3B4, but this was also the case in the absence of doxycycline, suggesting a clonal difference rather than an effect of the [D620N] mutation. Together, these results suggest that the [D620N] mutation does not affect the trafficking of CIMPR.

4.3.2 VPS35[D620N] does not perturb *trans*-Golgi morphology

Overexpression of hyperactive [G2019S] mutant LRRK2 has been shown to cause dispersal of the Golgi network, which can be rescued by LRRK2 inhibition (Purlyte et al., 2018). As the [D620N] mutation in VPS35 also causes hyperactivation of LRRK2 (Mir et al., 2018), I sought to look at the effect of VPS35[D620N] expression on the

morphology of the *trans*-Golgi network. RPE1 FlpIn WT 3B4 and [D620N] 1F3 cells were co-stained with p230 and HA after induction of HA-VPS35 expression with doxycycline for 24 hours (**Figure 4.5A**). The area occupied by the trans-Golgi network was not significantly altered upon expression of either wild type or [D620N] mutant VPS35 (**Figure 4.5B**). This is in agreement with data from a previous study which showed that VPS35[D620N] patient fibroblasts display a normal Golgi morphology (McGough et al., 2014), but contrasts with other work which showed HeLa cells expressing VPS35 [D620N] display an abnormal Golgi morphology (Zavodszky et al., 2014). As I did not observe any change to the morphology of *trans*-Golgi network, I was therefore unable to investigate a role for LRRK2 in this context.

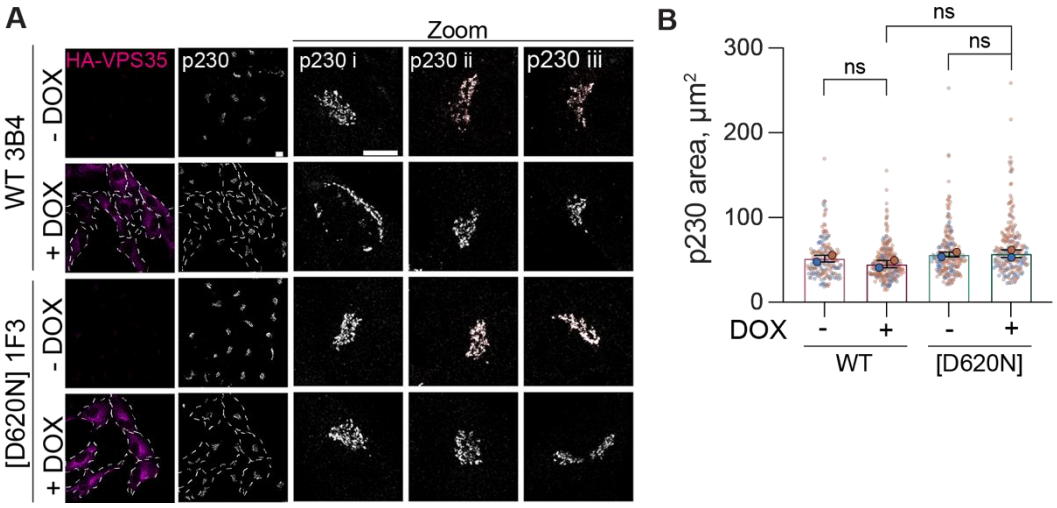

Figure 4.5 VPS35[D620N] does not cause dispersal of the Golgi in RPE1 cells
A RPE1 FlpIn VPS35 WT 3B4 and [D620N] 1F3 cells were treated with 0.1 µg/ml doxycycline for 24 hours before being fixed and stained with the indicated antibodies. Single slice images were acquired on a Zeiss LSM900 confocal microscope using a 40x objective. Scale bar 10 µm. **B** Quantification of the *trans*-Golgi area occupied by p230. *n* = 2. Each independent experiment is colour-coded. Transparent circles with no outline represent values for each cell in an experiment, opaque circles with black outlines correspond to mean values for each experiment. Bars represent mean and range. One-way ANOVA with Tukey's multiple comparisons test. ns, not significant.

4.3.3 Depletion of VPS35 does not alter the steady-state distribution of CIMPR

Recently, the role of retromer in CIMPR trafficking has been called into question. Despite studies from several independent groups showing that depletion of VPS35 causes a redistribution of CIMPR from the Golgi to peripheral endosomal structures (Arighi et al., 2004; Cui et al., 2021; Harbour et al., 2010; MacDonald et al., 2014; McGough et al., 2014; Seaman, 2004), it is now thought that CIMPR is instead an

ESCPE-1 complex cargo. Contrary to initial studies, more recent work has, in fact, found recycling of CI-MPR to the TGN to be enhanced in VPS35 knockout HeLa cells (Kvainickas et al., 2017; Simonetti et al., 2017). To investigate the role of retromer in CIMPR trafficking in RPE1 cells, I performed a 72-hour siRNA knockdown to deplete cells of VPS35 and processed the cells for immunofluorescence microscopy, probing for CIMPR and the *trans*-Golgi marker p230 (**Figure 4.6A**). Knockdown of VPS35 did not cause a redistribution of CIMPR from the trans-Golgi network in RPE1 cells. The Pearson's correlation co-efficient between CIMPR and p230 staining was not significantly changed between control and VPS35 knockdown conditions (**Figure 4.6B**). By western blotting, knockdown of VPS35 caused a small increase in total levels of CIMPR (**Figure 4.6C**).

Disruption of the mannose-6-phosphate-dependent lysosomal hydrolase trafficking pathway can cause mistargeting of pro-cathepsin D into the extracellular medium via the secretory pathway (Davidson, 1995; Gaffet et al., 1997; MacDonald et al., 2014). To assess whether depletion of VPS35 caused misdirection of cathepsin D to the secretory pathway in RPE1 cells, I analysed the amount of cathepsin D in the growth medium (**Figure 4.6D**). After 56 hours of siRNA-mediated knockdown of VPS35, adherent cells were washed thoroughly with PBS and the regular DMEM/F12 growth media were replaced with serum free Opti-MEM media. The condition media were then collected, and proteins were precipitated from the media using sodium deoxycholate and TCA (method described in detail in **Section 2.3.6**). Precipitated proteins were resuspended in sample buffer and resolved using SDS-PAGE and western blotting. Adherent cells were lysed in NP40 and processed as usual for immunoblotting. In the whole cell lysate samples, depletion of VPS35 did not affect the expression of the different Cathepsin D forms (**Figure 4.6F-H**). In the media, a band at approximately 50 kDa was detectable, corresponding to the molecular weight of the pro form of cathepsin D. The levels of this were unaffected by VPS35 knockdown (**Figure 4.6D and E**). These results support the hypothesis that CIMPR trafficking occurs via a retromer-independent pathway in RPE1 FlpIn cells. However, it cannot be excluded that there is a potential defect in the biosynthetic pathway in retromer-depleted cells which would block the secretion of pro-cathepsin D from the Golgi.

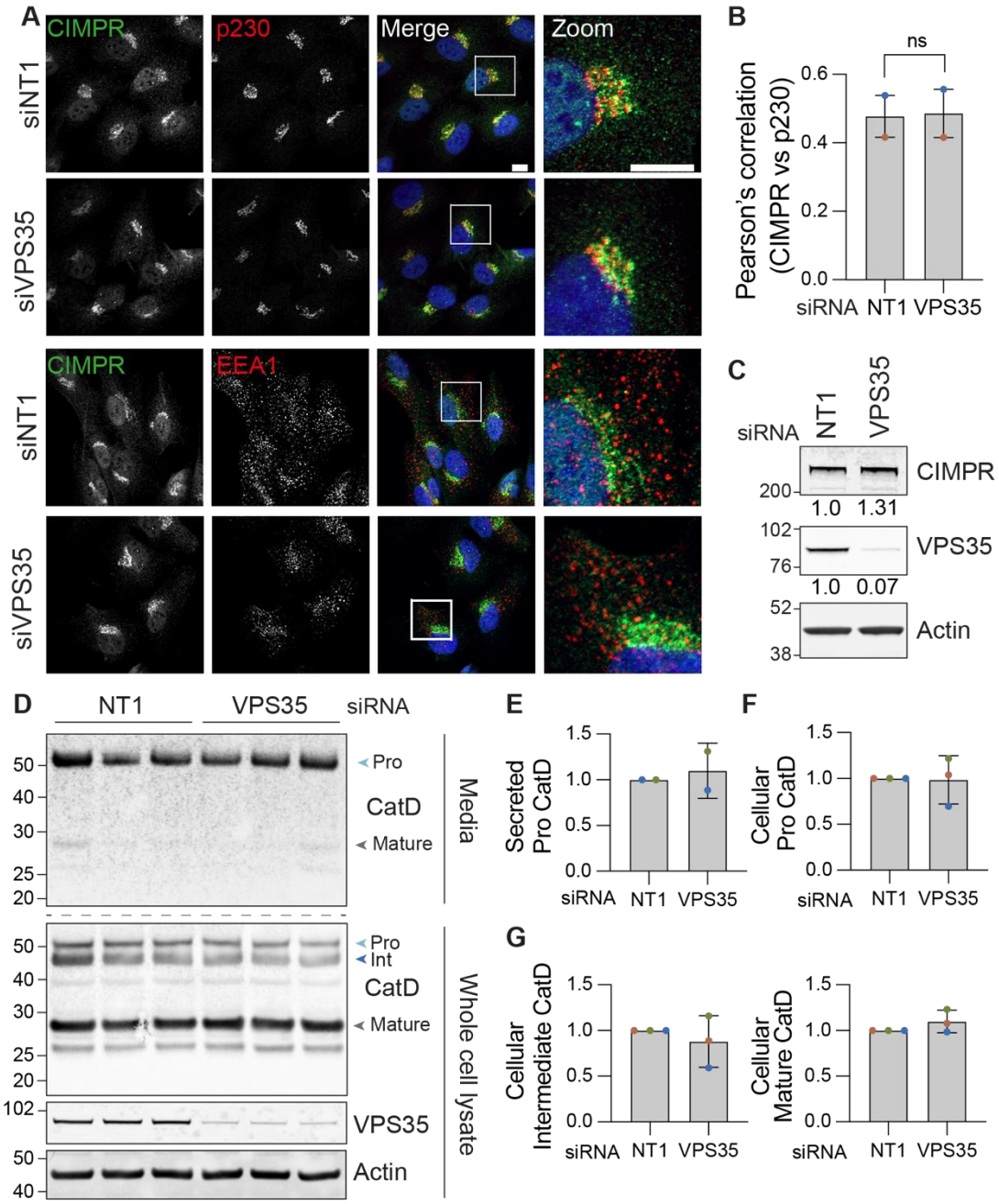

Figure 4.6 Depletion of VPS35 does not affect CIMPR trafficking in RPE1 cells

A RPE1 FlpIn Parental cells were subjected to siRNA knockdown for 72 hours with control (non-targeting #1; NT1) or VPS35 (pooled) targeting oligonucleotides before being fixed and stained with the indicated antibodies. z-stack images (3 slices, 0.2µm step) were acquired on a Zeiss LSM900 confocal microscope using a 63x objective. Max projections are shown. Scale bar 10 µm. **B** Pearson's correlation of CIMPR vs p230. *n* = 2. Each independent experiment is colour-coded. Bars represent mean and range. Paired t-test. ns, not significant. **C** RPE1 FlpIn Parental cells were subjected to siRNA knockdown for 72 hours with control (non-targeting #1; NT1) or VPS35 (pooled) targeting oligonucleotides before being lysed and subjected to immunoblotting. Values represent signal intensity of CIMPR and VPS35 signal, normalised to actin and then NT1 control. **D** Immunoblot of levels of cathepsin D (CatD) species in media and whole cell lysates in RPE1 FlpIn Parental cells subjected to siRNA knockdown for 72 hours with control (non-targeting #1; NT1) or VPS35 (pooled)

targeting oligonucleotides. A representative western blot is shown. **E-F** Quantification of D. Signals were quantified and normalised to actin then to the NT1 control condition. Graphs represent CIMPR (E), pro CatD, intermediate CatD (G) and mature CatD (H). *n* = 2-3. Each independent experiment is colour-coded. Bars represent mean ± SD.

4.3.4 VPS35[D620N] does not alter steady-state distribution of sortilin

Retromer has been reported to be required for the retrograde trafficking of the lysosomal hydrolase receptor sortilin from the endosome to the TGN in HeLa and COS-7 cells (Canuel et al., 2008; Seaman, 2007). Depletion of VPS26A led to the accumulation of sortilin in peripheral structures and reduced localisation at the Golgi compared to control cells (Canuel et al., 2008). However, overexpression of VPS35 wild-type or [D620N] was not seen to cause a change in the steady-state distribution of sortilin in cortical neurons in another study (Tsika et al., 2014). I next assessed the effect of the [D620N] mutation on the distribution of sortilin in the RPE1 FlpIn cell lines.

RPE1 FlpIn WT 3B4 and [D620N] 1F3 cells were processed for immunocytochemistry 72 hours after doxycycline induction and stained for sortilin, HA and TGN46 (**Figure 4.7A**). The majority of sortilin was localised in a tight perinuclear area that co-localised with the *trans*-Golgi marker TGN46. There was also a population of peripheral sortilin puncta which co-localised with HA-VPS35, suggesting this belonged to an endosomal compartment. There was no observable redistribution of sortilin upon expression of either wild-type or [D620N] VPS35 by eye, suggesting the trafficking of this receptor is unaffected by the [D620N] mutation in RPE1 cells. Assessment of sortilin by immunoblotting 24 hours after of induction HA-VPS35 likewise showed no impact on sortilin expression levels (**Figure 4.7B**).

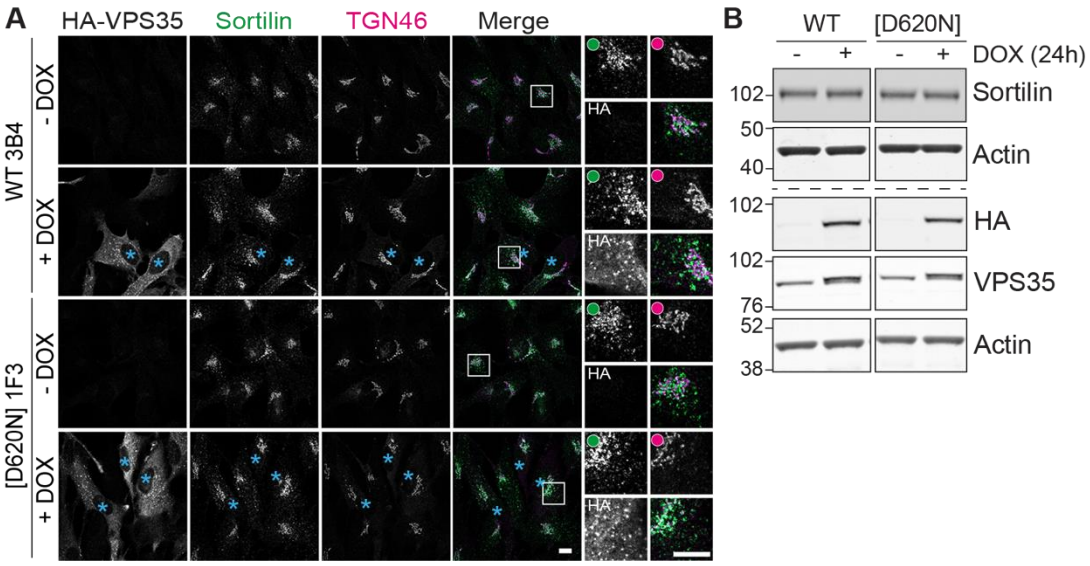

Figure 4.7 VPS35 [D620N] does not affect the steady-state levels and distribution of sortilin
A RPE1 FlpIn VPS35 WT 3B4 and [D620N] 1F3 cells were treated with 0.1 µg/ml doxycycline and after 72 hours fixed and stained with the indicated antibodies. Images were acquired on a Zeiss LSM800 confocal microscope using a 63x objective. Scale bar 10 µm. Images are representative of two experiments, *n* = 2. Blue asterisks indicate cells expressing HA-VPS35. **B** RPE1 FlpIn VPS35 WT 3B4 and [D620N] 1F3 cells were treated with 0.1 µg/ml doxycycline for 24 hours, then lysed and analysed by immunoblotting.

4.3.5 Depletion of VPS35 does not alter steady-state distribution of sortilin

I next performed an siRNA knockdown of VPS35 and looked at the distribution of sortilin by immunofluorescence. The cells were co-stained with the Golgi marker p230, early endosome marker EEA1 or the late endosome/lysosome marker LAMP1 (**Figure 4.8**). As described previously, most sortilin resided at the Golgi compartment with a population present at early endosomes in control cells. There was no observable co-localisation of sortilin with LAMP1-positive late endosomes/lysosomes. By qualitative assessment, this distribution has not affected by depletion of VPS35.

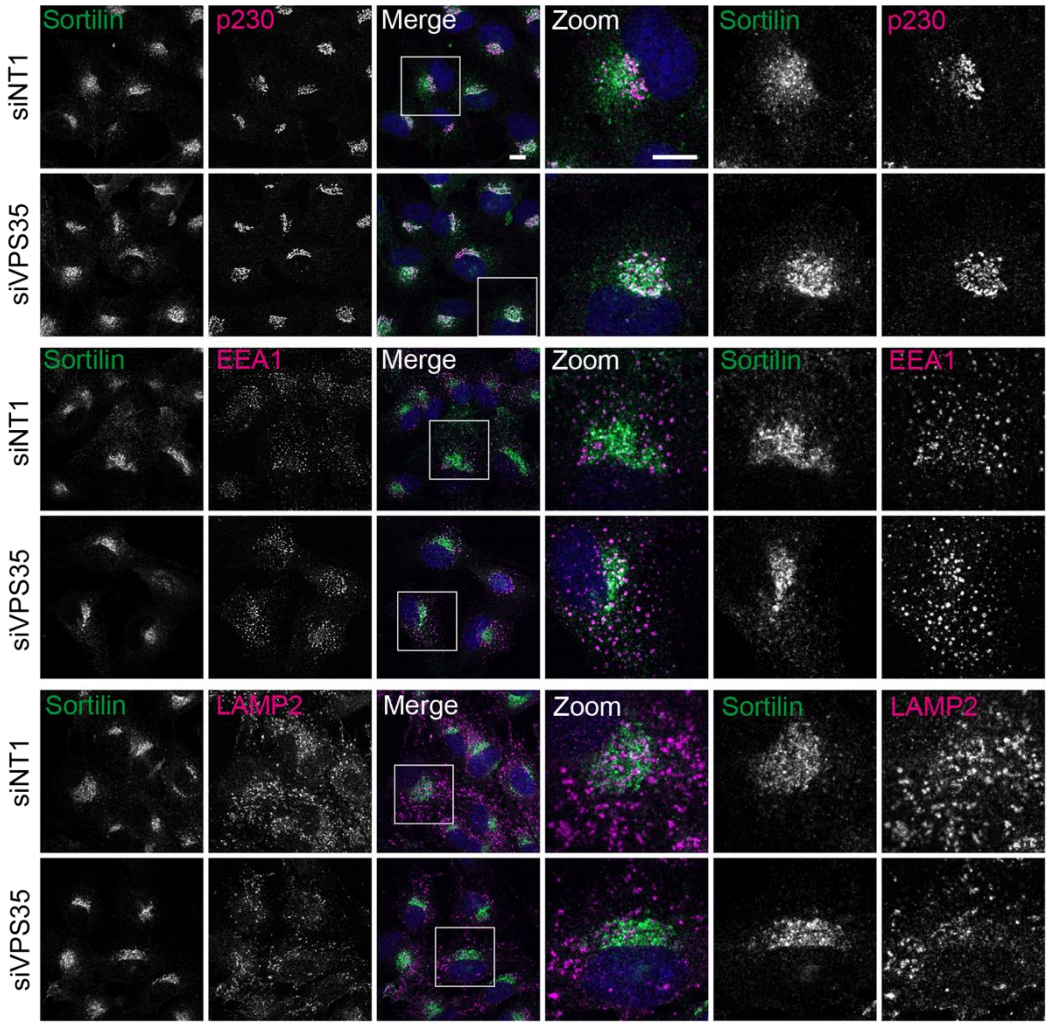

Figure 4.8 VPS35 depletion does not affect the steady-state distribution of sortilin

A RPE1 FlpIn Parental cells were subjected to siRNA knockdown for 72 hours with control (non-targeting #1; NT1) or VPS35 (pooled) targeting oligonucleotides before being fixed and stained with the indicated antibodies. Images were acquired on a Zeiss LSM800 confocal microscope using a 63x objective. Scale bar 10 µm. Data from a single experiment, *n* = 1.

4.4 VPS35, LRRK2 and Rab7

4.4.1 Depletion of VPS35 causes a reduction in total Rab7

When optimising the VPS35 knockdown protocol, I observed that depletion of VPS35 caused a small but reproducible reduction of Rab7 by approximately 30% (**Figure 4.9A and B**). To confirm that this reduction of Rab7 was not caused by an off-target effect of the siRNA, I performed a deconvolution of the VPS35-directed siRNA oligonucleotide pool (**Figure 4.9C**). The individual oligonucleotides targeting VPS35 showed variability in the degree of Rab7 reduction, but Rab7 expression was reduced with all four oligonucleotides, confirming this effect is specific and correlates with depletion of VPS35 (**Figure 4.9D**). To see if the variability in the decrease in Rab7 as

a result of VPS35 knockdown was related to the efficiency of VPS35 depletion, I plotted the VPS35 signal against the Rab7 signal in the pooled and deconvoluted knockdowns relative to NT1 (**Figure 4.9E**). I then performed a simple linear regression on the data, which yielded an r^2 value of 0.13, suggesting there was a poor correlation between the efficiency of VPS35 knockdown and Rab7 reduction.

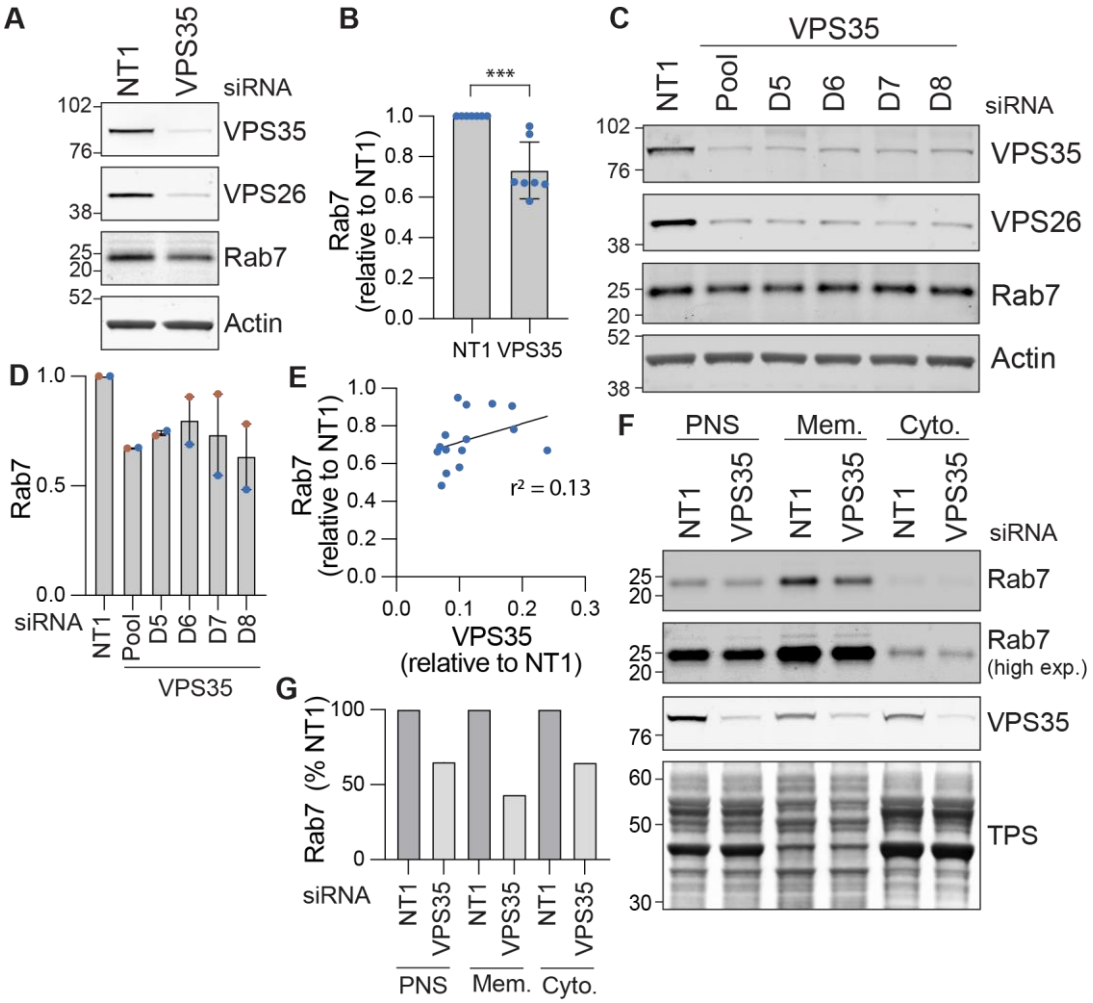

Figure 4.9 Depletion of VPS35 causes a reduction in Rab7

A Representative immunoblot of Rab7 levels in RPE1 FlpIn Parental cells subjected to siRNA knockdown with control (non-targeting #1; NT1) or VPS35 (pooled) targeting oligonucleotides before for 72 hours. **B** Quantification of A. Values were normalised to actin then to NT1 control. *n* = 7 independent experiments. Bars represent mean ± SD. Unpaired t-tests performed on values normalised to sum of signal within a replicate then to actin. P *** < 0.001. **C** siRNA deconvolution of pooled VPS35 targeting oligonucleotides. 72-hour knockdown. A representative western blot is shown. **D** Quantification of C. Values were normalised to actin then NT1 control. *n* = 2. Each independent experiment is colour-coded. Bars represent mean and range. **E** Scatter plot of VPS35 and Rab7 signal in VPS35 knockdown conditions relative to NT1 control from experiments shown in B and D. Values were normalised to actin then NT1 control. Line of best fit calculated using simple linear regression model. **F** Subcellular fractionation of 72-hour NT1 control and pooled VPS35

knockdown. PNS; post-nuclear supernatant, TPS; total protein stain. **G** Quantification of F. Values were normalised to NT1 control for each fraction. Data from a single experiment, *n* = 1.

I wondered whether this reduction of Rab7 corresponded to a loss of a specific pool of Rab7 i.e. active, membrane-bound Rab7 or inactive cytosolic Rab7. To look at the distribution of Rab7, I isolated total membranes from the cytosol using centrifugation in control and VPS35 knockdown cells (**Figure 4.9E**). A decrease in Rab7 could be observed in the post-nuclear supernatant and cytosolic and membrane fractions, indicating that the loss of Rab7 is not specific to a particular pool and rather affects the whole population (**Figure 4.9F**). However, the degree of loss appeared to be slightly greater in the membrane fraction.

The fractionation experiment showed that there was little change in the distribution of Rab7 between the membrane and the cytosol, but this does not provide information on whether the distribution of Rab7 to different membrane compartments is altered as only a total membrane fraction was collected. To investigate whether this loss of Rab7 upon knockdown of VPS35 affected the subcellular localisation of Rab7, I co-stained control and VPS35 knockdown cells with antibodies against Rab7 and LAMP2 (**Figure 4.10A**). Previous studies have shown that knockout of retromer increases Rab7 localisation to lysosomes in H4 and Hela cells (Daly et al., 2023; Jimenez-Orgaz et al., 2018). In contrast to these previously reported findings, knockdown of VPS35 did not result in an increase in the co-localisation of Rab7 and LAMP2 in the RPE1 cell model. In agreement with the immunoblotting data, there was a trend towards a decrease in Rab7 puncta and the total area occupied by Rab7 punctate structures in the cell (**Figure 4.10C and E**). However, the Rab7 reduction by western blotting did not translate into a decrease in the total intensity of Rab7 fluorescence staining (**Figure 4.10B**). The average size of these puncta was also not affected by VPS35 knockdown (**Figure 4.10D**).

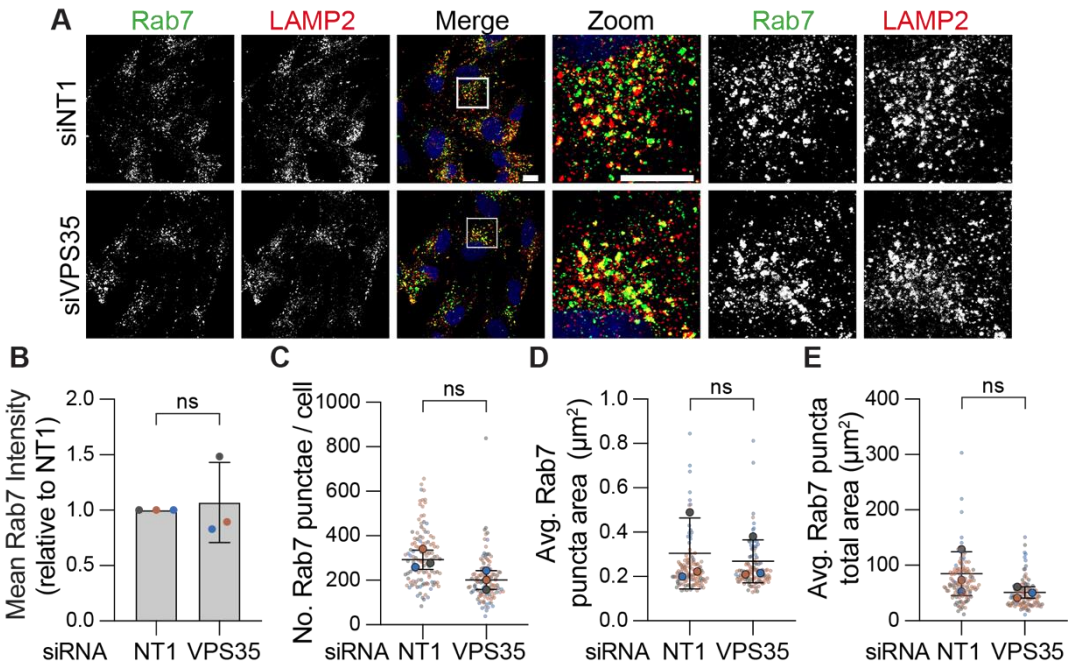

Figure 4.10 Depletion of VPS35 does not affect Rab7 localisation to lysosomes

A RPE1 FlpIn Parental cells were subjected to siRNA knockdown for 72 hours with NT1 control or pooled VPS35 targeting oligonucleotides before being fixed and stained with the indicated antibodies. Images were acquired on a Zeiss LSM800 confocal microscope using a 63x objective. Scale bar 10 µm. **B** Corrected total cell fluorescence (CTCF) of Rab7 staining normalised to NT1 control. **C** Quantification of the number (**C**), average size (**D**) and total area (**E**) of Rab7 particles. *n* = 3, > 15 cells quantified per condition per independent. Each independent experiment is colour-coded. Transparent circles with no outline represent values for each cell in an experiment, opaque circles with black outlines correspond to mean values for each experiment. Bars represent mean ± SD. Paired t-tests. ns, not significant.

Next, I investigated whether this change in Rab7 expression altered the activity status of Rab7. To do this I utilised the GST-RILP active Rab7 binding assay (**Figure 4.11A**). Knockdown of VPS35 reduced the amount of GTP-bound, active Rab7 pulled down with the GST-RILP beads (**Figure 4.11D**). However, after normalising the amount of active Rab7 to the total Rab7 in the input, the proportion of active Rab7 did not change on average (**Figure 4.11E**). It must be noted that the results are variable between replicate experiments making it difficult to draw firm conclusions from this data. This may reflect the poor Rab7 pulldown signal in the assay, making it sensitive to slight differences in loading of samples. As shown before in **Section 3.5.2**, and consistent with its role as a Rab7 GAP, depletion of TBC1D5 increased the proportion of active GTP-bound Rab7. However, the high variability in the increase in active Rab7 compared to untransfected controls illustrates the high variability of the assay.

In the same set of experiments, I also looked at the effect of depletion of LRRK2, Rab29 and Rab10 on Rab7 activity status. Confirmation of the knockdown of these proteins is shown in **Figure 4.11B**. Knockdown of LRRK2 and Rab29 caused no change in the proportion of Rab7 that was active, whereas depletion of Rab10 caused a small decrease in the proportion of active Rab7 relative to total levels.

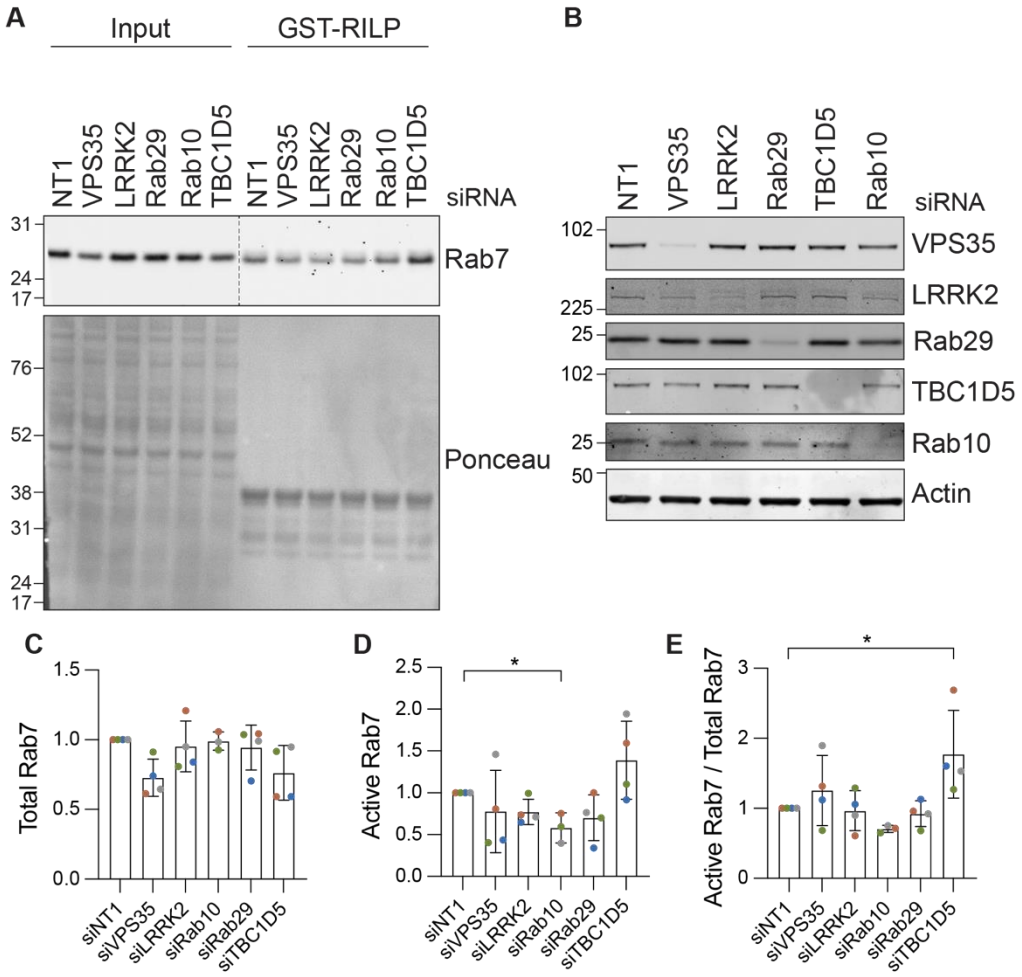

Figure 4.11 Effect of various knockdowns on active Rab7

A RPE1 FlpIn Parental cells were subjected to siRNA knockdown for 72 hours with NT1 control or pooled oligonucleotides as indicated before being lysed and incubated with immobilised GST-RILP for 2 hours. Eluted GST-RILP-bound Rab7 was analysed by immunoblotting. A representative western blot is shown. **B** Immunoblot of samples processed as in A. **C-E** Quantification of A. Values were normalised to NT1 control. *n* = 4. Each independent experiment is colour-coded. Bars represent mean ± SD. One-way ANOVA with Dunnett's multiple comparisons test performed on values normalised to sum of signal within a replicate. * P < 0.05.

4.4.2 VPS35[D620N] does not affect Rab7 distribution and activity

The effect the [D620N] mutation in VPS35 has on Rab7 localisation and activity is not known and so I set out to explore this. Firstly, I looked at the distribution of Rab7 in

the FlpIn VPS35 cell lines after 72 hours of doxycycline induction using immunofluorescence microscopy. Qualitatively, there appeared to be no change in the co-occurrence of Rab7 and the lysosomal marker LAMP2, suggesting that the [D620N] mutation does not disrupt the localisation of Rab7 (**Figure 4.12A**). When assessed by fractionation, the membrane-cytosol distribution of Rab7 was not changed by expression of either wild-type of mutant VPS35 (**Figure 4.12B**).

I also assessed whether expression of [D620N] VPS35 altered the amount of active Rab7 using the GST-RILP assay (**Figure 4.13A**). For each experiment, duplicate samples were prepared to ascertain technical reproducibility. Quantification revealed a trend towards an increase in the amount of proportion of active Rab7 in the [D620N]-expressing cells, despite a significant degree of variability between experiments and technical replicates (**Figure 4.13B**). I also repeated the experiment using more GST-RILP bound to the beads (**Figure 4.13C**). This gave the same result but also the same degree of variability (**Figure 4.13D**). Given the degree of variability and the fact that the change is rather small, I decided that the assay would not be sensitive enough to look at the effect of LRRK2 inhibition on this change.

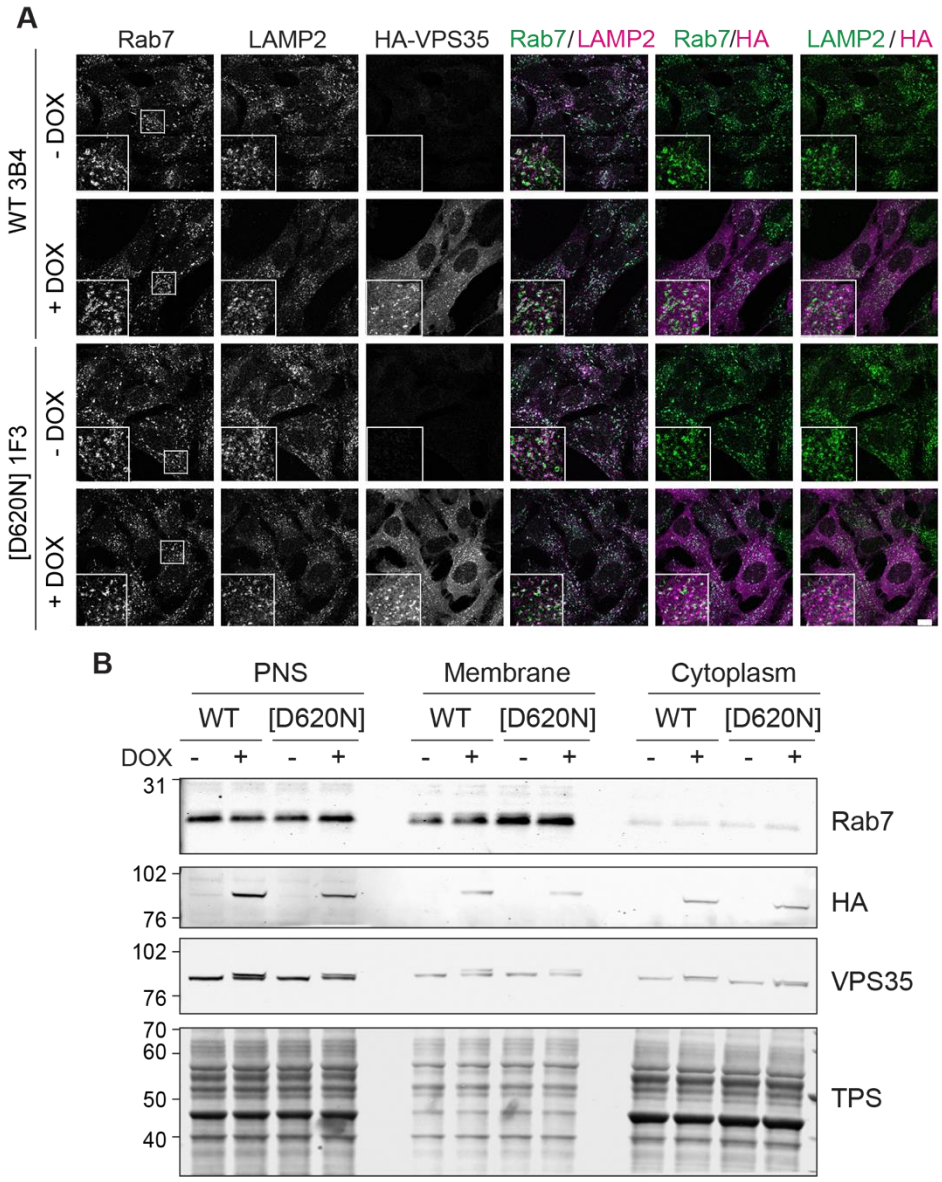

Figure 4.12 Expression of VPS35 [D620N] does not affect distribution of Rab7

A RPE1 FlpIn VPS35 WT 3B4 and [D620N] 1F3 cells were treated with 0.1 µg/ml doxycycline and after 72 hours fixed and stained for the indicated antibodies. Images were acquired on a Zeiss LSM800 confocal microscope using a 63x objective. Scale bar 10 µm. Representative images shown from one of two independent experiments, *n* = 2. **B** Subcellular fractionation of RPE1 FlpIn VPS35 WT 3B4 and [D620N] 1F3 cells treated with 0.1 µg/ml doxycycline for 24 hours. Samples analysed are the same as in Figure 3.13A. TPS; total protein stain. Data from a single experiment, *n* = 1.

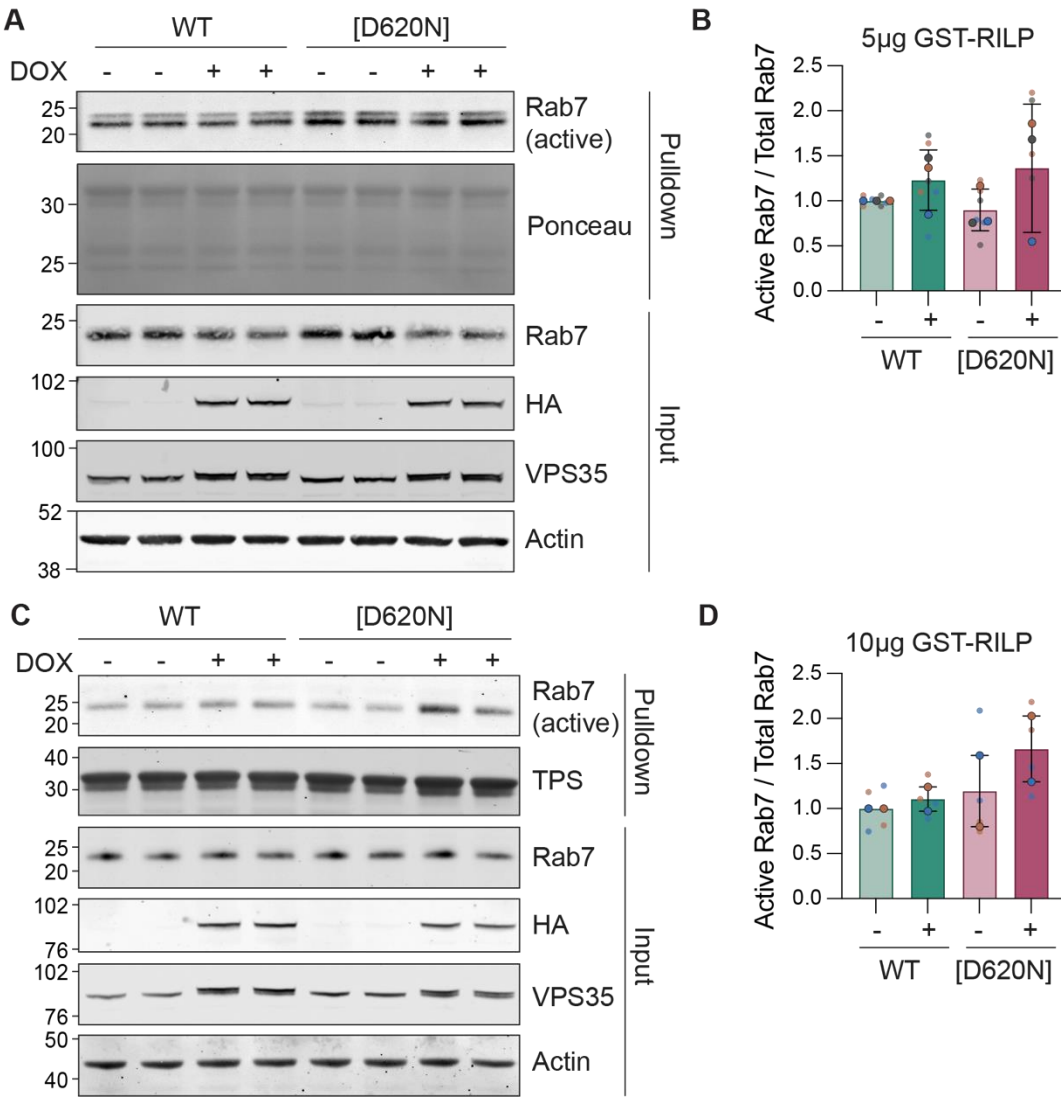

Figure 4.13 Assessment of levels of active Rab7 in HA-VPS35 wild type and [D620N]-expressing RPE1 cells

A RPE1 FlpIn VPS35 WT 3B4 and [D620N] 1F3 cells were treated with 0.1 µg/ml doxycycline for 24 hours before being lysed and incubated with 5 µg immobilised GST-RILP for 2 hours. Eluted GST-RILP-bound Rab7 was analysed by immunoblotting. TPS; total protein stain. **B** Quantification of A. Values were normalised to mean of WT – DOX in each experiment. *n* = 3 independent experiments with duplicate samples. Each independent experiment is colour-coded. Transparent circles with no outline represent values for each sample in an experiment, opaque circles with black outlines correspond to mean values for each experiment. Bars represent mean ± SD. **C** RPE1 FlpIn VPS35 WT 3B4 and [D620N] 1F3 cells treated with 0.1 µg/ml doxycycline for 24 hours before being lysed and incubated with 10 µg immobilised GST-RILP for 2 hours. Eluted GST-RILP-bound Rab7 was analysed by immunoblotting. **D** Quantification of C. Values were normalised to mean of WT – DOX in each experiment. *n* = 2 independent experiments with duplicate samples. Each independent experiment is colour-coded. Transparent circles with no outline represent values for each sample in an experiment, opaque circles with black outlines correspond to mean values for each experiment. Bars represent mean ± range.

4.4.3 LRRK2 inhibition does not alter Rab7 distribution and activity

Even though I was unable to test the effect of LRRK2 inhibition on active Rab7 levels in cells expressing mutant VPS35, I did investigate the effect of LRRK2 inhibition in RPE1 Parental cells (**Figure 4.14A**). Treatment with MLi-2 for one and 24 hours did not change the proportion of active Rab7 when compared to DMSO treated controls (**Figure 4.14B-D**). By immunofluorescence microscopy, there was no change to Rab7 distribution following one, four and 24 hours of LRRK2 inhibition with MLi-2 (**Figure 4.14E**).

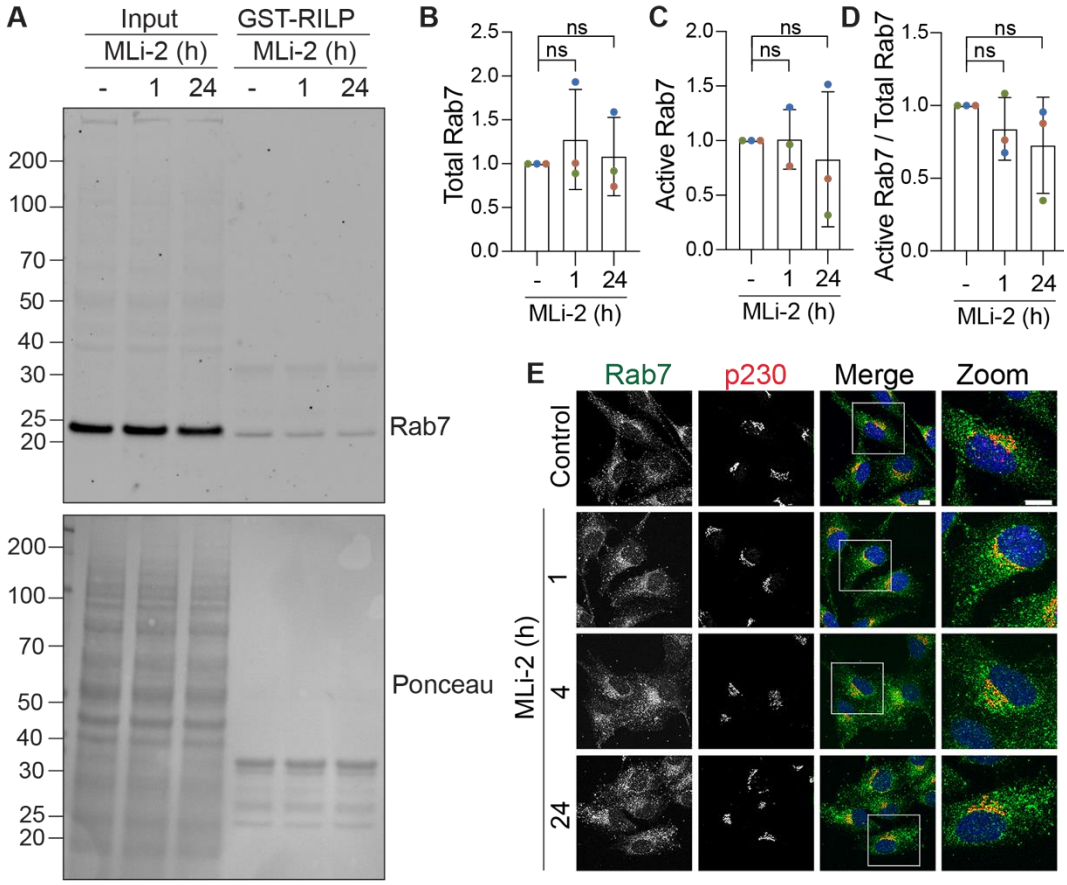

Figure 4.14 Effect of LRRK2 inhibition on Rab7 activity and distribution

A RPE1 FlpIn Parental cells were treated with 200 nM MLi-2 for one or 24 hours or vehicle (DMSO, 24 h) before being lysed and incubated with 5 µg immobilised GST-RILP for 2 hours. Eluted GST-RILP-bound Rab7 was analysed by immunoblotting. **B-D** Quantification of A. Values were normalised to vehicle control. *n* = 3. Each independent experiment is colour-coded. Bars represent mean ± SD. One-way ANOVA with Dunnett's multiple comparisons test performed on values normalised to sum of signal within a replicate. ns, not significant. **E** RPE1 FlpIn Parental cells were treated with 200 nM MLi-2 for one, four or 24 hours or vehicle control (DMSO, 24 h) before being fixed and stained with the indicated antibodies. Images were acquired on a Zeiss LSM800 confocal microscope using a 63x objective. Scale bar 10 µm. Data from a single experiment, *n* = 1.

4.5 Discussion

In this chapter I have used the RPE1 FlpIn system to investigate the effect of the VPS35[D620N] mutation in VPS35 on the endosomal network and retromer's role in trafficking and control of Rab7. To do so I have used the cell lines generated in **Chapter 3** to look at a range of phenotypes that have previously been reported in the literature, with a specific focus on those where independent groups have come to conflicting conclusions. A comparison of the effects of the [D620N] mutation and knockdown of VPS35 in RPE1 cells with previous studies are summarised in **Table 4.2**. The [D620N] mutation did not cause any observable changes to endosomal function and trafficking in the RPE1 FlpIn system, suggesting the effects of the mutation are subtle, lie elsewhere or arise from long-term low-level dysfunction.

Table 4.2 Comparison of trafficking and endosomal phenotypes upon VPS35 loss or mutation between RPE1 FlpIn cells and those previously reported in the literature. kd; knockdown.

Phenotype	**Retromer loss/depletion/inactivation**		**VPS35 [D20N] mutation**	
	Previously reported	**RPE1 with VPS35 kd**	**Previously reported**	**RPE1 FlpIn VPS35 [D20N] cells**
CIMPR trafficking	Impaired or Unchanged	Unchanged	Impaired or Unchanged	Unchanged
Sortilin trafficking	Impaired	Unchanged	Unchanged	Unchanged
SorLA trafficking	Impaired	Not tested	Unchanged	Not tested
GLUT1 trafficking	Impaired	Not tested	Impaired or unchanged	Not tested
Rab7 activity	Increased	Small increase	Not tested	Unchanged
Rab7 localisation	Accumulation on lysosomes	Unchanged	Not tested	Unchanged

4.5.1 Retromer and the WASH complex

Using the RPE1 FlpIn VPS35 cells, I confirmed previous work and demonstrated that the [D620N] mutation exhibits a 60% decrease in association with WASHC1 of the WASH complex (McGough et al., 2014). By immunofluorescence microscopy, WASHC1 and FAM21 were localised to HA-VPS35-positive structures, and the number and size of these WASHC1 or FAM21 puncta was not changed by the

[D620N] mutation, suggesting that the endosomal localisation of WASH is not perturbed by the mutation. This is in agreement with one study (McGough et al., 2014), but not another (Zavodszky et al., 2014). This discrepancy may arise through the different methods of image analysis used in the different studies, where I measured number and size of the FAM21/WASHC1 puncta, Zavodszky and colleagues quantified their signal intensity, and McGough and colleagues calculated the degree of overlap between FAM21 and the expressed VPS35 constructs (McGough et al., 2014; Zavodszky et al., 2014).

Using Airyscan microscopy, I did not observe a change in the overlap between HRS-positive degradative and WASH/VPS35-positive recycling endosomal subdomains upon expression of VPS35[D620N]. This suggests that the [D620N] mutation does not perturb the maintenance of discrete recycling and degradative subdomains at the endosome. To further investigate this, it may be beneficial to artificially enlarge early endosomes to allow for better separation of the subdomains. This can be achieved by through transfection with constitutively active Rab5[Q79L] which causes endosomal swelling and enlargement (Barbieri et al., 1996; MacDonald et al., 2018).

In agreement with previous studies, I found that knockdown of VPS35 had a profound effect on WASH complex localisation to endosomes (Harbour et al., 2012; Jia et al., 2012). The observation by Zavodszky and colleagues that the [D620N] mutation reduced WASH complex association to endosomes was performed with siRNA-mediated silencing of endogenous VPS35 whilst overexpressing the mutant, then measuring the intensity of FAM21 puncta by immunofluorescence microscopy (Zavodszky et al., 2014). The authors also performed membrane fractionation experiments and showed that the membrane association of strumpellin, another component of the WASH complex, was decreased in cells stably VPS35[D620N] compared to cells overexpressing wild type VPS35. Furthermore, they showed that this difference became more pronounced when endogenous VPS35 was simultaneously silenced (Zavodszky et al., 2014). Together this suggests that this effect is due to [D620N] mutation and not simply a failure to rescue a knockdown phenotype. In the RPE1 FlpIn VPS35 system, endogenous VPS35 is still present and so it is possible that a decrease in FAM21 localisation to endosomes would be too subtle to detect by imaging. Future examination of WASH complex distribution through cellular fractionation in the RPE1 FlpIn cells would help shed light on the effect of the [D620N] mutation in my system.

4.5.2 Role of VPS35 in receptor trafficking

In the RPE1 FlpIn system, the [D620N] mutation in VPS35 did not alter the steady-state distribution of the lysosomal hydrolase receptors CIMPR or sortilin, suggesting that the mutation does not perturb their trafficking. The lack of disruption to CIMPR trafficking in this system is in agreement with the work described in some previous studies (Tsika et al., 2014; Zavodszky et al., 2014), but at odds with others (Follett et al., 2014; MacLeod et al., 2013; McGough et al., 2014). Tsika and colleagues also found that there was no alteration to sortilin trafficking in when VPS35 harbouring the [D620N] mutation was overexpressed in primary cortical neurons (Tsika et al., 2014).

That I do not see a difference in CIMPR trafficking due to the [D620N] mutation where other studies have may be reflective of the cell model or type of assay used to assess trafficking. Some previous studies have looked at the effect of the mutation in the context of a simultaneous knockdown of endogenous VPS35, and asked whether the mutant rescued the knockdown phenotype (McGough et al., 2014; Zavodszky et al., 2014). In contrast, endogenous VPS35 is still present in the RPE1 FlpIn model. Looking at the consequences of the [D620N] mutation when wild type endogenous VPS35 is still present is more akin to the situation in the heterozygous PD patient, who will have one wild type and one [D620N] VPS35 allele. Retaining endogenous VPS35 expression also avoids changes that may arise due to compensatory effects resulting from long-term VPS35 depletion or knockout. In studies using patient-derived fibroblasts, CIMPR trafficking was not altered by the [D620N] mutation (Tsika et al., 2014), supporting the argument that our RPE1 FlpIn system is a more physiologically relevant model.

I used fixed cell microscopy to look at the staining pattern of CIMPR and sortilin in cells, but this only provides a snapshot of their distribution and does not provide information on the kinetics of their trafficking. A commonly used method for monitoring the dynamics of receptor trafficking is taking advantage of CD8-receptor chimeras (MacDonald et al., 2014; Seaman, 2007). These comprise the intracellular domains of CIMPR or sortilin linked to an extracellular CD8 domain which can then be surface labelled using anti-CD8 antibodies on ice. The transit of the CD8-chimeras can then be followed by fixing cells at specific time-points after primary antibody labelling.

In addition to not observing any differences in the distribution of CIMPR and sortilin, there was no substantial change in their expression in presence of VPS35[D620N], nor did the mutation affect the levels of the different forms of cathepsin D. Together with the immunofluorescence data, this supports a model where trafficking is not

acutely affected by the [D620N] mutation. In contrast, VPS35[D620N] mice have been shown to have a 1.7-fold increase in CIMPR levels (Kalogeropulou et al., 2020). Knockout of retromer has been shown to lead to upregulation of sortilin, CIMPR and cathepsin D and is attributed to a long term compensatory feedback mechanism aimed at restoring lysosomal function (Evans et al., 2020). It is possible that the increase in CIMPR expression seen in VPS35[D620N] knockin mice also results from longer term dysfunction in the endolysosomal network as a result of the mutation. In the RPE1 FlpIn system, we are only looking at short timescales of VPS35[D620N] expression and so may only see the acute effects of the mutation and not the longer-term consequences.

In the RPE1 cells, siRNA-mediated silencing of VPS35 also did not affect the cellular localisation of CIMPR or sortilin. This supports the proposal that CIMPR is not a true retromer cargo and calls into question whether sortilin is either. Knockdown resulted in a small increase in CIMPR levels, which, as discussed above, may reflect a compensatory mechanism rather than a direct effect on trafficking of the receptor. McGough and colleagues showed dispersal of CIMPR from the Golgi upon VPS35 knockdown in RPE1 cells, whereas I did not (McGough et al., 2014). This disparity may reflect differences in the knockdown protocol, antibodies and fixation methods used or a difference between our RPE1 FlpIn Parental cells and the human RPE1 cells used in their study. Later work from the same group used a ‘knock sideways’ approach in HeLa cells to trap retromer on an unrelated organelle, rendering it non-functional, and found that this led to defects in GLUT1, but not CIMPR, sorting (Evans et al., 2020).

Future studies may benefit from utilising a knock sideways approach to inactivate sorting complexes married with CD8-receptor chimera trafficking assays to better understand the role of different sorting complexes in receptor trafficking. This would allow the kinetics of receptor trafficking to be measured and avoids potential compensatory effects of longer-term sorting complex depletion or deletion. It would be interesting to use this approach to look at the role of retromer in sortilin trafficking, as, in my hands, VPS35 knockdown does not affect its distribution.

4.5.3 Retromer as a regulator of Rab7

I found that knockdown of VPS35 caused a minor decrease in the expression of Rab7 in whole cell lysates. This decrease was seen both in membrane and cytosolic fractions. Using the GST-RILP assay, I did not observe a change in proportion of active Rab7. This contrasts previous work which has shown a more than 3.5-fold

increase in active Rab7 in VPS35 KO HeLa cells (Jimenez-Orgaz et al., 2018). This disparity could mean that a complete loss of VPS35 is needed to observe this phenotype and that the partial depletion achieved by siRNA-mediated silencing is not sufficient. The increase in Rab7 activity following knockout of retromer may also reflect a longer-term compensatory mechanism. It may also be cell line dependent or reflect the lack of sensitivity of the assay in RPE1 cells.

Unlike other studies that reported Rab7 accumulation on late endosomes/lysosomes in retromer knockout cells, I did not observe any change in Rab7 distribution after VPS35 knockdown (Daly et al., 2023; Jimenez-Orgaz et al., 2018). This difference may reflect the substantial co-occurrence of Rab7 and LAMP2 at steady state in RPE1 cells, which would make an increase of this co-localisation harder to detect compared with the cell models used in the studies above where the majority of Rab7 localises with other structures in control cells. For instance, Jimenez-Orgaz and colleagues observe a predominantly mitochondrial localisation of Rab7 at steady state in HeLa cells (Jimenez-Orgaz et al., 2018). Following knockdown of VPS35 in RPE1 cells, there was a trend towards fewer Rab7 puncta. This may reflect a decrease in the number of late endosomes/lysosomes in the cells. With less Rab7, the ability of endosomes to undergo the Rab5 to Rab7 switch, a critical aspect of endosome maturation, may be reduced (Poteryaev et al., 2010). To see if this decrease in Rab7 is due to a decrease in transcription it would be valuable to perform RT-qPCR.

Although expression of VPS35[D620N] had little effect on the distribution and activity of Rab7 in the RPE1 FlpIn system, this may only speak to the acute effects of the [D620N] mutation. It is possible that, like what has been reported in knock out cells, dysfunction in Rab7 localisation and activity may arise over longer time periods. If there were longer term effects on Rab7, it would suggest that these are not due to a change in the function of retromer and TBC1D5 in control of Rab7 activity but may reflect a more general disruption to organelle homeostasis.

4.5.4 LRRK2 and Rab7

Rab7 is not a direct substrate of LRRK2, but in fact, is a substrate of LRRK2's homolog LRRK1. Phosphorylation of Rab7 by LRRK1 occurs at the equivalent switch-II motif site targeted by LRRK2 on Rab8A and Rab10 (Malik et al., 2021). Despite not being a direct substrate, work by the Hilfiker lab has shown that hyperactivating mutations in LRRK2 result in a decrease in active Rab7 (Gómez-Suaga et al., 2014). Given this, one might expect that a reduction in LRRK2 kinase activity, either by knockdown or pharmacological inhibition, would induce the opposite effect, an increase in Rab7

activity. However, in RPE1 cells, I found that knockdown and inhibition of LRRK2 cells did not cause a measurable effect on Rab7 activity. This difference between the effect of gain and loss of LRRK2 function on levels of active Rab7 may reflect the actions of LRRK2 substrate Rabs at steady state, when only 1-2% of Rabs are phosphorylated. As basal Rab phosphorylation is so low, a reduction in LRRK2 activity may have little effect. Whereas gain of function mutations in LRRK2 will increase the proportion of phosphorylated Rabs, influencing their preference for different effectors and therefore perhaps disrupting their normal function. That depletion of the LRRK2 substrate Rab10 caused a mild decrease in Rab7 activity could suggest that it is the 'normal' function of this Rab, in its unphosphorylated form, that influences Rab7, and this is then disrupted by enhanced phosphorylation in the presence of LRRK2 PD mutations. Supporting this, the Hilfiker lab have also shown that knockdown of Rab8a and Rab10 causes a decrease in Rab7 activity (Rivero-Ríos et al., 2020, 2019).

Inhibition of LRRK2 kinase activity in RPE1 cells did not affect the staining pattern of Rab7 by immunofluorescence microscopy. This contrasts with work from a previous PhD student in the lab, Hannah Elcocks, who found that in Melan-a cells, LRRK2 inhibition increased the number of Rab7 puncta by microscopy and caused an increase in Rab7 activity using the GST-RILP assay (manuscript in preparation). In Melan-a cells, knockdown of LRRK2 also increased Rab7 staining by immunofluorescence microscopy. A recent pre-print has shown that LRRK2 suppresses the transcription factor TFE3 and acute inhibition or depletion of LRRK2 leads to an upregulation of lysosomal genes in macrophages and microglia (Yadavalli and Ferguson, 2023). The lack of effect of LRRK2 inhibition on Rab7 in the RPE1 cells may indicate that this function of LRRK2 is cell type specific or depends on LRRK2 expression levels or basal activity status.

5 VPS35, LRRK2 and the mitochondria

5.1 Introduction

Impaired mitochondrial function and dynamics have been extensively linked to neurodegenerative disease, including PD. Mitochondrial dysfunction can arise from a number of alterations, including compromised mitochondrial biogenesis, increased mitochondrial ROS production, electron transport chain dysfunction, disruptions to mitochondrial fission and fusion and impaired mitophagy (Prasuhn et al., 2021). These changes can be both primary, resulting from alterations to the mitochondria themselves, or a secondary consequence of iron homeostasis, Ca^{2+} influx, accumulation of protein aggregates or UPS and lysosome dysfunction (Prasuhn et al., 2021).

Parkinson's disease-causing mutations in both VPS35 and LRRK2 have been widely shown to disrupt mitochondrial bioenergetics and morphology. These changes include increased mitochondrial ROS production, decreased ATP production, reduced mitochondrial membrane potential (MMP) (Hanss et al., 2021; Hsieh et al., 2016; Ma et al., 2021; Mortiboys et al., 2010; Niu et al., 2012, 2021; Tang et al., 2015b; Toyofuku et al., 2020; Wang et al., 2017, 2016, 2012b; Wauters et al., 2019). The different mitochondrial phenotypes reported as a result of the [D620N] mutation and the model in which they were studied are summarised in **Table 5.1**. Introduction of the [D620N] VPS35 mutation is widely reported to induce mitochondrial fragmentation (Hanss et al., 2021; Ma et al., 2021; Niu et al., 2021; Tang et al., 2015b; Wang et al., 2017, 2016). However, overexpression of wild type VPS35 and LRRK2 both cause mitochondrial fragmentation, calling in to question the utility of overexpression models when studying the mitochondrial effects of these mutations (Niu et al., 2012; Wang et al., 2017, 2016, 2012b).

It has been reported that basal mitophagy is unaffected by the [D620N] mutation, whilst depolarisation-induced mitophagy is impaired (Hanss et al., 2021; Ma et al., 2021). However, whether this impairment is due to a defect in initiation of mitophagy or a block in degradation is debated. Ma and colleagues found that heterozygous [D620N] knockin SH-SY5Y cells stably expressing the mitophagy reporter COX8-EGFP-mCherry had fewer mitolysosomes in response to CCCP treatment compared to controls, indicating a failure in initiation of mitophagy (Ma et al., 2021). Conversely, Hanss and colleagues found that the [D620N] mutant caused an increase in the number of mitolysosomes upon CCCP treatment in iPSC-derived neurons expressing

the mitophagy reporter ATP5C1-DsRed-pHluorin (Hanss et al., 2021). Unlike in healthy control cells, the number of mitolysosomes did not fall over time, indicating a failure in clearance.

Likewise, LRRK2 mutations have been shown to impair mitophagy (Bonello et al., 2019; Hsieh et al., 2016; Singh et al., 2021; Tasegian et al., 2021; Wauters et al., 2019). The [G2019S] mutation in LRRK2 has been reported to suppress basal PINK1-independent mitophagy which can be rescued by pharmacological inhibition of LRRK2 (Singh et al., 2021). In the context of depolarisation-induced mitophagy, LRRK2 has been reported to act upstream (Bonello et al., 2019), downstream (Wauters et al., 2019) and in parallel to Parkin (Hsieh et al., 2016). Clearly the exact molecular mechanisms of LRRK2's involvement in mitophagy remain unclear.

Table 5.1 Reported phenotypes for mitochondrial parameters in D620N models.
DA, dopaminergic; iDA, induced dopaminergic

Phenotype	Previously reported	Cell model	Reference
Morphology	Fragmented	Knockin mice	Niu *et al.* (2021)
		Mouse primary DA neurons – expression on top of depletion	Tang *et al.* (2015)
		Patient-derived iDA neurons	Hanss *et al.* (2020)
		Overexpression in rat primary cortical neurons, M17 cells and mice. Patient-derived fibroblasts	Wang *et al.* (2016) Wang *et al.* (2017)
		SH-SY5Y $^{WT/D620N}$	Ma *et al.* (2021)
Mitochondrial membrane potential	Decreased	Patient-derived iDA neurons	Hanss *et al.* (2020)
		Overexpression in rat primary cortical neurons and M17 cells. Patient-derived fibroblasts	Wang *et al.* (2016)
		SH-SY5Y $^{WT/D620N}$	Ma *et al.* (2021)
ROS production	Increased	Patient-derived iDA neurons	Hanss *et al.* (2020)
		Overexpression in rat primary cortical neurons and M17 cells	Wang *et al.* (2016)
ATP levels	Decreased	Patient-derived iDA neurons	Hanss *et al.* (2020)
		Overexpression in M17 cells. Patient-derived fibroblasts	Wang *et al.* (2016)
Respiration	Decreased	Knockin mice	Niu *et al.* (2021)
		Patient-derived iDA neurons	Hanss *et al.* (2020)

		Stable overexpression in M17 cells. Patient-derived fibroblasts	Wang *et al.* (2017)
Basal mitophagy	Unaffected	Patient-derived iDA neurons	Hanss *et al.* (2020)
Depolarisation-induced mitophagy	Impaired	Patient-derived iDA neurons	Hanss *et al.* (2020)
		SH-SY5Y $^{WT/D620N}$	Ma *et al.* (2021)

The similarities in mitochondrial phenotypes reported in LRRK2 and VPS35 mutant models strengthens the notion that mitochondrial dysfunction is important to Parkinson's disease pathogenesis. It also begs the question as to whether the observed impairments are caused by dysfunction to the same pathway. In this chapter, I describe the benchmarking of the RPE1 FlpIn VPS35 WT and [D620N] cells against mitochondrial phenotypes that have previously been reported, with the final aim being to investigate whether these occur in a pathway involving LRRK2.

5.2 VPS35 and mitochondrial dynamics

5.2.1 VPS35[D620N] does not alter total levels of proteins involved in mitochondrial fission and fusion

The [D620N] mutation in VPS35 has been widely reported to cause mitochondrial fragmentation (Hanss et al., 2021; Ma et al., 2021; Niu et al., 2021; Tang et al., 2015b; Wang et al., 2017, 2016). However, there have been contrasting reports as to whether this is due to a decrease in fusion (Tang et al., 2015b), increased fission (Niu et al., 2021; Wang et al., 2017, 2016), or as a secondary consequence of other cellular dysfunction (Hanss et al., 2021). The consequence of VPS35 loss on mitochondrial morphology is also not conclusive, with elongation and fragmentation of the mitochondrial network both reported in the literature (Tang et al., 2015b; Wang et al., 2016).

Given these conflicting findings on the effect of the [D620N] mutation, I sought to investigate this in the RPE1 FlpIn system. First, I induced HA-VPS35 WT or [D620N] expression for 48 hours and performed western blotting against proteins involved in mitochondrial fission (OPA1, FIS1) and fusion (MFN2) and the E3 ligase MUL1 (Tang et al., 2015b). Induction of wild-type or mutant VPS35 expression had no significant effect on the total expression of any of these proteins (**Figure 5.1**).

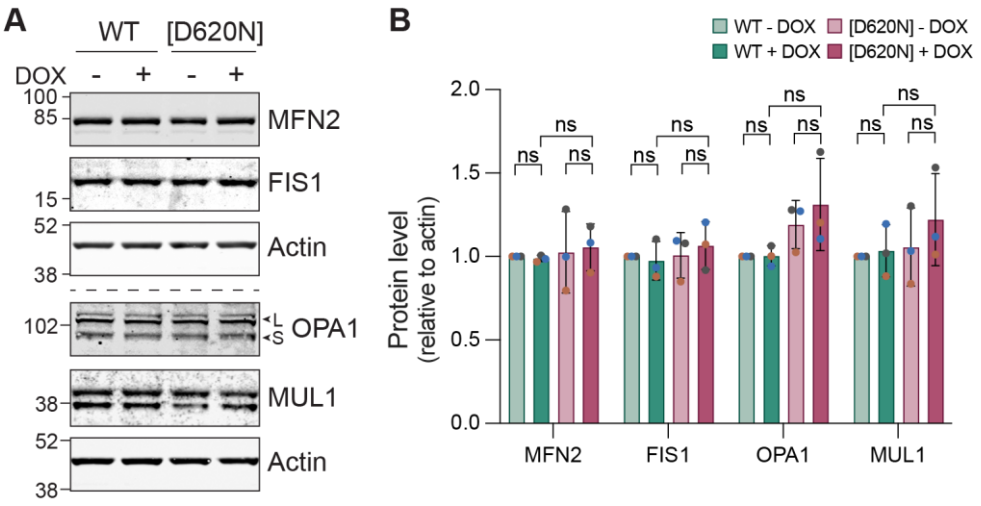

Figure 5.1 Mitochondrial fission/fusion proteins are not changed upon expression of VPS35[D620N]

A RPE1 FlpIn HA-VPS35 WT 3B4 and [D620N] 1F3 were incubated for 24 hours with 0.1 µg/ml doxycycline to induce HA-VPS35 expression. After 24 hours, media containing doxycycline was replaced with fresh media and left for a further 24 hours. Cells were then lysed in NP40 buffer. Lysates were immunoblotted against mitochondrial fission/fusion proteins, a representative blot is shown. Samples analysed are the same as in Figure 5.2 and Figure 5.6. **B** Quantification of A relative to actin and normalised to WT-DOX. *n* = 3. Each independent experiment is colour-coded. Bars represent mean ± SD. One-way ANOVA with Tukey's multiple comparisons test. ns, not significant.

5.2.2 VPS35[D620N] does not alter mitochondrial mass

As the VPS35 [D620N] mutation has been reported to cause mitochondrial fragmentation and impaired mitophagy, this may affect turnover of mitochondria, and by extension alter mitochondrial mass. To investigate whether mitochondrial mass was affected by the [D620N] mutation, I used immunoblotting to assess the levels of several mitochondrial proteins: the outer mitochondrial membrane proteins TOM20, TOM40 and VDAC1 (voltage-dependent anion channel 1), and the mitochondrial matrix protein HSP60 (heat shock protein 60). After 48 hours of HA-VPS35 expression, the levels of these mitochondrial proteins remained unchanged in VPS35 wild type- and [D620N]-expressing cells (**Figure 5.2**). This suggests that mitochondrial mass is not affected by the VPS35 [D620N] mutation in this cell model.

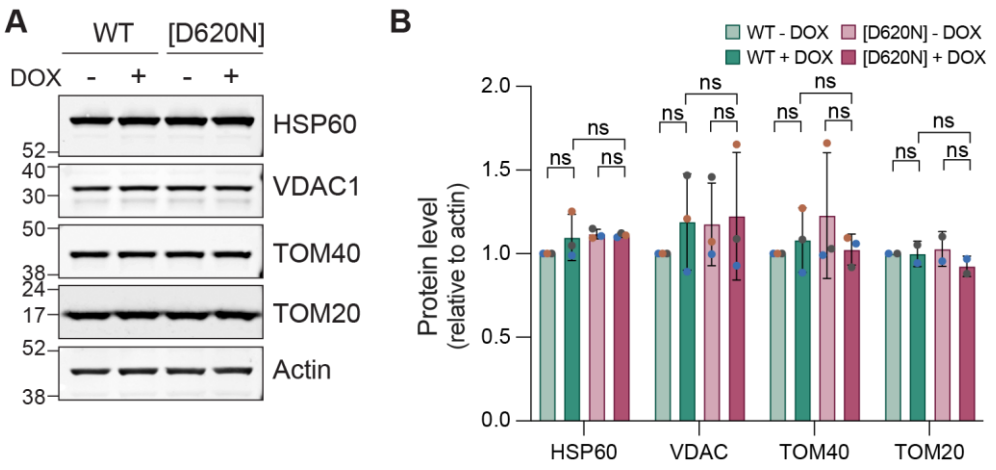

Figure 5.2 Mitochondrial mass markers are not changed upon expression of VPS35[D620N]
A RPE1 FlpIn HA-VPS35 WT 3B4 and [D620N] 1F3 were incubated for 24 hours with 0.1 µg/ml doxycycline to induce HA-VPS35 expression. After 24 hours, media containing doxycycline was replaced with fresh media and left for a further 24 hours. Cells were then lysed in NP40 buffer. Lysates were immunoblotted against mitochondrial proteins. A representative western blot is shown. Samples analysed are the same as in Figure 5.1 and Figure 5.6. **B** Quantification of A relative to actin and normalised WT-DOX. *n* = 2-3. Each independent experiment is colour-coded. Bars represent mean ± SD. One-way ANOVA with Tukey's multiple comparisons test. ns, not significant.

5.2.3 VPS35[D620N] does not alter mitochondrial network morphology

Several of the existing studies investigating the [D620N] mutation and mitochondrial morphology in immortalised cell lines and rodent models have relied upon overexpression (Niu et al., 2021; Tang et al., 2015b; Wang et al., 2017, 2016). These studies have found the mitochondrial network more fragmented when VPS35 [D620N] is expressed. However, the significance of these findings is complicated by the fact that overexpression of wild-type VPS35 also results in mitochondrial network disruption, albeit less severe than with the [D620N] mutant (Wang et al., 2017, 2016). The level of overexpression is only two-fold in the RPE1 FlpIn system, thus avoiding artefacts caused by a large excess of VPS35 and allowing differences caused by the [D620N] mutation to be observed. To assess this, RPE1 cells induced for WT and [D620N] VPS35 expression were fixed and stained for the outer mitochondrial membrane protein TOM20 (**Figure 5.3A**). I then measured the area of the cell occupied by mitochondria and the length and number of mitochondrial branches using the Mitochondrial Network Analysis (MiNA) Fiji plug-in (**Figure 5.3B-D**). I found no significant differences in these parameters comparing WT and [D620N] VPS35-expressing cells.

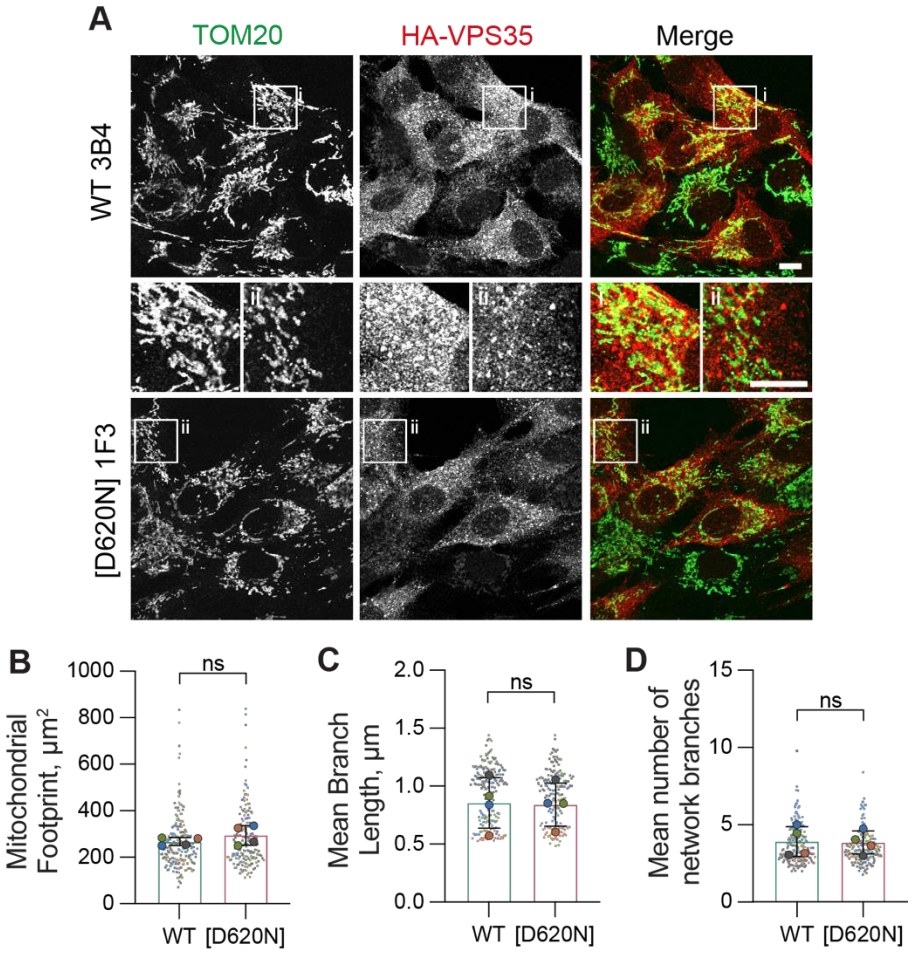

Figure 5.3 Mitochondrial morphology is not changed upon expression of VPS35[D620N]
A RPE1 FlpIn VPS35 WT 3B4 and [D620N] 1F3 cells were treated with 0.1 µg/ml doxycycline to induce HA-VPS35 expression. After 24 hours cells were mixed with RPE1 FlpIn Parental cells (green only in the merge) and replated onto coverslips. Cells were fixed 48 hours after replating and stained for the indicated antibodies. Single slice images were acquired on a Zeiss LSM800 confocal microscope using a 63x objective. Scale bar 10 µm. **B - D** Mitochondrial network analysis was performed using Fiji MiNA plug-in to calculate mitochondrial footprint (area of cell occupied by mitochondria) (B), mean length of network branches (C) and mean number of network branches (D). 26-88 cells analysed per condition per experiment, *n* = 3. Each independent experiment is colour-coded. Transparent circles with no outline represent values for each cell in an experiment, opaque circles with black outlines correspond to mean values for each experiment. Error bars represent mean ± SD. Paired t-test of mean values. ns, not significant.

One observation I made was the occurrence of small punctate TOM20-positive structures. I hypothesised that these could be small, fragmented mitochondria, mitochondrial derived vesicles or mitolysosomes. To determine the identity of these puncta, I fixed and stained cells with TOM20 and co-stained with either the inner mitochondrial membrane protein Translocase of Inner Mitochondrial Membrane 44 (TIMM44), the mitochondrial matrix protein HSP60 or the autophagy marker LC3

(**Figure 5.4**). A subset of TOM20 puncta co-localised with TIMM44, however none were found to co-localise with HSP60 (**Figure 5.4A**), suggesting these structures may only contain mitochondrial membrane content. Some larger TOM20 puncta co-localised with LC3, suggesting they were mitophagosomes or mitolysosomes (**Figure 5.4B**). Simultaneous staining for TOM20, TIMM44 and LC3 would be required to determine whether TIMM44 is also present in these TOM20+ and LC3+ structures.

I was unable to robustly quantify these structures as they could not be distinguished from the mitochondrial network by thresholding. However, they appeared at a similar frequency in both WT and [D620N] cells, both with and without doxycycline addition, suggesting they were not directly linked to VPS35 expression.

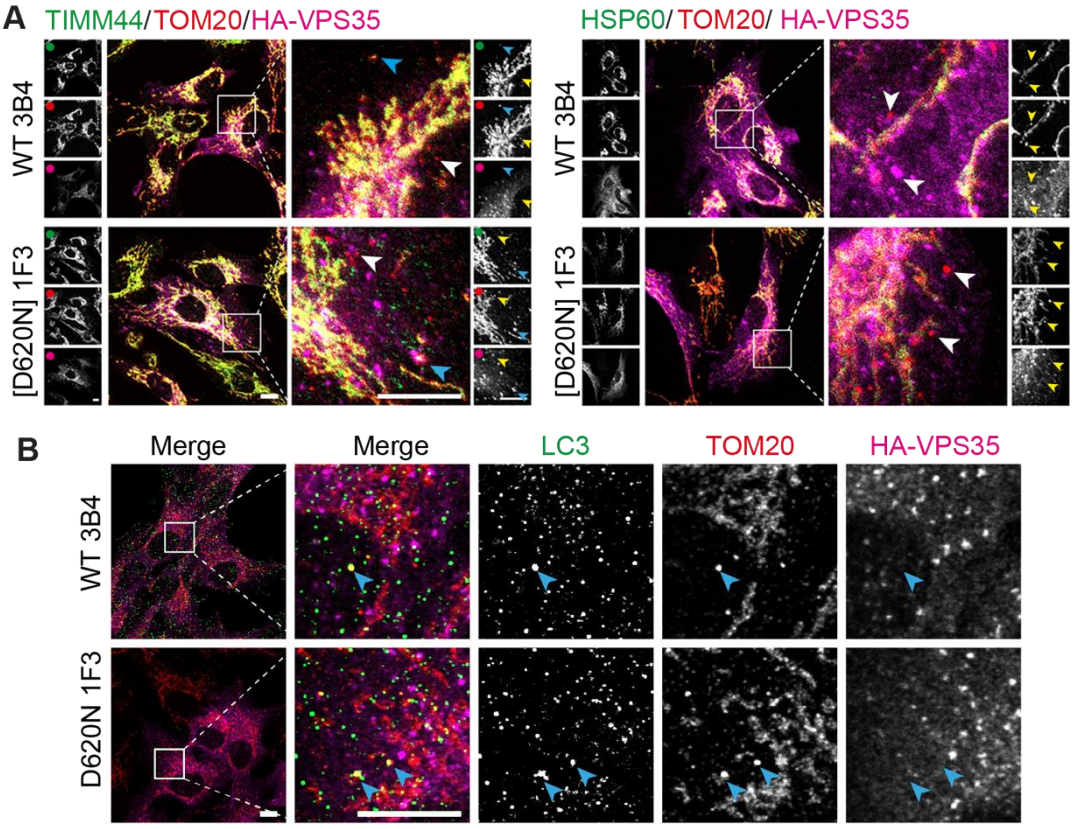

Figure 5.4 Determining the identity of TOM20 puncta

A RPE1 FlpIn VPS35 WT 3B4 and [D620N] 1F3 cells were treated with 0.1 µg/ml doxycycline to induce HA-VPS35 expression. After 24 hours cells were mixed with RPE1 FlpIn Parental cells (not shown) and replated onto coverslips. Cells were fixed 48 hours after replating and stained for the indicated antibodies. Single slice images were acquired on a Zeiss LSM800 confocal microscope using a 63x objective. Scale bar 10 µm. Blue arrowheads indicate puncta with co-localisation, white and yellow arrowheads indicate puncta that are only positive for TOM20. Data from a single experiment, *n* = 1. **B** RPE1 FlpIn VPS35 WT 3B4 and [D620N] 1F3 cells were treated with 0.1 µg/ml doxycycline to induce HA-VPS35 expression. After 24 hours cells were mixed with RPE1 FlpIn

Parental cells (not shown) and replated onto coverslips. Cells were fixed 48 hours after replating and stained for the indicated antibodies. Single slice images were acquired on a Zeiss LSM800 confocal microscope at 63x objective. Scale bar 10 µm. Blue arrowheads indicate puncta with TOM20 and LC3 co-localisation. Data from a single experiment, *n* = 1.

5.2.4 VPS35[D620N] does not impair mitophagy induction

Two recent studies have shown that depolarisation-induced mitophagy is impaired in the presence of the VPS35[D620N] mutation but disagreed about the cause of this dysfunction. Hanss and colleagues showed a deficit in clearance of mitophagosomes after CCCP treatment in patient-derived induced dopaminergic neurons, and attributed this to a more general defect in autophagy (Hanss et al., 2021). Conversely, Ma and colleagues reported impaired mitophagy in response to CCCP treatment in VPS35[D620N] heterozygous knockin SH-SY5Y cells, resulting in a decrease in the number mitolysosomes after 24 hours (Ma et al., 2021). The authors suggested that this is due to a defect in the initiation of mitophagy as the recruitment of PINK1 and Parkin to mitochondria following CCCP treatment was also impaired (Ma et al., 2021). These results point towards an effect of the VPS35 [D620N] mutation on mitophagy, but the exact mechanism by which this is altered is not clear. Therefore, I sought to test the effect of the [D620N] mutation on mitophagy in my cell system.

I first tested a small panel of agents which have been shown to induce mitophagy by different mechanisms and looked at their effect on read-outs of mitochondrial depolarisation (cleavage of OPA1 and stabilisation of PINK1) and mitophagy induction (LC3-II formation) (**Figure 5.5**). CCCP is a protonophore which causes a loss of the mitochondrial membrane potential which triggers PINK1 stabilisation at the mitochondrial membrane and subsequent PINK1/Parkin dependent mitophagy (Matsuda et al., 2010; Narendra et al., 2008, 2010). Antimycin A and oligomycin A are inhibitors of complex III and the F_1F_0-ATPase of the respiratory chain, respectively. Using these compounds as an inhibitor cocktail causes mitochondrial depolarisation and induces PINK1-dependent mitophagy (Allen et al., 2013).

MLN4924 inhibits neddylation by the Nedd8-E1 conjugating enzyme, a process required for activation of Cullin-RING E3 ligases (Brownell et al., 2010). Our lab in conjunction with another have recently shown that MLN4924 potently induces mitophagy through up-regulation of the mitophagy adaptors BNIP3 and NIX (Elcocks et al., 2023a; Nguyen-Dien et al., 2023). MLN4924 inhibits the action of two Cullin-RING E3 ligases which act as negative regulators of BNIP3 and NIX expression: VHL,

which suppresses HIF1α-dependent transcription of BNIP3 and NIX, and FBXL4, which promotes their proteasomal degradation (Elcocks et al., 2023b).

As expected, treatment with an Antimycin A and oligomycin A (AO) cocktail and with CCCP resulted in mitochondrial depolarisation, as evidenced by the accumulation of cleaved OPA1 (S-OPA1) and PINK1 after 4 hours of treatment. After 24 hours, the levels of PINK1 continued to increase, whereas OPA-1 levels decreased despite not regaining more full-length OPA1. Conversely, MLN4924 did not induce cleavage of OPA1 or robust PINK1 stabilisation, in agreement with the hypothesis that MLN4924 induces mitophagy independently of acute depolarisation (Elcocks et al., 2023b). All compounds caused a detectable increase in LC3-II formation, indicating an initiation of mitophagy (or autophagy generally), but this was much more pronounced upon CCCP treatment.

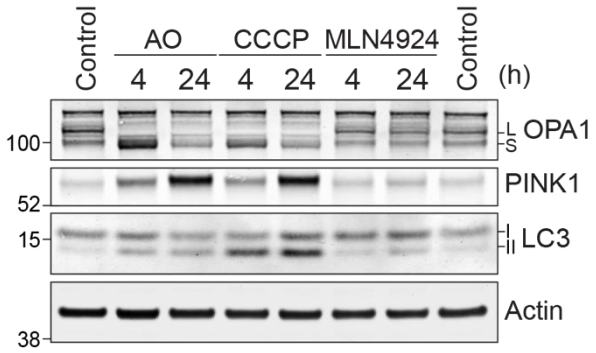

Figure 5.5 Evaluation of mitophagy inducers in RPE1 parental cells

A RPE1 FlpIn Parental cells were treated with 1μM Antimycin A and 1μM Oligomycin A cocktail, 10μM CCCP or 1μM MLN4924 for 4 and 24 hours, or vehicle (DMSO, 24 hours).Cells were then lysed in NP40 buffer. Lysates were immunoblotted against markers of mitochondrial depolarisation and autophagy. Data from a single experiment, *n* = 1.

To investigate whether the VPS35[D620N] mutation caused a defect in the initiation of mitophagy in RPE1 FlpIn VPS35 cells, I looked at the effect of expression of wild-type or mutant HA-VPS35 on OPA1 cleavage (increase in OPA-S form), PINK1 stabilisation and phospho-ubiquitin accumulation after 4 and 24 hours of CCCP and AO treatment (**Figure 5.6**). In all treatment conditions I observed an increase in OPA1-S, phospho-ubiquitin and PINK1, indicative of depolarisation and mitophagy induction. However, these changes did not differ in the presence of VPS35[D620N], suggesting that in this system induction of depolarisation-induced mitophagy is not impaired.

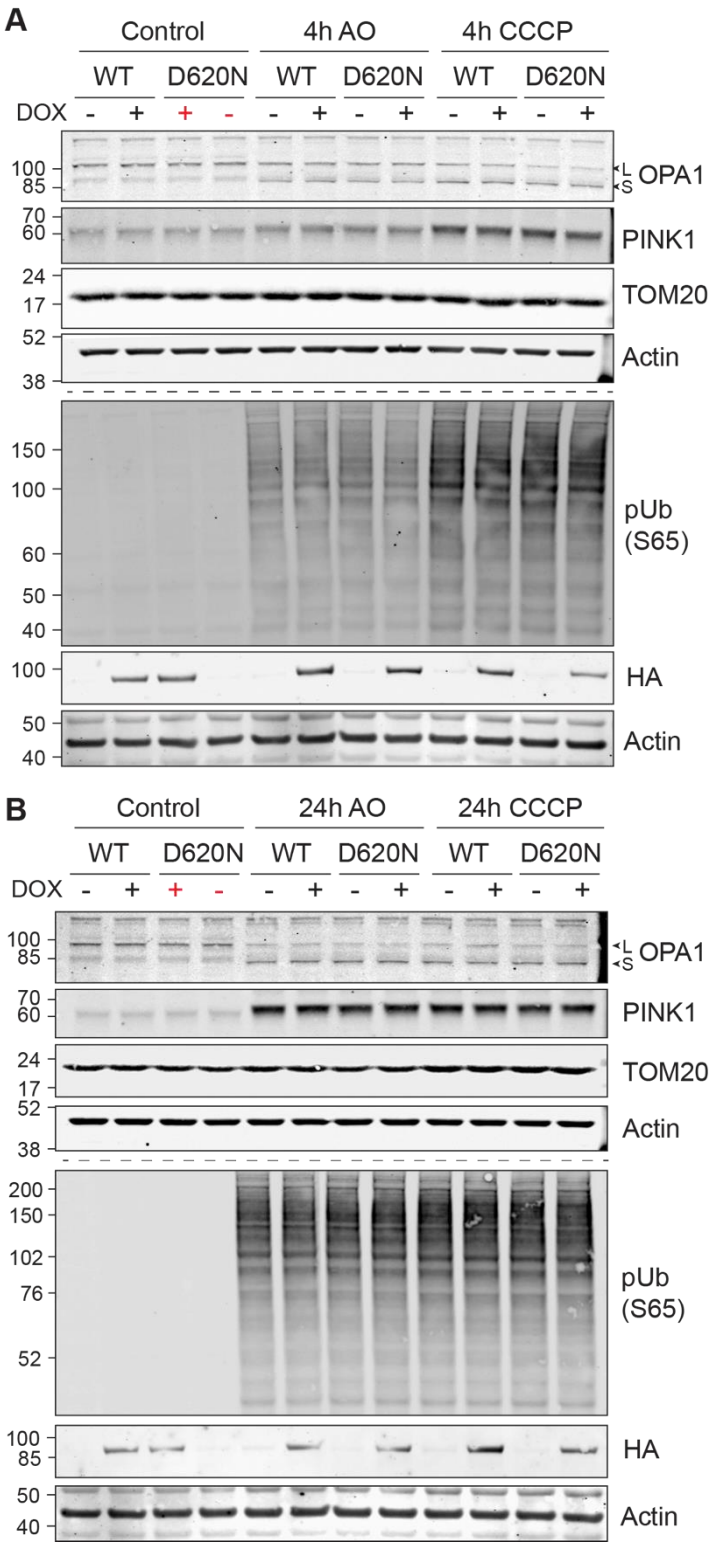

Figure 5.6 The [D620N] mutation does not affect induction of mitophagy in RPE1 cells

A - **B** RPE1 FlpIn VPS35 WT 3B4 and [D620N] 1F3 cells were treated with 0.1 µg/ml doxycycline to induce HA-VPS35 expression. Cells were then treated with 1µM Antimycin A and 1µM Oligomycin A cocktail, 10µM CCCP for 4 (A) or 24 hours (B), or with vehicle (DMSO, 24h) and lysed in NP40 buffer and analysed by immunoblotting. Representative blots from 2 (A) and 5 (B) experiments. Vehicle control samples analysed are the same as in Figure 5.1 and Figure 5.2.

5.2.5 VPS35[D620N] does not alter resting mitochondrial membrane potential

The mitochondrial membrane potential (MMP) drives ATP synthesis by complex V of the respiratory chain and is crucial for normal cell functioning (Zorova et al., 2018). Transient changes to MMP in response to physiological processes are considered normal for mitochondrial homeostasis. Furthermore, mitochondrial depolarisation acts as an important signal to initiate clearance of damaged mitochondria by PINK1-parkin-dependent mitophagy (Kondapalli et al., 2012).

However, sustained perturbation of the MMP may have pathologic consequences (Zorova et al., 2018). An increasing body of evidence suggests a reduction in MMP may be a common pathological mechanism in PD and has so far been linked to mutations in PINK1 (Abramov et al., 2011; Wang et al., 2011), Parkin (Mortiboys et al., 2008; Zilocchi et al., 2020), VPS35 (Hanss et al., 2021; Ma et al., 2021; Wang et al., 2016) and LRRK2 (Mortiboys et al., 2010).

To see whether mitochondrial membrane potential was affected by VPS35 [D620N] in the RPE FlpIn system model, I performed live cell imaging using the fluorescent rhodamine dye TMRE which is sequestered in fully polarised mitochondria (**Figure 5.7**). As a read-out of membrane potential, I measured TMRE intensity by calculating the 'corrected total cell fluorescence' in Fiji (described in **Section 2.4.6.1**). The fluorescence intensity between the two repeats I carried out for this experiment differed greatly and thus it was not possible to plot these together without normalisation (**Figure 5.7B**). Experiment number one (#1) showed little difference in TMRE intensity between the different conditions, whereas experiment two (#2) revealed an increase in TMRE fluorescence only when VPS35[D620N] was expressed. When normalised to the average CTCF in the uninduced WT 3B4 condition, there was a small increase in the mitochondrial membrane potential in the VPS35[D620N] expressing cells (**Figure 5.7C**).

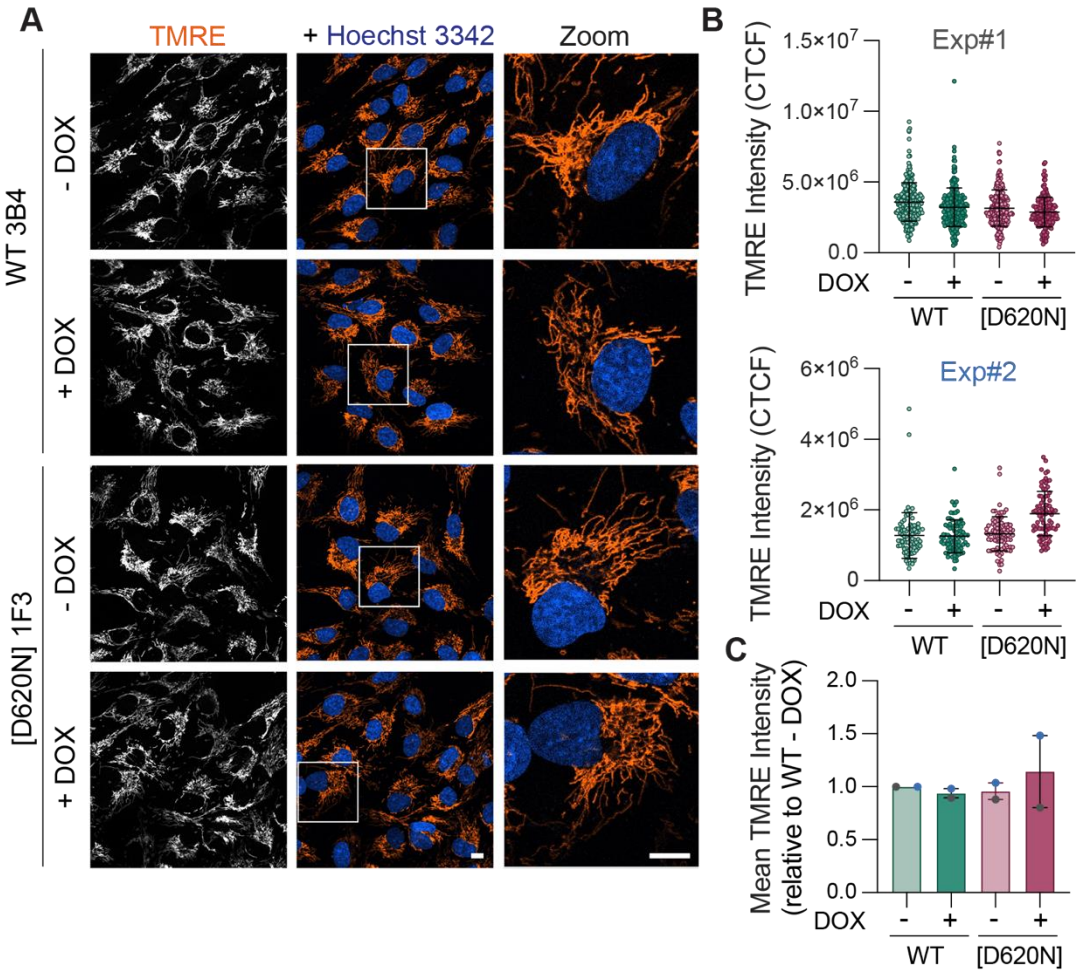

Figure 5.7 Mitochondrial membrane potential is unchanged upon expression of VPS35[D620N] **A** RPE1 FlpIn HA-VPS35 WT 3B4 and [D620N] 1F3 were incubated for 24 hours with 0.1 µg/ml doxycycline to induce HA-VPS35 expression and then stained with 50 µM TMRE and 0.5 µg/ml Hoechst 33342 for 30 minutes before being analysed by live-cell imaging using a 40x objective on an LSM900 confocal microscope. **B** Individual cell values of corrected total cell fluorescence (CTCF) of TMRE staining from two independent experiments. Bars represent mean ± SD. **C** Mean values from quantification in B normalised to WT - DOX. *n* = 2. Each independent experiment is colour-coded. Bars represent mean and range.

5.2.6 Rab7 does not localise to mitochondria in RPE1 cells

A pool of Rab7 localised to the mitochondrial network at steady state has been shown to become redistributed to lysosomes upon deletion of VPS35 in HeLa cells (Jimenez-Orgaz et al., 2018). I set out to investigate the effect of the [D620N] mutation on Rab7 distribution. To do so I analysed Rab7 distribution by immunofluorescence microscopy using both the 'mixed' and 'single' clones and looking after 24 and 72 hours of induction of HA-VPS35 expression. I hypothesised that for some phenotypes such as trafficking and localisation it may take more time for defects to become

pronounced and so these may only be revealed after longer expression of mutant VPS35. As established in **Section 3.3.5** (**Figure 3.12**), HA-VPS35 remains stable over this time. In the representative experiment shown in **Figure 5.8**, RPE1 FlpIn WT and [D620N] cells were mixed at a 2:1 ratio with RPE1 FlpIn Parental cells and induced with doxycycline for 24 hours, which was then chased out for 48 hours. Cells were fixed and stained for Rab7, TOM20 and HA. I did not observe a pool of Rab7 that co-localised with TOM20 in the RPE1 FlpIn Parental cells, nor in cells expressing wild type or mutant VPS35. Rab7 maintained a vesicular staining pattern in all the conditions.

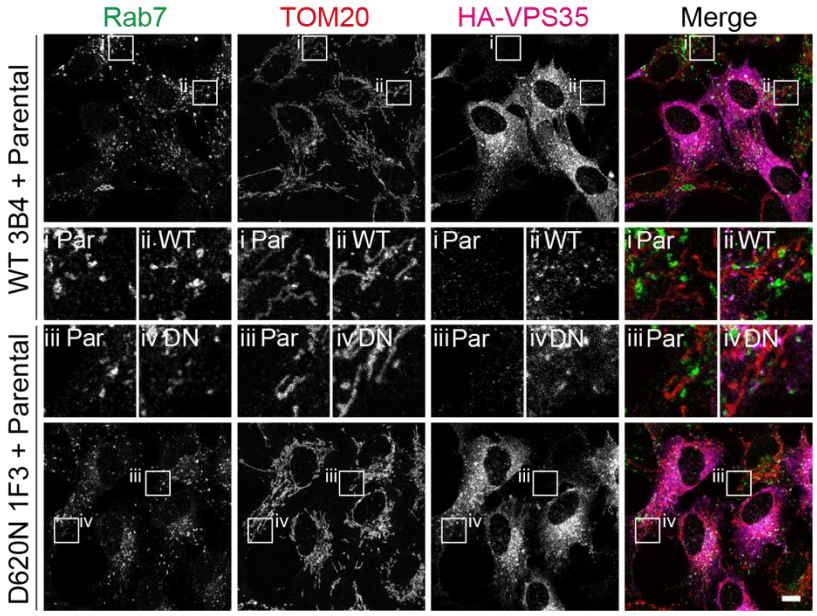

Figure 5.8 Rab7 does not localise to mitochondria in RPE1 FlpIn HA-VPS35 cells
A RPE1 FlpIn VPS35 WT 3B4 and [D620N] 1F3 (DN) cells were treated with 0.1 µg/ml doxycycline to induce HA-VPS35 expression. After 24 hours cells were mixed with RPE1 FlpIn Parental cells and replated onto coverslips. Cells were fixed 48 hours after replating and stained for the indicated antibodies. Single slice images were acquired on a Zeiss LSM800 confocal microscope using a 63x objective. Scale bar 10 µm. Representative images shown from one of two independent experiments, *n* = 2.

5.3 LRRK2 and mitochondrial dynamics

5.3.1 LRRK2 inhibition does not alter mitochondrial morphology

Like VPS35, PD-causing mutations in LRRK2 have been reported to alter mitochondrial morphology (Hsieh et al., 2016; Mortiboys et al., 2010; Niu et al., 2012; Papkovskaia et al., 2012; Su et al., 2015; Wang et al., 2012b). I set out to see if acute pharmacological perturbation of LRRK2 activity altered the distribution of mitochondrial networks in RPE1 cells. Cells were treated for one, four and 24 hours with 200 nM MLi-2 before fixation and staining for the mitochondrial marker TOM20 (**Figure 5.9A**). Analysis of mitochondrial networks was performed using the MiNA plugin, as described previously (**Section 5.2.2**), to assess mitochondrial branch length and number and area occupied by mitochondria (mitochondrial footprint) (**Figure 5.9B-D**). I also included two control treatments in this experiment which perturb mitochondrial morphology: AO, which causes fragmentation of mitochondria, and MLN4924, which previous colleagues in the lab, Dr Elena Marcassa and Dr Jane Jardine, have found causes an elongated mitochondrial network. Pharmacological activity of these compounds was confirmed biochemically using immunoblotting; treatment with AO caused accumulation of phospho-ubiquitin, MLN4924 treatment resulted in a loss of neddylated Cullin 2 indicating Nedd8-activating enzyme inhibition (**Figure 5.9E**).

Treatment with MLi-2 caused no visible differences in mitochondrial morphology, although quantification suggested a trend towards a more branched network at longer time points of MLi-2 treatment. However, this was small and the spread of data within each condition (excluding AO condition) was large. This variation is likely due to the heterogeneity in size and appearance of RPE1 cells, which affects whether the mitochondrial network is clustered at the perinuclear area or projects across the cell.

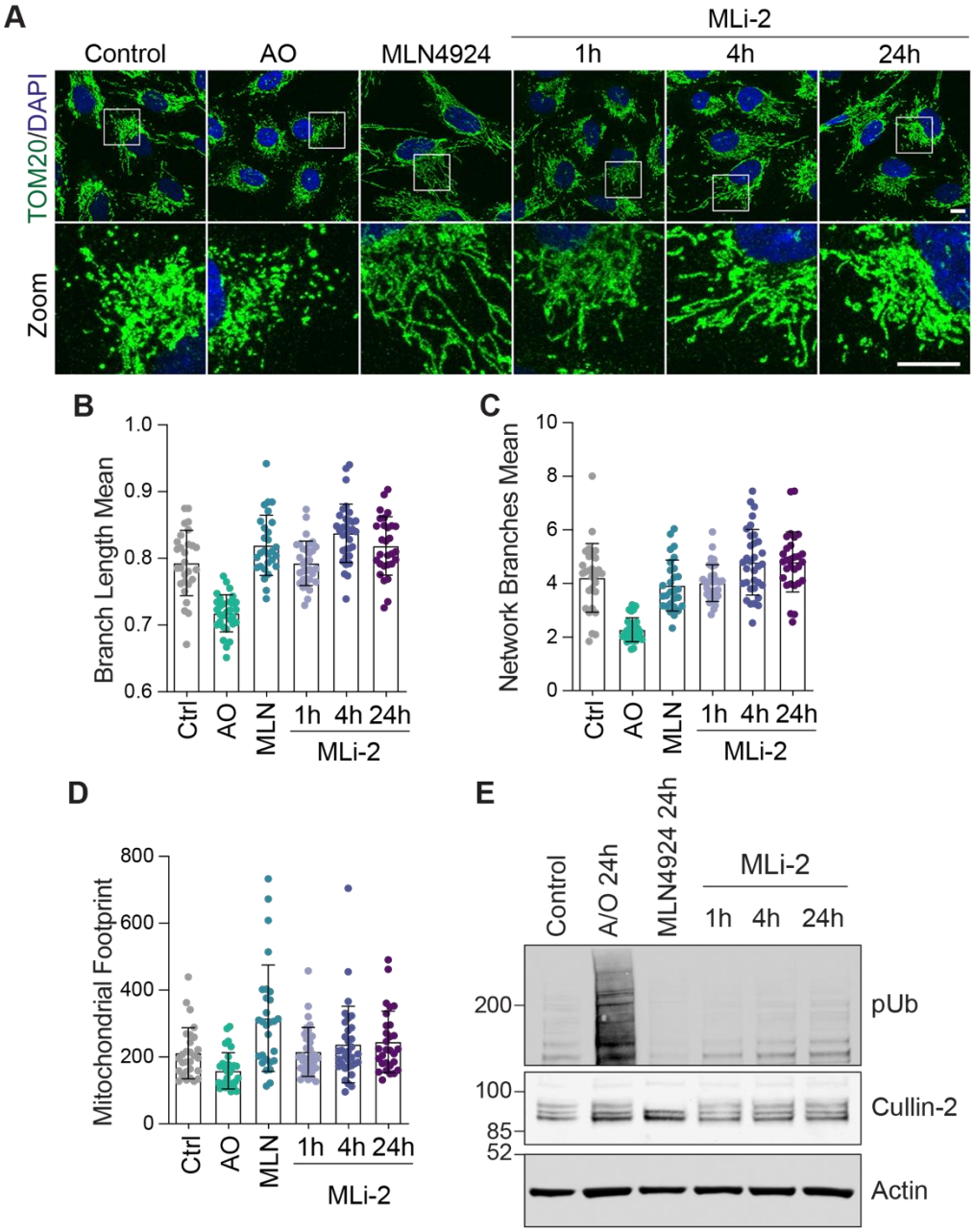

Figure 5.9 Assessment of mitochondrial morphology upon pharmacological LRRK2 inhibition
A RPE1 FlpIn parental cells were treated with DMSO (24 hours), Antimycin A / Oligomycin A cocktail (1 µM/1 µM, 24 hours), MLN4924 (1 µM, 24 hours) and MLi-2 (200 nM, 1, 4, and 24 hours). Cells were then fixed and stained for TOM20 and imaged on an LSM800 confocal microscope using a 63x objective. Scale bar represents 10µm. Mitochondrial network analysis was performed using Fiji MiNA plug-in. **B** mean length of network branches, **C** mean number of network branches and **D** Mitochondrial footprint (area of cell occupied by mitochondria). Data from a single experiment, 31-35 cells analysed per condition, *n* = 1. Error bars represent mean ± SD. **E** Western blot confirming pharmacological activity of compounds used. Cells were treated in the same manner as in A, lysed in RIPA buffer and analysed by immunoblotting. Representative western blot from one of two independent experiments, *n* = 2.

5.3.2 LRRK2 inhibition does not alter basal mitophagy in RPE1 cells

To explore whether LRRK2 plays a role in basal mitophagy, I used RPE1 cells stably expressing using the fluorescent reporter mitokeima. mKeima is a fluorescent protein which undergoes a pH-dependent shift in excitation wavelength and is resistant to lysosomal proteases (Sun et al., 2017). Tagging mKeima with a mitochondrial targeting sequence leads to its localisation to the matrix of mitochondria. At healthy mitochondria, mitokeima will be in a pH 8 environment and so will be optimally excited at 440nm and emit fluorescence at 620 nm. When damaged mitochondria fuse with lysosomes through the process of mitophagy, the mitokeima reporter will then be in the acidic lysosomal environment at pH 4.5 and so its peak excitation wavelength shifts to 586 nm. By evaluating the ratio of pH 8 to pH 4.5 fluorescence it is possible to identify mitolysosomes and thus measure mitophagy (Sun et al., 2017).

RPE1 mitokeima cells were treated with increasing concentrations of MLi-2 to inhibit LRRK2 activity for 24 hours and imaged live (**Figure 5.10A**). Using the semi-automated 'mito-QC' counter plug-in described in Montava-Garriga *et al*. (2020), the number and average area of mitolysosomes per cell was quantified. I found LRRK2 inhibition did not affect the average number or size of mitolysosomes in RPE1 cells (**Figure 5.10B and C**). There appeared to be a decrease in the number of cells with very high levels of mitophagy (>100 mitolysosomes per cell) following Mli-2 treatment when compared to control cells (**Figure 5.10B**).

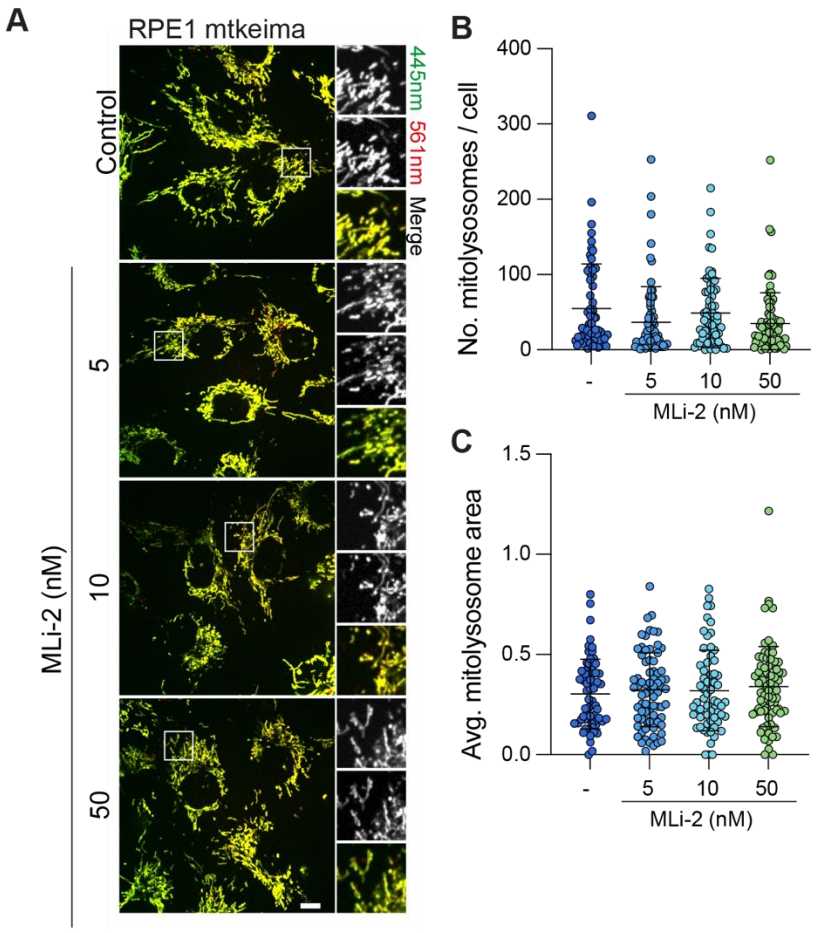

Figure 5.10 LRRK2 inhibition does not affect basal mitophagy in RPE1 cells

A RPE1-mitokeima cells were treated with Mli-2 at the concentrations indicated or vehicle (DMSO) for 24 hours before imaging on a 3i spinning disk confocal microscope using a 63x objective. Scale bar 10µm. **B** – **C** Quantification of the data was performed using the mito-QC counter Fiji plug-in to calculate number of mitolysosomes per cell (B) and average are of mitolysosomes per cell (C). Data are from a single experiment with 61-75 cells analysed per condition, *n* = 1. Bars represent mean ± SD.

5.4 Discussion

Multiple studies have reported mitochondrial phenotypes when studying PD-linked mutations in VPS35 and LRRK2, including impaired mitochondrial bioenergetics and defective mitophagy. Using the isogenic RPE1 FlpIn VPS35 cells, in this chapter I set out to explore whether mitochondrial function was disrupted by the [D620N] mutation in this model and if so, whether this was LRRK2 dependent. My findings, compared with those previously reported in the literature, are summarised in **Table 5.2**. As I observed no mitochondrial phenotypes as a result of VPS35 [D620N] expression in RPE1 cells, I was unable to test the effect of LRRK2 inhibition in this context.

Table 5.2 Comparison between VPS35 [D620N] mitochondrial phenotypes in RPE1 FlpIn VPS35 and previously reported models.

Phenotype	Previously reported	RPE1 FlpIn VPS35 cell model
Morphology	Fragmented	Unchanged
Mitochondrial membrane potential	Decreased	Unchanged
ROS production	Increased	Not tested
ATP levels	Decreased	Not tested
Respiration	Decreased	Not tested
Basal mitophagy	Unchanged	Not tested
Depolarisation-induced mitophagy	Impaired	Initiation not affected

5.4.1 VPS35, LRRK2 and the fission/fusion balance

I did not observe any disruption to morphology caused by the [D620N] mutation. This contrasts with multiple previous studies which have shown VPS35[D620N] to cause mitochondrial fragmentation (Hanss et al., 2021; Ma et al., 2021; Niu et al., 2021; Tang et al., 2015b; Wang et al., 2017, 2016). Several of these studies used overexpression of VPS35 to study the effects of this mutation and one group noted that overexpression of wild-type VPS35 also induced mitochondrial fragmentation, albeit to a lesser extent, which calls in to question the physiological relevance of this finding and the utility of overexpression models to measure mitochondrial phenotypes (Wang et al., 2017, 2016). That being said, the [D620N] mutation has been shown to cause mitochondrial fragmentation in more physiologically relevant models, including PD patient-derived VPS35[D620N fibroblasts and induced neurons, and a heterozygous [D620N] knockin SH-SY5Y cell model (Hanss et al., 2021; Ma et al.,

2021; Wang et al., 2017, 2016). It is worth noting that Ma and colleagues reported that they were only able to visualise the increased fragmentation of mitochondria using electron microscopy and not by confocal microscopy (Ma et al., 2021).

By western blotting, I found no differences in the total levels of proteins involved in mitochondrial fission (OPA1, FIS1) and fusion (MFN2, MUL1). This finding is in agreement with a previous study that found no change in the expression of DRP1, MFN2, OPA1 and MFF in ventral midbrain and striatum extracts between homozygous[D620N] knockin mice and wild type controls (Niu et al., 2021). Despite overall protein abundance of DLP1 not changing in this study, the authors found that expression of the [D620N] mutation decreased the amount of monomeric DRP1 in mitochondrial fractions. This supports previous work which found that overexpression of VPS35[D620N] promoted the removal of inactive DRP1 oligomers via MDVs, leading to more active monomeric DRP1 at mitochondria, thus promoting mitochondrial fragmentation (Wang et al., 2016). In contrast to my results, SH-SY5Y cells overexpressing [D620N], but not wild type, VPS35 have been shown to have increased MUL1 and decreased MFN2 expression (Tang et al., 2015b). This was attributed to impaired removal of MUL1 from mitochondria via MDVs, leading to increased ubiquitylation and subsequent degradation of the fusion protein MFN2, and in turn, decreasing mitochondrial fusion. The authors assessed levels of MUL1 and MFN2 in mitochondrial fractions rather than whole cell lysates which may explain the difference to my results (Tang et al., 2015b). It is not clear at what level VPS35 was overexpressed in these experiments, therefore it is possible that these effects could be an artefact due to gross overexpression of VPS35. Despite these studies all concluding that the [D620N] mutation causes mitochondrial fragmentation by perturbing MDV-dependent turnover of mitochondrial proteins, these studies contrast in whether turnover is enhanced (DRP1) or impaired (MUL1).

The influence of LRRK2 and its PD-causing mutations on mitochondrial morphology is more contentious. Like with VPS35, overexpression of wild-type and PD-mutant ([G2019S] and [R1441C]) LRRK2 causes mitochondrial fragmentation in SH-SY5Y and mouse primary cortical neurons (Niu et al., 2012; Wang et al., 2012b). In patient fibroblasts derived from [G2019S] carrier PD patients, loss of mitochondrial mass (Su et al., 2015), elongation of mitochondria (Mortiboys et al., 2010) or no change to mitochondrial morphology have all been described (Hsieh et al., 2016; Papkovskaia et al., 2012). These differing findings may arise from differences in the patient-derived cell models, or the assays used to measure morphology. Looking at the effect of LRRK2 inhibition on mitochondrial morphology, I found no obvious changes, in line

with a previous study that assessed mitochondrial network morphology of MEFs treated with LRRK2 inhibitors by transmission electron microscopy (Singh et al., 2021).

5.4.2 VPS35, LRRK2 and mitophagy

Focussing on mitophagy initiation, I found that expression of VPS35[D620N] did not impair PINK1 stabilisation and subsequent phosphorylation of ubiquitin when cells were treated with either AO cocktail or CCCP. A previous study using heterozygous [D620N] knockin SH-SY5Y cells showed that expression of [D620N] lowered basal mitochondrial membrane potential, rendering the cells less sensitive to the depolarising agent CCCP, thus impairing the recruitment of PINK1 and Parkin to initiate mitophagy (Ma et al., 2021). In the RPE1 FlpIn VPS35 model, expression of VPS35[D620N] does not alter mitochondrial membrane potential and so we may not observe this insensitivity to CCCP treatment. Ma and colleagues also found that AO-induced mitophagy was unaffected by expression of VPS35[D620N] (Ma et al., 2021). They attribute this to the initiation of mitophagy upon AO treatment being independent of mitochondrial membrane potential collapse (Ma et al., 2021).

Another study found that VPS35[D620N] causes impaired lysosomal clearance of mitochondria in CCCP-induced PINK1/Parkin-dependent mitophagy, suggesting that the effects of the VPS35[D620N] mutation lie further in this pathway (Hanss et al., 2021). The authors also report that basal mitophagy is unaffected, perhaps as the lysosomes can clear lower levels of damaged mitochondria but become overwhelmed on the onset of widespread mitophagy such as upon treatment with CCCP. It is also worth noting that CCCP will also dissipate the proton gradient at other organelles, including lysosomes, which will exacerbate the defect in clearance of mitolysosomes (Llopis et al., 1998; Padman et al., 2013).

As mitophagy can be initiated by several different mechanisms, some of which are independent of PINK1 and Parkin, it would be interesting to look at whether other forms of mitophagy, such as MLN4924-induced NIX-dependent mitophagy, is affected by the [D620N] mutation. I have only performed experiments to look at the initiation of mitophagy, so it would be valuable to look at whether downstream progression of induced mitophagy is affected in our model. To do so, a mitophagy reporter such as mitokeima could be introduced into the RPE1 FlpIn VPS35 cells to look at the number and size of mitolysosomes basally and following depolarisation.

I also analysed the effect of inhibition of LRRK2 on basal mitophagy in RPE1 mitokeima-expressing cells. I did not observe an effect on the number nor area of

mitolysosomes at any of the MLi-2 concentrations tested, suggesting that mitophagy is not impacted by LRRK2 inhibition in this cell line. This contrasts with two studies by the Muqit group which have shown using knockin LRRK2 [G2019S] MEFs that inhibition of LRRK2 using distinct inhibitor compounds decreases basal mitophagy in a PINK1-independent manner using a similar fluorescent reporter assay, mito-QC (Singh et al., 2021; Tasegian et al., 2021). They found that LRRK2 [G2019S] expression reduced basal mitophagy which could be rescued by LRRK2 inhibition and that knockout of LRRK2 enhanced mitophagy, suggesting that LRRK2 plays a role in suppressing basal mitophagy (Singh et al., 2021; Tasegian et al., 2021). RPE1 cells express low levels of LRRK2 and so LRRK2 may not play a significant role in basal mitophagy in this cell line.

6 Investigating the roles of VPS35 and LRRK2 in the response to lysosomal damage

6.1 Introduction

Pharmacological agents which cause lysosomal stress have been shown to activate LRRK2, leading to its recruitment to membranes and subsequent Rab phosphorylation (Bonet-Ponce et al., 2020; Eguchi et al., 2018; Herbst et al., 2020; Kalogeropulou et al., 2020; Kuwahara et al., 2020). LRRK2 has been suggested to limit lysosomal damage by several different mechanisms.

Eguchi and colleagues showed that chloroquine induces LRRK2 dependent recruitment of the Rab8/10 effectors EHBP1 and EHBP1L1 to the lysosome (Eguchi et al., 2018). These effectors then act to limit lysosomal swelling and promote release of lysosomal contents, such as cathepsin D, into the medium to prevent lysosome overload (Eguchi et al., 2018). The Iwatsubo lab propose that Rab29 is required for the recruitment of LRRK2 to the lysosome and subsequent Rab8 and Rab10 phosphorylation following chloroquine treatment (Eguchi et al., 2018; Kuwahara et al., 2020). However this has been contested by a recent study which failed to see an effect of Rab29 knockout on chloroquine-induced Rab phosphorylation by LRRK2 (Kalogeropulou et al., 2020).

LRRK2 has also been implicated in the ESCRT-mediated membrane repair of ruptured lysosomes (Herbst et al., 2020). Following treatment with the lysosomotropic agent LLOMe (discussed in detail in **Section 6.2 below**), calcium efflux triggers LRRK2 recruitment to the lysosomal membrane. Here, LRRK2 mediates the recruitment of Galectin-3 and the ESCRT-III machinery to sites of damage to promote repair. In the absence of LRRK2 activity, lysosomes are unable to be repaired and are instead targeted for removal by lysophagy. The authors show these effects are also Rab8 dependent, but how LRRK2 and Rab8 are linked mechanistically to the ESCRT machinery is unknown (Herbst et al., 2020).

Recently, the phosphoRab effector JIP4 has been shown to promote lysosomal tubulation in response to LLOMe treatment in a LRRK2-dependent manner by linking lysosomes to motor proteins and microtubules (Bonet-Ponce et al., 2020). JIP4 is capable of binding to both the anterograde motor protein kinesin and the retrograde motor protein dynein and so could function in tubule elongation and retraction (Montagnac et al., 2009). This lysosomal tubulation driven by LRRK2 has been

proposed to sort undegraded cargo from damaged lysosomes to active lysosomes to resolve the lysosomal insult.

Given the body of evidence implicating LRRK2 in the response to lysosomal damage, I investigated whether enhanced LRRK2 activation by VPS35[D620N] influences the resolution from endolysosomal stress. In this chapter, I characterise the effect of endolysosomal stressors on lysosomal pH, morphology, and Rab phosphorylation in RPE1 cells. Then, using these pharmacological agents, I investigate the role of VPS35 in the response to lysosomal damage and the functional consequences of the [D620N] mutation.

6.2 Characterisation of lysosomal damaging agents in RPE1 cells

The arsenal of compounds that researchers use to study lysosomal stress and damage act via varied mechanisms, and are summarised in **Table 6.1** below. I focused on three compounds, nigericin, chloroquine and LLOMe which have all been shown to induce LRRK2-dependent Rab phosphorylation, but are proposed to act by diverse mechanisms (Eguchi et al., 2018; Herbst et al., 2020; Kalogeropulou et al., 2020).

Nigericin is a K^+/H^+ antiporter which enhances the flow of potassium and hydrogen ions in opposite directions along the K^+ concentration gradient. At the lysosome, this results in K^+ influx and H^+ efflux, increasing the lysosomal pH (Jacquin et al., 2017; Tapper and Sundler, 1990). Chloroquine is widely used in autophagy and lysosome research to alkalinise lysosomes and prevent autophagosome-lysosome fusion. Upon entering the lysosome, chloroquine is thought to become protonated, preventing its diffusion back across the membrane, and so it accumulates in the lysosomal lumen. As chloroquine is a weak base, this neutralises the lysosome, but this also leads to osmotic swelling (Seglen et al., 1979; Solomon and Lee, 2009). LLOMe is thought to be taken up by cells via endocytosis and when it reaches the lysosomes it undergoes condensation by the enzyme cathepsin C, converting it into a membranolytic form (Thiele and Lipsky, 1990).

Table 6.1 Commonly used lysosomotropic agents and their mechanisms of action
Cat C, cathepsin C. (Florey et al., 2015; Jacquin et al., 2017; Morgan et al., 2020; Thiele and Lipsky, 1990)

Group	Compound	Mechanism of action
Rupturing dipeptides	LLOMe	Condensed in lysosomes by cathepsin C into membranolytic detergent form

	GPN	Degraded in lysosomes by CatC into a dipeptide which accumulates, causing osmotic swelling and membrane rupture
v-ATPase inhibitors	Bafilomycin A	Selectively inhibit lysosomal vacuolar H^+-ATPase
	Concanamycin A	
Weak bases	Chloroquine	Accumulate in lysosomes, causing osmotic swelling
	Hydroxychloroquine	
	Ammonium chloride (NH_4Cl)	
Ionophores	Monensin	Na^+/H^+ ionophore, proton efflux
	Nigericin	K^+/H^+ ionophore, proton efflux

6.2.1 Assessment of the effect of endolysosomal stressors on lysosomal acidification

I first looked at the effect of the chosen endolysosomal stressors on lysosomal pH. RPE1 cells were stained with Lysotracker Red, which consists of a weak base linked to a fluorophore. Like chloroquine, Lysotracker probes accumulate in the lysosome and so can be used to visualise lysosomes by live cell microscopy. Furthermore, loss of Lysotracker Red staining has previously been used as a readout of an increase in lysosomal pH or evidence of lysosomal rupture (Jacquin et al., 2017; Radulovic et al., 2018). To allow visualisation of cells and at the same time assess if any of the compounds affected mitochondrial morphology, cells were counterstained with Mitotracker Green. The dyes were removed, and cells were treated with compound for one hour before imaging (**Figure 6.1**). In addition to chloroquine, nigericin, LLOMe and a vehicle control, treatments with concanamycin A, apilimod and MLi-2 were also included. Concanamycin inhibits the lysosomal vacuolar H^+-ATPase and so increases lysosomal pH. Conversely, the PIKfyve inhibitor apilimod has been reported to cause hyperacidification of lysosomes by removing the tonic inhibitory effect of $PI(3,5)P_2$ on the lysosomal Cl^-/H^+ antiporter ClC-7 (Leray et al., 2022). A previous PhD student in the lab, Hannah Elcocks, has shown that acute inhibition of LRRK2 with MLi-2 causes an increase in Lysotracker staining in mouse melanocytes and in human melanoma MNT1 cells.

In control cells, bright puncta corresponding to lysosomes were visible as well as a low background signal. Treatment with concanamycin A caused a visible decrease in the number and intensity of Lysotracker puncta (**Figure 6.1B**). The morphology of stained lysosomes was unaffected by concanamycin A, in contrast to chloroquine which caused an enlargement of lysosomes with reduced staining intensity.

Chloroquine-treated enlarged lysosomes in the cell periphery overall showed a higher staining intensity than those in the perinuclear area.

Upon addition of LLOMe, lysosomes appeared enlarged and unexpectedly displayed an increased Lysotracker staining intensity (**Figure 6.1B**). The representative images in **Figure 6.1A** were processed equally across all conditions to an extent that allowed visualisation of Lysotracker particles even in the conditions that had a decreased staining intensity, such as with chloroquine. In these images, the LLOMe-treated, Lysotracker-positive lysosomes appear as uniformly stained puncta. However, when the LLOMe-treated cells are displayed using an optimal dynamic range, it is possible to discern multiple individual small bright puncta within larger Lysotracker stained vesicles (**Figure 6.1C**). It is tempting to speculate that these bright internal puncta represent damaged lysosomes that have been autophagocytosed. In addition, LLOMe caused a drastic fragmentation of the mitochondrial network. This supports previous work which has shown that LLOMe-induced leakage of lysosomal enzymes into the cytosol causes impaired mitochondrial function and network fragmentation due to degradation of mitochondrial proteins (Bussi et al., 2022).

As expected, treatment with nigericin caused an overall decrease in the intensity of Lysotracker stained lysosomes (**Figure 6.1B**). However, approximately half the cells analysed retained a bright peripheral Lysotracker signal. Lysosome size was not affected, suggesting that nigericin does not cause a change in lysosomal morphology. Like LLOMe, nigericin treatment also caused fragmentation of the mitochondrial network.

Apilimod caused a dramatic swelling of Lysotracker-stained structures, without a change in overall signal intensity (**Figure 6.1B**). Given that apilimod has previously been shown to cause lysosomal hyperacidification in U2OS cells, it was expected that Lysotracker Red staining would increase (Leray et al., 2022). Although the accumulation of Lysotracker probes is sensitive to pH, they do not allow a quantitative assessment of pH changes, in contrast to Oregon Green-dextran 488 which was used in the aforementioned study (Leray et al., 2022). Thus, the lack of hyperacidification observed in RPE1 may reflect the methodology used rather than a difference between the different cell lines. Finally, treatment with the LRRK2 inhibitor MLi-2 did not affect the staining pattern of Lysotracker Red in RPE1 cells.

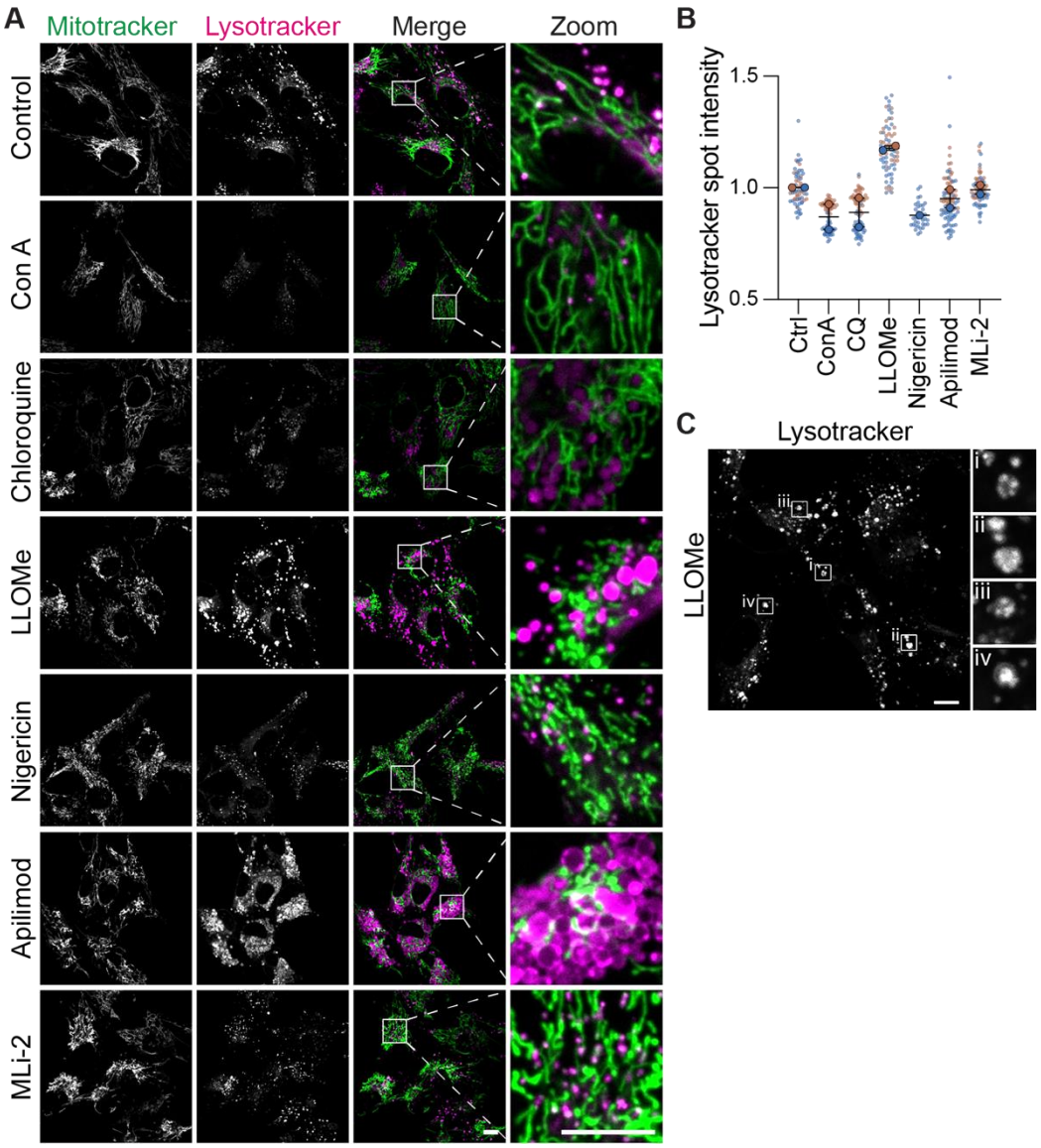

Figure 6.1 Effect of endolysosomal stressors on lysosomal pH and mitochondrial morphology
A RPE1 FlpIn Parental cells were stained with Mitotracker Green and Lysotracker Red DND-99 and then treated with 100 nM concanamycin A, 100 µM chloroquine, 500 µM LLOMe, 2 µM nigericin, 150 nM apilimod, 100 nM MLi-2 or a vehicle control (DMSO) for 1 hour before live-cell imaging using a 63x objective on a 3i spinning disk confocal microscope. Scale bar 10 µm. **B** Quantification of the intensity of Lysotracker puncta. *n* = 1 – 2, 26 - 49 cells quantified per condition per experiment. Each independent experiment is colour-coded. Transparent circles with no outline represent values for each cell in an experiment, opaque circles with black outlines correspond to mean values for each experiment. Bars represent mean and range. **C** Representative image of LLOMe condition in A. Scale bar 10 µm.

6.2.2 Assessment of the effect of endolysosomal stressors on endolysosomal morphology

To further investigate the morphological changes induced upon treatment with these agents, I stained cells for LAMP1 and CD63 after a 3-hour treatment with chloroquine, nigericin and LLOMe (**Figure 5.3**). Proteins known to reside at lysosomes, such as LAMP1 and LAMP2, and late endosomes, such as CD63 and Rab7, show overlapping distributions (Shearer and Petersen, 2019). For ease, this compartment will be referred to simply as lysosomes henceforth. In agreement with the Lysotracker staining in **Figure 6.1**, I found that LLOMe and chloroquine treatment caused a substantial enlargement and perinuclear clustering of lysosomes. Nigericin caused mild lysosomal swelling and caused a general decrease in the intensity of LAMP1 and CD63 staining, except for a population of resistant lysosomes in the cell periphery.

By creating a region of interest around the borders of a cell and using this to generate smaller concentric regions of interest, the cumulative intensity of a fluorescent stain can be mapped from the centre of the cell to the periphery. Utilising this technique with a lysosomal marker allows the generation of a curve illustrative of lysosomal positioning within a cell (Starling et al., 2016). A shift of the baseline curve to the right indicates a redistribution of lysosomes to the periphery, whereas a shift leftwards indicates perinuclear clustering. Using this method, I created concentric regions of interest at 10% size decrements and measured the integrated density within each region. For each region, this was plotted relative to the total integrated density of the whole cell area to create a curve of cumulative LAMP1 signal intensity (**Figure 5.3B**). Supporting the changes that were visible by eye, the lysosomal positioning curves for LLOMe and chloroquine treatment were shifted leftwards, representing a redistribution of lysosomes towards the perinuclear area. Nigericin treatment did not induce such a substantial curve shift. There was a minor shift rightwards, which is consistent with the small clusters of bright puncta that are visible in the periphery of some cells, however more repeats would be necessary to ascertain whether this small shift was significant.

The size and area of LAMP1 puncta were also quantified (**Figure 5.3C**). Treatment with LLOMe and nigericin reduced the number of LAMP1-positive lysosomes, whereas chloroquine had no effect. Given the decrease in staining intensity in nigericin-treated cells, it is possible that the remaining lysosomes are less robustly identified after thresholding, which may cause the apparent decrease in number. Lysosomal clustering may also interfere with the ability to distinguish and quantify

individual lysosomes. After chloroquine and LLOMe treatment, there was a doubling in the size of lysosomes, indicative of lysosomal swelling. Nigericin, on the other hand, did not affect the lysosomal area, but again, this may be due to a thresholding issue.

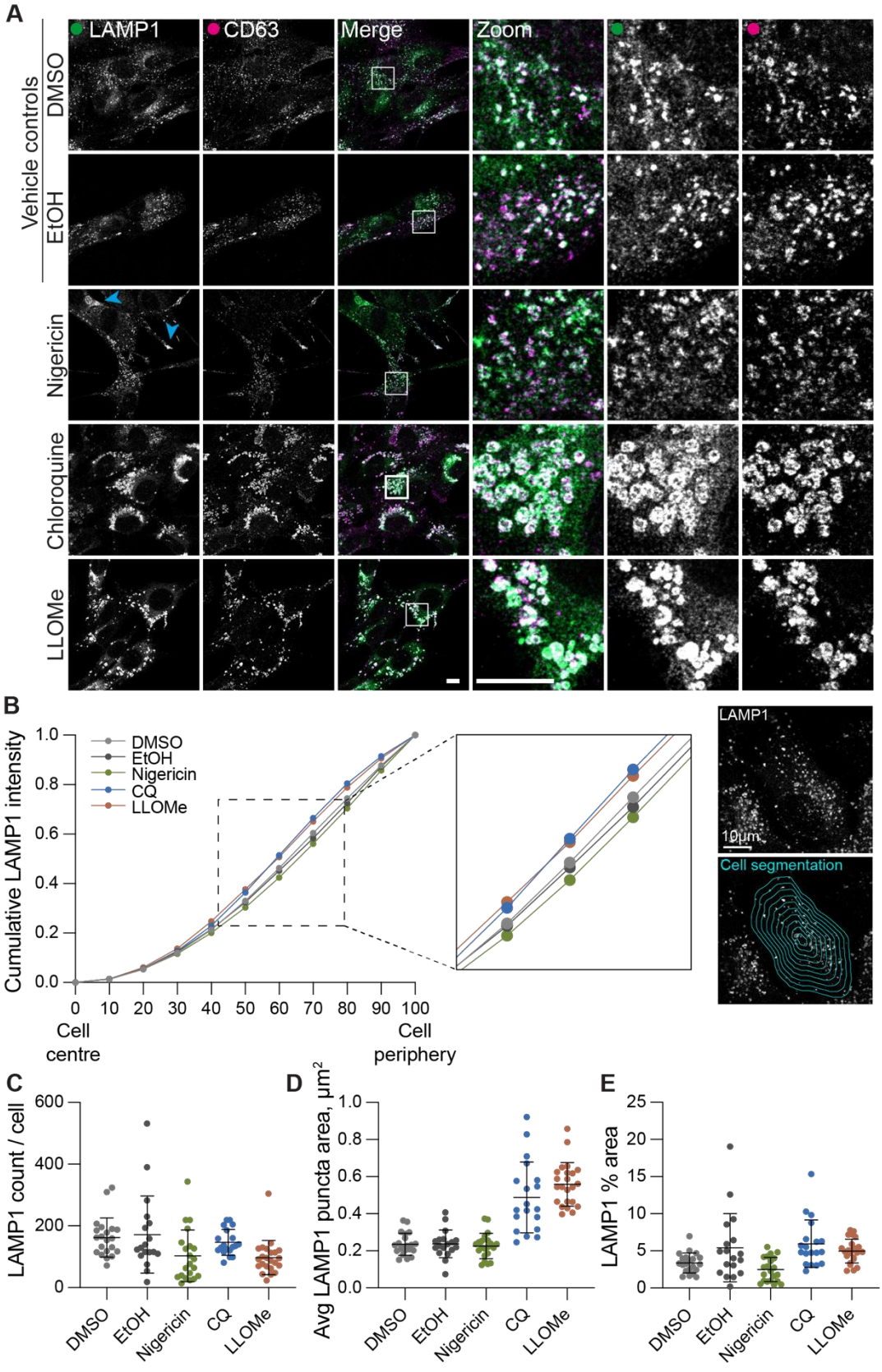

Figure 6.2 Chemical stressors of the endolysosomal system cause enlargement of lysosomes
A RPE1 FlpIn Parental cells were treated with 2 µM nigericin or vehicle (ethanol, EtOH), 500 µM LLOMe or vehicle (DMSO), or 100 µM chloroquine (CQ) for 3 hours, then fixed and stained with the indicated antibodies. Single slice images were acquired on a Zeiss LSM900 confocal microscope using a 63x objective. Scale bar 10 µm. Blue arrowheads indicate peripheral clustering phenotype. **B** Quantification of cumulative LAMP1 intensity as a function of total LAMP1 intensity by concentric cell segmentation at 10% decrements (illustrated right). **C-E** Quantification of number (C), average size (D) and percentage of total area (E) of LAMP1 puncta. Data from a single experiment, 18-23 cells counted per condition, *n* = 1. Bars represent mean ± SD.

Acute treatment with nigericin has been shown to cause an enlargement of Rab5-and Rab7-positive endosomes (Podinovskaia et al., 2021). To investigate whether nigericin affects the morphology of early endosomes, RPE1 cells were treated with nigericin for three hours and then fixed and stained for EEA1 and VPS35 (**Figure 6.3**). The number, average size and total area occupied by EEA1 puncta was then quantified (**Figure 6.3B-D**). In addition, cumulative EEA1 and VPS35 signal intensities were plotted to generate 'endosome positioning' curves (**Figure 6.3E and F**). Nigericin treatment led to a visible swelling of endosomes in the perinuclear region, which is reflected in the quantification as a clear positive trend in both number and size of early endosomes. Combining these measurements to calculate the percentage area of the cell occupied by EEA1 reveals the extent of the overall effect (**Figure 6.3D**). The distribution of EEA1-positive endosomes was not affected by nigericin treatment (**Figure 6.3E**). In contrast, VPS35 staining became more prominent at the cell edges (in particular the leading edges), reminiscent of the LAMP1 and CD63 staining in **Figure 6.2**. Measurement of the cumulative VPS35 intensity in the cells revealed a small rightwards shift of the endosome positioning curve, which is consistent with an increase in staining in the cell periphery (**Figure 6.3F**).

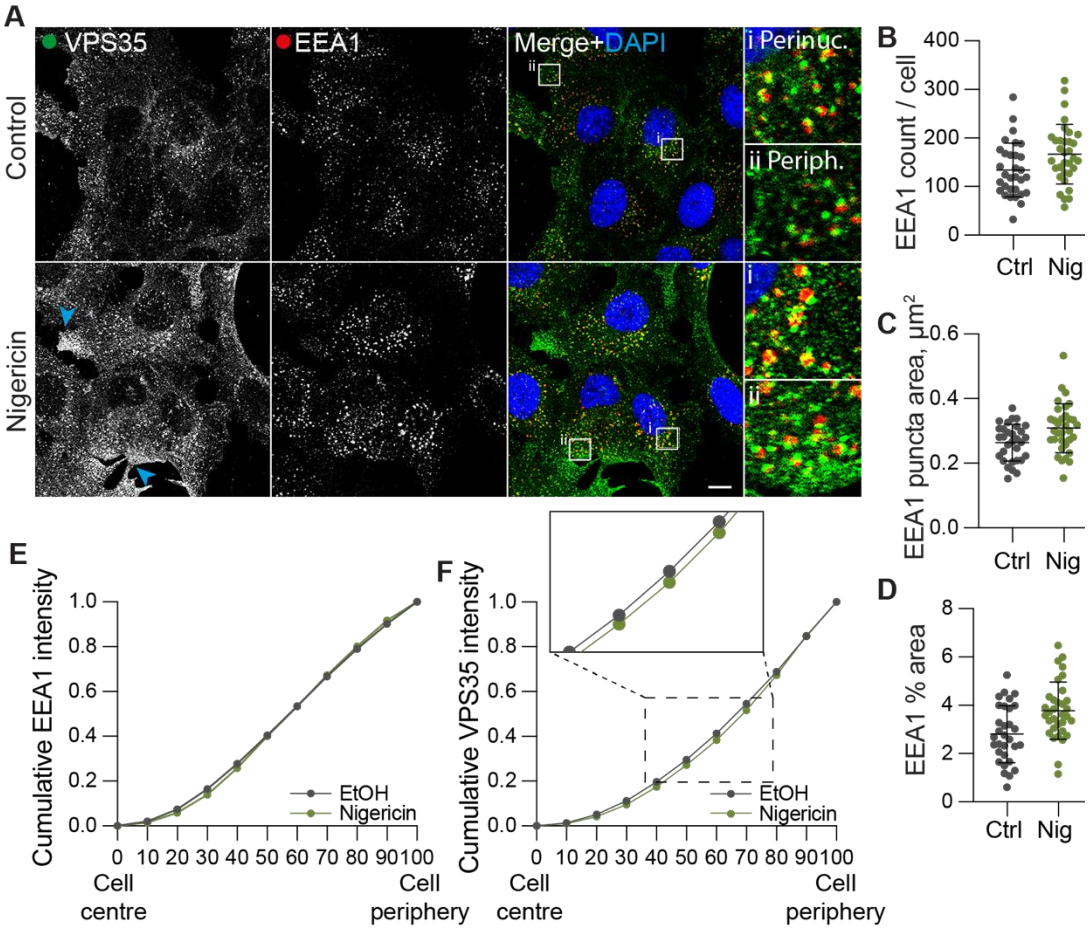

Figure 6.3 Nigericin causes enlargement of early endosomes

A RPE1 FlpIn Parental cells were treated with 2µM nigericin or vehicle (ethanol) for 3 hours, then fixed and stained with the indicated antibodies and DAPI (DNA, blue). Single slice images were acquired on a Zeiss LSM900 confocal microscope using a 63x objective. Scale bar 10 µm. Blue arrowheads indicate peripheral lysosome clustering phenotype. Perinuc, perinuclear; periph, peripheral. **B-D** Quantification of number (B), average size (C) and percentage of total area (D) of EEA1 puncta. Bars represent mean ± SD. **E** Mean cumulative EEA1 intensity as a function of total EEA1 intensity by concentric cell segmentation at 10% decrements. **F** Mean cumulative VPS35 intensity as a function of total VPS35 intensity by concentric cell segmentation at 10% decrements. Data from a single experiment, 31-33 cells quantified per condition, *n* = 1.

In the Lysotracker staining experiments (**Figure 6.1**), treatment with apilimod caused substantial lysosomal swelling. To look at the effect of apilimod on the endolysosomal system in more detail, RPE1 cells were treated with 30, 150 or 300 nM of apilimod for 30 minutes before fixation and processing for immunofluorescence using antibodies against the early endosome marker EEA1 and the lysosome marker LAMP1 (**Figure 6.4**). These concentrations were chosen based on the reported apilimod IC_{50} of 14 nM for PIKfyve based on an *in vitro* kinase assay (Cai et al., 2013). Even at the lowest concentration tested, apilimod caused a marked change in endosome and lysosome

morphology. Early endosomes were enlarged (**Figure 6.4B**) and became more clustered towards the perinuclear area of the cell (**Figure 6.4D**). Conversely, the lysosome positioning curve was shifted rightwards, indicating an increase in LAMP1 staining towards the periphery of the cell (**Figure 6.4E**). Lysosomes were also enlarged by eye in all the conditions but was only reflected in the quantification at the lowest concentration as the decreased staining intensity at higher apilimod concentrations interfered with the segmentation process (**Figure 6.4C**).

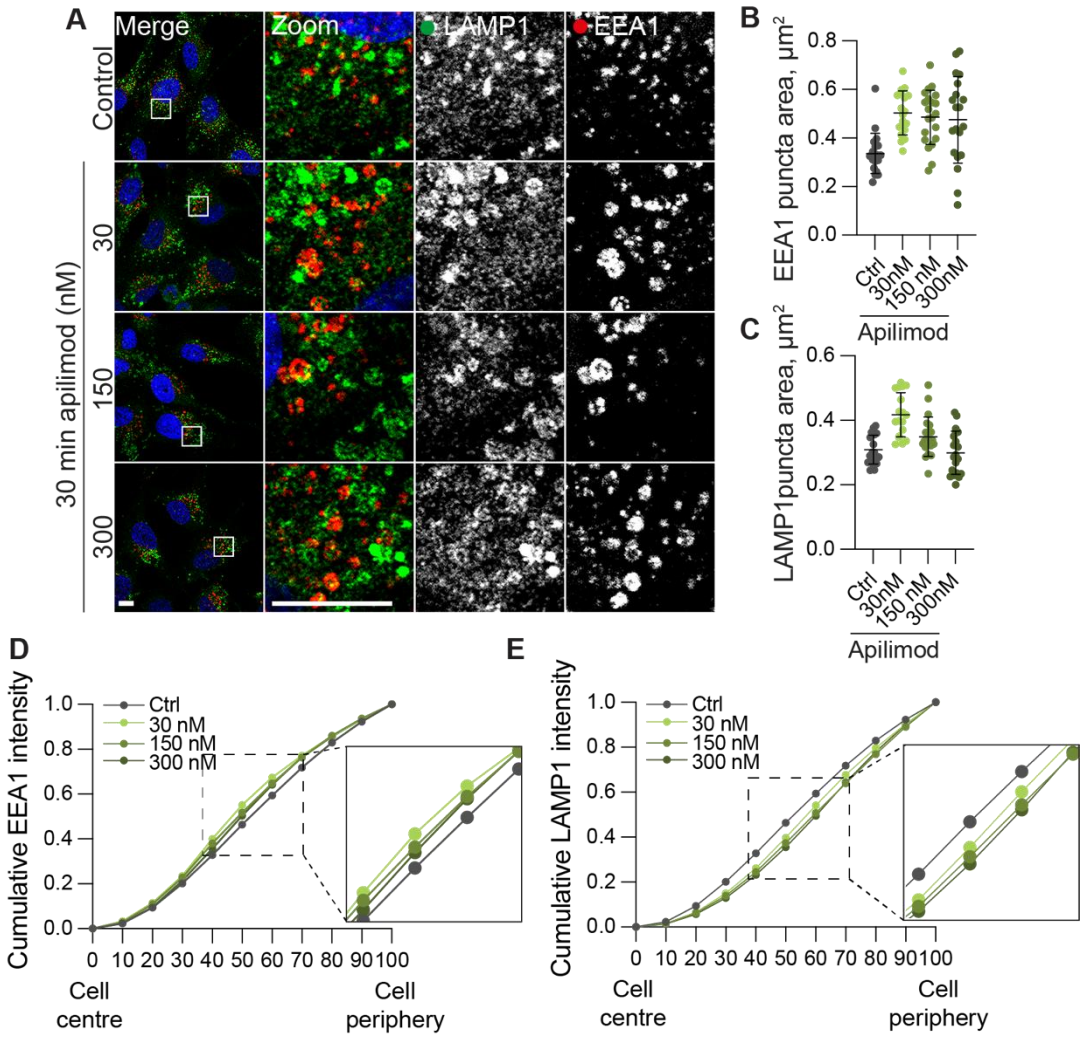

Figure 6.4 Apilimod treatment causes enlargement of early endosomes and lysosomes
A RPE1 FlpIn Parental cells were treated with apilimod for 30 minutes at the concentrations indicated or vehicle control (DMSO), then fixed and stained with the indicated antibodies and DAPI (DNA, blue). Single slice images were acquired on a Zeiss LSM900 confocal microscope using a 63x objective. Scale bar 10 µm. **B** Quantification of the size of EEA1 puncta. Bars represent mean ± SD. **C** Quantification of the size of LAMP1 puncta. Bars represent mean ± SD. **D** Mean cumulative EEA1 intensity as a function of total EEA1 intensity by concentric cell segmentation at 10% decrements. **E** Mean cumulative LAMP1 intensity as a function of total LAMP1 intensity by concentric cell

segmentation at 10% decrements. Data from a single experiment, 18-21 cells counted per condition, *n* = 1.

6.2.3 Assessment of the effect of endolysosomal stressors on the phosphorylation of LRRK2 substrate Rabs

Treatment of cells with nigericin, LLOMe and chloroquine have all been reported to increase the phosphorylation of Rab proteins by LRRK2 (Eguchi et al., 2018; Herbst et al., 2020; Kalogeropulou et al., 2020). I set out to ascertain the optimal incubation times and concentrations of LLOMe, chloroquine and nigericin in RPE1 cells to measure Rab phosphorylation.

RPE1 cells were treated with 2 μM nigericin over one and eight hours and the degree of Rab10 phosphorylation was assessed by western blotting (**Figure 6.5A**). Within one and two hours, Rab10 phosphorylation increased four- and six-fold, respectively, after which the levels plateaued (**Figure 6.5B**). Addition of the LRRK2 inhibitor MLi-2 one hour prior to lysis caused a reduction in Rab10 phosphorylation, confirming that nigericin-induced Rab10 phosphorylation is dependent on LRRK2. The expression of LRRK2 was not altered by nigericin treatment, indicating that the effect of nigericin is on the kinase activity of LRRK2 and not level of expression. As maximal Rab phosphorylation appeared to have been reached at later time points, I chose to focus on the shorter treatment lengths. RPE1 cells were treated with concentrations of nigericin between 0.1 and 4 μM for 30 or 60 minutes before lysis and analysis of Rab10 and Rab12 phosphorylation by western blotting (**Figure 6.5C**). Phosphorylation of Rab10 increased with increasing concentrations of nigericin, however there was little difference in response between 30 and 60 minutes of treatment (**Figure 6.5D**). Unlike in **Figure 6.5A**, one hour treatment with nigericin only caused a two-fold increase in pT73-Rab10 signal. Immunoblotting for total Rab10 revealed that this was not affected by nigericin treatment, confirming that the increase in Rab10 phosphorylation was not due to an increase in total levels of Rab10. Treatment with nigericin also increased phosphorylation of Rab12, another LRRK2 substrate Rab. A near two-fold increase in Rab12 phosphorylation was observed at concentrations higher than 0.5 μM after 60 minutes of treatment. At 30 minutes of treatment, there was little effect on the levels of pS106-Rab12.

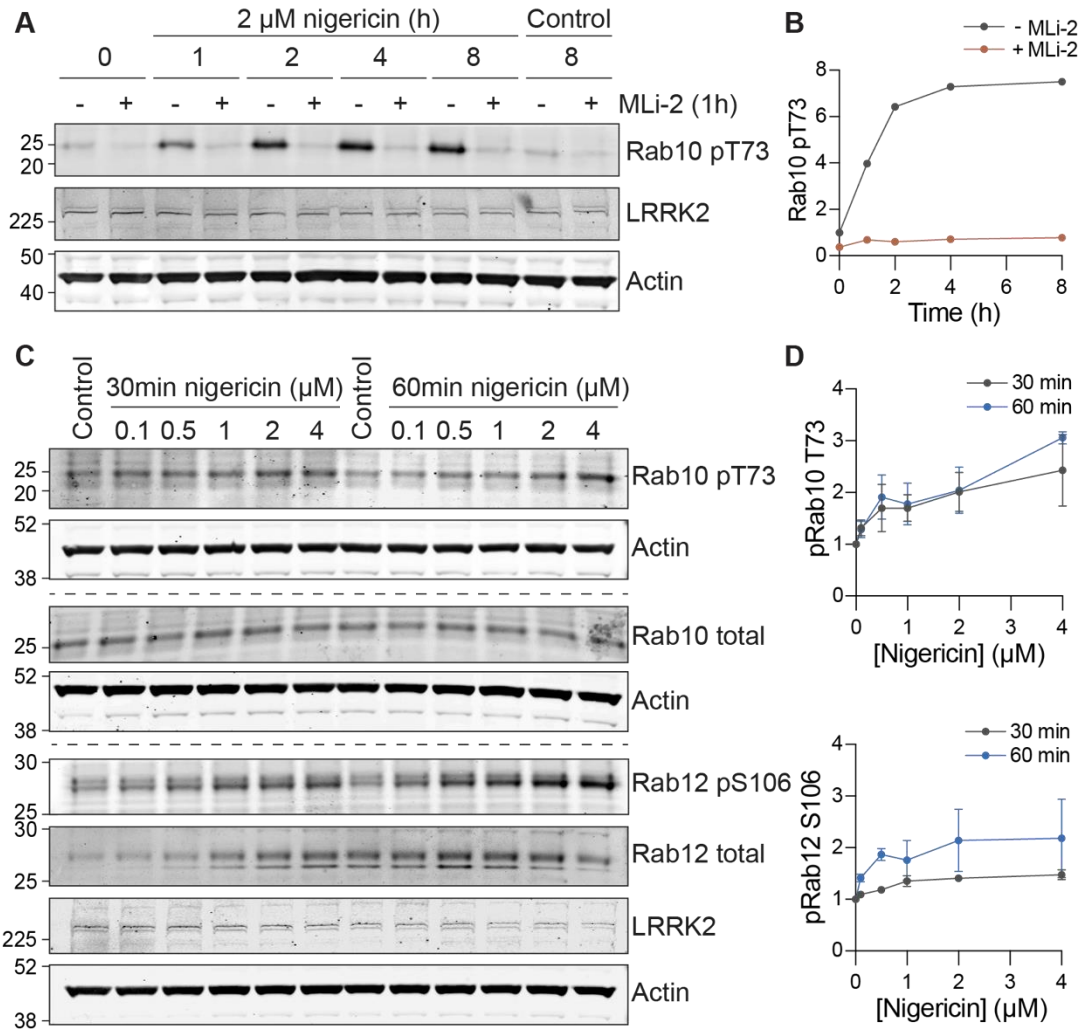

Figure 6.5 Nigericin treatment induces a time- and concentration-dependent increase in Rab phosphorylation via the action of LRRK2

A RPE1 FlpIn Parentals cells were treated with 2 μM nigericin or vehicle (ethanol) for the indicated times. Cells were treated with 100 nM MLi-2 or vehicle (DMSO) for one hour prior to lysis and analysis by immunoblotting. Data from a single experiment, *n* = 1. **B** Quantification of A. Data are normalised to 0-hour untreated control. *n* = 1. **C** RPE1 FlpIn Parentals cells were treated with nigericin at the indicated concentrations for 30 or 60 minutes before lysis and analysis by immunoblotting. A representative western blot is shown. The lower signal in the first four lanes of the total Rab12 indicate a problem with staining with Rab12 total antibody as non-specific bands are also reduced but there was no transfer issue evident on the Ponceau staining. **D** Quantification of C. Data are normalised to control for each time point. *n* = 2. Data represent mean and range (some error bars are too small to be shown).

Next, I looked at LLOMe-induced Rab phosphorylation in RPE1 cells. Cells were treated with 500 μM LLOMe for 15 to 120 minutes before lysis and analysis by western blotting (**Figure 6.6A**). LLOMe caused a steady increase in Rab12 phosphorylation from 15 to 90 minutes, plateauing at approximately 3-fold at the 90-minute timepoint

(Figure 6.6B). Total Rab12 levels were unchanged, indicating that it is specifically the phosphorylation status of Rab12 that is increased upon LLOMe treatment.

The concentration of LLOMe was then optimised using a 90-minute treatment length in the presence and absence of MLi-2 to help discriminate specific LRRK2 dependent pT73-Rab10 signal from background (Figure 6.6C). At concentrations of 250 µM and above, I found that Rab12 phosphorylation plateaued at a three-fold increase (Figure 6.6D). In contrast, Rab10 phosphorylation only reached a 1.3-fold (± 0.11) increase at the highest concentration tested (1000 µM), which was abolished by Mli-2. Rab12 phosphorylation was only partially inhibited by Mli-2 at LLOMe concentrations above 250 µM.

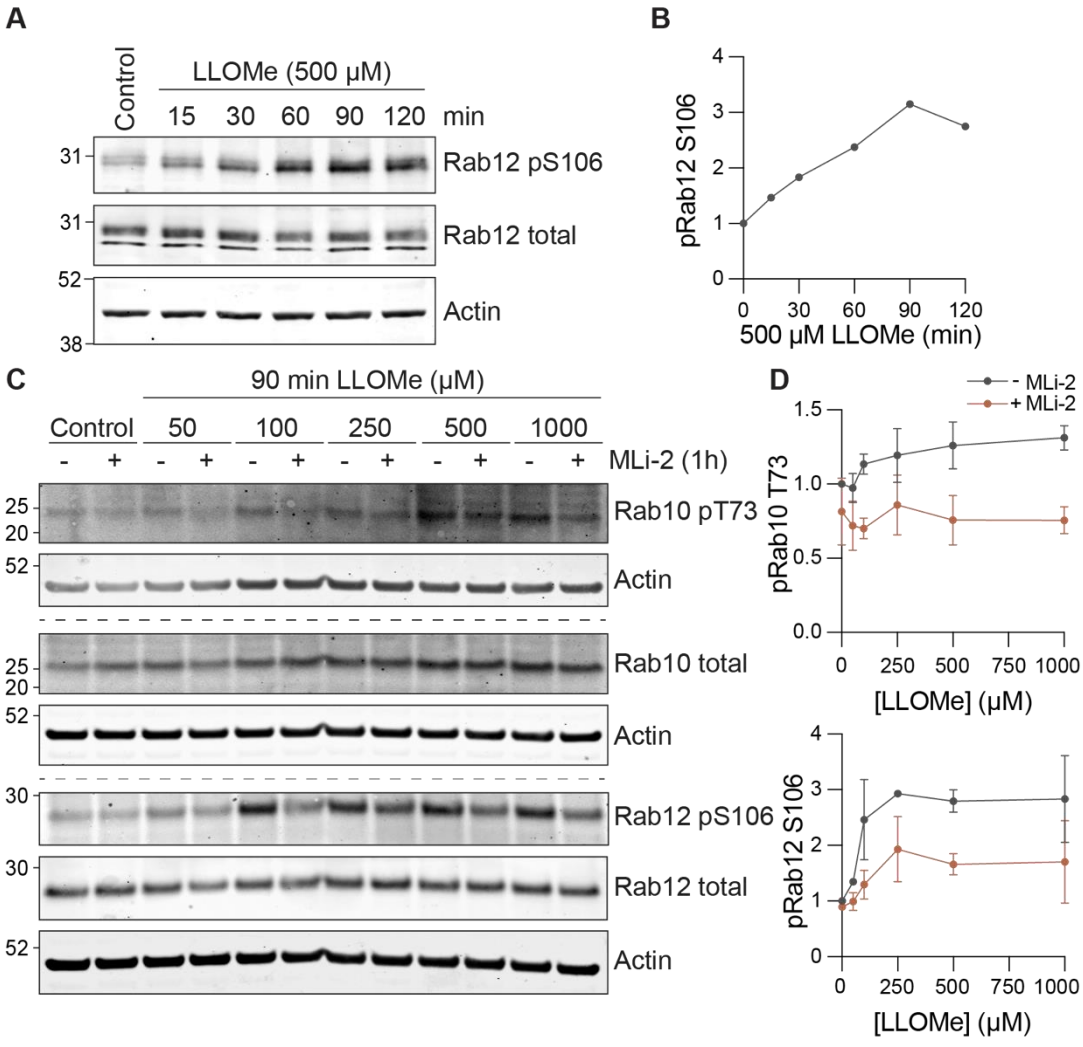

Figure 6.6 LLOMe treatment induces a time- and concentration-dependent increase in Rab phosphorylation via the action of LRRK2

A RPE1 FlpIn Parentals cells were treated with 500 µM LLOMe or vehicle (DMSO) for the indicated times prior to lysis and analysis by immunoblotting. **B** Quantification of A. Data are normalised to vehicle control. Data from a single experiment, *n* = 1. **C** RPE1 FlpIn Parentals cells were treated with LLOMe at the indicated concentrations for 90 minutes. Cells were treated with 100 nM MLi-2 or vehicle

(DMSO) for one hour prior to lysis and analysis by immunoblotting. A representative western blot is shown. **D** Quantification of C. Data are normalised to untreated control. *n* = 2. Data represent mean and range (some error bars are too small to be shown).

Finally, I looked at the Rab phosphorylation response to chloroquine. RPE1 cells were treated with 50 μM chloroquine over 30 minutes to six hours (**Figure 6.7A**). Phosphorylation of Rab10 reached a peak four hours after addition of chloroquine, with an approximately 1.5-fold increase compared to untreated controls and plateaued thereafter (**Figure 6.7B**). Treatment with MLi-2 reduced Rab10 phosphorylation to baseline untreated levels. A higher fold increase in Rab12 phosphorylation was observed in response to chloroquine with a 2.3-fold increase, which also reached plateaued after 4 hours. This increase was attenuated by the addition of MLi-2, but Rab12 phosphorylation remained higher than baseline when the duration of chloroquine treatment was longer than one hour.

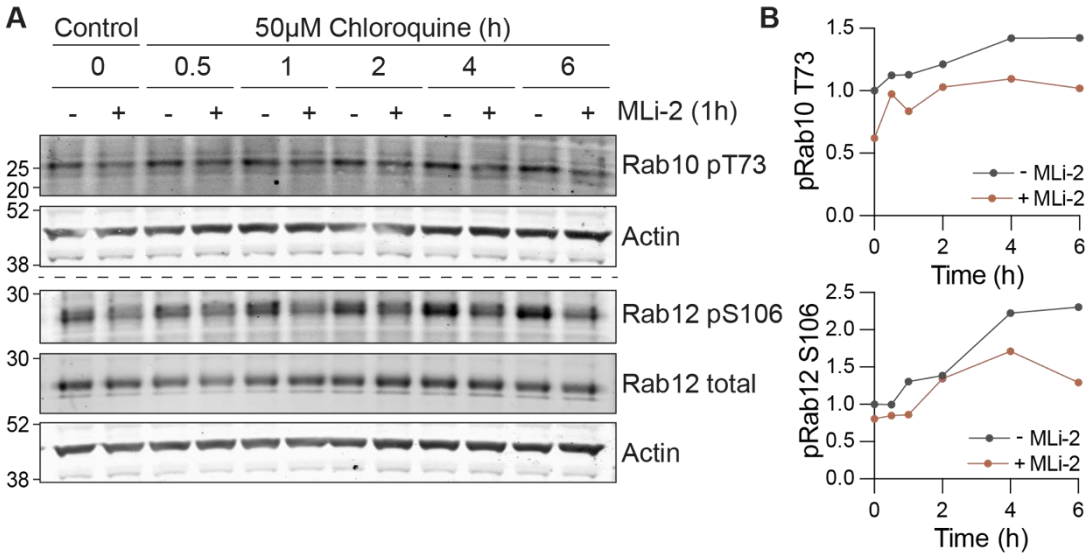

Figure 6.7 Chloroquine treatment induces a time-dependent increase in Rab phosphorylation via the action of LRRK2

A RPE1 FlpIn Parentals cells were treated with 50 μM chloroquine for the indicated times. Cells were treated with DMSO or 100 nM MLi-2 for one hour prior to lysis and analysis by immunoblotting **B** Quantification of A. Data are normalised to untreated control. Data from a single experiment, *n* = 1.

The mechanism by which LRRK2 is recruited to the membrane following lysosomal damage is debated. The Iwatsubo group proposed that Rab29 is responsible for LRRK2 membrane recruitment and showed that knockdown of Rab29 blunts chloroquine-induced phosphorylation of Rab10 (Eguchi et al., 2018; Kuwahara et al., 2016). However, this was called in to question when the Alessi group showed that

knockout of Rab29 had no effect on Rab phosphorylation induced by a range of stressors, including chloroquine, LLOMe and nigericin (Kalogeropulou et al., 2020). Furthermore, they showed that this was not due to a compensatory mechanism involving the closely related Rab, Rab32. To gain clarity on this, I investigated the effect of Rab29 depletion on stress-induced Rab phosphorylation in RPE1 cells (**Figure 6.8A**). As nigericin had given the most robust signal increase in Rab phosphorylation in my experiments, I chose to use it as an alternative stressor to chloroquine. I also included knockdown of Rab7 in the experiment. Although Rab7 is not a LRRK2 substrate (Steger et al., 2016), I hypothesised that as it is present at late endosomes it could still be involved in LRRK2 recruitment. Furthermore, it plays a role both upstream and downstream of VPS35 (Seaman et al., 2009). Depletion of both Rab29 and Rab7 caused a mild increase in nigericin-induced Rab12 phosphorylation compared to NT1 control (**Figure 6.8B**). This suggests that neither of these Rabs recruits LRRK2 for activation in response to nigericin treatment and if anything, they could play a negative regulatory role in this process. However, this would need to be validated using individual siRNAs and ideally include a rescue condition to exclude off-target effects. Since I carried out these experiments, two independent groups have proposed that Rab12 itself may be the critical Rab for membrane recruitment of LRRK2 (Bondar et al., 2023; Dhekne et al., 2023).

I also performed western blot analysis to analyse LC3 lipidation. Nigericin treatment induced LC3 lipidation which was potentiated by knockdown of Rab7 and, to a lesser extent, knockdown of Rab29. This suggests that nigericin-induced autophagy could be upregulated under these conditions. A minor increase in LC3-II is also seen upon Rab7 knockdown in untreated cells, which may indicate an upregulation of autophagy or an inability to clear autophagosomes.

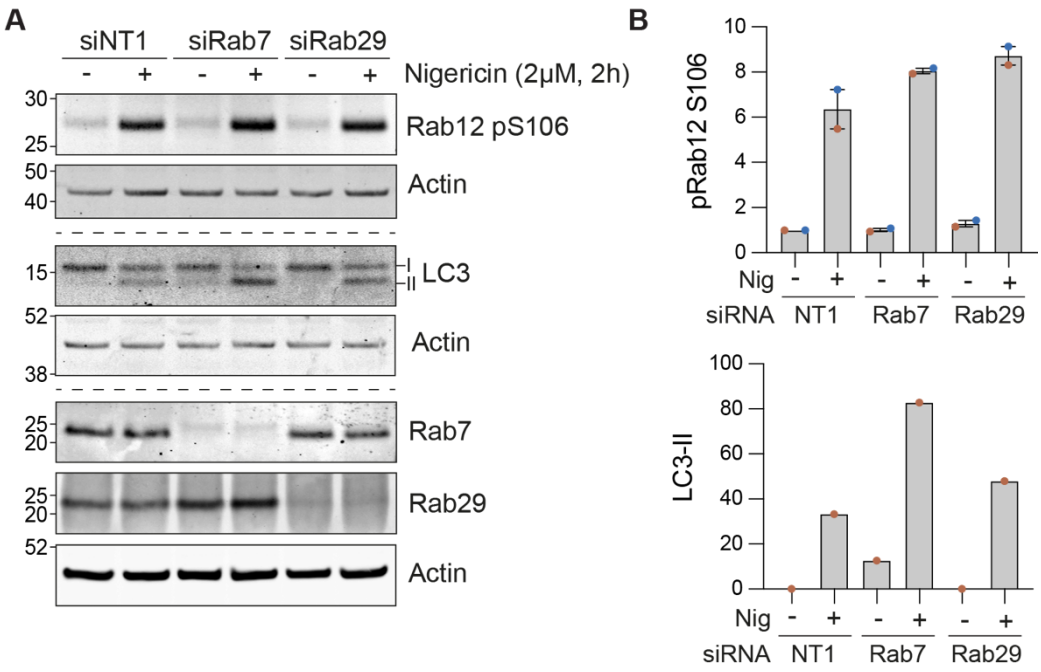

Figure 6.8 Rab29 is not required for nigericin-induced Rab phosphorylation in RPE1
A RPE1 FlpIn Parental cells were treated with 40 nM of non-targeting control (NT1) or a pool of Rab7 or Rab29 targeting siRNA oligonucleotides for 72 hours and then treated with 2 μM nigericin or vehicle (ethanol) for 2 hours prior to lysis and analysis by immunoblotting. A representative western blot is shown. **B** Quantification of A. Values are normalised to NT1 vehicle control (pS106-Rab12) or raw intensities (LC3-II). *n* = 1 - 2. Each independent experiment is colour-coded. Bars represent mean ± range.

6.2.3.1 Summary

By systematically assessing the effects of chloroquine, LLOMe and nigericin on the lysosome, I have found that they differ in the phenotypes that they produce (**Table 6.2**). Despite causing different changes to the morphology and distribution of lysosomes, all three agents induced Rab phosphorylation. Next, I investigated whether the consequences of lysosomal stress induced by LLOMe and nigericin treatment were different, and whether LRRK2 played a role.

Table 6.2 Summary of the different lysosomal phenotypes observed in response to treatment with the lysosome stressors chloroquine, LLOMe and nigericin

	Chloroquine	LLOMe	Nigericin
Morphology	Enlarged	Enlarged	Slightly enlarged?
Distribution	Perinuclear	Perinuclear	Peripheral
Lysotracker staining	Decreased	Increased	Decreased
Rab phosphorylation	Increased	Increased	Increased

6.3 Investigating the downstream consequences of endolysosomal stress

6.3.1 Assessment of the effect of endolysosomal stressors on extracellular release of lysosomal contents

LRRK2 has been reported to negatively regulate extracellular release of lysosomal contents in response to lysosomal overload (Eguchi et al., 2018). Using RAW264.7 macrophage cells, the authors showed that chloroquine treatment causes the release of the intermediate active form of the lysosomal protease cathepsin D into the media and that this was attenuated by LRRK2 inhibition (Eguchi et al., 2018).

To characterise the effects of different pharmacological endolysosomal stressors on cathepsin D release, RPE1 cells were treated with concanamycin A, chloroquine, LLOMe or nigericin for 3 hours before the cells were lysed and the conditioned media collected for TCA precipitation. Cathepsin D levels were then analysed by western blotting (**Figure 6.9A**). Levels of pro, intermediate and mature forms of cathepsin D in the whole cell lysates were quantified (**Figure 6.9D**) and the proportion of each form relative to total cathepsin D was calculated (**Figure 6.9C**). In the media samples collected from control conditions, the Cathepsin D banding pattern revealed two bands close to one another at ~50 kDa, and another band at ~27 kDa. The two upper bands on the media blot ran at the expected molecular weight of pro cathepsin D. These two bands were not resolved enough to discriminate between them during quantification and so are labelled as 'pro' cathepsin D (**Figure 6.9B**).

LLOMe treatment caused an 80% loss of mature cathepsin D in the whole cell lysates. This was accompanied by a 1.8- and 1.7-fold rise in the amount of pro and intermediate forms, respectively. Intriguingly, the mature cathepsin D was not recovered in the media fraction, suggesting that the loss of mature cathepsin D from the whole cell lysates does not correspond to its extracellular release.

Both concanamycin A and chloroquine treatment caused an approximately 5-fold increase in the extracellular release of pro cathepsin D and a 2-fold increase for the mature form. Treatment with these agents also lead to the appearance of a 25 kDa band in the media samples in some experimental repeats. The mature cathepsin D light chain is expected to run at 14 kDa, thus this band is more likely corresponding to a degradation product of cathepsin D. Looking at the whole cell lysates, concanamycin A and chloroquine treatments both caused an increase in pro cathepsin D, whilst having little effect on intermediate and mature cathepsin D forms.

This is likely due to the neutralising effect that concanamycin A and chloroquine have on lysosomes, which will prevent the pH-dependent processing of pro-cathepsin D.

Unlike chloroquine and concanamycin A treatment which promoted secretion of pro but not mature cathepsin D, nigericin caused an equivalent increase in the secretion of both pro and mature cathepsin D. Nigericin treatment did not have a strong impact on the absolute levels or the relative proportions of the intracellular cathepsin D species, expect for a mild increase in the intermediate form. These results exemplify how, despite all acting on the endolysosomal system, these agents lead to different downstream consequences.

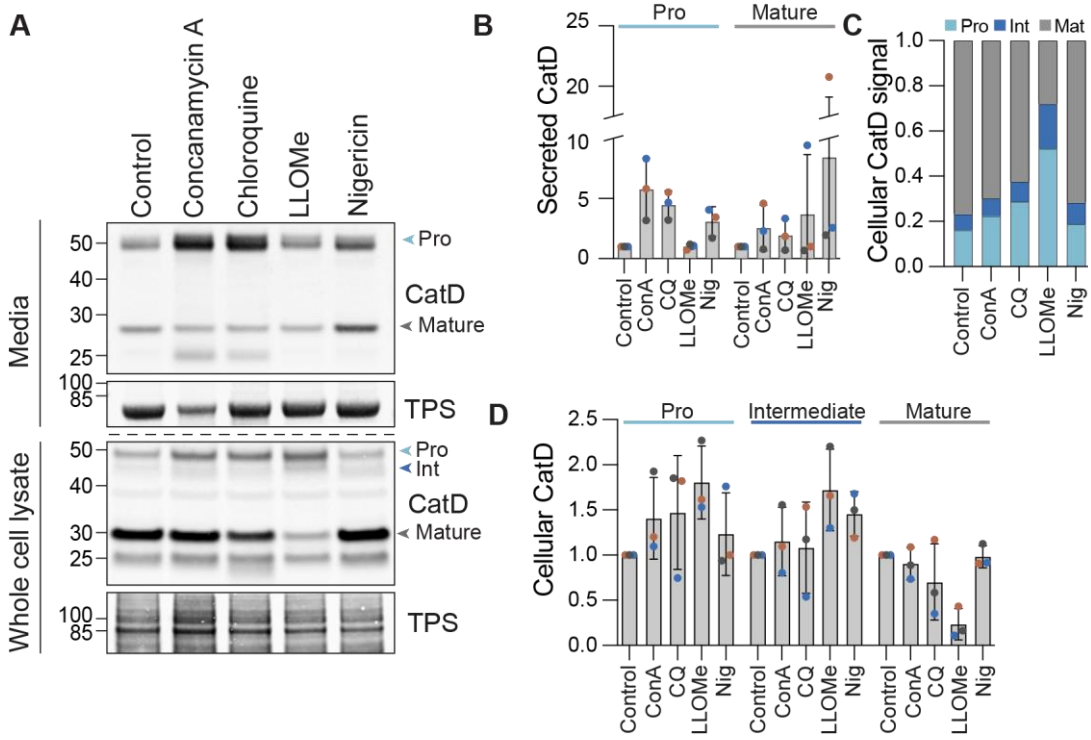

Figure 6.9 Effect of endolysosomal stress on extracellular release of cathepsin D

A RPE1 FlpIn Parentals cells were treated for 3 hours with 2 µM nigericin, 500 µM LLOMe or 100 µM chloroquine or DMSO control in serum-free Opti-MEM media. Adherent cells were then lysed in NP40 buffer. Media were collected and proteins were precipitated using TCA. Samples were analysed by western blotting and a representative western blot is shown. **B** Quantification of secreted cathepsin D in A. Values normalised to DMSO for each form of cathepsin D. *n* = 3. Each independent experiment is colour-coded. Bars represent mean ± SD. Angled line on y-axis represents a break in the axis. **C** Quantification of mean proportion of cellular cathepsin D forms in A as a function of total cathepsin D signal for each condition. *n* = 3. **D** Quantification of secreted cathepsin D in A. Values normalised to control for each form of cathepsin D. *n* = 3. Each independent experiment is colour-coded. Bars represent mean ± SD.

As the loss of mature cathepsin D after treatment with LLOMe did not lead to a corresponding increase in mature cathepsin D in the extracellular medium, I investigated whether it was subject to degradation by the proteasome or in some remaining functional residual lysosomes. RPE1 cells were treated with LLOMe in the presence of the proteasome inhibitor epoxomicin or concanamycin A (**Figure 6.10**). Neither treatment with epoxomicin nor concanamycin A prevented the LLOMe-induced loss of mature cathepsin D, suggesting that it is not being degraded by either the proteasome or the lysosome.

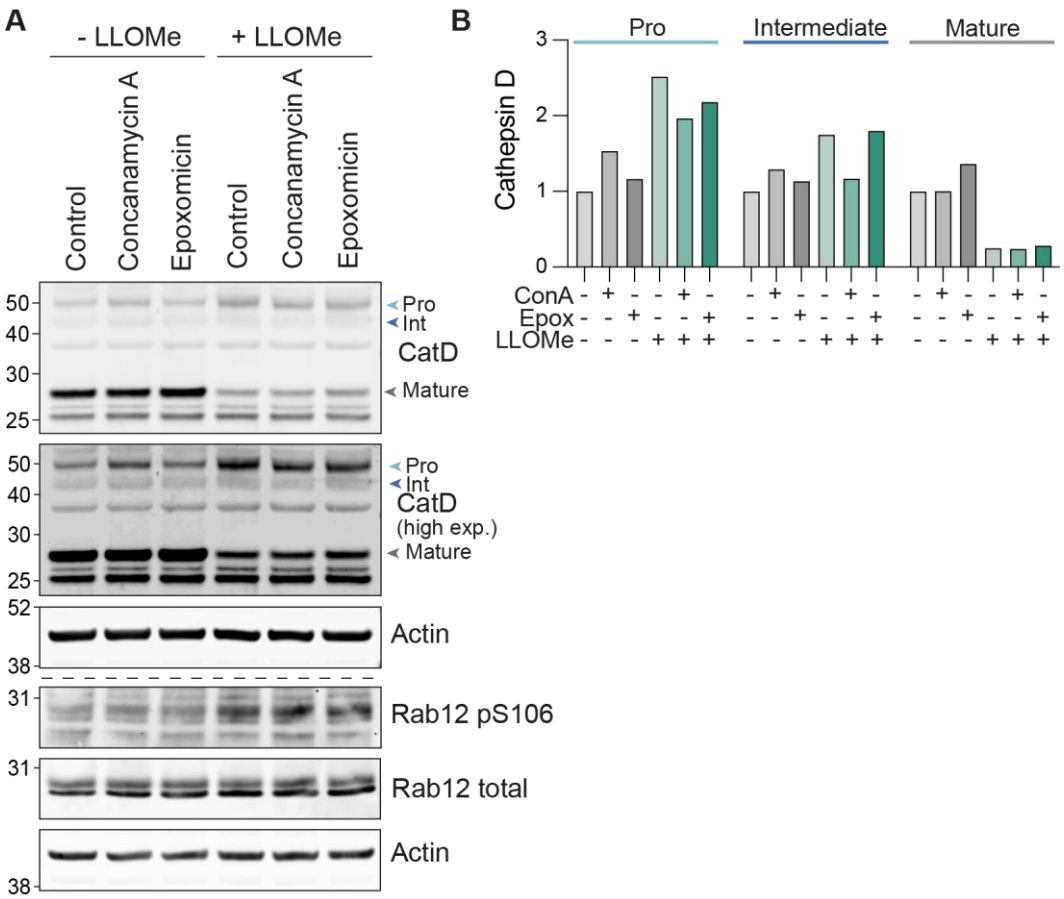

Figure 6.10 LLOMe treatment results in a loss of mature cathepsin D
A RPE1 FlpIn Parentals cells were treated for 3 hours with 500 µM LLOMe alone or with co-treatment with 100 nM concanamycin A (ConA) or 100 nM epoxomicin (Epox) prior to lysis and analysis by immunoblotting. **B** Quantification of A. Values are normalised to vehicle control for each cathepsin D (CatD) species. Data from a single experiment, *n* = 1.

To look at the dynamics of mature cathepsin D loss after LLOMe treatment, cells were treated with either 250 or 500 µM LLOMe, lysed after 15 , 30, 60, 90 or 120 minutes and the levels of cathepsin D analysed by western blotting (**Figure 6.11A**). A time-course of nigericin treatment was also included and the blots were probed for other

markers of lysosomal damage, including p62, LC3 and pS106-Rab12. Treatment with LLOMe caused a time-dependent decrease in mature cathepsin D and increase of pro cathepsin D (**Figure 6.11B**). The loss of mature cathepsin D occurred faster with higher concentrations of LLOMe. This indicates that the loss of mature cathepsin D is not an 'all-or-nothing' response after lysosomal rupture and may be due to gradual leakage from lysosomes over time. As seen previously, nigericin treatment did not cause loss of mature cathepsin D but caused a mild increase in pro and intermediate forms of cathepsin D.

Treatment with nigericin and LLOMe caused a comparable two-fold increase in Rab12 phosphorylation over two hours (**Figure 6.11C**). In contrast, lipidation of LC3-I to LC3-II was much more pronounced after LLOMe treatment compared to nigericin treatment. This suggests that there is no simple linear correlation between LC3 conversion and Rab phosphorylation in response to endolysosomal stress. Both treatment with LLOMe and with nigericin caused a mild loss of p62 over time.

After characterising the different effects of endolysosomal damage agents on cathepsin D, I investigated the effect of LRRK2 on these responses. RPE1 cells were pre-treated with MLi-2 for 15 minutes and then treated with chloroquine, LLOMe or nigericin. After 3 hours, conditioned media were collected and precipitated, adherent cells were lysed, and samples assessed for cathepsin D levels by immunoblotting (**Figure 6.12**). In the absence of lysosomal stress, inhibition of LRRK2 caused a mild decrease in the secretion of pro, intermediate and mature cathepsin D. In the presence of MLi-2, the nigericin-induced secretion of all forms of cathepsin D was mildly reduced. In contrast to published work, inhibition of LRRK2 did not reduce the secretion of intermediate cathepsin D in response to chloroquine treatment (Eguchi et al., 2018). Taken together, and with the caveat that these experiments require further validation with additional experimental repeats, this may suggest that in RPE1 cells, LRRK2 plays a role in cathepsin D secretion at steady state and in response to endolysosomal stress triggered by nigericin, but not by chloroquine. However, the mechanism by which the different forms of cathepsin D are secreted, and how LRRK2 plays a role in this, are not clear. Although the deacidification may cause an accumulation of unprocessed pro and intermediate forms of cathepsin D in the lysosome which are secreted via exocytosis in response to the endolysosomal stressors, the possibility that cathepsin D is secreted via the biosynthetic pathway under this setting cannot be excluded.

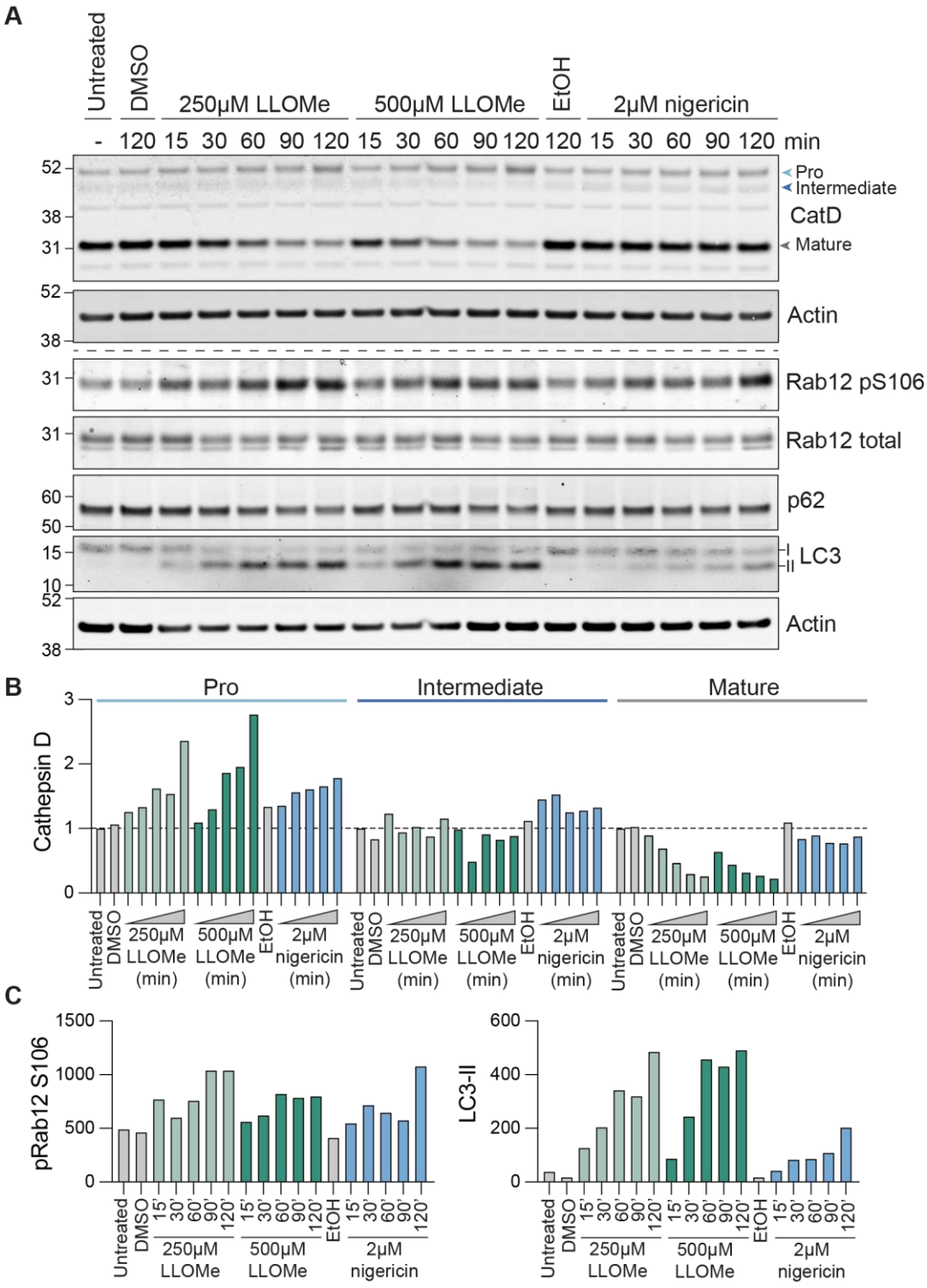

Figure 6.11 LLOMe treatment causes a time-dependent loss of mature cathepsin D

A RPE1 FlpIn Parentals cells were treated with LLOMe (250 or 500 μM) or nigericin (2 μM) for the times indicated. DMSO and ethanol (EtOH) vehicle treatments were for 120 minutes. Cells were then lysed and analysed by immunoblotting. **B** Quantification of A. Data are normalised to untreated control for each form of cathepsin D. **C** Quantification of A. Data are raw intensity values. Data from a single experiment, *n* = 1.

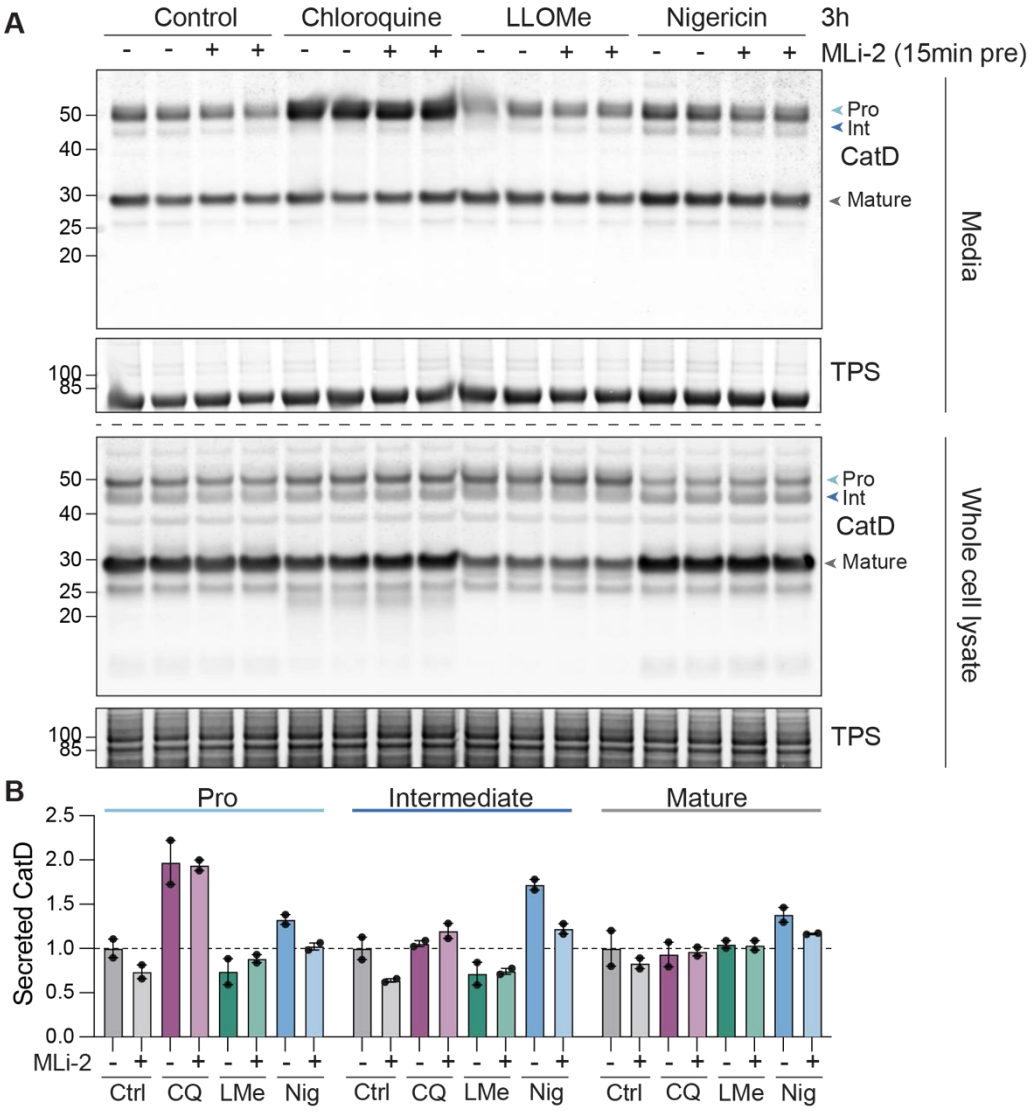

Figure 6.12 Effect of LRRK2 on endolysosomal damage-induced cathepsin D secretion

A RPE1 FlpIn Parental cells were pre-treated with 100 nM MLi-2 for 15 minutes before 3-hour treatment with 100 µM chloroquine (CQ), 500 µM LLOMe (LMe) or 2µM nigericin in serum-free Opti-MEM media. Adherent cells were then lysed in NP40 buffer. Media were collected and proteins were precipitated using TCA. Samples were analysed by western blotting. **B** Quantification of secreted cathepsin D in A. Values normalised to DMSO for each form of cathepsin D. Duplicate samples from a single experiment, *n* = 1. Bars represent mean and range.

6.3.2 Assessment of the effect of endolysosomal stressors on LC3 lipidation and recruitment to lysosomes

Osmotic stress has been shown to trigger the activation of the canonical autophagy pathway, resulting in v-ATPase-dependent lipidation of LC3 to the lysosomal membrane (Florey et al., 2015). Treatment with chloroquine, LLOMe and nigericin have all been shown to activate both canonical and non-canonical autophagy pathways (Cross et al., 2023; Florey et al., 2015; Jacquin et al., 2017).

To look at whether LLOMe and nigericin induced recruitment of LC3 to the lysosomes in RPE1 cells, the localisation of LC3 was assessed using immunofluorescence microscopy. Cells were treated with nigericin or LLOMe for 30 or 120 minutes and then fixed and stained with antibodies against LC3 and LAMP1 (**Figure 6.13**). In vehicle control-treated cells, LC3 showed a diffuse signal with few bright punctate structures. After 30 minutes treatment with LLOMe, LC3 recruitment to LAMP1 positive lysosomes could be observed. After two hours, many LC3-positive lysosomes could be seen engulfed within enlarged LAMP1-positive structures. These structures may represent autolysosomes, wherein damaged lysosomes are in the process of being cleared through lysophagy. Only minimal recruitment of LC3 to lysosomes was observed in nigericin-treated samples at the 30-minute timepoint. After two hours of incubation, LC3 recruitment was more prominent but the majority did not co-localise with LAMP1. This suggests that at longer time points nigericin is triggering general autophagy or selective autophagy of other organelles.

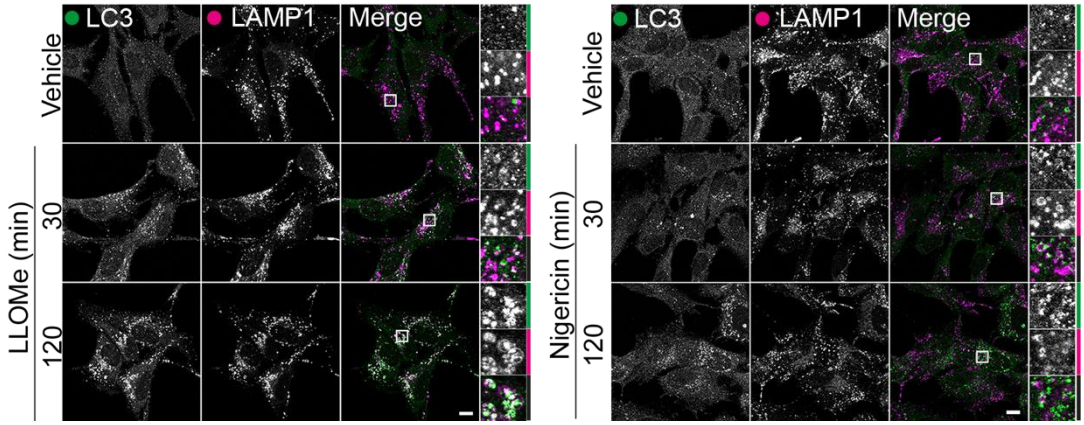

Figure 6.13 Endolysosomal damage triggers LC3 recruitment at lysosomes
RPE1 FlpIn Parental cells were treated with 500 µM LLOMe or 2 µM nigericin, or DMSO or EtOH vehicle control, for 30 or 120 minutes as indicated, then fixed and stained with the indicated antibodies. Single slice images were acquired on a Zeiss LSM900 confocal microscope using a 63x objective. Scale bar 10 µm. Data from a single experiment, *n* = 1.

Next, I looked at the effect of nigericin, LLOMe and chloroquine treatment on LC3 lipidation by western blotting (**Figure 6.14**). To investigate the contribution of non-canonical autophagy to this response, cells were pre-treated with concanamycin A. As non-canonical autophagy is v-ATPase dependent, addition of concanamycin A should abrogate non-canonical autophagy-driven LC3 lipidation. To look at the role of PI(3,5)P_2 and PIKfyve in the endolysosomal stress response, another set of conditions included pre-treatment with apilimod (**Figure 6.14**).

Treatment with apilimod alone caused a small increase in Rab12 phosphorylation and LC3 lipidation. Concanamycin A treatment did not affect basal Rab12 phosphorylation but caused a small increase in LC3-II, as expected by inhibiting autophagy flux. LRRK2 inhibition decreased Rab12 phosphorylation and on its own did not trigger LC3 lipidation. Nigericin caused an increase in pS106-Rab12 and LC3-II levels, which were both further amplified by apilimod. This suggests that PIKfyve plays a negative regulatory role in nigericin-induced endolysosomal damage. Conversely, concanamycin A reduced both Rab12 phosphorylation and LC3-II levels, suggesting that the nigericin-induced endolysosomal damage response depends on v-ATPase activity. In contrast, Rab12 phosphorylation and LC3 lipidation induced by LLOMe treatment was insensitive to concanamycin A or apilimod. Chloroquine caused an increase in Rab12 phosphorylation and an accumulation of LC3-II. This was unaffected by inhibition of PIKfyve by apilimod. In the presence of concanamycin A, chloroquine-induced lipidation of LC3 and Rab12 phosphorylation was blunted. As expected, inhibition of LRRK2 reduced Rab12 phosphorylation but had little effect on LC3 lipidation induced by nigericin, LLOMe or chloroquine.

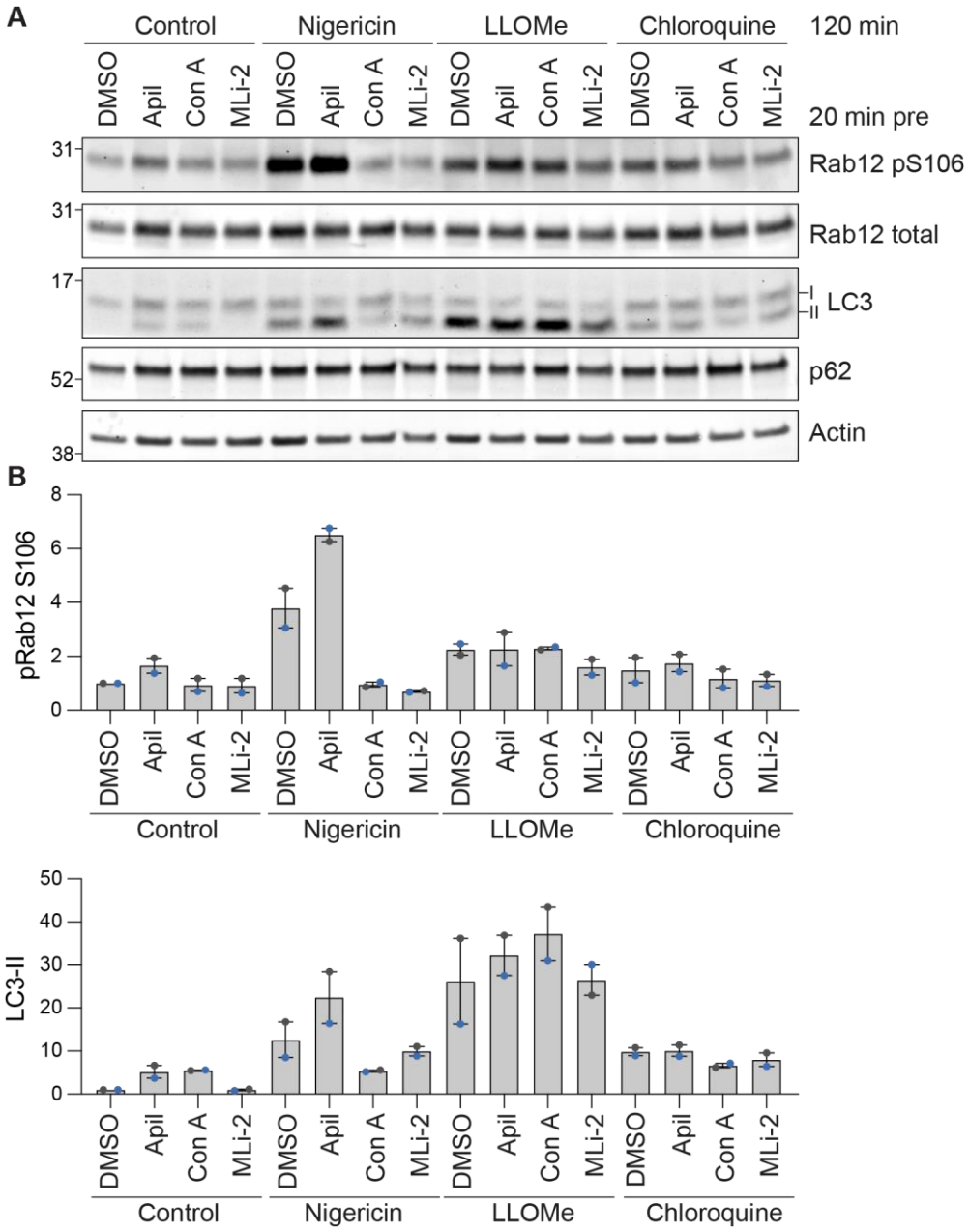

Figure 6.14 Effect of PIKfyve, v-ATPase and LRRK2 inhibition on the endolysosomal damage response

A RPE1 FlpIn Parentals cells were pre-treated with 150 nM apilimod, 100 nM concanamycin A, 100 nM MLi-2 or vehicle (DMSO) for 20 minutes before being treated for 2 hours with 2 µM nigericin, 500 µM LLOMe, 100 µM chloroquine or a vehicle control (DMSO). Cells lysates were analysed by western blotting. A representative western blot is shown. **B** Quantification of A. Values are normalised to DMSO control. *n* = 2. Each independent experiment is colour-coded. Bars represent mean and range.

6.3.3 Assessment of the effect of endolysosomal stressors on recruitment of the ESCRT machinery to lysosomes

Treatment with LLOMe has been shown to trigger the recruitment of ESCRT machinery components which function to repair the damaged lysosomal membrane (Radulovic et al., 2018; Skowyra et al., 2018). I wondered whether ESCRT recruitment to the lysosome is a specific response to LLOMe or is elicited by with other endolysosomal stressors. RPE1 cells were treated with LLOMe or nigericin for 30 minutes before fixation and processing for immunocytochemistry, probing for CHMP2B and ALIX with the lysosomal markers CD63 and LAMP1 (**Figure 6.15**). CHMP2B is a component of the ESCRT-III complex which, along with VPS4, facilitates membrane deformation and sealing (McCullough et al., 2018). The assembly of the ESCRT machinery to sites of lysosomal damage is mediated by ALIX, which itself is recruited by the Ca^{2+} sensor ALG2 (Shukla et al., 2022; Skowyra et al., 2018).

In vehicle control cells, both CHMP2B and ALIX showed a weak, diffuse signal with no clear localisation to late endosomes/lysosomes. After 30 minutes of LLOMe, but not nigericin, treatment, CHMP2B and ALIX showed a striking relocalisation to lysosomes. This reveals yet another difference between the damage induced by nigericin versus LLOMe and suggests that nigericin does not disrupt the integrity of the lysosomal membrane.

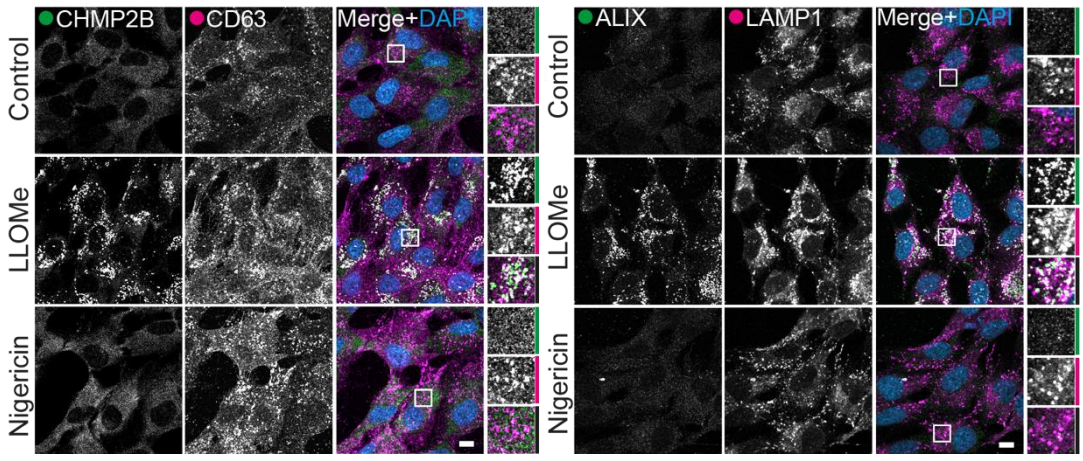

Figure 6.15 LLOMe treatment triggers recruitment of ESCRT machinery components to lysosomes

RPE1 FlpIn Parental cells were treated with 500 µM LLOMe, 2 µM nigericin or vehicle control (EtOH) for 30 minutes, then fixed and stained with the indicated antibodies and DAPI (DNA). Single slice images were acquired on a Zeiss LSM900 confocal microscope using a 63x objective. Scale bar 10 µm. Data from a single experiment, *n* = 1.

It has been previously shown that LRRK2 and Rab8a function in the recruitment of the ESCRT machinery to damaged lysosomes in macrophages (Herbst et al., 2020). The authors of the manuscript showed that in the absence of LRRK2 activity, achieved either by gene knockout or pharmacological inhibition, CHMP4B failed to be recruited to LLOMe-damaged lysosomes (Herbst et al., 2020). To investigate whether LRRK2 was required for the recruitment of the ESCRT machinery in the face of lysosomal damage in RPE1 cells, cells were pre-treated with MLi-2 for 15 minutes before lysosomal damage was induced with LLOMe. Cells were treated with LLOMe for 15 or 30 minutes and then fixed and stained with antibodies against CHMP2B and LAMP1 (**Figure 6.16A**). The number and average size of CHMP2B puncta within a cell over a set threshold value were quantified (**Figure 6.16B**). LAMP1 images were segmented to create a 'lysosome mask' which was then used to calculate the mean intensity of CHMP2B signal within the lysosome mask for each cell (**Figure 6.16C**). In control cells, few CHMP2B puncta were present. After 15- and 30-minutes treatment with LLOMe, a substantial amount of CHMP2B was recruited to lysosomes, illustrated by the increase in fluorescence signal and number of CHMP2B particles (>100 per cell) at lysosomes (**Figure 6.16B and C**). In the presence of LRRK2 inhibition, CHMP2B recruitment was slightly reduced after 15, but not 30, minutes of LLOMe treatment.

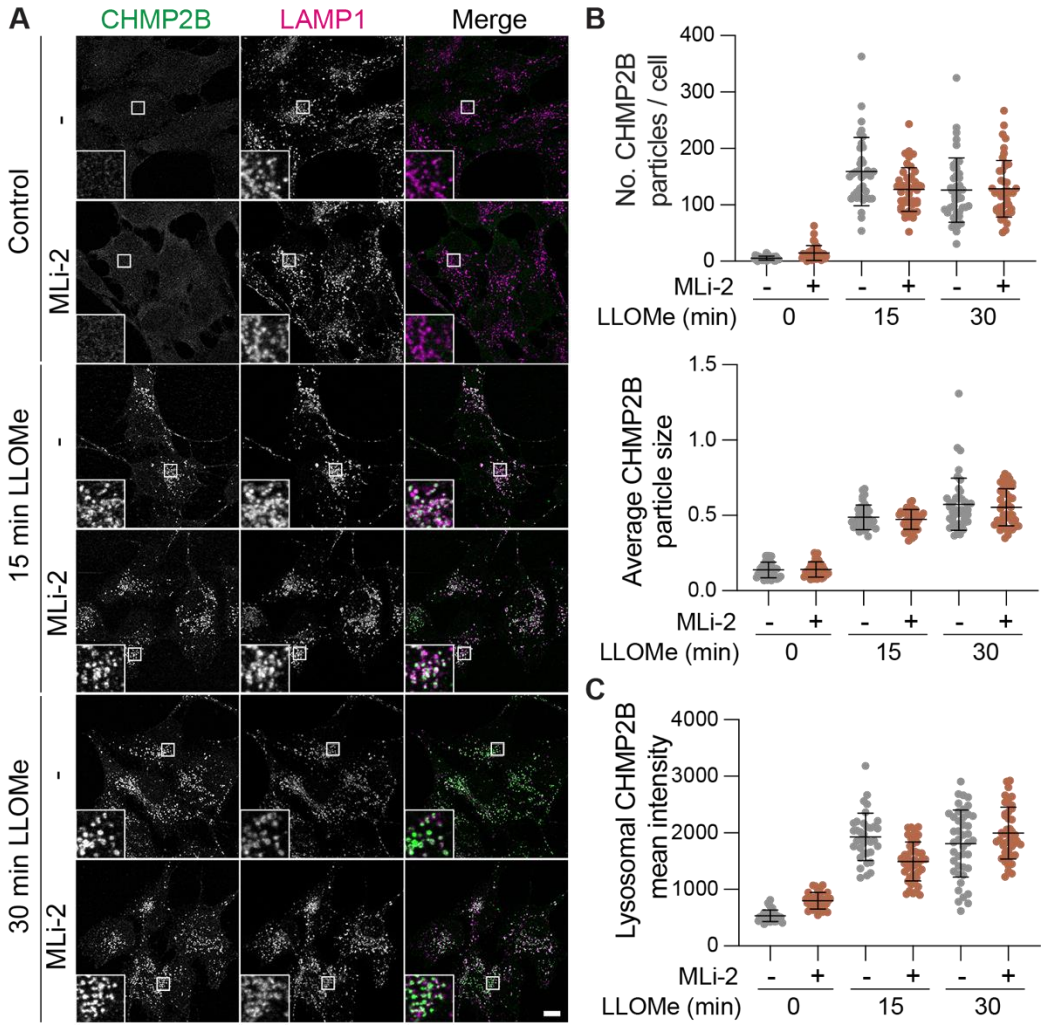

Figure 6.16 ESCRT recruitment to damaged lysosomes proceeds in the presence of LRRK2 inhibition

A RPE1 FlpIn Parental cells were pre-treated with 100 nM MLi-2 or vehicle (DMSO) for 15 minutes and then treated with 500μM LLOMe for 15 or 30 minutes before fixation and staining with the indicated antibodies. Single slice images were acquired on a Zeiss LSM900 confocal microscope using a 63x objective. Scale bar 10 μm. **B** Quantification of the number and size of CHMP2B puncta per cell. Bars represent mean ± SD. 33-44 cells quantified per condition, *n* = 1. **C** Quantification of mean CHMP2B intensity within LAMP1 puncta per cell. Bars are mean ± SD. 33-44 cells quantified per condition, *n* = 1.

6.3.4 Assessment of effect of endolysosomal stressors on Galectin-3 recruitment to lysosomes

Upon rupture of the lysosomal membrane, a subset of galectins bind to the exposed carbohydrate-rich luminal tails of lysosomal transmembrane proteins (Aits et al., 2015). As such, galectins can be used as markers of lysosomal damage. The galectins implicated in this process include galectin-1, galectin-3 and galectin-8 (Aits et al., 2015; Eapen et al., 2021; Jia et al., 2020, 2018). Galectin-3 has been shown to

be the primary galectin involved in lysosomal damage repair through co-ordinating the recruitment of the ESCRT machinery, whereas galectin-1 and galectin-8 promote lysosome clearance or lysosome biogenesis (Jia et al., 2020).

I was unable to visualise recruitment of galectin-3 to lysosomes after LLOMe treatment in RPE1 cells using several commercially available antibodies. I therefore introduced a tagged galectin construct to investigate galectin recruitment. I made use of a recently described 'lysokeima' probe which allows assessment of lysophagy in live cells (Eapen et al., 2021). The lysokeima reporter consists of monomeric mKeima linked to galectin-3. As discussed in **Section 5.3.2**, under neutral pH, mKeima has an emission spectrum that peaks at 620 nm and an excitation spectrum that peaks at 438 nm. Under acidic conditions, such as those within the lysosome, mKeima has an excitation spectrum which peaks at 550 nm while retaining the same emission spectrum. Therefore, the bimodal, pH-dependent excitation spectrum of mKeima facilitates the measurement of autophagic flux (Katayama et al., 2011).

In the case of mKeima-Gal3, the construct is cytosolic at steady state and emits fluorescence when excited by a 455 nm laser. Upon rupture of the lysosomal membrane, it is recruited to the lumen of the damaged lysosomes (**Figure 6.17A**). As the damage neutralises the lysosomal pH, mKeima-Gal3 is still excited by the 455 nm, but now has a punctate appearance. When the damaged lysosomes are autophagocytosed they retain a neutral pH until they fuse with functional lysosomes, creating an acidic environment and shifting the excitation peak of mKeima-Gal3. The lysokeima construct was stably introduced into the RPE1 FlpIn VPS35 WT 3B4 and [D620N] 1F3 cell lines using lentiviral transduction by Dr Hannah Elcocks. For experiments that weren't focussed on VPS35, uninduced RPE1 FlpIn VPS35 WT 3B4 lysokeima cells were used.

Using this reporter line, I investigated whether galectin-3 recruitment was unique to rupturing dipeptides (e.g. LLOMe) or whether it could be triggered by other agents which disrupt the endolysosomal system. To do this, cells expressing the lysokeima reporter were treated with LLOMe, chloroquine and nigericin for one hour and imaged (**Figure 6.17B**). A set of samples where the drugs were washed out after one hour and chased for 12 hours were also included to look at the progression of lysophagy. In untreated cells, the construct gave a largely cytosolic signal at 455 nm excitation and some faint punctate structures at 561 nm excitation. One hour incubation with LLOMe caused a strong recruitment of the lysokeima reporter to pH neutral, damaged lysosomes which fluoresced at 455 nm excitation. In contrast, there was no

observable lysosomal recruitment of lysokeima after treatment with nigericin or chloroquine. After LLOMe washout, punctate structures appeared in the 561 nm channel, signalling that lysophagy had occurred and the lysokeima reporter was now in autolysosomes.

To further understand the dynamics of lysophagy in the RPE1 cells, I repeated the LLOMe chase but this time acquired images at one-hour intervals following washout (**Figure 6.17C**). Unlike the previous experiment, some acidic lysokeima-positive lysosomes could be observed after one hour of LLOMe incubation. These could represent damaged lysosomes that have already undergone lysophagy or lysosomes which have undergone membrane repair via the action of the ESCRT machinery, and thus regained an acidic pH. In immunofluorescence experiments, I have observed LC3 puncta within enlarged lysosomes after 2 hours of LLOMe treatment (**Figure 6.13**), so it is possible that lysophagy could proceed within this timeframe. After one hour of washout, there was an increase in the number of lysosomes which had undergone an excitation shift and fluoresced in the 561 nm channel. This further increased up until 6 hours after washout, at which point there were few neutral lysosomes remaining. This indicates that the bulk of lysophagy occurs within 6 hours of insult with LLOMe in RPE1 cells.

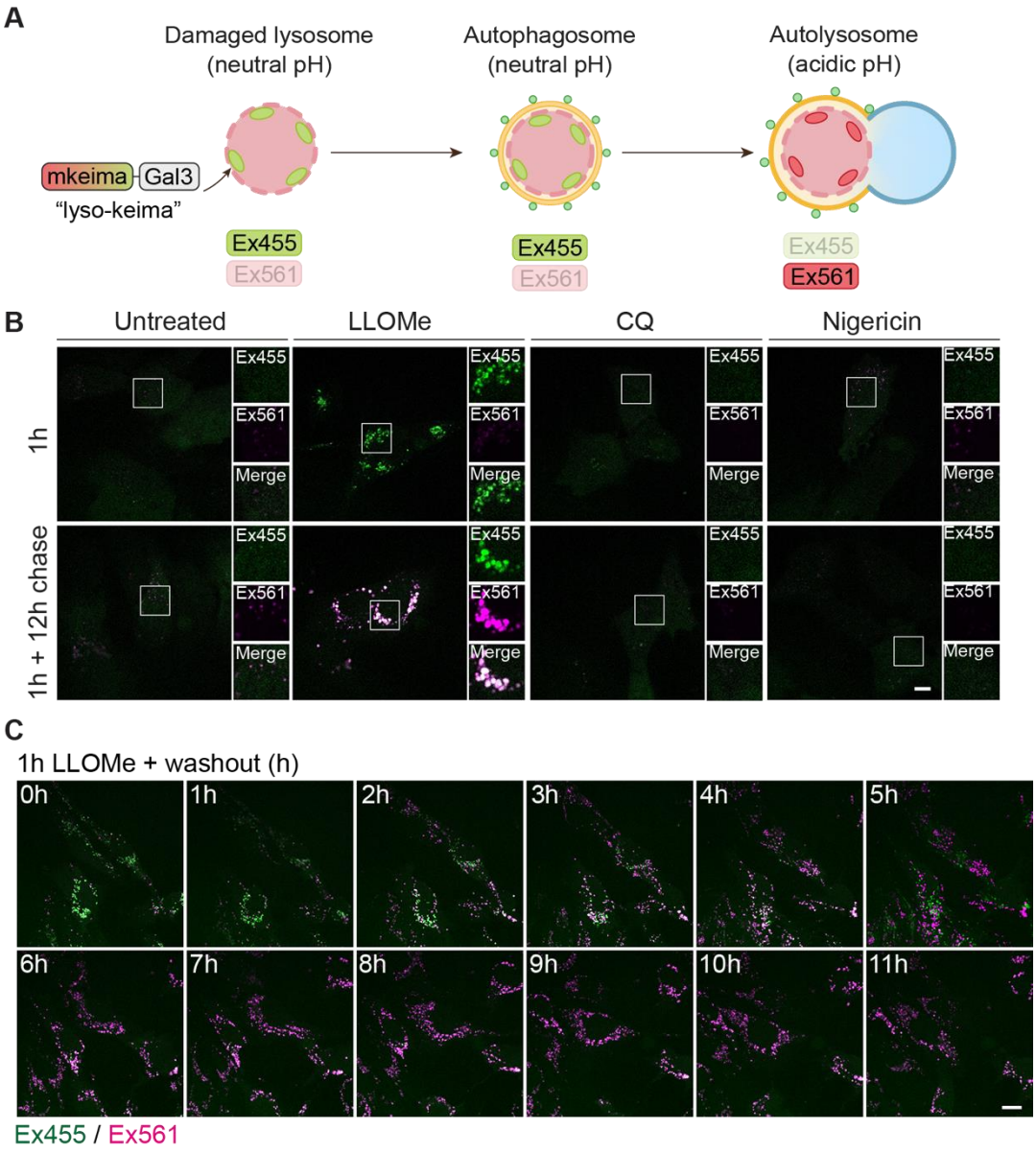

Figure 6.17 Assessment of lysophagy using lysokeima reporter

A Schematic of lysokeima reporter. At steady state, the mKeima-Gal3 "lysokeima" construct is cytosolic and emits fluorescence when excited with a 455 nm laser. Upon lysosomal membrane damage, lysosomes are neutralised and lysokeima is recruited. Damaged lysosomes are autophagocytosed. When autophagosomes fuse with functional lysosomes, the environment becomes acidic and the mKeima undergoes a spectral shift to emit fluorescence when excited with a 561 nm laser. **B** RPE1 FlpIn VPS35 WT 3B4 lysokeima cells (HA-VPS35 not induced with doxycycline) were treated with 500 μM LLOMe, 2 μM nigericin or 100 μM chloroquine and imaged after one hour of treatment or the treatments were washed out for 12 hours before imaging (1h + 12h chase). Live-cell images were acquired on a 3i spinning disk confocal microscope using a 63x objective. Scale bar 10 μm. Images were acquired by Dr Hannah Elcocks. Data from a single experiment, *n* = 1. **C** RPE1 FlpIn VPS35 WT 3B4 lysokeima cells (HA-VPS35 not induced with doxycycline) were treated with 500μM LLOMe for one hour. LLOMe was then washed out and live-cell images were acquired at one-hour intervals on a 3i spinning disk confocal microscope using a 40x objective. Scale bar 20 μm. Data from a single experiment, *n* = 1.

6.4 A role for VPS35 in the endolysosomal damage response

6.4.1 Knockdown of VPS35 attenuates endolysosomal damage-induced Rab phosphorylation

As the [D620N] mutation in VPS35 has been shown to cause hyperphosphorylation of LRRK2-substrate Rabs, I wondered whether VPS35 influences LRRK2's functions in the response to lysosomal damage. First, I investigated whether endogenous VPS35 was involved in LRRK2-mediated Rab phosphorylation in response to lysosomal damage. RPE1 FlpIn Parental cells were depleted of VPS35 using siRNA, then treated with nigericin, LLOMe or chloroquine for two hours before lysis and analysis of pS106-Rab12 levels by immunoblotting (**Figure 6.18A**). As in previous experiments (**Figure 6.14**), the strongest phosphorylation response was seen with nigericin (4-fold increase), which was significantly dampened upon depletion of VPS35 (**Figure 6.18B**). Likewise, the weaker Rab12 phosphorylation induced by LLOMe and chloroquine was also reduced by VPS35 depletion, although these changes did not reach significance. I also measured the levels of LC3 as another marker of endolysosomal damage. As seen previously (**Figure 6.14**), LLOMe treatment caused the greatest degree of LC3 lipidation, with a 14-fold increase in LC3-II levels. In contrast to Rab12 phosphorylation, depletion of VPS35, if anything, enhanced LC3 lipidation induced by endolysosomal damage.

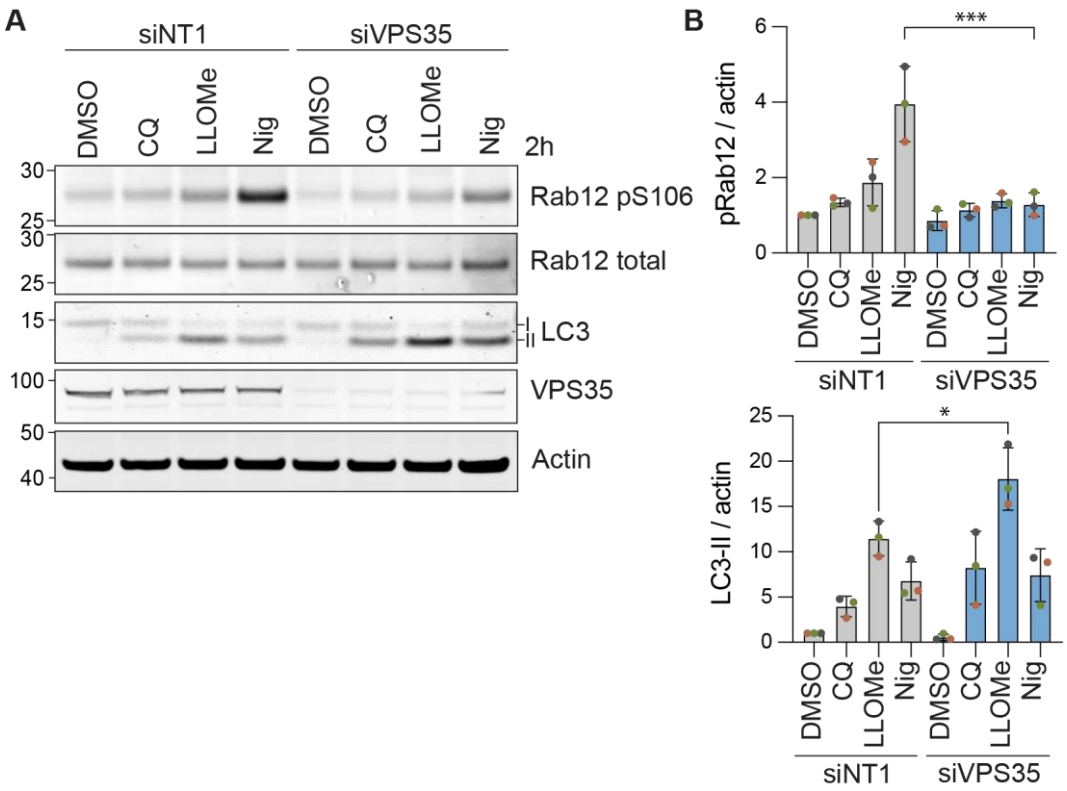

Figure 6.18 VPS35 is required for LRRK2-mediated Rab phosphorylation in response to lysosomal damage

A RPE1 FlpIn Parental cells were treated with 40 nM of control (non-targeting #1; NT1) or VPS35 (pooled) targeting siRNA oligonucleotides for 72 hours and then treated with 2 μM nigericin, 100 μM chloroquine, 500 μM LLOMe or vehicle (DMSO) for 2 hours prior to lysis and analysis by immunoblotting. A representative western blot is shown. **B** Quantification of A. Values are normalised to actin then to siNT1 DMSO only control. *n* = 3. Each independent experiment is colour-coded. Bars represent mean ± SD. One-way ANOVA with Šídák's multiple comparisons test performed on values normalised to sum of signal within a replicate then to actin. * $P < 0.05$, *** $P < 0.001$.

6.4.2 VPS35[D620N] amplifies endolysosomal damage-induced Rab phosphorylation

Given that VPS35 appeared to play a role in the response to endolysosomal damage, I next investigated the effect of the [D620N] mutation in this context. RPE1 FlpIn VPS35 WT 3B4 and [D620N] 1F3 cells were induced to express HA-VPS35 for 24 hours and then treated with either 0.1 or 2 μM nigericin for one hour. Rab phosphorylation was then assessed by immunoblotting (**Figure 6.19A**). As shown previously (**Figure 6.5**), treatment with nigericin induced a concentration-dependent increase in the phosphorylation of Rab10 and Rab12. At both concentrations of nigericin, Rab12 phosphorylation was significantly enhanced in induced RPE1 FlpIn VPS35 [D620N] cells compared with non-induced controls (**Figure 6.19B**). Moreover, VPS35[D620N] significantly enhanced pT73-Rab10 levels at the higher nigericin

concentration. This was not the case in the isogenic wild type VPS35-expressing cells. This demonstrates that the amplification effect is specific to the mutation and not due to VPS35 overexpression.

To confirm that the enhancement in Rab phosphorylation seen in the [D620N] mutant cells in response to nigericin was mediated by LRRK2, cells were treated with nigericin in the presence of the LRRK2 inhibitor MLi-2 (**Figure 6.20**). For all cell lines, including those expressing VPS35[D620N], co-treatment with MLi-2 abolished nigericin-induced Rab phosphorylation. This confirms that the enhanced Rab phosphorylation observed in VPS35[D620N]-expressing cells is dependent on LRRK2 kinase activity.

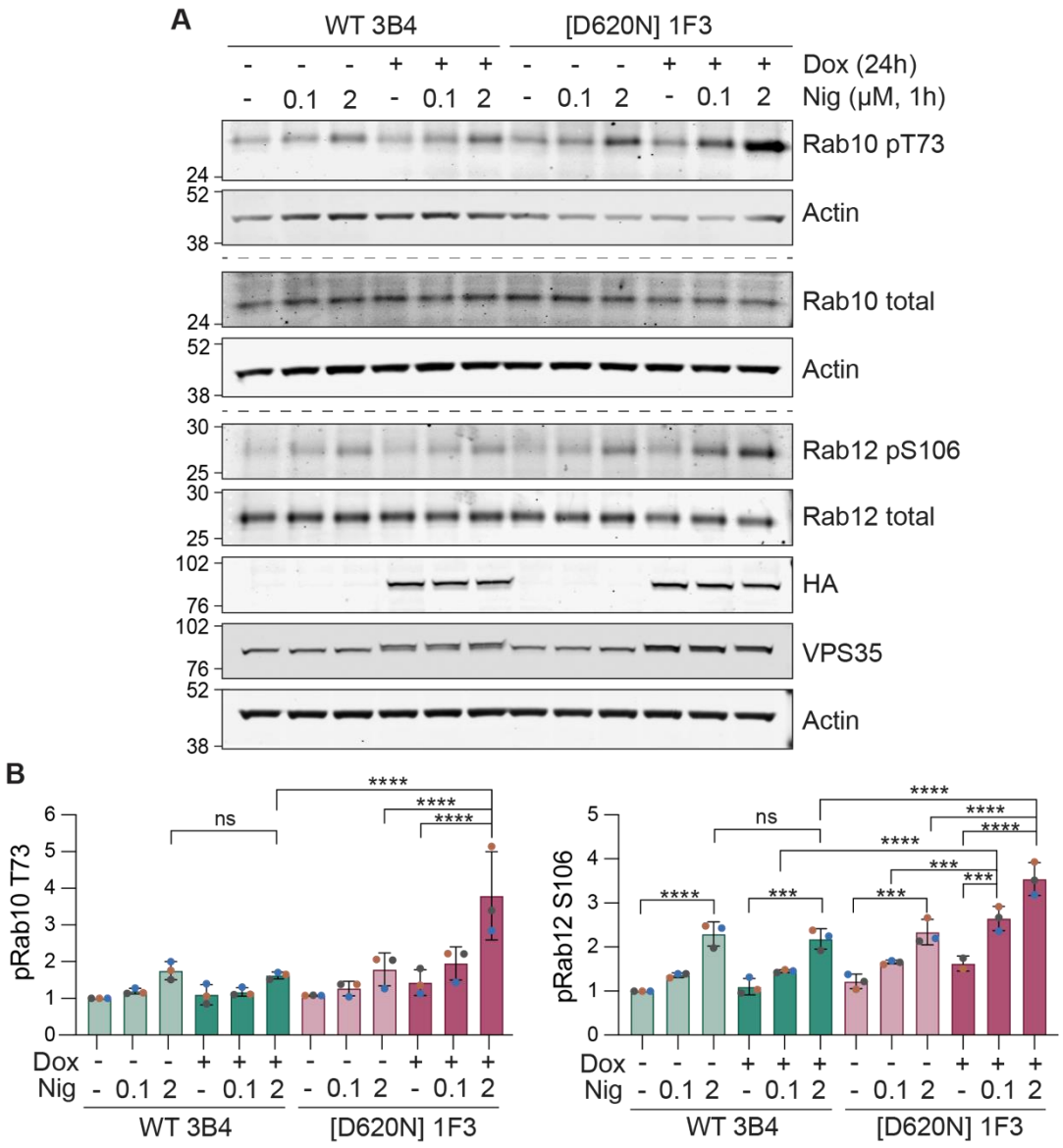

Figure 6.19 Mutation of VPS35 causes an enhancement of Rab10 and Rab12 phosphorylation in response to nigericin treatment

A RPE1 FlpIn HA-VPS35 WT 3B4 and [D620N] 1F3 cells were induced with doxycycline for 24 hours before being treated with ethanol vehicle control or nigericin at the indicated concentrations for 60 minutes, lysed and analysed by western blotting. **B** Quantification of A. Signals normalised to 'WT – DOX' vehicle control sample per replicate. *n* = 3. Each independent experiment is colour-coded. Bars represent mean ± SD. One-way ANOVA with Tukey's multiple comparisons test performed on values normalised to sum of signal within a replicate. *** $P < 0.001$, **** $P < 0.0001$.

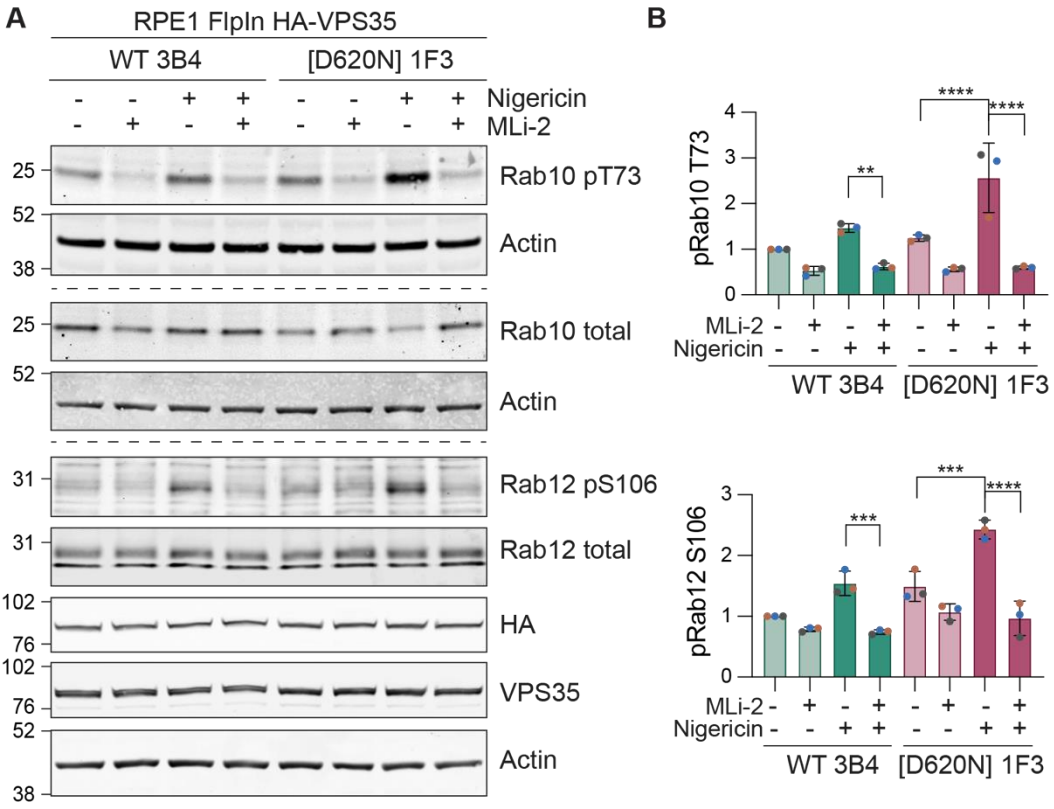

Figure 6.20 LRRK2 mediates [D620N] sensitised Rab phosphorylation in response to nigericin

A RPE1 FlpIn HA-VPS35 WT 3B4 and [D620N] 1F3 cells were induced with doxycycline for 24 hours before being treated with 2 μM nigericin or vehicle (EtOH) and 100 nM MLi-2 or vehicle (DMSO) for 60 minutes, lysed and analysed by western blotting. A representative western blot is shown. **B** Quantification of A. Signals normalised to 'WT – DOX' vehicle only control treated samples per replicate. *n* = 3. Each independent experiment is colour-coded. Bars represent mean ± SD. One-way ANOVA with Tukey's multiple comparisons test performed on values normalised to sum of signal within a replicate. ** $P < 0.01$, *** $P < 0.001$, **** $P < 0.0001$.

I next investigated whether the amplification of Rab phosphorylation seen after nigericin treatment in the VPS35[D620N] cells was specific to nigericin treatment or was common to other agents causing endolysosomal damage. To this end, I treated

cells with 50 μM or 500 μM LLOMe and analysed the levels of phopshoRab12 S106 by western blotting (**Figure 6.21A**). At 500 μM LLOMe, but not 50 μM, a robust increase in Rab phosphorylation could be measured (**Figure 6.21B**). Upon expression of VPS35[D620N], treatment with 500 μM LLOMe led to a 4.7-fold increase in Rab12 phosphorylation, which was significantly higher than in uninduced and wild type-expressing cells. I also probed for the autophagy markers LC3 and p62. Treatment with 500 μM LLOMe caused an increase in lipidated LC3, which was not significantly altered by expression of wild type or [D620N] mutant VPS35. Total p62 levels were not affected by LLOMe treatment not expression of wild type nor mutant VPS35. It was possible to discern a small upshift in the p62 band after LLOMe treatment, which I hypothesised could represent phosphorylation or ubiquitylation of p62. There was no difference to this upshift upon expression of wild type or [D620N] mutant VPS35.

Next, I investigated whether the enhancement of LLOMe-induced Rab phosphorylation was LRRK2 dependent. Addition of the LRRK2 inhibitor MLi-2 abolished all LLOMe-induced Rab phosphorylation in the absence and presence of VPS35 wild type and mutant expression (**Figure 6.22**).

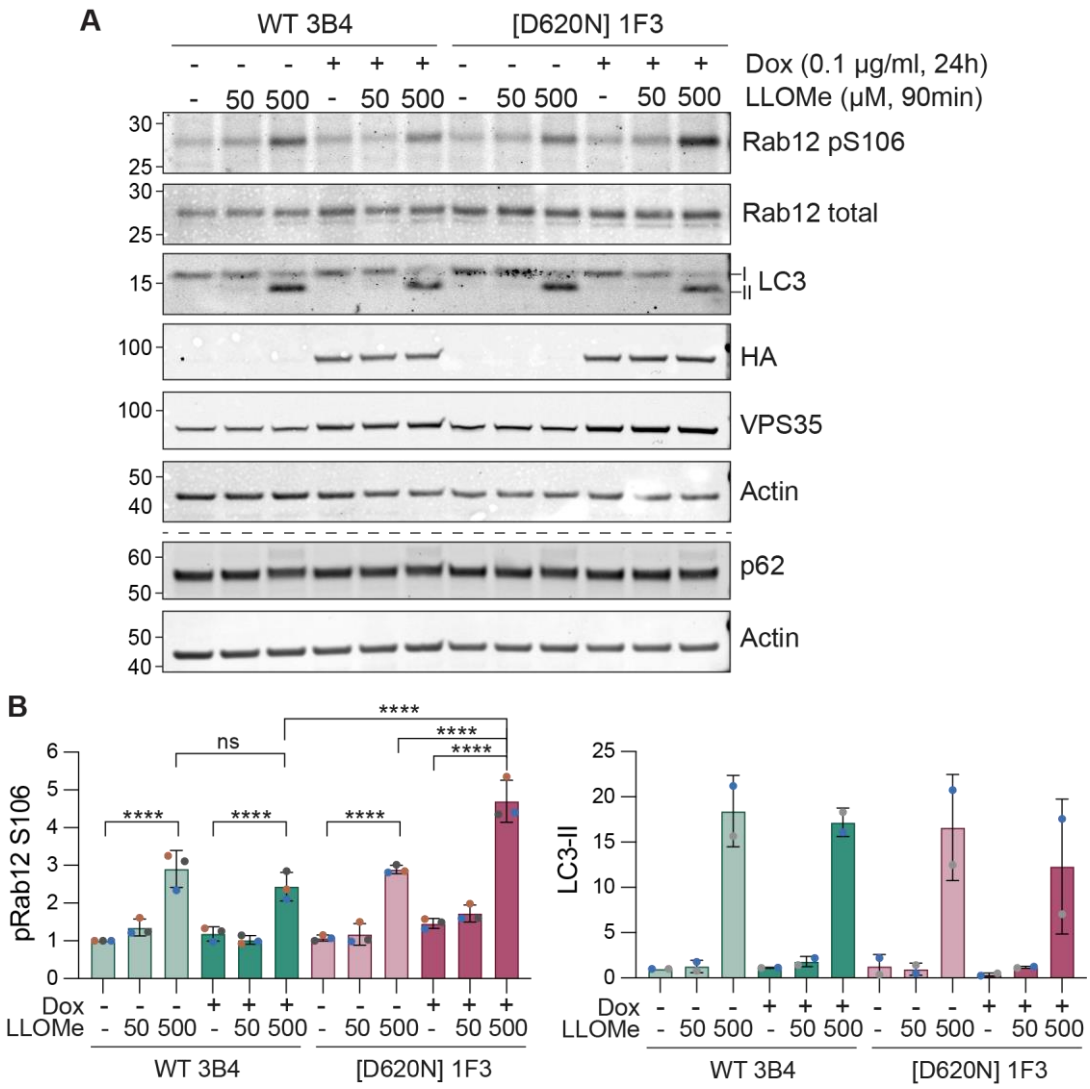

Figure 6.21 Mutation of VPS35 causes an enhancement of Rab10 and Rab12 phosphorylation in response to LLOMe treatment

A RPE1 FlpIn HA-VPS35 WT 3B4 and [D620N] 1F3 cells were induced with doxycycline for 24 hours before being treated with LLOMe at the indicated concentrations vehicle (EtOH) for 90 minutes, lysed and analysed by immunoblotting. A representative western blot is shown. **B** Quantification of A. Signals normalised to 'WT – DOX' vehicle control samples per replicate. *n* = 2 – 3 independent experiments. Each independent experiment is colour-coded. Bars represent mean ± SD. One-way ANOVA with Tukey's multiple comparisons test performed on values normalised to sum of signal within a replicate. **** $P < 0.0001$.

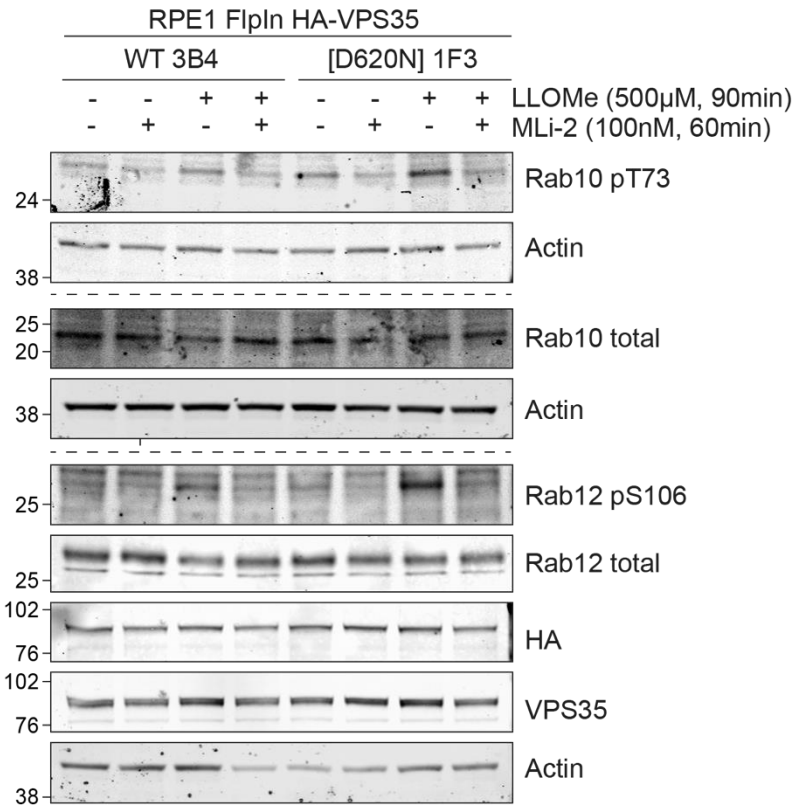

Figure 6.22 LRRK2 mediates [D620N] sensitised Rab phosphorylation in response to LLOMe
A RPE1 FlpIn HA-VPS35 WT 3B4 and [D620N] 1F3 cells were induced with doxycycline for 24 hours before being treated with 500 µM LLOMe or vehicle (DMSO) for 90 minutes. Cells were treated with 100 nM Mli-2 or vehicle (DMSO) for one hour prior to lysis and analysis by immunoblotting. Data from a single experiment, *n* = 1.

After establishing that the [D620N] VPS35 mutant enhanced Rab phosphorylation basally and under conditions of endolysosomal stress, I wondered whether this was reflecting greater recruitment of LRRK2 substrate Rabs to the lysosomal membrane. To investigate this, I performed subcellular fractionation to isolate total membrane and cytosol fractions from cells expressing wild type or [D620N] HA-VPS35 treated with nigericin or LLOMe for one hour prior to fractionation (**Figure 6.23A**). As expected, Rab12 phosphorylation was enhanced in control [D620N] cells compared to wild type when looking at the post-nuclear supernatant. This was further elevated after nigericin and LLOMe treatment. This pattern was mirrored in the membrane fraction (**Figure 6.23B**). Little pS106-Rab12 was detectable in the cytosolic fraction. In cells expressing wild type VPS35, treatment with LLOMe and nigericin led to a ~1.5-fold increase in Rab12 at membranes. In VPS35 [D620N]-expressing cells, total Rab12 levels were elevated in the membrane fractions at steady state, and this was not further increased by nigericin or LLOMe treatment. Looking at pS106-Rab12 levels at

membranes, this was elevated under basal conditions and further enhanced by nigericin and LLOMe treatment upon expression of [D620N] mutant, but not wild type VPS35.

Analysis of LRRK2 levels revealed no difference in the amount associated to membranes in wild type and [D620N] mutant VPS35-expressing cells. Treatment with LLOMe caused a decrease in the amount of LRRK2 in the membrane fraction. This was surprising as LLOMe has previously been shown to trigger recruitment of LRRK2 to the lysosomal membrane by immunofluorescence microscopy (Herbst et al., 2020). It is possible that the apparent loss of LRRK2 at membranes in this experiment is due to dissociation of LRRK2 from the lysosomes during fractionation.

JIP4 is a Rab10 effector which preferentially binds to Rab10 when it is phosphorylated by LRRK2 at the T73 site (Waschbüsch et al., 2020). Furthermore, treatment with LLOMe has been shown to cause a recruitment of JIP4 to the lysosome where it orchestrates the formation of lysosomal tubules (Bonet-Ponce et al., 2020). I probed the fractionated samples for JIP4 to investigate whether I could observe this proposed recruitment to membranes following LLOMe treatment, and whether this was influenced by the VPS35[D620N] mutation. However, I could only detect JIP4 in the cytosolic fractions.

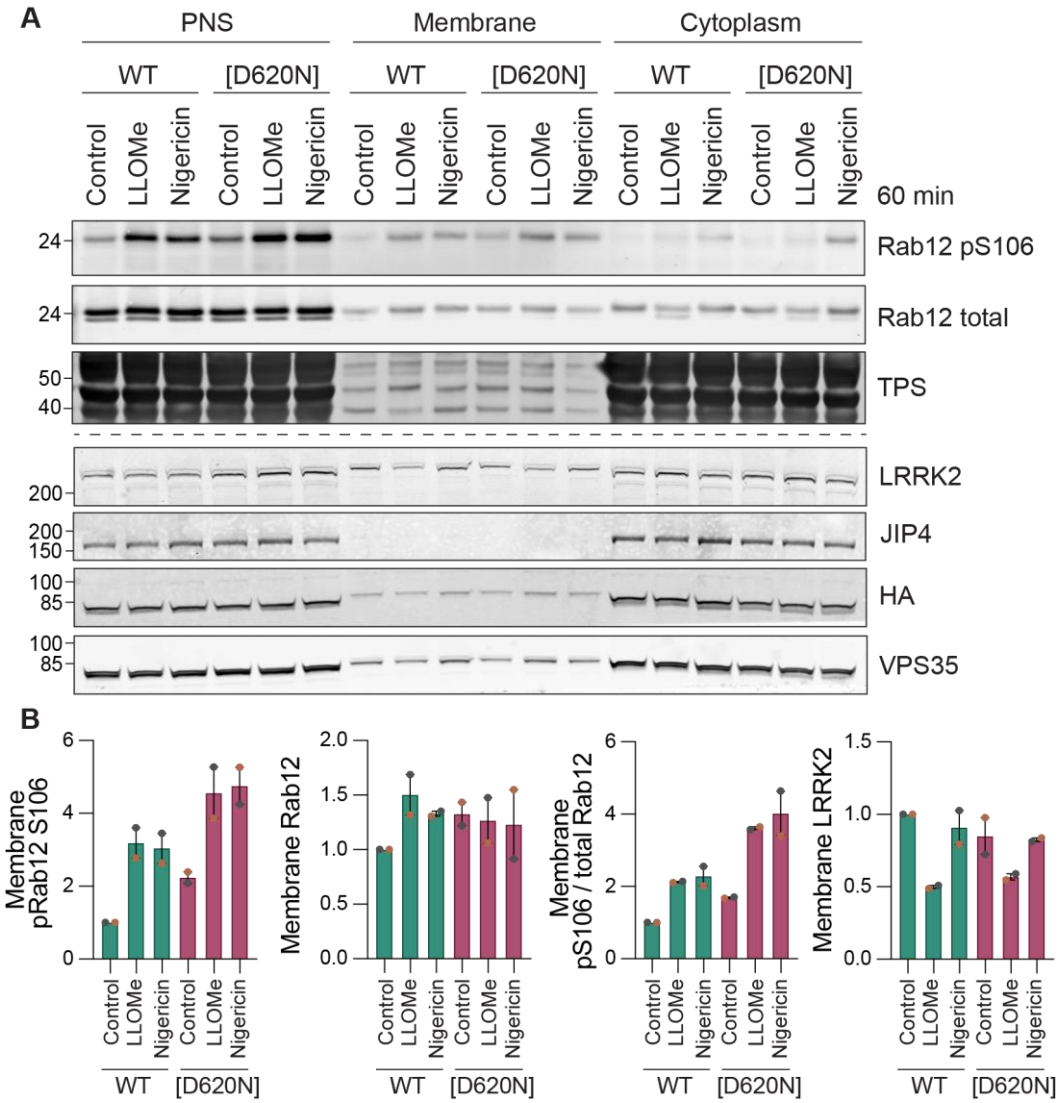

Figure 6.23 VPS35[D620N] enhances phosphorylated membrane-bound Rab12

A Subcellular fractionation of RPE1 FlpIn VPS35 WT 3B4 and [D620N] 1F3 cells induced with 0.1 µg/ml doxycycline for 24 hours and then treated with 500 µM LLOMe, 3 µM nigericin or vehicle control (DMSO) for 60 minutes. PNS; post nuclear supernatant, TPS; total protein stain. **B** Quantification of A. Signals normalised to 'WT – DOX' control samples per replicate. *n* = 2. Each independent experiment is colour-coded. Bars represent mean and range.

Based on the finding that treatment with apilimod alone did affect Rab phosphorylation but potentiated nigericin-induced Rab phosphorylation (**Figure 6.14**), I wondered what the consequence of apilimod treatment would be in VPS35[D620N] mutant cells. To investigate this, RPE1 FlpIn VPS35 WT 3B4 and [D620N] 1F3 were induced with doxycycline, treated with apilimod for two hours and Rab12 phosphorylation was analysed by western blotting (**Figure 6.24**). In uninduced cells and cells expressing wild type VPS35, treatment with apilimod resulted in a very small increase in Rab phosphorylation (**Figure 6.24B**). In cells expressing [D620N] mutant VPS35, basal

Rab phosphorylation was elevated, and this was further increased by addition of apilimod. This suggests that PIKfyve inhibition may also activate LRRK2 to a small extent, which is more apparent when LRRK2 activity is already increased, such as when VPS35[D620N] is expressed.

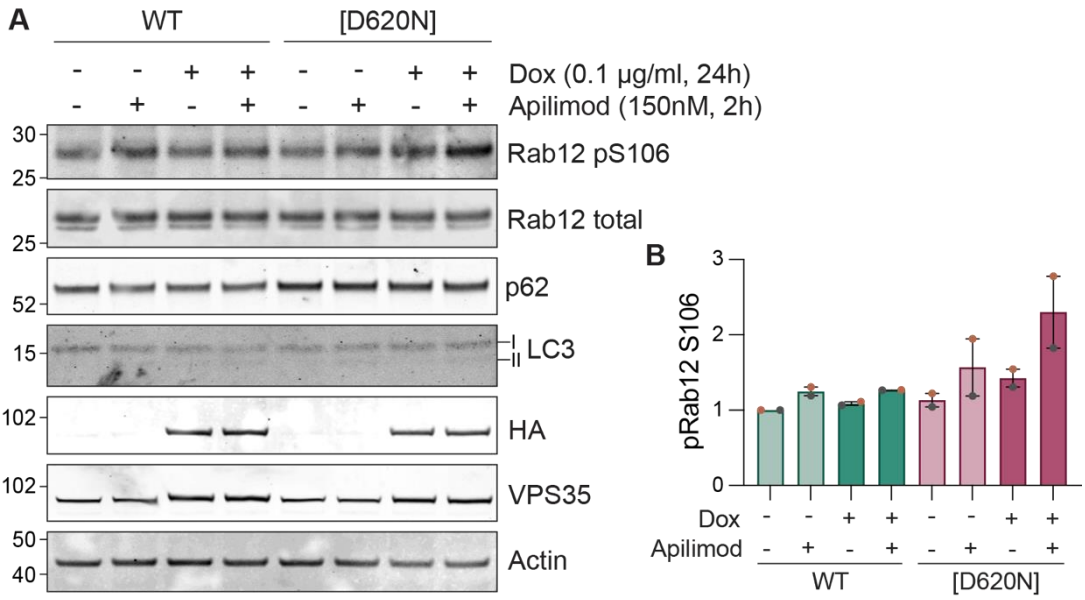

Figure 6.24 PIKfyve inhibition further increases Rab12 phosphorylation in RPE1 FlpIn VPS35[D620N] cells

A RPE1 FlpIn HA-VPS35 3B4 and [D620N] 1F3 cells were induced with 0.1 µg/ml doxycycline for 24 hours, then treated with 150 nM apilimod or vehicle (DMSO) for 2 hours prior to lysis and analysis by immunoblotting. A representative western blot is shown. **B** Quantification of A. Values normalised to 'WT – DOX' control. *n* = 2. Each independent experiment is colour-coded. Bars represent mean and range.

6.4.3 VPS35[D620N] does not affect basal lysosome morphology and distribution

As cells expressing [D620N] mutant VPS35 displayed greater localisation of Rab12 to membranes at steady state, I speculated whether the [D620N] mutation was causing lysosomal stress, which, in turn, was triggering LRRK2 activation. RPE1 FlpIn cells expressing wild type or [D620N] mutant HA-VPS35 were stained for LAMP1 by immunocytochemistry (**Figure 6.25A**). The average size of LAMP1 positive lysosomes was not significantly affected by expression of VPS35[D620N], suggesting that the mutation does not impact lysosomal morphology (**Figure 6.25B**). In addition, the distribution of lysosomes was assessed by plotting lysosome positioning curves

and found to be unaffected by wild type or [D620N] mutant VPS35 expression (**Figure 6.25C**).

RPE1 FlpIn VPS35 WT 3B4 and [D620N] 1F3 cells were next stained with Lysotracker Red to visualise lysosomes by live-cell imaging (**Figure 6.25D**). In line with the immunofluorescence data, there were no differences in the lysosome size or distribution between wild type and [D620N]-expressing cells, nor between uninduced controls. Quantification of the intensity of Lysotracker puncta revealed no differences between the conditions (**Figure 6.25E**). Together, these results suggest that the [D620N] mutation does not cause overt lysosomal stress.

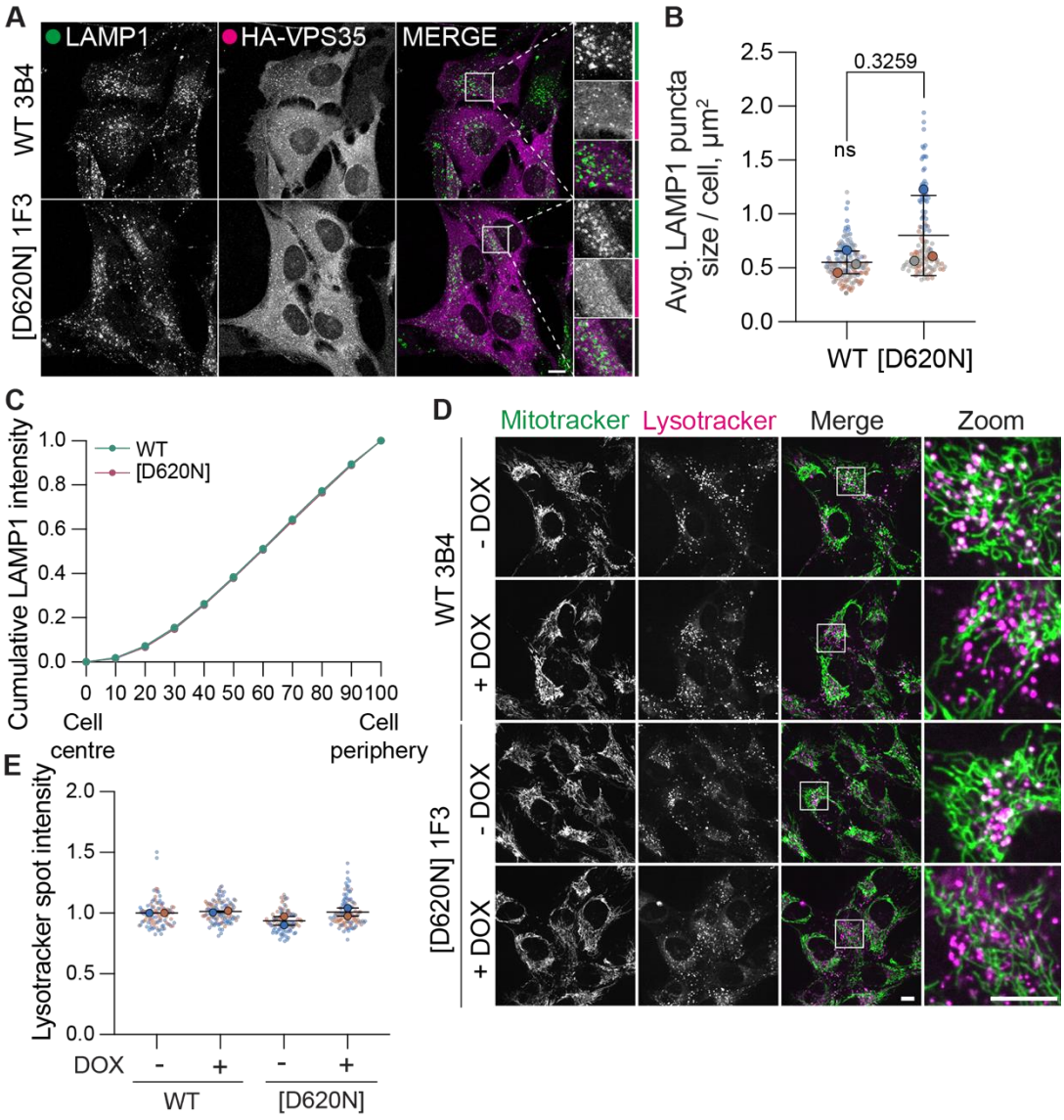

Figure 6.25 VPS35[D620N] does not alter lysosomal morphology and positioning

A RPE1 FlpIn VPS35 WT 3B4 and [D620N] 1F3 cells were induced with doxycycline for 24 hours before fixation and staining with the indicated antibodies. Images were acquired on a Zeiss LSM900 confocal microscope using a 63x objective. 10 µm scale bar. **B** Quantification of the average size of

LAMP1-positive lysosomes per cell. *n* = 3, 36-54 cells quantified per condition per experiment. Each independent experiment is colour-coded. Transparent circles with no outline represent values for each cell in an experiment, opaque circles with black outlines correspond to mean values for each experiment. Bars represent mean ± SD. **C** Mean cumulative LAMP1 intensity as a function of total LAMP1 intensity by concentric cell segmentation at 10% decrements. 36-54 cells quantified per condition, *n* = 3. Data represent mean ± standard deviation (not visible). **D** RPE1 FlpIn VPS35 WT 3B4 and [D620N] 1F3 cells were induced with doxycycline for 24 hours and stained with Mitotracker Green and Lysotracker Red DND-99 before live-cell imaging using a 63x objective on a 3i spinning disk confocal microscope. Scale bar 10 µm. **E** Quantification of the intensity of Lysotracker particles. 46 - 55 cells quantified per condition per experiment, *n* = 2. Each independent experiment is colour-coded. Transparent circles with no outline represent values for each cell in an experiment, opaque circles with black outlines correspond to mean values for each experiment. Bars represent mean and range.

6.4.4 VPS35[D620N] does not affect lysosome damaged-induced cathepsin D release

Given that the [D620N] mutation in VPS35 was causing enhanced lysosomal stress-induced Rab phosphorylation, I set out to investigate what the downstream consequences of this may be. As previous work in the literature and my work above (**Figure 6.12** and **Figure 6.16**) has shown LRRK2 to play a role in lysosomal stress-induced lysosomal exocytosis and ESCRT recruitment, these were the natural areas to explore.

Therefore, I looked at the effect of the VPS35[D620N] mutation on cathepsin D levels in the context of lysosomal damage. Expression of HA-VPS35 was induced for 24 hours in RPE1 FlpIn VPS35 WT 3B4 and [D620N] 1F3 cells and then adherent cells were washed thoroughly and incubated with nigericin in serum-free Opti-MEM media for 3 hours. The conditioned media were collected and subjected to protein precipitation using TCA and the adherent cells were lysed. The samples were then analysed by western blotting for cathepsin D (**Figure 6.26A**). Steady-state cellular levels of cathepsin D were unaltered by the [D620N] mutation, consistent with the results from a previous experiment (**Figure 4.4**). As previously shown (**Figure 6.9**), nigericin treatment caused an increase of pro, intermediate and mature cathepsin D into the media, which was unaffected by expression of either wild type or [D620N] VPS35. This suggests that, despite the enhanced LRRK2 activation in the VPS35[D620N] cells, secretion of lysosomal contents following nigericin treatment is not altered. This contrasts with pharmacological inhibition of LRRK2 activity, which decreased nigericin-induced cathepsin D secretion (**Figure 6.12**).

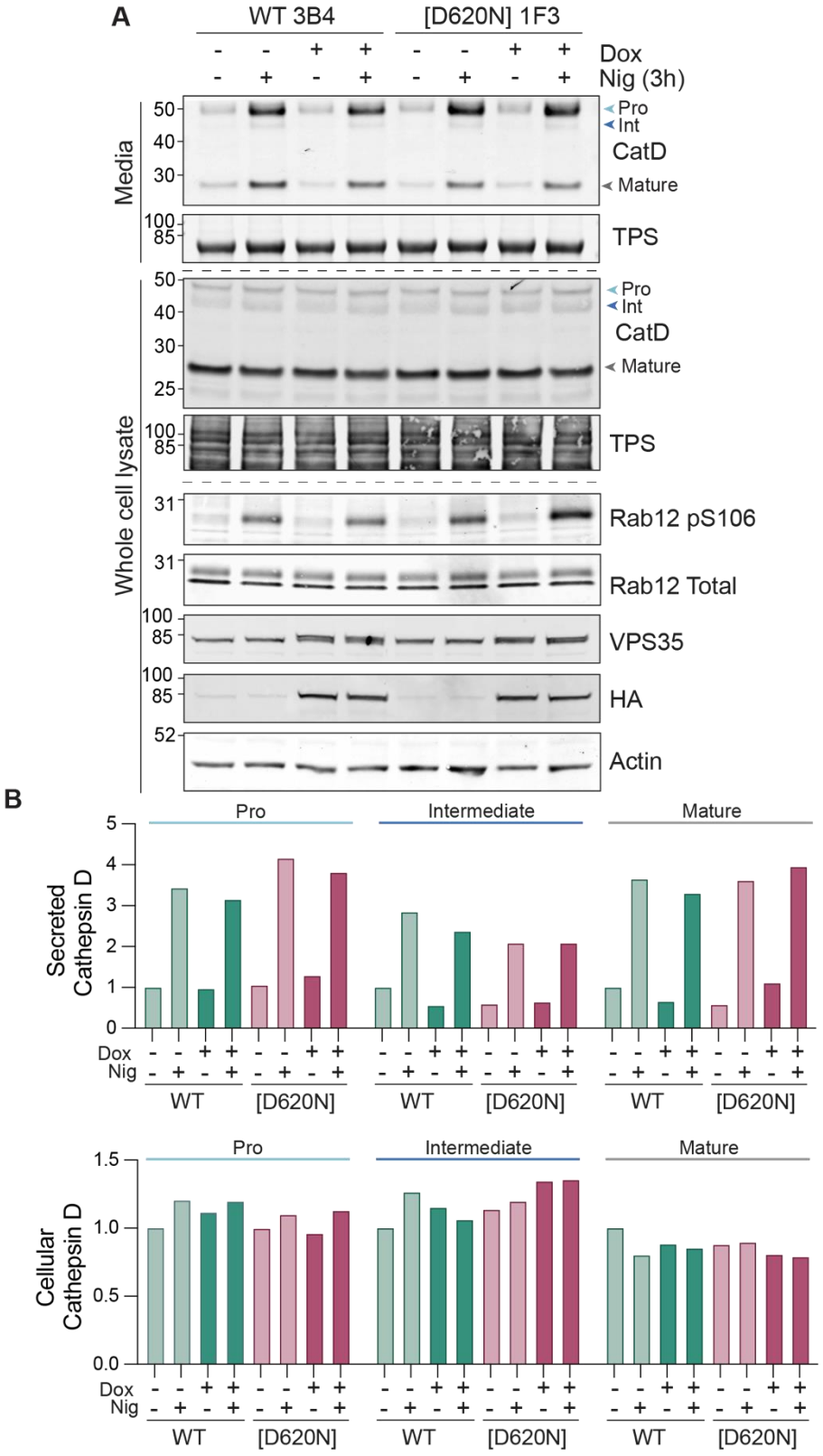

Figure 6.26 VPS35[D620N] does not affect nigericin-induced extracellular cathepsin D secretion

A RPE1 FlpIn HA-VPS35 3B4 and [D620N] 1F3 cells were induced with 0.1 µg/ml doxycycline for 24 hours before adherent cells were washed in PBS and treated with 2 µM nigericin or vehicle (EtOH) in serum-free Opti-MEM media for 3 hours. Media were collected and subjected to TCA protein

precipitation. Adherent cells were lysed in NP40 buffer. Samples were analysed by immunoblotting. **B** Quantification of A. Values are normalised to 'WT – DOX' vehicle control for each cathepsin D species. Data from a single experiment, *n* = 1.

As LLOMe causes a rupture of the cell membrane and subsequent leakage of lysosomal contents, I wondered whether it would be possible to visualise the leakage of cathepsin D from the lysosome into the cytosol using subcellular fractionation. Total membranes were isolated from the cytosolic fraction by ultracentrifugation from induced RPE1 FlpIn VPS35 WT and [D620N] cells treated with LLOMe or nigericin (**Figure 6.27**). Western blot analysis of cathepsin D revealed that treatment with LLOMe, but not nigericin, caused a clear increase in mature and intermediate cathepsin D in the cytosolic fraction and a concomitant loss of these species in the membrane fraction (**Figure 6.27B**). This leakage of cathepsin D into the cytosol was not affected by expression of [D620N] mutant VPS35.

In the basal condition, expression of VPS35[D620N] appeared to increase intermediate cathepsin D levels in the membrane fraction and PNS. However, in experiments looking at total cell lysates, an increase in intermediate cathepsin D as a result of VPS35[D620N] expression was not observed in one previous experiment (**Figure 6.26**) and another showed enhanced cathepsin D in uninduced RPE1 VPS35[D620N] 1F3 cells (**Figure 4.4**), calling in to question how reproducible or meaningful this finding is.

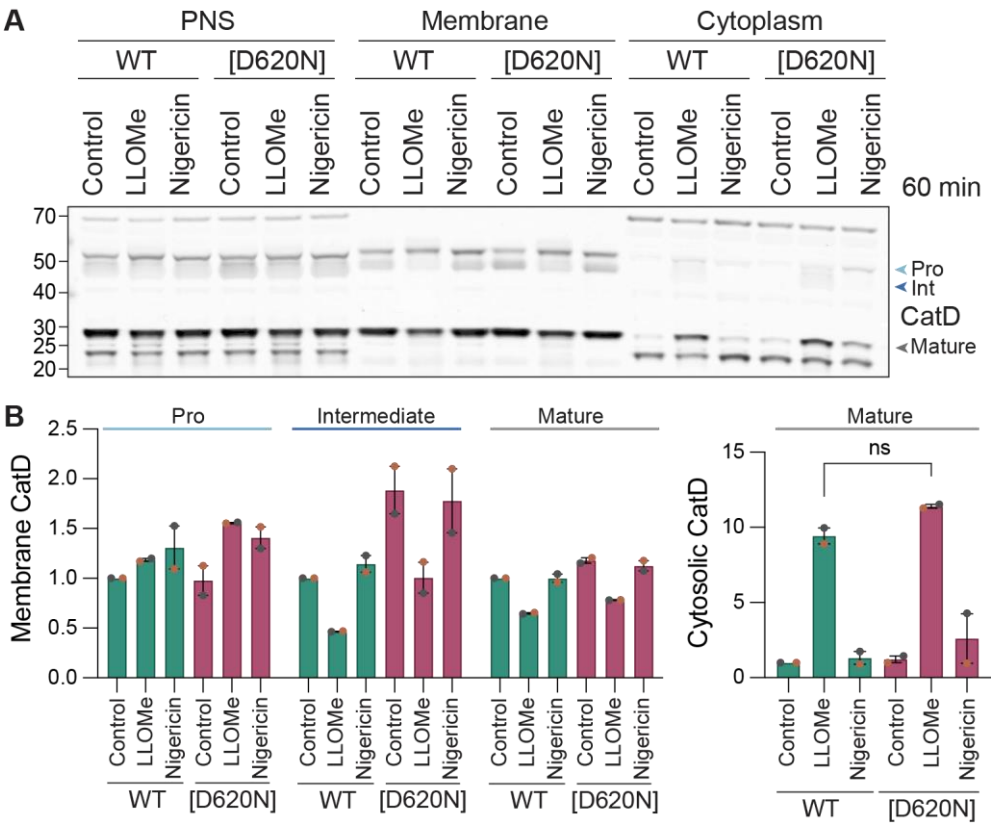

Figure 6.27 VPS35[D620N] does not enhance leakage of mature cathepsin D into the cytosol
A Subcellular fractionation of RPE1 FlpIn VPS35 WT 3B4 and [D620N] 1F3 cells induced with 0.1 µg/ml doxycycline for 24 hours and then treated with 500 µM LLOMe, 3 µM nigericin or vehicle (DMSO) for 60 minutes. Samples analysed are the same as in Figure 6.23. A representative western blot is shown. PNS; post nuclear supernatant, TPS; total protein stain. **B** Quantification of A. Signals normalised to WT - DOX control samples per replicate. *n* = 2. Each independent experiment is colour-coded. Bars represent mean and range. One-way ANOVA with Šídák's multiple comparisons test. ns, not significant.

6.4.5 VPS35[D620N] does not affect ESCRT recruitment in response to lysosomal damage

The western blots from the subcellular fractionation experiments described in **Sections 6.4.2** and **6.4.4** were also probed for ESCRT machinery components to see if their recruitment to membranes in response to LLOMe treatment was affected by the [D620N] mutation in VPS35 (**Figure 6.28**). As seen previously by immunofluorescence (**Figure 6.15** and **Figure 6.16**), LLOMe induced the recruitment of ALIX to the membranes (**Figure 6.28**). There was also a small increase in ALIX with nigericin treatment, despite not seeing ALIX localisation to lysosomes by immunofluorescence microscopy previously (**Figure 6.15**). Treatment with LLOMe caused the loss of a lower molecular weight band in the membrane fraction. One of

my colleagues, Francesca Frigenti, has performed siRNA knockdown of ALIX in HeLa cells and has shown that the bands at approximately 85 and 100 kDa are both specific. These may represent different ALIX isoforms or unmodified and post-translationally modified forms of ALIX. Accordingly, quantification of ALIX signal was performed including both bands (**Figure 6.28B**). Neither the banding pattern nor the amount of ALIX recruited to membranes in response to endolysosomal damage was affected by the expression of the [D620N] mutant.

Furthermore, at a higher exposure, the appearance of an additional band above ALIX could be seen after treatment with LLOMe which I would suggest represents a monoubiquitylated species. ALIX has recently been identified in a ubiquitylomics study investigating the effect of one-hour LLOMe treatment in HeLa cells (Kravić et al., 2022). The ESCRT-0 component HRS was also identified as being ubiquitylated after LLOMe treatment in the ubiquitylomics experiment described above, despite a previous study failing to observe HRS recruitment to lysosomes upon LLOMe treatment using immunofluorescence microscopy (Radulovic et al., 2018). In light of this, I probed the fractionation blots for HRS and quantified the levels of membrane-localised HRS (**Figure 6.28B**). There was a mild increase in membrane HRS following LLOMe, but not nigericin, treatment. Furthermore, like ALIX, LLOMe treatment led to the appearance of an additional modified membrane-bound form of HRS that may represent ubiquitylation. Expression of VPS35[D620N] did not affect the levels or banding pattern of HRS at membranes basally or following endolysosomal damage.

Rab7 was also identified by and Kravić and colleagues to be ubiquitylated following LLOMe treatment (Kravić et al., 2022). Given this finding and the close link between Rab7 and retromer, I also analysed the membrane cytosol distribution of Rab7. Treatment with LLOMe induced a clear downshift in the Rab7 band in both the post-nuclear supernatant and the membrane fraction. As this is also seen in the membrane-bound fraction, the lower band is unlikely to represent Rab7 that is not geranylgeranylated because this would be unable to be localised to membranes. It is possible that at steady state in RPE1 cells, Rab7 is post-translationally modified and this modification is lost with LLOMe treatment, and this accounts for the downshift. Expression of wild type or [D620N] mutant VPS35 did not affect the total levels of Rab7 at membranes nor the electrophoretic mobility following LLOMe treatment.

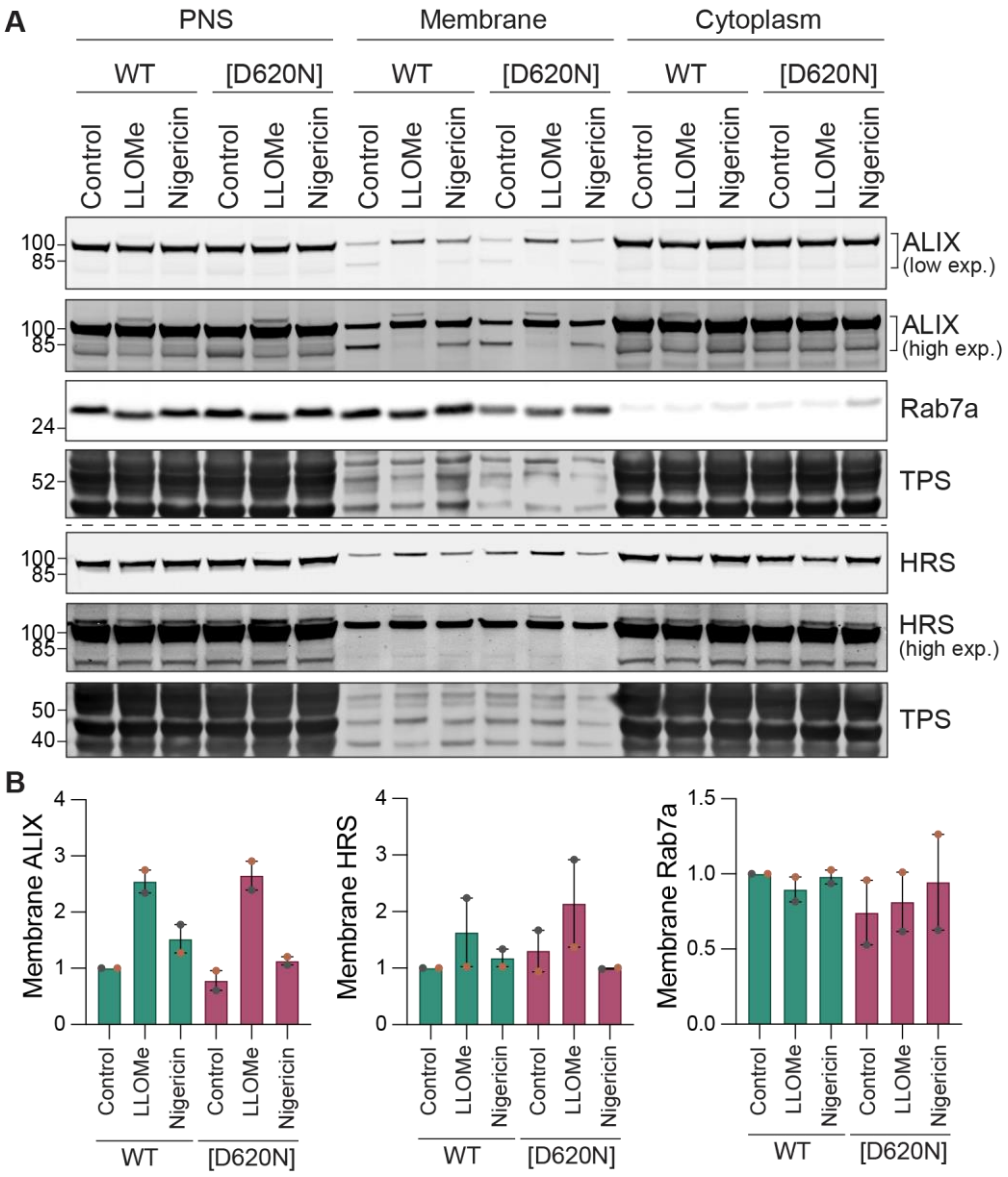

Figure 6.28 VPS35[D620N] does not affect ESCRT recruitment to membranes in response to endolysosomal damage

A Subcellular fractionation of RPE1 FlpIn VPS35 WT 3B4 and [D620N] 1F3 cells induced with 0.1 µg/ml doxycycline for 24 hours and then treated with 500 µM LLOMe or 3 µM nigericin or vehicle (DMSO) for 60 minutes. A representative western blot is shown. Samples analysed are the same as in Figure 6.23 and Figure 6.27. TPS; total protein stain. **B** Quantification of A. Signals normalised to WT - DOX DMSO samples per replicate. *n* = 2. Each independent experiment is colour-coded. Bars represent mean and range.

To further corroborate that the [D620N] mutation did not affect recruitment of the ESCRT machinery following lysosomal damage, ESCRT recruitment to lysosomes was also analysed by immunofluorescence microscopy. RPE1 FlpIn VPS35 WT and [D620N] cells were treated with LLOMe for 30 or 120 minutes and then fixed and stained for ALIX or CHMP2B and counterstained for LAMP1 and CD63, respectively

(**Figure 6.29**). The number and total area of CHMPB2B and ALIX puncta were then quantified, along with the intensity of their signal within a lysosome mask (**Figure 6.29B and C**). After 30 minutes of LLOMe treatment, I found an increase in the overall number of ALIX and CHMP2B puncta present within cells, which declined slightly with 120 minutes of LLOMe treatment. This was mirrored by an increase in the signal intensity at lysosomes, indicating the recruitment of the ESCRT machinery to this compartment. Expression of VPS35 [D620N] did not affect the number, total area nor lysosomal signal intensity of CHMP2B or ALIX compared to cells expressing wild type VPS35, confirming the subcellular fractionation results above.

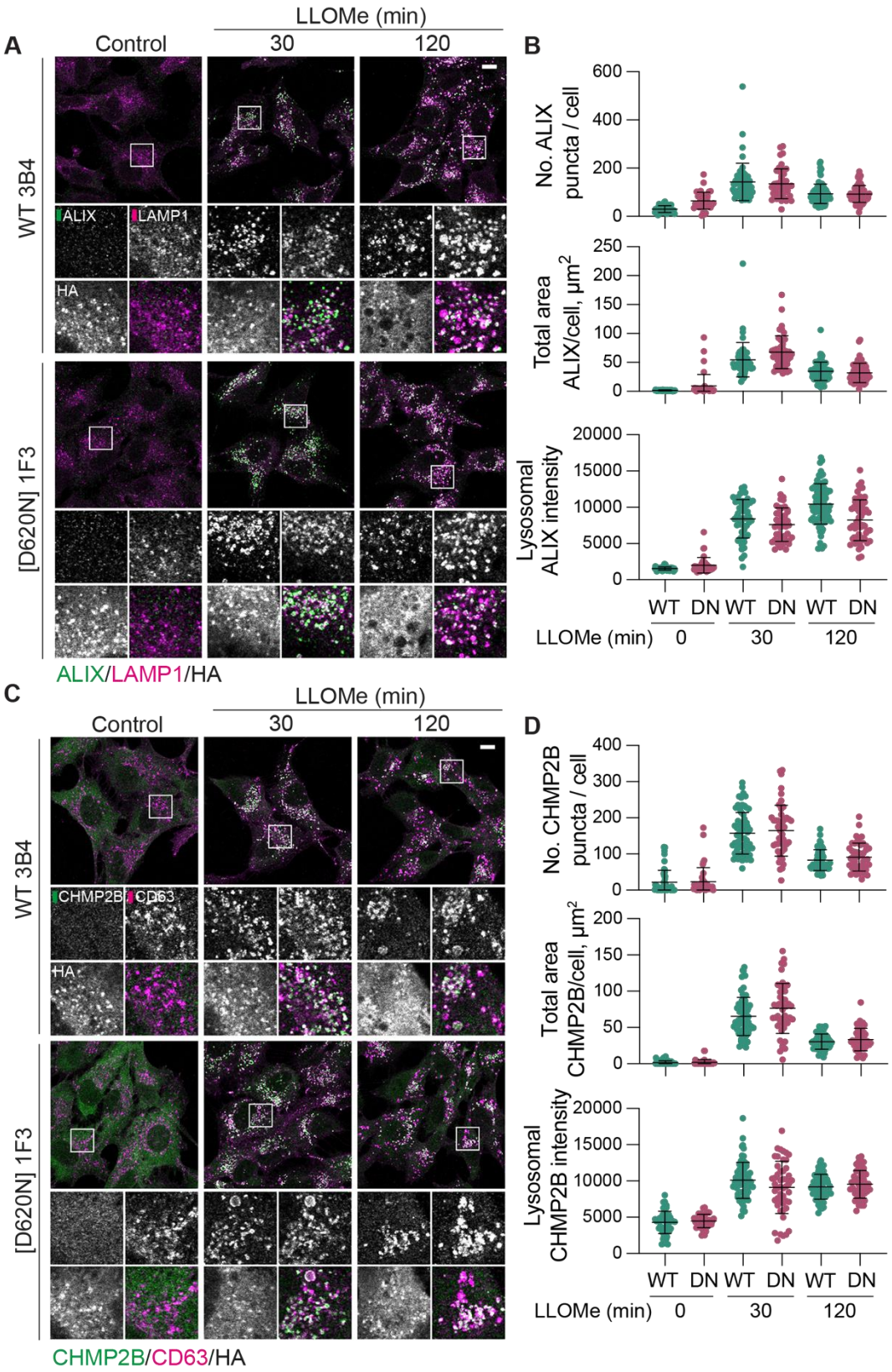

Figure 6.29 VPS35 [D620N] does not affect recruitment of the ESCRT machinery to lysosomes following LLOMe treatment

A RPE1 FlpIn VPS35 WT 3B4 and [D620N] 1F3 (DN) cell lines were induced with doxycycline for 24 hours. Cells were then treated with 500 µM LLOMe (30 or 120 minutes) or vehicle (DMSO, 120 minutes) prior to fixation and staining with the indicated antibodies. Scale bar 10 µm. **B** Quantification

of the number and total area of ALIX puncta and mean ALIX intensity within lysosomes per cell. *n* = 1, > 37 cells quantified per condition. Bars represent mean ± SD. **C** RPE1 FlpIn VPS35 WT 3B4 and [D620N] 1F3 cell lines were induced with doxycycline for 24 hours. Cells were then treated with DMSO vehicle control (120 minutes) or 500 µM LLOMe (30 or 120 minutes) prior to fixation and staining with the indicated antibodies. Scale bar 10 µm. **D** Quantification of the number and total area of CHMP2B puncta and mean CHMP2B intensity within lysosomes per cell. *n* = 1, > 37 cells quantified per condition. Bars represent mean ± SD.

6.4.6 VPS35[D620N] impairs the recovery from lysosomal damage

As the mechanisms by which lysosomes try to repair damage did not appear to be affected by the [D620N] mutation, I wondered whether clearance of damaged lysosomes might be affected. LLOMe-damaged lysosomes have previously been shown to be cleared via both canonical and non-canonical autophagy (CASM) pathways (Cross et al., 2023; Maejima et al., 2013). Both pathways induce the recruitment of LC3 to the lysosome. To investigate whether LC3 recruitment was affected by the expression of VPS35 [D620N], RPE1 FlpIn cells expressing wild type or [D620N] HA-tagged VPS35 were treated with LLOMe for two hours and fixed and stained for LC3 and LAMP1. To assess resolution from lysosome damage, one set of samples had the LLOMe-containing media replaced and the cells were left to recover in fresh media for 16 hours (**Figure 6.30A**). After two hours of treatment with LLOMe, LC3 was clearly recruited to lysosomes (**Figure 6.30B**). Quantification of the number and average size of LC3 puncta and the total area occupied by LC3 per cell revealed no significant differences between wild type and [D620N] VPS35-expressing cells at this time point (**Figure 6.30C-E**). Following wash out of LLOMe, LC3 punctate staining reduced back to near-baseline levels in wild type VPS35-expressing cells. In contrast, in cells expressing VPS35[D620N], some LC3 puncta persisted after the washout. In some experiments this manifested as a greater number of LC3 puncta, and in others the remaining LC3 puncta were larger. Across three replicate experiments, there was a clear trend towards an increase in number (**Figure 6.30C**) and size (**Figure 6.30D**) of LC3 puncta. Computation of total area of the cell occupied by LC3 puncta, which combines information about their number and size, revealed this to be significantly increased by the [D620N] mutation (**Figure 6.30E**). This suggests that the [D620N] mutation in VPS35 impairs the ability to resolve lysosomal damage.

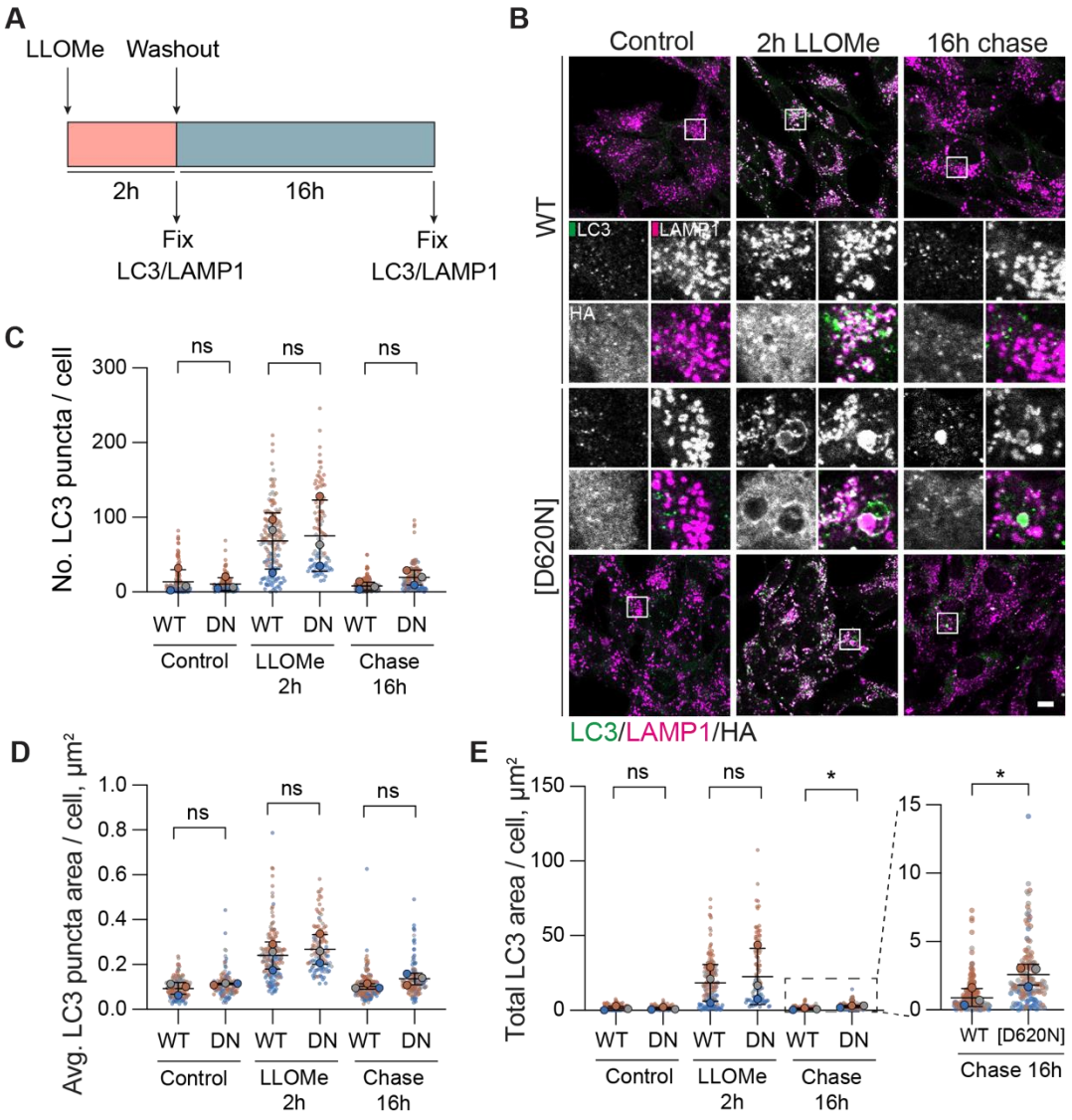

Figure 6.30 VPS35 [D620N] impairs LC3 clearance following lysosomal damage

A Schematic of experimental set-up **B** RPE1 FlpIn VPS35 WT 3B4 and [D620N] 1F3 (DN) cells were induced with doxycycline for 24 hours and then treated with 500 µM LLOMe or vehicle (DMSO) control for 2 hours. Cells were either fixed or LLOMe was chased out for 16 hours and then the cells were fixed and stained with the indicated antibodies. Scale bar 10 µm. **C-E** Quantification of the number (C), average size and total area (E) of LC3 puncta per cell. > 20 cells quantified per condition per repeat, *n* = 3. Each independent experiment is colour-coded. Transparent circles with no outline represent values for each cell in an experiment, opaque circles with black outlines correspond to mean values for each experiment. Bars represent mean ± SD. Paired Student's t-tests. * $P < 0.05$.

The [D620N] mutation in VPS35 has previously been shown to impair autophagy (Zavodszky et al., 2014). To confirm whether the failure to resolve lysosomal damage was due to a general dysfunction in autophagy or specific to lysophagy, RPE1 FlpIn VPS35 WT and [D620N] cells were treated with concanamycin A to block autolysosome fusion and inhibit autophagy flux. LC3 conversion was then measured

by immunoblotting (**Figure 6.31A**). As expected, treatment with concanamycin caused an increase in LC3-II levels and a mild rise in p62, consistent with a block in autophagosome turnover. Lipidation of LC3 was not differentially affected in the wild type and [D620N]-expressing cell lines (**Figure 6.31B**). Levels of p62 were mildly elevated in [D620N] 1F3 cells before and after concanamycin A treatment, however this was also the case in uninduced cells, suggesting a clonal variation. Altogether, these results suggest that general autophagic flux is not affected by the VPS35 [D620N] mutation.

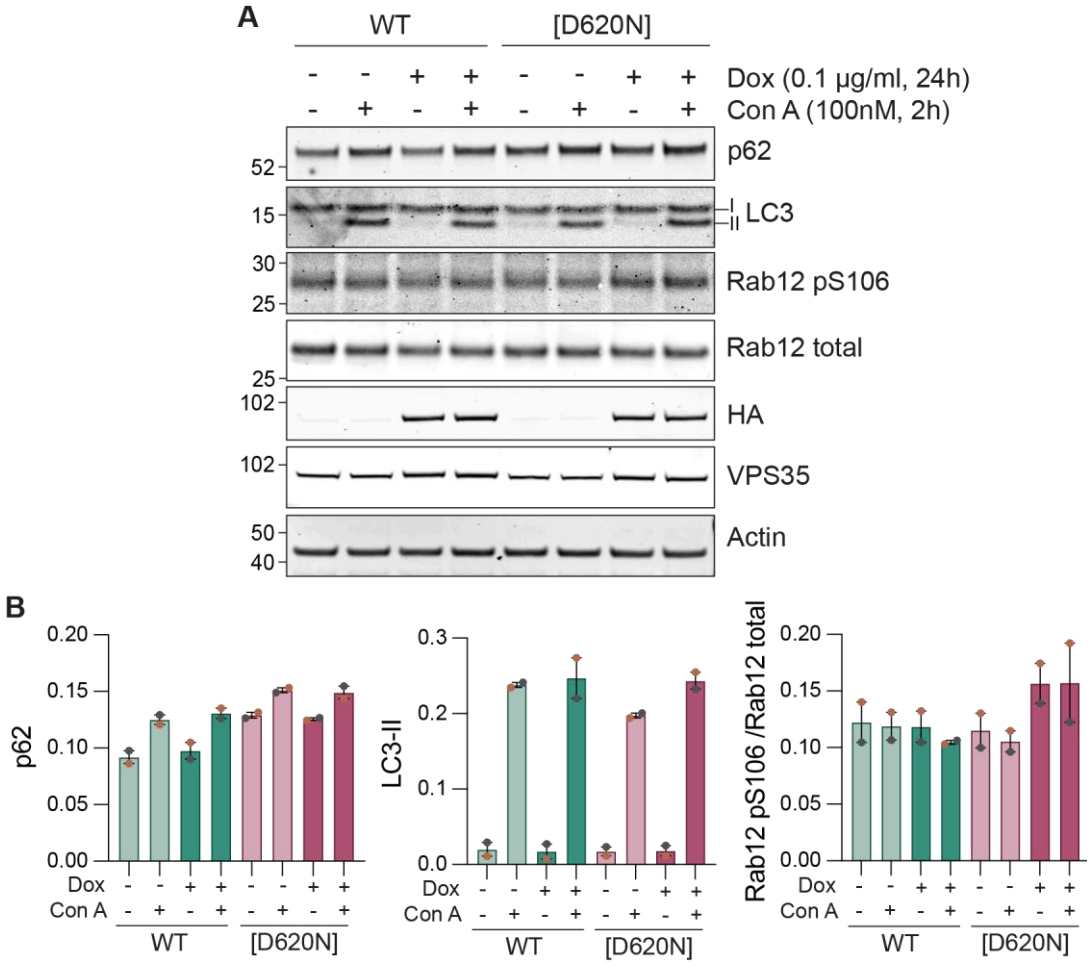

Figure 6.31 VPS35[D620N] does not impair general autophagy

A RPE1 FlpIn HA-VPS35 3B4 and [D620N] 1F3 cells were induced with 0.1 µg/ml doxycycline for 24 hours, then treated with 100 nM concanamycin A for 2 hours prior to lysis and analysis by immunoblotting. **B** Quantification of A. Values normalised to sum of all bands in a replicate. *n* = 2. Each independent experiment is colour-coded. Bars represent mean and range.

6.5 Discussion

6.5.1 Pharmacological endolysosome stressors elicit different phenotypes

Multiple ion channels and transporters are responsible for maintaining a concentration gradient for protons and other ions across the lysosomal membrane (Freeman et al., 2023). Maintenance of this environment is key to the degradative function of lysosomes. However, this makes them particularly sensitive to perturbations by various ionophores and weak bases, which can have wide-ranging consequences for the cell.

In this chapter, I have investigated the actions of three compounds reported to cause lysosomal damage and LRRK2 activation, LLOMe, nigericin and chloroquine, and I have studied the signatures of lysosomal damage they produce. The phenotypes induced by the different agents are summarised in **Table 6.3** below.

Table 6.3 Summary of the different lysosomal phenotypes observed in response to treatment to the lysosome stressors chloroquine, LLOMe and nigericin

	Chloroquine	LLOMe	Nigericin
Morphology	Enlarged	Enlarged	Slightly enlarged
Distribution	Perinuclear	Perinuclear	Peripheral
pH	Increased	Increased	Increased
Lysotracker staining	Decreased	Increased	Decreased
LC3 lipidation	Yes, v-ATPase dependent	Yes, v-ATPase independent	Yes, v-ATPase dependent
Rab phosphorylation	Increased	Increased	Increased
ESCRT recruitment	-	Yes	No (?)
Gal3 recruitment	No	Yes	No
Cathepsin D	Released extracellularly	Released into cytosol	Released extracellularly

As expected, chloroquine caused swelling of lysosomes and no change to their abundance. LLOMe also caused enlarged swollen lysosomes, in agreement with previous reports, but caused a decrease in their number (Herbst et al., 2020; Repnik et al., 2017; Tan and Finkel, 2022; Vest et al., 2022). It is possible that rather than osmotic swelling, the enlarged lysosomes seen upon LLOMe treatment are large autolysosomes that have engulfed damaged lysosomes, and as such the decrease in lysosome number represents their clearance. Upon nigericin treatment, I observed

only some minor swelling in a subset of lysosomes. In a previous study, two-hour treatment with nigericin was reported to cause an enlargement of lysosomes in MCF10A mammary epithelial cells (Lee et al., 2020). However, this effect was recorded in ATG13 knockout cells and the effect of nigericin on wild-type cells was not reported.

Clustering of lysosomes in the perinuclear region can be induced by lysosomal stress, nutrient starvation and mTORC inactivation (Cabukusta and Neefjes, 2018). In line with a previous report, I found that LLOMe triggered perinuclear clustering of lysosomes (Kluss et al., 2022). Chloroquine treatment also showed a perinuclear shift of lysosome distribution. In contrast, I observed a dispersal of lysosomes to the periphery following nigericin treatment. These peripheral clusters of lysosomes are reminiscent of the phenotype observed by Kluss and colleagues following JIP4 knockout or Arl8 overexpression (Kluss et al., 2022). As nigericin induced the release of cathepsin D into the extracellular media, it is possible that this peripheral, plasma membrane proximal population of lysosomes is primed to undergo exocytosis and release their contents.

Nigericin, chloroquine and LLOMe all caused alkalinisation of lysosomes. This was evident by the loss of Lysotracker staining following nigericin and chloroquine treatment. Although I observed an overall increase in staining intensity of Lysotracker with LLOMe that is suggestive of increased acidification (discussed below), the lysokeima experiments told a different story. Following LLOMe treatment, the lysokeima mKeima-Gal3 construct relocalised to lysosomes that were pH neutral, suggesting that LLOMe does cause an alkalinisation of damaged lysosomes.

The increase in Lysotracker staining following LLOMe treatment I observed stands in contrast to previous reports which have shown a loss of Lysotracker staining after treatment with LLOMe (Eriksson et al., 2020; Jia et al., 2020; Radulovic et al., 2018). However, it is worth noting that following an initial reduction in Lysotracker staining, Radulovic and colleagues observed that Lysotracker staining was recovered within 30-60 minutes (Radulovic et al., 2018). In fact, their experiments show that fluorescence continued to increase to above the level recorded before addition of LLOMe. The authors showed that this was indicative of lysosomal membrane repair. It is possible that after an hour of treatment I had already missed the initial leakage of Lysotracker probe from lysosomes after membrane permeabilisation and was witnessing the subsequent reaccumulation after membrane repair. However, it should be noted that in my experiments, the Lysotracker dye was removed before the LLOMe

insult, and so it might be assumed that the concentration was not high enough to facilitate re-staining after repair. Alternatively, it is also possible that these high intensity puncta I observed represent autophagocytosed lysosomes which have been targeted for clearance via lysophagy. It would be beneficial to look at this with time-lapse microscopy starting immediately after LLOMe addition to see if there is an initial loss of Lysotracker signal which is then regained before the one-hour timepoint that was used in my experiments.

Nigericin, chloroquine and LLOMe all induced lipidation of LC3, signalling the activation of autophagy. Treatment with LLOMe has been shown to trigger lysophagy via the ubiquitin-dependent selective autophagy machinery (Maejima et al., 2013). It is possible the monoubiquitylation that I may have observed on membrane-associated ALIX and HRS serves as a signal to trigger lysophagy as monoubuitylation of substrates has previously been shown to be sufficient to trigger selective autophagy (Kim et al., 2008). Furthermore, I also observed recruitment of Gal3 (lysokeima) following LLOMe treatment, which is reported to recruit the E3 ligase TRIM16 and the ULK1 complex to promote lysophagy (Chauhan et al., 2016).

It has been previously shown that chloroquine, nigericin and LLOMe all trigger v-ATPase-dependent non-canonical autophagy at the lysosomal membrane (Cross et al., 2023; Hooper et al., 2022; Jacquin et al., 2017). I observed a failure of cells treated with nigericin and chloroquine to accumulate lipidated LC3 when the v-ATPase was inhibited, which is consistent with these agents activating non-canonical autophagy in RPE1 cells. In contrast, LC3-II levels following LLOMe treatment were not affected by the presence of concanamycin A. This suggests that LC3-II recruitment is not formed by non-canonical autophagy mechanisms in this setting but instead reports on the engagement of the selective autophagy machinery for execution of lysophagy.

The contribution of CASM to driving LC3 recruitment at the lysosome has been proposed to be most important in the acute phase of LLOMe treatment (Cross et al., 2023). Therefore, it is possible that at the two hours of LLOMe treatment used in my experiments, the contribution of the non-canonical autophagy to LC3 lipidation is negligible compared to that of the canonical autophagy pathway and so shows little v-ATPase dependence. Repeating the experiment using shorter LLOMe treatments might yield a different result.

6.5.2 All roads lead to LRRK2 activation

Despite causing different changes to lysosome pH, morphology, distribution, membrane integrity, and fate (lysophagy via LC3 recruitment, or secretion of contents)

the unifying feature of the compounds tested was that they induced LRRK2-dependent Rab phosphorylation. This raises the question of how these diverse insults trigger LRRK2 recruitment and activation.

Given that all three compounds cause deacidification of lysosomes, it could be proposed that an increase in lysosome pH triggers LRRK2 recruitment by an unknown mechanism. This hypothesis has recently been put forward by the Grinstein lab, who have shown that dissipation of endosomal pH by co-treatment with nigericin and concanamycin A causes recruitment of LRRK2 to Rab5- and Rab7-positive endosomal structures and phosphorylation of Rab10 and Rab12 (Maxson et al., 2023). The authors showed that LRRK2 recruitment lead to vacuolation of endosomes and altered the activation state of Rab5 and Rab7, leading to their increased retention at endosomal membranes (Maxson et al., 2023). However, in my hands, treatment with the v-ATPase inhibitor concanamycin A caused an increase in lysosomal pH, yet failed to trigger Rab12 phosphorylation, suggesting that the mechanism by which LRRK2 is activated is not as straightforward as simply sensing dissipated pH. In fact, in contrast to the previously reported finding, I observed that inhibition of the v-ATPase with concanamycin A dampened nigericin and chloroquine-induced Rab phosphorylation. Concanamycin A inhibits v-ATPase proton pump activity by driving the dissociation of the V_0 and V_1 domains. Could the correct assembly of the v-ATPase be an important component in the sensing of lysosomal damage by LRRK2? Indeed, LRRK2 has been shown to interact with the a1 subunit of the V_0 domain of the v-ATPase, thus it is possible that LRRK2 requires a fully assembled v-ATPase for recruitment (Wallings et al., 2019). Disruption of the lysosomal ion concentration and pH has been shown to drive engagement between the V_0 and V_1 subunits to regain normal lysosomal pH (Hooper et al., 2022). For activation of non-canonical autophagy, it is the proper assembly of the V-ATPase at the lysosomal membrane that is important, rather than its ability to transport H^+ (Hooper et al., 2022). It would be interesting to see if saliphenylhalamide, a v-ATPase inhibitor which blocks pump function but prevents its disassembly, also reduced nigericin-induced Rab phosphorylation. This would shed light on whether it is the proton pumping function or assembly of the V_0-V_1 v-ATPase complex that is necessary for the LRRK2 response to chloroquine and nigericin. Inhibition of the v-ATPase activity did not impact on Rab phosphorylation following LLOMe treatment. This suggests that LRRK2 may be recruited by a different mechanism altogether or is capable of being activated by different stimuli.

Another hypothesis for the mechanism of LRRK2 recruitment is that LRRK2 may be sensitive to osmotic imbalance and changes in lysosomal size. This is supported by the fact that LLOMe and chloroquine both induce lysosomal enlargement and Rab phosphorylation. However, I failed to observe any overt lysosomal swelling following nigericin treatment yet recorded a robust increase in Rab phosphorylation. Secondly, treatment with apilimod caused a dramatic swelling of lysosomes yet, when added alone, had a minimal effect on Rab phosphorylation. Overall, this suggests that lysosome size is not a sufficient trigger for LRRK2 activation.

Treatment with apilimod enhanced Rab phosphorylation and LC3 lipidation induced by nigericin, suggesting that phospholipid levels are important in the response to lysosomal damage. The tonic inhibitory effect of $PI(3,5)P_2$ on the lysosomal chloride channel ClC-7 has been shown to be important for regulating lysosomal pH (Leray et al., 2022). Inhibition of PIKfyve by apilimod will reduce $PI(3,5)P_2$ levels and so relieve this block, leading to chloride efflux and H^+ influx. Apilimod and nigericin may have an additive effect of disrupting lysosomal ion imbalance and stress. It is also possible that there is a more direct relationship between PIKfyve and LRRK2, that only becomes more apparent when paired with heightened LRRK2 activity by another means, akin to the effect I have seen with the [D620N] mutation. It has recently been shown that inhibition of VPS34 triggers LRRK2 recruitment to endosomes and subsequent Rab phosphorylation (Rinaldi et al., 2023). However, this was only observed in cells expressing hyperactivating mutant LRRK2 variants, and not wild type LRRK2. As VPS34 and PIKfyve are both part of the phosphoinositide pathway, it is possible we are seeing a similar phenomenon and phospholipid identity is important for LRRK2 recruitment and activation.

6.5.3 The role of LRRK2 in the lysosomal damage response

6.5.3.1 Lysosome positioning

When considering a possible relationship between LRRK2 and lysosomal positioning, it raises a ‘chicken and egg’ dilemma. Does the repositioning of lysosomes increase LRRK2 activation or does LRRK2 activation drive the movement of lysosomes to the perinuclear area? Kluss and colleagues reported that the retrograde movement of lysosomes to the perinuclear cloud is required for Rab10 phosphorylation (Kluss et al., 2022). Knockout of JIP4 or overexpression of Arl8 or SKIP, which caused peripheral dispersal of lysosomes, reduced Rab10 phosphorylation (Kluss et al., 2022). Conversely, overexpression of RILP, which caused lysosomal clustering, increased Rab10 phosphorylation. However, none of these interventions affected

Rab12 phosphorylation, showing there may be a distinct set of conditions required for LRRK2 to activate different substrate Rabs (Kluss et al., 2022).

Rab phosphorylation by LRRK2 increases their interaction with certain effectors: RILPL1 (Rab8A, Rab10), RILPL2 (Rab8A), JIP3 (Rab10) and JIP4 (Rab10) (Ito et al., 2023; Steger et al., 2017; Waschbüsch et al., 2020). It follows that increased LRRK2 activation would drive engagement of Rab10 with JIP4, promoting lysosome motility towards the perinuclear region. In addition to JIP4, two recent studies have found that LRRK2 may control lysosome positioning via RILPL1 (Ito et al., 2023; Pal et al., 2023). Ito and colleagues found that overexpression of hyperactive LRRK2 variants drove perinuclear clustering of lysosomes in a manner dependent on Rab12 and RILPL1 (Ito et al., 2023). Supporting this concept, Pal and colleagues have shown that upon lysosomal damage, LRRK2-dependent phosphorylation of Rab8A and Rab10 drives the formation of a RILPL1:TMEM55B complex at the lysosome (Pal et al., 2023). TMEM55B has also previously been shown to recruit JIP4 to the lysosome to promote perinuclear clustering, providing another possible layer to the regulation of lysosome motility (Willett et al., 2017). Taken together, these studies strongly suggest that LRRK2 can regulate positioning of lysosomes within the cell.

It is interesting then, that in response to nigericin, I observed an accumulation of lysosomes at peripheral sites yet also saw Rab10 phosphorylation. As the phosphatase for Rab10, PPM1H, is located at the Golgi (Berndsen et al., 2019), it is possible that the increased Rab phosphorylation under these conditions is, in part, amplified due to this physical separation of lysosome-localised Rabs and Golgi-localised PPM1H.

Interestingly, phosphorylation of Rab7 by LRRK1 promotes its interaction with RILP, stimulating movement of Rab7-positive vesicles towards the perinuclear area (Hanafusa et al., 2019). This finding supports a central role for LRRK-family proteins in regulating endolysosomal positioning.

6.5.3.2 Extracellular release of lysosomal contents

LRRK2 has been proposed to regulate lysosomal swelling and extracellular secretion of lysosomal contents (Eguchi et al., 2018). In contrast to this previous report, I failed to observe a change in chloroquine-induced extracellular release of cathepsin D following LRRK2 inhibition (Eguchi et al., 2018). However, in RPE1 cells, basal, as well as nigericin-induced, cathepsin D secretion was mildly reduced in the presence of MLi-2. These findings suggest that LRRK2 may promote lysosomal secretion. The

difference in response to different agents compared with the aforementioned study may represent cell type specific differences.

Eguchi and colleagues showed that treatment with chloroquine caused a LRRK2 dependent recruitment of the Rab8/10 effectors EHBP1 and EHBP1L1 which then promoted the release of lysosomal contents outside of the cell (Eguchi et al., 2018). Unlike in the case of RILPL1 and RILPL2, the binding of Rab8a to EHBP1 was not affected by its phosphorylation state (Eguchi et al., 2018; Steger et al., 2017). This may suggest that this pathway is promoted by the accumulation of Rab8 and Rab10 at membranes as they become resistant to extraction by GDIs in their phosphorylated state, rather than a switch in their binding affinity for specific effectors (Eguchi et al., 2018; Steger et al., 2017, 2016).

Unlike chloroquine and nigericin, treatment with LLOMe caused an apparent loss of cathepsin D from whole cell lysates, which was not recovered in the media. Subcellular fractionation also experiments revealed a redistribution of cathepsin D from membrane compartments to the cytosol upon LLOMe treatment. It is possible that the loss observed in total cell lysates represents the degradation of cathepsin D by cytosolic proteases such as calpains and caspases (Huang and Wang, 2001; Zhivotovsky et al., 1999).

6.5.3.3 ESCRT recruitment

LLOMe, but not nigericin, triggered recruitment of the ESCRT machinery to lysosomes. Inhibition of LRRK2 caused a mild decrease in the recruitment of ESCRT components after 15 minutes of LLOMe treatment, but this decrease was no longer seen after 30 minutes. The data came from a single experiment and so warrants repeating to ensure this is significant. However, this may signify that in RPE1 cells LRRK2 is not essential but may be rate-limiting for the initial recruitment of ESCRTs following lysosomal damage. With sustained insult, this difference may no longer be apparent. In addition, it is possible that a secondary LRRK2-independent mechanism of ESCRT recruitment takes over. This could align with the hypothesis outlined by Jia and colleagues, who proposed that there is an acute phase of ESCRT recruitment that is dependent on calcium and a secondary phase reliant on galectin 3 (Jia et al., 2020). In another study, chelation of calcium ions using BAPTA reduced LRRK2 recruitment, Rab phosphorylation and CHMP4B recruitment following lysosomal damage, supporting a role for LRRK2 in an acute, Ca^{2+}-dependent phase (Herbst et al., 2020). However, the authors of the manuscript also showed less galectin 3

recruitment in the absence of LRRK2, which could suggest a more general role for LRRK2 than specifically in the ESCRT-mediated repair pathway.

In my hands, only treatment with LLOMe triggered the recruitment of ESCRT components and galectin 3 to lysosomes. This suggests that LLOME is the only lysosomal damage inducing agent amongst the ones I used that causes breaks in the lysosomal membrane which need to be repaired and exposes luminal carbohydrates to which galectin 3 will bind. As treatment with nigericin and chloroquine also cause LRRK2 activation, a role in the ESCRT-mediated response cannot be the sole function of LRRK2 at the lysosome.

6.5.3.4 Activation of autophagy pathways

I found that inhibition of LRRK2 neither enhanced nor inhibited lysosomal damage-induced LC3 lipidation. This finding suggests that LRRK2 does not play a direct role in the activation of CASM or lysophagy following lysosomal damage. Despite causing similar levels of Rab phosphorylation, LLOMe and nigericin caused different degrees of LC3 lipidation. This lack of correlation further suggests that the LRRK2 phosphorylation response is separate from the induction of autophagy.

However, it is possible that LRRK2 indirectly influences autophagy pathways. If LRRK2 is playing a role in the recovery of damaged lysosomes, either by removal of undegraded cargo or by membrane repair, dysfunctional lysosomes may be pushed towards autophagic clearance in the absence of LRRK2. This idea is strengthened by the finding by Herbst and colleagues that in the absence of LRRK2 activity, either by pharmacological inhibition or knockout, there are higher levels of K63-linked ubiquitylation at lysosomes, consistent with an increase in lysophagy (Herbst et al., 2020). The authors showed reduced galectin 3 recruitment in the absence of LRRK2 activity but increased levels of galectin-8 at sites of damage, suggesting cells could be redirecting repair efforts towards a different lysophagy pathway (Herbst et al., 2020).

6.5.4 A role for VPS35 in the response to lysosomal stress

In this chapter, I have identified a role for VPS35 in the LRRK2 response to lysosomal damage. Using the RPE1 FlpIn system, I have shown that the [D620N] mutation in VPS35 causes a sensitisation to the Rab10 and 12 phosphorylation response to lysosomal stress induced by LLOMe and nigericin. Furthermore, I have shown that depletion of VPS35 blunts lysosome damage-induced Rab phosphorylation, suggesting that VPS35 is required for complete LRRK2 activation in this context.

6.5.4.1 VPS35 and activation of LRRK2

In control, wild type VPS35-expressing cells, LLOMe or nigericin treatment caused an increase in membrane recruitment and LRRK2-dependent phosphorylation of Rab12. In VPS35[D620N]-expressing cells, more Rab12 was already associated with membranes at steady state. This did not increase further following lysosomal damage, whereas Rab12 phosphorylation did further increase. This could mean that cells expressing mutant VPS35 are 'primed' for the damage response as Rab12 is already enriched at the membrane, allowing for the higher degree of Rab phosphorylation (**Figure 6.32**). This may explain why I was only able to see an effect of PIKfyve inhibition with apilimod on Rab phosphorylation in the VPS35[D620N]-expressing cells.

It has recently been shown by two independent groups that Rab12 is critical for the activation of LRRK2 and its recruitment to the lysosome following lysosomal damage (Bondar et al., 2023; Dhekne et al., 2023). More Rab12 at membranes will facilitate LRRK2 recruitment, which, in turn, will further increase Rab membrane localisation and phosphorylation in a positive feedback loop. Using the lyso-IP technique, Bondar and colleagues found a mild increase in LRRK2 at lysosomes in VPS35[D620N] knockin A549 cells, which was not further increased by LLOMe (Bondar et al., 2023). While I did not see any differences in the levels of LRRK2 membrane localisation by subcellular fractionation in my [D620N]-mutant expressing RPE1 cells, it is interesting that this pattern mirrors what I observed for Rab12. However, the authors draw a different conclusion, stating that with the PD pathogenic LRRK2 and VPS35 variants, the Rab12-LRRK2 axis is maximally stimulated, making cells unable to properly respond to additional stress. On the contrary, in my cell model, lysosomal damage clearly further increased Rab phosphorylation, with no change in membrane recruitment when VPS35[D620N] was expressed, suggesting these cells are more sensitive to additional lysosomal stress.

This begs the question as to why the [D620N] mutation causes increased localisation of Rab12 to membranes at steady state. It is possible that the VPS35[D620N] activates LRRK2, either directly or indirectly, in the absence of lysosomal damage or that in VPS35[D620N]- expressing cells there is some underlying lysosomal damage or dysfunction that is driving LRRK2 activation and subsequent Rab12 phosphorylation, which then 'traps' the Rabs at the membrane (**Figure 6.32**).

Changes to the cholesterol composition of the lysosomal membrane have previously been shown to be sufficient to trigger lysophagy (Hu et al., 2021). A recent study has

reported that knockin of VPS35[D620N] in MEFs caused changes to the expression of many lysosomal proteins, leading Pal and colleagues to hypothesise that this causes lysosome stress which, in turn, triggers LRRK2 recruitment and activation (Pal et al., 2023). I found no evidence of aberrant lysosome morphology in cells expressing VPS35[D620N]. However, it would be valuable for future study to investigate whether lysosomes in VPS35[D620N]-expressing cells have full functionality in my cell system. This could be achieved using live-cell imaging assays such as the Magic Red® Cathepsin B Activity Assay, or using DQ™ Green-BSA, which is taken up by endocytosis and undergoes fluorescence unquenching dependent on the activity of lysosomal proteases.

Given that deletion of VPS35 has been shown to cause lysosomal dysfunction and swelling (Daly et al., 2023), one might expect that knockdown of VPS35 would enhance Rab phosphorylation. However, I found the opposite effect: when cells were depleted of VPS35, basal Rab phosphorylation was reduced and the LRRK2 response to lysosomal stress was blunted. This suggests that in this context, the [D620N] mutation is acting with a gain of function. It further lends weight to the notion that it is not general lysosomal dysfunction in [D620N]-expressing cells that is promoting greater Rab12 and LRRK2 recruitment because knockdown of VPS35 likely also disrupts lysosomal function. However, it is possible that we may not see this after only a short knockdown of VPS35, as previous studies have reported that lysosomal dysfunction in the absence of retromer is due to longer term compensatory mechanisms (Evans et al., 2020). Likewise, induction of VPS35[D620N] for only 24 hours may not be long enough for widescale changes to the lysosomal proteome and the resulting dysfunction to manifest.

Considering the previously reported finding that merely driving lysosomes towards the perinuclear region is sufficient to induce Rab10 phosphorylation (Kluss et al., 2022), a change in lysosomal positioning in VPS35[D620N]-expressing cells could explain the enhanced Rab10 (and Rab12) phosphorylation that I, and others (Bu et al., 2023; Kadgien et al., 2021; Mir et al., 2018), observe. However, I found no difference in lysosomal distribution when comparing cells expressing either wild type or [D620N] mutant VPS35. Knockin VPS35[D620N] MEFs have been shown to display increased recruitment of RILPL1 to lysosomes in a LRRK2-dependent manner, suggesting that changes to lysosomal positioning are more likely to lie downstream of LRRK2 activation (Pal et al., 2023). Accordingly, recent work has shown that pathogenic LRRK2 variants promote perinuclear clustering in a manner dependent on a pRab12-RILPL1 axis (Ito et al., 2023).

The increased residency of Rab12 at membranes that I observe could indicate a decrease in engagement with its GAP or GDI, or increased activity of its GEF. Increased phosphorylation is likely to contribute to this as it has been shown by independent groups that phosphorylation of Rabs by LRRK2 interferes with their extraction from membranes by GDI (Eguchi et al., 2018; Steger et al., 2017). One previous study has shown that LRRK2-dependent phosphorylation of Rab10 decreases its interaction with its GAP AS160 (Liu et al., 2018). This would reduce Rab-GTP hydrolysis and subsequently interfere with membrane extraction by GDIs, which display higher affinity for Rabs in their GDP-bound state (Wu et al., 2010). Together, these studies demonstrate how phosphorylated Rabs can become trapped at membranes but does not account for the increase in unphosphorylated membrane bound Rab12 that I observe. It is possible that the expression of an as yet unidentified GAP for Rab12 is decreased in VPS35[D620N]-expressing cells and accounts for the Rab12 hyperaccumulation at membranes.

An alternative explanation for increased Rab12 at the membrane is increased activity or expression of its GEF, DENND3 (Yoshimura et al., 2010). It has previously been shown that phosphorylation of the Rab12 GEF DENND3 by ULK1 in response to starvation enhances its activity, leading to increased active Rab12 (Xu et al., 2015). It is possible that the [D620N] mutation somehow indirectly affects the phosphorylation status of DENND3 to lead to increased Rab12 at membranes in a similar manner.

The Rab10 GEF, DENND4C has been shown to interact with retromer (McMillan et al., 2016). In fact, the authors showed that the [K297X] mutation in VPS26A, which causes a Parkinson's-like syndrome, causes an increased association with DENND4C. It is therefore tempting to speculate that the VPS35[D620N] may perturb the regulation of Rab10 activity and localisation by affecting the localisation of DENND4C. It would be interesting to see if an increased interaction of DENND4C with retromer is also observed in the case of the VPS35[D620N] mutation, and whether this does contribute to increased Rab10 at membranes. Furthermore, it would also be interesting to look at whether retromer interacts with other DENND-family GEFs and whether the VPS26A [K297X] mutation enhances LRRK2-mediated Rab phosphorylation. It must be noted that whilst I have observed enhanced Rab12 at membranes, I did not look at Rab10. Therefore, before considering this hypothesis, it would be necessary to test whether expression of VPS35[D620N] also leads to accumulation of Rab10 at membranes, and if so, whether this is solely driven by

increased membrane recruitment of LRRK2 due to enrichment of Rab12 (Bondar et al., 2023; Dhekne et al., 2023).

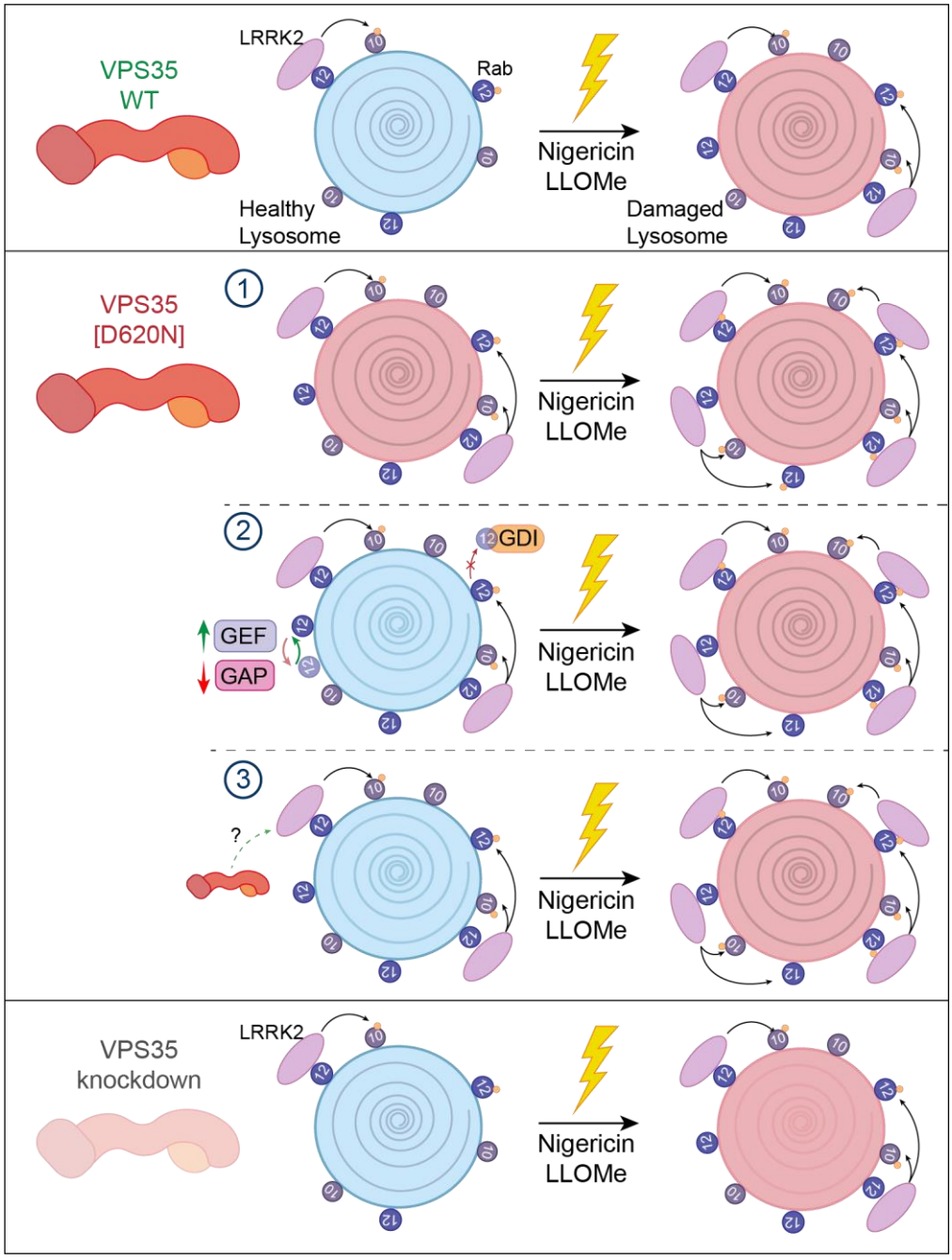

Figure 6.32 Proposed role for VPS35 in the LRRK2 lysosome damage response

In the presence of wild type VPS35, a small proportion of the Rab12 and Rab10 at membranes is phosphorylated. Upon lysosomal damage (e.g. by nigericin or LLOMe), Rab10, Rab12 and LRRK2 are recruited to the membrane. Here, LRRK2 is activated and phosphorylates Rab10 and Rab12. Expression of the [D620N] mutant VPS35 leads to accumulation of total and phosphorylated Rab12 at membranes, priming the cells for LRRK2 recruitment, activation, and subsequent Rab phosphorylation upon lysosomal damage. This may occur because the [D620N] mutation causes 1)

underlying lysosomal damage that triggers LRRK2 activation, 2) a disruption to Rab12 activity cycling by perturbing the expression or activity of its cognate GEF or GAP, or 3) enhanced LRRK2 activity, either indirectly or directly, by an unknown mechanism. Conversely, depletion of VPS35 leads to a decrease in lysosome damage-induced LRRK2-dependent Rab phosphorylation.

6.5.4.2 VPS35 and the response to lysosomal damage

Given the amplification of Rab phosphorylation in response to lysosomal damage in RPE1 cells expressing the VPS35[D620N] mutation, I wondered what downstream consequences this may have. I first looked at the responses to lysosomal damage that LRRK2 has been implicated in; JIP4 recruitment, ESCRT recruitment and secretion of cathepsin D extracellularly.

In the subcellular fractionation experiments, I failed to detect any membrane localisation of JIP4 in any conditions and so could not determine whether this was influenced by lysosomal damage and the [D620N] mutation. It would be interesting to explore this area further using microscopy to investigate JIP4 localisation and lysosome tubulation in the presence of VPS35[D620N] mutation, both basally and following lysosomal damage. This could be achieved by looking at endogenous JIP4 if possible or using fluorescently tagged constructs.

I observed no effect of VPS35[D620N] expression on the recruitment of CHMP2B and ALIX to lysosomes following LLOMe treatment. This result suggests that the [D620N] mutation does not influence this repair pathway. However, it is possible that an effect could have been missed by analysing only a single snapshot using fixed cell microscopy. It would be beneficial to monitor ESCRT recruitment in live cells to see if the kinetics of recruitment are affected, for example using the CHMP4B-eGFP construct utilised by Radulovic and colleagues (Radulovic et al., 2018). The time points that I tested were 30 and 120 minutes after LLOMe treatment, which also raises the possibility that an effect on acute recruitment may have been missed as I found that ESCRT recruitment was only sensitive to MLi-2 at the earliest 15-minute timepoint and gone by 30 minutes.

I was also unable to observe any effect of the [D620N] mutation on nigericin-induced Cathepsin D secretion into the extracellular media, which I had previously shown to be sensitive to LRRK2 kinase activity. This result was based on a single experiment, so it would be necessary to repeat this to ensure reproducibility, but it suggests that the [D620N] mutation does not influence lysosomal secretion. This is in contrast to

what has been recently reported in VPS35 knockout cells, which display an increase in lysosomal proteins in their secretome (Daly et al., 2023).

As there was no observable impact of the [D620N] mutation on LRRK2-dependent lysosomal recovery mechanisms, I turned to look at whether autophagic clearance of lysosomes was affected. Expression of the [D620N] mutation did not affect LLOMe-induced LC3 lipidation assessed by western blotting, or its recruitment to lysosomal membranes as measured by immunofluorescence microscopy. This suggests that lysophagy can be initiated in VPS35[D620N] cells unhindered. After a washout period, the clearance of LC3 puncta appeared less efficient in cells expressing VPS35[D620N] compared with cells expressing wild type VPS35. This suggests that there is an impairment in the ability of the [D620N] mutant cells to recover from lysosomal damage. It would be interesting to use the lysokeima reporter cell lines to further examine the progression and resolution of lysophagy in the VPS35 FlpIn cell lines. However, I did not have the time to examine this after discovering that a large percentage of the cell populations were no longer expressing the HA-VPS35 constructs, which could not be improved by culturing cells under antibiotic selection. As the lysokeima reporter can only be used in live cells, it was not possible to distinguish which cells were positive for HA-VPS35 expression.

I have confirmed that the impairment in clearing damaged lysosomes is not due to a general block in autophagy or autophagic flux, as LC3 lipidation levels were equivalent in wild type and mutant cells following concanamycin A treatment. This contrasts with two previous reports which have shown that cells overexpressing VPS35[D620N] exhibit a reduction in LC3-II levels basally and following bafilomycin A treatment (Rahman et al., 2020; Zavodszky et al., 2014). Zavodszky and colleagues attributed this to an impairment in autophagosome formation due to perturbed Atg9a trafficking, whereas Rahman and colleagues proposed this was due to transcription-level changes in components of PI3K-AKT signalling pathway which regulates mTOR (Rahman et al., 2020; Zavodszky et al., 2014).

Mammalian retromer has been suggested to play multiple roles in the regulation of autophagy, including in controlling mTOR activity, ATG9A trafficking and autophagic lysosome reformation (Daly et al., 2023; Jimenez-Orgaz et al., 2018; Rahman et al., 2020; Tang et al., 2015a; Zavodszky et al., 2014). Furthermore, knockdown of VPS35 and expression of VPS35[D620N] (endogenous knockin and overexpression) have both been reported to cause a defect in autophagic flux due to reduced lysosomal degradative capacity (Carosi et al., 2021; Hanss et al., 2021). I was unable to detect

any lipidated LC3 in VPS35-depleted cells by western blotting, which suggests that basal autophagic turnover is not affected by loss of VPS35 in RPE1 cells. Contrary to previous work in the literature, I found that VPS35 depletion caused an increase in LC3 lipidation when autophagy was initiated (in my case, using chloroquine and LLOMe) compared to controls (Jimenez-Orgaz et al., 2018; Kvainickas et al., 2019; Popovic and Dikic, 2014). This could suggest that these cells have increased autophagy induction in response to stress or that they are unable to properly degrade autolysosomes once challenged. To gain clarity on this, it would be necessary to co-treat with the endolysosomal damaging agents plus concanamycin A in the VPS35-depleted cells to see if autophagic flux was impaired.

In summary, I have demonstrated a role for VPS35 in the LRRK2-Rab axis in lysosomal damage. VPS35 is required for proper LRRK2 activation following lysosomal damage. Furthermore, in this context, the VPS35 [D620N] mutation behaves as a 'gain of function' mutation, enhancing LRRK2-dependent phosphorylation of substrate Rabs. This may occur due to a 'priming' effect whereby the [D620N] mutation increases Rab12 levels at the lysosome, facilitating greater recruitment of LRRK2 and, in turn, greater Rab recruitment and phosphorylation in a feed-forward mechanism. The [D620N] mutation did not affect LRRK2-dependent lysosomal repair mechanisms under the conditions tested but led to a defect in the clearance of damaged lysosomes by autophagy. This suggests that the [D620N] mutation impairs recovery following lysosomal insult, although it remains to been seen whether this delay in lysosomal recovery in the presence of the [D620N] mutation is dependent on the enhanced Rab phosphorylation observed.

7 Conclusion

The mainstay of PD treatment is levodopa, which was developed over 50 years ago and merely alleviates the symptoms of PD, not slowing or preventing disease progression (Fahn et al., 2004). This dearth of treatment options is, in part, because the molecular mechanisms underlying PD pathogenesis are poorly understood. Although most cases of PD are idiopathic, 10-15% are inherited, with seventeen different genes having been found to be mutated. Not only do these so-called 'PARK' genes provide potential drug targets, but they have been implicated in two overarching processes that emerge as central to PD pathology: endolysosomal trafficking and mitochondrial homeostasis. Furthermore, multiple studies have reported physical and functional interactions between 'PARK' proteins, suggesting that they may form common pathways that underpin pathology. One such link is the finding that the PD-mutation [D620N] within VPS35 leads to the hyperactivation of LRRK2 (Mir et al., 2018). The work presented in this thesis aimed to gain a deeper understanding of the relationship between VPS35 and LRRK2 and how this relates to PD.

7.1 Isogenic RPE1 FlpIn VPS35 cell lines as a model system for studying the [D620N] mutation

To study the pathogenic effects of the [D620N] mutation, I generated cell lines stably expressing either wild type or [D620N] mutant VPS35 in RPE1 cells using the Flp-In™ system, which has many benefits over transient overexpression and more traditional modes of stable cell line generation. As only one copy of VPS35 is introduced at a unique site, the wild type and [D620N] mutant cell line pair are isogenic and have equivalent levels of VPS35 expression. Furthermore, expression of VPS35 is inducible by introduction of doxycycline. This means that exogenous VPS35 expression can be titrated to achieve near-endogenous levels. The attainment of a 1:1 ratio between exogenous and endogenous VPS35 allows us to recapitulate the stoichiometry that prevails in the autosomal dominant PD patient setting.

Overexpression of wild type and [D620N] VPS35 has often been reported to mirror the effects of VPS35 depletion or deletion, suggesting that high levels of VPS35 overexpression may give rise to dominant negative phenotypes (MacLeod et al., 2013; Munsie et al., 2015; Tang et al., 2015b; Tian et al., 2015). This complicates the study of the true effects of the [D620N] mutation and highlights the need for more physiologically relevant model systems. The fact that I observe differential effects on LRRK2-dependent Rab phosphorylation between VPS35 depletion and expression of

VPS35[D620N] demonstrates that the RPE1 FlpIn system is not victim to this phenomenon.

To study the effect of the [D620N] mutation at truly endogenous protein expression levels, VPS35[D620N] would need to be introduced by knockin substitution. This technique has been successfully executed to create heterozygous and homozygous [D620N] knockin mammalian cell and mouse models (Bondar et al., 2023; Cataldi et al., 2018; Ma et al., 2021; Mir et al., 2018; Pal et al., 2023). However, the long-term expression of VPS35[D620N] in these systems may give rise to compensatory changes to account for any functional deficits, which could make the study of the acute effects of the [D620N] mutation challenging. The inducible nature of VPS35 expression in my cell model makes it more amenable to the study of the acute consequences of the [D620N] mutation without the complication of compensatory effects.

Whilst working with the RPE1 FlpIn VPS35 cell lines, I have observed that a population of the cells lose the expression of the construct. Therefore, care must be taken to ensure that a high percentage of the cells express HA-VPS35 by maintaining them under antibiotic selection. This is particularly important for experiments that look at the whole cell population (e.g. via western blotting) or live cell imaging where it is not possible to distinguish expressing cells from those that have lost expression.

Although the RPE1 cells utilised in this project are valuable for researching the molecular biology of PD, the most physiologically relevant model would be the cell type that is most affected in PD patients, dopaminergic neurons. Working with patient-derived iPSCs fibroblasts or induced dopaminergic neurons provides more translational power but presents its own challenges as there can be high variability in the behaviour of cells from different donors, including between different ‘healthy’ controls, even when donors are carefully matched for sex and age. To overcome these challenges, the iPSC Neurodegenerative Disease Initiative (iNDI) project is a multi-centre effort to generate a standardised catalogue of isogenic iPSC cell lines with over 100 different mutations associated with Alzheimer’s Disease and other neurodegenerative disorders (Ramos et al., 2021). It is an exciting possibility that soon an isogenic VPS35[D620N] iPSC model capable of being differentiated into dopaminergic neurons may exist.

7.2 [D620N] gives rise to a subtle phenotype

Using the isogenic RPE1 FlpIn VPS35 cell line, I have systematically tested the effects of the [D620N] mutation on a range of different phenotypes that have previously been reported in the literature. In doing so, I was only able to recapitulate two of the previously reported consequences of the [D620N] mutation: loss of interaction with the WASH complex and enhanced phosphorylation of LRRK2-substrate Rabs.

Although the interaction of retromer with the WASH complex was reduced by approximately half in cells expressing the [D620N] mutation, I found no loss of WASH complex localisation to endosomes. Looking at the steady-state distribution of the lysosomal hydrolase receptors CIMPR and sortilin I found no changes in their localisation, suggesting that the [D620N] does not perturb endosome-to-TGN trafficking. I did not test the effect of the [D620N] mutation on the trafficking from the endosome to the plasma membrane, such as retromer cargo GLUT1. It would be valuable to test this in the future to see whether this recycling route is also unaffected by the [D620N] mutation.

As VPS35 has been implicated in mitochondrial quality control and multiple studies have reported disruptions to mitochondrial dynamics and mitophagy as a result of the [D620N] mutation, I also examined several mitochondrial phenotypes in the RPE1 FlpIn VPS35 model (Braschi et al., 2010; Hanss et al., 2021; Ma et al., 2021; Niu et al., 2021; Tang et al., 2015b; Wang et al., 2017, 2016). I was unable to observe any changes in mitochondrial morphology nor expression of proteins responsible for maintaining the balance between mitochondrial fission and fusion. I did not find changes to the basal mitochondrial membrane potential which suggests that mitochondrial function is not impaired. Furthermore, I found no effect of the [D620N] mutation on the induction of depolarisation-induced mitophagy. Together, these results suggest that the [D620N] mutation does not cause any overt changes to mitochondrial function and homeostasis in the RPE1 FlpIn cell system.

Deletion of VPS35 has been reported to cause hyperaccumulation of Rab7 on late endosome-lysosome compartments, perturbing endolysosomal morphology and function (Daly et al., 2023; Jimenez-Orgaz et al., 2018). In RPE1 cells, Rab7 mostly co-localised with lysosomes at steady state, and this was not changed by expression of the VPS35[D620N] mutant. Furthermore, I found no changes to lysosomal morphology or distribution following expression of VPS35[D620N].

From this work, I conclude that the [D620N] mutation gives rise to a subtle phenotype in the RPE1 FlpIn VPS35 cell model as very few alterations were observed at steady state. On the one hand, this is surprising as retromer clearly plays an indispensable role in the cell given that knockout of VPS35 is embryonically lethal (Wen et al., 2011). On the other hand, perhaps only a subtle perturbation explains why PD patients that harbour the [D620N] mutation have a late age of onset (Vilariño-Güell et al., 2011; Zimprich et al., 2011). This indicates that the mutation is not a simple loss of function, and it may be that only in combination with the stresses of ageing do the negative consequences of the [D620N] mutation begin to take hold.

7.3 VPS35[D620N] and LRRK2

Using the RPE1 FlpIn model, I confirmed the work of others that the VPS35[D620N] mutation causes enhanced phosphorylation of LRRK2-substrate Rabs (Mir et al., 2018). Mir and colleagues demonstrated that the [D620N] mutation in VPS35 enhances LRRK2-mediated autophosphorylation at S1292, suggesting that the enhanced Rab phosphorylation observed is due to increased LRRK2 kinase activity rather than a decreased activity of Rab phosphatases such as PPM1H (Mir et al., 2018). I was unable to detect pS1292-LRRK2 by immunoblotting, possibly owing to the relatively low endogenous LRRK2 expression in RPE1 cells. The molecular mechanism by which VPS35[D620N] enhances LRRK2 activity is not understood, including whether it occurs directly or indirectly.

I found that the [D620N] mutation caused an increased localisation of both unphosphorylated and phosphorylated Rab12 to membranes. The finding that there is an increase in the pool of unphosphorylated Rab12 at membranes is interesting as it suggests that it is not solely being trapped there by LRRK2-dependent phosphorylation, which prevents its extraction from membranes by GDIs (Steger et al., 2016). As Rab12 has recently been discovered to be critical for recruitment and activation of LRRK2, it is possible that the accumulation of Rab12 at membranes that I observe is driving a feed-forward mechanism to increase LRRK2 recruitment, activation, and subsequent Rab phosphorylation (Bondar et al., 2023; Dhekne et al., 2023). A change in membrane-cytosol distribution of Rab12 may suggest that VPS35[D620N] causes a disruption to Rab12 activity cycling by altering the expression or activity of its cognate GEF and GAP.

It would be valuable to examine Rab12 localisation by immunofluorescence to ascertain which membrane compartment Rab12 is accumulating at. In light of the findings by other groups that the VPS35[D620N] mutation increases the localisation

of LRRK2 and the Rab12 effector RILPL1 to lysosomes, I would speculate that Rab12 would be accumulating at lysosomes in my system (Bondar et al., 2023; Fukuda et al., 2008; Pal et al., 2023).

It would also be valuable in the future to investigate the effect of the [D620N] mutation on the localisation and distribution of other LRRK2-substrate Rabs such as Rab10 and Rab8A to see whether there is a similar increase in their accumulation at membranes in their unphosphorylated form and whether this can be modulated by knockdown of Rab12. This may provide information as to whether enhanced Rab phosphorylation in [D620N]-expressing cells is due to the accumulated membrane-bound Rab12 lying upstream of LRRK2 activation.

7.4 VPS35 and lysosomal damage

LRRK2 is recruited to lysosomes in following lysosomal damage, where it has been suggested to play a role in the recovery from damage (Bonet-Ponce et al., 2020; Eguchi et al., 2018; Herbst et al., 2020). In this thesis I have shown that VPS35 is required for complete activation of LRRK2 in response to the lysosomal stressors nigericin, chloroquine and LLOMe. Conversely, I found that expression of [D620N] mutant VPS35 amplifies LRRK2-dependent Rab phosphorylation in response to lysosomal stress. These results suggest that in this capacity the [D620N] mutation acts in a ‘gain-of-function’ manner and implicates a role for VPS35 in the LRRK2-Rab axis in the lysosomal damage response. I hypothesise that this amplified response may occur due to a priming effect whereby the increased membrane-bound Rab12 at steady state facilitates heightened LRRK2 recruitment when lysosomal damage is triggered.

As above, the Rab12 accumulation may arise due to perturbation of the Rab GEF-GAP cycling, however, an alternative hypothesis is that the [D620N] mutation causes a low level of underlying lysosomal dysfunction that is causing Rab12 recruitment and LRRK2 recruitment and activation that is exacerbated in response to additional lysosomal stress. Recent work by Pal and colleagues has shown that the [D620N] mutation causes changes in expression of over 100 lysosomal proteins, making this a possibility (Pal et al., 2023). I found no changes to lysosomal morphology or distribution at steady state, but it would be valuable to use a read-out for lysosomal degradative capacity to inform on whether lysosomes are fully functional when VPS35[D620N] is expressed. It is also possible that changes to the lysosomal proteome as a result of the [D620N] mutation would take longer to manifest than the 24-hour time point I have used in experiments. If this is the case, lysosomal

dysfunction may contribute to enhanced LRRK2 activation or recruitment but may not be the sole driver of LRRK2 activation given that I observe enhanced Rab phosphorylation after a short duration of VPS35 expression.

I found that the [D620N] mutation impaired the ability to clear damaged lysosomes, suggesting that the mutation also affects the recovery from lysosomal damage. Future experiments could investigate whether this impairment is dependent on LRRK2 or if it is occurring by a separate mechanism. Daly and colleagues have shown that knockout of VPS35 impairs autophagic lysosome reformation in response to nutrient starvation, which will limit the ability to generate a functional pool of lysosomes. Furthermore, using LAMP1-APEX proximity labelling, Bhattacharya and colleagues found that VPS26 and VPS35 are enriched at lysosomes following treatment with LLOMe (Bhattacharya et al., 2023). Together these findings further suggest that VPS35 plays a role in the lysosome stress response in addition to its cargo sorting function at the endosome.

Overall, this thesis reveals a potential VPS35-LRRK2-Rab axis in the response to lysosomal damage and indicates that lysosomal dysfunction may be a key player in PD pathogenesis. I have demonstrated that, in this context, the VPS35[D620N] mutation causes a gain-of-function. Finally, this provides encouraging evidence that patients with the VPS35[D620N] mutation may benefit therapeutically from use of the LRRK2 inhibitor that is currently in clinical trials for treatment of LRRK2-variant PD.

8 References

Abramov, A.Y., Gegg, M., Grunewald, A., Wood, N.W., Klein, C., Schapira, A.H.V., 2011. Bioenergetic Consequences of PINK1 Mutations in Parkinson Disease. PLOS ONE 6, e25622. https://doi.org/10.1371/journal.pone.0025622

Adell, M.A.Y., Vogel, G.F., Pakdel, M., Müller, M., Lindner, H., Hess, M.W., Teis, D., 2014. Coordinated binding of Vps4 to ESCRT-III drives membrane neck constriction during MVB vesicle formation. J. Cell Biol. 205, 33–49. https://doi.org/10.1083/jcb.201310114

Aharon-Peretz, J., Rosenbaum, H., Gershoni-Baruch, R., 2004. Mutations in the glucocerebrosidase gene and Parkinson's disease in Ashkenazi Jews. N. Engl. J. Med. 351, 1972–1977. https://doi.org/10.1056/NEJMoa033277

Ahler, E., Sullivan, W.J., Cass, A., Braas, D., York, A.G., Bensinger, S.J., Graeber, T.G., Christofk, H.R., 2013. Doxycycline Alters Metabolism and Proliferation of Human Cell Lines. PLoS ONE 8, e64561. https://doi.org/10.1371/journal.pone.0064561

Aits, S., Kricker, J., Liu, B., Ellegaard, A.-M., Hämälistö, S., Tvingsholm, S., Corcelle-Termeau, E., Høgh, S., Farkas, T., Holm Jonassen, A., Gromova, I., Mortensen, M., Jäättelä, M., 2015. Sensitive detection of lysosomal membrane permeabilization by lysosomal galectin puncta assay. Autophagy 11, 1408–1424. https://doi.org/10.1080/15548627.2015.1063871

Akutsu, M., Dikic, I., Bremm, A., 2016. Ubiquitin chain diversity at a glance. J. Cell Sci. 129, 875–880. https://doi.org/10.1242/jcs.183954

Alexandrov, K., Horiuchi, H., Steele-Mortimer, O., Seabra, M.C., Zerial, M., 1994. Rab escort protein-1 is a multifunctional protein that accompanies newly prenylated rab proteins to their target membranes. EMBO J. 13, 5262–5273.

Allen, G.F.G., Toth, R., James, J., Ganley, I.G., 2013. Loss of iron triggers PINK1/Parkin-independent mitophagy. EMBO Rep. 14, 1127–1135. https://doi.org/10.1038/embor.2013.168

Alonso-Curbelo, D., Riveiro-Falkenbach, E., Pérez-Guijarro, E., Cifdaloz, M., Karras, P., Osterloh, L., Megías, D., Cañón, E., Calvo, T.G., Olmeda, D., Gómez-López, G., Graña, O., Sánchez-Arévalo Lobo, V.J., Pisano, D.G., Wang, H.-W., Ortiz-Romero, P., Tormo, D., Hoek, K., Rodríguez-Peralto, J.L., Joyce, J.A., Soengas, M.S., 2014. RAB7 Controls Melanoma Progression by Exploiting a Lineage-Specific Wiring of the Endolysosomal Pathway. Cancer Cell 26, 61–76. https://doi.org/10.1016/j.ccr.2014.04.030

Antony, P.M.A., Diederich, N.J., Krüger, R., Balling, R., 2013. The hallmarks of Parkinson's disease. FEBS J. 280, 5981–5993. https://doi.org/10.1111/febs.12335

Appelmans, F., De Duve, C., 1955. Tissue fractionation studies. 3. Further observations on the binding of acid phosphatase by rat-liver particles. Biochem. J. 59, 426–433.

Araki, S., Kikuchi, A., Hata, Y., Isomura, M., Takai, Y., 1990. Regulation of reversible binding of smg p25A, a ras p21-like GTP-binding protein, to synaptic plasma membranes and vesicles by its specific regulatory protein, GDP dissociation inhibitor. J. Biol. Chem. 265, 13007–13015. https://doi.org/10.1016/S0021-9258(19)38260-2

Arighi, C.N., Hartnell, L.M., Aguilar, R.C., Haft, C.R., Bonifacino, J.S., 2004. Role of the mammalian retromer in sorting of the cation-independent mannose 6-phosphate receptor. J. Cell Biol. 165, 123–133. https://doi.org/10.1083/jcb.200312055

Azeggagh, S., Berwick, D.C., 2022. The development of inhibitors of leucine-rich repeat kinase 2 (LRRK2) as a therapeutic strategy for Parkinson's disease:

the current state of play. Br. J. Pharmacol. 179, 1478–1495. https://doi.org/10.1111/bph.15575
Babst, M., Katzmann, D.J., Estepa-Sabal, E.J., Meerloo, T., Emr, S.D., 2002a. Escrt-III: An endosome-associated heterooligomeric protein complex required for mvb sorting. Dev. Cell 3, 271–282. https://doi.org/10.1016/S1534-5807(02)00220-4
Babst, M., Katzmann, D.J., Snyder, W.B., Wendland, B., Emr, S.D., 2002b. Endosome-associated complex, ESCRT-II, recruits transport machinery for protein sorting at the multivesicular body. Dev. Cell 3, 283–289. https://doi.org/10.1016/s1534-5807(02)00219-8
Babst, M., Sato, T.K., Banta, L.M., Emr, S.D., 1997. Endosomal transport function in yeast requires a novel AAA-type ATPase, Vps4p. EMBO J. 16, 1820–1831. https://doi.org/10.1093/emboj/16.8.1820
Babst, M., Wendland, B., Estepa, E.J., Emr, S.D., 1998. The Vps4p AAA ATPase regulates membrane association of a Vps protein complex required for normal endosome function. EMBO J. 17, 2982–2993. https://doi.org/10.1093/emboj/17.11.2982
Bakula, D., Müller, A.J., Zuleger, T., Takacs, Z., Franz-Wachtel, M., Thost, A.-K., Brigger, D., Tschan, M.P., Frickey, T., Robenek, H., Macek, B., Proikas-Cezanne, T., 2017. WIPI3 and WIPI4 β-propellers are scaffolds for LKB1-AMPK-TSC signalling circuits in the control of autophagy. Nat. Commun. 8, 15637. https://doi.org/10.1038/ncomms15637
Barbieri, M.A., Li, G., Mayorga, L.S., Stahl, P.D., 1996. Characterization of Rab5:Q79L-Stimulated Endosome Fusion. Arch. Biochem. Biophys. 326, 64–72. https://doi.org/10.1006/abbi.1996.0047
Barone, F.G., Urbé, S., Clague, M.J., 2023. Segregation of pathways leading to pexophagy. Life Sci. Alliance 6. https://doi.org/10.26508/lsa.202201825
Barretina, J., Caponigro, G., Stransky, N., Venkatesan, K., Margolin, A.A., Kim, S., Wilson, C.J., Lehár, J., Kryukov, G.V., Sonkin, D., Reddy, A., Liu, M., Murray, L., Berger, M.F., Monahan, J.E., Morais, P., Meltzer, J., Korejwa, A., Jané-Valbuena, J., Mapa, F.A., Thibault, J., Bric-Furlong, E., Raman, P., Shipway, A., Engels, I.H., Cheng, J., Yu, G.K., Yu, J., Aspesi, P., de Silva, M., Jagtap, K., Jones, M.D., Wang, L., Hatton, C., Palescandolo, E., Gupta, S., Mahan, S., Sougnez, C., Onofrio, R.C., Liefeld, T., MacConaill, L., Winckler, W., Reich, M., Li, N., Mesirov, J.P., Gabriel, S.B., Getz, G., Ardlie, K., Chan, V., Myer, V.E., Weber, B.L., Porter, J., Warmuth, M., Finan, P., Harris, J.L., Meyerson, M., Golub, T.R., Morrissey, M.P., Sellers, W.R., Schlegel, R., Garraway, L.A., 2012. The Cancer Cell Line Encyclopedia enables predictive modelling of anticancer drug sensitivity. Nature 483, 603–607. https://doi.org/10.1038/nature11003
Beilina, A., Bonet-Ponce, L., Kumaran, R., Kordich, J.J., Ishida, M., Mamais, A., Kaganovich, A., Saez-Atienzar, S., Gershlick, D.C., Roosen, D.A., Pellegrini, L., Malkov, V., Fell, M.J., Harvey, K., Bonifacino, J.S., Moore, D.J., Cookson, M.R., 2020. The Parkinson's Disease Protein LRRK2 Interacts with the GARP Complex to Promote Retrograde Transport to the trans-Golgi Network. Cell Rep. 31, 107614. https://doi.org/10.1016/j.celrep.2020.107614
Beilina, A., Rudenko, I.N., Kaganovich, A., Civiero, L., Chau, H., Kalia, S.K., Kalia, L.V., Lobbestael, E., Chia, R., Ndukwe, K., Ding, J., Nalls, Mike A., Olszewski, M., Hauser, D.N., Kumaran, R., Lozano, A.M., Baekelandt, V., Greene, L.E., Taymans, J.-M., Greggio, E., Cookson, M.R., Nalls, Mike A., Plagnol, V., Martinez, M., Hernandez, D.G., Sharma, M., Sheerin, U.-M., Saad, M., Simón-Sánchez, J., Schulte, C., Lesage, S., Sveinbjörnsdóttir, S., Arepalli, S., Barker, R., Ben-Shlomo, Y., Berendse, H.W., Berg, D., Bhatia, K., de Bie, R.M.A., Biffi, A., Bloem, B., Bochdanovits, Z., Bonin, M., Bras, J.M., Brockmann, K., Brooks, J., Burn, D.J., Charlesworth, G., Chen, H., Chong, S., Clarke, C.E., Cookson,

M.R., Cooper, J.M., Corvol, J.C., Counsell, C., Damier, P., Dartigues, J.-F., Deloukas, P., Deuschl, G., Dexter, D.T., van Dijk, K.D., Dillman, A., Durif, F., Dürr, A., Edkins, S., Evans, J.R., Foltynie, T., Gao, J., Gardner, M., Gibbs, J.R., Goate, A., Gray, E., Guerreiro, R., Gústafsson, Ó., Harris, C., van Hilten, J.J., Hofman, A., Hollenbeck, A., Holton, J., Hu, M., Huang, X., Huber, H., Hudson, G., Hunt, S.E., Huttenlocher, J., Illig, T., München, H.Z., Jónsson, P.V., Lambert, J.-C., Langford, C., Lees, A., Lichtner, P., München, H.Z., Limousin, P., Lopez, G., Lorenz, D., McNeill, A., Moorby, C., Moore, M., Morris, H.R., Morrison, K.E., Mudanohwo, E., O'Sullivan, S.S., Pearson, J., Perlmutter, J.S., Pétursson, H., Pollak, P., Post, B., Potter, S., Ravina, B., Revesz, T., Riess, O., Rivadeneira, F., Rizzu, P., Ryten, M., Sawcer, S., Schapira, A., Scheffer, H., Shaw, K., Shoulson, I., Sidransky, E., Smith, C., Spencer, C.C.A., Stefánsson, H., Steinberg, S., Stockton, J.D., Strange, A., Talbot, K., Tanner, C.M., Tashakkori-Ghanbaria, A., Tison, F., Trabzuni, D., Traynor, B.J., Uitterlinden, A.G., Velseboer, D., Vidailhet, M., Walker, R., van de Warrenburg, B., Wickremaratchi, M., Williams, N., Williams-Gray, C.H., Winder-Rhodes, S., Stefánsson, K., Hardy, J., Heutink, P., Brice, A., Gasser, T., Singleton, A.B., Wood, N.W., Chinnery, P.F., Arepalli, S., Cookson, M.R., Dillman, A., Ferrucci, L., Gibbs, J.R., Hernandez, D.G., Johnson, R., Longo, D.L., Majounie, E., Nalls, Michael A, O'Brien, R., Singleton, A.B., Traynor, B.J., Troncoso, J., van der Brug, M., Zielke, H.R., Zonderman, A.B., 2014. Unbiased screen for interactors of leucine-rich repeat kinase 2 supports a common pathway for sporadic and familial Parkinson disease. Proc. Natl. Acad. Sci. U. S. A. 111, 2626–2631. https://doi.org/10.1073/pnas.1318306111

Bento, C.F., Ashkenazi, A., Jimenez-Sanchez, M., Rubinsztein, D.C., 2016. The Parkinson's disease-associated genes ATP13A2 and SYT11 regulate autophagy via a common pathway. Nat. Commun. 7. https://doi.org/10.1038/ncomms11803

Berger, Z., Smith, K.A., LaVoie, M.J., 2010. Membrane localization of LRRK2 is associated with increased formation of the highly active LRRK2 dimer and changes in its phosphorylation. Biochemistry 49, 5511–5523. https://doi.org/10.1021/bi100157u

Berge-Seidl, V., Pihlstrøm, L., Maple-Grødem, J., Forsgren, L., Linder, J., Larsen, J.P., Tysnes, O.-B., Toft, M., 2017. The GBA variant E326K is associated with Parkinson's disease and explains a genome-wide association signal. Neurosci. Lett. 658, 48–52. https://doi.org/10.1016/j.neulet.2017.08.040

Berndsen, K., Lis, P., Yeshaw, W.M., Wawro, P.S., Nirujogi, R.S., Wightman, M., Macartney, T., Dorward, M., Knebel, A., Tonelli, F., Pfeffer, S.R., Alessi, D.R., 2019. PPM1H phosphatase counteracts LRRK2 signaling by selectively dephosphorylating Rab proteins. eLife 8, e50416. https://doi.org/10.7554/eLife.50416

Berwick, D.C., Heaton, G.R., Azeggagh, S., Harvey, K., 2019. LRRK2 Biology from structure to dysfunction: research progresses, but the themes remain the same. Mol. Neurodegener. 14. https://doi.org/10.1186/s13024-019-0344-2

Besemer, A.S., Maus, J., Ax, M.D.A., Stein, A., Vo, S., Freese, C., Nalbach, K., von Hilchen, C., Pfalzgraf, I.F., Koziollek-Drechsler, I., Silva, B., Huesmann, H., Boukhallouk, F., Florin, L., Kern, A., Behl, C., Clement, A.M., 2020. Receptor-mediated endocytosis 8 (RME-8)/DNAJC13 is a novel positive modulator of autophagy and stabilizes cellular protein homeostasis. Cell. Mol. Life Sci. https://doi.org/10.1007/s00018-020-03521-y

Bhattacharya, A., Mukherjee, R., Kuncha, S.K., Brunstein, M.E., Rathore, R., Junek, S., Münch, C., Dikic, I., 2023. A lysosome membrane regeneration pathway depends on TBC1D15 and autophagic lysosomal reformation proteins. Nat. Cell Biol. 25, 685–698. https://doi.org/10.1038/s41556-023-01125-9

Bindoff, L.A., Birch-Machin, M., Cartlidge, N.E.F., Parker, W.D., Turnbull, D.M., 1989. MITOCHONDRIAL FUNCTION IN PARKINSON'S DISEASE. The Lancet, Originally published as Volume 2, Issue 8653 334, 49. https://doi.org/10.1016/S0140-6736(89)90291-2

Biogen, 2023. A Phase 3, Multicenter, Randomized, Double-Blind, Placebo-Controlled Study to Determine the Efficacy and Safety of BIIB122/DNL151 in Participants With Parkinson's Disease and Pathogenic LRRK2 Variants (Clinical trial registration No. NCT05418673). clinicaltrials.gov.

Biskup, S., Moore, D.J., Celsi, F., Higashi, S., West, A.B., Andrabi, S.A., Kurkinen, K., Yu, S.-W., Savitt, J.M., Waldvogel, H.J., Faull, R.L.M., Emson, P.C., Torp, R., Ottersen, O.P., Dawson, T.M., Dawson, V.L., 2006. Localization of LRRK2 to membranous and vesicular structures in mammalian brain. Ann. Neurol. 60, 557–569. https://doi.org/10.1002/ana.21019

Bissig, C., Gruenberg, J., 2014. ALIX and the multivesicular endosome: ALIX in Wonderland. Trends Cell Biol., Special Issue: Membrane Trafficking 24, 19–25. https://doi.org/10.1016/j.tcb.2013.10.009

Blauwendraat, C., Bras, J.M., Nalls, M.A., Lewis, P.A., Hernandez, D.G., Singleton, A.B., 2018. Coding Variation in GBA Explains the Majority of the SYT11-GBA Parkinson's Disease GWAS Locus. Mov. Disord. Off. J. Mov. Disord. Soc. 33, 1821–1823. https://doi.org/10.1002/mds.103

Blauwendraat, C., Nalls, M.A., Singleton, A.B., 2020. The genetic architecture of Parkinson's disease. Lancet Neurol. 19, 170–178. https://doi.org/10.1016/S1474-4422(19)30287-X

Blümer, J., Rey, J., Dehmelt, L., Mazel, T., Wu, Y.-W., Bastiaens, P., Goody, R.S., Itzen, A., 2013. RabGEFs are a major determinant for specific Rab membrane targeting. J. Cell Biol. 200, 287–300. https://doi.org/10.1083/jcb.201209113

Bodnar, A.G., Ouellette, M., Frolkis, M., Holt, S.E., Chiu, C.-P., Morin, G.B., Harley, C.B., Shay, J.W., Lichtsteiner, S., Wright, W.E., 1998. Extension of Life-Span by Introduction of Telomerase into Normal Human Cells. Science 279, 349–352. https://doi.org/10.1126/science.279.5349.349

Boesch, D.J., Singla, A., Han, Y., Kramer, D.A., Liu, Q., Suzuki, K., Juneja, P., Zhao, X., Long, X., Medlyn, M.J., Billadeau, D.D., Chen, Z., Chen, B., Burstein, E., 2023. Structural Organization of the Retriever-CCC Endosomal Recycling Complex. https://doi.org/10.1101/2023.06.06.543888

Bondar, V.V., Wang, X., Davis, O.B., Maloney, M.T., Agam, M., Chin, M.Y., Ho, A.C.-N., Joy, D., Lewcock, J.W., Paolo, G.D., Thorne, R.G., Sweeney, Z.K., Henry, A.G., 2023. Rab12 regulates LRRK2 activity by promoting its localization to lysosomes. https://doi.org/10.1101/2023.02.21.529466

Bonello, F., Hassoun, S.-M., Mouton-Liger, F., Shin, Y.S., Muscat, A., Tesson, C., Lesage, S., Beart, P.M., Brice, A., Krupp, J., Corvol, J.-C., Corti, O., 2019. LRRK2 impairs PINK1/Parkin-dependent mitophagy via its kinase activity: pathologic insights into Parkinson's disease. Hum. Mol. Genet. 28, 1645–1660. https://doi.org/10.1093/hmg/ddz004

Bonet-Ponce, L., Beilina, A., Williamson, C.D., Lindberg, E., Kluss, J.H., Saez-Atienzar, S., Landeck, N., Kumaran, R., Mamais, A., Bleck, C.K.E., Li, Y., Cookson, M.R., 2020. LRRK2 mediates tubulation and vesicle sorting from lysosomes. Sci. Adv. 6, eabb2454. https://doi.org/10.1126/sciadv.abb2454

Bove, C., Travagli, R.A., 2019. Neurophysiology of the brain stem in Parkinson's disease. J. Neurophysiol. 121, 1856–1864. https://doi.org/10.1152/jn.00056.2019

Boya, P., Kroemer, G., 2008. Lysosomal membrane permeabilization in cell death. Oncogene 27, 6434–6451. https://doi.org/10.1038/onc.2008.310

Braschi, E., Goyon, V., Zunino, R., Mohanty, A., Xu, L., McBride, H.M., 2010. Vps35 mediates vesicle transport between the mitochondria and peroxisomes. Curr. Biol. CB 20, 1310–1315. https://doi.org/10.1016/j.cub.2010.05.066

Braulke, T., Bonifacino, J.S., 2009. Sorting of lysosomal proteins. Biochim. Biophys. Acta BBA - Mol. Cell Res., Lysosomes 1793, 605–614. https://doi.org/10.1016/j.bbamcr.2008.10.016

Bright, N.A., Davis, L.J., Luzio, J.P., 2016. Endolysosomes Are the Principal Intracellular Sites of Acid Hydrolase Activity. Curr. Biol. 26, 2233–2245. https://doi.org/10.1016/j.cub.2016.06.046

Brownell, J.E., Sintchak, M.D., Gavin, J.M., Liao, H., Bruzzese, F.J., Bump, N.J., Soucy, T.A., Milhollen, M.A., Yang, X., Burkhardt, A.L., Ma, J., Loke, H.-K., Lingaraj, T., Wu, D., Hamman, K.B., Spelman, J.J., Cullis, C.A., Langston, S.P., Vyskocil, S., Sells, T.B., Mallender, W.D., Visiers, I., Li, P., Claiborne, C.F., Rolfe, M., Bolen, J.B., Dick, L.R., 2010. Substrate-Assisted Inhibition of Ubiquitin-like Protein-Activating Enzymes: The NEDD8 E1 Inhibitor MLN4924 Forms a NEDD8-AMP Mimetic In Situ. Mol. Cell 37, 102–111. https://doi.org/10.1016/j.molcel.2009.12.024

Bu, M., Follett, J., Tatarnikov, I., Wall, S., Guenther, D., Deng, I., Wimsatt, G., Milnerwood, A., Moehle, M.S., Khoshbouei, H., Farrer, M.J., 2023. Inhibition of LRRK2 kinase activity rescues deficits in striatal dopamine dynamics in VPS35 p.D620N knock-in mice. https://doi.org/10.1101/2023.05.14.540654

Bucci, C., Parton, R.G., Mather, I.H., Stunnenberg, H., Simons, K., Hoflack, B., Zerial, M., 1992. The small GTPase rab5 functions as a regulatory factor in the early endocytic pathway. Cell 70, 715–728. https://doi.org/10.1016/0092-8674(92)90306-w

Burd, C., Cullen, P.J., 2014. Retromer: A Master Conductor of Endosome Sorting. Cold Spring Harb. Perspect. Biol. 6. https://doi.org/10.1101/cshperspect.a016774

Burré, J., Sharma, M., Südhof, T.C., 2018. Cell Biology and Pathophysiology of α-Synuclein. Cold Spring Harb. Perspect. Med. 8. https://doi.org/10.1101/cshperspect.a024091

Bussi, C., Heunis, T., Pellegrino, E., Bernard, E.M., Bah, N., Dos Santos, M.S., Santucci, P., Aylan, B., Rodgers, A., Fearns, A., Mitschke, J., Moore, C., MacRae, J.I., Greco, M., Reinheckel, T., Trost, M., Gutierrez, M.G., 2022. Lysosomal damage drives mitochondrial proteome remodelling and reprograms macrophage immunometabolism. Nat. Commun. 13, 7338. https://doi.org/10.1038/s41467-022-34632-8

Bussi, C., Peralta Ramos, J.M., Arroyo, D.S., Gallea, J.I., Ronchi, P., Kolovou, A., Wang, J.M., Florey, O., Celej, M.S., Schwab, Y., Ktistakis, N.T., Iribarren, P., 2018. Alpha-synuclein fibrils recruit TBK1 and OPTN to lysosomal damage sites and induce autophagy in microglial cells. J. Cell Sci. 131, jcs226241. https://doi.org/10.1242/jcs.226241

Cabezas, A., Pattni, K., Stenmark, H., 2006. Cloning and subcellular localization of a human phosphatidylinositol 3-phosphate 5-kinase, PIKfyve/Fab1. Gene 371, 34–41. https://doi.org/10.1016/j.gene.2005.11.009

Cabrera, M., Ungermann, C., 2013. Guanine Nucleotide Exchange Factors (GEFs) Have a Critical but Not Exclusive Role in Organelle Localization of Rab GTPases. J. Biol. Chem. 288, 28704–28712. https://doi.org/10.1074/jbc.M113.488213

Cabukusta, B., Neefjes, J., 2018. Mechanisms of lysosomal positioning and movement. Traffic 19, 761–769. https://doi.org/10.1111/tra.12587

Cadete, V.J.J., Deschênes, S., Cuillerier, A., Brisebois, F., Sugiura, A., Vincent, A., Turnbull, D., Picard, M., McBride, H.M., Burelle, Y., 2016. Formation of mitochondrial-derived vesicles is an active and physiologically relevant mitochondrial quality control process in the cardiac system. J. Physiol. 594, 5343–5362. https://doi.org/10.1113/JP272703

Cai, X., Xu, Y., Cheung, A.K., Tomlinson, R.C., Alcázar-Román, A., Murphy, L., Billich, A., Zhang, B., Feng, Y., Klumpp, M., Rondeau, J.-M., Fazal, A.N., Wilson, C.J.,

Myer, V., Joberty, G., Bouwmeester, T., Labow, M.A., Finan, P.M., Porter, J.A., Ploegh, H.L., Baird, D., De Camilli, P., Tallarico, J.A., Huang, Q., 2013. PIKfyve, a Class III PI Kinase, Is the Target of the Small Molecular IL-12/IL-23 Inhibitor Apilimod and a Player in Toll-like Receptor Signaling. Chem. Biol. 20, 912–921. https://doi.org/10.1016/j.chembiol.2013.05.010

Cantalupo, G., Alifano, P., Roberti, V., Bruni, C.B., Bucci, C., 2001. Rab-interacting lysosomal protein (RILP): the Rab7 effector required for transport to lysosomes. EMBO J. 20, 683–693. https://doi.org/10.1093/emboj/20.4.683

Canuel, M., Lefrancois, S., Zeng, J., Morales, C.R., 2008. AP-1 and retromer play opposite roles in the trafficking of sortilin between the Golgi apparatus and the lysosomes. Biochem. Biophys. Res. Commun. 366, 724–730. https://doi.org/10.1016/j.bbrc.2007.12.015

Carlton, J.G., Cullen, P.J., 2005. Coincidence detection in phosphoinositide signaling. Trends Cell Biol. 15, 540–547. https://doi.org/10.1016/j.tcb.2005.08.005

Carosi, J.M., Hein, L.K., van den Hurk, M., Adams, R., Milky, B., Singh, S., Bardy, C., Denton, D., Kumar, S., Sargeant, T.J., 2021. Retromer regulates the lysosomal clearance of MAPT/tau. Autophagy 17, 2217–2237. https://doi.org/10.1080/15548627.2020.1821545

Cataldi, S., Follett, J., Fox, J.D., Tatarnikov, I., Kadgien, C., Gustavsson, E.K., Khinda, J., Milnerwood, A.J., Farrer, M.J., 2018. Altered dopamine release and monoamine transporters in Vps35 p.D620N knock-in mice. NPJ Park. Dis. 4, 27. https://doi.org/10.1038/s41531-018-0063-3

Chang, D., Nalls, M.A., Hallgrímsdóttir, I.B., Hunkapiller, J., van der Brug, M., Cai, F., Kerchner, G.A., Ayalon, G., Bingol, B., Sheng, M., Hinds, D., Behrens, T.W., Singleton, A.B., Bhangale, T.R., Graham, R.R., 2017. A meta-analysis of genome-wide association studies identifies 17 new Parkinson's disease risk loci. Nat. Genet. 49, 1511–1516. https://doi.org/10.1038/ng.3955

Chang, H.C., Hull, M., Mellman, I., 2004. The J-domain protein Rme-8 interacts with Hsc70 to control clathrin-dependent endocytosis in Drosophila. J. Cell Biol. 164, 1055–1064. https://doi.org/10.1083/jcb.200311084

Chauhan, S., Kumar, S., Jain, A., Ponpuak, M., Mudd, M.H., Kimura, T., Choi, S.W., Peters, R., Mandell, M., Bruun, J.-A., Johansen, T., Deretic, V., 2016. TRIMs and Galectins Globally Cooperate and TRIM16 and Galectin-3 Co-direct Autophagy in Endomembrane Damage Homeostasis. Dev. Cell 39, 13–27. https://doi.org/10.1016/j.devcel.2016.08.003

Chavrier, P., Parton, R.G., Hauri, H.P., Simons, K., Zerial, M., 1990. Localization of low molecular weight GTP binding proteins to exocytic and endocytic compartments. Cell 62, 317–329. https://doi.org/10.1016/0092-8674(90)90369-p

Chen, X., Kordich, J.K., Williams, E.T., Levine, N., Cole-Strauss, A., Marshall, L., Labrie, V., Ma, J., Lipton, J.W., Moore, D.J., 2019. Parkinson's disease-linked D620N VPS35 knockin mice manifest tau neuropathology and dopaminergic neurodegeneration. Proc. Natl. Acad. Sci. 116, 5765–5774. https://doi.org/10.1073/pnas.1814909116

Christoforidis, S., Miaczynska, M., Ashman, K., Wilm, M., Zhao, L., Yip, S.-C., Waterfield, M.D., Backer, J.M., Zerial, M., 1999. Phosphatidylinositol-3-OH kinases are Rab5 effectors. Nat. Cell Biol. 1, 249–252. https://doi.org/10.1038/12075

Clague, M.J., Heride, C., Urbé, S., 2015. The demographics of the ubiquitin system. Trends Cell Biol. 25, 417–426. https://doi.org/10.1016/j.tcb.2015.03.002

Clague, M.J., Urbé, S., 2010. Ubiquitin: Same Molecule, Different Degradation Pathways. Cell 143, 682–685. https://doi.org/10.1016/j.cell.2010.11.012

Clague, M.J., Urbé, S., 2006. Endocytosis: the DUB version. Trends Cell Biol. 16, 551–559. https://doi.org/10.1016/j.tcb.2006.09.002

Clague, M.J., Urbé, S., Komander, D., 2019. Breaking the chains: deubiquitylating enzyme specificity begets function. Nat. Rev. Mol. Cell Biol. 20, 338–352. https://doi.org/10.1038/s41580-019-0099-1

Clark, I.E., Dodson, M.W., Jiang, C., Cao, J.H., Huh, J.R., Seol, J.H., Yoo, S.J., Hay, B.A., Guo, M., 2006. Drosophila pink1 is required for mitochondrial function and interacts genetically with parkin. Nature 441, 1162–1166. https://doi.org/10.1038/nature04779

Clark, L.N., Ross, B.M., Wang, Y., Mejia-Santana, H., Harris, J., Louis, E.D., Cote, L.J., Andrews, H., Fahn, S., Waters, C., Ford, B., Frucht, S., Ottman, R., Marder, K., 2007. Mutations in the glucocerebrosidase gene are associated with early-onset Parkinson disease. Neurology 69, 1270–1277. https://doi.org/10.1212/01.wnl.0000276989.17578.02

Collins, G.A., Goldberg, A.L., 2017. The Logic of the 26S Proteasome. Cell 169, 792–806. https://doi.org/10.1016/j.cell.2017.04.023

Cremona, O., Di Paolo, G., Wenk, M.R., Lüthi, A., Kim, W.T., Takei, K., Daniell, L., Nemoto, Y., Shears, S.B., Flavell, R.A., McCormick, D.A., De Camilli, P., 1999. Essential role of phosphoinositide metabolism in synaptic vesicle recycling. Cell 99, 179–188. https://doi.org/10.1016/s0092-8674(00)81649-9

Cross, J., Durgan, J., McEwan, D.G., Florey, O., 2023. Lysosome damage triggers direct ATG8 conjugation and ATG2 engagement via CASM. https://doi.org/10.1101/2023.03.22.533754

Cui, Y., Carosi, J.M., Yang, Z., Ariotti, N., Kerr, M.C., Parton, R.G., Sargeant, T.J., Teasdale, R.D., 2018. Retromer has a selective function in cargo sorting via endosome transport carriers. J. Cell Biol. 218, 615–631. https://doi.org/10.1083/jcb.201806153

Cui, Y., Yang, Z., Flores-Rodriguez, N., Follett, J., Ariotti, N., Wall, A.A., Parton, R.G., Teasdale, R.D., 2021. Formation of retromer transport carriers is disrupted by the Parkinson disease-linked Vps35 D620N variant. Traffic 22, 123–136. https://doi.org/10.1111/tra.12779

Cullen, P.J., Steinberg, F., 2018. To degrade or not to degrade: mechanisms and significance of endocytic recycling. Nat. Rev. Mol. Cell Biol. 19, 679–696. https://doi.org/10.1038/s41580-018-0053-7

Curnock, R., Calcagni, A., Ballabio, A., Cullen, P.J., 2019. TFEB controls retromer expression in response to nutrient availability. J. Cell Biol. 218, 3954–3966. https://doi.org/10.1083/jcb.201903006

Daly, J.L., Danson, C.M., Lewis, P.A., Zhao, L., Riccardo, S., Di Filippo, L., Cacchiarelli, D., Lee, D., Cross, S.J., Heesom, K.J., Xiong, W.-C., Ballabio, A., Edgar, J.R., Cullen, P.J., 2023. Multi-omic approach characterises the neuroprotective role of retromer in regulating lysosomal health. Nat. Commun. 14, 3086. https://doi.org/10.1038/s41467-023-38719-8

Damgaard, R.B., 2021. The ubiquitin system: from cell signalling to disease biology and new therapeutic opportunities. Cell Death Differ. 28, 423–426. https://doi.org/10.1038/s41418-020-00703-w

Daniëls, V., Vancraenenbroeck, R., Law, B.M.H., Greggio, E., Lobbestael, E., Gao, F., De Maeyer, M., Cookson, M.R., Harvey, K., Baekelandt, V., Taymans, J.-M., 2011. Insight into the mode of action of the LRRK2 Y1699C pathogenic mutant. J. Neurochem. 116, 304–315. https://doi.org/10.1111/j.1471-4159.2010.07105.x

Davidson, H.W., 1995. Wortmannin causes mistargeting of procathepsin D. evidence for the involvement of a phosphatidylinositol 3-kinase in vesicular transport to lysosomes. J. Cell Biol. 130, 797–805. https://doi.org/10.1083/jcb.130.4.797

De Luca, M., Cogli, L., Progida, C., Nisi, V., Pascolutti, R., Sigismund, S., Di Fiore, P.P., Bucci, C., 2014. RILP regulates vacuolar ATPase through interaction with the V1G1 subunit. J. Cell Sci. 127, 2697–2708. https://doi.org/10.1242/jcs.142604

de Oliveira, G.A.P., Silva, J.L., 2019. Alpha-synuclein stepwise aggregation reveals features of an early onset mutation in Parkinson's disease. Commun. Biol. 2, 1–13. https://doi.org/10.1038/s42003-019-0598-9

Dehay, B., Ramirez, A., Martinez-Vicente, M., Perier, C., Canron, M.-H., Doudnikoff, E., Vital, A., Vila, M., Klein, C., Bezard, E., 2012. Loss of P-type ATPase ATP13A2/PARK9 function induces general lysosomal deficiency and leads to Parkinson disease neurodegeneration. Proc. Natl. Acad. Sci. U. S. A. 109, 9611–9616. https://doi.org/10.1073/pnas.1112368109

Delgado-Camprubi, M., Esteras, N., Soutar, M.P., Plun-Favreau, H., Abramov, A.Y., 2017. Deficiency of Parkinson's disease-related gene Fbxo7 is associated with impaired mitochondrial metabolism by PARP activation. Cell Death Differ. 24, 120–131. https://doi.org/10.1038/cdd.2016.104

Demirsoy, S., Martin, S., Motamedi, S., van Veen, S., Holemans, T., Van den Haute, C., Jordanova, A., Baekelandt, V., Vangheluwe, P., Agostinis, P., 2017. ATP13A2/PARK9 regulates endo-/lysosomal cargo sorting and proteostasis through a novel PI(3, 5)P2-mediated scaffolding function. Hum. Mol. Genet. 26, 1656–1669. https://doi.org/10.1093/hmg/ddx070

Deng, H., Fan, K., Jankovic, J., 2018. The Role of TMEM230 Gene in Parkinson's Disease. J. Park. Dis. 8, 469–477. https://doi.org/10.3233/JPD-181421

Deng, H.-X., Shi, Y., Yang, Y., Ahmeti, K.B., Miller, N., Huang, C., Cheng, L., Zhai, H., Deng, S., Nuytemans, K., Corbett, N.J., Kim, M.J., Deng, H., Tang, B., Yang, Z., Xu, Y., Chan, P., Huang, B., Gao, X.-P., Song, Z., Liu, Z., Fecto, F., Siddique, N., Foroud, T., Jankovic, J., Ghetti, B., Nicholson, D.A., Krainc, D., Melen, O., Vance, J.M., Pericak-Vance, M.A., Ma, Y.-C., Rajput, A.H., Siddique, T., 2016. Identification of TMEM230 mutations in familial Parkinson's disease. Nat. Genet. 48, 733–739. https://doi.org/10.1038/ng.3589

Derivery, E., Helfer, E., Henriot, V., Gautreau, A., 2012. Actin Polymerization Controls the Organization of WASH Domains at the Surface of Endosomes. PLOS ONE 7, e39774. https://doi.org/10.1371/journal.pone.0039774

Derivery, E., Sousa, C., Gautier, J.J., Lombard, B., Loew, D., Gautreau, A., 2009. The Arp2/3 Activator WASH Controls the Fission of Endosomes through a Large Multiprotein Complex. Dev. Cell 17, 712–723. https://doi.org/10.1016/j.devcel.2009.09.010

Dhekne, H.S., Tonelli, F., Yeshaw, W.M., Chiang, C.Y., Limouse, C., Jaimon, E., Purlyte, E., Alessi, D.R., Pfeffer, S.R., 2023. Genome-wide screen reveals Rab12 GTPase as a critical activator of pathogenic LRRK2 kinase. https://doi.org/10.1101/2023.02.17.529028

Dhekne, H.S., Yanatori, I., Gomez, R.C., Tonelli, F., Diez, F., Schüle, B., Steger, M., Alessi, D.R., Pfeffer, S.R., 2018. A pathway for Parkinson's Disease LRRK2 kinase to block primary cilia and Sonic hedgehog signaling in the brain. eLife 7. https://doi.org/10.7554/eLife.40202

Di Nottia, M., Masciullo, M., Verrigni, D., Petrillo, S., Modoni, A., Rizzo, V., Di Giuda, D., Rizza, T., Niceta, M., Torraco, A., Bianchi, M., Santoro, M., Bentivoglio, A. r., Bertini, E., Piemonte, F., Carrozzo, R., Silvestri, G., 2017. DJ-1 modulates mitochondrial response to oxidative stress: clues from a novel diagnosis of PARK7. Clin. Genet. 92, 18–25. https://doi.org/10.1111/cge.12841

Dirac-Svejstrup, A.B., Soldati, T., Shapiro, A.D., Pfeffer, S.R., 1994. Rab-GDI presents functional Rab9 to the intracellular transport machinery and contributes selectivity to Rab9 membrane recruitment. J. Biol. Chem. 269, 15427–15430. https://doi.org/10.1016/S0021-9258(17)40696-X

Do, J., McKinney, C., Sharma, P., Sidransky, E., 2019. Glucocerebrosidase and its relevance to Parkinson disease. Mol. Neurodegener. 14, 36. https://doi.org/10.1186/s13024-019-0336-2

Dodson, M.W., Zhang, T., Jiang, C., Chen, S., Guo, M., 2012. Roles of the Drosophila LRRK2 homolog in Rab7-dependent lysosomal positioning. Hum. Mol. Genet. 21, 1350–1363. https://doi.org/10.1093/hmg/ddr573

Dolgacheva, L.P., Berezhnov, A.V., Fedotova, E.I., Zinchenko, V.P., Abramov, A.Y., 2019. Role of DJ-1 in the mechanism of pathogenesis of Parkinson's disease. J. Bioenerg. Biomembr. 51, 175–188. https://doi.org/10.1007/s10863-019-09798-4

Dooley, H.C., Razi, M., Polson, H.E.J., Girardin, S.E., Wilson, M.I., Tooze, S.A., 2014. WIPI2 Links LC3 Conjugation with PI3P, Autophagosome Formation, and Pathogen Clearance by Recruiting Atg12–5-16L1. Mol. Cell 55, 238–252. https://doi.org/10.1016/j.molcel.2014.05.021

Dostál, V., Humhalová, T., Beránková, P., Pácalt, O., Libusová, L., 2023. SWIP mediates retromer-independent membrane recruitment of the WASH complex. Traffic 24, 216–230. https://doi.org/10.1111/tra.12884

Dove, S.K., McEwen, R.K., Mayes, A., Hughes, D.C., Beggs, J.D., Michell, R.H., 2002. Vac14 controls PtdIns(3,5)P(2) synthesis and Fab1-dependent protein trafficking to the multivesicular body. Curr. Biol. CB 12, 885–893. https://doi.org/10.1016/s0960-9822(02)00891-6

Durgan, J., Florey, O., 2022. Many roads lead to CASM: Diverse stimuli of noncanonical autophagy share a unifying molecular mechanism. Sci. Adv. 8, eabo1274. https://doi.org/10.1126/sciadv.abo1274

Durgan, J., Lystad, A.H., Sloan, K., Carlsson, S.R., Wilson, M.I., Marcassa, E., Ulferts, R., Webster, J., Lopez-Clavijo, A.F., Wakelam, M.J., Beale, R., Simonsen, A., Oxley, D., Florey, O., 2021. Non-canonical autophagy drives alternative ATG8 conjugation to phosphatidylserine. Mol. Cell 81, 2031-2040.e8. https://doi.org/10.1016/j.molcel.2021.03.020

Dzamko, N., Deak, M., Hentati, F., Reith, A.D., Prescott, A.R., Alessi, D.R., Nichols, R.J., 2010. Inhibition of LRRK2 kinase activity leads to dephosphorylation of Ser910/Ser935, disruption of 14-3-3 binding and altered cytoplasmic localization. Biochem. J. 430, 405–413. https://doi.org/10.1042/BJ20100784

Eapen, V.V., Swarup, S., Hoyer, M.J., Paulo, J.A., Harper, J.W., 2021. Quantitative proteomics reveals the selectivity of ubiquitin-binding autophagy receptors in the turnover of damaged lysosomes by lysophagy. eLife 10, e72328. https://doi.org/10.7554/eLife.72328

Ebanks, K., Lewis, P.A., Bandopadhyay, R., 2020. Vesicular Dysfunction and the Pathogenesis of Parkinson's Disease: Clues From Genetic Studies. Front. Neurosci. 13. https://doi.org/10.3389/fnins.2019.01381

Edler, E., Stein, M., 2019. Recognition and stabilization of geranylgeranylated human Rab5 by the GDP Dissociation Inhibitor (GDI). Small GTPases 10, 227–242. https://doi.org/10.1080/21541248.2017.1371268

Eguchi, T., Kuwahara, T., Sakurai, M., Komori, T., Fujimoto, T., Ito, G., Yoshimura, S., Harada, A., Fukuda, M., Koike, M., Iwatsubo, T., 2018. LRRK2 and its substrate Rab GTPases are sequentially targeted onto stressed lysosomes and maintain their homeostasis. Proc. Natl. Acad. Sci. 115, E9115–E9124. https://doi.org/10.1073/pnas.1812196115

Elcocks, H., Brazel, A.J., McCarron, K.R., Kaulich, M., Husnjak, K., Mortiboys, H., Clague, M.J., Urbé, S., 2023a. FBXL4 ubiquitin ligase deficiency promotes mitophagy by elevating NIX levels. EMBO J. 42, e112799. https://doi.org/10.15252/embj.2022112799

Elcocks, H., Brazel, A.J., McCarron, K.R., Kaulich, M., Husnjak, K., Mortiboys, H., Clague, M.J., Urbé, S., 2023b. FBXL4 deficiency promotes mitophagy by elevating NIX. https://doi.org/10.1101/2022.10.11.511735

Erb, M.L., Moore, D.J., 2020. LRRK2 and the Endolysosomal System in Parkinson's Disease. J. Park. Dis. 10, 1271–1291. https://doi.org/10.3233/JPD-202138

Eriksson, I., Wäster, P., Öllinger, K., 2020. Restoration of lysosomal function after damage is accompanied by recycling of lysosomal membrane proteins. Cell Death Dis. 11, 1–16. https://doi.org/10.1038/s41419-020-2527-8

Evans, A.J., Daly, J.L., Anuar, A.N.K., Simonetti, B., Cullen, P.J., 2020. Acute inactivation of retromer and ESCPE-1 leads to time-resolved defects in endosomal cargo sorting. J. Cell Sci. 133. https://doi.org/10.1242/jcs.246033

Fahn, S., Oakes, D., Shoulson, I., Kieburtz, K., Rudolph, A., Lang, A., Olanow, C.W., Tanner, C., Marek, K., Parkinson Study Group, 2004. Levodopa and the progression of Parkinson's disease. N. Engl. J. Med. 351, 2498–2508. https://doi.org/10.1056/NEJMoa033447

Farmer, T., Naslavsky, N., Caplan, S., 2018. Tying Trafficking to Fusion and Fission at the Mighty Mitochondria. Traffic Cph. Den. 19, 569–577. https://doi.org/10.1111/tra.12573

Fasano, D., Parisi, S., Pierantoni, G.M., De Rosa, A., Picillo, M., Amodio, G., Pellecchia, M.T., Barone, P., Moltedo, O., Bonifati, V., De Michele, G., Nitsch, L., Remondelli, P., Criscuolo, C., Paladino, S., 2018. Alteration of endosomal trafficking is associated with early-onset parkinsonism caused by SYNJ1 mutations. Cell Death Dis. 9, 1–15. https://doi.org/10.1038/s41419-018-0410-7

Fedoseienko, A., Wijers, M., Wolters, J.C., Dekker, D., Smit, M., Huijkman, N., Kloosterhuis, N., Klug, H., Schepers, A., Willems van Dijk, K., Levels, J.H.M., Billadeau, D.D., Hofker, M.H., van Deursen, J., Westerterp, M., Burstein, E., Kuivenhoven, J.A., van de Sluis, B., 2018. The COMMD Family Regulates Plasma LDL Levels and Attenuates Atherosclerosis Through Stabilizing the CCC Complex in Endosomal LDLR Trafficking. Circ. Res. 122, 1648–1660. https://doi.org/10.1161/CIRCRESAHA.117.312004

Feng, X., Liu, S., Xu, H., 2023. Not just protons: Chloride also activates lysosomal acidic hydrolases. J. Cell Biol. 222, e202305007. https://doi.org/10.1083/jcb.202305007

Fernandes, H.J.R., Hartfield, E.M., Christian, H.C., Emmanoulidou, E., Zheng, Y., Booth, H., Bogetofte, H., Lang, C., Ryan, B.J., Sardi, S.P., Badger, J., Vowles, J., Evetts, S., Tofaris, G.K., Vekrellis, K., Talbot, K., Hu, M.T., James, W., Cowley, S.A., Wade-Martins, R., 2016. ER Stress and Autophagic Perturbations Lead to Elevated Extracellular α-Synuclein in GBA-N370S Parkinson's iPSC-Derived Dopamine Neurons. Stem Cell Rep. 6, 342–356. https://doi.org/10.1016/j.stemcr.2016.01.013

Finley, D., 2009. Recognition and Processing of Ubiquitin-Protein Conjugates by the Proteasome. Annu. Rev. Biochem. 78, 477–513. https://doi.org/10.1146/annurev.biochem.78.081507.101607

Fjorback, A.W., Seaman, M., Gustafsen, C., Mehmedbasic, A., Gokool, S., Wu, C., Militz, D., Schmidt, V., Madsen, P., Nyengaard, J.R., Willnow, T.E., Christensen, E.I., Mobley, W.B., Nykjær, A., Andersen, O.M., 2012. Retromer Binds the FANSHY Sorting Motif in SorLA to Regulate Amyloid Precursor Protein Sorting and Processing. J. Neurosci. 32, 1467–1480. https://doi.org/10.1523/JNEUROSCI.2272-11.2012

Fletcher, K., Ulferts, R., Jacquin, E., Veith, T., Gammoh, N., Arasteh, J.M., Mayer, U., Carding, S.R., Wileman, T., Beale, R., Florey, O., 2018. The WD40 domain of ATG16L1 is required for its non-canonical role in lipidation of LC3 at single membranes. EMBO J. 37, e97840. https://doi.org/10.15252/embj.201797840

Florey, O., Gammoh, N., Kim, S.E., Jiang, X., Overholtzer, M., 2015. V-ATPase and osmotic imbalances activate endolysosomal LC3 lipidation. Autophagy 11, 88–99. https://doi.org/10.4161/15548627.2014.984277

Follett, J., Fox, J.D., Gustavsson, E.K., Kadgien, C., Munsie, L.N., Cao, L.P., Tatarnikov, I., Milnerwood, A.J., Farrer, M.J., 2019. DNAJC13 p.Asn855Ser,

implicated in familial parkinsonism, alters membrane dynamics of sorting nexin 1. Neurosci. Lett. 706, 114–122. https://doi.org/10.1016/j.neulet.2019.04.043
Follett, J., Norwood, S.J., Hamilton, N.A., Mohan, M., Kovtun, O., Tay, S., Zhe, Y., Wood, S.A., Mellick, G.D., Silburn, P.A., Collins, B.M., Bugarcic, A., Teasdale, R.D., 2014. The Vps35 D620N Mutation Linked to Parkinson's Disease Disrupts the Cargo Sorting Function of Retromer. Traffic 15, 230–244. https://doi.org/10.1111/tra.12136
Frankel, E.B., Audhya, A., 2018. ESCRT-dependent cargo sorting at multivesicular endosomes. Semin. Cell Dev. Biol. 74, 4–10. https://doi.org/10.1016/j.semcdb.2017.08.020
Freeman, C.L., Hesketh, G., Seaman, M.N.J., 2014. RME-8 coordinates the activity of the WASH complex with the function of the retromer SNX dimer to control endosomal tubulation. J. Cell Sci. 127, 2053–2070. https://doi.org/10.1242/jcs.144659
Freeman, S.A., Grinstein, S., Orlowski, J., 2023. Determinants, maintenance, and function of organellar pH. Physiol. Rev. 103, 515–606. https://doi.org/10.1152/physrev.00009.2022
Fukuda, M., 2016. Multiple Roles of VARP in Endosomal Trafficking: Rabs, Retromer Components and R-SNARE VAMP7 Meet on VARP. Traffic 17, 709–719. https://doi.org/10.1111/tra.12406
Fukuda, M., Kanno, E., Ishibashi, K., Itoh, T., 2008. Large Scale Screening for Novel Rab Effectors Reveals Unexpected Broad Rab Binding Specificity. Mol. Cell. Proteomics 7, 1031–1042. https://doi.org/10.1074/mcp.M700569-MCP200
Funayama, M., Hasegawa, K., Kowa, H., Saito, M., Tsuji, S., Obata, F., 2002. A new locus for Parkinson's disease (PARK8) maps to chromosome 12p11.2–q13.1. Ann. Neurol. 51, 296–301. https://doi.org/10.1002/ana.10113
Funayama, M., Ohe, K., Amo, T., Furuya, N., Yamaguchi, J., Saiki, S., Li, Y., Ogaki, K., Ando, M., Yoshino, H., Tomiyama, H., Nishioka, K., Hasegawa, K., Saiki, H., Satake, W., Mogushi, K., Sasaki, R., Kokubo, Y., Kuzuhara, S., Toda, T., Mizuno, Y., Uchiyama, Y., Ohno, K., Hattori, N., 2015. CHCHD2 mutations in autosomal dominant late-onset Parkinson's disease: a genome-wide linkage and sequencing study. Lancet Neurol. 14, 274–282. https://doi.org/10.1016/S1474-4422(14)70266-2
Fuse, A., Furuya, N., Kakuta, S., Inose, A., Sato, M., Koike, M., Saiki, S., Hattori, N., 2015. VPS29–VPS35 intermediate of retromer is stable and may be involved in the retromer complex assembly process. FEBS Lett. 589, 1430–1436. https://doi.org/10.1016/j.febslet.2015.04.040
Gaffet, P., Jones, A.T., Clague, M.J., 1997. Inhibition of Calcium-independent Mannose 6-Phosphate Receptor Incorporation into trans-Golgi Network-derived Clathrin-coated Vesicles by Wortmannin*. J. Biol. Chem. 272, 24170–24175. https://doi.org/10.1074/jbc.272.39.24170
Gallon, M., Clairfeuille, T., Steinberg, F., Mas, C., Ghai, R., Sessions, R.B., Teasdale, R.D., Collins, B.M., Cullen, P.J., 2014. A unique PDZ domain and arrestin-like fold interaction reveals mechanistic details of endocytic recycling by SNX27-retromer. Proc. Natl. Acad. Sci. U. S. A. 111, E3604–E3613. https://doi.org/10.1073/pnas.1410552111
Galluzzi, L., Baehrecke, E.H., Ballabio, A., Boya, P., Bravo-San Pedro, J.M., Cecconi, F., Choi, A.M., Chu, C.T., Codogno, P., Colombo, M.I., Cuervo, A.M., Debnath, J., Deretic, V., Dikic, I., Eskelinen, E.-L., Fimia, G.M., Fulda, S., Gewirtz, D.A., Green, D.R., Hansen, M., Harper, J.W., Jäättelä, M., Johansen, T., Juhasz, G., Kimmelman, A.C., Kraft, C., Ktistakis, N.T., Kumar, S., Levine, B., Lopez-Otin, C., Madeo, F., Martens, S., Martinez, J., Melendez, A., Mizushima, N., Münz, C., Murphy, L.O., Penninger, J.M., Piacentini, M., Reggiori, F., Rubinsztein, D.C., Ryan, K.M., Santambrogio, L., Scorrano, L., Simon, A.K.,

Simon, H.-U., Simonsen, A., Tavernarakis, N., Tooze, S.A., Yoshimori, T., Yuan, J., Yue, Z., Zhong, Q., Kroemer, G., 2017. Molecular definitions of autophagy and related processes. EMBO J. 36, 1811–1836. https://doi.org/10.15252/embj.201796697

Ganley, I.G., Simonsen, A., 2022. Diversity of mitophagy pathways at a glance. J. Cell Sci. 135, jcs259748. https://doi.org/10.1242/jcs.259748

Gautreau, A., Oguievetskaia, K., Ungermann, C., 2014. Function and Regulation of the Endosomal Fusion and Fission Machineries. Cold Spring Harb. Perspect. Biol. 6, a016832. https://doi.org/10.1101/cshperspect.a016832

Gegg, M.E., Burke, D., Heales, S.J.R., Cooper, J.M., Hardy, J., Wood, N.W., Schapira, A.H.V., 2012. Glucocerebrosidase deficiency in substantia nigra of parkinson disease brains. Ann. Neurol. 72, 455–463. https://doi.org/10.1002/ana.23614

Gerondopoulos, A., Langemeyer, L., Liang, J.-R., Linford, A., Barr, F.A., 2012. BLOC-3 Mutated in Hermansky-Pudlak Syndrome Is a Rab32/38 Guanine Nucleotide Exchange Factor. Curr. Biol. 22, 2135–2139. https://doi.org/10.1016/j.cub.2012.09.020

Gillooly, D.J., Morrow, I.C., Lindsay, M., Gould, R., Bryant, N.J., Gaullier, J.-M., Parton, R.G., Stenmark, H., 2000. Localization of phosphatidylinositol 3-phosphate in yeast and mammalian cells. EMBO J. 19, 4577–4588. https://doi.org/10.1093/emboj/19.17.4577

Giridharan, S.S.P., Luo, G., Rivero-Rios, P., Steinfeld, N., Tronchere, H., Singla, A., Burstein, E., Billadeau, D.D., Sutton, M.A., Weisman, L.S., 2022. Lipid kinases VPS34 and PIKfyve coordinate a phosphoinositide cascade to regulate retriever-mediated recycling on endosomes. eLife 11, e69709. https://doi.org/10.7554/eLife.69709

Gloeckner, C.J., Kinkl, N., Schumacher, A., Braun, R.J., O'Neill, E., Meitinger, T., Kolch, W., Prokisch, H., Ueffing, M., 2006. The Parkinson disease causing LRRK2 mutation I2020T is associated with increased kinase activity. Hum. Mol. Genet. 15, 223–232. https://doi.org/10.1093/hmg/ddi439

Gómez-Suaga, P., Rivero-Ríos, P., Fdez, E., Blanca Ramírez, M., Ferrer, I., Aiastui, A., López De Munain, A., Hilfiker, S., 2014. LRRK2 delays degradative receptor trafficking by impeding late endosomal budding through decreasing Rab7 activity. Hum. Mol. Genet. 23, 6779–6796. https://doi.org/10.1093/hmg/ddu395

Goodwin, J.M., Walkup, W.G., Hooper, K., Li, T., Kishi-Itakura, C., Ng, A., Lehmberg, T., Jha, A., Kommineni, S., Fletcher, K., Garcia-Fortanet, J., Fan, Y., Tang, Q., Wei, M., Agrawal, A., Budhe, S.R., Rouduri, S.R., Baird, D., Saunders, J., Kiselar, J., Chance, M.R., Ballabio, A., Appleton, B.A., Brumell, J.H., Florey, O., Murphy, L.O., 2021. GABARAP sequesters the FLCN-FNIP tumor suppressor complex to couple autophagy with lysosomal biogenesis. Sci. Adv. 7, eabj2485. https://doi.org/10.1126/sciadv.abj2485

Gorvel, J.-P., Chavrier, P., Zerial, M., Gruenberg, J., 1991. rab5 controls early endosome fusion in vitro. Cell 64, 915–925. https://doi.org/10.1016/0092-8674(91)90316-Q

Goud, B., Liu, S., Storrie, B., 2018. Rab proteins as major determinants of the Golgi complex structure. Small GTPases 9, 66–75. https://doi.org/10.1080/21541248.2017.1384087

Greene, A.W., Grenier, K., Aguileta, M.A., Muise, S., Farazifard, R., Haque, M.E., McBride, H.M., Park, D.S., Fon, E.A., 2012. Mitochondrial processing peptidase regulates PINK1 processing, import and Parkin recruitment. EMBO Rep. 13, 378–385. https://doi.org/10.1038/embor.2012.14

Guerra, F., Bucci, C., 2016. Multiple Roles of the Small GTPase Rab7. Cells 5, 34. https://doi.org/10.3390/cells5030034

Gusdon, A.M., Zhu, J., Van Houten, B., Chu, C.T., 2012. ATP13A2 regulates mitochondrial bioenergetics through macroautophagy. Neurobiol. Dis. 45, 962–972. https://doi.org/10.1016/j.nbd.2011.12.015

Hanafusa, H., Yagi, T., Ikeda, H., Hisamoto, N., Nishioka, T., Kaibuchi, K., Shirakabe, K., Matsumoto, K., 2019. LRRK1 phosphorylation of Rab7 at S72 links trafficking of EGFR-containing endosomes to its effector RILP. J. Cell Sci. 132, jcs228809. https://doi.org/10.1242/jcs.228809

Hanna, R.A., Quinsay, M.N., Orogo, A.M., Giang, K., Rikka, S., Gustafsson, Å.B., 2012. Microtubule-associated Protein 1 Light Chain 3 (LC3) Interacts with Bnip3 Protein to Selectively Remove Endoplasmic Reticulum and Mitochondria via Autophagy. J. Biol. Chem. 287, 19094–19104. https://doi.org/10.1074/jbc.M111.322933

Hanss, Z., Larsen, S.B., Antony, P., Mencke, P., Massart, F., Jarazo, J., Schwamborn, J.C., Barbuti, P.A., Mellick, G.D., Krüger, R., 2021. Mitochondrial and Clearance Impairment in p.D620N VPS35 Patient-Derived Neurons. Mov. Disord. 36, 704–715. https://doi.org/10.1002/mds.28365

Hao, L.-Y., Giasson, B.I., Bonini, N.M., 2010. DJ-1 is critical for mitochondrial function and rescues PINK1 loss of function. Proc. Natl. Acad. Sci. 107, 9747–9752. https://doi.org/10.1073/pnas.0911175107

Hao, Y.-H., Doyle, J.M., Ramanathan, S., Gomez, T.S., Jia, D., Xu, M., Chen, Z.J., Billadeau, D.D., Rosen, M.K., Potts, P.R., 2013. Regulation of WASH-dependent actin polymerization and protein trafficking by ubiquitination. Cell 152, 1051–1064. https://doi.org/10.1016/j.cell.2013.01.051

Harbour, M.E., Breusegem, S.Y., Seaman, M.N.J., 2012. Recruitment of the endosomal WASH complex is mediated by the extended 'tail' of Fam21 binding to the retromer protein Vps35. Biochem. J. 442, 209–220. https://doi.org/10.1042/BJ20111761

Harbour, M.E., Breusegem, S.Y.A., Antrobus, R., Freeman, C., Reid, E., Seaman, M.N.J., 2010. The cargo-selective retromer complex is a recruiting hub for protein complexes that regulate endosomal tubule dynamics. J. Cell Sci. 123, 3703–3717. https://doi.org/10.1242/jcs.071472

Harterink, M., Port, F., Lorenowicz, M.J., McGough, I.J., Silhankova, M., Betist, M.C., van Weering, J.R.T., van Heesbeen, R.G.H.P., Middelkoop, T.C., Basler, K., Cullen, P.J., Korswagen, H.C., 2011. A SNX3-dependent retromer pathway mediates retrograde transport of the Wnt sorting receptor Wntless and is required for Wnt secretion. Nat. Cell Biol. 13, 914–923. https://doi.org/10.1038/ncb2281

Healy, M.D., McNally, K.E., Butkovič, R., Chilton, M., Kato, K., Sacharz, J., McConville, C., Moody, E.R.R., Shaw, S., Planelles-Herrero, V.J., Yadav, S.K.N., Ross, J., Borucu, U., Palmer, C.S., Chen, K.-E., Croll, T.I., Hall, R.J., Caruana, N.J., Ghai, R., Nguyen, T.H.D., Heesom, K.J., Saitoh, S., Berger, I., Schaffitzel, C., Williams, T.A., Stroud, D.A., Derivery, E., Collins, B.M., Cullen, P.J., 2023. Structure of the endosomal Commander complex linked to Ritscher-Schinzel syndrome. Cell 186, 2219-2237.e29. https://doi.org/10.1016/j.cell.2023.04.003

Henry, A.G., Aghamohammadzadeh, S., Samaroo, H., Chen, Y., Mou, K., Needle, E., Hirst, W.D., 2015. Pathogenic LRRK2 mutations, through increased kinase activity, produce enlarged lysosomes with reduced degradative capacity and increase ATP13A2 expression. Hum. Mol. Genet. 24, 6013–6028. https://doi.org/10.1093/hmg/ddv314

Herbst, S., Campbell, P., Harvey, J., Bernard, E.M., Papayannopoulos, V., Wood, N.W., Morris, H.R., Gutierrez, M.G., 2020. LRRK2 activation controls the repair of damaged endomembranes in macrophages. EMBO J. n/a, e104494. https://doi.org/10.15252/embj.2020104494

Heride, C., Urbé, S., Clague, M.J., 2014. Ubiquitin code assembly and disassembly. Curr. Biol. 24, R215–R220. https://doi.org/10.1016/j.cub.2014.02.002
Hirst, J., Futter, C.E., Hopkins, C.R., 1998. The kinetics of mannose 6-phosphate receptor trafficking in the endocytic pathway in HEp-2 cells: the receptor enters and rapidly leaves multivesicular endosomes without accumulating in a prelysosomal compartment. Mol. Biol. Cell 9, 809–816. https://doi.org/10.1091/mbc.9.4.809
Ho, P.W.-L., Leung, C.-T., Liu, H., Pang, S.Y.-Y., Lam, C.S.-C., Xian, J., Li, L., Kung, M.H.-W., Ramsden, D.B., Ho, S.-L., 2019. Age-dependent accumulation of oligomeric SNCA/α-synuclein from impaired degradation in mutant LRRK2 knockin mouse model of Parkinson disease: role for therapeutic activation of chaperone-mediated autophagy (CMA). Autophagy 16, 347–370. https://doi.org/10.1080/15548627.2019.1603545
Hockey, L.N., Kilpatrick, B.S., Eden, E.R., Lin-Moshier, Y., Brailoiu, G.C., Brailoiu, E., Futter, C.E., Schapira, A.H., Marchant, J.S., Patel, S., 2015. Dysregulation of lysosomal morphology by pathogenic LRRK2 is corrected by TPC2 inhibition. J. Cell Sci. 128, 232–238. https://doi.org/10.1242/jcs.164152
Hooper, K.M., Jacquin, E., Li, T., Goodwin, J.M., Brumell, J.H., Durgan, J., Florey, O., 2022. V-ATPase is a universal regulator of LC3-associated phagocytosis and non-canonical autophagy. J. Cell Biol. 221, e202105112. https://doi.org/10.1083/jcb.202105112
Hsieh, C.-H., Shaltouki, A., Gonzalez, A.E., da Cruz, A.B., Burbulla, L.F., St Lawrence, E., Schüle, B., Krainc, D., Palmer, T.D., Wang, X., 2016. Functional Impairment in Miro Degradation and Mitophagy Is a Shared Feature in Familial and Sporadic Parkinson's Disease. Cell Stem Cell 19, 709–724. https://doi.org/10.1016/j.stem.2016.08.002
Hu, P., Li, H., Sun, W., Wang, H., Yu, X., Qing, Y., Wang, Z., Zhu, M., Xu, J., Guo, Q., Hui, H., 2021. Cholesterol-associated lysosomal disorder triggers cell death of hematological malignancy: Dynamic analysis on cytotoxic effects of LW-218. Acta Pharm. Sin. B 11, 3178–3192. https://doi.org/10.1016/j.apsb.2021.02.004
Huang, X., Wu, B.P., Nguyen, D., Liu, Y.-T., Marani, M., Hench, J., Bénit, P., Kozjak-Pavlovic, V., Rustin, P., Frank, S., Narendra, D.P., 2018. CHCHD2 accumulates in distressed mitochondria and facilitates oligomerization of CHCHD10. Hum. Mol. Genet. 27, 3881–3900. https://doi.org/10.1093/hmg/ddy270
Huang, Y., Wang, K.K.W., 2001. The calpain family and human disease. Trends Mol. Med. 7, 355–362. https://doi.org/10.1016/S1471-4914(01)02049-4
Huotari, J., Helenius, A., 2011. Endosome maturation. EMBO J. 30, 3481–3500. https://doi.org/10.1038/emboj.2011.286
Ignatev, A., Kravchenko, S., Rak, A., Goody, R.S., Pylypenko, O., 2008. A Structural Model of the GDP Dissociation Inhibitor Rab Membrane Extraction Mechanism. J. Biol. Chem. 283, 18377–18384. https://doi.org/10.1074/jbc.M709718200
Inoshita, T., Arano, T., Hosaka, Y., Meng, H., Umezaki, Y., Kosugi, S., Morimoto, T., Koike, M., Chang, H.-Y., Imai, Y., Hattori, N., 2017. Vps35 in cooperation with LRRK2 regulates synaptic vesicle endocytosis through the endosomal pathway in Drosophila. Hum. Mol. Genet. 26, 2933–2948. https://doi.org/10.1093/hmg/ddx179
International Parkinson Disease Genomics Consortium, Nalls, M.A., Plagnol, V., Hernandez, D.G., Sharma, M., Sheerin, U.-M., Saad, M., Simón-Sánchez, J., Schulte, C., Lesage, S., Sveinbjörnsdóttir, S., Stefánsson, K., Martinez, M., Hardy, J., Heutink, P., Brice, A., Gasser, T., Singleton, A.B., Wood, N.W., 2011. Imputation of sequence variants for identification of genetic risks for Parkinson's disease: a meta-analysis of genome-wide association studies.

Lancet Lond. Engl. 377, 641–649. https://doi.org/10.1016/S0140-6736(10)62345-8
Invitrogen, 2012. Flp-In System: For Generating Constitutive Expression Cell Lines - UK [WWW Document]. URL https://www.thermofisher.com/uk/en/home/references/protocols/proteins-expression-isolation-and-analysis/protein-expression-protocol/flp-in-system-for-generating-constitutive-expression-cell-lines.html (accessed 5.23.23).
Ito, G., Katsemonova, K., Tonelli, F., Lis, P., Baptista, M.A.S., Shpiro, N., Duddy, G., Wilson, S., Ho, P.W.-L., Ho, S.-L., Reith, A.D., Alessi, D.R., 2016. Phos-tag analysis of Rab10 phosphorylation by LRRK2: a powerful assay for assessing kinase function and inhibitors. Biochem. J. 473, 2671–2685. https://doi.org/10.1042/BCJ20160557
Ito, K., Araki, M., Katai, Y., Nishimura, Y., Imotani, S., Inoue, H., Ito, G., Tomita, T., 2023. Pathogenic LRRK2 compromises the subcellular distribution of lysosomes in a Rab12-RILPL1-dependent manner. FASEB J. 37, e22930. https://doi.org/10.1096/fj.202200780RR
Itzen, A., Goody, R.S., 2011. GTPases involved in vesicular trafficking: Structures and mechanisms. Semin. Cell Dev. Biol., GTPases in Intracellular Trafficking 22, 48–56. https://doi.org/10.1016/j.semcdb.2010.10.003
Jacquin, E., Leclerc-Mercier, S., Judon, C., Blanchard, E., Fraitag, S., Florey, O., 2017. Pharmacological modulators of autophagy activate a parallel noncanonical pathway driving unconventional LC3 lipidation. Autophagy 13, 854–867. https://doi.org/10.1080/15548627.2017.1287653
Jeong, G.R., Jang, E.-H., Bae, J.R., Jun, S., Kang, H.C., Park, C.-H., Shin, J.-H., Yamamoto, Y., Tanaka-Yamamoto, K., Dawson, V.L., Dawson, T.M., Hur, E.-M., Lee, B.D., 2018. Dysregulated phosphorylation of Rab GTPases by LRRK2 induces neurodegeneration. Mol. Neurodegener. 13, 8. https://doi.org/10.1186/s13024-018-0240-1
Jia, D., Gomez, T.S., Billadeau, D.D., Rosen, M.K., 2012. Multiple repeat elements within the FAM21 tail link the WASH actin regulatory complex to the retromer. Mol. Biol. Cell 23, 2352–2361. https://doi.org/10.1091/mbc.e11-12-1059
Jia, D., Zhang, J.-S., Li, F., Wang, J., Deng, Z., White, M.A., Osborne, D.G., Phillips-Krawczak, C., Gomez, T.S., Li, H., Singla, A., Burstein, E., Billadeau, D.D., Rosen, M.K., 2016. Structural and mechanistic insights into regulation of the retromer coat by TBC1d5. Nat. Commun. 7. https://doi.org/10.1038/ncomms13305
Jia, J., Abudu, Y.P., Claude-Taupin, A., Gu, Y., Kumar, S., Choi, S.W., Peters, R., Mudd, M.H., Allers, L., Salemi, M., Phinney, B., Johansen, T., Deretic, V., 2018. Galectins Control mTOR in Response to Endomembrane Damage. Mol. Cell 70, 120-135.e8. https://doi.org/10.1016/j.molcel.2018.03.009
Jia, J., Claude-Taupin, A., Gu, Y., Choi, S.W., Peters, R., Bissa, B., Mudd, M.H., Allers, L., Pallikkuth, S., Lidke, K.A., Salemi, M., Phinney, B., Mari, M., Reggiori, F., Deretic, V., 2020. Galectin-3 Coordinates a Cellular System for Lysosomal Repair and Removal. Dev. Cell 52, 69-87.e8. https://doi.org/10.1016/j.devcel.2019.10.025
Jimenez-Orgaz, A., Kvainickas, A., Nägele, H., Denner, J., Eimer, S., Dengjel, J., Steinberg, F., 2018. Control of RAB7 activity and localization through the retromer-TBC1D5 complex enables RAB7-dependent mitophagy. EMBO J. 37, 235–254. https://doi.org/10.15252/embj.201797128
Jin, S.M., Lazarou, M., Wang, C., Kane, L.A., Narendra, D.P., Youle, R.J., 2010. Mitochondrial membrane potential regulates PINK1 import and proteolytic destabilization by PARL. J. Cell Biol. 191, 933–942. https://doi.org/10.1083/jcb.201008084
Jordens, I., Fernandez-Borja, M., Marsman, M., Dusseljee, S., Janssen, L., Calafat, J., Janssen, H., Wubbolts, R., Neefjes, J., 2001. The Rab7 effector protein

RILP controls lysosomal transport by inducing the recruitment of dynein-dynactin motors. Curr. Biol. 11, 1680–1685. https://doi.org/10.1016/S0960-9822(01)00531-0

Kadgien, C.A., Kamesh, A., Milnerwood, A.J., 2021. Endosomal traffic and glutamate synapse activity are increased in VPS35 D620N mutant knock-in mouse neurons, and resistant to LRRK2 kinase inhibition. Mol. Brain 14, 143. https://doi.org/10.1186/s13041-021-00848-w

Kaksonen, M., Roux, A., 2018. Mechanisms of clathrin-mediated endocytosis. Nat. Rev. Mol. Cell Biol. 19, 313–326. https://doi.org/10.1038/nrm.2017.132

Kalogeropulou, A.F., Freemantle, J.B., Lis, P., Vides, E.G., Polinski, N.K., Alessi, D.R., 2020. Endogenous Rab29 does not impact basal or stimulated LRRK2 pathway activity. Biochem. J. 477, 4397–4423. https://doi.org/10.1042/BCJ20200458

Kane, L.A., Lazarou, M., Fogel, A.I., Li, Y., Yamano, K., Sarraf, S.A., Banerjee, S., Youle, R.J., 2014. PINK1 phosphorylates ubiquitin to activate Parkin E3 ubiquitin ligase activity. J. Cell Biol. 205, 143–153. https://doi.org/10.1083/jcb.201402104

Karayel, Ö., Tonelli, F., Virreira Winter, S., Geyer, P.E., Fan, Y., Sammler, E.M., Alessi, D.R., Steger, M., Mann, M., 2020. Accurate MS-based Rab10 Phosphorylation Stoichiometry Determination as Readout for LRRK2 Activity in Parkinson's Disease. Mol. Cell. Proteomics MCP 19, 1546–1560. https://doi.org/10.1074/mcp.RA120.002055

Karimi-Moghadam, A., Charsouei, S., Bell, B., Jabalameli, M.R., 2018. Parkinson Disease from Mendelian Forms to Genetic Susceptibility: New Molecular Insights into the Neurodegeneration Process. Cell. Mol. Neurobiol. 38, 1153–1178. https://doi.org/10.1007/s10571-018-0587-4

Katayama, H., Kogure, T., Mizushima, N., Yoshimori, T., Miyawaki, A., 2011. A Sensitive and Quantitative Technique for Detecting Autophagic Events Based on Lysosomal Delivery. Chem. Biol. 18, 1042–1052. https://doi.org/10.1016/j.chembiol.2011.05.013

Kato, K., Oka, Y., Muramatsu, H., Vasilev, F.F., Otomo, T., Oishi, H., Kawano, Y., Kidokoro, H., Nakazawa, Y., Ogi, T., Takahashi, Y., Saitoh, S., 2020. Biallelic VPS35L pathogenic variants cause 3C/Ritscher-Schinzel-like syndrome through dysfunction of retriever complex. J. Med. Genet. 57, 245–253. https://doi.org/10.1136/jmedgenet-2019-106213

Kazlauskaite, A., Martínez-Torres, R.J., Wilkie, S., Kumar, A., Peltier, J., Gonzalez, A., Johnson, C., Zhang, J., Hope, A.G., Peggie, M., Trost, M., van Aalten, D.M., Alessi, D.R., Prescott, A.R., Knebel, A., Walden, H., Muqit, M.M., 2015. Binding to serine 65-phosphorylated ubiquitin primes Parkin for optimal PINK1-dependent phosphorylation and activation. EMBO Rep. 16, 939–954. https://doi.org/10.15252/embr.201540352

Kee, T.R., Espinoza Gonzalez, P., Wehinger, J.L., Bukhari, M.Z., Ermekbaeva, A., Sista, A., Kotsiviras, P., Liu, T., Kang, D.E., Woo, J.-A.A., 2021. Mitochondrial CHCHD2: Disease-Associated Mutations, Physiological Functions, and Current Animal Models. Front. Aging Neurosci. 13, 660843. https://doi.org/10.3389/fnagi.2021.660843

Kim, P.K., Hailey, D.W., Mullen, R.T., Lippincott-Schwartz, J., 2008. Ubiquitin signals autophagic degradation of cytosolic proteins and peroxisomes. Proc. Natl. Acad. Sci. U. S. A. 105, 20567–20574. https://doi.org/10.1073/pnas.0810611105

Klein, C., Westenberger, A., 2012. Genetics of Parkinson's Disease. Cold Spring Harb. Perspect. Med. 2. https://doi.org/10.1101/cshperspect.a008888

Klinkert, K., Echard, A., 2016. Rab35 GTPase: A Central Regulator of Phosphoinositides and F-actin in Endocytic Recycling and Beyond. Traffic 17, 1063–1077. https://doi.org/10.1111/tra.12422

Klumperman, J., Raposo, G., 2014. The Complex Ultrastructure of the Endolysosomal System. Cold Spring Harb. Perspect. Biol. 6, a016857. https://doi.org/10.1101/cshperspect.a016857
Kluss, J.H., Beilina, A., Williamson, C.D., Lewis, P.A., Cookson, M.R., Bonet-Ponce, L., 2022. Lysosomal positioning regulates Rab10 phosphorylation at LRRK2+ lysosomes. Proc. Natl. Acad. Sci. 119, e2205492119. https://doi.org/10.1073/pnas.2205492119
Koerver, L., Papadopoulos, C., Liu, B., Kravic, B., Rota, G., Brecht, L., Veenendaal, T., Polajnar, M., Bluemke, A., Ehrmann, M., Klumperman, J., Jäättelä, M., Behrends, C., Meyer, H., 2019. The ubiquitin-conjugating enzyme UBE2QL1 coordinates lysophagy in response to endolysosomal damage. EMBO Rep. 20, e48014. https://doi.org/10.15252/embr.201948014
Kondapalli, C., Kazlauskaite, A., Zhang, N., Woodroof, H.I., Campbell, D.G., Gourlay, R., Burchell, L., Walden, H., Macartney, T.J., Deak, M., Knebel, A., Alessi, D.R., Muqit, M.M.K., 2012. PINK1 is activated by mitochondrial membrane potential depolarization and stimulates Parkin E3 ligase activity by phosphorylating Serine 65. Open Biol. 2, 120080. https://doi.org/10.1098/rsob.120080
König, T., Nolte, H., Aaltonen, M.J., Tatsuta, T., Krols, M., Stroh, T., Langer, T., McBride, H.M., 2021. MIROs and DRP1 drive mitochondrial-derived vesicle biogenesis and promote quality control. Nat. Cell Biol. 23, 1271–1286. https://doi.org/10.1038/s41556-021-00798-4
Kornfeld, R., Bao, M., Brewer, K., Noll, C., Canfield, W., 1999. Molecular Cloning and Functional Expression of Two Splice Forms of Human N-Acetylglucosamine-1-phosphodiester α-N-Acetylglucosaminidase*. J. Biol. Chem. 274, 32778–32785. https://doi.org/10.1074/jbc.274.46.32778
Korolchuk, V.I., Saiki, S., Lichtenberg, M., Siddiqi, F.H., Roberts, E.A., Imarisio, S., Jahreiss, L., Sarkar, S., Futter, M., Menzies, F.M., O'Kane, C.J., Deretic, V., Rubinsztein, D.C., 2011. Lysosomal positioning coordinates cellular nutrient responses. Nat. Cell Biol. 13, 453–460. https://doi.org/10.1038/ncb2204
Koumandou, V.L., Klute, M.J., Herman, E.K., Nunez-Miguel, R., Dacks, J.B., Field, M.C., 2011. Evolutionary reconstruction of the retromer complex and its function in Trypanosoma brucei. J. Cell Sci. 124, 1496–1509. https://doi.org/10.1242/jcs.081596
Kovtun, O., Leneva, N., Bykov, Y.S., Ariotti, N., Teasdale, R.D., Schaffer, M., Engel, B.D., Owen, D.J., Briggs, J.A.G., Collins, B.M., 2018. Structure of the membrane-assembled retromer coat determined by cryo-electron tomography. Nature 561, 561–564. https://doi.org/10.1038/s41586-018-0526-z
Koyano, F., Okatsu, K., Kosako, H., Tamura, Y., Go, E., Kimura, M., Kimura, Y., Tsuchiya, H., Yoshihara, H., Hirokawa, T., Endo, T., Fon, E.A., Trempe, J.-F., Saeki, Y., Tanaka, K., Matsuda, N., 2014. Ubiquitin is phosphorylated by PINK1 to activate parkin. Nature 510, 162–166. https://doi.org/10.1038/nature13392
Kraus, F., Goodall, E.A., Smith, I.R., Jiang, Y., Paoli, J.C., Adolf, F., Zhang, J., Paulo, J.A., Schulman, B.A., Harper, J.W., 2023. PARK15/FBXO7 is dispensable for PINK1/Parkin mitophagy in iNeurons and HeLa cell systems. EMBO Rep. n/a, e56399. https://doi.org/10.15252/embr.202256399
Kravić, B., Bionda, T., Siebert, A., Gahlot, P., Levantovsky, S., Behrends, C., Meyer, H., 2022. Ubiquitin profiling of lysophagy identifies actin stabilizer CNN2 as a target of VCP/p97 and uncovers a link to HSPB1. Mol. Cell 82, 2633-2649.e7. https://doi.org/10.1016/j.molcel.2022.06.012
Kumar, N., Leonzino, M., Hancock-Cerutti, W., Horenkamp, F.A., Li, P., Lees, J.A., Wheeler, H., Reinisch, K.M., De Camilli, P., 2018. VPS13A and VPS13C are

lipid transport proteins differentially localized at ER contact sites. J. Cell Biol. 217, 3625–3639. https://doi.org/10.1083/jcb.201807019
Kuwahara, T., Funakawa, K., Komori, T., Sakurai, M., Yoshii, G., Eguchi, T., Fukuda, M., Iwatsubo, T., 2020. Roles of lysosomotropic agents on LRRK2 activation and Rab10 phosphorylation. Neurobiol. Dis. 145, 105081. https://doi.org/10.1016/j.nbd.2020.105081
Kuwahara, T., Inoue, K., D'Agati, V.D., Fujimoto, T., Eguchi, T., Saha, S., Wolozin, B., Iwatsubo, T., Abeliovich, A., 2016. LRRK2 and RAB7L1 coordinately regulate axonal morphology and lysosome integrity in diverse cellular contexts. Sci. Rep. 6. https://doi.org/10.1038/srep29945
Kvainickas, A., Jimenez-Orgaz, A., Nägele, H., Hu, Z., Dengjel, J., Steinberg, F., 2017. Cargo-selective SNX-BAR proteins mediate retromer trimer independent retrograde transport. J. Cell Biol. 216, 3677–3693. https://doi.org/10.1083/jcb.201702137
Kvainickas, A., Nägele, H., Qi, W., Dokládal, L., Jimenez-Orgaz, A., Stehl, L., Gangurde, D., Zhao, Q., Hu, Z., Dengjel, J., De Virgilio, C., Baumeister, R., Steinberg, F., 2019. Retromer and TBC1D5 maintain late endosomal RAB7 domains to enable amino acid–induced mTORC1 signaling. J. Cell Biol. 218, 3019–3038. https://doi.org/10.1083/jcb.201812110
Lara Ordónez, A.J., Fernández, B., Fdez, E., Romo-Lozano, M., Madero-Pérez, J., Lobbestael, E., Baekelandt, V., Aiastui, A., López de Munaín, A., Melrose, H.L., Civiero, L., Hilfiker, S., 2019. RAB8, RAB10 and RILPL1 contribute to both LRRK2 kinase–mediated centrosomal cohesion and ciliogenesis deficits. Hum. Mol. Genet. 28, 3552–3568. https://doi.org/10.1093/hmg/ddz201
Lauffer, B.E.L., Melero, C., Temkin, P., Lei, C., Hong, W., Kortemme, T., von Zastrow, M., 2010. SNX27 mediates PDZ-directed sorting from endosomes to the plasma membrane. J. Cell Biol. 190, 565–574. https://doi.org/10.1083/jcb.201004060
Laulumaa, S., Kumpula, E.-P., Huiskonen, J.T., Varjosalo, M., 2023. Structure and Interactions of the Endogenous Human Commander Complex. https://doi.org/10.1101/2023.04.03.535349
Lawe, D.C., Patki, V., Heller-Harrison, R., Lambright, D., Corvera, S., 2000. The FYVE Domain of Early Endosome Antigen 1 Is Required for Both Phosphatidylinositol 3-Phosphate and Rab5 Binding: CRITICAL ROLE OF THIS DUAL INTERACTION FOR ENDOSOMAL LOCALIZATION *. J. Biol. Chem. 275, 3699–3705. https://doi.org/10.1074/jbc.275.5.3699
Lazarou, M., Sliter, D.A., Kane, L.A., Sarraf, S.A., Wang, C., Burman, J.L., Sideris, D.P., Fogel, A.I., Youle, R.J., 2015. The ubiquitin kinase PINK1 recruits autophagy receptors to induce mitophagy. Nature 524, 309–314. https://doi.org/10.1038/nature14893
Lee, C., Lamech, L., Johns, E., Overholtzer, M., 2020. Selective Lysosome Membrane Turnover Is Induced by Nutrient Starvation. Dev. Cell 55, 289-297.e4. https://doi.org/10.1016/j.devcel.2020.08.008
Lee, R.G., Sedghi, M., Salari, M., Shearwood, A.-M.J., Stentenbach, M., Kariminejad, A., Goullee, H., Rackham, O., Laing, N.G., Tajsharghi, H., Filipovska, A., 2018. Early-onset Parkinson disease caused by a mutation in CHCHD2 and mitochondrial dysfunction. Neurol. Genet. 4, e276. https://doi.org/10.1212/NXG.0000000000000276
Lee, S., Chang, J., Blackstone, C., 2016. FAM21 directs SNX27–retromer cargoes to the plasma membrane by preventing transport to the Golgi apparatus. Nat. Commun. 7, 10939. https://doi.org/10.1038/ncomms10939
Leneva, N., Kovtun, O., Morado, D.R., Briggs, J.A.G., Owen, D.J., 2021. Architecture and mechanism of metazoan retromer:SNX3 tubular coat assembly. Sci. Adv. 7, eabf8598. https://doi.org/10.1126/sciadv.abf8598

Leonzino, M., Reinisch, K.M., De Camilli, P., 2021. Insights into VPS13 properties and function reveal a new mechanism of eukaryotic lipid transport. Biochim. Biophys. Acta BBA - Mol. Cell Biol. Lipids 1866, 159003. https://doi.org/10.1016/j.bbalip.2021.159003

Leray, X., Hilton, J.K., Nwangwu, K., Becerril, A., Mikusevic, V., Fitzgerald, G., Amin, A., Weston, M.R., Mindell, J.A., 2022. Tonic inhibition of the chloride/proton antiporter ClC-7 by PI(3,5)P2 is crucial for lysosomal pH maintenance. eLife 11, e74136. https://doi.org/10.7554/eLife.74136

Lesage, S., Drouet, V., Majounie, E., Deramecourt, V., Jacoupy, M., Nicolas, A., Cormier-Dequaire, F., Hassoun, S.M., Pujol, C., Ciura, S., Erpapazoglou, Z., Usenko, T., Maurage, C.-A., Sahbatou, M., Liebau, S., Ding, J., Bilgic, B., Emre, M., Erginel-Unaltuna, N., Guven, G., Tison, F., Tranchant, C., Vidailhet, M., Corvol, J.-C., Krack, P., Leutenegger, A.-L., Nalls, M.A., Hernandez, D.G., Heutink, P., Gibbs, J.R., Hardy, J., Wood, N.W., Gasser, T., Durr, A., Deleuze, J.-F., Tazir, M., Destée, A., Lohmann, E., Kabashi, E., Singleton, A., Corti, O., Brice, A., 2016. Loss of VPS13C Function in Autosomal-Recessive Parkinsonism Causes Mitochondrial Dysfunction and Increases PINK1/Parkin-Dependent Mitophagy. Am. J. Hum. Genet. 98, 500–513. https://doi.org/10.1016/j.ajhg.2016.01.014

Lewis, P.A., Greggio, E., Beilina, A., Jain, S., Baker, A., Cookson, M.R., 2007. The R1441C mutation of LRRK2 disrupts GTP hydrolysis. Biochem. Biophys. Res. Commun. 357, 668–671. https://doi.org/10.1016/j.bbrc.2007.04.006

Li, G., Marlin, M.C., 2015. Rab Family of GTPases. Methods Mol. Biol. Clifton NJ 1298, 1–15. https://doi.org/10.1007/978-1-4939-2569-8_1

Li, P., Lees, J.A., Lusk, C.P., Reinisch, K.M., 2020. Cryo-EM reconstruction of a VPS13 fragment reveals a long groove to channel lipids between membranes. J. Cell Biol. 219. https://doi.org/10.1083/jcb.202001161

Li, X., Wang, Q.J., Pan, N., Lee, S., Zhao, Y., Chait, B.T., Yue, Z., 2011. Phosphorylation-dependent 14-3-3 binding to LRRK2 is impaired by common mutations of familial Parkinson's disease. PloS One 6, e17153. https://doi.org/10.1371/journal.pone.0017153

Li, Y., Zheng, W., Lu, Y., Zheng, Y., Pan, L., Wu, X., Yuan, Y., Shen, Z., Ma, S., Zhang, Xingxian, Wu, J., Chen, Z., Zhang, Xiangnan, 2021. BNIP3L/NIX-mediated mitophagy: molecular mechanisms and implications for human disease. Cell Death Dis. 13, 1–11. https://doi.org/10.1038/s41419-021-04469-y

Lin, K.-J., Lin, K.-L., Chen, S.-D., Liou, C.-W., Chuang, Y.-C., Lin, H.-Y., Lin, T.-K., 2019. The Overcrowded Crossroads: Mitochondria, Alpha-Synuclein, and the Endo-Lysosomal System Interaction in Parkinson's Disease. Int. J. Mol. Sci. 20. https://doi.org/10.3390/ijms20215312

Lind-Holm Mogensen, F., Scafidi, A., Poli, A., Michelucci, A., 2023. PARK7/DJ-1 in microglia: implications in Parkinson's disease and relevance as a therapeutic target. J. Neuroinflammation 20, 95. https://doi.org/10.1186/s12974-023-02776-z

Linhart, R., Wong, S.A., Cao, J., Tran, M., Huynh, A., Ardrey, C., Park, J.M., Hsu, C., Taha, S., Peterson, R., Shea, S., Kurian, J., Venderova, K., 2014. Vacuolar protein sorting 35 (Vps35) rescues locomotor deficits and shortened lifespan in Drosophila expressing a Parkinson's disease mutant of Leucine-rich repeat kinase 2 (LRRK2). Mol. Neurodegener. 9, 23. https://doi.org/10.1186/1750-1326-9-23

Lis, P., Burel, S., Steger, M., Mann, M., Brown, F., Diez, F., Tonelli, F., Holton, J.L., Ho, P.W., Ho, S.-L., Chou, M.-Y., Polinski, N.K., Martinez, T.N., Davies, P., Alessi, D.R., 2018. Development of phospho-specific Rab protein antibodies to monitor in vivo activity of the LRRK2 Parkinson's disease kinase. Biochem. J. 475, 1–22. https://doi.org/10.1042/BCJ20170802

Liu, M., Bender, S.A., Cuny, G.D., Sherman, W., Glicksman, M., Ray, S.S., 2013. Type II Kinase Inhibitors Show an Unexpected Inhibition Mode against Parkinson's Disease-Linked LRRK2 Mutant G2019S. Biochemistry 52, 1725–1736. https://doi.org/10.1021/bi3012077

Liu, Z., Bryant, N., Kumaran, R., Beilina, A., Abeliovich, A., Cookson, M.R., West, A.B., 2018. LRRK2 phosphorylates membrane-bound Rabs and is activated by GTP-bound Rab7L1 to promote recruitment to the trans-Golgi network. Hum. Mol. Genet. 27, 385–395. https://doi.org/10.1093/hmg/ddx410

Llopis, J., McCaffery, J.M., Miyawaki, A., Farquhar, M.G., Tsien, R.Y., 1998. Measurement of cytosolic, mitochondrial, and Golgi pH in single living cells with green fluorescent proteins. Proc. Natl. Acad. Sci. U. S. A. 95, 6803–6808.

López-Jiménez, A.T., Cardenal-Muñoz, E., Leuba, F., Gerstenmaier, L., Barisch, C., Hagedorn, M., King, J.S., Soldati, T., 2018. The ESCRT and autophagy machineries cooperate to repair ESX-1-dependent damage at the Mycobacterium-containing vacuole but have opposite impact on containing the infection. PLOS Pathog. 14, e1007501. https://doi.org/10.1371/journal.ppat.1007501

Lopez-Robles, C., Scaramuzza, S., Astorga-Simon, E.N., Ishida, M., Williamson, C.D., Baños-Mateos, S., Gil-Carton, D., Romero-Durana, M., Vidaurrazaga, A., Fernandez-Recio, J., Rojas, A.L., Bonifacino, J.S., Castaño-Díez, D., Hierro, A., 2023. Architecture of the ESCPE-1 membrane coat. Nat. Struct. Mol. Biol. 1–12. https://doi.org/10.1038/s41594-023-01014-7

Lucas, M., Gershlick, D.C., Vidaurrazaga, A., Rojas, A.L., Bonifacino, J.S., Hierro, A., 2016. Structural Mechanism for Cargo Recognition by the Retromer Complex. Cell 167, 1623-1635.e14. https://doi.org/10.1016/j.cell.2016.10.056

Luzio, J.P., Hackmann, Y., Dieckmann, N.M.G., Griffiths, G.M., 2014. The Biogenesis of Lysosomes and Lysosome-Related Organelles. Cold Spring Harb. Perspect. Biol. 6. https://doi.org/10.1101/cshperspect.a016840

Lwin, A., Orvisky, E., Goker-Alpan, O., LaMarca, M.E., Sidransky, E., 2004. Glucocerebrosidase mutations in subjects with parkinsonism. Mol. Genet. Metab. 81, 70–73. https://doi.org/10.1016/j.ymgme.2003.11.004

Lystad, A.H., Simonsen, A., 2016. Phosphoinositide-binding proteins in autophagy. FEBS Lett. 590, 2454–2468. https://doi.org/10.1002/1873-3468.12286

Ma, K.Y., Fokkens, M.R., Reggiori, F., Mari, M., Verbeek, D.S., 2021. Parkinson's disease–associated VPS35 mutant reduces mitochondrial membrane potential and impairs PINK1/Parkin-mediated mitophagy. Transl. Neurodegener. 10, 19. https://doi.org/10.1186/s40035-021-00243-4

MacDonald, E., Brown, L., Selvais, A., Liu, H., Waring, T., Newman, D., Bithell, J., Grimes, D., Urbé, S., Clague, M.J., Zech, T., 2018. HRS-WASH axis governs actin-mediated endosomal recycling and cell invasion. J. Cell Biol. 217, 2549–2564. https://doi.org/10.1083/jcb.201710051

MacDonald, E., Savage, B., Zech, T., 2020. Connecting the dots: combined control of endocytic recycling and degradation. Biochem. Soc. Trans. 48, 2377–2386. https://doi.org/10.1042/BST20180255

MacDonald, E., Urbé, S., Clague, M.J., 2014. USP8 Controls the Trafficking and Sorting of Lysosomal Enzymes. Traffic 15, 879–888. https://doi.org/10.1111/tra.12180

MacLeod, D.A., Rhinn, H., Kuwahara, T., Zolin, A., Di Paolo, G., McCabe, B.D., Clark, L.N., Small, S.A., Abeliovich, A., 2013. RAB7L1 interacts with LRRK2 to modify intraneuronal protein sorting and Parkinson's disease risk. Neuron 77, 425–439. https://doi.org/10.1016/j.neuron.2012.11.033

Maejima, I., Takahashi, A., Omori, H., Kimura, T., Takabatake, Y., Saitoh, T., Yamamoto, A., Hamasaki, M., Noda, T., Isaka, Y., Yoshimori, T., 2013. Autophagy sequesters damaged lysosomes to control lysosomal biogenesis

and kidney injury. EMBO J. 32, 2336–2347. https://doi.org/10.1038/emboj.2013.171
Malik, A.U., Karapetsas, A., Nirujogi, R.S., Mathea, S., Chatterjee, D., Pal, P., Lis, P., Taylor, M., Purlyte, E., Gourlay, R., Dorward, M., Weidlich, S., Toth, R., Polinski, N.K., Knapp, S., Tonelli, F., Alessi, D.R., 2021. Deciphering the LRRK code: LRRK1 and LRRK2 phosphorylate distinct Rab proteins and are regulated by diverse mechanisms. Biochem. J. 478, 553–578. https://doi.org/10.1042/BCJ20200937
Malik, B.R., Godena, V.K., Whitworth, A.J., 2015. VPS35 pathogenic mutations confer no dominant toxicity but partial loss of function in Drosophila and genetically interact with parkin. Hum. Mol. Genet. 24, 6106–6117. https://doi.org/10.1093/hmg/ddv322
Mamais, A., Chia, R., Beilina, A., Hauser, D.N., Hall, C., Lewis, P.A., Cookson, M.R., Bandopadhyay, R., 2014. Arsenite Stress Down-regulates Phosphorylation and 14-3-3 Binding of Leucine-rich Repeat Kinase 2 (LRRK2), Promoting Self-association and Cellular Redistribution. J. Biol. Chem. 289, 21386–21400. https://doi.org/10.1074/jbc.M113.528463
Mamais, A., Kluss, J.H., Bonet-Ponce, L., Landeck, N., Langston, R.G., Smith, N., Beilina, A., Kaganovich, A., Ghosh, M.C., Pellegrini, L., Kumaran, R., Papazoglou, I., Heaton, G.R., Bandopadhyay, R., Maio, N., Kim, C., LaVoie, M.J., Gershlick, D.C., Cookson, M.R., 2021. Mutations in LRRK2 linked to Parkinson disease sequester Rab8a to damaged lysosomes and regulate transferrin-mediated iron uptake in microglia. PLoS Biol. 19, e3001480. https://doi.org/10.1371/journal.pbio.3001480
Marchand, A., Drouyer, M., Sarchione, A., Chartier-Harlin, M.-C., Taymans, J.-M., 2020. LRRK2 Phosphorylation, More Than an Epiphenomenon. Front. Neurosci. 14.
Marcos, A.L., Corradi, G.R., Mazzitelli, L.R., Casali, C.I., Fernández Tome, M. del C., Adamo, H.P., de Tezanos Pinto, F., 2019. The Parkinson-associated human P5B-ATPase ATP13A2 modifies lipid homeostasis. Biochim. Biophys. Acta BBA - Biomembr. 1861, 182993. https://doi.org/10.1016/j.bbamem.2019.05.015
Martina, J.A., Chen, Y., Gucek, M., Puertollano, R., 2012. MTORC1 functions as a transcriptional regulator of autophagy by preventing nuclear transport of TFEB. Autophagy 8, 903–914. https://doi.org/10.4161/auto.19653
Martinez, A., Lectez, B., Ramirez, J., Popp, O., Sutherland, J.D., Urbé, S., Dittmar, G., Clague, M.J., Mayor, U., 2017. Quantitative proteomic analysis of Parkin substrates in Drosophila neurons. Mol. Neurodegener. 12, 29. https://doi.org/10.1186/s13024-017-0170-3
Martinez, J., Malireddi, R.S., Lu, Q., Cunha, L.D., Pelletier, S., Gingras, S., Orchard, R., Guan, J.-L., Tan, H., Peng, J., Kanneganti, T.-D., Virgin, H.W., Green, D.R., 2015. Molecular characterization of LC3-associated phagocytosis (LAP) reveals distinct roles for Rubicon, NOX2, and autophagy proteins. Nat. Cell Biol. 17, 893–906. https://doi.org/10.1038/ncb3192
Matheoud, D., Sugiura, A., Bellemare-Pelletier, A., Laplante, A., Rondeau, C., Chemali, M., Fazel, A., Bergeron, J.J., Trudeau, L.-E., Burelle, Y., Gagnon, E., McBride, H.M., Desjardins, M., 2016. Parkinson's Disease-Related Proteins PINK1 and Parkin Repress Mitochondrial Antigen Presentation. Cell 166, 314–327. https://doi.org/10.1016/j.cell.2016.05.039
Matsuda, N., Sato, S., Shiba, K., Okatsu, K., Saisho, K., Gautier, C.A., Sou, Y., Saiki, S., Kawajiri, S., Sato, F., Kimura, M., Komatsu, M., Hattori, N., Tanaka, K., 2010. PINK1 stabilized by mitochondrial depolarization recruits Parkin to damaged mitochondria and activates latent Parkin for mitophagy. J. Cell Biol. 189, 211–221. https://doi.org/10.1083/jcb.200910140

Matsui, Y., Kikuchi, A., Araki, S., Hata, Y., Kondo, J., Teranishi, Y., Takai, Y., 1990. Molecular cloning and characterization of a novel type of regulatory protein (GDI) for smg p25A, a ras p21-like GTP-binding protein. Mol. Cell. Biol. 10, 4116–4122. https://doi.org/10.1128/mcb.10.8.4116-4122.1990

Maxfield, F.R., 2014. Role of Endosomes and Lysosomes in Human Disease. Cold Spring Harb. Perspect. Biol. 6, a016931. https://doi.org/10.1101/cshperspect.a016931

Maxson, M.E., Huynh, K.K., Grinstein, S., 2023. Endocytosis is regulated through the pH-dependent phosphorylation of Rab GTPases by Parkinson's kinase LRRK2. https://doi.org/10.1101/2023.02.15.528749

Mayor, S., Parton, R.G., Donaldson, J.G., 2014. Clathrin-Independent Pathways of Endocytosis. Cold Spring Harb. Perspect. Biol. 6, a016758. https://doi.org/10.1101/cshperspect.a016758

McCullough, J., Clippinger, A.K., Talledge, N., Skowyra, M.L., Saunders, M.G., Naismith, T.V., Colf, L.A., Afonine, P., Arthur, C., Sundquist, W.I., Hanson, P.I., Frost, A., 2015. Structure and membrane remodeling activity of ESCRT-III helical polymers. Science 350, 1548–1551. https://doi.org/10.1126/science.aad8305

McCullough, J., Frost, A., Sundquist, W.I., 2018. Structures, Functions, and Dynamics of ESCRT-III/Vps4 Membrane Remodeling and Fission Complexes. Annu. Rev. Cell Dev. Biol. 34, 85–109. https://doi.org/10.1146/annurev-cellbio-100616-060600

McEwen, R.K., Dove, S.K., Cooke, F.T., Painter, G.F., Holmes, A.B., Shisheva, A., Ohya, Y., Parker, P.J., Michell, R.H., 1999. Complementation analysis in PtdInsP kinase-deficient yeast mutants demonstrates that Schizosaccharomyces pombe and murine Fab1p homologues are phosphatidylinositol 3-phosphate 5-kinases. J. Biol. Chem. 274, 33905–33912. https://doi.org/10.1074/jbc.274.48.33905

McGough, Steinberg, F., Jia, D., Barbuti, P.A., McMillan, K.J., Heesom, K.J., Whone, A.L., Caldwell, M.A., Billadeau, D.D., Rosen, M.K., Cullen, P.J., 2014. Retromer Binding to FAM21 and the WASH Complex Is Perturbed by the Parkinson Disease-Linked VPS35(D620N) Mutation. Curr. Biol. 24, 1670–1676. https://doi.org/10.1016/j.cub.2014.06.024

McGrath, E., Waschbüsch, D., Baker, B.M., Khan, A.R., 2021. LRRK2 binds to the Rab32 subfamily in a GTP-dependent manner *via* its armadillo domain. Small GTPases 12, 133–146. https://doi.org/10.1080/21541248.2019.1666623

McLelland, G.-L., Lee, S.A., McBride, H.M., Fon, E.A., 2016. Syntaxin-17 delivers PINK1/parkin-dependent mitochondrial vesicles to the endolysosomal system. J. Cell Biol. 214, 275–291. https://doi.org/10.1083/jcb.201603105

McLelland, G.-L., Soubannier, V., Chen, C.X., McBride, H.M., Fon, E.A., 2014. Parkin and PINK1 function in a vesicular trafficking pathway regulating mitochondrial quality control. EMBO J. 33, 282–295. https://doi.org/10.1002/embj.201385902

McMillan, K.J., Gallon, M., Jellett, A.P., Clairfeuille, T., Tilley, F.C., McGough, I., Danson, C.M., Heesom, K.J., Wilkinson, K.A., Collins, B.M., Cullen, P.J., 2016. Atypical parkinsonism–associated retromer mutant alters endosomal sorting of specific cargo proteins. J. Cell Biol. 214, 389–399. https://doi.org/10.1083/jcb.201604057

McNally, K.E., Cullen, P.J., 2018. Endosomal Retrieval of Cargo: Retromer Is Not Alone. Trends Cell Biol. 28, 807–822. https://doi.org/10.1016/j.tcb.2018.06.005

McNally, K.E., Faulkner, R., Steinberg, F., Gallon, M., Ghai, R., Pim, D., Langton, P., Pearson, N., Danson, C.M., Nägele, H., Morris, L.L., Singla, A., Overlee, B.L., Heesom, K.J., Sessions, R., Banks, L., Collins, B.M., Berger, I., Billadeau, D.D., Burstein, E., Cullen, P.J., 2017. Retriever is a multiprotein complex for

retromer-independent endosomal cargo recycling. Nat. Cell Biol. 19, 1214–1225. https://doi.org/10.1038/ncb3610
McPherson, P.S., Garcia, E.P., Slepnev, V.I., David, C., Zhang, X., Grabs, D., Sossini, W.S., Bauerfeind, R., Nemoto, Y., De Camilli, P., 1996. A presynaptic inositol-5-phosphatase. Nature 379, 353–357. https://doi.org/10.1038/379353a0
Medina, D.L., Di Paola, S., Peluso, I., Armani, A., De Stefani, D., Venditti, R., Montefusco, S., Scotto-Rosato, A., Prezioso, C., Forrester, A., Settembre, C., Wang, W., Gao, Q., Xu, H., Sandri, M., Rizzuto, R., De Matteis, M.A., Ballabio, A., 2015. Lysosomal calcium signalling regulates autophagy through calcineurin and TFEB. Nat. Cell Biol. 17, 288–299. https://doi.org/10.1038/ncb3114
Melia, T.J., Lystad, A.H., Simonsen, A., 2020. Autophagosome biogenesis: From membrane growth to closure. J. Cell Biol. 219, e202002085. https://doi.org/10.1083/jcb.202002085
Mercer, T.J., Gubas, A., Tooze, S.A., 2018. A molecular perspective of mammalian autophagosome biogenesis. J. Biol. Chem. 293, 5386–5395. https://doi.org/10.1074/jbc.R117.810366
Mills, I.G., Jones, A.T., Clague, M.J., 1998. Involvement of the endosomal autoantigen EEA1 in homotypic fusion of early endosomes. Curr. Biol. 8, 881–884. https://doi.org/10.1016/S0960-9822(07)00351-X
Mir, R., Tonelli, F., Lis, P., Macartney, T., Polinski, N.K., Martinez, T.N., Chou, M.-Y., Howden, A.J.M., König, T., Hotzy, C., Milenkovic, I., Brücke, T., Zimprich, A., Sammler, E., Alessi, D.R., 2018. The Parkinson's disease VPS35[D620N] mutation enhances LRRK2-mediated Rab protein phosphorylation in mouse and human. Biochem. J. 475, 1861–1883. https://doi.org/10.1042/BCJ20180248
Montagnac, G., Sibarita, J.-B., Loubéry, S., Daviet, L., Romao, M., Raposo, G., Chavrier, P., 2009. ARF6 Interacts with JIP4 to control a motor switch mechanism regulating endosome traffic in cytokinesis. Curr. Biol. CB 19, 184–195. https://doi.org/10.1016/j.cub.2008.12.043
Montava-Garriga, L., Singh, F., Ball, G., Ganley, I.G., 2020. Semi-automated quantitation of mitophagy in cells and tissues. Mech. Ageing Dev. 185, 111196. https://doi.org/10.1016/j.mad.2019.111196
Morgan, A.J., Yuan, Y., Patel, S., Galione, A., 2020. Does lysosomal rupture evoke Ca2+ release? A question of pores and stores. Cell Calcium 86, 102139. https://doi.org/10.1016/j.ceca.2019.102139
Mortiboys, H., Johansen, K.K., Aasly, J.O., Bandmann, O., 2010. Mitochondrial impairment in patients with Parkinson disease with the G2019S mutation in LRRK2. Neurology 75, 2017–2020. https://doi.org/10.1212/WNL.0b013e3181ff9685
Mortiboys, H., Thomas, K.J., Koopman, W.J.H., Klaffke, S., Abou-Sleiman, P., Olpin, S., Wood, N.W., Willems, P.H.G.M., Smeitink, J.A.M., Cookson, M.R., Bandmann, O., 2008. Mitochondrial function and morphology are impaired in parkin mutant fibroblasts. Ann. Neurol. 64, 555–565. https://doi.org/10.1002/ana.21492
Mu, F.-T., Callaghan, J.M., Steele-Mortimer, O., Stenmark, H., Parton, R.G., Campbell, P.L., McCluskey, J., Yeo, J.-P., Tock, E.P.C., Toh, B.-H., 1995. EEA1, an Early Endosome-Associated Protein.: EEA1 IS A CONSERVED α-HELICAL PERIPHERAL MEMBRANE PROTEIN FLANKED BY CYSTEINE "FINGERS" AND CONTAINS A CALMODULIN-BINDING IQ MOTIF ∗. J. Biol. Chem. 270, 13503–13511. https://doi.org/10.1074/jbc.270.22.13503
Muda, K., Bertinetti, D., Gesellchen, F., Hermann, J.S., Zweydorf, F. von, Geerlof, A., Jacob, A., Ueffing, M., Gloeckner, C.J., Herberg, F.W., 2014. Parkinson-related LRRK2 mutation R1441C/G/H impairs PKA phosphorylation of LRRK2

and disrupts its interaction with 14-3-3. Proc. Natl. Acad. Sci. 111, E34–E43. https://doi.org/10.1073/pnas.1312701111
Munsie, L.N., Milnerwood, A.J., Seibler, P., Beccano-Kelly, D.A., Tatarnikov, I., Khinda, J., Volta, M., Kadgien, C., Cao, L.P., Tapia, L., Klein, C., Farrer, M.J., 2015. Retromer-dependent neurotransmitter receptor trafficking to synapses is altered by the Parkinson's disease VPS35 mutation p.D620N. Hum. Mol. Genet. 24, 1691–1703. https://doi.org/10.1093/hmg/ddu582
Murphy, K.E., Gysbers, A.M., Abbott, S.K., Tayebi, N., Kim, W.S., Sidransky, E., Cooper, A., Garner, B., Halliday, G.M., 2014. Reduced glucocerebrosidase is associated with increased α-synuclein in sporadic Parkinson's disease. Brain 137, 834–848. https://doi.org/10.1093/brain/awt367
Nakamura, S., Shigeyama, S., Minami, S., Shima, T., Akayama, S., Matsuda, T., Esposito, A., Napolitano, G., Kuma, A., Namba-Hamano, T., Nakamura, J., Yamamoto, K., Sasai, M., Tokumura, A., Miyamoto, M., Oe, Y., Fujita, T., Terawaki, S., Takahashi, A., Hamasaki, M., Yamamoto, M., Okada, Y., Komatsu, M., Nagai, T., Takabatake, Y., Xu, H., Isaka, Y., Ballabio, A., Yoshimori, T., 2020. LC3 lipidation is essential for TFEB activation during the lysosomal damage response to kidney injury. Nat. Cell Biol. 22, 1252–1263. https://doi.org/10.1038/s41556-020-00583-9
Nakatogawa, H., 2020. Mechanisms governing autophagosome biogenesis. Nat. Rev. Mol. Cell Biol. 21, 439–458. https://doi.org/10.1038/s41580-020-0241-0
Nalls, M.A., Pankratz, N., Lill, C.M., Do, C.B., Hernandez, D.G., Saad, M., DeStefano, A.L., Kara, E., Bras, J., Sharma, M., Schulte, C., Keller, M.F., Arepalli, S., Letson, C., Edsall, C., Stefansson, H., Liu, X., Pliner, H., Lee, J.H., Cheng, R., International Parkinson's Disease Genomics Consortium (IPDGC), Parkinson's Study Group (PSG) Parkinson's Research: The Organized GENetics Initiative (PROGENI), 23andMe, GenePD, NeuroGenetics Research Consortium (NGRC), Hussman Institute of Human Genomics (HIHG), Ashkenazi Jewish Dataset Investigator, Cohorts for Health and Aging Research in Genetic Epidemiology (CHARGE), North American Brain Expression Consortium (NABEC), United Kingdom Brain Expression Consortium (UKBEC), Greek Parkinson's Disease Consortium, Alzheimer Genetic Analysis Group, Ikram, M.A., Ioannidis, J.P.A., Hadjigeorgiou, G.M., Bis, J.C., Martinez, M., Perlmutter, J.S., Goate, A., Marder, K., Fiske, B., Sutherland, M., Xiromerisiou, G., Myers, R.H., Clark, L.N., Stefansson, K., Hardy, J.A., Heutink, P., Chen, H., Wood, N.W., Houlden, H., Payami, H., Brice, A., Scott, W.K., Gasser, T., Bertram, L., Eriksson, N., Foroud, T., Singleton, A.B., 2014. Large-scale meta-analysis of genome-wide association data identifies six new risk loci for Parkinson's disease. Nat. Genet. 46, 989–993. https://doi.org/10.1038/ng.3043
Narendra, D., Tanaka, A., Suen, D.-F., Youle, R.J., 2008. Parkin is recruited selectively to impaired mitochondria and promotes their autophagy. J. Cell Biol. 183, 795–803. https://doi.org/10.1083/jcb.200809125
Narendra, D.P., Jin, S.M., Tanaka, A., Suen, D.-F., Gautier, C.A., Shen, J., Cookson, M.R., Youle, R.J., 2010. PINK1 Is Selectively Stabilized on Impaired Mitochondria to Activate Parkin. PLOS Biol. 8, e1000298. https://doi.org/10.1371/journal.pbio.1000298
Naslavsky, N., Caplan, S., 2018. The enigmatic endosome – sorting the ins and outs of endocytic trafficking. J. Cell Sci. 131. https://doi.org/10.1242/jcs.216499
Neumann, J., Bras, J., Deas, E., O'Sullivan, S.S., Parkkinen, L., Lachmann, R.H., Li, A., Holton, J., Guerreiro, R., Paudel, R., Segarane, B., Singleton, A., Lees, A., Hardy, J., Houlden, H., Revesz, T., Wood, N.W., 2009. Glucocerebrosidase mutations in clinical and pathologically proven Parkinson's disease. Brain J. Neurol. 132, 1783–1794. https://doi.org/10.1093/brain/awp044

Neuspiel, M., Schauss, A.C., Braschi, E., Zunino, R., Rippstein, P., Rachubinski, R.A., Andrade-Navarro, M.A., McBride, H.M., 2008. Cargo-Selected Transport from the Mitochondria to Peroxisomes Is Mediated by Vesicular Carriers. Curr. Biol. 18, 102–108. https://doi.org/10.1016/j.cub.2007.12.038

Ng, C.-H., Mok, S.Z.S., Koh, C., Ouyang, X., Fivaz, M.L., Tan, E.-K., Dawson, V.L., Dawson, T.M., Yu, F., Lim, K.-L., 2009. Parkin protects against LRRK2 G2019S mutant-induced dopaminergic neurodegeneration in Drosophila. J. Neurosci. Off. J. Soc. Neurosci. 29, 11257–11262. https://doi.org/10.1523/JNEUROSCI.2375-09.2009

Nguyen, M., Krainc, D., 2018. LRRK2 phosphorylation of auxilin mediates synaptic defects in dopaminergic neurons from patients with Parkinson's disease. Proc. Natl. Acad. Sci. U. S. A. 115, 5576–5581. https://doi.org/10.1073/pnas.1717590115

Nguyen-Dien, G.T., Kozul, K.-L., Cui, Y., Townsend, B., Kulkarni, P.G., Ooi, S.S., Marzio, A., Carrodus, N., Zuryn, S., Pagano, M., Parton, R.G., Lazarou, M., Millard, S.S., Taylor, R.W., Collins, B.M., Jones, M.J., Pagan, J.K., 2023. FBXL4 suppresses mitophagy by restricting the accumulation of NIX and BNIP3 mitophagy receptors. EMBO J. n/a, e112767. https://doi.org/10.15252/embj.2022112767

Nichols, R.J., Dzamko, N., Morrice, N.A., Campbell, D.G., Deak, M., Ordureau, A., Macartney, T., Tong, Y., Shen, J., Prescott, A.R., Alessi, D.R., 2010. 14-3-3 binding to LRRK2 is disrupted by multiple Parkinson's disease-associated mutations and regulates cytoplasmic localization. Biochem. J. 430, 393–404. https://doi.org/10.1042/BJ20100483

Niu, J., Yu, M., Wang, C., Xu, Z., 2012. Leucine-rich repeat kinase 2 disturbs mitochondrial dynamics via Dynamin-like protein. J. Neurochem. 122, 650–658. https://doi.org/10.1111/j.1471-4159.2012.07809.x

Niu, M., Zhao, F., Bondelid, K., Siedlak, S.L., Torres, S., Fujioka, H., Wang, W., Liu, J., Zhu, X., 2021. VPS35 D620N knockin mice recapitulate cardinal features of Parkinson's disease. Aging Cell 20, e13347. https://doi.org/10.1111/acel.13347

Norris, A., Grant, B.D., 2020. Endosomal microdomains: Formation and function. Curr. Opin. Cell Biol. 65, 86–95. https://doi.org/10.1016/j.ceb.2020.02.018

Norris, A., Tammineni, P., Wang, S., Gerdes, J., Murr, A., Kwan, K.Y., Cai, Q., Grant, B.D., 2017. SNX-1 and RME-8 oppose the assembly of HGRS-1/ESCRT-0 degradative microdomains on endosomes. Proc. Natl. Acad. Sci. 114, E307–E316. https://doi.org/10.1073/pnas.1612730114

Novak, I., Kirkin, V., McEwan, D.G., Zhang, J., Wild, P., Rozenknop, A., Rogov, V., Löhr, F., Popovic, D., Occhipinti, A., Reichert, A.S., Terzic, J., Dötsch, V., Ney, P.A., Dikic, I., 2010. Nix is a selective autophagy receptor for mitochondrial clearance. EMBO Rep. 11, 45–51. https://doi.org/10.1038/embor.2009.256

Nthiga, T.M., Shrestha, B.K., Bruun, J.-A., Larsen, K.B., Lamark, T., Johansen, T., 2021. Regulation of Golgi turnover by CALCOCO1-mediated selective autophagy. J. Cell Biol. 220, e202006128. https://doi.org/10.1083/jcb.202006128

Obeso, J.A., Stamelou, M., Goetz, C.G., Poewe, W., Lang, A.E., Weintraub, D., Burn, D., Halliday, G.M., Bezard, E., Przedborski, S., Lehericy, S., Brooks, D.J., Rothwell, J.C., Hallett, M., DeLong, M.R., Marras, C., Tanner, C.M., Ross, G.W., Langston, J.W., Klein, C., Bonifati, V., Jankovic, J., Lozano, A.M., Deuschl, G., Bergman, H., Tolosa, E., Rodriguez-Violante, M., Fahn, S., Postuma, R.B., Berg, D., Marek, K., Standaert, D.G., Surmeier, D.J., Olanow, C.W., Kordower, J.H., Calabresi, P., Schapira, A.H.V., Stoessl, A.J., 2017. Past, Present, and Future of Parkinson's Disease: A Special Essay on the 200th Anniversary of the Shaking Palsy. Mov. Disord. Off. J. Mov. Disord. Soc. 32, 1264–1310. https://doi.org/10.1002/mds.27115

Ohkuma, S., Moriyama, Y., Takano, T., 1982. Identification and characterization of a proton pump on lysosomes by fluorescein-isothiocyanate-dextran fluorescence. Proc. Natl. Acad. Sci. 79, 2758–2762. https://doi.org/10.1073/pnas.79.9.2758

Olson, L.J., Hindsgaul, O., Dahms, N.M., Kim, J.-J.P., 2008. Structural Insights into the Mechanism of pH-dependent Ligand Binding and Release by the Cation-dependent Mannose 6-Phosphate Receptor. J. Biol. Chem. 283, 10124–10134. https://doi.org/10.1074/jbc.M708994200

Otsuji, S., Nishio, Y., Tsujita, M., Rio, M., Huber, C., Antón-Plágaro, C., Mizuno, S., Kawano, Y., Miyatake, S., Simon, M., Binsbergen, E. van, Jaarsveld, R.H. van, Matsumoto, N., Cormier-Daire, V., J.Cullen, P., Saitoh, S., Kato, K., 2023. Clinical diversity and molecular mechanism of VPS35L-associated Ritscher-Schinzel syndrome. J. Med. Genet. 60, 359–367. https://doi.org/10.1136/jmg-2022-108602

Padman, B.S., Bach, M., Lucarelli, G., Prescott, M., Ramm, G., 2013. The protonophore CCCP interferes with lysosomal degradation of autophagic cargo in yeast and mammalian cells. Autophagy 9, 1862–1875. https://doi.org/10.4161/auto.26557

Paisán-Ruíz, C., Jain, S., Evans, E.W., Gilks, W.P., Simón, J., Brug, M. van der, Munain, A.L. de, Aparicio, S., Gil, A.M., Khan, N., Johnson, J., Martinez, J.R., Nicholl, D., Carrera, I.M., Peña, A.S., Silva, R. de, Lees, A., Martí-Massó, J.F., Pérez-Tur, J., Wood, N.W., Singleton, A.B., 2004. Cloning of the Gene Containing Mutations that Cause PARK8-Linked Parkinson's Disease. Neuron 44, 595–600. https://doi.org/10.1016/j.neuron.2004.10.023

Pal, P., Taylor, M., Lam, P.Y., Tonelli, F., Hecht, C.A., Lis, P., Nirujogi, R.S., Phung, T.K., Dickie, E.A., Wightman, M., Macartney, T., Pfeffer, S.R., Alessi, D.R., 2023. Parkinson's VP535[D620N] mutation induces LRRK2 mediated lysosomal association of RILPL1 and TMEM55B. https://doi.org/10.1101/2023.06.07.544051

Palmieri, M., Impey, S., Kang, H., di Ronza, A., Pelz, C., Sardiello, M., Ballabio, A., 2011. Characterization of the CLEAR network reveals an integrated control of cellular clearance pathways. Hum. Mol. Genet. 20, 3852–3866. https://doi.org/10.1093/hmg/ddr306

Pankratz, N., Beecham, G.W., DeStefano, A.L., Dawson, T.M., Doheny, K.F., Factor, S.A., Hamza, T.H., Hung, A.Y., Hyman, B.T., Ivinson, A.J., Krainc, D., Latourelle, J.C., Clark, L.N., Marder, K., Martin, E.R., Mayeux, R., Ross, O.A., Scherzer, C.R., Simon, D.K., Tanner, C., Vance, J.M., Wszolek, Z.K., Zabetian, C.P., Myers, R.H., Payami, H., Scott, W.K., Foroud, T., PD GWAS Consortium, 2012. Meta-analysis of Parkinson's disease: identification of a novel locus, RIT2. Ann. Neurol. 71, 370–384. https://doi.org/10.1002/ana.22687

Papadopoulos, C., Kirchner, P., Bug, M., Grum, D., Koerver, L., Schulze, N., Poehler, R., Dressler, A., Fengler, S., Arhzaouy, K., Lux, V., Ehrmann, M., Weihl, C.C., Meyer, H., 2017. VCP/p97 cooperates with YOD1, UBXD1 and PLAA to drive clearance of ruptured lysosomes by autophagy. EMBO J. 36, 135–150. https://doi.org/10.15252/embj.201695148

Papadopoulos, C., Kravic, B., Meyer, H., 2020. Repair or Lysophagy: Dealing with Damaged Lysosomes. J. Mol. Biol., Molecular Mechanisms of Selective Autophagy 432, 231–239. https://doi.org/10.1016/j.jmb.2019.08.010

Papadopoulos, V.E., Nikolopoulou, G., Antoniadou, I., Karachaliou, A., Arianoglou, G., Emmanouilidou, E., Sardi, S.P., Stefanis, L., Vekrellis, K., 2018. Modulation of β-glucocerebrosidase increases α-synuclein secretion and exosome release in mouse models of Parkinson's disease. Hum. Mol. Genet. 27, 1696–1710. https://doi.org/10.1093/hmg/ddy075

Papkovskaia, T.D., Chau, K.-Y., Inesta-Vaquera, F., Papkovsky, D.B., Healy, D.G., Nishio, K., Staddon, J., Duchen, M.R., Hardy, J., Schapira, A.H.V., Cooper, J.M., 2012. G2019S leucine-rich repeat kinase 2 causes uncoupling protein-mediated mitochondrial depolarization. Hum. Mol. Genet. 21, 4201. https://doi.org/10.1093/hmg/dds244

Park, J., Lee, S.B., Lee, S., Kim, Y., Song, S., Kim, S., Bae, E., Kim, J., Shong, M., Kim, J.-M., Chung, J., 2006. Mitochondrial dysfunction in Drosophila PINK1 mutants is complemented by parkin. Nature 441, 1157–1161. https://doi.org/10.1038/nature04788

Park, J.-S., Blair, N.F., Sue, C.M., 2015. The role of ATP13A2 in Parkinson's disease: Clinical phenotypes and molecular mechanisms. Mov. Disord. 30, 770–779. https://doi.org/10.1002/mds.26243

Parkinson, J., 2002. An Essay on the Shaking Palsy. J. Neuropsychiatry Clin. Neurosci. 14, 223–236. https://doi.org/10.1176/jnp.14.2.223

Perez Carrion, M., Pischedda, F., Biosa, A., Russo, I., Straniero, L., Civiero, L., Guida, M., Gloeckner, C.J., Ticozzi, N., Tiloca, C., Mariani, C., Pezzoli, G., Duga, S., Pichler, I., Pan, L., Landers, J.E., Greggio, E., Hess, M.W., Goldwurm, S., Piccoli, G., 2018. The LRRK2 Variant E193K Prevents Mitochondrial Fission Upon MPP+ Treatment by Altering LRRK2 Binding to DRP1. Front. Mol. Neurosci. 11, 64. https://doi.org/10.3389/fnmol.2018.00064

Pfeffer, S.R., 2017. Rab GTPases: master regulators that establish the secretory and endocytic pathways. Mol. Biol. Cell 28, 712–715. https://doi.org/10.1091/mbc.e16-10-0737

Phillips-Krawczak, C.A., Singla, A., Starokadomskyy, P., Deng, Z., Osborne, D.G., Li, H., Dick, C.J., Gomez, T.S., Koenecke, M., Zhang, J.-S., Dai, H., Sifuentes-Dominguez, L.F., Geng, L.N., Kaufmann, S.H., Hein, M.Y., Wallis, M., McGaughran, J., Gecz, J., van de Sluis, B., Billadeau, D.D., Burstein, E., 2015. COMMD1 is linked to the WASH complex and regulates endosomal trafficking of the copper transporter ATP7A. Mol. Biol. Cell 26, 91–103. https://doi.org/10.1091/mbc.E14-06-1073

Piotrowski, J.T., Gomez, T.S., Schoon, R.A., Mangalam, A.K., Billadeau, D.D., 2013. WASH Knockout T Cells Demonstrate Defective Receptor Trafficking, Proliferation, and Effector Function. Mol. Cell. Biol. 33, 958–973. https://doi.org/10.1128/MCB.01288-12

Podinovskaia, M., Prescianotto-Baschong, C., Buser, D.P., Spang, A., 2021. A novel live-cell imaging assay reveals regulation of endosome maturation. eLife 10, e70982. https://doi.org/10.7554/eLife.70982

Pohl, C., Dikic, I., 2019. Cellular quality control by the ubiquitin-proteasome system and autophagy. Science 366, 818–822. https://doi.org/10.1126/science.aax3769

Pohlmann, R., Boeker, M.W.C., von Figura, K., 1995. The Two Mannose 6-Phosphate Receptors Transport Distinct Complements of Lysosomal Proteins (*). J. Biol. Chem. 270, 27311–27318. https://doi.org/10.1074/jbc.270.45.27311

Pollock, L., Jardine, J., Urbé, S., Clague, M.J., 2021. The PINK1 repertoire: Not just a one trick pony. BioEssays 43, 2100168. https://doi.org/10.1002/bies.202100168

Polson, H.E.J., de Lartigue, J., Rigden, D.J., Reedijk, M., Urbé, S., Clague, M.J., Tooze, S.A., 2010. Mammalian Atg18 (WIPI2) localizes to omegasome-anchored phagophores and positively regulates LC3 lipidation. Autophagy 6, 506–522. https://doi.org/10.4161/auto.6.4.11863

Polymeropoulos, M.H., Lavedan, C., Leroy, E., Ide, S.E., Dehejia, A., Dutra, A., Pike, B., Root, H., Rubenstein, J., Boyer, R., Stenroos, E.S., Chandrasekharappa, S., Athanassiadou, A., Papapetropoulos, T., Johnson, W.G., Lazzarini, A.M., Duvoisin, R.C., Di Iorio, G., Golbe, L.I., Nussbaum, R.L., 1997. Mutation in the

alpha-synuclein gene identified in families with Parkinson's disease. Science 276, 2045–2047. https://doi.org/10.1126/science.276.5321.2045
Popoff, V., Mardones, G.A., Bai, S.-K., Chambon, V., Tenza, D., Burgos, P.V., Shi, A., Benaroch, P., Urbé, S., Lamaze, C., Grant, B.D., Raposo, G., Johannes, L., 2009. Analysis of Articulation Between Clathrin and Retromer in Retrograde Sorting on Early Endosomes. Traffic 10, 1868–1880. https://doi.org/10.1111/j.1600-0854.2009.00993.x
Popovic, D., Dikic, I., 2014. TBC1D5 and the AP2 complex regulate ATG9 trafficking and initiation of autophagy. EMBO Rep. 15, 392–401. https://doi.org/10.1002/embr.201337995
Posor, Y., Jang, W., Haucke, V., 2022. Phosphoinositides as membrane organizers. Nat. Rev. Mol. Cell Biol. 23, 797–816. https://doi.org/10.1038/s41580-022-00490-x
Poteryaev, D., Datta, S., Ackema, K., Zerial, M., Spang, A., 2010. Identification of the Switch in Early-to-Late Endosome Transition. Cell 141, 497–508. https://doi.org/10.1016/j.cell.2010.03.011
Prasuhn, J., Davis, R.L., Kumar, K.R., 2021. Targeting Mitochondrial Impairment in Parkinson's Disease: Challenges and Opportunities. Front. Cell Dev. Biol. 8. https://doi.org/10.3389/fcell.2020.615461
Press, B., Feng, Y., Hoflack, B., Wandinger-Ness, A., 1998. Mutant Rab7 Causes the Accumulation of Cathepsin D and Cation-independent Mannose 6–Phosphate Receptor in an Early Endocytic Compartment. J. Cell Biol. 140, 1075–1089.
Pu, J., Guardia, C.M., Keren-Kaplan, T., Bonifacino, J.S., 2016. Mechanisms and functions of lysosome positioning. J. Cell Sci. 129, 4329–4339. https://doi.org/10.1242/jcs.196287
Purlyte, E., Dhekne, H.S., Sarhan, A.R., Gomez, R., Lis, P., Wightman, M., Martinez, T.N., Tonelli, F., Pfeffer, S.R., Alessi, D.R., 2018. Rab29 activation of the Parkinson's disease-associated LRRK2 kinase. EMBO J. 37, 1–18. https://doi.org/10.15252/embj.201798099
Puthenveedu, M.A., Lauffer, B., Temkin, P., Vistein, R., Carlton, P., Thorn, K., Taunton, J., Weiner, O.D., Parton, R.G., von Zastrow, M., 2010. Sequence-dependent sorting of recycling proteins by actin-stabilized endosomal microdomains. Cell 143, 761–773. https://doi.org/10.1016/j.cell.2010.10.003
Pylypenko, O., Rak, A., Durek, T., Kushnir, S., Dursina, B.E., Thomae, N.H., Constantinescu, A.T., Brunsveld, L., Watzke, A., Waldmann, H., Goody, R.S., Alexandrov, K., 2006. Structure of doubly prenylated Ypt1:GDI complex and the mechanism of GDI-mediated Rab recycling. EMBO J. 25, 13. https://doi.org/10.1038/sj.emboj.7600921
Qureshi, Y.H., Berman, D.E., Marsh, S.E., Klein, R.L., Patel, V.M., Simoes, S., Kannan, S., Petsko, G.A., Stevens, B., Small, S.A., 2022. The neuronal retromer can regulate both neuronal and microglial phenotypes of Alzheimer's disease. Cell Rep. 38, 110262. https://doi.org/10.1016/j.celrep.2021.110262
Radulovic, M., Schink, K.O., Wenzel, E.M., Nähse, V., Bongiovanni, A., Lafont, F., Stenmark, H., 2018. ESCRT-mediated lysosome repair precedes lysophagy and promotes cell survival. EMBO J. 37, e99753. https://doi.org/10.15252/embj.201899753
Radulovic, M., Wenzel, E.M., Gilani, S., Holland, L.K., Lystad, A.H., Phuyal, S., Olkkonen, V.M., Brech, A., Jäättelä, M., Maeda, K., Raiborg, C., Stenmark, H., 2022. Cholesterol transfer via endoplasmic reticulum contacts mediates lysosome damage repair. EMBO J. 41, e112677. https://doi.org/10.15252/embj.2022112677
Rafiq, N.M., Lyons, L.L., Gowrishankar, S., De Camilli, P., Ferguson, S.M., 2022. JIP3 links lysosome transport to regulation of multiple components of the axonal cytoskeleton. Commun. Biol. 5, 1–10. https://doi.org/10.1038/s42003-021-02945-x

Rahman, A.A., Morrison, B.E., 2019. Contributions of VPS35 mutations to Parkinson's Disease. Neuroscience 401, 1–10. https://doi.org/10.1016/j.neuroscience.2019.01.006

Rahman, A.A., Soto-Avellaneda, A., Jin, H.Y., Stojkovska, I., Lai, N.K., Albright, J.E., Webb, A.R., Oe, E., Valarde, J.P., Oxford, A.E., Urquhart, P.E., Wagner, B., Brown, C., Amado, I., Vasquez, P., Lehning, N., Grozdanov, V., Pu, X., Danzer, K.M., Morrison, B.E., 2020. Enhanced hyaluronan signaling and autophagy dysfunction by VPS35 D620N. Neuroscience 441, 33–45. https://doi.org/10.1016/j.neuroscience.2020.06.009

Raiborg, C., Bremnes, B., Mehlum, A., Gillooly, D.J., D'Arrigo, A., Stang, E., Stenmark, H., 2001. FYVE and coiled-coil domains determine the specific localisation of Hrs to early endosomes. J. Cell Sci. 114, 2255–2263. https://doi.org/10.1242/jcs.114.12.2255

Ramirez, A., Heimbach, A., Gründemann, J., Stiller, B., Hampshire, D., Cid, L.P., Goebel, I., Mubaidin, A.F., Wriekat, A.-L., Roeper, J., Al-Din, A., Hillmer, A.M., Karsak, M., Liss, B., Woods, C.G., Behrens, M.I., Kubisch, C., 2006. Hereditary parkinsonism with dementia is caused by mutations in ATP13A2 , encoding a lysosomal type 5 P-type ATPase. Nat. Genet. 38, 1184–1191. https://doi.org/10.1038/ng1884

Ramonet, D., Podhajska, A., Stafa, K., Sonnay, S., Trancikova, A., Tsika, E., Pletnikova, O., Troncoso, J.C., Glauser, L., Moore, D.J., 2012. PARK9-associated ATP13A2 localizes to intracellular acidic vesicles and regulates cation homeostasis and neuronal integrity. Hum. Mol. Genet. 21, 1725–1743. https://doi.org/10.1093/hmg/ddr606

Ramos, D.M., Skarnes, W.C., Singleton, A.B., Cookson, M.R., Ward, M.E., 2021. Tackling neurodegenerative diseases with genomic engineering: A new stem cell initiative from the NIH. Neuron 109, 1080–1083. https://doi.org/10.1016/j.neuron.2021.03.022

Ravanelli, S., den Brave, F., Hoppe, T., 2020. Mitochondrial Quality Control Governed by Ubiquitin. Front. Cell Dev. Biol. 8.

Raymond, C.K., Howald-Stevenson, I., Vater, C.A., Stevens, T.H., 1992. Morphological classification of the yeast vacuolar protein sorting mutants: evidence for a prevacuolar compartment in class E vps mutants. Mol. Biol. Cell 3, 1389–1402.

Reeve, A., Simcox, E., Turnbull, D., 2014. Ageing and Parkinson's disease: Why is advancing age the biggest risk factor? Ageing Res. Rev. 14, 19–30. https://doi.org/10.1016/j.arr.2014.01.004

Repnik, U., Borg Distefano, M., Speth, M.T., Ng, M.Y.W., Progida, C., Hoflack, B., Gruenberg, J., Griffiths, G., 2017. L-leucyl-L-leucine methyl ester does not release cysteine cathepsins to the cytosol but inactivates them in transiently permeabilized lysosomes. J. Cell Sci. 130, 3124–3140. https://doi.org/10.1242/jcs.204529

Rinaldi, C., Waters, C.S., Li, Z., Kumbier, K., Rao, L., Nichols, R.J., Jacobson, M.P., Wu, L.F., Altschuler, S.J., 2023. Dissecting the effects of GTPase and kinase domain mutations on LRRK2 endosomal localization and activity. Cell Rep. 42. https://doi.org/10.1016/j.celrep.2023.112447

Rink, J., Ghigo, E., Kalaidzidis, Y., Zerial, M., 2005. Rab conversion as a mechanism of progression from early to late endosomes. Cell 122, 735–749. https://doi.org/10.1016/j.cell.2005.06.043

Rivero-Ríos, P., Romo-Lozano, M., Fernández, B., Fdez, E., Hilfiker, S., 2020. Distinct Roles for RAB10 and RAB29 in Pathogenic LRRK2-Mediated Endolysosomal Trafficking Alterations. Cells 9, 1719. https://doi.org/10.3390/cells9071719

Rivero-Ríos, P., Romo-Lozano, M., Madero-Pérez, J., Thomas, A.P., Biosa, A., Greggio, E., Hilfiker, S., 2019. The G2019S variant of leucine-rich repeat kinase 2 (LRRK2) alters endolysosomal trafficking by impairing the function of

the GTPase RAB8A. J. Biol. Chem. jbc.RA118.005008. https://doi.org/10.1074/jbc.RA118.005008
Rivero-Ríos, P., Weisman, L.S., 2022. Roles of PIKfyve in multiple cellular pathways. Curr. Opin. Cell Biol. 76, 102086. https://doi.org/10.1016/j.ceb.2022.102086
Rohrer, J., Kornfeld, R., 2001. Lysosomal Hydrolase Mannose 6-Phosphate Uncovering Enzyme Resides in the trans-Golgi Network. Mol. Biol. Cell 12, 1623–1631. https://doi.org/10.1091/mbc.12.6.1623
Rojas, R., van Vlijmen, T., Mardones, G.A., Prabhu, Y., Rojas, A.L., Mohammed, S., Heck, A.J.R., Raposo, G., van der Sluijs, P., Bonifacino, J.S., 2008. Regulation of retromer recruitment to endosomes by sequential action of Rab5 and Rab7. J. Cell Biol. 183, 513–526. https://doi.org/10.1083/jcb.200804048
Roosen, D.A., Landeck, N., Conti, M., Smith, N., Saez-Atienzar, S., Ding, J., Beilina, A., Kumaran, R., Kaganovich, A., Hoffmann, J. du, Williamson, C.D., Gershlick, D.C., Bonet-Ponce, L., Sampieri, L., Bleck, C.K.E., Liu, C., Bonifacino, J.S., Li, Y., Lewis, P.A., Cookson, M.R., 2019. Mutations in Auxilin cause parkinsonism via impaired clathrin-mediated trafficking at the Golgi apparatus and synapse. bioRxiv 830802. https://doi.org/10.1101/830802
Row, P.E., Liu, H., Hayes, S., Welchman, R., Charalabous, P., Hofmann, K., Clague, M.J., Sanderson, C.M., Urbé, S., 2007. The MIT Domain of UBPY Constitutes a CHMP Binding and Endosomal Localization Signal Required for Efficient Epidermal Growth Factor Receptor Degradation *. J. Biol. Chem. 282, 30929–30937. https://doi.org/10.1074/jbc.M704009200
Rozhin, J., Sameni, M., Ziegler, G., Sloane, B.F., 1994. Pericellular pH Affects Distribution and Secretion of Cathepsin B in Malignant Cells1. Cancer Res. 54, 6517–6525.
Rusilowicz-Jones, E.V., Urbé, S., Clague, M.J., 2022. Protein degradation on the global scale. Mol. Cell 82, 1414–1423. https://doi.org/10.1016/j.molcel.2022.02.027
Sachse, M., Urbé, S., Oorschot, V., Strous, G.J., Klumperman, J., 2002. Bilayered Clathrin Coats on Endosomal Vacuoles Are Involved in Protein Sorting toward Lysosomes. Mol. Biol. Cell 13, 1313–1328. https://doi.org/10.1091/mbc.01-10-0525
Saftig, P., Klumperman, J., 2009. Lysosome biogenesis and lysosomal membrane proteins: trafficking meets function. Nat. Rev. Mol. Cell Biol. 10, 623–635. https://doi.org/10.1038/nrm2745
Sanchez-Vega, F., Mina, M., Armenia, J., Chatila, W.K., Luna, A., La, K.C., Dimitriadoy, S., Liu, D.L., Kantheti, H.S., Saghafinia, S., Chakravarty, D., Daian, F., Gao, Q., Bailey, M.H., Liang, W.-W., Foltz, S.M., Shmulevich, I., Ding, L., Heins, Z., Ochoa, A., Gross, B., Gao, J., Zhang, H., Kundra, R., Kandoth, C., Bahceci, I., Dervishi, L., Dogrusoz, U., Zhou, W., Shen, H., Laird, P.W., Way, G.P., Greene, C.S., Liang, H., Xiao, Y., Wang, C., Iavarone, A., Berger, A.H., Bivona, T.G., Lazar, A.J., Hammer, G.D., Giordano, T., Kwong, L.N., McArthur, G., Huang, C., Tward, A.D., Frederick, M.J., McCormick, F., Meyerson, M., Van Allen, E.M., Cherniack, A.D., Ciriello, G., Sander, C., Schultz, N., 2018. Oncogenic Signaling Pathways in The Cancer Genome Atlas. Cell 173, 321-337.e10. https://doi.org/10.1016/j.cell.2018.03.035
Sardiello, M., Palmieri, M., di Ronza, A., Medina, D.L., Valenza, M., Gennarino, V.A., Di Malta, C., Donaudy, F., Embrione, V., Polishchuk, R.S., Banfi, S., Parenti, G., Cattaneo, E., Ballabio, A., 2009. A gene network regulating lysosomal biogenesis and function. Science 325, 473–477. https://doi.org/10.1126/science.1174447
Sasaki, T., Kikuchi, A., Araki, S., Hata, Y., Isomura, M., Kuroda, S., Takai, Y., 1990. Purification and characterization from bovine brain cytosol of a protein that inhibits the dissociation of GDP from and the subsequent binding of GTP to

smg p25A, a ras p21-like GTP-binding protein. J. Biol. Chem. 265, 2333–2337. https://doi.org/10.1016/S0021-9258(19)39980-6
Sawa-Makarska, J., Baumann, V., Coudevylle, N., von Bülow, S., Nogellova, V., Abert, C., Schuschnig, M., Graef, M., Hummer, G., Martens, S., 2020. Reconstitution of autophagosome nucleation defines Atg9 vesicles as seeds for membrane formation. Science 369, eaaz7714. https://doi.org/10.1126/science.aaz7714
Sbrissa, D., Ikonomov, O.C., Shisheva, A., 1999. PIKfyve, a Mammalian Ortholog of Yeast Fab1p Lipid Kinase, Synthesizes 5-Phosphoinositides: EFFECT OF INSULIN *. J. Biol. Chem. 274, 21589–21597. https://doi.org/10.1074/jbc.274.31.21589
Schäfer, I.B., Hesketh, G.G., Bright, N.A., Gray, S.R., Pryor, P.R., Evans, P.R., Luzio, J.P., Owen, D.J., 2012. The binding of Varp to VAMP7 traps VAMP7 in a closed, fusogenically inactive conformation. Nat. Struct. Mol. Biol. 19, 1300–1309. https://doi.org/10.1038/nsmb.2414
Schapansky, J., Khasnavis, S., DeAndrade, M.P., Nardozzi, J.D., Falkson, S.R., Boyd, J.D., Sanderson, J.B., Bartels, T., Melrose, H.L., LaVoie, M.J., 2018. Familial knockin mutation of LRRK2 causes lysosomal dysfunction and accumulation of endogenous insoluble α-synuclein in neurons. Neurobiol. Dis. 111, 26–35. https://doi.org/10.1016/j.nbd.2017.12.005
Schapira, A.H.V., Cooper, J.M., Dexter, D., Clark, J.B., Jenner, P., Marsden, C.D., 1990. Mitochondrial Complex I Deficiency in Parkinson's Disease. J. Neurochem. 54, 823–827. https://doi.org/10.1111/j.1471-4159.1990.tb02325.x
Schaub, J.R., Stearns, T., 2013. The Rilp-like proteins Rilpl1 and Rilpl2 regulate ciliary membrane content. Mol. Biol. Cell 24, 453–464. https://doi.org/10.1091/mbc.E12-08-0598
Schmidt, O., Teis, D., 2012. The ESCRT machinery. Curr. Biol. 22, R116–R120. https://doi.org/10.1016/j.cub.2012.01.028
Schöndorf, D.C., Aureli, M., McAllister, F.E., Hindley, C.J., Mayer, F., Schmid, B., Sardi, S.P., Valsecchi, M., Hoffmann, S., Schwarz, L.K., Hedrich, U., Berg, D., Shihabuddin, L.S., Hu, J., Pruszak, J., Gygi, S.P., Sonnino, S., Gasser, T., Deleidi, M., 2014. iPSC-derived neurons from GBA1-associated Parkinson's disease patients show autophagic defects and impaired calcium homeostasis. Nat. Commun. 5, 4028. https://doi.org/10.1038/ncomms5028
Schu, P.V., Takegawa, K., Fry, M.J., Stack, J.H., Waterfield, M.D., Emr, S.D., 1993. Phosphatidylinositol 3-kinase encoded by yeast VPS34 gene essential for protein sorting. Science 260, 88–91. https://doi.org/10.1126/science.8385367
Schwanhäusser, B., Busse, D., Li, N., Dittmar, G., Schuchhardt, J., Wolf, J., Chen, W., Selbach, M., 2011. Global quantification of mammalian gene expression control. Nature 473, 337–342. https://doi.org/10.1038/nature10098
Seaman, M.N.J., 2007. Identification of a novel conserved sorting motif required for retromer-mediated endosome-to-TGN retrieval. J. Cell Sci. 120, 2378–2389. https://doi.org/10.1242/jcs.009654
Seaman, M.N.J., 2004. Cargo-selective endosomal sorting for retrieval to the Golgi requires retromer. J. Cell Biol. 165, 111–122. https://doi.org/10.1083/jcb.200312034
Seaman, M.N.J., Harbour, M.E., Tattersall, D., Read, E., Bright, N., 2009. Membrane recruitment of the cargo-selective retromer subcomplex is catalysed by the small GTPase Rab7 and inhibited by the Rab-GAP TBC1D5. J. Cell Sci. 122, 2371–2382. https://doi.org/10.1242/jcs.048686
Seaman, M.N.J., Michael McCaffery, J., Emr, S.D., 1998. A Membrane Coat Complex Essential for Endosome-to-Golgi Retrograde Transport in Yeast. J. Cell Biol. 142, 665–681.

Seegobin, S.P., Heaton, G.R., Liang, D., Choi, I., Blanca Ramirez, M., Tang, B., Yue, Z., 2020. Progress in LRRK2-Associated Parkinson's Disease Animal Models. Front. Neurosci. 14.

Seglen, P.O., Grinde, B., Solheim, A.E., 1979. Inhibition of the Lysosomal Pathway of Protein Degradation in Isolated Rat Hepatocytes by Ammonia, Methylamine, Chloroquine and Leupeptin. Eur. J. Biochem. 95, 215–225. https://doi.org/10.1111/j.1432-1033.1979.tb12956.x

Settembre, C., Ballabio, A., 2014. Lysosomal Adaptation: How the Lysosome Responds to External Cues. Cold Spring Harb. Perspect. Biol. 6. https://doi.org/10.1101/cshperspect.a016907

Settembre, C., Malta, C.D., Polito, V.A., Arencibia, M.G., Vetrini, F., Erdin, S., Erdin, S.U., Huynh, T., Medina, D., Colella, P., Sardiello, M., Rubinsztein, D.C., Ballabio, A., 2011. TFEB Links Autophagy to Lysosomal Biogenesis. Science 332, 1429–1433. https://doi.org/10.1126/science.1204592

Shapiro, A.D., Pfeffer, S.R., 1995. Quantitative Analysis of the Interactions between Prenyl Rab9, GDP Dissociation Inhibitor-α, and Guanine Nucleotides *. J. Biol. Chem. 270, 11085–11090. https://doi.org/10.1074/jbc.270.19.11085

Shearer, L.J., Petersen, N.O., 2019. Distribution and Co-localization of endosome markers in cells. Heliyon 5, e02375. https://doi.org/10.1016/j.heliyon.2019.e02375

Sheng, Z., Zhang, S., Bustos, D., Kleinheinz, T., Le Pichon, C.E., Dominguez, S.L., Solanoy, H.O., Drummond, J., Zhang, X., Ding, X., Cai, F., Song, Q., Li, X., Yue, Z., van der Brug, M.P., Burdick, D.J., Gunzner-Toste, J., Chen, H., Liu, X., Estrada, A.A., Sweeney, Z.K., Scearce-Levie, K., Moffat, J.G., Kirkpatrick, D.S., Zhu, H., 2012. Ser1292 Autophosphorylation Is an Indicator of LRRK2 Kinase Activity and Contributes to the Cellular Effects of PD Mutations. Sci. Transl. Med. 4, 164ra161-164ra161. https://doi.org/10.1126/scitranslmed.3004485

Shisheva, A., Rusin, B., Ikonomov, O.C., DeMarco, C., Sbrissa, D., 2001. Localization and insulin-regulated relocation of phosphoinositide 5-kinase PIKfyve in 3T3-L1 adipocytes. J. Biol. Chem. 276, 11859–11869. https://doi.org/10.1074/jbc.M008437200

Shukla, S., Larsen, K.P., Ou, C., Rose, K., Hurley, J.H., 2022. In vitro reconstitution of calcium-dependent recruitment of the human ESCRT machinery in lysosomal membrane repair. Proc. Natl. Acad. Sci. 119, e2205590119. https://doi.org/10.1073/pnas.2205590119

Sidransky, E., Nalls, M.A., Aasly, J.O., Aharon-Peretz, J., Annesi, G., Barbosa, E.R., Bar-Shira, A., Berg, D., Bras, J., Brice, A., Chen, C.-M., Clark, L.N., Condroyer, C., De Marco, E.V., Dürr, A., Eblan, M.J., Fahn, S., Farrer, M.J., Fung, H.-C., Gan-Or, Z., Gasser, T., Gershoni-Baruch, R., Giladi, N., Griffith, A., Gurevich, T., Januario, C., Kropp, P., Lang, A.E., Lee-Chen, G.-J., Lesage, S., Marder, K., Mata, I.F., Mirelman, A., Mitsui, J., Mizuta, I., Nicoletti, G., Oliveira, C., Ottman, R., Orr-Urtreger, A., Pereira, L.V., Quattrone, A., Rogaeva, E., Rolfs, A., Rosenbaum, H., Rozenberg, R., Samii, A., Samaddar, T., Schulte, C., Sharma, M., Singleton, A., Spitz, M., Tan, E.-K., Tayebi, N., Toda, T., Troiano, A.R., Tsuji, S., Wittstock, M., Wolfsberg, T.G., Wu, Y.-R., Zabetian, C.P., Zhao, Y., Ziegler, S.G., 2009. Multicenter analysis of glucocerebrosidase mutations in Parkinson's disease. N. Engl. J. Med. 361, 1651–1661. https://doi.org/10.1056/NEJMoa0901281

Simoes, S., Guo, J., Buitrago, L., Qureshi, Y.H., Feng, X., Kothiya, M., Cortes, E., Patel, V., Kannan, S., Kim, Y.-H., Chang, K.-T., Hussaini, S.A., Moreno, H., Di Paolo, G., Andersen, O.M., Small, S.A., 2021. Alzheimer's vulnerable brain region relies on a distinct retromer core dedicated to endosomal recycling. Cell Rep. 37, 110182. https://doi.org/10.1016/j.celrep.2021.110182

Simonetti, B., Cullen, P.J., 2019. Actin-dependent endosomal receptor recycling. Curr. Opin. Cell Biol., Cell Architecture 56, 22–33. https://doi.org/10.1016/j.ceb.2018.08.006
Simonetti, B., Danson, C.M., Heesom, K.J., Cullen, P.J., 2017. Sequence-dependent cargo recognition by SNX-BARs mediates retromer-independent transport of CI-MPR. J. Cell Biol. 216, 3695–3712. https://doi.org/10.1083/jcb.201703015
Simonetti, B., Paul, B., Chaudhari, K., Weeratunga, S., Steinberg, F., Gorla, M., Heesom, K.J., Bashaw, G.J., Collins, B.M., Cullen, P.J., 2019. Molecular identification of a BAR domain-containing coat complex for endosomal recycling of transmembrane proteins. Nat. Cell Biol. 21, 1219–1233. https://doi.org/10.1038/s41556-019-0393-3
Simonsen, A., Lippe, R., Christoforidis, S., Gaullier, J.-M., Brech, A., Callaghan, J., Toh, B.-H., Murphy, C., Zerial, M., Stenmark, H., 1998. EEA1 links PI(3)K function to Rab5 regulation of endosome fusion. Nature 394, 494–498. https://doi.org/10.1038/28879
Singh, A., Zhi, L., Zhang, H., 2019. LRRK2 and mitochondria: Recent advances and current views. Brain Res. 1702, 96–104. https://doi.org/10.1016/j.brainres.2018.06.010
Singh, F., Prescott, A.R., Rosewell, P., Ball, G., Reith, A.D., Ganley, I.G., 2021. Pharmacological rescue of impaired mitophagy in Parkinson's disease-related LRRK2 G2019S knock-in mice. eLife 10, e67604. https://doi.org/10.7554/eLife.67604
Singla, A., Fedoseienko, A., Giridharan, S.S.P., Overlee, B.L., Lopez, A., Jia, D., Song, J., Huff-Hardy, K., Weisman, L., Burstein, E., Billadeau, D.D., 2019. Endosomal PI(3)P regulation by the COMMD/CCDC22/CCDC93 (CCC) complex controls membrane protein recycling. Nat. Commun. 10, 4271. https://doi.org/10.1038/s41467-019-12221-6
Sivars, U., Aivazian, D., Pfeffer, S.R., 2003. Yip3 catalyses the dissociation of endosomal Rab–GDI complexes. Nature 425, 856–859. https://doi.org/10.1038/nature02057
Skowyra, M.L., Schlesinger, P.H., Naismith, T.V., Hanson, P.I., 2018. Triggered recruitment of ESCRT machinery promotes endolysosomal repair. Science 360, eaar5078. https://doi.org/10.1126/science.aar5078
Slagsvold, T., Aasland, R., Hirano, S., Bache, K.G., Raiborg, C., Trambaiolo, D., Wakatsuki, S., Stenmark, H., 2005. Eap45 in Mammalian ESCRT-II Binds Ubiquitin via a Phosphoinositide-interacting GLUE Domain * ♦. J. Biol. Chem. 280, 19600–19606. https://doi.org/10.1074/jbc.M501510200
Small, S.A., Kent, K., Pierce, A., Leung, C., Kang, M.S., Okada, H., Honig, L., Vonsattel, J.-P., Kim, T.-W., 2005. Model-guided microarray implicates the retromer complex in Alzheimer's disease. Ann. Neurol. 58, 909–919. https://doi.org/10.1002/ana.20667
Soldati, T., Riederer, M.A., Pfeffer, S.R., 1993. Rab GDI: a solubilizing and recycling factor for rab9 protein. Mol. Biol. Cell 4, 425–434.
Soldati, T., Shapiro, A.D., Svejstrup, A.B., Pfeffer, S.R., 1994. Membrane targeting of the small GTPase Rab9 is accompanied by nucleotide exchange. Nature 369, 76–78. https://doi.org/10.1038/369076a0
Solomon, V.R., Lee, H., 2009. Chloroquine and its analogs: A new promise of an old drug for effective and safe cancer therapies. Eur. J. Pharmacol., New Vistas in Anti-Cancer Therapy 625, 220–233. https://doi.org/10.1016/j.ejphar.2009.06.063
Song, P., Trajkovic, K., Tsunemi, T., Krainc, D., 2016. Parkin Modulates Endosomal Organization and Function of the Endo-Lysosomal Pathway. J. Neurosci. 36, 2425–2437. https://doi.org/10.1523/JNEUROSCI.2569-15.2016
Soubannier, V., McLelland, G.-L., Zunino, R., Braschi, E., Rippstein, P., Fon, E.A., McBride, H.M., 2012a. A Vesicular Transport Pathway Shuttles Cargo from

Mitochondria to Lysosomes. Curr. Biol. 22, 135–141. https://doi.org/10.1016/j.cub.2011.11.057
Soubannier, V., Rippstein, P., Kaufman, B.A., Shoubridge, E.A., McBride, H.M., 2012b. Reconstitution of Mitochondria Derived Vesicle Formation Demonstrates Selective Enrichment of Oxidized Cargo. PLOS ONE 7, e52830. https://doi.org/10.1371/journal.pone.0052830
Spillantini, M.G., Schmidt, M.L., Lee, V.M.-Y., Trojanowski, J.Q., Jakes, R., Goedert, M., 1997. α-Synuclein in Lewy bodies. Nature 388, 839–840. https://doi.org/10.1038/42166
Stafa, K., Tsika, E., Moser, R., Musso, A., Glauser, L., Jones, A., Biskup, S., Xiong, Y., Bandopadhyay, R., Dawson, V.L., Dawson, T.M., Moore, D.J., 2014. Functional interaction of Parkinson's disease-associated LRRK2 with members of the dynamin GTPase superfamily. Hum. Mol. Genet. 23, 2055–2077. https://doi.org/10.1093/hmg/ddt600
Starling, G.P., Yip, Y.Y., Sanger, A., Morton, P.E., Eden, E.R., Dodding, M.P., 2016. Folliculin directs the formation of a Rab34–RILP complex to control the nutrient-dependent dynamic distribution of lysosomes. EMBO Rep. 17, 823–841. https://doi.org/10.15252/embr.201541382
Steger, M., Diez, F., Dhekne, H.S., Lis, P., Nirujogi, R.S., Karayel, O., Tonelli, F., Martinez, T.N., Lorentzen, E., Pfeffer, S.R., Alessi, D.R., Mann, M., 2017. Systematic proteomic analysis of LRRK2-mediated Rab GTPase phosphorylation establishes a connection to ciliogenesis. eLife 6. https://doi.org/10.7554/eLife.31012
Steger, M., Tonelli, F., Ito, G., Davies, P., Trost, M., Vetter, M., Wachter, S., Lorentzen, E., Duddy, G., Wilson, S., Baptista, M.A., Fiske, B.K., Fell, M.J., Morrow, J.A., Reith, A.D., Alessi, D.R., Mann, M., 2016. Phosphoproteomics reveals that Parkinson's disease kinase LRRK2 regulates a subset of Rab GTPases. eLife 5. https://doi.org/10.7554/eLife.12813
Steinberg, F., Gallon, M., Winfield, M., Thomas, E., Bell, A.J., Heesom, K.J., Tavaré, J.M., Cullen, P.J., 2013. A global analysis of SNX27-retromer assembly and cargo specificity reveals a function in glucose and metal ion transport. Nat. Cell Biol. 15, 461–471. https://doi.org/10.1038/ncb2721
Steinberg, F., Heesom, K.J., Bass, M.D., Cullen, P.J., 2012. SNX17 protects integrins from degradation by sorting between lysosomal and recycling pathways. J. Cell Biol. 197, 219–230. https://doi.org/10.1083/jcb.201111121
Stenmark, H., 2009. Rab GTPases as coordinators of vesicle traffic. Nat. Rev. Mol. Cell Biol. 10, 513–525. https://doi.org/10.1038/nrm2728
Stoorvogel, W., Strous, G.J., Geuze, H.J., Oorschot, V., Schwartz, A.L., 1991. Late endosomes derive from early endosomes by maturation. Cell 65, 417–427. https://doi.org/10.1016/0092-8674(91)90459-c
Stransky, L.A., Forgac, M., 2015. Amino Acid Availability Modulates Vacuolar H+-ATPase Assembly. J. Biol. Chem. 290, 27360–27369. https://doi.org/10.1074/jbc.M115.659128
Su, Y.-C., Guo, X., Qi, X., 2015. Threonine56 phosphorylation of Bcl-2 is required for LRRK2 G2019S-induced mitochondrial depolarization and autophagy. Biochim. Biophys. Acta 1852, 12–21. https://doi.org/10.1016/j.bbadis.2014.11.009
Sugiura, A., Mattie, S., Prudent, J., McBride, H.M., 2017. Newly born peroxisomes are a hybrid of mitochondrial and ER-derived pre-peroxisomes. Nature 542, 251–254. https://doi.org/10.1038/nature21375
Sugiura, A., McLelland, G.-L., Fon, E.A., McBride, H.M., 2014. A new pathway for mitochondrial quality control: mitochondrial-derived vesicles. EMBO J. 33, 2142–2156. https://doi.org/10.15252/embj.201488104
Sun, J., Deghmane, A.-E., Bucci, C., Hmama, Z., 2009. Detection of Activated Rab7 GTPase with an Immobilized RILP Probe, in: Reiner, N.E. (Ed.), Macrophages

and Dendritic Cells: Methods and Protocols, Methods in Molecular Biology™. Humana Press, Totowa, NJ, pp. 57–69. https://doi.org/10.1007/978-1-59745-396-7_5

Sun, N., Malide, D., Liu, J., Rovira, I.I., Combs, C.A., Finkel, T., 2017. A fluorescence-based imaging method to measure in vitro and in vivo mitophagy using mt-Keima. Nat. Protoc. 12, 1576–1587. https://doi.org/10.1038/nprot.2017.060

Swatek, K.N., Komander, D., 2016. Ubiquitin modifications. Cell Res. 26, 399–422. https://doi.org/10.1038/cr.2016.39

Szczepanowska, K., Trifunovic, A., 2022. Mitochondrial matrix proteases: quality control and beyond. FEBS J. 289, 7128–7146. https://doi.org/10.1111/febs.15964

Szulc-Dąbrowska, L., Bossowska-Nowicka, M., Struzik, J., Toka, F.N., 2020. Cathepsins in Bacteria-Macrophage Interaction: Defenders or Victims of Circumstance? Front. Cell. Infect. Microbiol. 10.

Tan, J., Zhang, T., Jiang, L., Chi, J., Hu, D., Pan, Q., Wang, D., Zhang, Z., 2011. Regulation of Intracellular Manganese Homeostasis by Kufor-Rakeb Syndrome-associated ATP13A2 Protein. J. Biol. Chem. 286, 29654–29662. https://doi.org/10.1074/jbc.M111.233874

Tan, J.X., Finkel, T., 2022. A phosphoinositide signalling pathway mediates rapid lysosomal repair. Nature 609, 815–821. https://doi.org/10.1038/s41586-022-05164-4

Tang, F.-L., Erion, J.R., Tian, Y., Liu, W., Yin, D.-M., Ye, J., Tang, B., Mei, L., Xiong, W.-C., 2015a. VPS35 in Dopamine Neurons Is Required for Endosome-to-Golgi Retrieval of Lamp2a, a Receptor of Chaperone-Mediated Autophagy That Is Critical for α-Synuclein Degradation and Prevention of Pathogenesis of Parkinson's Disease. J. Neurosci. 35, 10613–10628. https://doi.org/10.1523/JNEUROSCI.0042-15.2015

Tang, F.-L., Liu, W., Hu, J.-X., Erion, J.R., Ye, J., Mei, L., Xiong, W.-C., 2015b. VPS35 Deficiency or Mutation Causes Dopaminergic Neuronal Loss by Impairing Mitochondrial Fusion and Function. Cell Rep. 12, 1631–1643. https://doi.org/10.1016/j.celrep.2015.08.001

Tapper, H., Sundler, R., 1990. Role of lysosomal and cytosolic pH in the regulation of macrophage lysosomal enzyme secretion. Biochem. J. 272, 407–414.

Tasegian, A., Singh, F., Ganley, I.G., Reith, A.D., Alessi, D.R., 2021. Impact of Type II LRRK2 inhibitors on signalling and mitophagy. Biochem. J. https://doi.org/10.1042/BCJ20210375

Taylor, M., Alessi, D.R., 2020. Advances in elucidating the function of leucine-rich repeat protein kinase-2 in normal cells and Parkinson's disease. Curr. Opin. Cell Biol. 63, 102–113. https://doi.org/10.1016/j.ceb.2020.01.001

Temkin, P., Lauffer, B., Jäger, S., Cimermancic, P., Krogan, N.J., von Zastrow, M., 2011. SNX27 mediates retromer tubule entry and endosome-to-plasma membrane trafficking of signalling receptors. Nat. Cell Biol. 13, 715–721. https://doi.org/10.1038/ncb2252

Thiele, D.L., Lipsky, P.E., 1990. Mechanism of L-leucyl-L-leucine methyl ester-mediated killing of cytotoxic lymphocytes: dependence on a lysosomal thiol protease, dipeptidyl peptidase I, that is enriched in these cells. Proc. Natl. Acad. Sci. U. S. A. 87, 83–87.

Thirstrup, K., Dächsel, J.C., Oppermann, F.S., Williamson, D.S., Smith, G.P., Fog, K., Christensen, K.V., 2017. Selective LRRK2 kinase inhibition reduces phosphorylation of endogenous Rab10 and Rab12 in human peripheral mononuclear blood cells. Sci. Rep. 7. https://doi.org/10.1038/s41598-017-10501-z

Thomas, L.L., Fromme, J.C., 2016. GTPase cross talk regulates TRAPPII activation of Rab11 homologues during vesicle biogenesis. J. Cell Biol. 215, 499–513. https://doi.org/10.1083/jcb.201608123

Thomas, L.L., van der Vegt, S.A., Fromme, J.C., 2019. A steric gating mechanism dictates the substrate specificity of a Rab-GEF. Dev. Cell 48, 100-114.e9. https://doi.org/10.1016/j.devcel.2018.11.013

Thurston, T.L.M., Wandel, M.P., von Muhlinen, N., Foeglein, Á., Randow, F., 2012. Galectin 8 targets damaged vesicles for autophagy to defend cells against bacterial invasion. Nature 482, 414–418. https://doi.org/10.1038/nature10744

Tian, Y., Tang, F.-L., Sun, X., Wen, L., Mei, L., Tang, B.-S., Xiong, W.-C., 2015. VPS35-deficiency results in an impaired AMPA receptor trafficking and decreased dendritic spine maturation. Mol. Brain 8, 70. https://doi.org/10.1186/s13041-015-0156-4

Toyofuku, T., Okamoto, Y., Ishikawa, T., Sasawatari, S., Kumanogoh, A., 2020. LRRK2 regulates endoplasmic reticulum–mitochondrial tethering through the PERK-mediated ubiquitination pathway. EMBO J. 39, e100875. https://doi.org/10.15252/embj.2018100875

Tsika, E., Glauser, L., Moser, R., Fiser, A., Daniel, G., Sheerin, U.-M., Lees, A., Troncoso, J.C., Lewis, P.A., Bandopadhyay, R., Schneider, B.L., Moore, D.J., 2014. Parkinson's disease-linked mutations in VPS35 induce dopaminergic neurodegeneration. Hum. Mol. Genet. 23, 4621–4638. https://doi.org/10.1093/hmg/ddu178

Tsukada, M., Ohsumi, Y., 1993. Isolation and characterization of autophagy-defective mutants of Saccharomyces cerevisiae. FEBS Lett. 333, 169–174. https://doi.org/10.1016/0014-5793(93)80398-E

Tsunemi, T., Krainc, D., 2014. Zn2+ dyshomeostasis caused by loss of ATP13A2/PARK9 leads to lysosomal dysfunction and alpha-synuclein accumulation. Hum. Mol. Genet. 23, 2791–2801. https://doi.org/10.1093/hmg/ddt572

Turco, E., Fracchiolla, D., Martens, S., 2020. Recruitment and Activation of the ULK1/Atg1 Kinase Complex in Selective Autophagy. J. Mol. Biol. 432, 123–134. https://doi.org/10.1016/j.jmb.2019.07.027

Ullrich, O., Horiuchi, H., Bucci, C., Zerial, M., 1994. Membrane association of Rab5 mediated by GDP-dissociation inhibitor and accompanied by GDP/GTP exchange. Nature 368, 157–160. https://doi.org/10.1038/368157a0

Ullrich, O., Reinsch, S., Urbé, S., Zerial, M., Parton, R.G., 1996. Rab11 regulates recycling through the pericentriolar recycling endosome. J. Cell Biol. 135, 913–924. https://doi.org/10.1083/jcb.135.4.913

Ullrich, O., Stenmark, H., Alexandrov, K., Huber, L.A., Kaibuchi, K., Sasaki, T., Takai, Y., Zerial, M., 1993. Rab GDP dissociation inhibitor as a general regulator for the membrane association of rab proteins. J. Biol. Chem. 268, 18143–18150. https://doi.org/10.1016/S0021-9258(17)46822-0

Unapanta, A., Shavarebi, F., Porath, J., Balen, C., Nguyen, A., Tseng, J., Shen, Y., Liu, M., Lis, P., Pietro, S.M.D., Hiniker, A., 2022. Endogenous Rab38 regulates LRRK2's membrane recruitment and substrate Rab phosphorylation in melanocytes. https://doi.org/10.1101/2022.06.20.496629

Urbé, S., Mills, I.G., Stenmark, H., Kitamura, N., Clague, M.J., 2000. Endosomal Localization and Receptor Dynamics Determine Tyrosine Phosphorylation of Hepatocyte Growth Factor-Regulated Tyrosine Kinase Substrate. Mol. Cell. Biol. 20, 7685–7692.

Usenovic, M., Tresse, E., Mazzulli, J.R., Taylor, J.P., Krainc, D., 2012. Deficiency of ATP13A2 Leads to Lysosomal Dysfunction, α-Synuclein Accumulation, and Neurotoxicity. J. Neurosci. 32, 4240–4246. https://doi.org/10.1523/JNEUROSCI.5575-11.2012

Valente, A.J., Maddalena, L.A., Robb, E.L., Moradi, F., Stuart, J.A., 2017. A simple ImageJ macro tool for analyzing mitochondrial network morphology in mammalian cell culture. Acta Histochem. 119, 315–326. https://doi.org/10.1016/j.acthis.2017.03.001

van Heesbeen, H.J., Smidt, M.P., 2019. Entanglement of Genetics and Epigenetics in Parkinson's Disease. Front. Neurosci. 13. https://doi.org/10.3389/fnins.2019.00277

Van Vliet, A.R., Chiduza, G.N., Maslen, S.L., Pye, V.E., Joshi, D., De Tito, S., Jefferies, H.B.J., Christodoulou, E., Roustan, C., Punch, E., Hervás, J.H., O'Reilly, N., Skehel, J.M., Cherepanov, P., Tooze, S.A., 2022. ATG9A and ATG2A form a heteromeric complex essential for autophagosome formation. Mol. Cell 82, 4324-4339.e8. https://doi.org/10.1016/j.molcel.2022.10.017

Vanhauwaert, R., Kuenen, S., Masius, R., Bademosi, A., Manetsberger, J., Schoovaerts, N., Bounti, L., Gontcharenko, S., Swerts, J., Vilain, S., Picillo, M., Barone, P., Munshi, S.T., de Vrij, F.M., Kushner, S.A., Gounko, N.V., Mandemakers, W., Bonifati, V., Meunier, F.A., Soukup, S.-F., Verstreken, P., 2017. The SAC1 domain in synaptojanin is required for autophagosome maturation at presynaptic terminals. EMBO J. 36, 1392–1411. https://doi.org/10.15252/embj.201695773

Vargas, J.N.S., Hamasaki, M., Kawabata, T., Youle, R.J., Yoshimori, T., 2023. The mechanisms and roles of selective autophagy in mammals. Nat. Rev. Mol. Cell Biol. 24, 167–185. https://doi.org/10.1038/s41580-022-00542-2

Vest, R.T., Chou, C.-C., Zhang, H., Haney, M.S., Li, L., Laqtom, N.N., Chang, B., Shuken, S., Nguyen, A., Yerra, L., Yang, A.C., Green, C., Tanga, M., Abu-Remaileh, M., Bassik, M.C., Frydman, J., Luo, J., Wyss-Coray, T., 2022. Small molecule C381 targets the lysosome to reduce inflammation and ameliorate disease in models of neurodegeneration. Proc. Natl. Acad. Sci. 119, e2121609119. https://doi.org/10.1073/pnas.2121609119

Vides, E.G., Adhikari, A., Chiang, C.Y., Lis, P., Purlyte, E., Limouse, C., Shumate, J.L., Spínola-Lasso, E., Dhekne, H.S., Alessi, D.R., Pfeffer, S.R., 2022. A feed-forward pathway drives LRRK2 kinase membrane recruitment and activation. eLife 11, e79771. https://doi.org/10.7554/eLife.79771

Vilariño-Güell, C., Rajput, A., Milnerwood, A.J., Shah, B., Szu-Tu, C., Trinh, J., Yu, I., Encarnacion, M., Munsie, L.N., Tapia, L., Gustavsson, E.K., Chou, P., Tatarnikov, I., Evans, D.M., Pishotta, F.T., Volta, M., Beccano-Kelly, D., Thompson, C., Lin, M.K., Sherman, H.E., Han, H.J., Guenther, B.L., Wasserman, W.W., Bernard, V., Ross, C.J., Appel-Cresswell, S., Stoessl, A.J., Robinson, C.A., Dickson, D.W., Ross, O.A., Wszolek, Z.K., Aasly, J.O., Wu, R.-M., Hentati, F., Gibson, R.A., McPherson, P.S., Girard, M., Rajput, M., Rajput, A.H., Farrer, M.J., 2014. DNAJC13 mutations in Parkinson disease. Hum. Mol. Genet. 23, 1794–1801. https://doi.org/10.1093/hmg/ddt570

Vilariño-Güell, C., Wider, C., Ross, O.A., Dachsel, J.C., Kachergus, J.M., Lincoln, S.J., Soto-Ortolaza, A.I., Cobb, S.A., Wilhoite, G.J., Bacon, J.A., Behrouz, B., Melrose, H.L., Hentati, E., Puschmann, A., Evans, D.M., Conibear, E., Wasserman, W.W., Aasly, J.O., Burkhard, P.R., Djaldetti, R., Ghika, J., Hentati, F., Krygowska-Wajs, A., Lynch, T., Melamed, E., Rajput, A., Rajput, A.H., Solida, A., Wu, R.-M., Uitti, R.J., Wszolek, Z.K., Vingerhoets, F., Farrer, M.J., 2011. VPS35 Mutations in Parkinson Disease. Am. J. Hum. Genet. 89, 162–167. https://doi.org/10.1016/j.ajhg.2011.06.001

Volpicelli-Daley, L.A., Luk, K.C., Patel, T.P., Tanik, S.A., Riddle, D.M., Stieber, A., Meany, D.F., Trojanowski, J.Q., Lee, V.M.-Y., 2011. Exogenous α-Synuclein Fibrils Induce Lewy Body Pathology Leading to Synaptic Dysfunction and Neuron Death. Neuron 72, 57–71. https://doi.org/10.1016/j.neuron.2011.08.033

Wallings, R., Connor-Robson, N., Wade-Martins, R., 2019. LRRK2 interacts with the vacuolar-type H+-ATPase pump a1 subunit to regulate lysosomal function. Hum. Mol. Genet. 28, 2696–2710. https://doi.org/10.1093/hmg/ddz088

Wallings, R.L., Tansey, M.G., 2019. LRRK2 regulation of immune-pathways and inflammatory disease. Biochem. Soc. Trans. 47, 1581–1595. https://doi.org/10.1042/BST20180463

Wandinger-Ness, A., Zerial, M., 2014. Rab Proteins and the Compartmentalization of the Endosomal System. Cold Spring Harb. Perspect. Biol. 6, a022616. https://doi.org/10.1101/cshperspect.a022616

Wang, H.-L., Chou, A.-H., Wu, A.-S., Chen, S.-Y., Weng, Y.-H., Kao, Y.-C., Yeh, T.-H., Chu, P.-J., Lu, C.-S., 2011. PARK6 PINK1 mutants are defective in maintaining mitochondrial membrane potential and inhibiting ROS formation of substantia nigra dopaminergic neurons. Biochim. Biophys. Acta BBA - Mol. Basis Dis. 1812, 674–684. https://doi.org/10.1016/j.bbadis.2011.03.007

Wang, W., Ma, X., Zhou, L., Liu, J., Zhu, X., 2017. A conserved retromer sorting motif is essential for mitochondrial DLP1 recycling by VPS35 in Parkinson's disease model. Hum. Mol. Genet. 26, 781–789. https://doi.org/10.1093/hmg/ddw430

Wang, W., Wang, X., Fujioka, H., Hoppel, C., Whone, A.L., Caldwell, M.A., Cullen, P.J., Liu, J., Zhu, X., 2016. Parkinson's disease-associated mutant VPS35 causes mitochondrial dysfunction by recycling DLP1 complexes. Nat. Med. 22, 54–63. https://doi.org/10.1038/nm.3983

Wang, X., Petrie, T.G., Liu, Y., Liu, J., Fujioka, H., Zhu, X., 2012a. Parkinson's disease-associated DJ-1 mutations impair mitochondrial dynamics and cause mitochondrial dysfunction. J. Neurochem. 121, 830–839. https://doi.org/10.1111/j.1471-4159.2012.07734.x

Wang, X., Yan, M.H., Fujioka, H., Liu, J., Wilson-Delfosse, A., Chen, S.G., Perry, G., Casadesus, G., Zhu, X., 2012b. LRRK2 regulates mitochondrial dynamics and function through direct interaction with DLP1. Hum. Mol. Genet. 21, 1931–1944. https://doi.org/10.1093/hmg/dds003

Waschbüsch, D., Michels, H., Strassheim, S., Ossendorf, E., Kessler, D., Gloeckner, C.J., Barnekow, A., 2014. LRRK2 Transport Is Regulated by Its Novel Interacting Partner Rab32. PLOS ONE 9, e111632. https://doi.org/10.1371/journal.pone.0111632

Waschbüsch, D., Purlyte, E., Pal, P., McGrath, E., Alessi, D.R., Khan, A.R., 2020. Structural Basis for Rab8a Recruitment of RILPL2 via LRRK2 Phosphorylation of Switch 2. Structure 28, 406-417.e6. https://doi.org/10.1016/j.str.2020.01.005

Wauters, F., Cornelissen, T., Imberechts, D., Martin, S., Koentjoro, B., Sue, C., Vangheluwe, P., Vandenberghe, W., 2019. LRRK2 mutations impair depolarization-induced mitophagy through inhibition of mitochondrial accumulation of RAB10. Autophagy 0, 1–20. https://doi.org/10.1080/15548627.2019.1603548

Wen, L., Tang, F.-L., Hong, Y., Luo, S.-W., Wang, C.-L., He, W., Shen, C., Jung, J.-U., Xiong, F., Lee, D., Zhang, Q.-G., Brann, D., Kim, T.-W., Yan, R., Mei, L., Xiong, W.-C., 2011. VPS35 haploinsufficiency increases Alzheimer's disease neuropathology. J. Cell Biol. 195, 765–779. https://doi.org/10.1083/jcb.201105109

Wen, S., Aki, T., Unuma, K., Uemura, K., 2020. Chemically Induced Models of Parkinson's Disease: History and Perspectives for the Involvement of Ferroptosis. Front. Cell. Neurosci. 14.

West, A.B., Moore, D.J., Biskup, S., Bugayenko, A., Smith, W.W., Ross, C.A., Dawson, V.L., Dawson, T.M., 2005. Parkinson's disease-associated mutations in leucine-rich repeat kinase 2 augment kinase activity. Proc. Natl. Acad. Sci. U. S. A. 102, 16842–16847. https://doi.org/10.1073/pnas.0507360102

Westerlund, M., Belin, A.C., Anvret, A., Bickford, P., Olson, L., Galter, D., 2008. Developmental regulation of leucine-rich repeat kinase 1 and 2 expression in the brain and other rodent and human organs: Implications for Parkinson's

disease. Neuroscience 152, 429–436. https://doi.org/10.1016/j.neuroscience.2007.10.062
Wilhelm, L.P., Zapata-Muñoz, J., Villarejo-Zori, B., Pellegrin, S., Freire, C.M., Toye, A.M., Boya, P., Ganley, I.G., 2022. BNIP3L/NIX regulates both mitophagy and pexophagy. EMBO J. 41, e111115. https://doi.org/10.15252/embj.2022111115
Willett, R., Martina, J.A., Zewe, J.P., Wills, R., Hammond, G.R.V., Puertollano, R., 2017. TFEB regulates lysosomal positioning by modulating TMEM55B expression and JIP4 recruitment to lysosomes. Nat. Commun. 8, 1580. https://doi.org/10.1038/s41467-017-01871-z
Williams, E.T., Chen, X., Moore, D.J., 2017. VPS35, the Retromer Complex and Parkinson's Disease. J. Park. Dis. 7, 219–233. https://doi.org/10.3233/JPD-161020
Williams, E.T., Chen, X., Otero, P.A., Moore, D.J., 2022. Understanding the contributions of VPS35 and the retromer in neurodegenerative disease. Neurobiol. Dis. 170, 105768. https://doi.org/10.1016/j.nbd.2022.105768
Williams, E.T., Glauser, L., Tsika, E., Jiang, H., Islam, S., Moore, D.J., 2018. Parkin mediates the ubiquitination of VPS35 and modulates retromer-dependent endosomal sorting. Hum. Mol. Genet. 27, 3189–3205. https://doi.org/10.1093/hmg/ddy224
Williams, R.L., Urbé, S., 2007. The emerging shape of the ESCRT machinery. Nat. Rev. Mol. Cell Biol. 8, 355–368. https://doi.org/10.1038/nrm2162
Wu, J.Z., Zeziulia, M., Kwon, W., Jentsch, T.J., Grinstein, S., Freeman, S.A., 2023. ClC-7 drives intraphagosomal chloride accumulation to support hydrolase activity and phagosome resolution. J. Cell Biol. 222, e202208155. https://doi.org/10.1083/jcb.202208155
Wu, Y.-W., Oesterlin, L.K., Tan, K.-T., Waldmann, H., Alexandrov, K., Goody, R.S., 2010. Membrane targeting mechanism of Rab GTPases elucidated by semisynthetic protein probes. Nat. Chem. Biol. 6, 534–540. https://doi.org/10.1038/nchembio.386
Xhabija, B., Taylor, G.S., Fujibayashi, A., Sekiguchi, K., Vacratsis, P.O., 2011. Receptor mediated endocytosis 8 is a novel PI(3)P binding protein regulated by myotubularin-related 2. FEBS Lett. 585, 1722–1728. https://doi.org/10.1016/j.febslet.2011.04.016
Xhabija, B., Vacratsis, P.O., 2015. Receptor-mediated Endocytosis 8 Utilizes an N-terminal Phosphoinositide-binding Motif to Regulate Endosomal Clathrin Dynamics. J. Biol. Chem. 290, 21676–21689. https://doi.org/10.1074/jbc.M115.644757
Xie, J., Nair, A., Hermiston, T.W., 2008. A comparative study examining the cytotoxicity of inducible gene expression system ligands in different cell types. Toxicol. In Vitro 22, 261–266. https://doi.org/10.1016/j.tiv.2007.08.019
Xu, J., Fotouhi, M., McPherson, P.S., 2015. Phosphorylation of the exchange factor DENND3 by ULK in response to starvation activates Rab12 and induces autophagy. EMBO Rep. 16, 709–718. https://doi.org/10.15252/embr.201440006
Yadavalli, N., Ferguson, S.M., 2023. LRRK2 Suppresses Lysosome Degradative Activity in Macrophages and Microglia Through MiT-TFE Transcription Factor Inhibition. https://doi.org/10.1101/2022.12.17.520834
Yamano, K., Wang, C., Sarraf, S.A., Münch, C., Kikuchi, R., Noda, N.N., Hizukuri, Y., Kanemaki, M.T., Harper, W., Tanaka, K., Matsuda, N., Youle, R.J., 2018. Endosomal Rab cycles regulate Parkin-mediated mitophagy. eLife 7. https://doi.org/10.7554/eLife.31326
Yamano, K., Youle, R.J., 2013. PINK1 is degraded through the N-end rule pathway. Autophagy 9, 1758–1769. https://doi.org/10.4161/auto.24633

Yang, C., Wang, X., 2021. Lysosome biogenesis: Regulation and functions. J. Cell Biol. 220, e202102001. https://doi.org/10.1083/jcb.202102001
Yang, H., Tan, J.X., 2023. Lysosomal quality control: molecular mechanisms and therapeutic implications. Trends Cell Biol. https://doi.org/10.1016/j.tcb.2023.01.001
Yang, Z., Klionsky, D.J., 2010. Eaten alive: a history of macroautophagy. Nat. Cell Biol. 12, 814–822. https://doi.org/10.1038/ncb0910-814
Yim, W.W.-Y., Mizushima, N., 2020. Lysosome biology in autophagy. Cell Discov. 6, 1–12. https://doi.org/10.1038/s41421-020-0141-7
Yoshida, S., Hasegawa, T., Suzuki, M., Sugeno, N., Kobayashi, J., Ueyama, M., Fukuda, M., Ido-Fujibayashi, A., Sekiguchi, K., Ezura, M., Kikuchi, A., Baba, T., Takeda, A., Mochizuki, H., Nagai, Y., Aoki, M., 2018. Parkinson's disease-linked DNAJC13 mutation aggravates alpha-synuclein-induced neurotoxicity through perturbation of endosomal trafficking. Hum. Mol. Genet. 27, 823–836. https://doi.org/10.1093/hmg/ddy003
Yoshida, Y., Yasuda, S., Fujita, T., Hamasaki, M., Murakami, A., Kawawaki, J., Iwai, K., Saeki, Y., Yoshimori, T., Matsuda, N., Tanaka, K., 2017. Ubiquitination of exposed glycoproteins by SCFFBXO27 directs damaged lysosomes for autophagy. Proc. Natl. Acad. Sci. 114, 8574–8579. https://doi.org/10.1073/pnas.1702615114
Yoshimura, S., Gerondopoulos, A., Linford, A., Rigden, D.J., Barr, F.A., 2010. Family-wide characterization of the DENN domain Rab GDP-GTP exchange factors. J. Cell Biol. 191, 367–381. https://doi.org/10.1083/jcb.201008051
Ysselstein, D., Nguyen, M., Young, T.J., Severino, A., Schwake, M., Merchant, K., Krainc, D., 2019. LRRK2 kinase activity regulates lysosomal glucocerebrosidase in neurons derived from Parkinson's disease patients. Nat. Commun. 10, 5570. https://doi.org/10.1038/s41467-019-13413-w
Zahraoui, A., Touchot, N., Chardin, P., Tavitian, A., 1989. The Human Rab Genes Encode a Family of GTP-binding Proteins Related to Yeast YPT1 and SEC4 Products Involved in Secretion. J. Biol. Chem. 264, 12394–12401. https://doi.org/10.1016/S0021-9258(18)63872-4
Zavodszky, E., Seaman, M.N.J., Moreau, K., Jimenez-Sanchez, M., Breusegem, S.Y., Harbour, M.E., Rubinsztein, D.C., 2014. Mutation in VPS35 associated with Parkinson's disease impairs WASH complex association and inhibits autophagy. Nat. Commun. 5, 1–16. https://doi.org/10.1038/ncomms4828
Zecchini, V., Paupe, V., Herranz-Montoya, I., Janssen, J., Wortel, I.M.N., Morris, J.L., Ferguson, A., Chowdury, S.R., Segarra-Mondejar, M., Costa, A.S.H., Pereira, G.C., Tronci, L., Young, T., Nikitopoulou, E., Yang, M., Bihary, D., Caicci, F., Nagashima, S., Speed, A., Bokea, K., Baig, Z., Samarajiwa, S., Tran, M., Mitchell, T., Johnson, M., Prudent, J., Frezza, C., 2023. Fumarate induces vesicular release of mtDNA to drive innate immunity. Nature 615, 499–506. https://doi.org/10.1038/s41586-023-05770-w
Zhang, G., Xia, Y., Wan, F., Ma, K., Guo, X., Kou, L., Yin, S., Han, C., Liu, L., Huang, J., Xiong, N., Wang, T., 2018. New Perspectives on Roles of Alpha-Synuclein in Parkinson's Disease. Front. Aging Neurosci. 10. https://doi.org/10.3389/fnagi.2018.00370
Zhang, L., Shimoji, M., Thomas, B., Moore, D.J., Yu, S.-W., Marupudi, N.I., Torp, R., Torgner, I.A., Ottersen, O.P., Dawson, T.M., Dawson, V.L., 2005. Mitochondrial localization of the Parkinson's disease related protein DJ-1: implications for pathogenesis. Hum. Mol. Genet. 14, 2063–2073. https://doi.org/10.1093/hmg/ddi211
Zhang, P., Wu, Y., Belenkaya, T.Y., Lin, X., 2011. SNX3 controls Wingless/Wnt secretion through regulating retromer-dependent recycling of Wntless. Cell Res. 21, 1677–1690. https://doi.org/10.1038/cr.2011.167

Zhang, Q., Li, Y., Jian, Y., Li, M., Wang, X., 2023. Lysosomal chloride transporter CLH-6 protects lysosome membrane integrity via cathepsin activation. J. Cell Biol. 222, e202210063. https://doi.org/10.1083/jcb.202210063

Zhang, W., Yang, X., Chen, L., Liu, Y.-Y., Venkatarangan, V., Reist, L., Hanson, P., Xu, H., Wang, Y., Li, M., 2021. A conserved ubiquitin- and ESCRT-dependent pathway internalizes human lysosomal membrane proteins for degradation. PLOS Biol. 19, e3001361. https://doi.org/10.1371/journal.pbio.3001361

Zhen, Y., Radulovic, M., Vietri, M., Stenmark, H., 2021. Sealing holes in cellular membranes. EMBO J. 40, e106922. https://doi.org/10.15252/embj.2020106922

Zhen, Y., Stenmark, H., 2015. Cellular functions of Rab GTPases at a glance. J. Cell Sci. 128, 3171–3176. https://doi.org/10.1242/jcs.166074

Zhivotovsky, B., Samali, A., Gahm, A., Orrenius, S., 1999. Caspases: their intracellular localization and translocation during apoptosis. Cell Death Differ. 6, 644–651. https://doi.org/10.1038/sj.cdd.4400536

Zilocchi, M., Colugnat, I., Lualdi, M., Meduri, M., Marini, F., Corasolla Carregari, V., Moutaoufik, M.T., Phanse, S., Pieroni, L., Babu, M., Garavaglia, B., Fasano, M., Alberio, T., 2020. Exploring the Impact of PARK2 Mutations on the Total and Mitochondrial Proteome of Human Skin Fibroblasts. Front. Cell Dev. Biol. 8, 423. https://doi.org/10.3389/fcell.2020.00423

Zimprich, A., Benet-Pagès, A., Struhal, W., Graf, E., Eck, S.H., Offman, M.N., Haubenberger, D., Spielberger, S., Schulte, E.C., Lichtner, P., Rossle, S.C., Klopp, N., Wolf, E., Seppi, K., Pirker, W., Presslauer, S., Mollenhauer, B., Katzenschlager, R., Foki, T., Hotzy, C., Reinthaler, E., Harutyunyan, A., Kralovics, R., Peters, A., Zimprich, F., Brücke, T., Poewe, W., Auff, E., Trenkwalder, C., Rost, B., Ransmayr, G., Winkelmann, J., Meitinger, T., Strom, T.M., 2011. A mutation in VPS35, encoding a subunit of the retromer complex, causes late-onset Parkinson disease. Am. J. Hum. Genet. 89, 168–175. https://doi.org/10.1016/j.ajhg.2011.06.008

Zimprich, A., Biskup, S., Leitner, P., Lichtner, P., Farrer, M., Lincoln, S., Kachergus, J., Hulihan, M., Uitti, R.J., Calne, D.B., Stoessl, A.J., Pfeiffer, R.F., Patenge, N., Carbajal, I.C., Vieregge, P., Asmus, F., Müller-Myhsok, B., Dickson, D.W., Meitinger, T., Strom, T.M., Wszolek, Z.K., Gasser, T., 2004. Mutations in LRRK2 Cause Autosomal-Dominant Parkinsonism with Pleomorphic Pathology. Neuron 44, 601–607. https://doi.org/10.1016/j.neuron.2004.11.005

Zoncu, R., Bar-Peled, L., Efeyan, A., Wang, S., Sancak, Y., Sabatini, D.M., 2011. mTORC1 senses lysosomal amino acids through an inside-out mechanism that requires the vacuolar H(+)-ATPase. Science 334, 678–683. https://doi.org/10.1126/science.1207056

Zoncu, R., Perera, R.M., 2022. Built to last: lysosome remodeling and repair in health and disease. Trends Cell Biol. https://doi.org/10.1016/j.tcb.2021.12.009

Zorova, L.D., Popkov, V.A., Plotnikov, E.Y., Silachev, D.N., Pevzner, I.B., Jankauskas, S.S., Babenko, V.A., Zorov, S.D., Balakireva, A.V., Juhaszova, M., Sollott, S.J., Zorov, D.B., 2018. Mitochondrial membrane potential. Anal. Biochem. 552, 50–59. https://doi.org/10.1016/j.ab.2017.07.009